The Dynamic Atmospheres of Classical Cepheids: Studies of Atmospheric Extension, Mass Loss, and Shocks

by

Hilding Raymond Neilson

A thesis submitted in conformity with the requirements
for the degree of Doctor of Philosophy,
Graduate Department of Astronomy and Astrophysics,
in the University of Toronto

© Copyright by Hilding Raymond Neilson (2009)

Abstract

The Dynamic Atmospheres of Classical Cepheids: Studies of Atmospheric Extension, Mass Loss, and Shocks

Hilding Raymond Neilson
Doctor of Philosophy
Graduate Department of Astronomy and Astrophysics
University of Toronto
2009

In this dissertation, we develop new tools for the study of stellar atmospheres, pulsating stellar atmospheres and mass loss from pulsating stars. These tools provide new insights into the structure and evolution of stars and complement modern observational techniques such as optical interferometry and high resolution spectroscopy. In the first part, a new spherically symmetric version of the ATLAS program is developed for modelling extended stellar atmospheres. The program is used to model interferometric observations from the literature and to study limb-darkening for stars with low gravity. It is determined that stellar limb-darkening can be used to constrain fundamental properties of stars. When this is coupled with interferometric or microlensing observations, stellar limb-darkening can predict the masses of isolated stars. The new SATLAS program is combined with the plane-parallel hydrodynamic program HERMES to develop a new spherically-symmetric radiative hydrodynamic program that models radial pulsation in the atmosphere of a star to depths including the pulsation-driving regions of the stars. Preliminary tests of this new program are discussed.

In the second part, we study the recent observations of circumstellar envelopes surrounding Cepheids and develop a mass-loss hypothesis to explain their formation. The hypothesis is studied using a modified version of the Castor, Abbott, & Klein theory for radiative-driven winds to contain the effects of pulsation. In the theory, pulsation is found to be a driving mechanism that increases the mass-loss rates of Cepheids by up to four orders of magnitude. These mass-loss rates are large enough to explain the formation of the envelopes from dust forming in the wind at large distances from the surface of the star. The mass-loss rates are found to be plausible explanation for the Cepheid mass discrepancy. We also compute mass-loss rates from optical and infrared observations of Large Magellanic Cloud Cepheids from the infrared excess and find mass loss to be an important phenomena in these stars. The amount of infrared excess is found to potentially affect the structure of the infrared Leavitt law.

To the two most important people in my life, Krista, and Xiaoke.

Acknowledgements

I am indebted to many people for their support and encouragement. First and foremost, I dedicate this thesis to my family and to my fiancee, Xiaoke. My parents have supported and encouraged me my entire life; they have taught me work ethic and determination and to appreciate education and family. My sister, Krista, is the bright light in my life, I cherish her happiness. Xiaoke has been my best friend and partner. I always appreciate her patience, support and encouragement, she has been my rock during my graduate career. I also want to thank my "new" parents; during my trip to China they showed great hospitality. I truly appreciate the encouragement and confidence they gave me.

I am very proud that Dr. John Lester is my Doctoral supervisor. His enthusiasm and research philosophy has motivated me. I appreciate the encouragement John has given me to pursue other directions and tangents in my research and the opportunities that John has allowed me to teach, travel to conferences and grow as a researcher. I wish to thank my PhD committee Dr. John Percy and Dr. Marten van Kerkwijk for their support and the interest they have shown in my work. Also, I want to thank Dr. Percy for teaching me about astronomy education and his support when I lectured AST201. A special thank you to both Dr. Tom Bolton and Dr. Yanqin Wu. It was Dr. Bolton's course on Stellar Winds that helped motivate much of the work presented in this thesis. Dr. Wu was a great supervisor for my first year project and I learned a lot from her.

I would like to thank my collaborators Dr. Chow-Choong Ngeow and Dr. Shashi Kanbur for their advice and help in studying mass loss in LMC Cepheids. I also want to thank Dr. Geoff Clayton for useful discussions about RCB stars. This thesis has been greatly improved because of the effort and interest of Dr. Lee Anne Willson, who has given me useful advice for studying pulsation mass-loss.

Life as a graduate student is only as good as the people you work with and I have worked with many great people. Thank you Fernando Pena, Rodrigo Fernández, Marija Stankovic, Lawrence Mudryk, Kevin Blagrave, Patrick Carey, Kaitlin Kratter, Bryce Croll, Nick Battaglia, Isamu Matsuyama, Silvia Bonoli, and Adam Muzzin.

Contents

1 Introduction **1**

1.1 Things in Perspective 1

1.2 History of Stellar Atmospheres 7

1.2.1 Stellar Spectroscopy and Classification 7

1.2.2 The Physics of Stellar Atmospheres 12

1.2.3 Development of Modern Stellar Atmosphere Programs 16

1.3 History of Cepheids 20

1.3.1 Observations of Cepheids 24

1.3.2 Statistical Properties of Cepheids 36

1.3.3 Theoretical Modeling 41

1.4 Cepheid Atmospheres 51

1.5 Thesis Outline 54

I Stellar Atmospheres & Radiative Hydrodynamics **61**

2 The SAtlas Code **63**

2.1 Introduction 63

2.2 Spherically Symmetric Radiative Transfer 64

2.3 Spherically Symmetric Hydrostatic Equilibrium 65

2.4 Spherically Symmetric Temperature Correction 66

2.5 Comparison of SAtlas Models to Phoenix Models 67

2.6 Testing the SAtlas Code Using Optical Interferometry 68

2.7 Method for Computing Visibilities and Determining Stellar Parameters 70

2.8 Results 72

2.9 Conclusions 76

3 The Study of Stellar Limb-Darkening **79**

3.1 Introduction . . . 79
3.2 Parameterization of Limb-darkening in Stars . . . 82
3.3 The Cause of the Fixed Point in Stellar Limb-Darkening Laws . . . 87
3.4 Limb-darkening and SAtlas Stellar Atmosphere Models . . . 95
3.5 Application of R_*/M_* Method to Microlensing Results . . . 107
3.6 Testing the Limb-darkening Parameterizations with Models . . . 110
3.7 Conclusions . . . 144

4 Developing the RHD Program **147**

4.1 Introduction . . . 147
4.2 Structure of Hermes . . . 148
4.3 Conversion to Spherical Symmetry . . . 153
4.4 Combining SAtlas with Hermes . . . 156
4.4.1 Equation of State . . . 156
4.4.2 Convergence Solver . . . 157
4.4.3 Convective Treatment . . . 158
4.5 The Current Status of the RHD Program . . . 159

II Cepheid Mass Loss **165**

5 The Analytic Derivation of Pulsation-Driven Mass Loss in Cepheids **167**

5.1 Introduction . . . 167
5.2 The Driving Mechanism of Cepheid Winds . . . 168
5.3 Pulsation Enhanced CAK Method . . . 169
5.4 Derivation for Pulsation Driven Winds . . . 169
5.5 Defining the Acceleration Due to Pulsation and Schocks . . . 173
5.6 Solution Space of the Wind Equation . . . 177
5.7 The Power–Law Dependence of the Pulsation and Shock Acceleration . . . 178
5.8 Comparison of Pulsating and Non–Pulsating Winds . . . 180
5.9 Conclusion . . . 182

6 Predicting Mass–Loss Rates of Galactic Cepheids **183**

6.1 Introduction . . . 183
6.2 The Dependence of Mass Loss on the Wind Boundary Conditions . . . 186
6.3 Predictions of Mass–Loss Rates of Observed Cepheids . . . 186
6.4 Uncertainty Analysis of Modified CAK Method . . . 192

6.5 Comparison to Observed Mass–Loss Rates . . . 195
6.6 Model Infrared Excess . . . 198
6.7 Mass Loss and Period Change . . . 204
6.8 Conclusions . . . 207

7 Predicting Mass–Loss Rates of Theoretical Cepheids with Varying Metallicity 211
7.1 Introduction . . . 211
7.2 The Metallicity Dependence of the Analytical Mass Loss Relation . . . 212
7.3 Comparison of the Analytic Predictions with Observations . . . 215
7.4 Predicting Mass–Loss Rates For Theoretical Model Cepheids . . . 218
7.5 Predictions of Infrared Excess Due to Mass Loss . . . 224
7.6 Mass Loss and the Mass Discrepancy . . . 225
7.7 Conclusions . . . 227

8 Testing Mass Loss in Large Magellanic Cloud Cepheids using Infrared and Optical Observations 231
8.1 Introduction . . . 231
8.2 The Data and Mass Loss Model . . . 232
8.3 Quality of Fit of Mass–Loss Rates . . . 237
8.4 The Effect of Mass Loss on Infrared Period Luminosity Relations . . . 243
8.5 What is the Driving Mechanism? . . . 247
8.6 Discussion and Conclusions . . . 250

III Summary 253

9 Conclusions and Future Work 255
9.1 Introduction . . . 255
9.2 The Big Picture . . . 255
9.2.1 The Mass-Loss Model . . . 255
9.2.2 Pulsation-Radiation Hydrodynamics . . . 260
9.3 Future Directions . . . 261

Bibliography 265

IV Appendices 301

A Methods for Calculating Spherically Symmetric Radiative Transfer 303

A.1 Introduction . . . 303
A.2 Geometry . . . 304
A.3 Derivation . . . 304
A.4 Numerical Derivation . . . 306
A.5 Feautrier Solution . . . 309
A.6 Rybicki Solution . . . 310
A.7 Hermitian Method Solution . . . 312

B Derivation of Spherically Symmetric Temperature Correction 317

B.1 Introduction . . . 317
B.2 Avrett–Krook Temperature Correction . . . 318
B.3 Formal Derivation . . . 319
B.4 Temperature Correction for ATLAS . . . 325

List of Tables

1.1 Typical Properties of Cepheid Variable stars 7

2.1 Best-Fit Parameters of the Three Stars 72

3.1 Best Fit Parameters for the Fixed Point and Intensity at the Fixed Point 107
3.2 Iterative Solution of R_*/M_* for Microlensing Event EROS-BLG-2000-5 108
3.3 Iterative Solution of R_*/M_* for Microlensing Event EROS-BLG-2000-5 With One Free Parameter Limb-Darkening 109

5.1 The Rate of Shock Acceleration as a Function of Phase for δ Cep 176

6.1 Global Parameters of Observed Galactic Cepheids 184
6.2 Predicted Pulsation Driven and Radiative Driven Mass–Loss Rates of Galactic Cepheids . . 185
6.3 Inferred Mass–Loss Rates from the Literature 195
6.4 Comparison of Predicted and Observed Circumstellar Envelope Fractional Luminosities . . 199
6.5 Observed Rates of Period Change 206

8.1 Best Fit Parameters for Predicted PL Relations 243

List of Figures

1.1 Stars and Vibrating Strings 2
1.2 Pulsation Hertzsprung-Russell Diagram 4
1.3 Observed Light Curves of δ Cephei 5
1.4 The Radial Velocity Curve of δ Cephei 6

2.1 Coordinate System for Solving the Spherically Symmetric Transfer Equation 65
2.2 Comparison Between SAtlas and Phoenix Models 69
2.3 The Best-Fit χ^2 Values for the Interferometric Observations of ψ Phe 71
2.4 Model Visibilities for ψ Phe 73
2.5 Model Visibilities for γ Sge 74
2.6 Model Visibilities for α Cet 75
2.7 The Dependence of Effective Temperatures on the Angular Diameters of Stars from Spectrophotometry and Interferometry 76
2.8 Predicted Effective Temperatures and Luminosities of the Three Observed Stars 77

3.1 The ratio of the Pseudo-Moment to the Mean Intensity 90
3.2 Dependence of the Fixed Point μ_0 on the Ratio of the Pseudo-moment to the Mean Intensity 92
3.3 The Ratio of the Pseudo-moment to the Mean Intensity and α as a function of wavelength . . 93
3.4 Dependence of the Fixed Point μ_0 on the Wavelength 94
3.5 Intensity Profiles for the γ Sge Grid of SAtlas Model Atmospheres 96
3.6 Distribution of Models on the H-R Diagram 97
3.7 Intensity Profiles for the $v_{\rm turb} = 0$ Cube of SAtlas Model Atmospheres at 555 *nm* 98
3.8 Intensity Profiles for the $v_{\rm turb} = 2$ Cube of SAtlas Model Atmospheres at 555 *nm* 99
3.9 Intensity Profiles for the $v_{\rm turb} = 4$ Cube of SAtlas Model Atmospheres at 555 *nm* 100
3.10 The Fixed Points Derived From Cubes of SAtlas Model Atmospheres 101
3.11 The Fixed Point and Intensity as a function of Gravity 103
3.12 The Fixed Point and Intensity as a function of Effective Temperature 104
3.13 The Fixed Point and Intensity as a function of R_*/M_* 106

3.14 The ratio of flux from four-parameter limb-darkening model and model atmospheres for $v_{\rm turb} = 0\ km/s$ at a function of effective temperature 111
3.15 The ratio of flux from four-parameter limb-darkening model and model atmospheres for $v_{\rm turb} = 2\ km/s$ at a function of effective temperature 112
3.16 The ratio of flux from four-parameter limb-darkening model and model atmospheres for $v_{\rm turb} = 4\ km/s$ at a function of effective temperature 113
3.17 The ratio of flux from four-parameter limb-darkening model and model atmospheres for $v_{\rm turb} = 0\ km/s$ at a function of gravity 115
3.18 The ratio of flux from four-parameter limb-darkening model and model atmospheres for $v_{\rm turb} = 2\ km/s$ at a function of gravity 116
3.19 The ratio of flux from four-parameter limb-darkening model and model atmospheres for $v_{\rm turb} = 4\ km/s$ at a function of gravity 117
3.20 Comparison between the four-parameter limb-darkening law coefficient a_1, determined from plane-parallel and spherical model atmospheres with $v_{\rm turb} = 0\ km/s$ 119
3.21 Comparison between the four-parameter limb-darkening law coefficient a_1, determined from plane-parallel and spherical model atmospheres with $v_{\rm turb} = 2\ km/s$ 120
3.22 Comparison between the four-parameter limb-darkening law coefficient a_1, determined from plane-parallel and spherical model atmospheres with $v_{\rm turb} = 4\ km/s$ 121
3.23 Comparison between the four-parameter limb-darkening law coefficient a_2, determined from plane-parallel and spherical model atmospheres with $v_{\rm turb} = 0\ km/s$ 122
3.24 Comparison between the four-parameter limb-darkening law coefficient a_1, determined from plane-parallel and spherical model atmospheres with $v_{\rm turb} = 2\ km/s$ 123
3.25 Comparison between the four-parameter limb-darkening law coefficient a_1, determined from plane-parallel and spherical model atmospheres with $v_{\rm turb} = 4\ km/s$ 124
3.26 Comparison between the four-parameter limb-darkening law coefficient a_3, determined from plane-parallel and spherical model atmospheres with $v_{\rm turb} = 0\ km/s$ 125
3.27 Comparison between the four-parameter limb-darkening law coefficient a_3, determined from plane-parallel and spherical model atmospheres with $v_{\rm turb} = 2\ km/s$ 126
3.28 Comparison between the four-parameter limb-darkening law coefficient a_3, determined from plane-parallel and spherical model atmospheres with $v_{\rm turb} = 4\ km/s$ 127
3.29 Comparison between the four-parameter limb-darkening law coefficient a_4, determined from plane-parallel and spherical model atmospheres with $v_{\rm turb} = 0\ km/s$ 128
3.30 Comparison between the four-parameter limb-darkening law coefficient a_4, determined from plane-parallel and spherical model atmospheres with $v_{\rm turb} = 2\ km/s$ 129
3.31 Comparison between the four-parameter limb-darkening law coefficient a_4, determined from plane-parallel and spherical model atmospheres with $v_{\rm turb} = 4\ km/s$ 130

3.32 Predicted values of the limb-darkening coefficient a_1 as a function of spherical extension for model atmospheres with $v_{\rm turb} = 0\ km/s$ . . . 132
3.33 Predicted values of the limb-darkening coefficient a_1 as a function of spherical extension for model atmospheres with $v_{\rm turb} = 2\ km/s$ . . . 133
3.34 Predicted values of the limb-darkening coefficient a_1 as a function of spherical extension for model atmospheres with $v_{\rm turb} = 4\ km/s$ . . . 134
3.35 Predicted values of the limb-darkening coefficient a_2 as a function of spherical extension for model atmospheres with $v_{\rm turb} = 0\ km/s$ . . . 135
3.36 Predicted values of the limb-darkening coefficient a_2 as a function of spherical extension for model atmospheres with $v_{\rm turb} = 2\ km/s$ . . . 136
3.37 Predicted values of the limb-darkening coefficient a_2 as a function of spherical extension for model atmospheres with $v_{\rm turb} = 4\ km/s$ . . . 137
3.38 Predicted values of the limb-darkening coefficient a_3 as a function of spherical extension for model atmospheres with $v_{\rm turb} = 0\ km/s$ . . . 138
3.39 Predicted values of the limb-darkening coefficient a_3 as a function of spherical extension for model atmospheres with $v_{\rm turb} = 2\ km/s$ . . . 139
3.40 Predicted values of the limb-darkening coefficient a_3 as a function of spherical extension for model atmospheres with $v_{\rm turb} = 4\ km/s$ . . . 140
3.41 Predicted values of the limb-darkening coefficient a_4 as a function of spherical extension for model atmospheres with $v_{\rm turb} = 0\ km/s$ . . . 141
3.42 Predicted values of the limb-darkening coefficient a_4 as a function of spherical extension for model atmospheres with $v_{\rm turb} = 2\ km/s$ . . . 142
3.43 Predicted values of the limb-darkening coefficient a_4 as a function of spherical extension for model atmospheres with $v_{\rm turb} = 4\ km/s$ . . . 143

4.1 Comparison Between Initial and Hydrodynamic Model . . . 162
4.2 The Lagrangian Variables in the Hydrodynamic Model . . . 163
4.3 Change of Radius & Velocity in the RHD Simulation . . . 164

6.1 The Continuum Optical Depth and Mass–Loss Rates for δ Cep and l Car . . . 187
6.2 Radiative Driven Mass–Loss Rates of Observed Galactic Cepheids . . . 188
6.3 Pulsation Driven Mass–Loss Rates of Observed Galactic Cepheids Ignoring the Effect of Shocks . . . 190
6.4 Pulsation and Shock Driven Mass–Loss Rates of Observed Galactic Cepheids . . . 191
6.5 The Distribution of Mass Loss on the Cepheid Instability Strip . . . 193
6.6 The Predicted Mass–Loss Rate as a Function of Stellar Mass for S Mus. . . . 194
6.7 The Uncertainty of Pulsation Driven Mass Loss . . . 196

6.8 Predicted Luminosities of Observed Galactic Cepheids at 2.2 μm 200
6.9 The Ratio of 25 and 12 μm Luminosities of Observed Galactic Cepheids Based on Radiative and Pulsation Driven Mass Loss Predictions 201
6.10 Predicted Infrared Excesses at Spitzer Wavelengths 202
6.11 The Effect of Mass Loss on the Rate of Period Change 205
6.12 The Efficiency of Pulsation Driving as a Function of the Rate of Period Change 207

7.1 The Dependence of the Analytical Model of Mass Loss on Metallicity and Other Parameters 214
7.2 The Relative Mass–Loss Rates of LMC/SMC Cepheids as a Function of Radius 217
7.3 Predictions of Mass–Loss Rates of Cepheids with a Canonical Mass–Luminosity Relation . 219
7.4 Predicted Mass–Loss Rates of Cepheids with a Convective Overshooting Mass–Luminosity Relation 220
7.5 The Color–Magnitude Diagram of the Theoretical Cepheids with a Canonical Mass–Luminosity Relation 221
7.6 The Color–Magnitude Diagram of the Theoretical Cepheids with a Convective Overshooting Mass–Luminosity Relation 222
7.7 Comparison of the Predicted 3.6 μm Luminosities of the Theoretical Cepheids with an Observed Period–Luminosity Relation 223

8.1 Infrared Brightnesses of LMC Cepheids using the SAGE Survey 233
8.2 The Separation Between OGLE–II Cepheids and SAGE Sources 235
8.3 The Fit of the Radius of the Cepheids for Predicting Fluxes 238
8.4 Testing the Fit of Pulsation Phase to Observed Data 239
8.5 The Fit of the Mass–Loss Model to the OGLE–II and SAGE Observations 240
8.6 The Dependence of the Mass–Loss Rates on the Unknown Pulsation Phase 241
8.7 Application of the F-test on the Two Models for Fitting the Observations 242
8.8 The Predicted IR Brightnesses of the OGLE–II Cepheids and Period–Luminosity Relations . 244
8.9 Comparison of the predicted stellar and the observed fluxes of the OGLE–II Cepheids 246
8.10 Comparison of Predicted and Radiative Driven Mass–Loss Rates 249

9.1 Mass Loss in RR Lyrae Stars 257
9.2 Mass Loss on the Hertsprung-Russell Diagram 259

Chapter 1

Introduction

Bright star, would I were steadfast as thou art–
Not in lone splendour hung aloft the night
And watching, with eternal lids apart,
Like nature's patient, sleepless Eremite,
- **Bright Star, Would I Were Steadfast As Thou Art** by John Keats (Milnes, 1848)

1.1 Things in Perspective

The stars are fundamental building blocks of the universe; they are important for the structure of galaxies on the large scale, and for the structure of planets and disks on the small scale. They are the engines that form the elements necessary for life such as carbon, oxygen and nitrogen. They are also the locations where life forms and is supported by stellar radiation. Studying the stars in the sky is a study of how life is formed.

Stars, though, are interesting in their own right. It is remarkable that stars vary in mass from $1/10$ the mass of the Sun to $100\times$ the mass of the Sun, by four orders of magnitude. The amount of light different stars emit ranges from $10^{-2} - 10^{6}\times$ the amount of light emitted by the Sun and likewise stars range in radius from $0.01 - 1000\times$ the radius of the Sun. It is a remarkable feat of nature that all these different stars are related and use the same physics.

Thus it is a compelling challenge to study these objects and learn about their structures, how they evolve and how they relate to the formation of life and planets. However, gathering information about stars is a challenging endeavor. The only window to the stars is the light they emit. The observed light is emitted from the optically thin outer layers of a star called the atmosphere, and is a measure of the star's temperature, pressure, density, and composition in these layers. Furthermore, one may use this information to measure global properties of a star such as the effective temperature, gravity and even mass (or conversely luminosity and/or radius) as well as the complete atmospheric structure, although this is model dependent. Models use

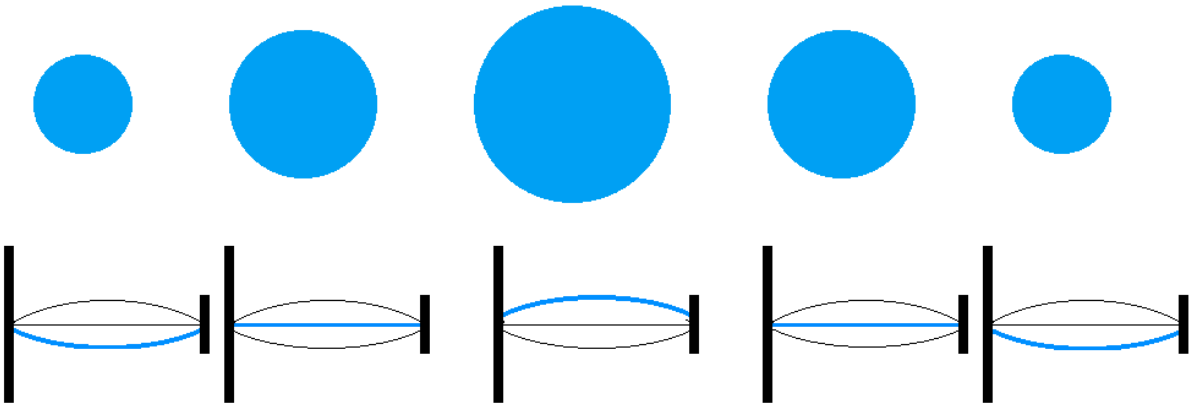

Figure 1.1: A pulsating star, shown as a blue circle, pulsating over one period at five different times, at minimum, mean, maximum, mean, and minimum radius. Below is a cartoon of a string vibrating as a standing wave, with the blue string corresponding to the same phase as the star above as minimum, mean, or maximum point in the wave.

atomic physics, radiation physics, and equations for the structure of a static fluid to describe the atmosphere of a star and attempt to reproduce the observations.

These observations do not yield any information about the interiors of stars, that is unless the star is pulsating. A pulsating star is a star that changes in brightness due to physical changes within that star. The simplest type of pulsating star is a radially pulsating star in which the star's volume expands and contracts periodically and this is seen as a change of light. A second type of pulsating star is one with non-radial pulsations, such that different parts of the surface are moving outward and inward at the same time.

A radially pulsating star is a powerful tool for understanding stellar interiors because the expansion and contraction is due to a standing wave. Therefore, observations of pulsation carries information about the interior structure of the pulsating star. This is analogous to a standing wave formed by a vibrating string as shown by the cartoon in Figure 1.1. When the star is smallest in size, the string is at a minimum and as the star expands, the string moves toward a maximum height and then the vibration moves back to a minimum. The two phenomena are similar. From classical mechanics, it is known that the period of oscillation for a string is

$$P = 2L\sqrt{\frac{\mu}{T}}, \tag{1.1}$$

where L is the length of the string, T is the tension, and μ is the mass density of the string. By measuring the period of oscillation of the string, one can learn about the properties of the string. Likewise, the period of pulsation for a star can tell us about the structure of the star.

Using the light from pulsating stars, one gains information about the interior of stars as well as information about the atmospheres of the same stars. However, pulsation is a dynamic effect, where a significant fraction of the star is moving at any time. Thus the atmosphere of the star is also moving and its structure is

being changed by these dynamic motions. Therefore, the standard models assuming a static fluid are a poor representation of reality. It is preferable to model the atmosphere of these stars using a hydrodynamic flow.

Luckily for astronomers, there are many pulsating variable stars in the universe, as is shown in the pulsation Hertzsprung-Russell (HR) diagram in Figure 1.2. The figure displays the luminosity and effective temperature of a star. The colored regions of the pulsation Hertzsprung-Russell Diagram denote different types of pulsating variable stars; the blue and green regions are non-radially pulsating variables and solar-like oscillators. The Mira and irregular pulsating stars (Irr) are radially pulsating and form dust in the atmosphere. The RR Lyrae stars and Cepheid stars are radial pulsators as well but do not form dust in the atmosphere. These two types of stars lie in what is called the Cepheid Instability Strip, a region of the HR diagram where the conditions in a star are just right for pulsation to occur.

The Cepheid variable stars, in particular, are interesting. They are evolved giant stars fusing helium in their cores, rapidly changing their structure as they evolve across the Cepheid Instability Strip. Cepheids pulsate and their brightness varies over a period of days to a few months as shown by the light curve for the prototype Cepheid, δ Cephei in Figure 1.3 for a number of wavelengths. The variation is regular and consistent with respect to time. Because Cepheids expand and contract, they also have a pulsational velocity; however, it is not possible to observe the pulsational velocity directly. Instead, one can measure its projection onto the radial velocity of a Cepheid, as shown in Figure 1.4 for δ Cephei. The variation of the radial velocity is also very regular, but it is interesting to note that the velocity curves do not correspond with the light curve as one might naively expect. When the velocity is zero, the radius of a Cepheid is either at its minimum or maximum value and one might expect this to also be the location of the minimum and maximum brightness. However, this is not the case, the minimum and maximum brightness occur at maximum and minimum velocity or conversely at the phase where the radius is about the mean radius.

The typical properties of Cepheids are listed in Table 1.1, adopted from Ngeow (2005). It is clear that Cepheids vary over a large range of luminosities and radii, providing a large parameter space for dynamic modelling, and their effective temperature is also idea for assuming local thermodynamic equilibrium.

While Cepheids are convenient for modelling, they are also important objects for astronomical research. Because Cepheids are massive stars, they are associated with young stellar populations and star formation. However, arguably their most significant property is that Cepheids are standard candles. If one measures how bright they appear to be and the period of pulsation then one can determine how bright the Cepheid actually is and its distance. This makes them powerful tools for extragalactic and cosmological studies.

In terms of stellar astrophysics, Cepheids are ideal laboratories because they present information that can be used to constrain their structure and hence help constrain the structure of stars, in general. The goal of this dissertation research is to study the dynamic atmospheres of these stars using numerical and analytical methods via the combination of stellar atmosphere modelling and Cepheid pulsation. These two topics have been studies extensively for more than a century and many questions answered, including why the light and velocity curves have a phase lag. There are also many questions unanswered and as such, they are reviewed

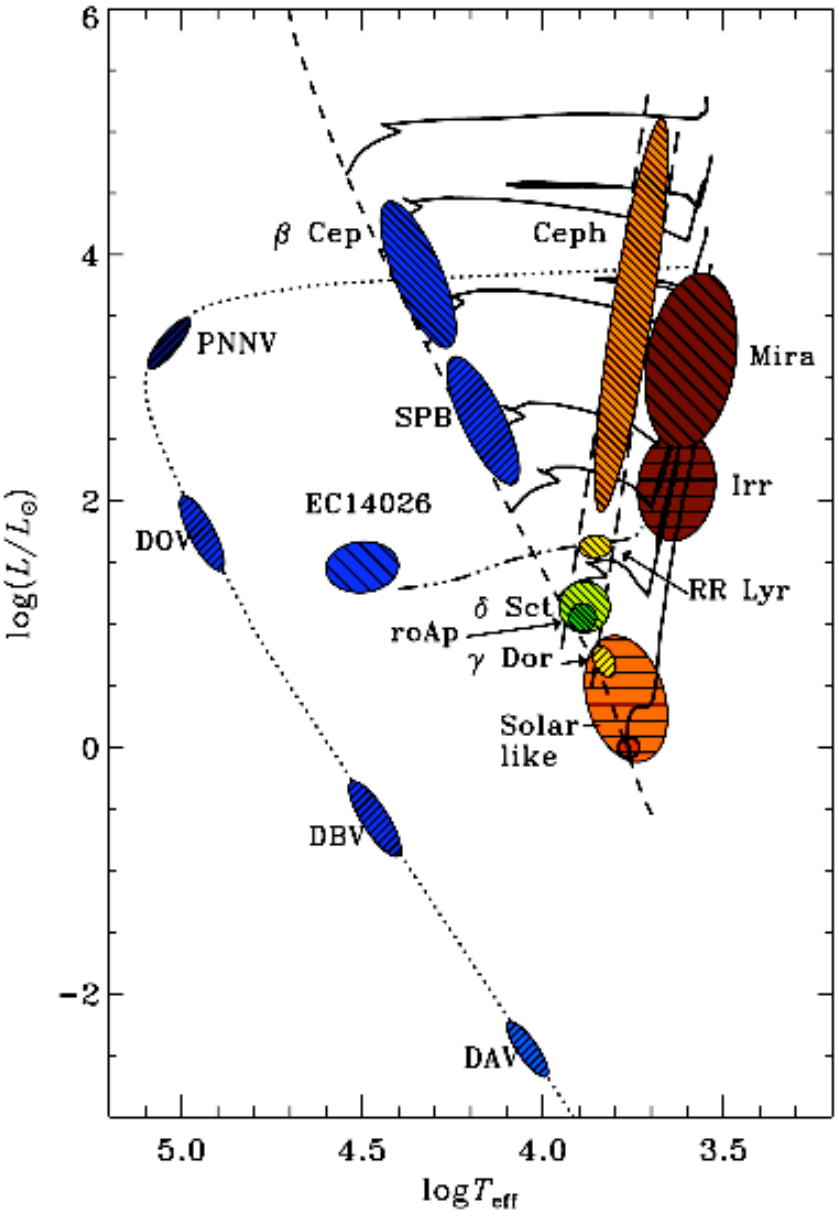

Figure 1.2: The pulsation Hertzsprung-Russell showing the effective temperatures and luminosities of different types of pulsating variable stars. The colors and labels are described in the text. The figure is adopted from Christensen-Dalsgaard (2003). Reproduced by permission of Dr. Christensen-Dalsgaard.

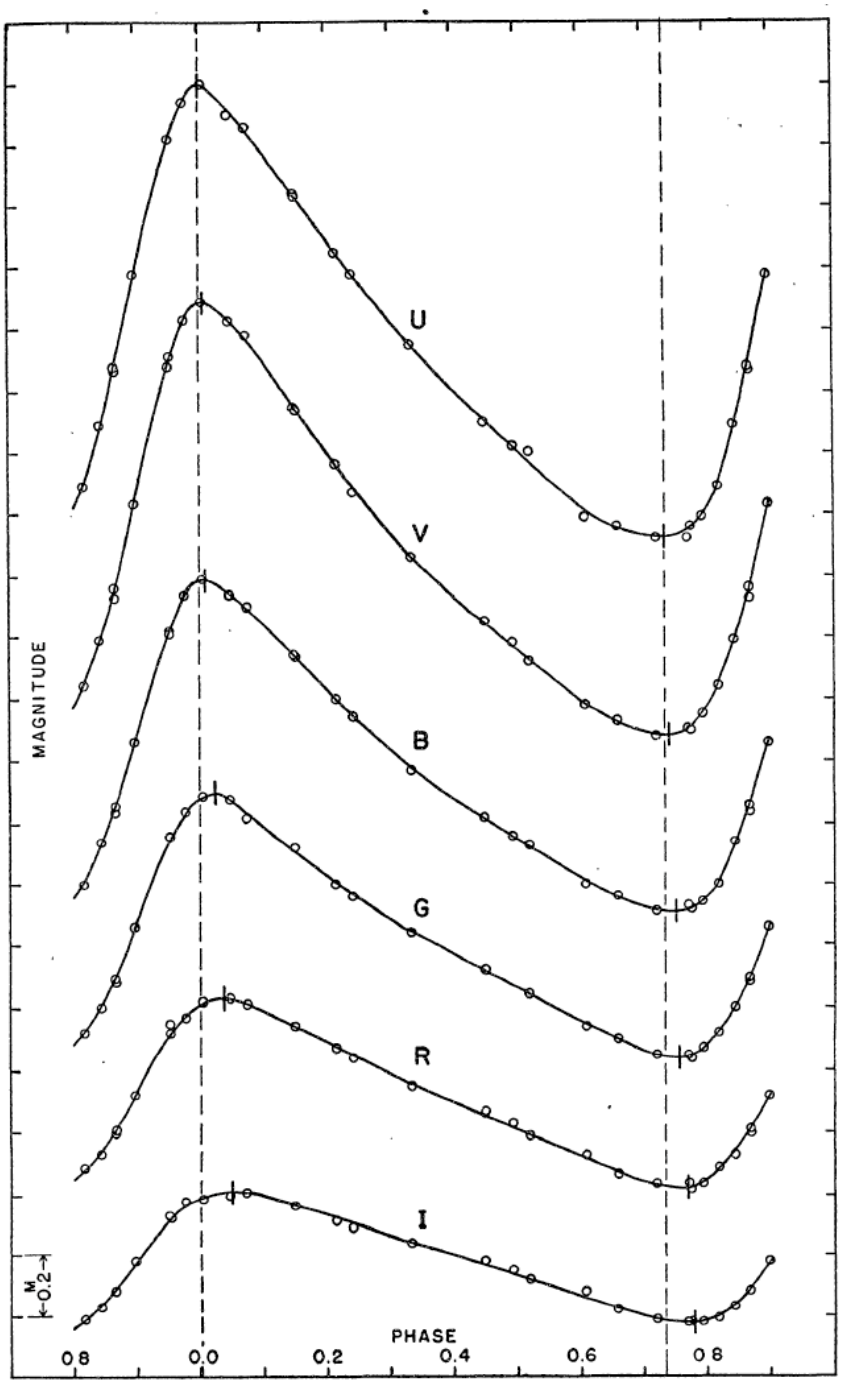

Figure 1.3: The observed variation of brightness for δ Cephei in the *UVBGRI*-bands. The figure is adopted from Stebbins (1945). Reproduced by permission of the American Astronomical Society.

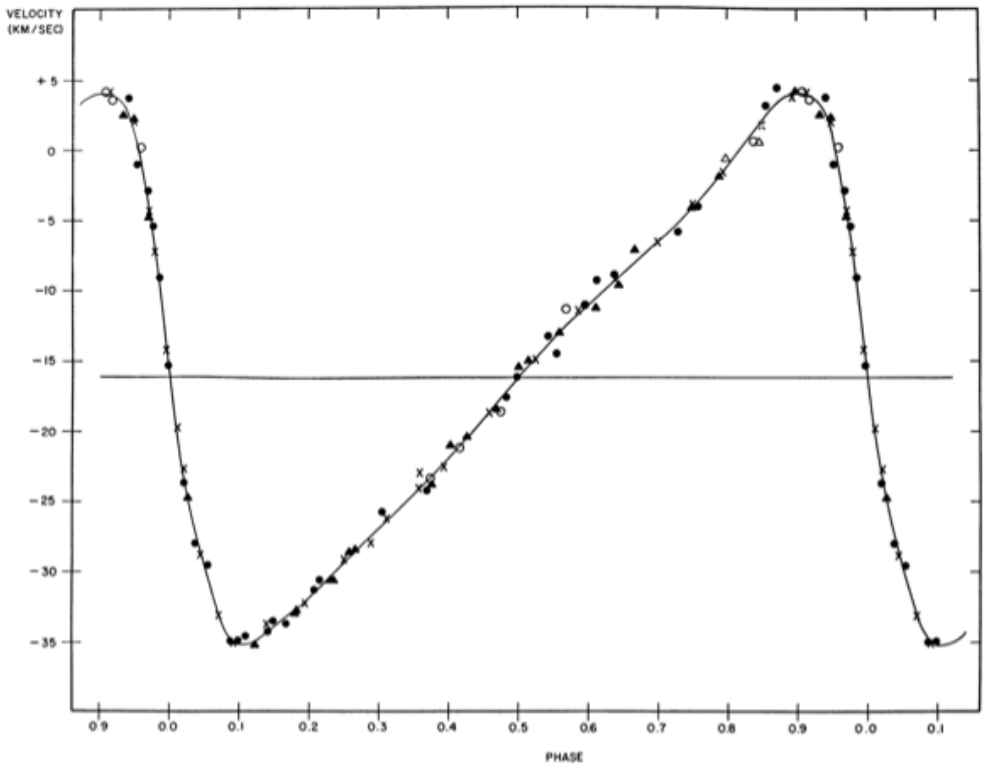

Figure 1.4: The radial velocity curve for δ Cephei. The figure is adopted from Shane (1958). Reproduced by permission of the American Astronomical Society.

Table 1.1: Typical Properties of Cepheid Variable stars

Parameter	Range
Period (days)	1 - 100
Mass ($M_\odot$)	3 - 15
Mean Luminosity ($L_\odot$)	300 - 45000
Effective Temperature (K)	4500 - 6500
Mean Radius ($R_\odot$)	15 - 200
Absolute Visual Magnitude (mag)	-0.5 - -8
V-Band Amplitude (mag)	0.3 - 1.2
Radial Velocity Amplitude (km/s)	30 - 60
Spectral Type	$F6$ - $K2$

here to outline the current understandings and open challenges.

1.2 History of Stellar Atmospheres

The history of the theory of stellar atmospheres is intertwined with the development of solar and stellar spectroscopy, stellar classification, atomic physics, and radiative transfer. It arguably began when Isaac Newton observed the continuous spectrum of the Sun through a glass prism almost 350 years ago. This simple observation sparked the field of stellar spectroscopy, which in turn motivated the development of stellar classification. The spectroscopic observations provided insight into atomic physics such as the discovery of helium, as well as a testbed for the theory of radiative transfer, that formed the basis for the field of stellar atmosphere modelling. Much of this review of stellar atmospheres is from Hearnshaw (1986), Gray & Corbally (2009), Mihalas (1978), and Pecker (1965).

1.2.1 Stellar Spectroscopy and Classification

While Isaac Newton observed the continuous spectrum of the Sun, he missed discovering absorption lines. That discovery was made by William Wollaston in 1802, in which he reported dark gaps between colors in the continuous spectrum. He attributed the dark gaps to a simple separation of colors. Joseph Fraunhofer observed the Solar spectra in more detail and found that the dark gaps varied in strength, some strong and some weak, and existed in regions where the color is same on both sides of the line. Because of this variation, Fraunhofer concluded that the lines are not a natural boundary. It was Kirchhoff, in 1859, who deduced that the Fraunhofer D line was due to the presence of sodium when he passed a continuous spectrum through a salt flame. This observation led to the Kirchhoff's Three Laws for radiation, and began the field of chemical analysis in stars.

The observations of Fraunhofer were instrumental in the development of solar spectroscopy but he was

also the first to observe absorption spectra of stars. In 1823, he reported observations of Sirius, Pollux, Castor, Betelgeuse, and Procyon. Fraunhofer's observations were repeated by Lamont in 1838 while he was director of the Royal Observatory in Munich, and by William Swan in 1856 (Swan, 1856). However, it was in the 1860's when the field of stellar spectroscopy became more common with observations in both Europe and North America. Lewis Rutherfurd observed seventeen stars from New York and classified them into three different groups (Rutherfurd, 1863). This was one of the first attempts at stellar classification. In London, the Astronomer Royal, George Airy, reported spectroscopic observations of eighteen stars. For some cases, these observations included only two absorption lines from some stars such as Arcturus (Airy, 1863). Donati (1863) discussed spectroscopic observations of fifteen stars. He noted many differences between the lines detected for different stars and did not detect certain lines. For instance, the author noted that the D line is not seen in any stars. It is remarkable that stellar spectra were observed by these astronomers given the difficulties they had obtaining consistent measurements, as noted by Donati (1863),

> Perhaps, as the stars change in color, their stria-positions change, or my more brilliant striæ may not have been the more brilliant ones to Fraunhofer's eyes. (Thus Fraunhofer is silent on the difficulties of Capella, and speaks of the difficulties of Procyon. I found Capella very troublesome, and the stria of Procyon much clearer and sharper than any in Capella.) I merely point out the utility of making these observations at various times with the extremest accuracy, without hazarding any hypothesis.

By 1864, William Huggins, from his private observatory in Upper Tulse Hill at the edge of London, had contributed greatly to the field of stellar astrophysics. Along with his partner, William Miller, a chemist, the two began a project to determine the chemical composition of stars. That year, they presented a paper on the spectra and composition of stars with particular emphasis on Aldebaran, Betelgeuse, β Pegasi, and Sirius (Huggins & Miller, 1864). In Aldebaran, the presence of sodium, magnesium, hydrogen, calcium, iron, bismuth, tellurium, antimony and mercury was detected, while in Betelgeuse the authors found sodium, magnesium, hydrogen, calcium, iron, and bismuth. In β Peg, only sodium, magnesium and barium were detected. For Sirius, they detected sodium, magnesium, hydrogen and iron. Huggins and Miller also presented results for another 41 stars. In another work, Huggins discussed laboratory experiments determining the spectra of air and 23 known elements from spark spectra (Huggins, 1864). This work was one of the first attempts to measure the composition of stars, which is remarkable considering that astronomers had not yet discovered how absorption/emission lines were formed. It was also a fundamental result as it provides constraints for modelling stellar atmospheres.

The field of stellar spectroscopy had grown so much by the 1860's that a plethora of stars had been observed and it was now possible to compare them with each other and the solar spectra. In conducting this comparison, it had been noted by a number of authors that there were significant differences between certain stars, (Rutherfurd, 1863; Huggins & Miller, 1864). Following the path taken in biology of categorizing

different species into classes, many astronomers began to devise schemes for classifying stellar spectra. Rutherfurd was among the first to take this approach of grouping stellar spectra; in his classification scheme there are three groups. The first group contains spectra like the Sun, those stars with many lines, while the second group uses Sirius as the prototype where the spectra are "wholly unlike the Sun, and are white stars" (Rutherfurd, 1863). The third class of stars show no lines, with Rigel as a typical star. In the modern MK system, the first group are G type and later, the second is late B to F, while the third type is early B stars or supergiants where the hydrogen lines are very narrow (Hearnshaw, 1986).

Another classification scheme was proposed by Father Secchi in 1863. In his system, there are two groups, the first Group I is defined as yellow or red stars and Group II is defined as white stars showing few lines. A third group was added in 1866 called the blue stars. This group was defined by broad spectral bands in the blue and near-violet due to hydrogen. In the english translation of an earlier paper, Secchi (1875) outlined the three classes using prototypical stars,

> I have shown from previous observations that the spectra of the fixed stars may be referred to three characteristic types, the representatives whereof are, firstly α Lyrae (Vega), secondly, α Herculis, thirdly, α Bootis (Arcturus), or by our Sun itself.

Soon after, this classification scheme was extended again to include the carbon stars in a fourth group, and a fifth group was defined as those stars with the broad hydrogen lines but also having emission lines such as Be stars.

In the 1870's, Hermann Carl Vogel in Potsdam proposed yet another stellar classification scheme (Vogel, 1873, 1874). This scheme is similar to that of Father Secchi but with the groups also defined by stellar evolution parameterized by estimates of the temperature of the star, presumably from the color. This was incredibly ambitious since in the 1870's there was no significant understanding of how stars evolved. The scheme was classified by three types. The first type is those stars that are so hot that metallic vapors have weak absorption lines, this is the white stars. The second type contains the stars that are similar to the Sun with strong absorption lines, and the third type contains those stars that are cool and are characterized by broad absorption bands. This scheme was further refined with subclasses. The first type contains three subclasses, with (a) weak metallic lines and visible hydrogen lines, (b) metallic lines are barely visible or not at all and the hydrogen lines are also missing and (c) stars with hydrogen emission lines. The second class has two subclasses defined as (a) stars with very numerous metallic lines that are easily recognized with either strong hydrogen lines or those stars where those lines are weak and (b) spectra with the weak bands but also a number of bright lines. This second subclass includes the Wolf-Rayet stars, novae, and Mira variables. The third class, which contains a number of dark lines and numerous dark bands, are separated into two subclasses. Vogel defined the first subclass by the dark bands that are strongest in the violet range of the spectra where they terminate sharply and become weaker at longer wavelengths. The second subclass was defined by having the opposite behavior where the lines are strongest in the red and weaken towards the

violet part of the spectrum (translation of Vogel (1874) by Hearnshaw, 1986).

Vogel had hoped he had devised a lasting classification scheme. However, the discovery of helium forced him to redefined the classification scheme. As a result, in 1899, sub-subclasses were created for Class Ia and Ic, and Class Ib was changed. The Class Ia was divided into three parts where they all show strong hydrogen lines but no helium with the metallic lines becoming stronger from the first sub-subclass to the third sub-subclass. The Class Ib was defined to include the helium stars which were mostly observed in the Orion nebula (also called Orion stars) and had helium absorption lines. The subclass Ic was divided into two parts with the first having stars with only hydrogen in emission and the other having emission lines of hydrogen and other elements.

One of the more fascinating attempts to devise a stellar classification system was attempted by Norman Lockyer that is based on his theory of star formation and evolution. The meteoric hypothesis states that the universe contains numerous meteorites that traveling throughout; these meteorites collide and vaporize into a gas. The gas condenses and forms young stars. The stars contract further causing the stellar temperature to increase until the radiation from the stars halts the contraction. At this point a star reaches a maximum temperature and begins to cool. Therefore, Lockyer argued that stars can be classified as being on one of two branches, one of increasing temperature and one a cooling branch (Lockyer, 1899, 1903). Thus Lockyer's classification scheme had two dimensions, one being a measure of temperature and the other is whether the star is on the ascending or descending branch. In his scheme, each branch is divided into seven parts and a peak division where the star reaches the maximum temperature. Each of the fifteen divisions are named after prototype star, starting on the ascending branch the divisions are based on Antares, Aldebaran, Polaris, α Cygni, Rigel, ζ Tau, and β Crucis. At the peak, the division is represented by ϵ Orionis, and γ Velorum. On the descending branch, the divisions have the prototypes Achernar, Algol, Markab, Sirius, Procyon, Arcturus, and 19 Piscium. These sequences are striking as the ascending branch is defined by giant and supergiant stars while the descending branch is defined by dwarfs. Lockyer and the meteoric hypothesis is an interesting cautionary tale of trying to fit a theory with observations but what is remarkable about the work is that Lockyer differentiated between giant/supergiant spectra and dwarf star spectra.

While Lockyer and Vogel were defining their classification systems in Europe during the 1870's and 1880's, work was also being done in the United States lead by the director of the Harvard College Observatory E.C. Pickering. One of the first goals of Pickering upon become director was to conduct a large spectroscopic survey for the Henry Draper Memorial Catalogue. The catalogue included spectra of more than 10000 stars and the duty of creating a classification system was given to Williamina Fleming. She proposed a classification scheme based on that of Father Secchi but with more divisions. In the words of Pickering (Pickering, 1890), Fleming's classification scheme is summarized as

> From this it appears that A, B, C, and D indicate varieties of the first type, E to L varieties of the second type, M the third type, N the fourth type, and O, P, and Q spectra which do not resemble those of any of the preceding types.

In this scheme, the letter J was not used, leaving sixteen different categories. In follow-up work on an extension of the Draper Memorial Catalogue for star clusters, Williamina Fleming made significant modifications to the classification scheme. The new classification scheme is A, B, F, E, G, H, M, N, O where C, D, I, and L are removed and F is moved ahead of E.

Being an ambitious researcher, Pickering began a detailed study of all bright stars and set Antonia Maury to classify these spectra. In this work, Antonia Maury devised a new classification scheme with 22 different groupings but also with a second dimension with three divisions. The 22 groups are similar to the four types specified by Father Secchi, but with groups I to V representing the Orion stars. The groups VII to XI represent Secchi's type I, while groups XIII to XVI represent the second type. The groups XVII to XX are equivalent to type III and group XXI represent carbon stars and XXII represent Wolf-Rayet stars. The groups VI, and XII are intermediate groups between Secchi types. The three divisions are defined as (a) in a spectra none of the lines are relatively wide with the exception of hydrogen and calcium, (b) spectra where all lines are relatively wide and (c) the hydrogen lines are narrow and strong, "the Orion lines are likewise narrow" (a reference to helium lines) (Maury & Pickering, 1897), and the calcium lines are more intense relative to other divisions, and contain metallic lines not seen in the solar spectrum.

Yet another systematic spectroscopic survey of stars was lead by Pickering starting in 1891 observing stars in the southern hemisphere. This survey included observed spectra for about 1100 stars and the task for classifying the stars was given to Annie Jump Cannon. Cannon adopted and modified Fleming's classification scheme, where various types were removed and others rearranged. She proposed a scheme with types O, B, A, F, G, K, and M with P for planetary nebulae, and Q for stars with particularly bright lines. The O-type was moved ahead of the B-type as it is recognized both exhibit Orion lines, "all the dark lines, except those due to hydrogen and calcium, in the spectra of classes Oe, Oe5B, B, B1A, B2A, B3A, and B5A." (Cannon & Pickering, 1901). In this notation B is equivalent to B0 and B3A is B3 in the current MK notation. It is here where we see that stellar classification is similar to the modern system used today.

Under the direction of Pickering and the dedication and creativity of Fleming, Maury and Cannon, almost 20000 stars were observed spectroscopically and classified. This historic work has also led to the development of the modern Morgan-Keenan classification scheme. In fact, the development and evolution of stellar classification from the system suggested by Annie Jump Cannon to the current system has a rich history but is beyond the scope of this work, and can be found in Gray & Corbally (2009). However, the early history of stellar spectroscopy and classification shows how observations provide necessary information that model atmospheres must reproduce. The two fields, stellar classification and atmospheric modelling are inherently related. In an analogy suggested by Dimitri Mihalas, to speak of only the theory of stellar atmospheres is akin to hearing only one side of a telephone conversation. Instead, the two fields work together as a good duet (Mihalas, 1994).

1.2.2 The Physics of Stellar Atmospheres

The first forty years of stellar spectroscopy had provided a plethora of information for theoretical astrophysicists to struggle with. In the early years of the twentieth century, researchers were using stellar spectroscopy to understand stellar temperatures (Wilsing & Scheiner, 1909) and luminosities (Hertzsprung, 1905, 1907; Russell, 1913a). However, there were still more questions. Some of these questions were related to the physical processes for forming absorption lines in a spectrum, how energy was transferred in a star, and how does a star maintain stability.

Some of the challenges of understanding of stellar atmospheres were not answered by astronomers but by physicists. The behavior of radiation was explained by Max Planck where he connected the wavelength dependence of light from an object emitting a continuous spectrum and that object's temperature. It was this result that Wilsing & Scheiner (1909) used to measure stellar temperatures from spectroscopy. Furthermore, the quantization of light was discovered by Albert Einstein. Niels Bohr and Ernest Rutherford devised the model for the structure of an atom by 1913. These two discoveries were used to explain how absorption and emission lines are formed in a stellar atmosphere. These three discoveries are fundamental to the understanding of quantum mechanics but also laid the foundation for the development of model stellar atmospheres.

Even though these theories laid a foundation for stellar atmospheres, progress was still to be made in the understanding of radiation transfer. Schuster (1905) studied radiative transfer in a foggy atmosphere, defined by having a significant amount of scattering of light. Rayleigh scattering was explored as a physical mechanism for generating bright line and dark line spectra. The light is treated as being emitted from a plane-parallel surface and travels a distance dx where some of the radiative energy is absorbed, and the remainder is scattered. One-half of the remainder is scattered in the forward direction and half backwards. The absorbing layer also re-emits radiation isotropically in all directions. In this model the emergent radiation can be calculated as well as the amount the radiation is diminished due to scattering. Without knowledge of atomic physics, Arthur Schuster constructed a solution for the equation of radiative transfer and was able to compute emission and absorption line strengths.

This work was followed by the seminal paper by Karl Schwarzschild, where he developed the concept of radiative equilibrium, as well as calculated the formal solution for the transfer equation in a plane-parallel atmosphere (Schwarzschild, 1906, english translation by Menzel & Milne (1966)). Prior to this work, most astronomers treated the solar atmosphere as either isothermal or adiabatic; here the concept of radiative equilibrium was developed

> If we assume that the outer regions of the Sun show a continuous transition to hotter and denser masses of gas, then we can no longer distinguish between radiating and absorbing layers, but must consider each layer as radiating and absorbing simultaneously. We know that a strong flux of energy from unknown sources in the solar interior permeates the Sun, and emerges into the

> surrounding space. In the absence of mixing motions, what must be the temperatures of the individual layers of the solar atmosphere so that, while remaining stationary, they could support such an energy flux without further temperature change within themselves?

Following this assumption, the author developed the two-stream approach for solving the equation of radiative transfer in a similar manner as Schuster (1905), but carried out the solution further to describe the blackbody emission as a linear function of the optical depth. Furthermore, he used this result to derive the temperature structure of the solar atmosphere under the assumption of a grey atmosphere (independent of wavelength) to be

$$T^4 = \frac{1}{2} T_{\rm eff}^4 (1 + \tau). \tag{1.2}$$

Combining this relation with the statement of hydrostatic equilibrium, and the ideal gas law, Schwarzchild computed the density structure of the atmosphere. He had effectively built one of the first model solar atmospheres. The process was also repeated under the assumption of adiabatic equilibrium. The two assumptions were tested by computing the center-to-limb variation of radiation and compared to observed solar limb-darkening profiles. He found that the assumption of radiative equilibrium produced a center-to-limb variation of the radiation that agreed better with the observations than did the results using adiabatic equilibrium. Schwarzschild (1906) developed, tested and confirmed the concept of radiative equilibrium in the Sun; a concept that is still heavily relied on for modelling both stellar and planetary atmospheres and interiors. The results of this work were soon tested and confirmed (Abbot et al., 1913; Shook, 1914) but was not fully appreciated until the work of Arthur Eddington (Eddington, 1926).

Schwarzschild continued his exploration of the solar atmosphere in a second article (Schwarzschild, 1914, english translation by Menzel & Milne (1966)). The second article focused on the formation mechanism for spectral lines, with tests of emission, absorption, and scattering that had been proposed by Schuster (1905). Here, he computed the radiation of the solar atmosphere for the cases of pure absorption, and pure diffusion as well as the case for scattering where again the scattering was assumed to be Rayleigh scattering. He determined that the Fraunhofer lines must form from scattering since lines formed by scattering can be seen as the solar limb while line formed by absorption would disappear. While this result is important as one of the first quantitative analyses of the formation of spectral lines, it was also the first time the concept of local thermodynamic equilibrium (LTE) was applied to a solar/stellar atmosphere. Local thermodynamic equilibrium assumes that the radiation at any point in the atmosphere is affected by only the local values of the density and temperature. The assumption of LTE has become a staple of model atmospheres still used today, almost one century later.

Schwarzschild (1914) concluded that the solar atmosphere was dominated by scattering was considered by Lundblad (1923), where he computed the integral solution of the equation of transfer. He also used the two stream method of inward and outward radiation being considered separately. He determined that the Sun must be dominated by absorption processes, Lundblad argued this result is not a contradiction of

Schwarzschild's earlier work because this work focused on the layers in the atmosphere where the continuous radiation is formed. Schwarzschild (1914) explored the Fraunhofer H and K lines which form in the "reversing layer" (chromosphere) of the Sun. The differences between these two works suggested a need to better understand the process of absorption in the solar atmosphere. The concept of Rayleigh scattering in the solar atmosphere was later ignored in favor of Compton scattering of free electrons (Compton, 1923a,b) by Dirac (1925). He showed that Compton scattering broadens the spectral lines, in the Sun by about 10 Å, but did not account for the shift of lines to longer wavelengths as seen in the limb of the Sun

A tremendous leap forward in the understanding of absorption was the development of a theory of ionization in stellar atmospheres (Saha, 1921). He developed the theory by building upon the results of Eddington (1917a), who explored ionization in the interiors of stars, and Eggert (1919), who first calculated the ionization temperatures for the outer eight electrons of iron in stellar interiors. However, Saha was the first to apply the theory to the solar atmosphere/chromosphere and the first to propose this as a quantitative explanation for the formation of spectral lines. Interestingly, this explanation was first qualitatively proposed by Lockyer (1893). Saha tested the theory by analyzing the spectra from the Harvard catalogue, in particular the H and K lines, and computed the effective temperatures of the stars. He found the temperatures of the stars agreed well with the color temperatures found by Wilsing et al. (1919), though he predicted higher temperatures for the G-type and later stars. For instance, Saha found that the solar temperature should be about 7500 K.

This analysis was carried further in the monumental work of Cecila Payne (Payne, 1925). She used line intensities from stellar spectra and was able to calculate the temperatures of the stars in the Harvard catalogue as well as using the variation of the line strengths to determine the composition of these stars for eighteen different elements. She found that stars are mostly composed of hydrogen and helium, although Cecila Payne, herself, was skeptical of the results. The application of quantum mechanics towards the understanding of stellar atmospheres was a great success to both fields and further analysis of ionization in stellar atmospheres was continued, in particular by Milne (1928a,b). The analysis of solar and stellar composition was pursued by Henry Russell (Adams & Russell, 1928; Russell et al., 1928; Russell, 1929) and Albrecht Unsöld (Unsöld, 1927, 1928).

The understanding of line opacity was a leap forward in the understanding of stellar atmospheres, but the vast amount of data needed regarding the structure of the atom for each element made the problem intractable. The problem was found to be simplified by the introduction of mean opacities. One of the first derivations of a mean opacity was by Rosseland (1925) where he determined the flux per unit frequency of a stellar atmosphere as a function of the energy density and opacity per unit frequency, $F_\nu d\nu = -(c/3\chi_\nu\rho)(\partial A_\nu/\partial r)d\nu$. He demonstrated that one can define a mean opacity such that $1/\chi = \int_0^\infty (\partial A_\nu/\partial r)d\nu/\chi_\nu$ and derive the frequency integrated flux as a function of the total energy density of radiation. This definition is a powerful tool for understanding stellar atmospheres because it is dependent on the local density and temperature as well as offering a simpler methodology for studying stellar atmospheres.

The concept of mean opacities was studied by others, in particular by Krook (1938), who derived mean opacities based on the moments of the radiative transfer equation meaning these opacities are weighted by either the mean intensity, flux or radiation pressure.

The culmination of these discoveries and theories was the development of the first models of stellar atmospheres with line dependent opacities, radiative transfer, hydrostatic equilibrium with the ability to test different compositions, effective temperatures and gravities. The first models of Schuster (1905) and Schwarzschild (1906) revealed significant information about the structure of the solar atmosphere, but they did not have knowledge of the necessary physics to model different chemistry and composition of other stars.

It was in the 1930's when the field modelling of stellar atmospheres matured. The term "model stellar atmosphere" was first coined by McCrea (1931) who modelled the solar atmosphere composed entirely of hydrogen.He assumed the atmosphere was composed entirely of hydrogen based on the observations of Payne (1925), who found that the Sun is primarily composed of hydrogen. McCrea built models with effective temperatures of 5700, 10000, and $15,000\ K$. He concluded that the solar model did not agree with observations as the model predicted a strong Balmer jump discontinuity that is not seen in the solar observations. He also found that the ultraviolet fluxes from the B and A-type models significantly deviated from blackbody fluxes. He could only match observed fluxes if the computed color temperatures are much larger than the effective temperatures.

The goal of matching model solar atmospheres to observations was further pursued by Biermann (1933), who considered a composition mostly hydrogen and some small fraction of metals, consistent with the amount suggested by Russell (1929). He claimed to produce absorption opacities consistent with the observations. Unsöld (1934a) repeated McCrea's analysis and also computed atmospheres with metals included as well. The results of the work led Unsöld to reject the solar composition suggested by Russell and Payne. Instead, he computed models composed of two-thirds metals and one-third hydrogen to reproduce the observed solar opacity (Unsöld, 1934b).

The discrepancy between the solar models and observations was solved by the astrophysical application of the negative hydrogen ion as the primary source of opacity in the solar atmosphere (Wildt, 1939). This result was confirmed using an empirical solar atmosphere model by Barbier (1946). Applying this opacity source to models of the solar atmosphere solved the discrepancy found earlier (Strömgren, 1940). The authors produced an atmospheric model with an effective temperature of 5740 K and $\log g = 4.44$ with hydrogen and metal abundances consistent with those suggested by Russell. The model reproduced the observed small Balmer jump that was not found by McCrea (1931). This result was a tremendous success as it is the first time that models accurately reproduced the solar composition, and solar structure. This success became a staging point for modelling the atmospheres of other stars.

Strömgren (1944) produced the first grid of stellar model atmospheres with spectral types A5 to G0 along the main sequence. In this grid, the H^- opacity was the dominant opacity for the cooler models and

the dominant opacity shifted to neutral hydrogen in the A-type stars. The work was extended to hotter stars by Rudkjøbing (1947) who attempted to model the B-type star τ Sco. One of the innovations of these models was the use of the Rosseland mean opacity. Aller (1942) computed models of early types stars as well attempting to analyze the spectra of Sirius and γ Geminorium.

In the 1950's and early 1960's, the number of model stellar atmospheres exploded and are listed in Table 4 of Pecker (1965). Some of the more interesting models were constructed by Pecker (1950), Underhill (1950) and Underhill (1957) of OB stars where they used Λ-iteration to enforce radiative equilibrium

$$\frac{\Delta T}{T} = \frac{1}{4}\left[\int_0^\infty \kappa_\nu (J_\nu - B_\nu) d\nu / \int_0^\infty \kappa_\nu B_\nu d\nu\right], \tag{1.3}$$

and achieved a constant flux of order a few percent for the first time. Hunger (1955), Swihart (1956), and Osawa (1956) compute models for α Lyrae, F5-G2 dwarfs and A-type dwarfs, respectively, and they each applied Φ iteration method to compute constant flux models. The Φ iteration method is an operator such that $\Phi[\Delta B(T)] = -\Delta F$, and the most common version of this type of iteration is the Unsöld-Lucy method (Lucy, 1964). Strom & Avrett (1964a), Strom (1964) and Mihalas (1965) to model stellar atmospheres in the spectral range of O5-F5 with gravities of $\log g$ = 1-4.44 using another type of iteration method for conserving radiative equilibrium based on the Avrett-Krook method (Avrett & Krook, 1963).

It was also in this timeframe where researchers began including convection into the model stellar atmospheres as suggested by Unsöld (1930), who showed that part of the solar photosphere is convective. This result was verified by observations of the solar granulation where it was concluded that granulation arises from convection in the solar atmosphere (Plaskett, 1936). The first models of stellar atmosphere that dealt with convection were by Ueno & Matsushima (1950) but the contribution of convection was very quickly incorporated into other models.

The early 1960's also saw the addition of different physics to the model atmospheres. Gingerich (1963) produced a grid of model atmospheres using molecular opacities to understand the M-type stars. There was also new work on understanding shock waves in stellar atmospheres (Kogure, 1962) and Collins (1965) explored how rotation affects continuum emission from stellar atmospheres.

1.2.3 Development of Modern Stellar Atmosphere Programs

In the latter half of the 1960's computing power was becoming better, computers were becoming more accessible and theorists were much more confident in the physics and the results of the model atmospheres. Hence, researchers began exploring different aspects of the model atmospheres, computing models of more exotic stars, reconsidering the applicability of the physics used in modelling atmospheres, and building the computer programs for computing model atmospheres that have become the workhorses of the field.

It was at this time, researchers began modelling stellar atmospheres with different temperatures, gravities, and compositions, different than the solar atmosphere and different than the main sequence and giant

stars that had been modelled before. The same techniques for modelling the solar atmosphere were applied to modelling the atmospheres of White Dwarfs with gravities ranging from $\log g$ = 6 - 9 and temperatures from 8000 to 25000 K (Terashita & Matsushima, 1966). Simarily, many researchers modelled helium stars where the composition is completely different from solar (Klinglesmith, 1967; Hunger & van Blerkom, 1967; Böhm-Vitense, 1967). Strom (1969) modelled RR Lyrae atmospheres to test the boundaries of the RR Lyrae instability strip. It was also one of the first works to understand the relation of the helium abundance and width of the instability strip. Auman (1969) and Krishna Swamy (1970) constructed models of late-type stars to an effective temperature of 2000 K.

While the model atmospheres were being used to explore more exotic stellar atmospheres, researchers were starting to explore the assumptions that were being used in the construction of model atmospheres. For instance, a number of researchers were testing departures from LTE in stellar atmospheres and began developing models using statistical equilibrium (Strom, 1967; Mihalas, 1967a,b; Mihalas & Stone, 1968; Mihalas, 1968; Auer & Mihalas, 1970; Mihalas & Auer, 1970). These authors found that the assumption of LTE was not applicable for understanding the atmospheres of OB stars.

The assumption of atmospheric geometry was also explored where plane-parallel geometries are replaced by a spherical geometry to explore the concept of extended atmospheres. The physics of extended atmospheres was originally explored Eddington (1930) and Chandrasekhar (1934), but it was not until the 1970's when the physics was applied to model stellar atmospheres. Some of the first articles involved finding solutions to the equation of radiative transfer in spherical symmetry (Chapman, 1966; Hummer & Rybicki, 1971; Castor, 1972; Peraiah, 1973) and spherically symmetric models were build by Cassinelli (1971) to understand planetary nebulae. Mihalas & Hummer (1974) developed computational methods to model extended atmospheres in non-LTE based on the method of Auer & Mihalas (1970) and presented first results for a $M = 60\ M_{\odot}$, $L = 10^6\ L_{\odot}$, and $R = 24\ R_{\odot}$ star. The problem of spherical symmetry was explored in subsequent articles (Kunasz et al., 1975; Mihalas et al., 1975, 1976a,b,c; Mihalas & Kunasz, 1978) as well as by other groups (Hundt et al., 1975; Schmid-Burgk & Scholz, 1975; Watanabe & Kodaira, 1978, 1979).

At the same time, there were other groups who used established techniques to construct "workhorse" programs for modelling stellar atmospheres. There are two programs, that have been important in the field of stellar atmospheres and astrophysics in general. The first is the Atlas stellar atmosphere program (Kurucz, 1970a,b) and the second is the MARCS stellar atmosphere program (Gustafsson et al., 1975). Both programs have been widely used and have helped shape the field of stellar atmosphere modelling and astrophysics in general. The impact of these works is difficult to measure but one may use citation count as a proxy. The Gustafsson et al. (1975) article has been cited 935 times while the Kurucz (1979) article has been cited 3053 times as of June 22, 2009. These citation counts would rank Kurucz (1979) as the 24th most cited article according to the NASA Astrophysics Data System and Gustafsson et al. (1975) the 328th most cited article.

The MARCS program, as described in Gustafsson et al. (1975), models stellar atmospheres under the assumptions of plane-parallel geometry, local thermodynamic equilibrium, and hydrostatic equilibrium. The

opacities are modelled using opacity distribution functions (ODF) that are fits to the opacity as a function of wavelength for some given composition over various ranges of wavelength. The purpose of using ODF's was to decrease computing time, as using all the opacities for each atomic and molecular transition would have been too computationally intensive. The ODF's included metallic and molecular lines. The radiative transfer was solved by the linearization scheme of Auer & Mihalas (1970) and the differential equations were solved using a scheme given by Nordlund (1974) that is based on the Feautrier method (Feautrier, 1964). The program enforced radiative equilibrium and solved for the condition of total flux simultaneously with the equation of radiative transfer and hydrostatic equilibrium. This is done by assuming a grey temperature scale $T^4 = T_{\rm eff}^4 A(\tau + 3^{-1/2})$, where $A = 1$ and perturbing the value of A until the flux error is minimized. Convection in the models are solved using a variant of the mixing length theory (Henyey et al., 1965). Using this program Gustafsson et al. (1975) computed models of low metallicity giants, $3750 \leq T_{\rm eff} \leq 6000\ K$, $0.75 \leq \log g \leq 3$ and $-3.0 \leq [A/H] \leq 0.0$ with a flux error less than 1% for each of the models after a number of iterations.

The Atlas program is described in Kurucz (1970c) and in many ways is very similar to the MARCS program. It assumes a plane-parallel geometry, LTE, and hydrostatic equilibrium, and it also uses ODF's to approximate the opacity as a function of wavelength. The opacities, however, were different because the original Atlas program did not use molecular opacities. Convection is solved using the mixing length theory. The radiative transfer, however, is solved by using the integral solution to the plane-parallel transfer equation, where the source function is guessed and iterated towards a solution (Kurucz, 1969). The flux is conserved using Λ-iteration near the surface of the atmosphere (Böhm-Vitense, 1964) and at deeper layers the Avrett-Krook method is used (Avrett & Krook, 1963). The first published grid of models ranged from $T_{\rm eff} = 5500\ K$ to $50000\ K$, and $0.0 \leq \log g \leq 4.5$ for abundances ranging from solar to $1/100$ of solar. Radiative equilibrium was conserved to about 2%, with the error being primarily due to not including molecular opacities. The Atlas program has been improved by adding more opacities (Kurucz et al., 1987; Kurucz, 1990) and different models of convection have been tested (Lester et al., 1982).

There have been other model atmospheres programs developed about the same time, including a set of non-LTE programs for computing atmospheres of hot, early-type stars (Husfeld et al., 1984; Anderson, 1985; Abbott & Hummer, 1985). The model atmospheres by Abbott & Hummer (1985) include wind blanketing, which has been used to model the atmosphere ζ Puppis (Bohannan et al., 1986). Also, Johnson & Krupp (1976) devised a numerical treatment for opacity sampling in model atmosphere calculations. They applied the method to the Atlas program, and has been applied to cool stars and in particular Arcturus with molecular opacities including TiO (Sneden et al., 1976; Johnson et al., 1977; Krupp et al., 1978; Johnson et al., 1980).

Advances in modelling stellar atmospheres continued in these two fronts. According to Gustafsson (1989), model atmospheres for cool stars had progressed due to advances in opacity calculations to include more molecules but also gave a list of necessary improvements for the modelling programs to be more real-

istic, such as better convection treatment, self-consistent dust opacities, and magnetic fields. On the hot star side, much progress was made in the treatment on non-LTE modelling with the development of approximate Λ operators to solve for the radiation field in statistical equilibrium instead of radiative equilibrium. In this method the equation for radiative transfer is solved by "guessing" the approximate matrix operator Λ^*_ν and iterating the solution for the equation such that $J^{(n)}_\nu = \Lambda^*_\nu S^{(n)}_\nu + (\Lambda_\nu - \Lambda^*_\nu) S^{(n-1)}_\nu$. The challenge of the method is what is the best choice of Λ^*_ν. The approximate lambda operators were first designed to calculate line formation in a velocity field (Hamann, 1985), The method was refined for multi-level atomic transitions (Werner & Husfeld, 1985) and for static stellar atmospheres of hot stars (Pauldrach & Herrero, 1988; Puls & Herrero, 1988; Hillier, 1990; Rybicki & Hummer, 1991; Puls, 1991).

In the 1990's, two new stellar atmosphere programs emerged, the first being TLUSTY (Hubeny, 1988; Hubeny et al., 1994; Hubeny & Lanz, 1995; Lanz & Hubeny, 1995), which uses the approximate lambda operator to solve for line-blanketed non-LTE atmospheres. This program has mostly been applied to the hot star range of the HR Diagram such as hot white dwarfs (Huang et al., 1995; Provencal et al., 2000; Godon et al., 2009), and hot OB stars (Lanz & Hubeny, 2003, 2007), with an emphasis on the ultraviolet spectra.

The second program is the Phoenix stellar atmospheres program (Hauschildt, 1992; Hauschildt et al., 1994; Allard & Hauschildt, 1995). Radiative transfer (the special relativistic version of the transfer equation) is treated in a similar manner as the TLUSTY program with approximate lambda operators that also calculates the non-LTE rate equations simultaneously (Hauschildt, 1993). The line opacities are calculated in situ such that depth dependencies of the line profiles can be accounted for and the geometry was assumed to be plane-parallel, though the spherically symmetric geometry was later added (Aufdenberg et al., 1999; Hauschildt et al., 1999b). The program was primarily developed to model supernovae (Baron et al., 1996) and novae (Hauschildt et al., 1996) but has also been used to model cool M-type dwarfs (Allard & Hauschildt, 1995) and brown dwarfs (Allard et al., 1996, 1997), with the addition of molecular opacities such as water (Allard et al., 1994). As well as the capabilities mentioned before, the Phoenix program is parallized, taking advantage of modern computing techniques that the Atlas and MARCS programs did not. There have been a number of grids of models constructed using this program (Hauschildt et al., 1999a,b; Allard et al., 2000).

More recently, the Phoenix program has been extended to model other systems and approach other problems, for instance, irradiated extrasolar planets (Chabrier et al., 2004), irradiated stars in binary systems (Barman et al., 2004), non-LTE modelling of solar-type stars to explore the effect of the known opacities on the UV flux (Short & Hauschildt, 2005, 2009), modelling chromospheres (Fuhrmeister et al., 2005, 2006), metal-poor stars in non-LTE (Short & Hauschildt, 2006), dust cloud formation in brown dwarfs (Helling et al., 2008), and circumstellar disks (Huegelmeyer et al., 2009).

The Phoenix program has become the benchmark for modelling stellar atmosphere and with constant advances in computational speed and memory, more stellar atmosphere programs are being written and tested while older programs are being upgraded. Kurucz (1996) modified the Atlas program to include

opacity sampling to replace the ODF's. Grupp (2004a) developed a new stellar atmosphere program for modelling stars of spectral types A, F, and G using opacity sampling and a plane-parallel geometry. He tested the program by modelling Procyon, the metal-poor star Groombride 1830, and HD 19445 and found differences between predicted stellar parameters and observed parameters for the latter two stars (Grupp, 2004b). Shulyak et al. (2004) developed a stellar atmospheres program based on the ATLAS program to solve the opacities line-by-line, which is in essence opacity sampling with $\Delta\lambda \rightarrow 0$. Likewise, Gustafsson et al. (2008) have modified the MARCS program to include spherical symmetry and opacity sampling.

Another set of model atmospheres have emerged using three dimensional hydrodynamics. The 3-D models have been constructed to model the solar convection zone and its interaction with the photosphere. Of particular importance is the results of Asplund et al. (2005), who argued the solar composition is much lower than the standard solar model (Grevesse & Sauval, 1998), such that the abundance of metals is one-half. Other models have been constructed with differing metallicities (Caffau et al., 2009). Most of the 3-D models have tended to focus on simulating convection, Freytag et al. (2002) modelled convection in Betelguese, and Aufdenberg et al. (2005) combined 3-D models with PHOENIX models to explore the behavior of convection of Procyon. The 3-D model atmospheres are a significant step towards a physical understanding of real stellar atmospheres but they are still somewhat impractical because they are box simulations, meaning the simulation covers only a portion of the surface and they are very computationally expensive, requiring a significant amount of resources. It will still be some time before 3-D simulations of stellar atmospheres are norm.

The development of all of these stellar atmosphere programs have been one of the great successes of stellar astrophysics but there are still a number of challenges to be addressed, as noted by Landstreet et al. (2008). Some of these challenges include a better understanding of stellar convection as is being done with the 3-D models, various aspects of abundances and line formation as well as solving the so-called solar crisis ignited by Asplund et al. (2005) and to understand the coupling of the various phenomena such as mass loss and pulsation to the structure of stellar atmospheres.

1.3 History of Cepheids

Like stellar atmospheres, the historical account of Cepheids spans a long period of time, since the discovery of variability in δ Cephei by John Goodricke in 1784 (Goodricke & Bayer, 1786) and η Aquilae by Edward Pigott. This type of star has been both an enigma and a godsend. The variation of light is a puzzle for stellar physics, stellar structure and stellar evolution but this variation provides an ideal laboratory for theories of stellar physics as well as providing a Period-Luminosity relation (Leavitt Law) that makes them powerful standard candles for extragalactic and cosmological studies. Much of this discussion is based on Hoffleit (1986) and Gautschy (2003).

The discovery of the variation of light in Cepheids and other stars provided a great mystery in astro-

physics as these observations violated the Aristotlean paradigm of a static universe. As well as discovering η Aql. Edward Pigott discovered about a dozen other variable stars although before 1600 AD, more than 500 variable stars were recorded in China (Ho & Ho, 1962; Hoffleit, 1986). By the mid 1800's, a large number of variable stars had been discovered (Argeländer, 1843, 1857, 1859) and under the leadership of E.C. Pickering many new variable stars were discovered (for example, Pickering, 1881; Pickering & Bailey, 1895).

Variable stars were first classified into a number of groups as suggested by Pickering (1880, 1881). The variable stars were divided into five classes. The first class, Class I, contains new stars or temporary stars such as supernovae; stars of Class II are the long period variables such as Miras; and the Class III stars have irregular variation of brightness. The Class IV stars are short period variables, including Cepheid variables and Class V stars are those of Algol type. The Class II stars were subdivided into Class IIa, which are "ordinary" long-period variables and Class IIb contained U Geminorum and SS Cygni (referring to dwarf novae). Likewise the Class IV stars were also subdivided with Class IVa being the ordinary short-period variables and Class IVb containing β Lyrae and U Scuti (stars of β Lyrae type). By 1900, the list of variable stars had grown substantially (Pickering, 1903).

The main mystery of Cepheids and other variable stars in the 1800's was the source of brightness variation. There were a number of theories proposed: such as starspots, binarity, ellipsoidal shape of the stars, that the variable stars are surrounded by some sort of nebular material that causes eclipses, and pulsation. Wolf (1863) proposed that variable stars have spots on the stellar surface analogous to those on the Sun which may cause the brightness variations, an argument supported by Backhouse (1882) who calculated the number of dark strips required to reproduce observations of δ Cephei (Pickering, 1881). Birmingham (1877) proposed that the variations are due to an orbiting body, "... but it appears to me that a nebulous ring revolving round the variable would best account for the different phases of the phenomenom." This ring would have more matter on one side and less on the other and have several points of material accumulation to account for secondary brightness variations. This idea is similar to that proposed by Klinkerfues (1865), who proposed that two stars have close encounters where tidal effects distort the star and cause traveling tidal waves along the surface (Clerke, 1903). Lockyer (1889) argued that brightness variations are due to swarms of cometary and meteoric material that orbit the star, left over from star formation. This theory was designed to fit in with his theory of stellar classification and evolution. Pickering (1881) used Wolf's idea of starspots and went further to explain the variation of the Class IV variables by suggesting that the stars must be non-spherical and instead be oblate ellipsoids with one side of the star being intrinsically brighter than the other. Roberts (1895) did an extensive analysis of the lightcurves of short-period variables in an attempt to show that they are all binary systems. While there were admitted flaws with the concept, it appeared that binarity was a reasonable possibility and was heavily advocated. Clerke (1903) wrote

> A large class of variable stars, in fact, undergo what may be called compulsory vicissitudes; they partake, in other words, of the character of "forced vibrations"; they are obviously prescribed

> by the revolutions of a companion. That all congeners of δ Cephei are spectroscopic binaries is beyond reasonable doubt; in all (it is safe to assert) motion and light-changes follow an identical period; yet none suffer eclipse.

Pulsation was first proposed in a series of articles on heat transfer in stars by (Ritter, 1879, described by Hoffleit (1986)) as well as by Plummer (1914) but no physical reason was given. The idea of Plummer (1914) that pulsation was the source of variation was based on the consideration that most of these stars could not be spectroscopic binaries from the doppler interpretation of line shifts.

Some of these theories proposed are interesting in their own right because, in hindsight, they are similar to modern theories. The theories of meteor swarms and nebular rings is analogous to the concept of debris disks that are observed, while starspots are being observed for a number of different stars and, in particular, the RS CVn stars. Pickering's concept of a distorted shape for stars is analogous to the idea that rapid rotation changes the shape of stars such as the Be stars. However, these various theories were not applicable to Cepheids and other short-period variables.

New observations near the end of the 19th century would aid in the understanding of brightness variation. Belopolsky (1895) analyzed time-series observations of the spectrum of δ Cephei and measured the velocity as a function of time as well as determining the velocities for η Aquilae. The work made an immediate impact on the understanding of Cepheids

> It will be seen the times of minimum brightness and the times for which the velocity in the line of sight is zero do not coincide. For this reason the changes in the brightness of the star cannot be explained as the result of eclipse, and some other explanation must be sought. It is very remarkable that this is also true of the variable star δ Cephei.

This one result disproved the starspot concept, the nebular ring and meteoric swarm theories. More observations were undertaken, for instance Belopolsky also studied Polaris and ζ Geminorum (Belopolsky, 1899, 1900). Frost (1907) measured the radial velocity of X Cygni and Campbell (1907) measured the velocity for Polaris as part of the large program at the Lick observatory to measure radial velocities.

The velocity curves of Cepheid variables were one piece of the puzzle and Schwarszchild (1900) added another piece. From observations of η Aquilae, he found that the stars color varied over the period of light variation, timplying that the temperature of the star was changing over time. From these two results, all theories but pulsation and binarity could be discarded, though the tidal theory did hang on for some time. However, Shapley (1914) provided sufficient evidence to eliminate the binary hypothesis by considering the vast amount of observations of the radial velocities of Cepheids (such as ζ Geminorum (Campbell, 1901; Russell, 1902; Plummer, 1913), W Sagittarii (Curtiss, 1904), Y Ophiuchi (Albrecht, 1907), and RT Aurigae (Duncan, 1909)) and the error of fitting binary orbits to that data. Furthermore, he noted the results of Russell (1913b) and Hertzsprung (1914) where Cepheids were found to be giant stars and hence have radii much larger than the Sun. This would suggest that if Cepheids were spectroscopic binaries then the orbital

separation of the two stars must be much less than the radius of a Cepheid. While this result did not end the debate right away (a number of authors continued to explore the binary hypothesis, most notably Jeans (1925)), this work did lead the way for researchers to explore the pulsation hypothesis.

The pulsation hypothesis was explored by both Ritter (1879) and Plummer (1914) but it was Arthur Eddington that developed the theory of pulsation. Eddington (1917b) argued that pulsation might occur in stars if the stars behaved as thermodynamic engines,

> There is an evident supply of energy which might be utilized, sine heat is continually liberated within the star and passes outward into space; this may be borrowed and converted into energy of pulsation. But, in order to convert hear of any kind into work, the star, or some part of it, must behave as an engine in the thermodynamical sense: that is to say, it must take in heat when it is at a higher temperature than the average and give out heat at a lower temperature – just the opposite to what usually happens in natural conditions.

In his following two articles (Eddington, 1918, 1919b), Eddington treated a Cepheid as a polytropic adiabatic gas sphere and used linear perturbation theory to derive the Period-Density (in this case Eddington used the central density of a polytrope) relation, $P\sqrt{\rho_c} \approx$ Constant. Using this relation, it was also determined that the observed rates of period change of Cepheids are too small for the stars to be generating energy from gravitational contraction. In the second article, Eddington (1919b) argued that the observed phase lag of pulsation, defined as the phase difference between the time of maximum brightness and the time of maximum compression, was the result of non-adiabatic effects. In the adiabatic case the phase lag would be zero because the temperature variation must be in phase with the radius variation. It is from these two articles that the field of pulsation modelling began.

At the same time, Cepheids were being observed along with many other stars under the leadership of Pickering at Harvard. In one article in the Annuals of the Harvard College Observatory (Leavitt, 1908), one of Pickerings assistants Henrietta Leavitt announced the discovery of 1777 variable stars in the Magellanic Clouds and the author pointed out that "It is worthy of notice that is Table VI (listing the properties of some of the observed Cepheids) the brighter variables have longer period. It is also noticable that those having the longest periods appear to be as regular in their variations as those which pass through their changes in a day or two." This short afterthought was one of the most profound insights in astrophysics. Miss Leavitt had discovered that Cepheids follow a Period-Luminsity relation (also now called the Leavitt Law). In Leavitt & Pickering (1912), the relation was plotted and shown that the brightness in units of magnitudes is a linear function of the logarithm of the period. A review of this discovery and the biography of Henrietta Leavitt is given by Johnson (2005).

The two monumental discoveries by Arthur Eddington and Henrietta Leavitt motivated a field of research that impacts stellar astrophysics, cosmology and everything in between. A historical review of the progress made in understanding these stars is divided into three parts: 1) observations and physical properties, 2)

statistical properties of Cepheids, and 3) theoretical Cepheid modelling.

1.3.1 Observations of Cepheids

Early History

Cepheids had been observed for a significant period of time before Eddington presented his pulsation theory and the theory became a topic of much interest. Observations were becoming plentiful, in particular time series observations of light curves and velocity curves. One just had to follow the Harvard Circulars or Annals of the Harvard Observatory (Robinson & Shapley, 1940). Radial velocity curves were observed by Jacobsen (1926), Sanford (1930), Sanford (1935b), and Sanford (1935a). In particular, Joy (1937) observed velocity curves for 128 Cepheids. There were other observations that had significant impact on the understanding of these stars. One of the most important contributions of continued monitoring of the light curves was the determination of a "hump" in the light curves following brightness maxima (Okunev, 1929). The existence of the hump in the lightcurve could not be explained Eddington's pulsation theory and was subsequently used as a reason to support the binary theory of Cepheid light variation (Perrine, 1919). The location of the secondary hump in the lightcurve was shown to shift as a function of period and became known as the Hertzsprung Progression (Hertzsprung, 1926).

One of the first measurements of distances to Galactic Cepheids was by Harlow Shapley (Shapley, 1918), where the measurements were supported by the results of Kapteyn & van Rhijn (1922). He determined the statistical parallax for 139 Cepheids. The precision was not ideal, for instance, he found the distance to ζ Geminorum to be about 280 parsecs while current estimates are about 500 pc (Kervella et al., 2001). Regardless of this fact, by determining the distances to these Cepheids Shapley changed the standard view of these stars as it meant that Cepheids were much more luminous than the Sun.

Along with finding the distances to Cepheids, researchers were beginning to measure the period of pulsation so accurately that they were also beginning to measure the rate of period change of the star. Eddington (1919a) determined the rate of period change for δ Cephei and found that the period was decreasing but at a very slow rate. He used this result and the fact that a Cepheid's period is inversely related to the mean density of the Cepheid to show that this means that the mean density of δ Cep is increasing. However, the rate of density increase was much too small to be consistent with the theory that a star generates its energy from contraction. Thus, Eddington began to disprove that hypothesis, and this led him to eventually consider that a star generates energy from nuclear reactions. Wylie (1922) measured the rate of period change for η Aquilae, as well, and found the rate of period change was increasing (Wylie, 1922). An increasing rate contradicted the idea that a Cepheid's rate of period change was from contraction generating energy.

The first spectral observations were done by Belopolsky (1899) and others soon followed, determining the velocity curves of Cepheids. It was not until almost twenty years later that other properties of Cepheids were determined from spectra. Cannon & Pickering (1912) noted changes in the intensity of the hydrogen

lines, especially those at ultraviolet wavelengths, in the spectra of δ Cep at different times. In terms of spectral type, Shapley (1916) observed that a Cepheid's spectral type varies over its period. He observed the spectra of twenty different Cepheids with a total of 328 photographs of spectra. The Cepheids were found to vary from late A-type to early G-type over a period, where the Cepheids appeared to be of A-type at maximum brightness and of late spectral type at minimum brightness. This results confirmed the results of Schwarszchild (1900) that a Cepheid's color changes with phase of a period, since, a stars spectral type is a measure of the temperature of the star.

Henroteau (1925) presented spectral observations of δ Cep, η Aql, ζ Gem, and Polaris and monitored the neutral and ionized titanium lines at λ 4534.953 and λ 4534.139, respectively. He found that these two lines varied, from one line being twice as intense as the other at one time and much weaker at other times. For δ Cep and η Aql, the minimum ionization corresponds to minimum brightness, however, for ζ Gem minimum ionization was seen by Henroteau at about a quarter of a period after maximum brightness. This was some of the first evidence for atmospheric dynamics related to the variation of light and that the time dependent behavior varies for different Cepheids. Similarly, Hughes (1931) studied the ionization of calcium in forty-two Cepheids and found that the phase at which maximum ionization occurs varies as a function of period. For long-period Cepheids, the phase of maximum ionization corresponds to the phase of maximum brightness with the phase of maximum ionization shifting towards minimum brightness with decreasing period.

Atmospheric motions in Cepheids were explored by Petrie (1934) for RT Aurigae by analyzing time series observations of a number of spectral lines and grouping them into bins of eight heights in the photosphere. He determined that the velocity profiles for each group varied but had the same period. The velocity profile for higher regions of the atmosphere had a phase lag for the maximum velocity compares to velocity profiles for groups of lines that exist deeper in the atmosphere. It was also found that the lines near the top of the atmosphere had a larger range of velocities. Petrie (1937) repeated the analysis for δ Cep with three groups of lines and found similar results. Jacobsen (1949), again, repeated the analysis for δ Cep, with three of the same groupings of lines corresponding to height in the photosphere plus a new group of lines representing the location of the chromosphere. The chromospheric lines show similar behavior as before, having a larger range of velocities.

A test of the pulsation model was devised by Baade (1926), who suggested that if a Cepheid is pulsating then the radius of the star should vary as well as the luminosity and velocity. The radius at any one time is proportional to the square-root of the luminosity and inversely proportional to the effective temperature squared, One can use the color of the star as a proxy for the effective temperature and the luminosity is the observed flux divided by the distance squared. If one considers the ratio of the radius of a Cepheid at times t_1 and t_2 then

$$\frac{R_*(t_1)}{R_*(t_2)} = \sqrt{\frac{F(t_1)/4\pi d^2}{F(t_2)/4\pi d^2} \times \frac{\mathrm{Color(t_2)}}{\mathrm{Color(t_1)}}}. \tag{1.4}$$

To get a value of the radius, the radial velocity curve is then integrated with respect to time to determine the amplitude of radius variation, assuming that the radial velocity, v_R, is directly proportional to the velocity of pulsation, v_P. The ratio of v_P/v_R, the projection factor, is typically assumed to be about 1.3 based on using a standard limb-darkening profile for the Cepheid. The method was refined by other authors, in particular Wesselink (1946), hence the accepted name, the Baade-Wesselink method. An example of its usage is the determination of the radius of δ Cep by Wesselink (1946, 1947), who found a value for the mean radius $R = 48\ R_\odot$.

The method suggested by Baade motivated more spectral observations for effective temperature determinations. Whipple (1932) observed a number of lines as a function of time for δ Cep and η Aql. Using these spectrophotometric observations, he determined the effective temperature of each Cepheid at maximum and minimum brightness. For δ Cep, the temperatures are 6800 and 4800 degrees and for η Aql the temperatures are 6000 and 4000 degrees, respectively. Using these results, Whipple computed the radii of the two Cepheids and found the radii were much smaller than radii determined using the Leavitt Law for the luminosity.

Cepheid radii were explored by Bleksley (1936), who assumed that Cepheids behaved as near perfect blackbodies to derive a relation for the radius in terms of the temperature and bolometric magnitude. The temperature is found from the bolometric correction to the visual brightness of the star. Using this result, the author found that rT, radius times temperature, and is roughly constant for Cepheids, suggesting a simple method of radius determination as well as the Baade-Wesselink method.

In the late 1940's, observers began detecting emission lines in Cepheids. van Hoof (1948) observed that the shorter wavelength component of the H & K lines was in emission for part of the period. The emission was observed when the Cepheid brightness was increasing near the phase of maximum brightness until just past maximum brightness when the emission line disappeared. The effect was also found in η Aql (Joy & Wilson, 1949; Jacobsen, 1950), ζ Gem (Joy & Wilson, 1949), and S Sagittae (Herbig, 1952b). van Hoof argued that the variable emission line is due to the superposition of a nearby absorption profile at certain phases. Herbig (1952a) found this behavior to be common, observing it in seven more Cepheids including δ Cep. Kraft (1957) compiled observations of the H & K lines and argued the emission was related to the formation of a hydrogen convection zone in the atmosphere. He also found that the behavior of the emission lines is dependent on the gravity of the Cepheid.

By the 1950's, only two Cepheids were known to be part of binary systems, Polaris was discovered to be in a spectroscopic binary (Moore, 1929) and δ Cep as discovered by Belopolsky (1899). Along with the analysis of the spectral lines of S Sagittae, Herbig & Moore (1952) discovered it was also in a spectroscopic binary with a period of 1.85 years. Abt (1959) discovered that FF Aquilae is in a binary with a period of 1435 days. Lloyd Evans (1968) compiled radial velocity observations for 24 Cepheids to search for binarity. He found that the Cepheids S Muscae, AH Velorum, AW Persei, and V Carinae are in binary systems. The binary Cepheid HR 8157 was studied by Millis (1969); Abt & Levy (1970), whiere the Cepheid has a close

visual companion. Binarity is important for understanding Cepheids as it is a potential measure of the mass of the Cepheid.

In a series of articles, the atmosphere of β Doradus was studied using nine spectrograms (Rodgers & Bell, 1964). The observations were used to construct curves of growth and determine the composition of the star. The abundances of β Dor are found to be approximately solar. In their second article (Bell & Rodgers, 1964), the authors compared Fe II line profiles at $\lambda = 4508$ Å observed throughout the pulsation cycle with line profiles from theoretical stellar atmospheres. The comparison was done to determine the microturbulent velocity as a function of phase; they found that the microturbulent velocity is roughly constant with respect to phase. A more important observation was asymmetries in the Fe II line profiles at phase about 0.3. This was interpreted to be a wave propagating in the atmosphere.

Bell & Rodgers (1967) repeated the analysis using time-varying Hα line profiles in β Dor and compared them to theoretical line profiles from model stellar atmospheres. They found that the line cores were not reproduced by the models but did fit the line wings well and could be used to predict the effective temperature of the Cepheid as a function of phase. The effective temperature of β Dor was found to range from 5900 K to 6350 K. Rodgers & Bell (1967) studied the Hα line profiles for S Muscae and determined the effective temperature for that Cepheid. The authors also studied unpublished Hα line profiles for the long-period Cepheids l Carinae and RS Puppis but found that effective temperatures could not be fit to the line profiles. This is because the Hα line profiles show "that the redward side of the profile is affected by reversed P Cygni type absorption and emission which persists throughout the cycle". Rodgers & Bell (1968) showed that the Hα line profiles for l Car are obscured by chromospheric lines and instead assumes an iron abundance to derive an effective temperature. The role of Hα as a temperature indicator was verified by Schmidt (1970).

High spectral resolution observations were taken of RT Aurigae and analyzed by Bappu & Raghavan (1969) with the goal of determining atmospheric parameters. The authors used the Baade-Wesselink method to find a radius of 33.7 $R_\odot$ and found the abundance to be nearly solar using the curve of growth. Breger (1970) found a larger Baade-Wesselink radius of of $49 \pm 6\ R_\odot$ for S Norma but found a radius $R = 60\ R_\odot$ by using other methods. Parsons (1972) presented new values for the radii of a number of Cepheids based on an analysis of the projection factor, p. He found that the value of the p-factor is lower than traditionally used based on line profile calculations. Better agreement was found between radii computed using the Baade-Wesselink method and those found using the Period-Luminosity-Color relation for Cepheids. Parson's work demonstrated the weakness of the Baade-Wesselink method, being the assumption of the p-factor. The Baade-Wesslink method was used by Evans (1976) to determine radii of 14 Cepheids using the traditional value of the p-factor. She found the radii differed from the radii predicted by theory and from earlier calculations. This suggested an uncertainty of about 10% for the Baade-Wesselink method and 30% discrepancy for the mass estimates using theoretical Period-Mass-Radius relationship.

Cepheids had been observed to be mono-periodic, with the exception of Cepheids in binary systems, but a number of Cepheids were being observed to have secondary periods. Oosterhoff (1957a) found a

secondary period for TU Cassiopeiae. The primary period is $P_0 = 2.139$ day and the beat period is 5.230 days. A secondary period was also observed for U Trianguli Australis (U TrA) by Oosterhoff (1957b), who found a fundamental period of $P_0 = 2.568$ day and the beat period is 6.9795 day. Other Cepheids were found to have beat periods such as AP Velorum (Oosterhoff, 1964), BK Centauri (Leotta-Janin, 1967), and V 439 Ophiuchi (Gusev, 1967). Faulkner (1977) further studied the Cepheid U TrA confirmed the beat period. The beat Cepheids were found to be an important tool for predicting stellar masses from theoretical pulsation studies.

Petersen (1973) used the ratio of the fundamental and secondary periods to determines masses for eight beat Cepheids and found masses ranging from $0.7 \leq M/M_\odot \leq 1.7$. Stobie (1977) did a similar analysis and found a mass range $1 \leq M/M_\odot \leq 3$ and noted that the beat Cepheid masses are inconsistent with normal Cepheids. This suggested that the beat Cepheids were of a different evolutionary sequence than other Cepheids or that the masses were dramatically underestimated.

Particular interest was shown in the Cepheid RS Puppis; Havlen (1972) observed the reflection nebula surrounding the Cepheid. He modelled the nebula as four concentric dust shells that surround the Cepheid due to mass loss when the Cepheid enters or exits the Instability Strip. Based on this assumption, the total dust mass of the nebula is determined to be $M = 0.03\ M_\odot$. Later, Deasy (1988) speculated that each shell corresponded to mass loss on the crossing of the Instability Strip, and the rate of period change required RS Pup to be a crossing the Instability Strip for the fifth time. However, there are no Cepheids confirmed to be on the fifth crossing, the behavior is predicted by some stellar evolution models (Iben, 1965; Xu & Li, 2004). It was also noted that it is strange that RS Pup is the only long-period Cepheid to have a dusty nebula. If the nebula were due to mass loss then surely more Cepheids would be embedded in nebulae. It must be noted that SU Cassiopea is also associated with a reflection nebula but has a pulsation period of 1.95 day (van den Bergh, 1966).

At this time, the evolutionary sequence and source of the variability in Cepheids was understood from theory; this will be reviewed in later sections. However, there were still a number of questions about Cepheids such as their masses, and by 1980 there were new options to study Cepheids at infrared and ultraviolet wavelengths.

Observations of Cepheids from 1980 - 2000

In the 1980's, new observing facilities were coming on-line; for instance, the International Ultraviolet Explorer was launched in 1978. Cepheid observations were becoming much more abundant and much more precise, with new, more exotic Cepheids being discovered. For instance the Cepheid, HR 7308, was discovered to have the shortest known period of any Galactic Cepheid and was first studied by Michel Breger from 1966 to 1969 (Breger, 1980). He found that HR 7308 has a varying brightness amplitude, and argued that it may be a double-mode Cepheid with a period ratio of almost unity. Burki & Mayor (1980) observed the Cepheid spectroscopically and measured the radial velocity. They observed that the Cepheid's radial veloc-

ity amplitude had decreased from 1977 to 1979. The decrease of radial velocity amplitude was confirmed by Percy & Evans (1980), where the authors also found that HR 7308 had metal abundances similar to the Sun.

The controversy of the masses and the structure of beat Cepheids was still alive in the 1980's; Barrell (1982) observed spectra of nine beat Cepheids and using stellar atmosphere models plus Baade-Wesselink radii calculated the masses for five of the Cepheids. He found the spectroscopic masses to be consistent with masses of other Classical Cepheids predicted from stellar evolution calculations and argued that beat Cepheids are not a different type of object. On the other hand, IUE observations of binary Cepheids were used to constrain the mass of the companion star. From this, Böhm-Vitense & Parsons (1983) found that the Cepheids are too luminous for the determined mass, meaning the determined masses are less than the masses from stellar evolution calculations. Gieren (1989) attempted to determine the masses of 101 Cepheids based on the Baade-Wesselink method. The predicted masses were found to differ by about 20% from those masses derived from stellar evolution models.

One of the best but most challenging methods for solving the mass discrepancy is to determine dynamical masses of Cepheids in binary systems. Based on IUE observations , Böhm-Vitense et al. (1990) determined the mass of S Muscae to be in the range of $4.6 < M/M_{\odot} < 6.1$, compatible with predictions from stellar pulsation theory but not stellar evolution. They also found the mass of SU Cygni to be $\geq 5.9 \pm 0.4\ M_{\odot}$, consistent with the masses determined from stellar evolution (Evans & Bolton, 1990). Böhm-Vitense et al. (1997b) used high resolution spectra for the binary system S Mus to determine the mass of the Cepheid to be $5.9^{+0.7}_{-0.6}\ M_{\odot}$ which indicates a disagreement with the results of standard stellar evolution models. A dynamic mass was also determined for the beat Cepheid Y Carinae to be $M = 3.8 \pm 1.2\ M_{\odot}$, which is consistent with masses from stellar pulsation models (Böhm-Vitense et al., 1997a) and Evans et al. (1997) found the mass of V350 Sgr to be $5.2 \pm 0.9\ M_{\odot}$. Evans et al. (1998a) determined a mass of U Aquilae of $5.1 \pm 0.7\ M_{\odot}$, again inconsistent with standard stellar evolution models. The dynamic mass of V636 Scorpii was found to be $M = 3.1 \pm 0.4\ M_{\odot}$, making it a very, low mass Cepheid and more inconsistent with stellar evolution (Böhm-Vitense et al., 1998). These results suggest that the pulsation masses are more accurate than those from stellar evolution calculations.

The usage of UV satellite observatories gathered significant information about the possibility of chromospheres around Cepheids. The first observations were of the Mg II line at 2795 Å in β Doradus (Schmidt & Weiler, 1979). The emission line was observed to vary with phase and normally be stronger than the same line in non-variable supergiants. They argued this result is due to a shock in the atmosphere traveling outwards heating the chromosphere near minimum radius where the emission line is strongest. Similar observations of β Dor and δ Cep were taken using IUE where the Mg II and O I emission was detected at all phases for β Dor but not detected at all in δ Cep (Parsons, 1980). From low resolution observations of five Cepheids, Schmidt & Parsons (1982) found that the amplitude of light variation in the Cepheids rises with decreasing wavelength near or shortward $\lambda = 1550$ Å where the amplitude suddenly decreases.

The decrease is argued to be due to the presence of Si I line at $\lambda = 1683$ based on the analysis of static plane-parallel stellar atmosphere models. In the second article of the series (Schmidt & Parsons, 1984b), the authors analyzed high resolution Mg II h and k line profiles for the same five Cepheids. Emission features were observed to be consistent with a weak chromosphere, and a central absorption feature was also discovered for each star indicating the presence of circumstellar gas at a few tenths of a stellar radii from the star. They noted that the emission lines from Cepheids differ from non-variable supergiants, suggesting pulsation tends to inhibit the formation of a chromosphere. In a third article Schmidt & Parsons (1984a) showed that δ Cep and other short-period Cepheids show very weak Mg II and O I line emission relative to the long-period Cepheids such as l Car and thus the atmospheric structures of short-period and long-period Cepheids must be different. Böhm-Vitense & Parsons (1983) observed δ Cep, β Dor and ζ Gem at X-ray wavelengths to explore the chromospheric structure of these stars. However, no X-ray flux was observed for the first stars with the possible detection for ζ Gem.

At the other end of the spectrum, Welch et al. (1984) observed sixty-nine Cepheids at infrared wavelengths, J, H, and K to determine infrared amplitudes of brightness variation. They found that IR amplitudes tend to be smaller than the amplitudes in U, B, and V magnitudes for the same Cepheid. McAlary & Welch (1986) detected Cepheids using the Infrared Astronomical Satellite (IRAS) at $\lambda = 12$ and 25 μm. Some of the Cepheids show IR excesses, assumed to be from dusty mass loss with rate $\approx 10^{-9} - 10^{-8}\ M_{\odot}/yr$. A similar analysis of IRAS observations of Cepheids was conducted by Deasy (1988) where the ratio of 25 μm flux and 12 μm flux from Cepheids are compared to that ratio for non-pulsating supergiants. They found that Cepheids have a significant range of IR excess, from almost no excess to an excess of about three times the stellar flux at these wavelengths. This suggests that the Cepheids have mass-loss rates ranging from $10^{-10} - 10^{-6}\ M_{\odot}/yr$.

At even longer wavelengths, Welch & Duric (1988) observed five Classical Cepheids using the Very Large Array (VLA) and found that the upper limits of the 5 GHz flux density was between 120 and 180 μJy. The goal of these observations was to test for mass loss in the form of ionized gas at temperatures of about $10^4\ K$. The mass-loss rates derived from the flux density are approximately $10^{-9} - 10^{-8}\ M_{\odot}/yr$.

Infrared (1.1 μm) spectra of the Cepheids X Sagittari and η Aquilae were obtained by Sasselov et al. (1989). They found line doubling and asymmetries in the spectral lines and argued that the asymmetry is the result of blending of two absorption components of differing strength. The combination of these two effects change the amplitude of the radial velocity variation suggesting that the true amplitudes are about 30% larger than the amplitudes derived from optical observations, with implications on the value of the Baade-Wesselink radii derived from infrared photometry. In a follow-up article, Sasselov & Lester (1990) presented high resolution IR spectra of seven Cepheids in the wavelength range $1.08 \leq \lambda \leq 1.6\ \mu m$. Again, IR line asymmetries and line-splitting were observed, in which the phenomenon was attributed to pulsation driving shock waves in the atmosphere.

The He I λ10830 line was first observed by Sasselov & Lester (1994a) for seven Cepheids including X

Sgr, η Aql, and ζ Gem. They found that the absorption line was present throughout the pulsation cycle of the Cepheids and also found to be blueshifted in four of the Cepheids indicating an outflow of material. For the case of δ Cep, the line was not seen at phase 0.95, while for ζ Gem the line was also seen in emission. The detection of this line in Cepheids is evidence for high-temperature ($>> T_{\rm eff}$) plasma in the atmospheres of Cepheids. For the case of ζ Gem, the plasma is about 0.25 R_* above the photosphere. Analysis showed that the He I λ10830 line was formed by collisional excitation in the atmosphere (Sasselov & Lester, 1994b).

Breitfellner & Gillet (1993a) analyzed high resolution spectra of δ Cep in two spectral domains and compared the Hα and Sodium D line widths with pulsation models to determine an upper limit of the rotational velocity $v_R \sin i = 9\ km\ s^{-1}$. In these observations line-doubling was not seen, consistent with the earlier results of Schmidt & Parsons (1982). The observations were repeated for η Aql and S Sge (Breitfellner & Gillet, 1993c), who found a higher rate of turbulence than for δ Cep. They argued the difference to be due to the periods of η Aql and S Sge being near the resonance period (around $P \approx 10$ days) causing the atmosphere to become compressed at a later phase. The timing of maximum compression coincides with the outward propagation of the acceleration front increasing the macroturbulent velocity. The rotational velocities were argued to be $v_R \sin i = 10\ km\ s^{-1}$ and $5\ km\ s^{-1}$ for η Aql and S Sge, respectively. The third article of the series (Breitfellner & Gillet, 1993b) focused on observations of the large amplitude Cepheid X Cygni. From the spectral observations, two consecutive accelerations were found in the stellar atmosphere. The first acceleration is due to the propagation of a slow wave in the atmosphere increasing the turbulent velocity, while the second acceleration is a shock propagating in the turbulent atmosphere.

By the mid 1990's, optical interferometry had developed to the point where Cepheid observations were possible, Mourard et al. (1997) measured the mean angular diameter of δ Cep with the Grand Interféromètre à deux Télescopes. The power of interferometry is the ability to directly measure the apparent diameter of a star. When interferometric observations are combined with other information such as the radial velocity observations or distance estimates using the Leavitt Law, one can measure the actual diameter of a Cepheid. Mourard et al. (1997) determined a value of 1.60 ± 0.12 mas and they used published values of the radius to calculate the distance the Cepheid, consistent with Hipparcos parallax and other methods. The Cepheid ζ Gem was observed using the IOTA interferometer and the mean angular diameter was observed to be $2.065^{+0.087}_{-0.091}$ mas with a marginal detection of the variation of angular diameter due to pulsation with an amplitude of $0.204^{+0.198}_{-0.187}$ mas (Kervella et al., 1999). Nordgren et al. (2000) measured the angular diameters of four Cepheids δ Cep, Polaris, η Aql, and ζ Gem to be 3.28 ± 0.02, 1.52 ± 0.02, 1.73 ± 0.05, and 1.55 ± 0.09 mas, respectively using the Navy Prototype Optical Interferometer.

Fouque & Gieren (1997) calibrated the surface brightness-color relation for Cepheids, allowing for better Baade-Wesselink radii to be determined. Thy calibrated the relation using Cepheids with known values of radii and color. The surface brightness technique assumes that the surface brightness of a Cepheid is related to the color of that Cepheid meaning=g that the surface brightness in the visual band is $F_V = 4.2207 - 0.1V_0 - 0.5 \log \theta$ and that it is also $F_V = b + m(V - R)_0$. The difficulty of the surface brightness

technique is the calibration of this second relation. Fouque & Gieren (1997) calibrated the technique for $F_V, (V-R)_0$, $F_V, (V-K)_0$, and $F_K, (J-K)_0$ relations to high accuracy allowing the determination of Cepheid distances to an accuracy of $5-10\%$ using the Baade-Wesselink method.

An interesting result was determined for Polaris by Fernie (1993), who discovered that the pulsation amplitude has been decreasing. Before 1900, the visual amplitude was about 0.12 mag and the velocity amplitude 6.0 $km\ s^{-1}$ while by 1992, Fernie (1993) found that the amplitudes were $0.59 \pm 0.19\ km\ s^{-1}$ and 0.010 ± 0.002 mag. The O-C (Observed minus Calculated period versus Julian Date) diagram for Polaris was also determined and the period was found to change not just because of stellar evolution. He suggested that Polaris is changing from a Cepheid to a non-pulsating star but strangely the star's location on the H-R Diagram coincides with other Cepheids of similar period that do not have decreasing amplitudes and are not near the red edge of the Cepheid Instability Strip.

The construction and funding of microlensing surveys to detect microlensing events in the halo of the Milky Way led to a plethora of observations of Cepheids. Three microlensing surveys were started in the 1990's with time-series observations of the Galactic bulge, and the Magellanic Clouds. The EROS survey presented results for the bar of the Large Magellanic Cloud (LMC) for 97 Cepheids (Beaulieu et al., 1995) as well as the discovery of eleven beat Cepheids in the Small Magellanic Cloud (SMC). Welch et al. (1997) presented observations of approximately 1500 Cepheids in the LMC from the MACHO project, of which 45 beat Cepheids were analyzed to understand the second overtone of pulsation (Alcock et al., 1999). The OGLE-II survey found 2049 Cepheids in the SMC (Udalski et al., 1999c) and 1333 Cepheids in the LMC (Udalski et al., 1999b) and presented data in the B, V, and I-bands. Also, in this survey 13 single-mode second overtone Cepheids were discovered in the SMC (Udalski et al., 1999b) as well as 93 double-mode Cepheids (Udalski et al., 1999a). The discovery of all these Cepheids in the three surveys is important for understanding the nature of Cepheids at different metallicities and for finding unique Cepheids to be studied.

Recent Observations

By the turn of the century, one hundred years after the observations of the variation of velocity by Belopolsky (1899), there were still more questions regarding the radii and masses of Cepheids, and the structure of Cepheid atmospheres. Probing these questions require better observations and observing facilities, and recent Cepheid observations have served to address these questions while further adding new and existing discoveries and challenges.

Spectropolarimetric observations of η Aql by Plachinda (2000) revealed that this Cepheids has a magnetic field with a longitudinal field varying from $-100\ G$ to $+60\ G$ (where the negative sign reflects a change in polarity). The field strength varies almost sinusoidally with the exception of two observations. These two observations are seen at phases where the fit of the magnetic field would approach a minimum but are sharp peaks, that the authors suggest may be caused by the propagation of a strong shock in the atmosphere of η Aql at this phase. However, this result has been disputed using Stokes V spectropolarimetry where no

significant magnetic field was detected for η Aql (Wade et al., 2002).

Deviations from regular pulsation, such as amplitude modulation or interference with non-radial modes, are also showing up in recent observations. Koen (2001) conducted a frequency analysis of the time-series data from HIPPARCOS observations and found a modulation period of about 1200 days, leading the author to conclude that the Cepheid is displaying the Blazhko effect. The Cepheids amplitude modulation was discussed by Breger (2006) to test if the modulation is due to the combination of pulsation modes to generate the Blazhko effect. However, the analysis was not precise enough to confirm that hypothesis, but the authors detect additional periodicities in the star. Spectra of four Cepheids observed by Kovtyukh et al. (2003) showed line asymmetries that the authors argued were consistent with bumps seen in the line profiles of non-radially pulsation stars. Since the four Cepheids are not in binary systems but are close to resonances between modes, these authors concluded that they may be undergoing non-radial as well as radial pulsation. Along with the observations that the four Cepheids are not in binary systems and that they have periods close to resonance values, the authors contend that the Cepheids may be undergoing non-radial pulsations as well. Moskalik & Kolaczkowski (2008) conducted a search for multiperiodic variations in Cepheids from the OGLE-II survey to determine if there are Cepheids with non-radial pulsations. The authors found no evidence of non-radial pulsation in the fundamental mode Cepheids but did find evidence in three double-mode (fundamental to first overtone) Cepheids.

Alcock et al. (2002) found three eclipsing binary Cepheids in the LMC from the MACHO survey, observed in three wavebands V, R, and I. The discovery of eclipsing binaries provides a useful measure of the radii and radius variations of Cepheids and the limb darkening of Cepheids (the change of intensity from the center of the stellar disk to the edge). In the work, the limb-darkening was assumed to vary as a linear function with a coefficient as a free parameter in the fit. The radius and variation of radius are well-constrained for the eclipsing binary system but the limb-darkening coefficients are not. The study of the dynamical masses of Cepheids in spectroscopic binaries has continued, Evans et al. (2006) redetermined the mass of S Muscae to be $6.0 \pm 0.4\ M_{\odot}$ from FUSE observations at UV wavelengths. The dynamic mass of Polaris has been determined by Evans et al. (2008) from Hubble Space Telescope observations of $M = 4.5^{+2.2}_{-1.4}\ M_{\odot}$, when combined with earlier observations Kamper (1996); Wielen et al. (2000).

While Fernie (1993) said goodbye to Polaris as a Cepheid, Bruntt et al. (2008) welcomed it back. Continuous observations from the WIRE star tracker and SMEI instrument on Coriolis satellite showed that the brightness amplitude has increased by 30% from 2003 to 2006. Bruntt et al. (2008) argued that the change of amplitude is periodic and is a pulsation phenomenon.

The evolution of Cepheids can been tested using measurements of the rate of period change for Cepheids. Turner et al. (2006) presented rates of period change for more than 200 Galactic Cepheids and showed that the value of the rate may be used to deduce which crossing of the Instability Strip is most likely to apply. A star crosses the Instability Strip for the first time after it has finished core hydrogen fusion and is evolving to the Red Giant Branch. A star passes through the second and third crossing after it starts core helium fusion

and contracts. The observed rates were also compared to the rates predicted from pulsation models and the observed rates were found to cover a larger range of values than the predicted rates.

Optical interferometry has allowed for the direct detection of the variation of the angular diameter in Cepheids. The first convincing detection was by Lane et al. (2000) using the Palomar Testbed Interferometer (PTI) for ζ Gem where the radius is found as a function of phase; they used their measurements with the Baade-Wesselink method to determine the amplitude of the radius and thus, with interferometric observations, to derive the distance to ζ Gem to an accuracy of 10%. This analysis is consistent with distance estimates from other methods but does demonstrate how interferometry will allow us to determine distances to Cepheids with high accuracy. Further observations of ζ Gem and η Aql yielded distances to the stars as 368 ± 38 pc and 320 ± 32 pc, respectively, using the same Interferometric Baade-Wesselink (IBW) method (Lane et al., 2002).

Kervella et al. (2004d) observed seven Cepheids using the Very Large Telescope Interferometer and determined mean angular diameters to an accuracy of $\leq 4\%$. They used the Interferometric Baade-Wesselink method to compute distances to each observed Cepheid. The angular diameter of l Car, observed previously, was compared to the angular diameter from the surface brightness technique (Fouque & Gieren, 1997) and found to agree to within 1.5%, verifying the potential of both techniques (Kervella et al., 2004c). Following this agreement, Kervella et al. (2004b) use the interferometric observations of the seven Cepheids to calibrate the surface brightness-color relations. On the oppositie side of the argument, Mérand et al. (2005) used CHARA Array interferometric observations of δ Cep to determine the projection factor of the Baade-Wesselink method by assuming the parallax to δ Cep for the distance (Benedict et al., 2002). The authors find a value of $p = 1.27$, suggesting significant uncertainty in the assumed value of the projection factor.

Circumstellar Envelopes (CSE's) have recently been observed from interferometry for the Cepheid l Car at both K and N-band (Kervella et al., 2006). The CSE for l Car was found based on IR excesses at these wavebands, similar to the IR excesses observed by Deasy (1988). Kervella et al. (2006) argued the excess to be due to the presence of dust in the CSE and that it may have been formed from mass loss. Likewise, CSE's have been detected around Polaris and δ Cep using CHARA contributing about 1 to 1.5% of the total K-band flux of the system (Mérand et al., 2006). Mérand et al. (2007) also detected a CSE surrounding Y Ophiuchi but no CSE around the non-pulsating yellow supergiant α Persei. This result suggests that the CSE's are specifically related to the structure and evolution of Cepheids. IR Observations from the Spitzer Space Telescope at 8.0 and 24 μm have confirmed the existence of CSE emissions for nearby Cepheids. In particular, CSE's have been resolved for δ Cep, SZ Tau, and RS Pup and are found to be as far as $10,000$ AU from the star (Marengo et al., 2009).

Light echos from CSE's provide another useful tool for measuring the distance to Cepheids. The light echos are caused by stellar flux being scattered off of the surrounding dust shell towards the observer and the echo is shown to vary due to the change of stellar luminosity. By knowing the apparent separation between the Cepheid and the dust that causes the light echo, and the difference between the phase of the

Cepheid and the phase of the light echo, it is possible to measure the time since the light was first emitted. One can then measure the absolute distance between the Cepheid and the light echo and measure of the distance to the Cepheid. Kervella et al. (2008) measured a distance to RS Pup using this method and found $d = 1992 \pm 28\ pc$. However, they assumed that the dust shell around RS Pup is perfectly spherical and that all observed light echos are generated from a shell that is between the observer and the Cepheid. Because of these assumptions and that the light echo distance differed from other distance estimates ($d = 1728\ pc$) from HIPPARCOS parallax. Feast (2008) found that by using the HIPPARCOS distance then the nebula around RS Pup can be fit by a disk inclined 9 degrees from the plane of the sky. Bond & Sparks (2009) noted that the structure of the nebula appears to be bi-polar and suggested that high spatial resolution polarimetry be used to solve the problem.

Multi-wavelength observations of l Car and RS Pup were used to compute the spectral energy distribution of the stars and search for IR excess due to the presence of CSE's by Kervella et al. (2009). The authors build the SED's using Spitzer archival data, interferometric observations, COBE, and optical data. They found that there is a warm dust component to the CSE's for both stars extending from about 100 to a few 1000 AU but only RS Pup shows a cold ($\approx 40\ K$) component. Kervella el al. argued that the warm component is due to mass loss and that the cold component is a relic due to an earlier stage of evolution. This argument is bolstered by the observations of a nebula surrounding the Herbig Be star HD 200775 that is a young analog of RS Pup.

Gieren et al. (2005) computed the projection factor based on an analysis of the distances from the IR surface brightness technique for Galactic Cepheids which are used to calibrate the Leavitt law for LMC Cepheids. They found that the distance to the LMC is a function of the period of the LMC Cepheids, and suggested that the dependence is due to using a constant value of the p-factor. Thus, to remove the period dependence of the distance the p-factor was computed to be a function of period.

The challenge of precision understanding of the projection factor for Cepheids has been explored by Nardetto et al. (2006) using high spectral resolution observations of nine Galactic Cepheids. From the observations, the authors found the rotation velocity of the Cepheids to be $v_R \sin i < 20\ km\ s^{-1}$ and that there is a systematic asymmetry in the line profiles at the 5% level. Further study of the spectral observations, with specific attention to 17 particular lines, showed that there exists an extra velocity component in the lines termed the γ-velocity (or γ-asymmetry) Nardetto et al. (2008b). The determined γ-velocities range from $-11\ km\ s^{-1}$ to $26\ km\ s^{-1}$ and the average value is a blueshift of about $2\ km\ s^{-1}$. While the γ-velocity had been known, they showed that the phenomenon is intrinsic to Cepheids. However, the authors did not argue for a physical source. Nardetto et al. (2008a) analyzed the structure of the Hα line profiles for the same Cepheids and found that the line profiles show different behaviors for short-period and long-period Cepheids. The line profiles in short-period Cepheids were found to vary along with the pulsating envelope of the Cepheid but the line profiles in long-period Cepheids show significant asymmetries. They argued that the asymmetries may be related to mass loss and the presence of a hydrogen circumstellar envelope. The

uncertainty of the projection factor factor due to the method of computing the radial velocity was tested using spectral observations of eight Cepheids (Nardetto et al., 2009). The radial velocity was computed using the cross correlation method and the authors showed that using a different method causes an additional 5% uncertainty in the measure of the amplitude of the Cepheid. They also found that the cross-correlation method leads to larger values of the γ-velocity.

From spectral observations of X Sgr, Mathias et al. (2006) observed that the line profiles show up to three asymmetric components during the pulsation cycle. They argued that the components are caused by the propagation of three different shocks in the atmosphere of the Cepheid. The existence of shocks may be related to far-UV and X-ray observations of Polaris and β Dor (Engle et al., 2009). The observations show the presence of very hot plasma ($50000 - 500000\ K$) based on strong carbon and oxygen emission lines in the UV. X-ray fluxes have been detected for both stars and may indicate the presence of shocks, warm winds, or magnetic fields.

Recently, the results from the OGLE-III 40 square degree survey of the LMC have been presented and a large number of Cepheids have been observed in V and I-band (Soszynski et al., 2008). There are 1848 fundamental mode, 1228 first overtone, and 14 second overtone Cepheids. A large number of double-mode Cepheids were found, 61 fundamental to first overtone, 203 first to second overtone, and 2 first to third overtone. Also, there are 5 triple-mode Cepheids and 23 ultra-low amplitude variable stars that may be Cepheids.

1.3.2 Statistical Properties of Cepheids

Cepheid pulsation makes these stars powerful tools for distance determination. The Period-Luminosity relation, discovered by Henrietta Leavitt, has been the subject of a great deal of rigorous study. The history of the Period-Luminosity relation or Leavitt Law includes the study of the Period-Color relation and the Period-Luminosity-Color relation and whether these relations are more precise. In this section, the history of the Leavitt Law is reviewed with reference to the Period-Color, and Period-Luminosity-Color relation when appropriate. Cepheids are also known to follow a Period-Radius relation. These statistical properties provide insight into the evolution and structure of Cepheids as a whole, as well as developing tools for cosmology and extragalactic astronomy.

Much of the history of the development of the Leavitt Law (P-L relation) has been discussed by Fernie (1969), so only the key results will be mentioned here. After Henrietta Leavitt's discovery of the relation in 1908, both Enjar Hertzsprung and Harlow Shapley were quick to realize its significance. Independently, each derived the P-L relation for Galactic Cepheids using statistical parallax methods to find the distances (Hertzsprung, 1914; Shapley, 1918). Statistical parallax measures the distance to a set of stars that are approximately the same distance from measurements of the radial velocity and proper motion. In the determination of the Shapley (1918) P-L relation, a Period-Color relation was assumed.

Shapley & Nicholson (1919) attempted to determine a physical cause of the P-L relation. They used

the pulsation hypothesis from Lord Kelvin (1890) and Emden (1907) to show that a Cepheid follows the Period-Mean Density relation $P\sqrt{\rho} = Q$ (also found by Eddington (1918)). By using the definition of the mean density, and noting the luminosity as a function of radius and temperature and that the temperature is a function of the color, they showed that Cepheids must follow a Period-Luminosity-Color relation. Then using the Period-Color relation from the earlier paper, the authors showed that Cepheids follow a P-L relation. It should be noted that the P-L relation had been determined using RR Lyraes and Population I and Population II Cepheids which had not yet been discovered to be distinct types of variable stars.

The P-L relation determined by Shapley had an important effect on astronomy as a whole. For instance the distance to M31 and M33 was found using this relation Hubble (1925) and laid the foundation for modern cosmology. However, Fernie (1969) noted two issues with Shapleys P-L relation: 1) it ignored interstellar absorption, and 2) it was derived using only eleven Cepheids. While there are issues with the results of Shapley (1918, 1919), it is clear that statistical studies of Cepheids can yield significant information.

The Leavitt Law (Period-Luminosity Relation)

Following the discovery of interstellar absorption by Trumpler (1930), Lundmark (1931) studied the effect of absorption on the zero-point of the P-L relation and concluded that the zero-point of Shapley's P-L relation (Shapley, 1918) was correct. The analysis of Gerasimovic (1931) used statistical parallax of Cepheids and determined that the zero-point is about one magnitude fainter. Shapley (1934) presented observations of LMC Cepheids and found a P-L relation that was steeper than the Galactic relation. He noted that the difference may be due to how the photographic magnitude scale is determined, but it was clear that there was no convergence on the structure of the P-L relation.

The linearity of the P-L relation was also first tested at this time, Kukarkin (1937) used Cepheid observations from multiple galaxies and found that the P-L relation was well-represented by a quadratic relation and even better by a bi-linear relation that is two linear relations with a period break at a period of 10 days. Shapley (1940) also found that the P-L relation was best-fit by a quadratic relation.

One of the errors in the determination the zero point of the P-L relation was the inclusion of RR Lyraes in the derivation. Baade (1956) and Sandage (1953) found that RR Lyrae stars do not fit on the Cepheid P-L relation. For instance, Sandage (1953) determined from the Color-Magnitude diagram of M3 that RR Lyrae absolute brightnesses are approximately zero but the Population II Cepheids are about 1.5 magnitudes brighter, therefore he suggested that the P-L relation zero-point must also be 1.5 magnitudes brighter. The same result was also found by Dartayet & Landi Dessy (1952) for the SMC, and by Weaver (1954) from comparing distance determinations to the Galactic Center.

The difference between the P-L relations for Population I and II Cepheids was explored by Payne-Gaposchkin & Gaposchkin (1966) where they found that the two different classes produced different P-L relations. The Population II Cepheids are about 0.5 magnitudes brighter than predicted by the P-L relation from Population I Cepheids. This result was important for reducing the uncertainty of the P-L relation

and for its calibration. A similar result was found for Classical Cepheids pulsating in the fundamental and first overtone by Böhm-Vitense (1994), where the P-L relation for first-overtone Cepheids is shift by $\Delta \log P = 0.15$ from the fundamental-mode P-L relation.

In a significant analysis of LMC, SMC M31, and NGC 6822 Cepheids, Sandage & Tammann (1968) computed the slopes of P-L relations in both the B and V-bands. They found that the slopes are universal for all four galaxies, where the zero-point was calibrated using nine Galactic Cepheids. The resulting fits to the data have dispersions of 0.6 and 0.5 magnitudes in the B and V-band, respectively. Conversely, Gascoigne (1969) found that the slope of the V-band P-L relation differed for LMC and SMC Cepheids, however the result was based on observations of seven LMC and thirteen SMC Cepheids.

Welch et al. (1985) extended the P-L relation to the near infrared J, H, and K-bands based on ten Galactic Cepheids. The relations are $M_J = -2.31(\pm 0.11) - 3.11(\pm 0.12) \log P$, $M_H = -2.46(\pm 0.13) - 3.20(\pm 0.14) \log P$, and $M_K = -2.52(\pm 0.14) - 3.22(\pm 0.15) \log P$. Similar relations were derived from 21 Galactic and 115 Magellanic Cloud Cepheids by Laney & Stobie (1994) where the determined slopes for the infrared relations are steeper (from 3.306 to 3.443) than the Welch et al. (1985) relations. Another set of J, H, and K P-L relations were computed by Persson et al. (2004) for 92 LMC Cepheids, with slopes that are similar to those computed by Welch et al. (1985) with a range from -3.153 to -3.281.

The calibration of the zero-point was done by Feast & Catchpole (1997) using the Hipparcos trignometric parallaxes for 223 Galactic Cepheids with an error for each parallax measurement of 1.5 mas. The P-L relation was fit to the Cepheids assuming the slope is that of the LMC P-L relation as a constraint. Further calibration has been done using the interferometric observations of Cepheid distances to determine the zero point Kervella et al. (2004a), where the computed zero point for V and K-bands agree with previous observations. A calibration of the Galactic P-L relations from the B to K-bands has been derived by Fouqué et al. (2007) using 59 Cepheids with distance measurements based on Hubble Space Telescope and *Hipparcos* parallax, Baade-Wesselink methods, and distances to associated clusters. It has been found that the Galactic P-L relations do not differ significantly from LMC relations suggesting that the slope of the P-L relation is universal.

One of the most important contributors to the uncertainty of the P-L relation is interstellar reddening, and to account for this, Madore (1985) derived the Wesenheit function defined as $W = V - \alpha(V - I)$, where α is the redding coefficient R_{VI}. This function has a resulting scatter of less than 0.2 magnitudes. The structure of the Wesenheit function has also been tested for non-linearity with respect to period by Ngeow et al. (2005) using the OGLE-II sample and it is found that the Wesenheit function is linear. The Wesenheit function was analyzed by Madore & Freedman (2009), who argued that it is very insensitive to the slopes of the monochromatic P-L relations used to derive it. This suggests that the scatter of the Wesenheit function is small relative to these relations and that the Wesenheit function should be linear even when the P-L relations used to derive it are non-linear.

The second uncertainty is the dependence of the P-L relation on the metallicity of Cepheids. It is

this uncertainty that causes the differences between Galactic, LMC and SMC Cepheid P-L relations. This uncertainty was first measured by Freedman & Madore (1990) using observations of Cepheids in three regions of M3 in B, V, R, and I-bands. The three regions differ significantly in metallicity therefore it is expected that the predicted distances using the same P-L relation would also differ significantly. However, the observed distance moduli to each region are not significantly different. The metallicity dependence was tested using the EROS survey of LMC and SMC Cepheids (Sasselov et al., 1997), where the change of the distance modulus μ was found to be due to the relative differences in metallicity from the LMC metallicity $\delta\mu = (0.44^{+0.1}_{-0.2}) \log(Z/Z_{LMC})$. This result helped solve the conflict between the lower values of H_0 suggested by Sandage et al. (1994) and the high values suggested by Freedman et al. (1994) as well as highlighting the dependence of a Cepheid's pulsation properties on the metallicity. Kennicutt et al. (1998) explored this further as part of the Hubble Space Telescope Key Project for determining the Hubble constant by observing different regions of M101 where the Cepheids have a range of oxygen abundances. The inferred distance modulus was found to vary as a function of abundance at a rate of $\delta\mu/\delta[O/H] = -0.24 \pm 0.16$ mag dex^{-1}.

Groenewegen et al. (2004) studied the individual metallicities of about 50 Cepheids in the Galaxy, LMC, and SMC and constructed a new P-L relation. They found that when the effect of metallicity is ignored, the best-fit P-L relation is quadratic though the quadratic term is important for long-period ($\log P > 1.65$) Cepheids only. The metallicity correction was found to be about -0.6 ± 0.4 mag dex^{-1}. Distance measurements using the Cepheid P-L relation have been compared to distance measurements using the Tip of the Red Giant Branch and the difference between the two methods is assumed to be due to the metallicity correction (Sakai et al., 2004). They found that the distance modulus varies as a function of oxygen abundance $\delta\mu/\delta[O/H] = -0.24 \pm 0.05$ mag dex^{-1}.

The metallicity correction is concerned with the variation of the zero-point of the P-L relation but not the slope. The reason is that it is generally assumed that the slope is universal, however, Tammann et al. (2003) showed that this may not be true. Period-Color relations for Galactic, LMC, and SMC Cepheids were found to differ and this suggests that the P-L relations for the three galaxies must also differ. The LMC Cepheid P-L relation was explored in the second article of the series (Sandage et al., 2004), who found that there is a period break at a period of 10 days like that found by Kukarkin (1937). They also noted that the LMC Cepheids are bluer than the Galactic ones. On the other hand, Gieren et al. (2005) argued that the slope of the P-L relation is universal up to solar abundances based on IR surface brightness distances to 13 LMC Cepheids. The Gieren P-L relation agrees well with the Galactic P-L relation but not with the results of Persson et al. (2004) or the OGLE-II P-L relations (Udalski et al., 1999b).

The structure of the P-L relations has been mostly assumed to be linear but there is no a priori reason for them to be so. From the EROS survey of SMC Cepheids, Bauer et al. (1999) found that there was a period break at a period of $\approx$ 2 days where the slope of the P-L relation was significantly steeper for fundamental-mode Cepheids. The author speculate that the non-linearity might be due to a non-linear blue edge of the Instability strip. The LMC P-L relations were tested for non-linearity using the MACHO and

2MASS surveys in the V, R, and J, H, K-bands (Ngeow et al., 2005). They found that the P-L relations for wavelengths shorter than K-band are consistent with being non-linear with a period break at 10 days, while the K-band relation is linear. The structure of the optical P-L relations has been reviewed by Ngeow & Kanbur (2006). They found them to be physical and not just a selection effect due to having a sample with many short-period Cepheids and relatively few long-period Cepheids.

Observations of Cepheids at longer wavelengths from $\lambda = 3.6$ to $8.0\ \mu m$ using the Spitzer Space Telescope as part of the SAGE (*Surveying the Agents of a Galaxy's Evolution*) survey of the LMC have been used to determine the mid-infrared P-L relation (Meixner et al., 2006). Freedman et al. (2008) used the sample of Cepheids from Persson et al. (2004) with mid-infrared observations and determined relations with slopes ranging from -3.29 to -3.44. They argued that the slopes are consistent with the limiting slope of the P-L relation due to the surface brightness contributing most of the long-wavelength flux. Similarly, Ngeow & Kanbur (2008) also computed IR P-L relations using the SAGE data but correlated with the entire OGLE-II database and found slopes ranging from -3.26 to -3.03 with the slopes becoming less steep with increasing wavelength. This result contradicts the limiting slope argument of Freedman et al. (2008). The authors tested the IR P-L relations for non-linearity and find that the $8.0\ \mu m$ P-L relation is non-linear while other relations are linear. Madore et al. (2009) computed the IR P-L relations from two epochs of SAGE observations and find similar results as the previous work of Freedman et al. (2008). Similarly, Ngeow et al. (2009) used the two epochs of SAGE data correlated to OGLE-III and 2MASS data to compute P-L relations from V-band to Spitzer IRAC bands. The relations for wavelengths shorter than K-band agree with previous results and the slopes of the IRAC P-L relations vary from -3.25 to -3.20. All of the relations are tested for non-linearity; only the V, I, J, and H-band relations are confirmed to be non-linear.

The Cepheid P-L relations are important measures of the evolutionary and pulsation states of Cepheids as well as an important tool for distance measurements. The current uncertainty of the P-L relation is about 5% and evidence suggests it may not be linear. There are significant questions regarding the structure of these relations that have an impact on the understanding of Cepheids themselves.

The Period-Radius Relation

The Period-Radius (P-R) relation is an useful measure of the physical structure of a Cepheid. The calibration of the relation has followed the development of various methods to measure the radius of a Cepheid, for example the Baade-Wesselink method.

The first presentation of a P-R relation was by Woolley & Carter (1973) for eighteen Galactic Cepheids with radii determined at maximum brightness using the Baade-Wesselink method. The best-fit linear relation is

$$\log R(\text{maxlight}) = 1.181(\pm 0.069) + 0.683(\pm 0.071) \log \text{P}. \tag{1.5}$$

Based on an improvement of the Baade-Wesselink method, Caccin et al. (1981) determined the mean radii

for ten Cepheids and computed a P-R relation that was similar, with a slope of 0.654 ± 0.052 and zero-point of 1.177 ± 0.058.

It was not until 1987 when the P-R relation was computed for a large sample of data. Moffett & Barnes (1987) determined the radii of 63 Cepheids using the Visual Surface Brightness technique. From the observations the best-fit P-R relation was found to be steeper than earlier results with a slope of 0.734 ± 0.034. Gieren (1989) conducted the same analysis with an extended data set containing 52 southern Cepheids where the same result was found for the P-R relation as Moffett & Barnes (1987).

Laney & Stobie (1995) derived the P-R relation for Galactic Cepheids using Baade-Wesselink radii for 49 Cepheids based on multi-wavelength data. However, they found that using different wavebands for compute radii and hence P-R relations yielded different slopes for the P-R relation that do not agree. The authors argued the near-IR observations produced the least uncertain P-R relations, for which a slope of 0.751 ± 0.026 was determined, even more steep than previous estimates.

The visual and IR surface brightness techniques have been used to calibrate the P-R relation. Based on improvements to the technique (Fouque & Gieren, 1997), Gieren et al. (1998) derived the radii for 28 Galactic Cepheids for which a P-R relation is derived that is identical to that of Laney & Stobie (1995) even thought the radii are derived using a completely different method. Gieren et al. (1999) extended the analysis by including ten LMC and six SMC Cepheids with radii determined using the IR surface brightness method and found that the P-R relation is universal in that it does not vary with metallicity and that the slope is much smaller 0.680 ± 0.017.

A third calibration method of the P-R relation has been done using radii from interferometric observations via the IBW method. Kervella et al. (2004a) used this method with determined radii for eight Cepheids and the resulting P-R relation has a slope of 0.767 ± 0.009 which is 1σ different from the results of Laney & Stobie (1995) and Gieren et al. (1998). The calibration was also considered by Groenewegen (2007) who established a relation between the projection factor and pulsation period and used this result to compute a P-R relation. The new P-R relation has a slope of 0.686 ± 0.036.

These results show two different P-R relations with different slopes. Groenewegen (2007) pointed out that the analyses resulting in a steeper slope took into account a projection factor while the other analyses do not include this. Determination of the appropriate projection factor is thus essential to finding the correct P-R relation.

1.3.3 Theoretical Modeling

The development of theoretical models of Cepheid variable stars following from the derivation of Arthur Eddington has become one of the great successes of theoretical and computational stellar astrophysics. Much of the history of stellar pulsation modelling discussed here is reviewed by Zhevakin (1963) and Gautschy (2003). The pulsation hypothesis for the variability of Cepheids was due to the speculation of Plummer (1913) and Shapley (1914) following the derivation of Lord Kelvin (1890) and Emden (1907). However,

Eddington (1917a) was the first to develop the theory to describe pulsation in a star (Eddington, 1918, 1919b). He recognized that stellar pulsation is a thermodynamic engine where energy gains and losses compensate for each other. In this case, pulsation could begin as a small perturbation to the structure of the star and grow to become the stable, continuous variations that are observed. Eddington (1918) applied linear perturbation theory to equations of hydrostatic equilibrium and conservation of mass and assumed that the gas is adiabatic. By combining these perturbed equation, he derived a second-order differential equation that could be solved to describe the pulsation period of the star. The derived differential equation was applied to a polytropic model of a star and the Period-Density relation was found. Eddington (1919b) discussed the decay rate of pulsation as well as the phase lag between the luminosity and velocity curves. The delay was not found in his analysis and he argued that the lag was due to non-adiabatic effects.

Discovery of the Driving Mechanism

The driving mechanism for stellar pulsation could not be understood from Eddington's calculations; however, he did propose two hypotheses (Eddington, 1926). The first hypothesis is that the nuclear reactions in the core of the star would cause pulsations: as the star contracts the temperature of the core heats up and is more dense. With higher temperatures and densities the nuclear reactions occur at a larger rate and more reactions generate an outward force that causes the star to expand again. When the star expands the rate of nuclear reactions decreases again and the cycle begins anew. This mechanism was proposed at a time when nuclear energy generation as the source of energy for a star was just becoming understood. The second mechanism is the valve mechanism: as the star contracts it becomes more opaque and opacity increases. The outward energy would then become "dammed up" and eventually forces the star to expand again. As the star expands the opacity decreases and the trapped energy escapes; when the energy escapes the outward force decreases and the outer layers fall back towards the center, compressing the star and starting the cycle again.

The first mechanism was explored by Cowling (1934, 1935), again using linear perturbation theory and assuming Kramer's opacity law $\kappa \propto \rho^m T^n$. In this case, nuclear reactions were found to be a viable source for radial pulsation. However, this mechanism tended to produce relative displacements that are much larger than pulsation amplitudes observed for Cepheids The result was later verified by Ledoux (1941) and Cox (1955).

Eddington had explored pulsation assuming that stars pulsate in the fundamental mode but there was no reason to conclude that the fundamental mode was the only important mode in Cepheids. Edgar (1933) conducted a linear perturbation analysis of a stellar polytope but assumed a quasi-adiabatic method. The quasi-adiabatic method is useful because it explores the complex term of the wave function and measures growth and decay times for the pulsation mode. He found that the first overtone mode may be important but the decay time is short, meaning the first overtone mode is much more strongly damped than the fundamental mode. Similarly, Woltjer (1936) derived an iterative method for solving the perturbation equations with

a non-adiabatic correction. In a subsequent article, Woltjer (1937) investigated the interaction between multiple modes of oscillation in a star, following Kluyver (1935) and discussed the possibly that modulations seen in light curves of RR Lyrae stars may be interactions between the fundamental and first overtone modes.

An alternative theory to pulsation by standing waves was proposed by Schwarzschild (1936, 1938) where the variability is driven by traveling waves in the atmosphere of the star. This theory could explain the phase lag between the luminosity and radius maxima by assuming that the atmospheric density is a function of both the luminosity and velocity. Therefore the resulting density wave must be traveling and not be a standing wave. Using the running wave hypothesis, Schwarzschild (1938) modelled the light and velocity curves of δ Cep and later found that the curves for η Aql were well modelled by the theory as well (Schwarzschild et al., 1948). This concept was also applied to Mira (Scott, 1942).

The source of excitation for pulsation in stars was an important challenge of the valve mechanism. Eddington had assumed that the entire star would act as a valve but this was inaccurate. However, Eddington (1941) argued that the source of pulsation might be the zone of partial ionization of hydrogen which lies below the photosphere. He associated this zone with the phase lag of the radiation and the existence of the Period-Luminosity relation. In this work, Eddington maintained that the ionization zone does not drive the pulsation but instead modifies the pulsation and supports driving from nuclear reactions. He concluded that "the hypothesis of negative dissipation (the valve mechanism) is not likely to be advocated except as a last resort."

One of the issues with the stellar pulsation mentioned above is that Eddington, Schwarzschild and others assumed a polytrope of index 3, for which is the mass of the star is not centrally concentrated. Sen (1948) made explicit note of this concern and recommended using a polytrope of index 4 such that the central density is larger and better represents the actual structure of a Cepheid. Using realistic stellar models with highly concentrated central densities, instead of polytropes, Epstein (1950) computationally solved the pulsation equations for the stellar models for the fundamental and first overtone modes. He found that the fundamental mode is influenced most by the structure of the star at about 0.7 R_* while the first overtone is influenced the by the layers at 0.8 R_*. This result suggested that nuclear driving is not the excitation mechanism for stellar puslation. Epstein also determined the Period-Density relation but found it differed from the observed relation for η Aql. The radius of η Aql was found using the Baade-Wesselink method (Schwarzschild et al., 1948) and the mass was found using an observed mass-luminosity relation (Kuiper, 1938).

The development of stellar pulsation theory continued on each side of the Atlantic; on one side was S. A. Zhevakin in the USSR and on the side was J.P. Cox and collaborators in the United States. Cox (1955) tested the pulsational stability of stars using a typical stellar model of a red giant with a centrally condensed core. He showed that nuclear reactions are insufficient for driving pulsation in Cepheids and that the pulsation amplitudes derived before were wrong due to the lower density of the core assumed in those models. This result confirmed earlier tests by Zhevakin (1963) and Ledoux et al. (1955). Pulsation in the

stellar model appeared to be influenced by the outer 15% of the structure. In a later article, Cox (1958) derived a linear first-order non-adiabatic treatment for stellar pulsation, similar to that discussed previously (Rosseland, 1931, 1949; Zhevakin, 1953, 1954a,b). The work was designed to test a modified version of Eddington (1941) hypothesis where the pulsation and phase lag is modified by a partial ionization zone for some unknown element (Eddington had considered hydrogen only). The models of pulsation showed that the phase lag between the phase of luminosity maximum and the phase of maximum radius could be reproduced if the flux variations showed an abrupt decrease with height in the envelope.

Cox & Whitney (1958) continued the analysis of the phase lag and related it to the partial ionization of helium. Using this hypothesis, the authors computed a theoretical Period-Luminosiy relation to compare to observations. He found that the helium ionization zone was important for the producing the phase lag and reproducing the zero-point of the P-L relation, as suggested by Zhevakin (1948, 1953). Zhevakin (1959a) developed a discretization model for solving the pulsation equation in a star. He used it to confirm the hypothesis that helium is responsible for driving pulsation in Cepheids and showed that helium could do this only if the abundance of helium is at least 15% of the total stellar mass (Zhevakin, 1959c). Furthermore, he found that the models were able to reproduce the zero-point of the P-L relation, providing more evidence for his hypothesis (Zhevakin, 1959b). Cox (1959) similarly found that the zero-point depended on the helium abundance in the stellar models and produced pulsation calculations that agreed with the results of Zhevakin (1959c) (Cox, 1960). It had been about forty years since Eddington had postulated that Cepheid variability is due to pulsation but the independent works of Cox and Zhevakin finally derived the driving mechanism for Cepheid pulsation.

Both Baker & Kippenhahn (1962) and Cox (1963) computed linear non-adiabatic pulsation models and yet again confirmed that pulsation is driven from the helium partial ionization zone. Baker & Kippenhahn (1962) solved the pulsation equations for five stellar envelope models corresponding to the known properties of Cepheids and determined that Cepheids have both fundamental and first-overtone pulsation. They also reproduced the phase lag. In a second article, Baker & Kippenhahn (1965) solved the pulsation equations for fifteen stellar models of 7 $M_{\odot}$ and provided estimates of the boundaries of the Cepheid Instability strip on the HR Diagram that is centered on an effective temperature of 5200 K.

The Shift to Non-Linear Models

All of the works discussed so far are primarily based on the linear approximation of the equations of stellar structure. The first numerical work computing non-linear models of stellar pulsation is Christy (1966a) for RR Lyrae stars. He computed 100 models of varying mass, luminosity and composition and found that the structure of the Instability strip is a function of helium abundance. One of the more challenging aspects of this work was the treatment of convection. Convection was treated in the stellar structure model via the mixing length theory but the connection between pulsation and convection was ignored. However, Christy speculated that convection improves the efficiency of energy transport in the hydrogen ionization

zone, which would have an effect on the phase lag. Christy (1966b) attempted to model the Cepheids δ Cep, and η Aql using his non-linear pulsation program. By trying to fit observed light curves, Christy found that δ Cep most likely pulsates in the fundamental mode and has a mass of 3.3 $M_{\odot}$ while η Aql pulsates in the first overtone and has a mass of 4.2 $M_{\odot}$.

Similarly, Cox et al. (1966) also computed non-linear pulsation models of Cepheids, where the authors model the star only to a depth where $T = 2 \times 10^5$ K. The calculations confirmed the results of Christy (1966a,b) and furthermore showed an additional mechanism to drive pulsation. In the helium II ionization zone, when the layer is becoming ionized the opacity in the layer remains constant and the temperature remains cool relative to the surrounding layers that are being compressed and heated. This temperature difference causes heat to flow from the hotter layers into the ionization zone and generates pulsation.

The interaction of convection and pulsation was an important question of the models raised by Christy. Unno (1967) developed a time-dependent treatment of convection based on the mixing length theory. Using this time-dependent theory with the non-linear pulsation calculations, Unno tested the pulsational stability. He found that the stability is sensitive to the interaction of the convection zone and the ionization zone that drives the pulsation. This dependence was measured by the ratio of the convective timescale and the pulsation period. If the ratio is less than unity then pulsation may be destabilized by convection.

Another set of non-linear models were developed based on the technique of Stobie (1969a). This numerical technique was used to compute models of Cepheids ranging in mass from 5 to 9 $M_{\odot}$ (Stobie, 1969b). The results of the calculations showed the dependence of the location of the Instability Strip on the helium abundance. By increasing the helium abundance by 15%, the Instability Strip is shifted to hotter temperatures by about 600 K. The model lightcurves tended to show a secondary bump similar to the Hertzsprung progression except that they appeared at the wrong phase. Stobie argued that the bumps would match observations if the mass of the input stellar model was a factor of two smaller. This hypothesis was confirmed in a third article of the series (Stobie, 1969c), exposing one of the great challenges for understanding the properties of Cepheids, the mass discrepancy. This challenge would haunt pulsation and stellar evolution theory for more than two decades.

The Masses of Cepheids

The search for the source of the mass discrepancy was the foremost task for stellar pulsation theorists in the 1970's. The early measurements computed the theoretical Period-Mean Density relation to calculate the mass of Cepheids when there are measurements of the radius. The results suggested Cepheid masses to be about 20-40% smaller than evolutionary masses (Cogan, 1970; Rodgers, 1970; Cox et al., 1972). Fricke et al. (1971) proposed a number of possible sources of uncertainty that could resolve the discrepancy, including changes to stellar opacities in the stellar evolution models, errors in the distance estimates to nearby Cepheids as well as the potential for mass loss to play a role. The authors computed stellar evolution tracks with opacity increased by a factor of two in the envelope of the stellar model where $T > 10^6$ K. The

resulting evolutionary masses were changed but not enough to agree with pulsation masses. They found that increasing the opacity by a factor of four or more brings the predicted masses into better agreement. The authors also applied stellar pulsation and evolution calculations to 53 Cepheids and confirmed the mass discrepancy as well as the larger mass differences for bump Cepheids. Furthermore, the authors found that the ratio of pulsation and evolution masses is a function of pulsation mass. The ratio is smaller for larger mass, meaning the discrepancy is worse for larger mass (or lower temperature) Cepheids (Fricke et al., 1972)

The source of the discrepancy was further analyzed by Iben & Tuggle (1972b,a) who explored issues with Cepheid observations and pulsation models. They found that the models and observations could be brought into agreement with stellar evolution calculations if the luminosities of Cepheids are actually dimmer by 0.3 magnitudes, or the effective temperatures measured from the colors are cooler by $\Delta \log T_{\rm eff} \approx 0.025$ or if the helium abundance is increased by $\Delta Y = 0.14$. The authors also argued that the observed Period-Luminosity-Color relation (Sandage & Tammann, 1968) is also not appropriate for computing Cepheid masses because it assumes that the physical properties of Cepheids are universal with respect to different galaxies.

King et al. (1975) tested how different Color-Temperature scaling relations affect the mass determination for a sample of eight bump Cepheids. They found that using a new scaling relation the masses could be brought into agreement with the exception of U TrA which was still less massive than predicted from stellar evolution.

The opacity hypothesis was tested by Carson & Stothers (1976) and Sastri & Stothers (1978) based on new opacity calculations. The authors found that the bump Cepheid masses agreed better with the evolutionary masses than predictions using other opacities. However, the pulsation masses for other Cepheids, such as the beat Cepheids (double mode pulsation) tended to have worse agreement with the new opacities. Another possible contributor is rotation, but pulsation models including rotation would predict masses agreeing with stellar evolution only if the rotation is very large at the surface. A rotation law consistent with observations has no effect on the pulsation mass (Cox et al., 1977; Deupree, 1978).

Cox et al. (1977) suggested that helium enrichment could solve the mass discrepancy. If helium is enriched in the envelope of the Cepheid in layers where $T < 7 \times 10^4\ K$, then predicted mass for bump Cepheids are in closer agreement with observations. A possible mechanism for enriching helium is a wind that depletes the Cepheid of hydrogen near the surface but leaves the helium unaffected (Cox et al., 1978b). Helium would be significantly enriched if the mass-loss rate of the wind is about $10^{-10}\ M_\odot/yr$ and is sustained for about one to ten million years. The timescale is reasonable for explaining the short-period (low mass) Cepheids but not the larger mass Cepheids. Cox et al. (1978a) tested the helium enriched model by predicting masses for triple-mode Cepheids and determined they have pulsation masses about $3-4\ M_\odot$ and to agree with evolutionary models would require a greater amount of helium enrichment a larger depths $T < 3 \times 10^5\ K$. Therefore the triple-mode Cepheid masses are inconsistent with the helium enrichment scenario.

Yet another possible solution is the presence of a magnetic field in the envelope of a Cepheid. Stothers (1979) argued that a tangled magnetic field of the order of 10^2 G near the surface and 10^4 G at the base of the envelope would solve the mass discrepancy by adding an additional pressure term in the pulsation analysis that would change the predicted period ratio of bump Cepheids and bring the pulsation masses into agreement with evolution models. Stothers (1982) reanalyzed the hypothesis using updated stellar models. He found that pulsation models including a tangled magnetic field produce longer pulsation periods, larger amplitudes and the secondary bump in the velocity curve appears at an earlier phase than for models not including a magnetic field. The effect of the magnetic fields on the secondary bump suggest that the pulsation masses agree with stellar evolution if Cepheids have magnetic fields. However, the larger amplitudes are inconsistent with observations.

Cox (1979) compared the mass determinations from a Period-Mass-Radius relation and Baade-Wesselink radii and from theoretical calculations of the period and effective temperature plus better distance and temperature-color relations. He determined that the Baade-Wesselink masses were smaller than evolution masses for 69 Cepheids while Cepheid masses from theoretical calculations and temperature-color relation tended to predict masses in agreement with the evolutionary masses. This result was true for both standard pulsation models and models with helium enrichment in the envelope. The mean ratio of the theoretical mass to evolution mass is 0.97 ± 0.25 and 1.07 ± 0.27 for the standard and helium enriched models, respectively. However, the predicted masses for bump Cepheids were still much lower than masses from stellar evolution.

One other solution to the mass discrepancy was devised by Huang & Weigert (1983) who assumed that the stellar evolution models may be wrong. The authors tested the impact of convective core overshoot in the evolution models of Cepheid progenitors on the main sequence. They found that convective core overshoot mixes additional hydrogen into the core of the main sequence star. Therefore, when the star evolves off of the main sequence, it has a larger helium core suggesting that the star will have a larger luminosity than a star of the same mass but no convective core overshooting. This method provides a simple solution to the mass discrepancy by predicting higher Cepheid luminosities for a given mass, in closer agreement to pulsation masses of bump Cepheids. A similar solution to the mass discrepancy is pulsation-driven mass loss from Cepheids on the Instability Strip. Brunish & Willson (1987) modelled the evolution of a Cepheid that is losing about 5×10^{-7} $M_{\odot}/yr$ and found that the structure of the blue loop is changed. When the Cepheid evolves blueward on the second crossing, the star will eventually loop back redwards on the HR diagram. Mass loss moves the turning point in the loop from outside of the Instability Strip to within it and the Cepheid becomes "trapped" and a significant period of time. Therefore the Cepheid may lose a few solar masses of material and potentially resolving the mass discrepancy.

Refining the Theoretical Models

During the time that the mass discrepancy was a concern, Gough (1977) and Gonczi & Osaki (1980) developed models of time-dependent convection in stars that can be solved simultaneously with pulsation. The model by Gough is based on the mixing length theory, who found that convection is important when the pulsation period is similar to the convective eddy growth rate. Deupree (1980) modelled a number of Cepheids with a two dimensional program with time-dependent convection included to determine the location of the red edge of the Cepheid Instability Strip. The red edge is defined as a region of the HR Diagram where the pulsation is quenched by convection. Gonczi (1981, 1982) confirmed the red edge by using time-dependent convection and including turbulent viscosity in the calculations. The red edge found in this case, though, is very sensitive to the viscosity.

The previous methods for computing time-dependent convection in a pulsating star assume the convection depends on the local conditions. Stellingwerf (1982b) derived a non-linear non-local convection scheme and applied it to model RR Lyrae stars (Stellingwerf, 1982a). He found similar results as the previous methods but did produce new methodology that is less dependent on free parameters.

Cox (1979) resolved the mass discrepancy with better pulsation models with the exception of the bump Cepheids. Models of bump Cepheids were computed using different opacities by Carson & Stothers (1988) in a similar manner to previous works. The predicted masses using these opacities are 15% less than evolutionary masses, bringing the bump mass discrepancy to closer to resolution. It is interesting to note that while the mass discrepancy was being explored for bump Cepheids, the cause of the bump was still not established. Buchler & Kovacs (1986) used an iterative perturbation method to calculate pulsation in Cepheids and found that there is a 2:1 period resonance between the fundamental and second overtone modes. It is this resonance that causes the secondary bump to appear in the light curves Cepheids. The conclusion was later confirmed by Kovács & Buchler (1989) and Buchler et al. (1990) using hydrodynamic models and proved that the 2:1 resonance caused the Hertzsprung progression.

The solution to the bump Cepheid mass discrepancy was finally determined after the release of the OPAL opacities (Iglesias & Rogers, 1991). Moskalik et al. (1992) computed non-linear models of beat (double-mode) and bump Cepheids using the new OPAL opacities. The calculations predicted bumps in the velocity curve such that the pulsation masses are revised upwards. While the change in mass tended to almost agree with the stellar evolution calculations, there were still small differences between pulsation and evolution mass predictions. Simon & Kanbur (1994) found that there was still a mass discrepancy for small-mass ($M = 4 - 5\ M_{\odot}$) Cepheids. Changing the opacity did not change the results; Kanbur & Simon (1994) tested OPAL and OP opacities and found negligible differences.

New models were computed by Antonello & Aikawa (1993) and Antonello & Aikawa (1995) for first overtone Cepheids. The authors found that there was still a mass discrepancy using the OPAL opacities. Also, a period resonance was discovered for $P_1/P_4 = 2$, where P_4 is the pulsation period of the fourth

overtone mode for first-overtone periods around 3 days.

The development of photometric surveys of the Large Magellanic Cloud has led to a number of investigations about the behavior of pulsation at sub-solar metallicity. Wood et al. (1997) modelled the LMC bump Cepheid HV 905 and predicted a pulsation mass of 5.15 $M_{\odot}$ while stellar evolution calculations predicted $M = 7.14\ M_{\odot}$, suggesting that the mass discrepancy was not solved. Morgan & Welch (1997) modelled the behavior of beat Cepheids in the LMC and made predictions regarding the behavior of Small Magellanic Cloud beat Cepheids. They found that the beat phenomenon occurs at shorter periods as a function of decreasing metallicity. Similarly, Buchler et al. (1997) considered the dearth of Galactic Cepheids in the period range of $8-10$ days while there are many in the LMC. Models of Galactic Cepheids in this period ranges are pulsationally unstable because of the influence of the 2:1 resonance of the second overtone to fundamental periods. The same resonance that causes the Hertzsprung progresson also causes the pulsation amplitude to decrease and destabilizes the pulsation. They found the destabilization to be metallicity dependent, working only in Cepheids with $Z \geq 0.013$ explaining the differences between the LMC and Galactic distributions of Cepheids.

Pulsation Modeling in the 21st Century

There are a number of groups computing non-linear models of Cepheid pulsation. For instance, Aikawa & Antonello (2000a,b) modelled pulsation in long-period Cepheids, while Feuchtinger et al. (2000) was interested in the structure of first overtone Cepheids. Models computed by Yecko et al. (1998) and Kollath et al. (1998) have focused on the contribution of turbulent convection on pulsation. However, the most impressive and largest set of models have been computed and presented by Bono et al. (1999b, 2000a). The authors computed a number of models with varying mass-luminosity relations representing standard stellar evolution and convective core overshoot in the progenitor stars and with different metallicities corresponding to Galactic and Magellanic Cloud compositions. The models range in mass from 5 to 11 $M_{\odot}$ and effective temperature $T_{\rm eff}$ = 7000 to 4000 K. Using these models, the authors calculated the boundaries of the Instability Strip and found that the boundaries are metallicity dependent. As the metallicity decreases, the effective temperature of the blue and red edges decrease. In the second article, Bono et al. (1999a) computed theoretical Period-Luminosity, Period-Color (P-C), and Period-Luminosity-Color (P-L-C) relations that agree with the observed relations. The metallicity dependence, however, was found to contradict observations such that metal-poor Cepheids are predicted to be brighter than metal-rich Cepheids. Furthermore, the P-L relation is better represented by a quadratic relation instead of a linear relation. These relations were explored further as a function of wavelength and applied to measurements of the distance scale Caputo et al. (1999, 2000a,b). The Hertzsprung Progression was also explored for LMC Cepheids (Bono et al., 2000c) and found to occur in the mass range of $M = 6.55$ to $7.45\ M_{\odot}$ and is centered at a period $P = 11.24 \pm 0.46$ days. The calculations of cool bump Cepheids show that the secondary bump replaces the primary maximum as the brighter maximum in the light curve, making the progression appear to shift to the rising branch of the light curve as

opposed to the descending branch.

The series of articles by the Bono and Caputo group continued by exploring how the helium and metal abundance affected the structure of the Cepheid Instability Strip (Fiorentino et al., 2002). The temperature boundaries of the Instability Strip were found to shift to higher temperature for decreasing metal abundance with fixed helium abundance and for increasing helium abundance with fixed metal abundance. This result provides a potential observational measure of mean helium and metal abundances of populations of Cepheids. They found that the variation of the helium and metal abundance affected the P-L and P-C relations as measured by the ratio of the change of Y to the change of Z $\Delta Y/\Delta Z$. Furthermore, the relations shift at periods > 10 days when $\Delta Y/\Delta Z > 1.5$. This group has produced significant results, but much of the assumed physics had not been tested for robustness. Petroni et al. (2003) tested how the pulsation models change with different assumptions for the equation of state. The equation of state changes the pulsation amplitude marginally, however tests of the spatial resolution of the helium and hydrogen ionization zones did have a significant effect on the distribution of bump Cepheid periods, with the center shifting to $P = 9.65 - 9.84$ days. The effect of varying convection in the Cepheid pulsation models has also been tested (Fiorentino et al., 2007). They modelled convection using the mixing length theory, which assumes a free parameter defined by the ratio of the distance a convective eddy travels l to the pressure scale height H_P. They computed models assuming $l/H_P = 1.5$ and 1.75. When the free parameter is increased the width of the Instability Strip is reduced because the red edge, defined by convective damping of pulsation, shifts to higher temperatures. However, convection was found to have a negligible effect on the P-L and Period-Wesenheit function.

An interesting application of the Bono et al. model program is the attempt to fit the observed light and velocity curves of δ Cep by Natale et al. (2008). The fit of the model estimates the composition, mass and effective temperature of the star. The helium abundance is $Y = 0.26$, lower than the standard $Y = 0.28$, and the metal abundance is also reduce from $Z = 0.02$ to 0.01. The deduced mass is $M = 5.7\ M_{\odot}$ and $T_{\rm eff} = 5700\ K$.

The results of Natale et al. (2008) suggest a possible difference between the metallicity of δ Cep and the Sun. Buchler & Szabó (2007) noted that the Petersen diagram, which shows the period ratio of beat Cepheids as a function of fundamental period, is a measure of the stars metallicity independent of the helium abundance. The authors computed hydrodynamic models of Galactic beat Cepheids using the OPAL opacities. The model Cepheids with lower metallicity tended to best fit the observed Cepheids with a range of $Z = 0.0089$ to 0.0221. The revised solar abundances suggested by Asplund et al. (2005) motivated a reanalysis of the model beat Cepheids (Buchler, 2008). Cepheids models with the Asplund et al. (2005) abundances give masses, radii, and periods in better agreement with observed properties of Galactic beat Cepheids.

The mass discrepancy that appeared to have been solved in the early 1990's was shown by a number of works to still exist; however, quantitative estimates for the difference between pulsation and evolution

masses were not determined. Beaulieu et al. (2001) used OGLE-II LMC Cepheid observations plus Atlas stellar atmosphere models to derive a period, effective temperature and luminosity of each Cepheid in the sample. The authors then used this information to compute pulsation models and derive a mass-luminosity (M-L) relation. The predicted M-L relation differs from the standard stellar evolution M-L relation suggesting the mass discrepancy is still important. It should be noted that this work makes an implicit assumption about the gravity of each Cepheid to compute the effective temperatures although the effect of thus assumption on the effective temperatrue is small. The mass discrepancy for Galactic Cepheids was computed using a theoretical Period-Mass-Radius relation to calculate the mass of Cepheids with observed radii (Bono et al., 2001). They showed that the mass discrepancy is still about 10%. Caputo et al. (2005) further tested the Galactic mass discrepancy using theoretical models to generate a Period-Mass-Luminosity-Color relation and compared it with Galactic Cepheids. The authors found that the difference between pulsation and evolutionary masses is a function of mass with the discrepancy being 20% for a $M = 4\ M_{\odot}$ Cepheid, decreasing to zero for a 13 $M_{\odot}$ Cepheid.

The bump Cepheid mass discrepancy was explored by Keller & Wood (2002) using a sample of 20 LMC bump Cepheids with V and R-band observations from the MACHO project. The observations were fitted using pulsation models for the stars where the masses of the best-fit models turned out to be smaller than suggested from stellar evolutionary tracks. On the other hand, Buchler et al. (2004) computed models to match LMC bump Cepheids and found that the pulsation masses agreed with the stellar evolution masses. Keller & Wood (2006) conducted a similar analysis as before for Large and Small Magellanic Cloud bump Cepheids. They found that the mass discrepancy is a function of metallicity with the Galactic Cepheids have a 14% discrepancy, LMC Cepheids have a 17% and SMC Cepheids have a 20% mass discrepancy. Keller (2008) reanalyzed the results of Caputo et al. (2005) and found that they had used a mass-luminosity relation that was linear over all masses considered. If one uses the mass-luminosity relation from Bono et al. (2000a) or Bressan et al. (1993) which are non-linear for masses $\geq 10\ M_{\odot}$ then the mass dependence of the mass discrepancy disappears. There is, however, a mass discrepancy of about 17% that is still not understood.

Cepheid and variable star research, in general, has a rich history. The extra information about stellar structure from pulsation periods and amplitudes make Cepheids an attractive research field and the discovery of the Leavitt Law makes these stars a powerful tool for extragalactic and cosmological studies. However, it is clear that while many properties of Cepheids can easily be observed and computed such as the Leavitt Law or the Period-Mean Density relation, there are many subtleties to be understood, such as the Cepheid mass discrepancy.

1.4 Cepheid Atmospheres

The previous two sections discussed the independent and separate developments of the fields of stellar atmosphere modelling and Cepheid variable stars with the purpose of bridging them into a study of Cepheid

atmospheres. However, the study and modelling of Cepheid atmospheres is not a novel idea. There has been much progress on understanding the outer layers of these stars as some of the research mentioned in the previous sections suggests, and there is also motivation for new generations of Cepheid atmosphere models to compare with high resolution spectroscopic and interferometric observations.

The first model Cepheid atmospheres were by Lautman (1957), who calculated the solutions to the hydrodynamic equations for an isothermal atmosphere undergoing adiabatic pulsation. At the base of the atmosphere the pulsation is driven by a sinusoidal wave similar to a piston moving back and forth. He found that the pulsation generated bumps in the velocity curve. He argued that when the piston pushes the atmosphere outward, a compression wave is generated and propagates outwards. The wave lifts the atmosphere and causes the primary peak of the velocity curve. Eventually, gravity begins to dominate and the outer layer falls again. However, before the layer returns to its starting point, another compression wave generated by the piston interferes with the infalling material and changes the velocity of the gas. Lautman argued this interference causes the secondary humps in the velocity curve, however, these waves do not become shocks in the numerical simulations.

It was fifteen years before the next attempt to model radial pulsation in stellar atmospheres was taken. Keller & Mutschlecner (1970) computed a hydrodynamic model of the atmosphere of a Cepheid with an 11.5 day period. They calculated pulsation in a manner similar to the nonlinear pulsation calculations mentioned previously, with the pulsation simulated by a piston-like boundary condition at the base of the model. Here, plane-parallel stellar atmosphere models by Strom & Avrett (1964b, 1965) were used as input for the program. The radiation field was calculated for the optically thin layers of the star. The results of the calculation were somewhat limited but they did agree with observed $T_{\rm eff}$-color relations. This result demonstrated the potential for hydrodynamic atmospheres to model the atmospheres of Cepheids.

Some investigations of Cepheid atmospheres have also ignored dynamic motions in the atmosphere. The atmosphere and spectra of δ Cep was studied by Haefner (1975) using static atmosphere models representing different phases of pulsation. He fitted the effective temperature and the gravity of the models to the observations and found that δ Cep has solar-like abundances.

Karp (1975a) developed a hydrodynamic model for a 12 day Cepheid and included radiative transfer. The model was similar to that of Keller & Mutschlecner (1970) except that it included the deep envelope of the star, meaning that the model included the driving region for pulsation. The atmosphere was sitting on top of the envelope. Radiative transfer was computed assuming that the atmosphere is plane-parallel, and in local thermodynamic equilibrium. The opacity of each layer was denoted by the Rosseland mean. The resulting models reproduced the phase lags and secondary bumps in the light curves. He argued that compression waves lead to the bump phenomena. In a second article, Karp (1975b) computed the colors from the models and found that they agree with the observed effective temperature-color relation while in the third article. He argues that the observed microturbulence in Cepheids is not caused primarily by the pulsation velocity (Karp, 1975c). The microturbulence was assumed to be due to shocks in the atmosphere.

Another set of hydrostatic model atmospheres for Cepheids were used to test the helium enrichment theory of Cox et al. (1977) by Kamp & Deupree (1979). The goal of the analysis was to compare synthetic spectra from model atmospheres with and without helium enrichment to search for spectral line differences that may be observed and thereby verify or disprove that hypothesis. They found that helium enrichment affected the equivalent width of the Fe I lines.

Hill & Willson (1979) and Willson & Hill (1979) analysed numerical models of Miras and RR Lyrae variables to develop an analytic theory of shock amplitudes. To force a period solution for the pulsation and shock formation, they argued that the atmosphere of the star must puff up, in a manner similar to that argued by Lautman (1957). When the atmosphere us puffed up, some of the material is ejected. The interaction between mass loss and pulsation in Cepheids was discussed by Willson & Bowen (1986), who noted that Cepheid mass loss could affect the star's evolution. Bowen (1988) computed non-linear models for Mira variables and noted that shocks puff up the atmosphere. For Mira variables, he found that both shocks and dust are necessary ingredients to drive mass loss. Bowen & Willson (1991) continued the analysis by computing models with parameters consistent with spanning the Asymptotic Giant Branch. They found that mass loss dominates the evolution along the Asymptotic Giant Branch. The Bowen-WIllson program assumes a spherically symmetric grey atmosphere but includes non-LTE effects to model radiative reheating and cooling. This makes the program a powerful tool for the study of mass loss and shocks. However, the program is not ideal for Cepheids because the Cepheid shock amplitudes are much larger than Mira shock amplitudes. There a more robust treatment of radiative cooling is needed for modelling Cepheid mass loss.

Sasselov & Raga (1992) developed a new plane-parallel hydrodynamic program that models atmospheres of Cepheids assuming non-local thermodynamic equilibrium for hydrogen, Ca II and Mg II. The program is based on the one-dimensional hydrodynamic scheme proposed by Colella & Woodward (1984). The authors assume piston-driving at the base of the atmosphere using the oscillation formalism found by Buchler et al. (1990). They used the program was used to calculate line profiles of Cepheid models and detect the causes of line asymmetries (Sasselov & Lester, 1994b; Sabbey et al., 1995).

As part of a numerical exploration of the dynamical atmospheres, Fokin et al. (1996) modelled the atmosphere of δ Cep as part of a broader program to model variable stars including the dynamic atmospheres of low-mass giants (Fokin, 1991), RR Lyrae (Fokin, 1992; Fokin & Gillet, 1997), and BL Herculis (Fokin & Gillet, 1994). The hydrodynamic program solves for non-linear, non-adiabatic pulsation in a spherically symmetric atmosphere and uses different opacity tables such as OPAL and OP. The radiative transfer includes time-dependent effects and artificial viscosity for modelling shocks. The purpose for modelling δ Cep was to explore the dynamic structure of the atmosphere and to understand the behavior of time-series observations of the Fe I λ 5576.0883 line as well as the cause of turbulence in the atmosphere. The models revealed that the change of turbulence is due to velocity gradients caused by a strong shock wave in the atmosphere that compresses the atmosphere. The observed iron lines are shown to be fitted well by the models suggesting that the line-forming layers are not affected by non-LTE effects.

The development of optical interferometry and the use of the interferometric Baade-Wesselink method has motivated the need for better model atmospheres. With this in mind, Marengo et al. (2002) modelled the atmosphere of ζ Gem using the hydrodynamic program of Sasselov & Raga (1992). From the model, the authors computed the temperature structure at various phases and fitted the temperature structure to static ATLAS models to estimate the radiative transfer at each phase. Using this quasi-static method, the limb-darkening of the atmosphere was calculated as a function of phase tested the assumption that the limb-darkening, and hence the projection factor for computing the pulsational velocity from the radial velocity is constant with respect to phase. They determined that the limb-darkening is, in fact, not constant and cannot be modelled hydrostatically. In subsequent articles, Marengo et al. (2003) and Marengo et al. (2004) developed limb-darkening corrections for interferometric observations and an error analysis for the interferometric Baade-Wesselink method.

Similarly, Nardetto et al. (2004) modelled the atmosphere of δ Cep using the Fokin program to calculate the dynamic structure of the atmosphere and the projection factor as a function of phase. The uncertainty of the projection factor is about 6% when one assumes it is a constant value with respect to phase. The variation of limb-darkening affectsf the projection factor and thus the predicted distance from the interferometric Baade-Wesselink method. However, the authors found that the uncertainty due to limb-darkening has little impact on distance estimates, leading to an uncertainty of about 1%.

Mihalas (2003) reviewed the field of Cepheid atmosphere modelling and discussed the necessary input physics. He argued that one needs an adaptive mesh to resolve the ionization zones because the zone's thickness is less than a pressure scale height but it travels several heights in one pulsation period. Convection is another challenge that is only going to be solved by three dimensional simulation;"the one-dimensional approximations are problematic at best". Mihalas also argued that the atmospheres should be computed in non-local thermodynamic equilibrium with varying rate equations to handle the change of structure and shocks. Furthermore, one needs to use complete frequency and angle-dependent radiative transfer for computing line profiles and stellar continuum.

The field of modelling Cepheid atmospheres has taken tentative steps; the total number of models in the articles cited is about one dozen. There are many more non-linear models for Cepheid interiors than for the atmospheres. The reason for the lack of models is clear; they require significant computing power. One of the Fokin et al. (1996) models requires calculations of about 1000 pulsation cycles with many iterations per cycle. To compute radiative transfer is computationally intensive as well using the majority of computing time (Mihalas, 2003).

1.5 Thesis Outline

From both historical perspectives and recent developments in stellar atmospheres, Cepheid pulsation and, in particular, Cepheid atmospheres, it is clear that there are many unanswered questions, more than enough

occupy any one person's lifetime much less a graduate career. Some of these questions are:

Cepheid Limb-Darkening & the Projection Factor

The works of Marengo et al. (2002, 2003, 2004) and Nardetto et al. (2004, 2007) suggest that limb-darkening affects results from optical interferometry to about a few percent, based on models for only three Cepheids. These results need to be confirmed by more dynamic model atmospheres for more Cepheids computed independently to have a larger, more robust sample. Furthermore, with the quality of interferometric observations expected in the next couple of years, it is possible to compute the distance and Cepheid properties without relying on the interferometric Baade-Wesselink method and its assumption of a projection factor. Instead, one could use the time-series observations to constrain dynamic model atmospheres and fit a distance to the Cepheid. This concept has been demonstrated to be possible for fitting interferometric plus spectro-photometric observations of red giant stars (Wittkowski et al., 2004, 2006a,b)

Cepheid Circumstellar Envelopes

The discovery of the CSE's or cocoons surrounding Cepheids from interferometric observations (Kervella et al., 2006) have changed the view of Cepheids as singular, isolated objects that are somewhat easier to model and understand. The inclusion of a shell of material requires one to study the circumstellar environment to understand infrared interferometric, photometric and spectroscopic observations. Furthermore, the nature of these shells is not understood, Kervella et al. (2006) suggested they may form in a manner similar to the formation of the circumstellar shells about Mira variables, that being mass loss. However, there is no obvious evidence for mass loss, the shells might be relics from an earlier stage of evolution. Therefore, from the perspective of stellar evolution and structure the origins of these shells needs to be understood, be it from observational or theoretical investigations. Because these shells emit in the IR, then they may influence the IR P-L relations (Madore et al., 2009; Ngeow et al., 2009), thus further motivating work to solve the problem.

Cepheid Mass Discrepancy

The Cepheid mass discrepancy has been a persistent problem in Cepheid pulsation and much progress has been made in resolving the difference from a factor of two for bump Cepheids to $\approx$ 20%. However, what is the source of error for this last 20%? Bono et al. (2006) reviewed four possibilities: convective core overshoot in progenitor main sequence stars, mass loss on the Cepheid Instability Strip, unknown opacities, or rotational mixing. These possibilities can be explored using theoretical Cepheid models and solutions such as the amount of mass loss can be tested observationally but there is still no resolution at this time. While a 20% uncertainty may be well within "astrophysical uncertainty", it is important to understand the

masses and the underlying differences between evolution and pulsation models both calibrate properly the P-L relation to high precision and to understand stellar evolution in general.

The Infrared Leavitt Law

The IR Leavitt Law is an important tool for measuring distances because it is much less influenced by metallicity effects than its optical counterpart. The benefit of the IR Leavitt Law is that it is not affected by metallicity effect compared to its optical counterpart. Thus it will have a much smaller uncertainty and holds great promise for cosmological studies. With enough observations of Cepheids in distant galaxies with the forthcoming *James Webb Space Telescope*, one can potentially measure the Hubble Constant to an accuracy of 1%. With this precision, the degeneracy of cosmological parameters in the WMAP year 5 results (Dunkley et al., 2009) can be broken, such that Ω_M can be constrained. The IR P-L relation can also be used to better understand the statistical nature of Cepheids. Because IR flux is in the Wein's tail of the spectral energy distribution then the temperature of the Cepheid has less of an effect on the luminosity. Therefore the luminosity is directly related to the stellar radius and the IR P-L relation is related to the Period-Radius relation. The two observed relations can be used to constrain each other and for studies of populations of Cepheids. The question about the IR P-L relation is, if there is a metallicity dependence, how significant is it and does the existence of CSE's affect the observed relations.

The Calibration of the Zero-Point of Optical P-L Relations

One of the goals of optical interferometry is to compute distances to nearby Cepheids to calibrate the zero-point of the P-L relation. So far, precision distance estimates have been done for about eight Cepheids. In the near future though, interferometry will be able to measure about fifty Cepheids using the VEGA instrument on the Center for High Angular Resolution Astronomy (CHARA) interferometer (Mourard et al., 2008b). The forthcoming Gaia satellite (Cacciari, 2009) will measure the parallax of all Galactic Cepheids to a precision $< 4\%$ and even the parallax of Magellanic Cloud Cepheids to $20-30\%$, and similar precision will be achieved by the Space Interferometry Mission (SIM) (Edberg et al., 2007). With such precise distance estimates, the largest source of uncertainty for the zero-point calibration is the effect of metallicity on the Cepheid luminosity at a given mass. Solving this uncertainty to high precision requires high resolution time-series spectroscopy coupled with Cepheid models containing a complete set of opacities to predict synthetic spectra for comparison.

Non-Radial Pulsation & the Blazhko Effect

These two phenomena summarize one of the grand challenges for modelling Cepheids suggested by Buchler (2009) based on recent observations of LMC Cepheids. He noted that non-radial modes have mixed p and g modes which are strongly damped in Cepheids and it is argued that non-radial pulsation in Cepheids

will require three-dimensional hydrodynamic simulations. The Blazhko effect has been observed in a few Cepheids and has even been proposed to operate in Polaris (Stothers, 2009) but the cause of the Blazhko effect is unknown. There are a number of hypotheses to explain the amplitude modulation including non-radial pulsation and pulsation resonances (Dziembowski & Mizerski, 2004), coupling between a subsurface magnetic field and convection (Stothers, 2006), and possibly shocks (Chadid et al., 2008).

Convection in Cepheids

Understanding convection is possibly the holy grail for stellar physicists and is important in every star, not just Cepheids. Convection occurs in the envelopes of stars with spectral type A and later, while convection occurs in the core for stars of earlier spectral type. Also, convection has been discovered to occur in the envelopes of some hot stars (Cantiello et al., 2009). Current techniques for solving convection in pulsating stars are all basically some variant of a time-dependent mixing length theory (Buchler, 2009). Both Buchler and Mihalas (2003) discussed convection as part of a "grand challenge" and noted that the only way to truly include convection rigorously is with three dimensional hydrodynamic models. This has been done for stars such as the Sun (Nordlund et al., 2009), and M-dwarfs (Browning, 2008). However, three dimensional simulations of convection have not been applied to Cepheids because of the scale required to include radial pulsation that moves the convection zone a significant number of pressure heights. While this goal is probably far off, it may be possible to use spectroscopic observations to constrain one-dimensional convection schemes. Gray (2009) used spectroscopic line bisectors to understand the surface granulation of the cool star γ Cygnus and has demonstrated that the shape and position of various line profiles can be used to calculate the change of radius of a Cepheid as a function of phase (Gray & Stevenson, 2007). It may be possible to couple this kind of analysis with one-dimensional hydrodynamic calculations to constrain time-dependent mixing length theory. This observational constraint would be a powerful tool for mapping the red edge of the Instability Strip.

These seven challenges hardly summarize all the potential unanswered questions in Cepheid research but they form a common theme. All these problems may be explored to some degree by radiative hydrodynamic (RHD) models of the atmospheres of Cepheids. Realistic RHD models require convective treatment, the ability to resolve shocks, and to be able to produce time-series intensities and spectra. Convection can be explored by various one-dimensional treatments and tested with observations, and the RHD program can test if shocks might reproduce the amplitude modulation that is the Blazhko effect as suggested by Chadid et al. (2008). It has been shown previously that RHD models are necessary to understand the variation of the projection factor with respect to period, phase, and wavelength and to further understand Cepheid limb-darkening and spectra.

The Cepheid mass discrepancy can also be explored by RHD modelling. A spherically symmetric

Cepheid atmosphere requires three input parameters, one of which is the mass of the star. Therefore, by modelling nearby Galactic Cepheids and comparing to observations, pulsation masses may be computed and the mass discrepancy can refined. The current mass discrepancy is not even consistently measured (Caputo et al., 2005; Keller, 2008). A RHD program will be able to test the underlying physics that may explain the mass discrepancy such as opacities or mass loss. The opacity tables may be varied to test its affect of mass predictions, and if one develops a physical description for mass loss then it may be added to the RHD program to test its connection with atmospheric dynamics, and pulsation to make observable predictions.

Mass loss needs to be explored in Cepheids to not just explain the mass discrepancy but also as an explanation for the existence of the circumstellar envelopes. Observational data regarding the CSE's is still sparse but there is enough data to begin constraining theories and potentially mass-loss prescriptions in RHD simulations. However, before one can attempt to explain the existence of CSE's using RHD models under the hypothesis of mass loss, one actually needs to develop a theory for Cepheid mass loss.

The goal of this dissertation is not to revolutionize the understanding of Cepheid pulsation, atmospheres and dynamics but to take the first steps in developing tools that can be used to study these stated problems among others. With this goal in mind, the dissertation is divided into two parts. The first part describes the derivation and development of an RHD program to model the effects of pulsation on the structure of a Cepheid atmosphere and the resultant emergent radiation. The RHD program is a combination of the stellar atmosphere program ATLAS (Kurucz, 1993) and the one-dimensional hydrodynamic program HERMES (Sasselov & Raga, 1992). The plane-parallel ATLAS program is rewritten in FORTRAN 95 from its earlier FORTRAN 77 form. New versions of the program are developed to include spherically symmetric geometry that is appropriate for modelling the extended atmospheres of Cepheids and other giant/supergiant stars and even pre-main sequences stars.

The conversion to spherical symmetry is discussed in Chapter 2. In that chapter, the new program is tested by comparing spherically symmetric model atmospheres with spherically symmetric PHOENIX model atmospheres and with optical interferometric plus spectrophotometric observations of K and M-type giants. This is the first step in verifying that the spherically symmetric version of the ATLAS program produces realistic model atmospheres.

In Chapter 3, a detour is taken from the development of the RHD program to investigate limb-darkening in static model atmospheres. The current paradigm of stellar limb-darkening, its measurement and parameterization is reviewed and is found to be lacking. Limb-darkening models are used in interferometric observations to calculate the angular diameters of both static stars and Cepheids, implying that a detailed understanding of limb-darkening is important for understanding the physical parameters of these stars. The limb-darkening relations derived in the literature ignore atmospheric extension, but the effect of the extension on the relations carries significant information about atmospheric structure.

The fourth chapter discusses the development of the RHD program with a review of the structure of

the HERMES program. The hydrodynamical program is converted from plane-parallel geometry to spherical symmetry and combined with the spherical ATLAS program. The appropriate modifications are described as well as new developments, and preliminary tests.

The second part of this thesis focuses on the hypothesis of mass loss in Cepheids with the goal of understanding the driving mechanism and testing it with known observational evidence. In Chapter 5, a theory for pulsation-driven mass loss in Cepheids is derived based on the Castor et al. (1975) analytic method for calculating radiatively-driven mass loss. An analytic solution for pulsation-driven mass loss is derived from the theory. In Chapter 6, the pulsation-driven mass-loss theory is applied to a sample of Galactic Cepheids with determined physical properties and is compared to predictions from radiation-driven mass loss. The mass-loss rates are used to predict IR excesses from dust produced in the wind generating CSE's and are also compared to rate of period change observations to test if mass loss has a significant effect on the evolution of a Cepheid.

The pulsation-driven mass-loss theory is applied to theoretical models of Cepheids with different metallicities in Chapter 7. The purpose of this experiment is to determine how pulsation-driven mass loss changes with decreasing metallicity. Understanding the metallicity dependence is important because the mass discrepancy is metallicity dependent (Keller & Wood, 2006) and mass loss is a testable solution to that problem.

In Chapter 8, the mass-loss hypothesis is explored from another angle. Using optical and infrared observations of LMC Cepheids from the OGLE-II and the *Surveying the Agents of Galactic Evolution* (SAGE) survey, the prevalence for mass loss is tested. For each Cepheid in the sample, the spectral energy distribution is tested for the existence of infrared excess due to the presence of CSE's, assuming the CSE's are generated from mass loss. In this analysis, the predicted mass-loss rates are independent of assumed driving mechanism thus providing a test for the pulsation-driven mass-loss theory. Also, the IR P-L relations are tested to see if and how much they are affected by presences of CSE's.

In the final Chapter of this dissertation, a summary and conclusions are presented. Furthermore, an outlook of future research directions stemming from this dissertation is discussed.

Part I

Stellar Atmospheres & Radiative Hydrodynamics

Chapter 2

Development of the Spherically Symmetric Stellar Atmospheres Program SAtlas

Part of this chapter is published as:
"Determining Parameters of Cool Giant Stars by Modeling Spectrophotometric and Interferometric Observations Using the SAtlas Program" [1]
Neilson, H.R., & Lester, J.B. 2008, A&A, 490, 807

> *"The problem of fitting a series of beautiful internally-consistent models to honest-to-goodness real stars that are up there, is horrible ... "* - A. B. Underhill (Pecker, 1965)

2.1 Introduction

One of the great successes of modern astrophysics is the development of programs to model stellar atmospheres. These models have increased the understanding of the radiative output of stars and enhanced the interpretation of the structure of the outer layers of stars. The models have been also used to understand the frequency-dependent luminosity of galaxies via spectral synthesis models.

The Atlas program (Kurucz, 1970c) is a stellar atmospheres program that has been instrumental in much of these successes. The Atlas program is designed to model the structure of the atmosphere of a star and compute the radiative output of the star that can be compared with observations. The program assumes a plane-parallel geometry for the computation because it is the simplest and is computationally quick. The Atlas program best models stars in the spectral range A-K, for hotter and cooler stars non-local thermodynamic equilibrium issues become more important.

The assumption of a plane-parallel geometry treats the atmosphere as an infinite slab that has a thickness

[1] Neilson & Lester (2008a), reproduced with permission by Astronomy & Astrophysics

that is insignificant relative to the radius of the star. This assumption works remarkably well for most stars however some stars have atmospheres that are significantly extended. The thickness of the atmospheres of these stars is a significant fraction of the stellar radius.

In these cases, the ATLAS program does not model the stellar atmospheres accurately, and the assumption of plane-parallel geometry needs to be revisited. This has been accomplished for other model stellar atmosphere programs such as the PHOENIX (Hauschildt et al., 1999b) and MARCS (Gustafsson et al., 2008). However, it is useful to include spherical symmetry in the ATLAS program because it is the only one of the three programs that is open source and can easily be used as a testbed for new physics. A second use that is related to the goals of this thesis is the spherically symmetric version of the program, SATLAS, is used as part of the hydrodynamic program for modeling Cepheid atmospheres that is presented in Chapter 4.

In this chapter, we discuss the inclusion of spherical symmetry into a Fortran 2003 version of the ATLAS program. The Fortran 2003 versions of the ATLAS9 and ATLAS12 programs are described in Lester & Neilson (2008) as well as the conversion to spherical symmetry. To change the program from the plane-parallel geometry to the spherical geometry requires changes to how the radiative transfer, hydrostatic equilibrium and temperature correction are calculated. In the next sections, we derive in detail the methodology for computing the spherically symmetric routines. In section 2.5, we compare the SATLAS models with PHOENIX models followed by analysis of optical interferometric observations using a large number of SATLAS models.

2.2 Spherically Symmetric Radiative Transfer

There are a number of methods for determining the radiative transfer in a stellar atmospheres program. For example, the PHOENIX uses a method of short characteristics (Hauschildt, 1992), while radiative transfer in the plane-parallel version of the ATLAS program is calculated by solving the integral version of the equation of transfer. In that scenario, the source function S_ν is guessed and iterated by solving the equation of transfer until convergence is reached.

In spherical symmetry, one cannot directly solve the integral version of the equation of transfer. Therefore, we solve the differential version of the transfer equation

$$\mu \frac{\partial I(\nu)}{\partial r} + \frac{(1-\mu^2)}{r} \frac{\partial I(\nu)}{\partial \mu} = k(\nu)[S(\nu) - I(\nu)], \tag{2.1}$$

following the Feautrier (1964) method that is reorganized using the Rybicki (1971) solution. The derivation of these techniques for solving the spherically symmetric equation of transfer is given in Appendix A, along with a derivation of a Hermitian solution from Auer (1976) that is fourth-order accurate.

In this solution, the equation of transfer is rewritten so the radiation is computed along rays that are parallel to the direction of the observer, as shown in Figure 2.1. In this system, there are two sets of rays: one that intersects the ”core” boundary and the other set penetrates the atmosphere to a depth that is half

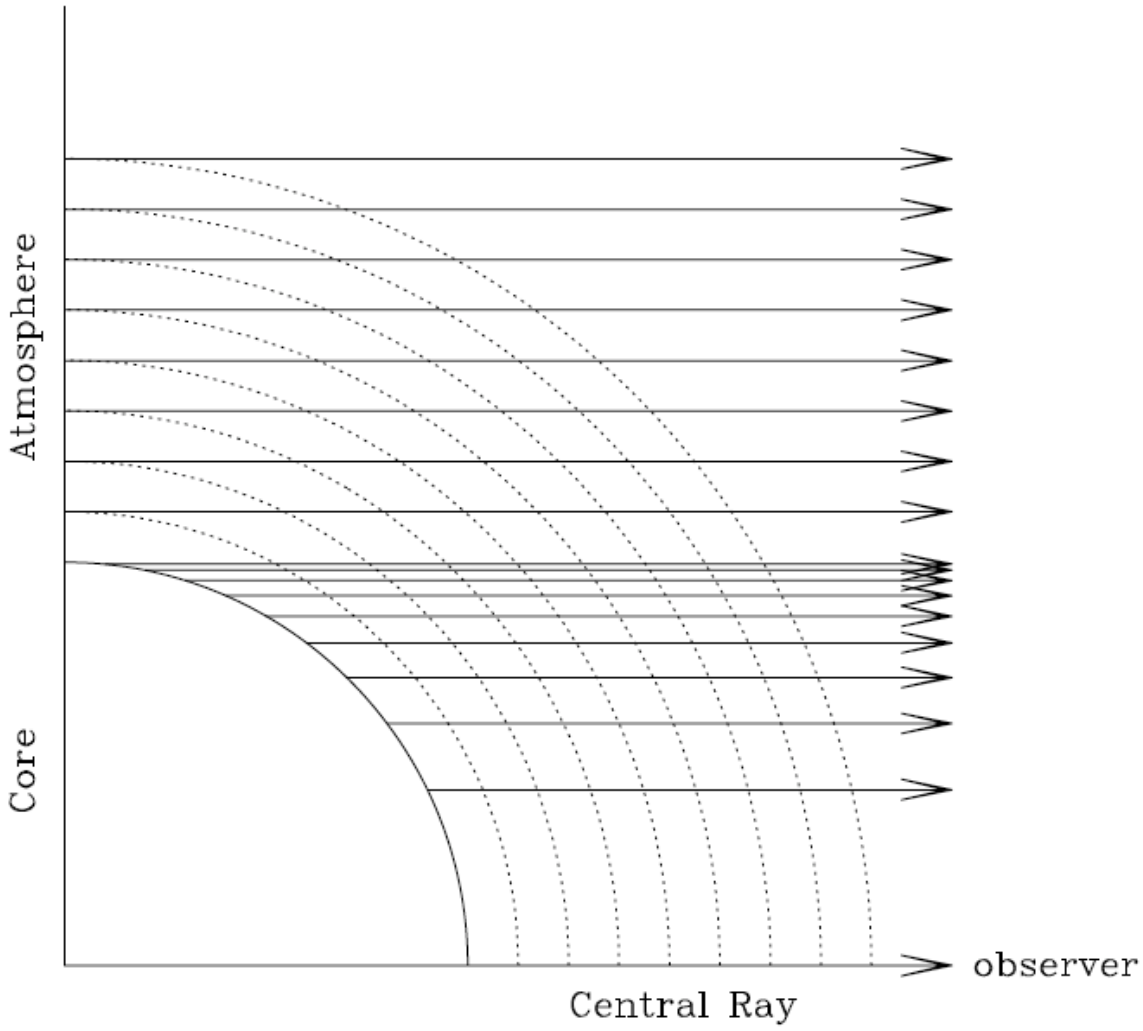

Figure 2.1: The geometry for solving the equation of transfer using the Rybicki (1971) method. Reproduced from the Lester & Neilson (2008) with permission.

way through the star. The rays that intersect the "core" terminate at an optical depth $\tau_R = 100$, although this depth may be changed by the user. The number of rays are arbitrary, we use 10 rays. The ten rays are spaced equally in terms of the angle $\mu = \cos\theta$. The number of rays that intersect the atmosphere is the number of depth points in the model. This number is typically set to 72, which translates to an optical depth step size of 0.125 from $\log \tau_R = -6.875$ to 2.

2.3 Spherically Symmetric Hydrostatic Equilibrium

The pressure structure of a stellar atmosphere depends on the assumed geometry of the atmosphere. In a plane-parallel atmosphere, the radius and mass interior to the atmosphere is constant, meaning the gravity ,g

at any layer in the atmosphere is constant. The pressure structure is then calculated by solving the equation

$$\frac{dP_{\rm tot}}{dm} = g, \tag{2.2}$$

where m is the mass column density defined as

$$dm = -\rho dr. \tag{2.3}$$

This equation is trivial to solve numerically, illustrating the benefits of assuming a plane-parallel atmosphere.

In spherical symmetry, the gravitational acceleration is not constant because the radius and mass interior to a layer is not constant. However, the mass of any shell in the atmosphere is orders of magnitude less than the mass interior the atmosphere. Therefore, we assume that the mass interior to any layer is just the mass of the star and the gravity scales as

$$g(r) = \frac{GM_*}{r^2}. \tag{2.4}$$

The equation for hydrostatic equilibrium therefore becomes

$$\frac{dP_{\rm tot}}{dm} = \frac{GM_*}{r^2}, \tag{2.5}$$

where $P_{\rm tot}$ is the sum of the gas, radiative, and turbulent pressures, or equivalently writing the pressure structure in terms of the Rossland optical depth, $\tau_{\rm R}$,

$$\frac{dP_{\rm tot}}{d\tau_{\rm R}} = \frac{GM_*}{k_{\rm R}(r)r^2}. \tag{2.6}$$

The Atlas program is written such that the Rossland optical depth is the independent variable of choice. One may use this or the mass column density or radius as the independent variable, all three choices are equivalent.

2.4 Spherically Symmetric Temperature Correction

The goal of a temperature correction routine is to enforce the principle of radiative equilibrium in the model stellar atmosphere. Radiative equilibrium is maintained when the luminosity at each layer in the atmosphere is constant. In a plane-parallel stellar atmosphere, this is equivalent to the flux being constant at each layer because the radius is assumed constant. In a spherically symmetric atmosphere, radiative equilibrium may be written as

$$\nabla \cdot \left[r^2 \int_0^\infty F_\nu d\nu \right] = 0. \tag{2.7}$$

There are a number of methods to enforce radiative equilibrium. One of the most simple is described in

Appendix B that is based on the integration of Equation 2.1 with respect to $\mu d\mu$, where $\mu = \cos\theta$,

$$\frac{\partial r^2 H_\nu}{\partial \tau_\nu} = r^2(J_\nu - S_\nu) \tag{2.8}$$

where the source function S_ν is approximated as the blackbody function, $B_\nu(T)$ and $d\tau_\nu = k_\nu dr$. If one integrates Equation 2.8 with respect to frequency then the left-hand side is zero and

$$\int_0^\infty k_\nu(B_\nu(T) - J_\nu)d\nu = 0. \tag{2.9}$$

When a stellar atmosphere is calculated this relation is not necessarily conserved so the routine changes the temperature at each layer so that Equation 2.9 is true. This is done by considering the linear perturbation of the blackbody function with respect to the temperature, $B_\nu(T) \rightarrow B_\nu(T) + \Delta T dB_\nu/dT$ and solving for the correction ΔT. This is a simple method with many flaws but it does illustrate the general theme to temperature correction methods to use linear perturbation theory and solve for a corrected temperature. However, this method is very slow and computationally expensive; the ideal temperature correction routine should be efficient if not as precise.

The Phoenix program uses a modified version of the Unsöld-Lucy temperature correction routine Lucy (1964). This method is the similar to the previous one, and is described by Mihalas (1978). This Unsöld-Lucy method produces a similar result as the above method but with an additional term that depends on the difference between the predicted and desired fluxes at layers above any layer that is being corrected. This additional term corrects the temperature at larger depths much more rapidly than the previous method and is thus more efficient.

The Atlas program uses the Avrett-Krook temperature correction routine (Avrett, 1964), which takes the equation of transfer and the second and third moments of the transfer equation and linearly perturbs them with respect to the temperature and the independent depth variable, be it the radius, mass column density or the optical depth. This differs from the other methods that perturb the variables with respect to the temperature only. Perturbing the independent variable rapidly corrects the temperature at large depths as well. Because experience has shown that the Avrett-Krook method to be robust and able to stabilize the temperature structure to $\leq 1\ mK$ (Tycner & Lester, 2002), we derive a spherically symmetric version of the Avrett-Krook method for the SAtlas program, and is described in detail in Appendix B.

2.5 Comparison of SAtlas Models to Phoenix Models

The spherical version of Atlas program is compared to stellar atmospheres modeled by the Phoenix program Hauschildt et al. (1999b) as a test of the quality of the models. The SAtlas program has been compared to the plane-parallel version of the program and to models from the spherical version of the Marcs program by Lester & Neilson (2008). We compare with the Phoenix models because the Phoenix program, arguably,

sets the current benchmark for precision stellar atmospheres.

In Figure 2.2, the temperature structure of four model stellar atmospheres computed using the SAtlas program are plotted as a function of gas pressure along with four Phoenix NextGen model stellar atmospheres (Hauschildt et al., 1999b). The model stellar atmosphere have effective temperatures of 3400 and 3800 K, have $\log g = 0.5$ and 1, and have a mass of $5M_{\odot}$. The predicted temperature structures from the SAtlas program agree with those from the Phoenix program. The structures are most different at depths where the temperature begins to increase at a greater rate in the range $T = 3000$ to 4000 K where convection is important. However, the differences are less than a 5%. The SAtlas computes model stellar atmospheres that agree with models from the Phoenix and the SAtlas program is a powerful tool for modeling stellar atmospheres but the program needs to be tested using observations.

2.6 Testing the SAtlas Code Using Optical Interferometry

Optical interferometry accurately measures the combination of the angular diameter and the structure of the intensity distribution of a stellar disk. The combination of interferometry with spectroscopy and/or spectrophotometry is a powerful tool for determining effective temperatures and other properties of stars, and the growth of optical interferometry is testing theoretical models of stellar atmospheres in new ways.

In a series of articles, Wittkowski et al. (2004, 2006a,b) fit Very Large Telescope Interferometer (VLTI) observations of cool giants using the VINCI instrument with spherically symmetric stellar atmosphere models in local thermodynamic equilibrium (LTE) computed with the Phoenix program (Hauschildt et al., 1999b), and with plane parallel models from Phoenix and Atlas (Kurucz, 1970c, 1993). The authors demonstrated that optical interferometry can detect the wavelength-dependent limb-darkening of cool giants and that the limb-darkening can be used to constrain model stellar atmospheres. These works are based on observations of three stars: ψ Phoenicis (M4 III), γ Sagittae (M0 III), and α Ceti (M1.5 III) also called Menkar.

We model these interferometric observations using the new spherically symmetric version of the Atlas program (SAtlas) developed by Lester & Neilson (2008) and to determine fundamental parameters of the three stars. There are two versions of the SAtlas program, one using opacity distribution functions while the other uses opacity sampling; in this work we use the first version. The radiation field is computed using the method suggested by Rybicki (1971), which is a reorganization of the Feautrier (1964) method.

In the remainder of this chapter, we compute cubes (three dimensional grids) of spherically symmetric stellar atmospheres with dimensions of luminosity, mass, and radius to model interferometric visibilities to fit the VLTI/VINCI observations and broadband spectrophotometry from Johnson & Mitchell (1975). This will provide a robust test of the program and a comparison to the results predicted using spherically symmetric Phoenix models. In the next section, we outline the method for computing synthetic visibilities and predicting radii, effective temperatures, luminosities, masses, and gravities. We present the results in

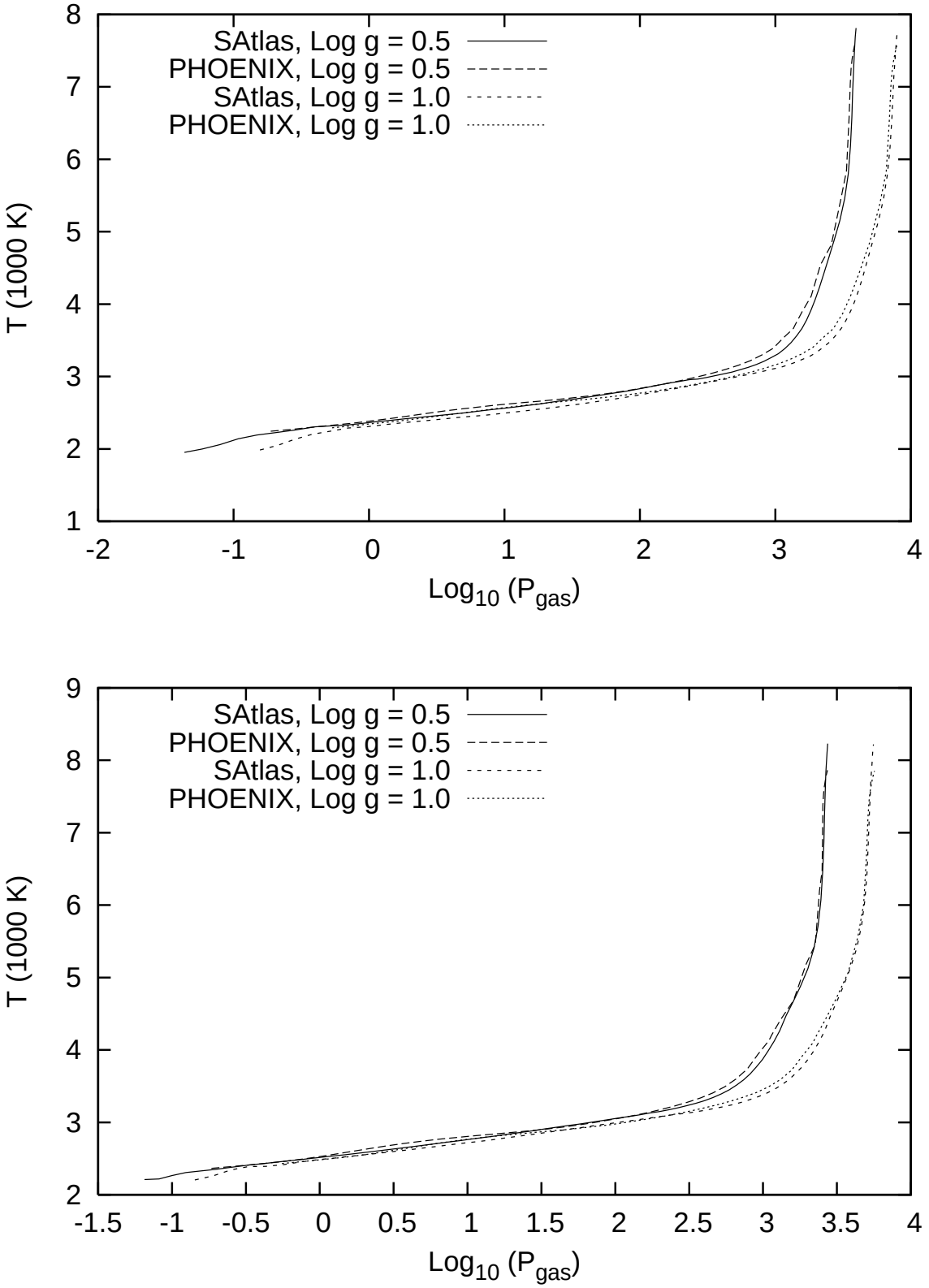

Figure 2.2: Comparison of model stellar atmospheres with gravity $\log g = 0.5$ and 1, mass of $5M\odot$ and effective temperature of (top) 3400 and (bottom) 3800 K.

the seventh section and the discussion in the eighth section.

2.7 Method for Computing Visibilities and Determining Stellar Parameters

The goal of these sections is to determine the global properties of the three observed stars. Interferometric observations are ideal for measuring the angular diameter, and with the HIPPARCOS parallax (Perryman & ESA, 1997) one can find the linear radii of the stars. The visibility (Davis et al., 2000; Tango & Davis, 2002) at wavelength λ is

$$V_{\rm LD}(\lambda) = \int_0^1 S_\lambda I_\lambda(\mu) J_0 \left[\pi\theta_{\rm LD}(B/\lambda)(1-\mu^2)^{1/2}\right] \mu {\rm d}\mu. \tag{2.10}$$

In this equation, S_λ is the sensitivity function of the instrument (VINCI in this case) (Kervella et al., 2000), J_0 is the zeroth-order Bessel function, B is the length of the baseline of the interferometer, and μ is the cosine of the angle between the center of the stellar disk and a distance from the center. The center of the disk corresponds to $\mu = 1$ and the edge of the disk is $\mu = 0$ as seen from the center of the star. To match the broadband VLTI/VINCI observations, the monochromatic model visibilities must be integrated and squared to get the squared visibility amplitudes,

$$|V_{\rm LD}|^2 = \frac{\int_0^\infty |V_{\rm LD}(\lambda)|^2 {\rm d}\lambda}{\int_0^\infty S_\lambda^2 F_\lambda^2 {\rm d}\lambda}. \tag{2.11}$$

The denominator of Eq. 2.11 normalizes the visibilities, where F_λ is the flux of model. For a given model atmosphere, we can find the best-fit angular diameter with a minimum χ^2 value.

The next step is to use the model stellar atmospheres to fit spectrophotometric observations. The purpose of fitting spectrophotometry is to constrain the effective temperature and the stellar flux; however, the effective temperature is dependent on the angular diameter. The modeled flux is scaled using the same method and assumptions as in Wittkowski et al. (2004) to fit the broadband data from Johnson & Mitchell (1975). The best-fit effective temperature is determined using the best-fit angular diameter from the interferometric fit to break the degeneracy.

The linear radius of the star is determined using the best-fit angular diameter and HIPPARCOS parallax, and the luminosity is calculated using the radius and the effective temperature. The mass and gravity are constrained by comparing the predicted effective temperature and luminosity with theoretical stellar evolution tracks (Girardi et al., 2000).

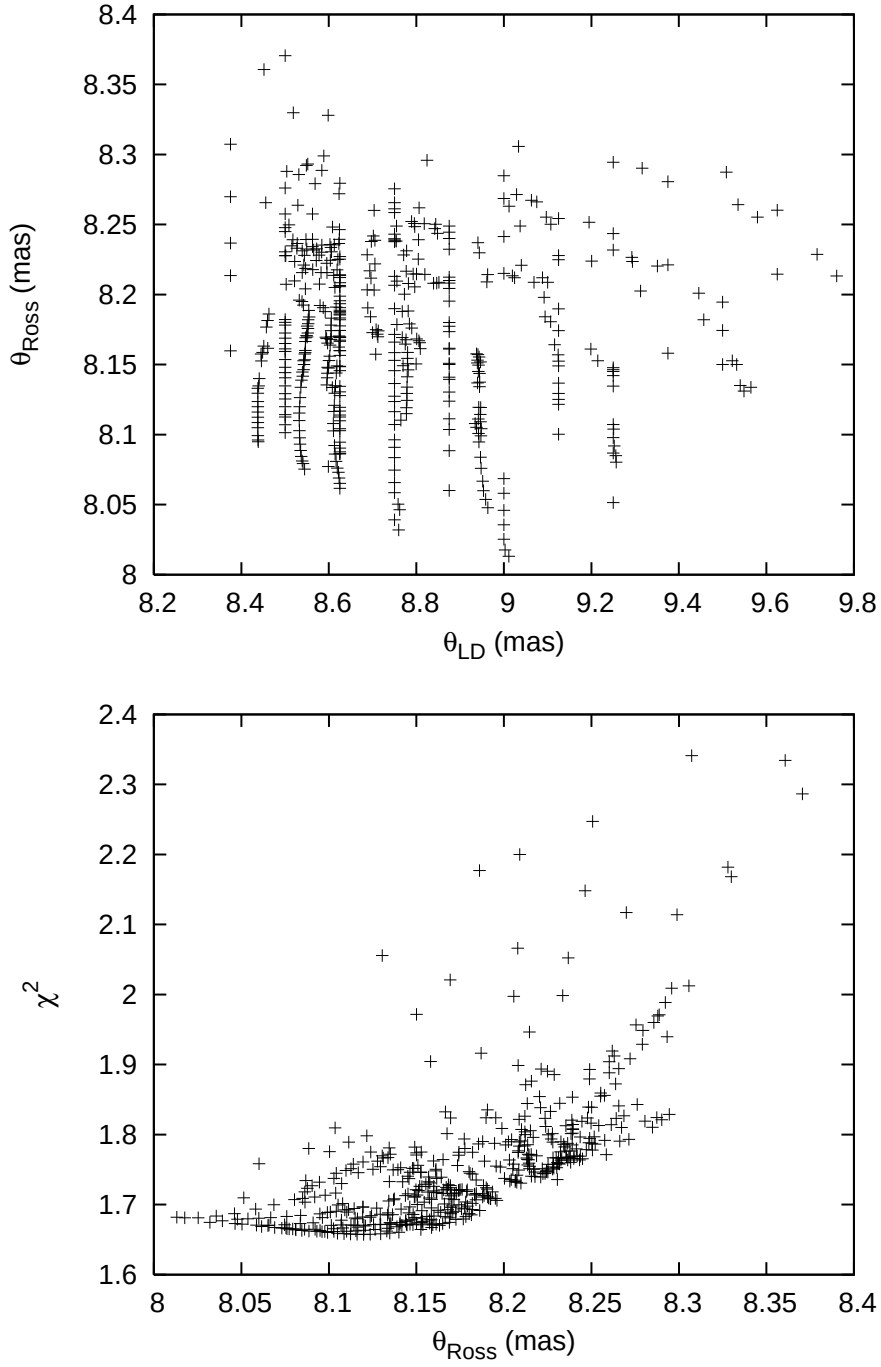

Figure 2.3: Values of minimum χ^2 for each model stellar atmosphere for fitting the interferometric data of ψ Phe as a function of (Top) $\theta_{\rm LD}$ and (Bottom) $\theta_{\rm Ross}$.

Table 2.1: Best-Fit Parameters of the Three Stars

	ψ Phe	γ Sge	α Cet
$\theta_{\rm LD}$(mas)	8.7 ± 0.3	6.3 ± 0.1	12.6 ± 0.2
$\theta_{\rm Ross}$(mas)	8.13 ± 0.1	6.02 ± 0.1	12.10 ± 0.05
χ^2	1.66	0.634	0.98
π(mas)	10.15 ± 0.15	11.9 ± 0.71	14.82 ± 0.83
$R(R_\odot)$	85 ± 1.6	54 ± 4	88 ± 5
$T_{\rm eff}$(K)	3415 ± 87	3650 ± 78	3584 ± 166
$L(L_\odot)$	882 ± 96	468 ± 81	1147 ± 249
$M(M_\odot)$	0.85 ± 0.1	0.9 ± 0.2	1.3 ± 0.4
$\log g$ (cm s^{-2})	$0.51^{+0.06}_{-0.02}$	$0.93^{+0.15}_{-0.17}$	$0.66^{+0.17}_{-0.20}$

2.8 Results

For each of the three stars, we compute a cube of models with luminosity, mass, and radius as input parameters. The metallicity is assumed to be solar, consistent with the conclusions of Feast et al. (1990), and the microturbulence is zero. These assumptions can be tested, but for this work variations of metallicity and microturbulence are ignored. The range of values for the input mass, luminosity and radius are chosen based on the results of Wittkowski et al. (2004, 2006a,b).

For ψ Phe, the mass range is chosen to be 0.6 to 1.6$M_\odot$ in steps of 0.2$M_\odot$; the luminosity range is 630 to 1580$L_\odot$ in steps of 50$L_\odot$ and the radius range is 60 to 120$R_\odot$ in steps of 20$R_\odot$. There are 480 models computed for ψ Phe. The mass range for γ Sge is 1.0 to 1.9$M_\odot$ in steps of 0.1$M_\odot$, the luminosity range is 400 to 700$L_\odot$ in steps of 50$L_\odot$ and the radius range is 30 to 70$R_\odot$ in steps of 10$R_\odot$, leading to 350 models for this star. There are 1680 models computed for α Cet to provide a larger range of parameters and a more robust test of the SAtlas program. The mass range is 1.5 to 3.0$M_\odot$ in steps of 0.1$M_\odot$, the luminosity range is 10^3 to $2 \times 10^3 L_\odot$ in steps of 50$L_\odot$ and the radius range is 60 to 100$R_\odot$ in steps of 10$R_\odot$.

We fit the limb-darkened angular diameter, $\theta_{\rm LD}$, to the interferometric observations of each star and find a minimum value of χ^2. The limb-darkened angular diameter is the angular diameter to the edge of the stellar disk corresponding to the the layer where $\mu = 0$, and from the stellar atmosphere models we determine the Rossland angular diameter by multiplying $\theta_{\rm LD}$ by the ratio of radius of the stellar atmosphere model at $\tau_{\rm Ross} = 2/3$ to the radius of the outermost shell of that model, although this outermost shell is determined by an arbitrary choice of the minimum $\tau_{\rm Ross}$ when the model is computed. The quality of fit to the interferometric data is sensitive to the Rossland angular diameter, as was noted by Wittkowski et al. (2004). The minimum χ^2 values are shown in Fig. 2.3 as a function of limb-darkened and Rossland angular diameter for each model for the case of ψ Phe. The best-fit Rossland angular diameter is well constrained by interferometry and the values of the Rossland and limb-darkened angular diameters, along with the uncertainty of the fit, for each star is given in Table 2.1. The Rossland angular diameter has a smaller uncertainty than the limb-darkened angular diameter for each star because the fits to the interferometric

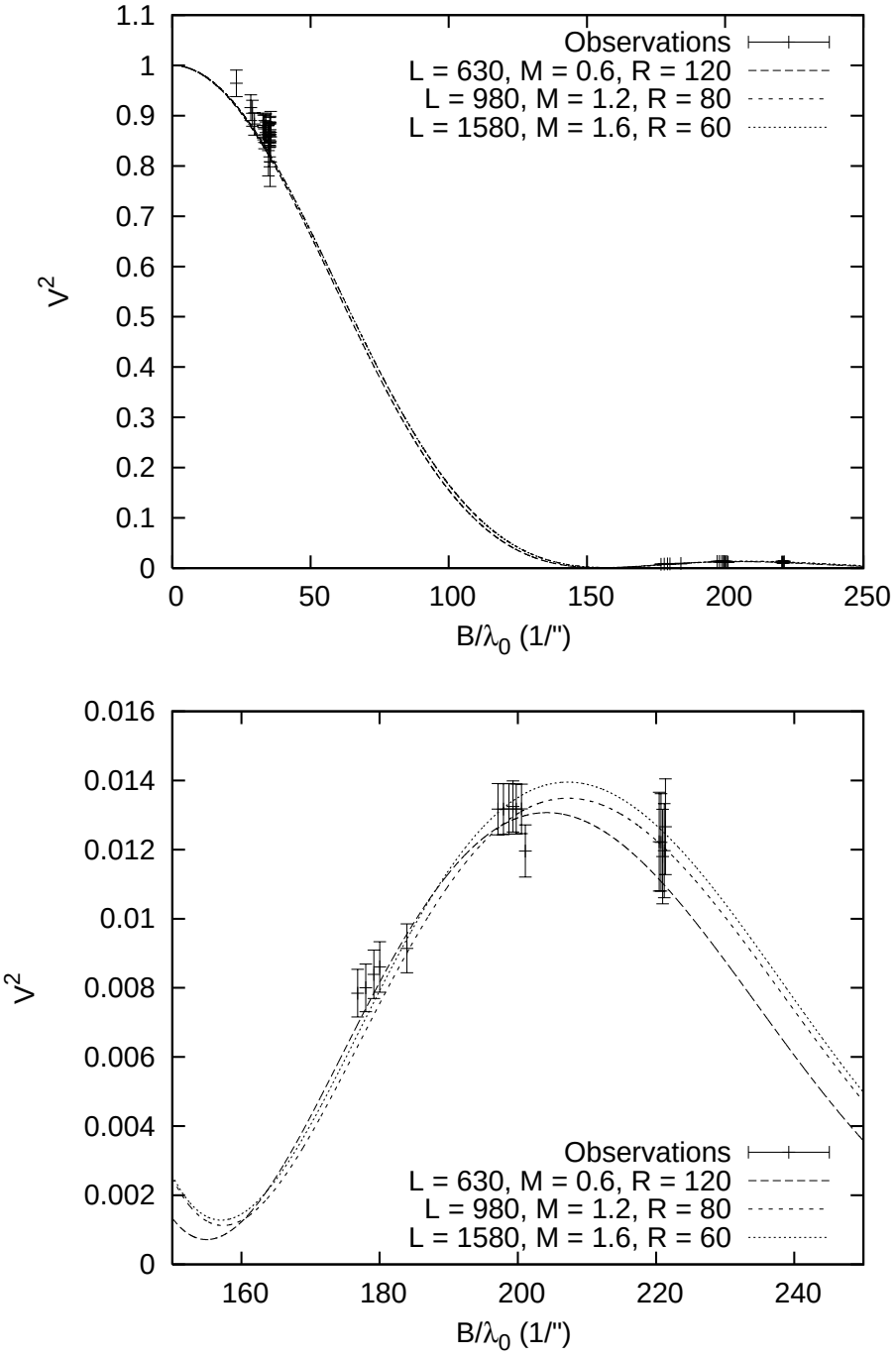

Figure 2.4: (Top) The visibilities calculated for three SAtlas models and the interferometric data for ψ Phe . (Bottom) Close-up of the second lobe of the visibility amplitude. The dotted line refers to the model stellar atmosphere for $L = 1580L_{\odot}$, M = $1.6M_{\odot}$, and $R = 60R_{\odot}$, the dot-dashed line represents a model with $L = 980L_{\odot}$, M = $1.2M_{\odot}$, and $R = 80R_{\odot}$, and the dashed line is for $L = 630L_{\odot}$, M = $0.6M_{\odot}$, and $R = 120R_{\odot}$.

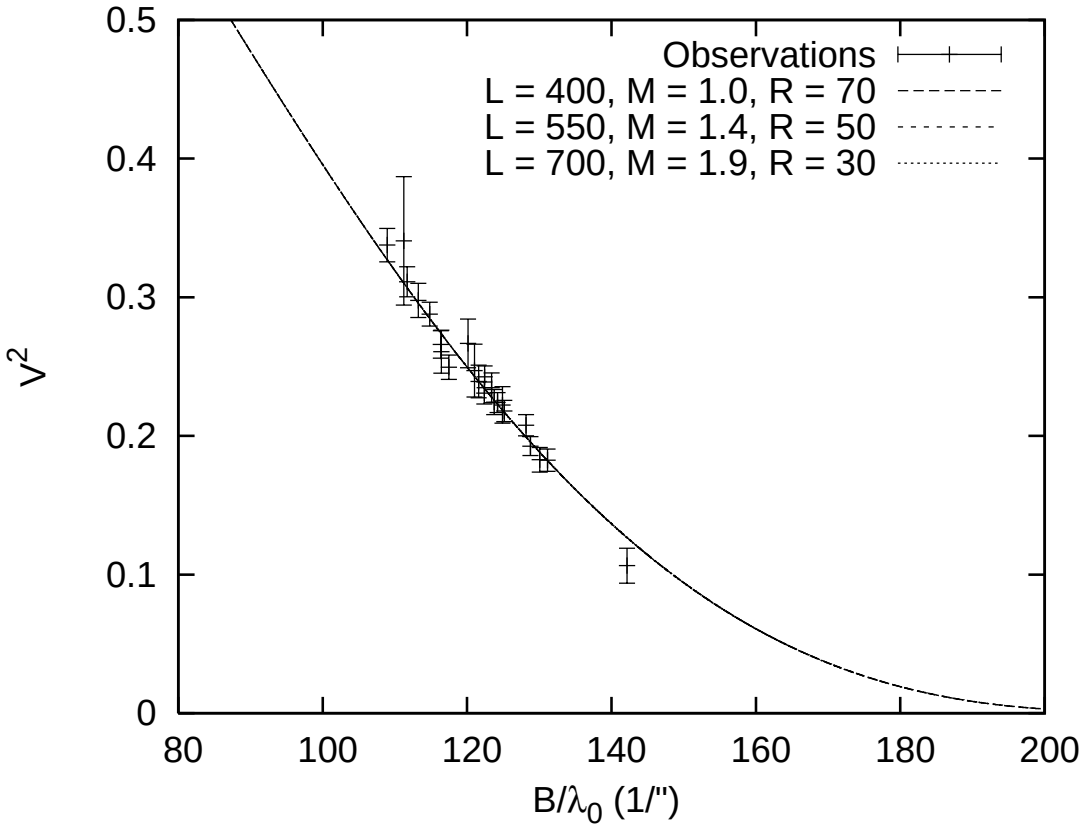

Figure 2.5: The visibilities calculated for three SAtlas models and the interferometric data for γ Sge. The dotted line refers to the model stellar atmosphere for $L = 700L_{\odot}$, M = $1.9M_{\odot}$, and $R = 30R_{\odot}$, the dot-dashed line represents a model with $L = 550L_{\odot}$, M = $1.4M_{\odot}$, and $R = 50R_{\odot}$, and the dashed line is for $L = 400L_{\odot}$, M = $1.0M_{\odot}$, and $R = 70R_{\odot}$.

data produce less variation of the Rossland angular diameter than the limb-darkened angular diameter. This variation is clearly shown in Fig. 2.3.

The model visibilities are shown in Fig. 2.4 for ψ Phe, with a close-up of the second lobe, Fig. 2.5 for γ Sge, and Fig. 2.6 for α Ceti with a close-up of the second lobe shown. The displayed model visibilities are chosen to be the smallest, middle and largest luminosity and gravity from each cube of models. The model visibilities for γ Sge and α Cet agree with the results of Wittkowski et al. (2006a,b). For γ Sge, there is not enough information to test the limb-darkening of the model atmospheres. While the model visibilities using SAtlas and Phoenix both fit the observed interferometric data well within the uncertainties of the observations, the minimum value of the χ^2 from fitting the SAtlas models is smaller than that using the Phoenix models. This implies that there are small differences in the model atmosphere intensity structures predicted from each program. It is not obvious why the predictions using Phoenix models and SAtlas models differ in this case.

Having fit the interferometric data, we next fit the broadband spectrophotometric data. One concern about fitting stellar atmosphere models to spectrophotometry is that the effective temperature and Rossland

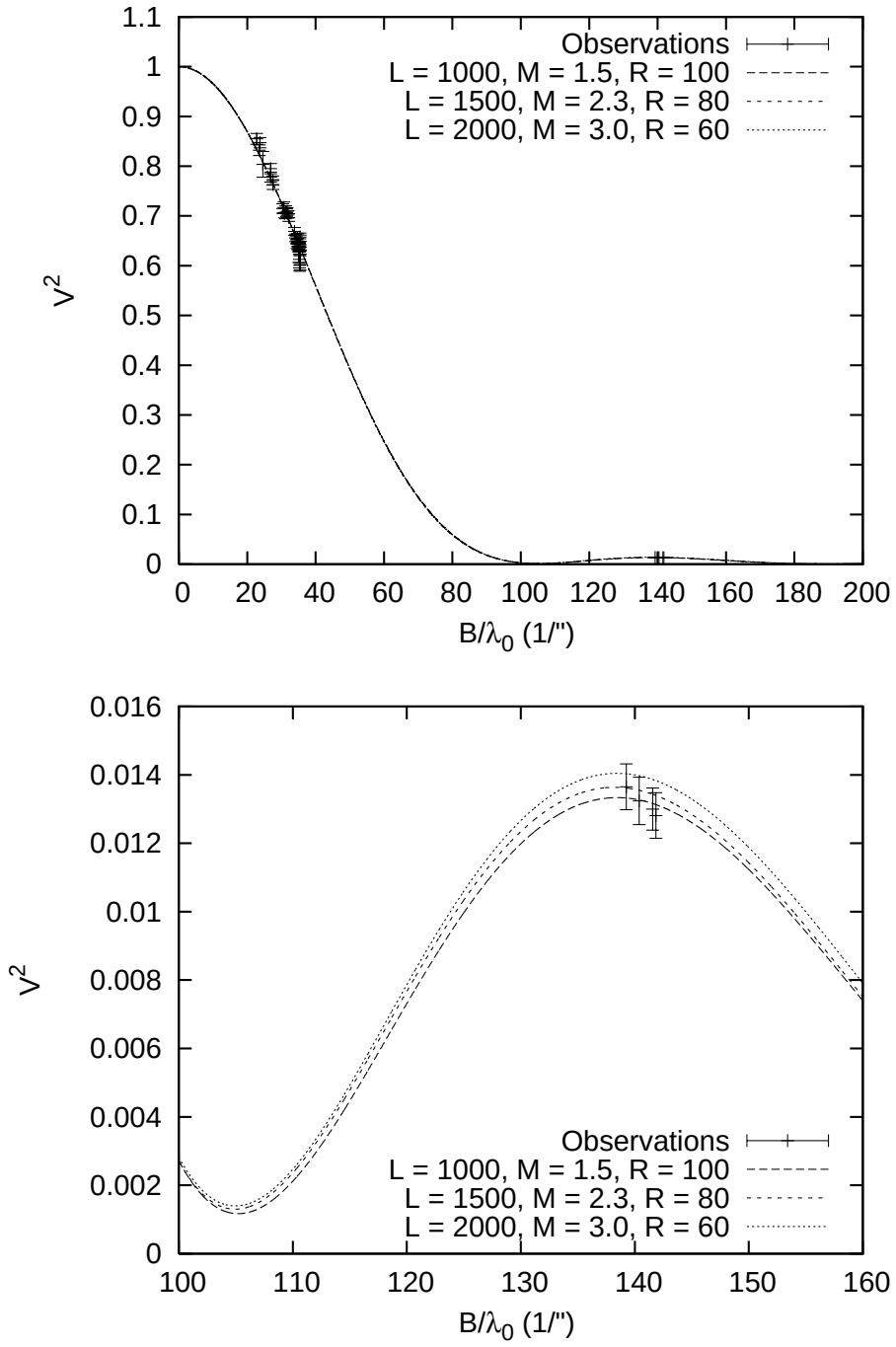

Figure 2.6: (Top) The visibilities calculated for three SAtlas models and the interferometric data for α Cet. (Bottom) Close-up of the second lobe of the visibility amplitude. The dotted line refers to the model stellar atmosphere for $L = 2000L_{\odot}$, M = $3.0M_{\odot}$, and $R = 60R_{\odot}$, the dot-dashed line represents a model with $L = 1500L_{\odot}$, M = $2.3M_{\odot}$, and $R = 80R_{\odot}$, and the dashed line is for $L = 1000L_{\odot}$, M = $1.5M_{\odot}$, and $R = 100R_{\odot}$.

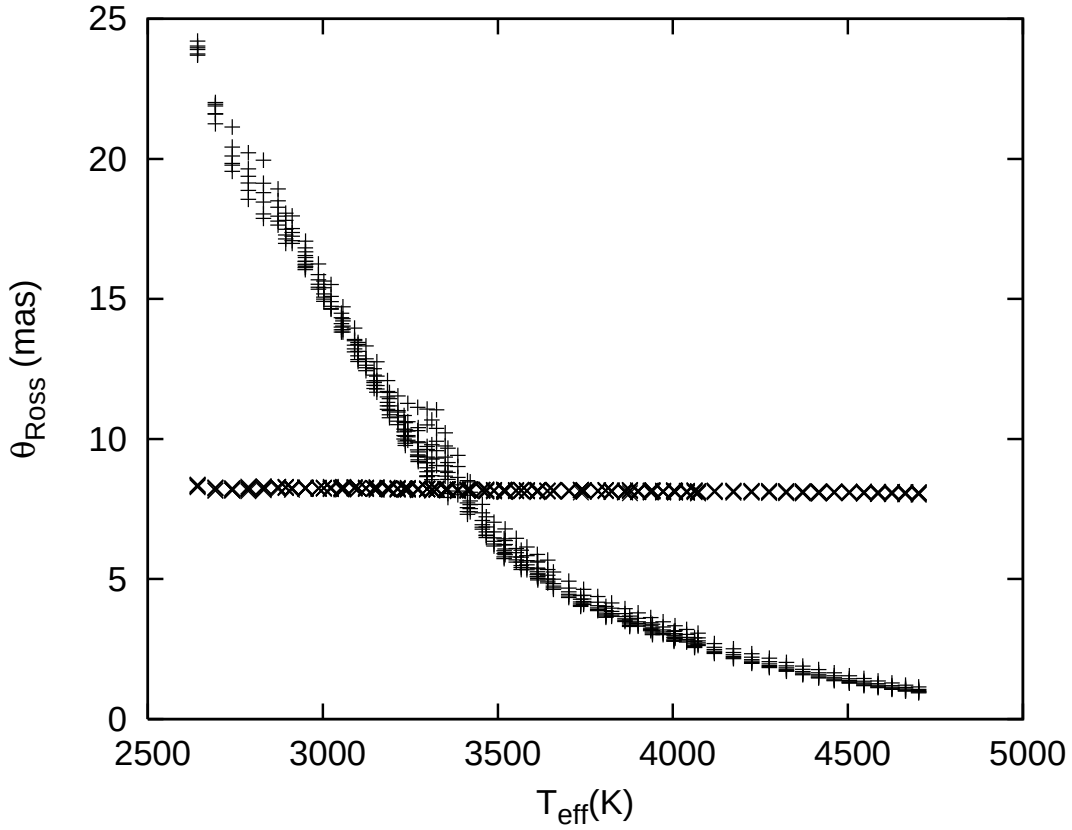

Figure 2.7: The best-fit effective temperature as a function of Rossland angular diameter found by fitting spectrophotometry (+'s) and interferometry (x's) for ψ Phe.

angular diameter are related. In Fig. 2.7, we compare the best-fit values of Rossland angular diameter as a function of the best-fit effective temperature for each model for fitting ψ Phe. The predicted angular diameter is almost constant with respect to effective temperature for the fit to interferometry. Therefore the interferometric fit of the Rossland angular diameter is used to constrain the predicted effective temperature. This process is repeated for the other two stars and the best-fit effective temperatures are given in Table 2.1.

The next step is to calculate the linear radius and luminosity of the stars. Using the HIPPARCOS parallax with the predicted Rossland angular diameter, we determine the radius of each star, the values of the parallax and radius are given in Table 2.1. The stellar luminosity is determined using the effective temperature and radius, $L = 4\pi R^2 \sigma T_{\rm eff}^4$. The best-fit effective temperature and luminosity for each star is plotted in Fig. 2.8 along with evolutionary tracks from Girardi et al. (2000) to determine the mass and gravity of each star.

2.9 Conclusions

The purpose of this chapter is to describe the changes to the ATLAS program to make it model a spherically symmetric geometry and test the spherical version of the ATLAS program. The program is modified by chang-

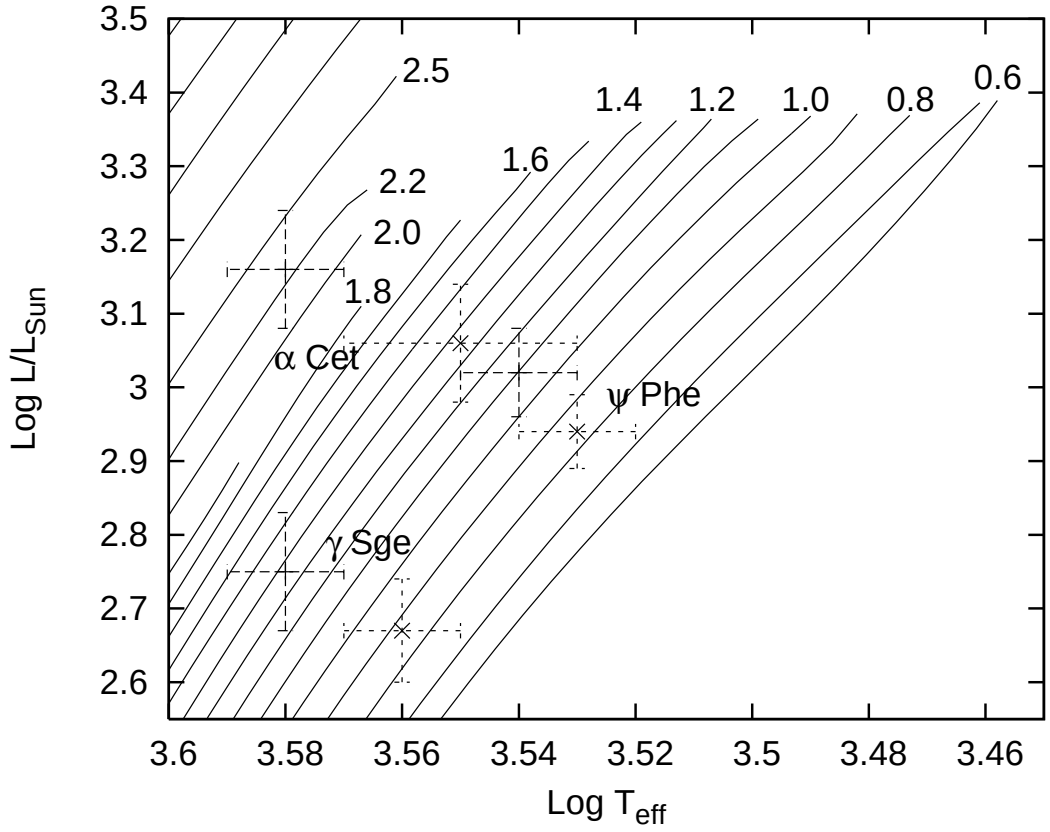

Figure 2.8: Comparison of the derived effective temperatures and luminosities of the three stars relative the derived parameters from previous analyses. The lines are evolutionary tracks from Girardi et al. (2000), the points given by x's are the predicted effective temperatures and luminosities found using the SAtlas models and the plusses are the values found using Phoenix models.

ing the radiative transfer, hydrostatic equilibrium and temperature correction routines. The transfer equation is solved using the Rybicki (1971) reorganization of the Feautrier (1964) solution. Hydrostatic equilibrium is solved using the method suggested by Mihalas & Hummer (1974) while the temperature correction is a generalization of the Avrett (1964) temperature correction for plane-parallel stellar atmospheres.

By fitting interferometric and spectrophotometric observations using model stellar atmospheres, we derive the properties of ψ Phe, γ Sge, and α Cet. The derived parameters are compared to earlier results. The angular diameters that are determined by fitting model stellar atmospheres to interferometric observations are the same, except for α Cet, for which we predict an angular diameter that is 0.1 mas smaller. The differences in predicted angular diameter are likely due to differences in limb-darkening of the model atmospheres generated using SAtlas and Phoenix. Also our minimum χ^2 value of the fit of the limb-darkened angular diameter for ψ Phe, 1.66, is smaller than the predicted value of χ^2 from the spherically symmetric Phoenix models, 1.8. The SAtlas models for ψ Phe that best fit the *interferometric* data have effective temperatures in the range of 4000 to 4500 K, while the Phoenix models from Wittkowski et al. (2004) are all 3550 and

3600 K. The fit of the SAtlas models to *spectrophotometric* observations predict an effective temperature of 3415 K conflicting with the prediction of a higher temperature. For the effective temperature range of 3400 to 3800 K, the minimum χ^2 values predicted by fitting SAtlas models are 1.70 to 1.72, similar to the values found using plane-parallel Atlas models.

The fit of the SAtlas models to broadband spectrophotometric observations are used to determine the effective temperatures of the three stars because spectrophotometry is much more sensitive to the effective temperature than interferometry. The predicted effective temperatures are smaller than those found in the previous works, but this difference is due to the methods used for determining the effective temperature, *not* differences in the stellar atmosphere programs. If we use the method from Wittkowski et al. (2004) where the bolometric flux $f_{\rm bol}$ is calculated by integrating the spectrophotometric data and then $T_{\rm eff}^4 = 4 f_{\rm bol}/(\sigma\theta_{\rm Ross}^2)$, we would predict similar effective temperatures. Any variation in that case would be due to differences in the calculation of the bolometric flux and differences in the angular diameter. This suggests the effective temperatures here would differ by at most 1%. Our results also differ because of the spectrophotometric data used. The difference is smallest for ψ Phe because the Phoenix and SAtlas fits both use the same spectrophotometric data for the fitting and agree within the uncertainty. For γ Sge, Wittkowski et al. (2006b) complement the Johnson & Mitchell (1975) data with narrow-band data from Alekseeva et al. (1997) while for α Cet, Wittkowski et al. (2006a) use optical (Glushneva et al., 1998a,b) and infrared (Cohen et al., 1996) spectrophotometry. The effective temperature difference for the remaining two stars are about 150 to 200 K.

Because the angular diameters are similar, the predicted radii are also similar for both fits with SAtlas and Phoenix. Therefore the differences between predicted luminosities are due to differences in effective temperatures and thus due to the different methods for determining the effective temperatures. The lower effective temperatures and luminosities imply lower masses when compared to Girardi et al. (2000) evolutionary tracks and smaller gravities.

The SAtlas models are consistent with previous results. Fitting the models to interferometric and spectrophotometric observations have provided a robust test of the spherically symmetric version of the Atlas program and have shown that the SAtlas program is a powerful tool for studies of stellar atmospheres.

Chapter 3

Using SAtlas Model Stellar Atmospheres as a Testbed for Understanding Center-To-Limb Intensity Distributions

Part of this chapter is submitted to the Astrophysical Journal:
"Limb-Darkening as a Test of Stellar Atmospheres"
Neilson, H.R., & Lester, J.B.

"It is the stars, The stars above us, govern our conditions" - William Shakespeare

3.1 Introduction

The center-to-limb intensity distribution, or limb-darkening, of a stellar atmosphere is a measure of the atmosphere's temperature and pressure structure and composition. This connection has been known for a long time, from the introduction of the simple yet profound Eddington-Barbier relation, $S(\tau) = I(\mu, \tau = 0)$ (Milne, 1930). The development of the theory of stellar atmospheres has led to more complicated relations between the source function and the emergent intensity of the stellar atmosphere (for example Mitchell, 1959), but as computers evolved then so did the atmospheric models. Today, a stellar atmosphere is modeled directly without making an assumption of how the source function relates to the intensity distribution. As a result, limb-darkening is still an ideal test of these model atmospheres.

Model stellar atmosphere can be tested by limb-darkening using a number of observational methods such as the change of flux from eclipsing binary stars (Popper, 1984), microlensing of stars (Fields et al., 2003), and optical interferometry, as discussed in the previous chapter. It is also possible that lunar occultations of stars by the Moon may provide an indirect test of the limb-darkening.

Understanding the structure of limb-darkening of stellar atmospheres is important for modeling the orbits

of transiting planets as well as eclipsing binaries when the orbit is not known. In both cases, the passage of one object in front of the other acts a mask removing a fraction of the total flux that is dependent on the intensity distribution of the eclipsed star. Having a precise understanding of the atmospheric structure and limb-darkening of each star provides better understanding of the orbits of these systems. Typically, the orbits of eclipsing binary stars and planetary transits are computed by assuming that the intensity distribution of the star is linear with respect to variable μ, which is the cosine of the angle between the line of sight of the observer and the line that is normal to the surface of the star. This simplifies the stellar limb-darkening and treats it as a single free-parameter in the model fit of the orbit.

The use of a linear limb-darkening law has been tested for better understanding of the orbits of extrasolar planets. Knutson et al. (2007) derived quadratic and four-parameter limb-darkening laws from Atlas models to reduce the uncertainty of the computed orbit of HD 209458b. Tingley et al. (2006), on the other hand, directly compared the intensity distribution of Phoenix models to Hubble Space Telescope observations and found significant discrepancies. Southworth (2008) used observations of a number of extrasolar planets to test the effect of different limb-darkening laws for fitting the orbit. He found that linear limb-darkening laws that have been traditionally used since first derived by Eddington, do not fit the data as well as nonlinear laws, although different nonlinear laws tend to produce similar results. Understanding the limb-darkening of planet-hosting stars is important if one is to use optical observations to characterize the transit to high precision.

Similar analyses have been applied to eclipsing binary systems. There is an extensive literature deriving orbital parameters of eclipsing binary systems using some parameterization of the stellar limb-darkening. However, there is not a significant volume of work that uses light curves of eclipsing binaries to test the limb-darkening of the star. The principal reason, as noted by Popper (1984), is that the observational errors (about 10%) of the analysis are too large to invert the light curve and constrain the stellar limb-darkening. Historically though, there have been a number of attempts to constrain the limb-darkening. Serkowski (1961) and Irwin (1963) modeled the differential stellar limb-darkening, defined as the difference between the intensity at two different wavelengths but same value of μ, from the lightcurve colors of eclipsing binaries but still were only able to constrain a linear limb-darkening model. It is likely that the better observations available today may provide better constraints, especially because the differential limb-darkening analysis is similar to the method Tingley et al. (2006) used to test Phoenix models.

There are a few examples of recent work on eclipsing binaries that attempt to constrain stellar limb-darkening. One unique idea was presented by Jeffers et al. (2006), where the authors modeled the first derivative of the observed eclipsing binaries lightcurve and directly compared this to the intensity distributions of Phoenix and Atlas models. They found that the best-fit Phoenix model fit the data only marginally better than the Atlas model, due to the fact that the Atlas models did not fit the limb of the star as well. This result is most likely because the Atlas models are plane-parallel and overestimates the intensity near the edge of the disk and produces an inaccurate first derivative of the intensity with respect to μ.

Southworth et al. (2007) fit the orbital parameters of an eclipsing binary using WIRE observations to a precision of about 1%. At this precision the conclusions of Popper (1984) become invalid, and it is possible to constrain stellar limb-darkening better than just a linear law. The authors fit three different types of nonlinear laws: quadratic, square-root and logarithmic. It is found that the quadratic law provides a marginally better fit than the linear and other nonlinear laws. It is also found that when bi-parametric laws, for example linear plus square-root, are used the best-fit coefficients are correlated. On the other hand, Torres & Sandberg Lacy (2009) observed VZ Cep and found that the data was not precise enough to distinguish between linear and nonlinear limb-darkening laws. Testing limb-darkening using eclipsing binaries is still in the early stages, but with better telescopes and more precise monitoring efforts they will provide a testbed for stellar limb-darkening.

Limb-darkening has also been explored through microlensing observations. This is a very challenging method because a microlensing event is a serendipitous discovery chosen by nature and not observer, and for a star, the event does not repeat. These observations are hence rare. Abe et al. (2003) compared microlensing observations of a solar-like star to linear plus square-root limb-darkening relations generated by Atlas and Phoenix stellar atmosphere models. The observations were fit by the atmospheric models with 95% confidence with no significant discrepancy between the stellar atmosphere codes. Likewise, Fields et al. (2003) conducted a similar analysis using observations of a K giant and found significant discrepancies between the Atlas and Phoenix models and the observed intensity profile. These observations suggest that microlensing is a powerful tool for constraining stellar atmosphere models, however, it is argued by Dominik (2004) that these microlensing observations constrain only the linear term of a linear plus square-root limb-darkening law due to the geometry of the fold caustics of the microlensing event. It is noted that microlensing observations of a K giant by Albrow et al. (1999) had a significantly larger magnitification than the other two results and hence could constrain the square-root term of the limb-darkening law. These observations suggest that, like eclipsing binaries, microlensing is almost able to provide robust tests for stellar atmosphere models through limb-darkening.

A third possible method for testing limb-darkening is observations of the lunar occultation of stars. As the Moon passes in front of a star in its motion about the Earth, it acts as a knife edge creating a diffraction pattern. This diffraction pattern is projected upon the Earth's surface and can be detected by telescopes with millisecond readouts. This technique has been applied primarily by Richichi and collaborators (Richichi et al., 2006; Fors, 2006; Richichi et al., 2008a,b) to determine the angular diameters of the occulted stars. More specifically, they determine the uniform-disk angular diameter, defined as the angular diameter if every point on the stellar disk has an intensity equal to the central intensity. This is the drawback of the lunar occultation technique, the intensity profile is degenerate with the angular diameter. However if one has an independent measurement of the angular diameter then it may be possible to use the occultation method to test limb-darkening technique to constrain stellar atmosphere models. For instance, if we observe a K or M-type giant then the angular diameter can be found using the calibration of Dyck et al. (1996), or

one can use the infrared surface brightness method (Di Benedetto, 2005). By comparing this limb-darkened angular diameter to the uniform-disk angular diameter then one has a measure of the limb-darkening profile. However, it is not clear how that this would provide any more of a robust test than the other techniques suggested.

The primary method for using these observations to test limb-darkening involves assuming a parameterized function for the limb-darkening. The parameterization assumes a structure for the center-to-limb intensity distribution. In the next section, the various choices for the parameterization of limb-darkening are reviewed with an attempt to derive a relation that is consistent with the equation of radiative transfer. In section 2.3, the fixed point of the intensity profiles found by Fields et al. (2003) is discussed and shown to not be real. The limb-darkening parameterizations are compared to stellar atmosphere models computed using the SAtlas code in Section 2.4. In Section 2.5, it is shown that the limb-darkening law can constrain stellar parameters using results from microlensing observations and in Section 2.6 more advanced limb-darkening parameterizations are computed using SAtlas stellar atmosphere models.

3.2 Parameterization of Limb-darkening in Stars

Limb-darkening laws have been very important for modeling the orbits of binary stars starting from the early works of Russell (1912a,b); Russell & Shapley (1912a,b). The Eddington approximation, derived in the pioneering work of Milne (1926), is the one of the first parameterizations of the limb-darkening of the star of the form

$$\frac{I(\mu)}{I(\mu=1)} = \frac{3}{5}\left(\mu + \frac{2}{3}\right), \tag{3.1}$$

where μ is the cosine of the angle between the observer's line-of-sight and the normal to the surface of the star, while the intensity, $I(\mu = 0)$ is the central intensity. This approximation is an early attempt to characterize the intensity distribution of stars, and began a small industry of defining new relations (see the early review by Wyse, 1939) and constraining the parameterizations (for example Russell, 1945; Huffer & Eggen, 1947).

More complex limb-darkening laws have been developed to include square-root, logarithmic or quadratic terms. Klinglesmith & Sobieski (1970) introduced two limb-darkening parameterizations for stars in the range $10000\ K \leq T_{\rm eff} \leq 40000\ K$ and $2.5 \leq \log g \leq 4.5$

$$\frac{I_\lambda(\mu)}{I_\lambda(1)} = 1 - A_\lambda(1-\mu) - B_\lambda(1-\mu^3), \tag{3.2}$$

and

$$\frac{I_\lambda(\mu)}{I_\lambda(1)} = 1 - A_\lambda(1-\mu) - B_\lambda\mu\log\mu, \tag{3.3}$$

where Equation 3.2 is from van't Veer (1960). The authors calculated model atmospheres and computed the

best-fit coefficients to Equation 3.3.

A similar analysis was conducted using models of late-type stellar atmospheres by Gustafsson et al. (1975), and Bell et al. (1976) by Manduca et al. (1977). The model atmospheres span a temperature and gravity range of $6000\ K \geq T_{\rm eff} \geq 3750\ K$ and $3.0 \geq \log g \geq 0.75$ with a metallicity range of $0.0 \geq [A/H] \geq -3.0$. The intensity profile was fit to two limb-darkening parameterizations, linear and quadratic

$$\frac{I_\lambda(\mu)}{I_\lambda(1)} = 1 - A_\lambda(1-\mu) - B_\lambda(1-\mu)^2, \tag{3.4}$$

for the U, B, V bands. It was found that the error of the linear fit increases as the effective temperature decreases, with the linear fit breaking down at about $T_{\rm eff} = 4500\ K$ in the U-band, $T_{\rm eff} = 4000\ K$ in the B-band and $T_{\rm eff} = 3750\ K$ in the V-band. The quadratic fit agrees to within ± 0.01 in all cases, suggesting that the quadratic fit is significantly better for modeling limb-darkening in cool stars. The analysis was repeated for infrared wavelengths (Manduca, 1979), where it was found that the limb-darkening is more nonlinear at infrared wavelengths than at optical wavelengths up to a wavelength of 1.6 μm, corresponding to the H^- opacity minimum. At longer wavelengths the author noted the limb-darkening becomes less nonlinear.

The behavior of linear limb-darkening coefficients as a function of wavelength was explored by Al-Naimiy (1978) using atmospheric models from Carbon & Gingerich (1969). For hotter stars, $T_{\rm eff} \geq 10000\ K$, the linear coefficients are continuous with respect to wavelength except for a break at about 380 nm, corresponding to the Balmer discontinuity. From the other perspective, the linear coefficients at constant wavelength are found to be roughly continuous with respective to effective temperature.

New linear and quadratic limb-darkening expressions were calculated by Wade & Rucinski (1985) using Kurucz (1979) stellar atmosphere models. The analysis by Wade & Rucinski (1985) differed from previous works in that it enforced flux conservation in the fit. In that case, the coefficients from the linear limb-darkening fit differed from those calculated by Al-Naimiy (1978) primarily due to the difference between the stellar atmosphere models. The fit of the linear model at UV wavelengths was also found to be a poor fit, predicting negative intensities near the limb of the star. The flux-conservation method for computing linear and quadratic limb-darkening laws was compared to least square fits using MARCS stellar atmospheres (Gustafsson et al., 1975; Bell et al., 1976). The least-square fitting method produces a more physical limb-darkening law than the flux-conservation method.

Yet another limb-darkening law was introduced by Diaz-Cordoves & Gimenez (1992) of the form

$$\frac{I_\lambda(\mu)}{I_\lambda(1)} = 1 - A_\lambda(1-\mu) - B_\lambda(1-\sqrt{\mu}) \tag{3.5}$$

and used Kurucz (1979) model stellar atmospheres (effective temperature range of 5500 K to 50000 K and surface gravity range $\log g = 0.0$ to 5.0) to produce limb-darkening relations using least squares. The authors also produces limb-darkening relations using the quadratic and linear parameterizations. The error of the fit is calculated for each model and each parameterization, and the authors note that the square-root law is a

better fit to the model limb-darkening for hotter stars $T_{\rm eff} \geq 8500\ K$ while the quadratic law is better a fit to the limb-darkening of cooler stars $T_{\rm eff} \leq 8000\ K$ corresponding to convective atmospheres.

Linear, logarithmic, and square-root limb-darkening laws were computed using Atlas model stellar atmospheres by van Hamme (1993). The laws are fit by enforcing flux conservation for the one parameter fit and both flux and mean intensity agrees with the model atmosphere. The author also tests how reasonable the quadratic law by defining a new, more general limb-darkening relation

$$\frac{I_\lambda(\mu)}{I_\lambda(1)} = 1 - A_\lambda(1-\mu) - B_\lambda(1-\mu)^p \tag{3.6}$$

and calculates the minimum value of p for the relation to best fit the model atmosphere. It is found that the value of $p = 2$ is not ideal; at UV wavelengths the best value of p is about 1 at $\log g = 0.0$, $1-3$ at $\log g = 2.0$ and $2-3$ at $\log g = 4.0$. In the optical regime, p is $2-5$ at all three gravities and the at IR wavelengths, $p = 5-8$. However, the polynomial fit to the limb-darkening is statistically equivalent to the square-root and logarithmic laws, so the author recommends not using the polynomial law as it has one more free parameter than the other two laws. The fits of the square-root and logarithmic laws are compared and it is found that the logarithmic law provides a better fit at UV wavelengths while the square-root laws gives a better fit at IR wavelengths. At optical wavelengths, the fit depends on the effective temperature, with the logarithmic law fitting better for model atmospheres with effective temperatures $T_{\rm eff} \leq 9000K$ with the square-root law fitting hotter stars better.

Diaz-Cordoves et al. (1995) recomputed limb-darkening laws from Kurucz (1979) model stellar atmospheres by for Strömgren *uvby* and UBV photometry bands using the linear, square-root and quadratic parameterizations. The relations were calculated using least-squares fitting, the flux conservation method of Wade & Rucinski (1985), and a hybrid method that uses flux conservation to determine one free parameter and least-square fitting to determine the second free parameter. For the linear laws, it is found that that least-squares fit laws are more stable than the flux conserved laws, while for the nonlinear laws, the fitting method does not cause significantly different results. Claret et al. (1995) computed the limb-darkening profiles at $RIJHK$, also using Kurucz (1979) models, and found that the square-root parameterization produced the most accurate representation. This confirmed previous claims (van Hamme, 1993) that the square-root law was best at near-IR and IR wavelengths. Another result seen in both Diaz-Cordoves et al. (1995) and Claret et al. (1995) is that the best-fit coefficients were not a continuous function of effective temperature for a specific gravity; there was a break near $T_{\rm eff} = 6300\ K$, due to the transition from radiative to convective atmospheres.

Claret (1998) calculated limb-darkening laws with the same three parameterizations from Phoenix models (Hauschildt et al., 1997a,b) over the effective temperature range of 2000 K to 50000 K. The best-fit coefficients from the linear law are systematically greater than the linear limb-darkening coefficients calculated using the Atlas models over the effective temperature range where the two sets of models overlap.

The Phoenix models were used again along with Atlas models to model a new limb-darkening law that is a hybrid of the square-root and quadratic laws

$$\frac{I(\mu)}{I(1)} = 1 - \sum_{k=1}^{4} A_k(1 - \mu^{k/2}) \tag{3.7}$$

by Claret (2000, 2003, 2004). The four parameter limb-darkening law is fit using both the least squares method and flux conservation, and it is found that the least squares method provides a better fit to the theoretical models; in some cases the error of the flux conservation method is 1000 times larger than the error from the least squares method.

The square-root limb-darkening law computed by Claret (2000) was applied to microlensing observations by Fields et al. (2003), where the intensity relation is transformed be of the form

$$\frac{I_\lambda(\mu)}{F_\lambda} = 2\left[(1 - \Gamma_\lambda - \Lambda_\lambda) + \frac{3\Gamma_\lambda}{2}\mu + \frac{5\Lambda_\lambda}{4}\sqrt{\mu}\right]. \tag{3.8}$$

This relation is designed to conserve the flux regardless of the fitting method. In this form the limb-darkening relations were shown to have the strange property of a fixed point, all limb-darkening relations from Atlas and Phoenix were shown to intersect at a particular value of μ. It is argued by Heyrovsky (2000) that the fixed point is related to the opacity of H^- that is the primary source of opacity in the stellar atmosphere models used in his study with a temperature range from 3500 to 4000 K. The analysis of Fields et al. (2003) used models with an effective temperature range of 3000 to 18000 K to show the fixed point, thus contradicting the argument that the H^- opacity is the source of the fixed point.

Claret & Hauschildt (2003) calculated limb-darkening laws using spherically symmetric stellar atmospheres (Hauschildt et al., 1999b) with $\log g$ = 3.5-5.5 and $T_{\rm eff}$ = 5000-10000 K for linear, quadratic, square-root and the four parameter laws. The author also fits an exponential limb-darkening law

$$\frac{I(\mu)}{I(1)} = 1 - A(1 - \mu) - \frac{B}{1 - e^{\mu}}. \tag{3.9}$$

For the spherical model atmospheres, it was found that the four parameter and exponential limb-darkening laws fit best while the other laws fit poorly compared to how well they fit plane-parallel model atmospheres. The authors suggest that it may be best to fit the limb-darkening laws from the center of the disk to the point where $I(\mu) \approx 0$ near the limb ignoring the extension of the atmosphere.

Barban et al. (2003) computed limb-darkening laws from Atlas using two different convection routines: the Mixing Length Theory and the Turbulent Convection approach (Canuto et al., 1996). They find that the discontinuity that was found in the limb-darkening coefficients as a function of effective temperature (Diaz-Cordoves et al., 1995; Claret et al., 1995; Claret, 2000) does not appear in the limb-darkening coefficients computed using the turbulent convection models. It is shown that the discontinuity is due to the use of

convective overshooting in the Atlas models with the mixing length theory as in Diaz-Cordoves et al. (1995), Claret et al. (1995), and Claret (2000), and not to the onset of convection. The Atlas models constructed by Barban et al. (2003) do not use convective overshoot and the resulting limb-darkening laws did not show the discontinuity.

The method of fitting the intensity parameterizations to the model stellar atmospheres was tested by Heyrovský (2007). It is argued that least-squared fitting is not the best method for fitting atmosphere models, in particular Atlas models, because the model have less than 20 value of $I(\mu)$ for each wavelength and that the spacing of μ is not even. To counter this problem, the fitting method should be based on cubic spline interpolation and minimizing the integral

$$\Delta^2 = \int (I_M - \tilde{I})^2 d\mu, \tag{3.10}$$

where $\tilde{I}$ is the assumed limb-darkening law, and I_M is the model intensity. It is also argued that minimizing the fit with respect to μ constrains the fit more to the limb of the disk. The author prefers to constrain the fit more so to the center of the disk by minimizing the similar integral

$$\Delta^2 = \int (I_M - \tilde{I})^2 \frac{\mu}{(1-\mu^2)^{1/2}} d\mu \tag{3.11}$$

to reproduce the light curves of eclipsing binaries and microlensing events more accurately. The technique is tested using the five different limb-darkening laws: linear, quadratic, square-root, logarithmic, and the four parameter model with Atlas models, and it is found that minimizing Equation 3.11 had an error significantly less than the error from least squares fitting with the exception of the four parameter law where the least squares method was equivalent. The ability of each to conserve flux was also tested by calculating the fractional difference between the flux of the model atmosphere and integrated value of the limb-darkening relation. The method minimizing Equation 3.10 had a fractional flux error of 10^{-16} for all relation while the other methods had errors of 10^{-5} to 10^{-3}.

The least-squares method was tested recently using Atlas and Phoenix models with 100 equally spaced μ-points (Claret, 2008). It is found that with a factor of ten more data points, it is possible to obtain limb-darkening laws with errors similar to the errors from minimizing Equation 3.11 but with smaller flux errors. However, the flux errors are still orders of magnitude larger than from minimizing Equation 3.10.

There has been significant progress regarding the study of stellar limb-darkening and how it relates to the physical processes in the atmosphere. In this age of computing it is becoming possible to directly compare the limb-darkening from model stellar atmospheres to observations (for example, Wittkowski et al., 2004, 2006a,b), but for most observations the errors are too large to provide a useful test. Parameterizations of stellar limb-darkening allow us to fit observations such as eclipsing binary lightcurves, but they can also be used to provide insight into how limb-darkening varies across the Hertzsprung-Russell Diagram, for instance, how the structure of the limb-darkening relations changes at the transition between convective and

radiative atmospheres.

This review highlights some of the knowledge gained from studying the parameterizations of limb-darkening, but there are more questions that should be addressed. One such question is the existence of the fixed point in the intensity as a function of μ discovered by Heyrovsky (2000) using both principle component analysis and linear limb-darkening laws. Another question of interest is how well the limb-darkening parameterizations represent limb-darkening in stars with low gravity $\log g = 0 - 2$ with very extended atmospheres. Most of the limb-darkening relations are tested using plane-parallel stellar atmosphere models which are adequate for modeling stars with gravity similar to the Sun but this approximation is poor at lower gravity.

In this chapter, we explore the existence of the fixed point in spherically symmetric model stellar atmospheres from the SAtlas stellar atmospheres code and propose an alternative explanation for why it is seen in the limb-darkening profiles. Using the models, we test which of the limb-darkening parameterizations described in this section most accurately describe the modeled intensity profiles, and also which of the proposed minimization techniques, least squares fitting, minimizing the flux error, etc. is most accurate. In particular, we test how well the parameterizations fit the intensity at the limb of the disk, which is important for fitting planetary transits, and interferometric observations.

3.3 The Cause of the Fixed Point in Stellar Limb-Darkening Laws

Heyrovsky (2000) and Fields et al. (2003) found the fixed point of the limb-darkening laws for center-to-limb intensity profiles of cool red giants and for the predicted limb-darkening profile of the Sun. Heyrovsky (2000) argues that the fixed point is related to the fact that H^- is the dominant continuous opacity source in these stars. In both cases, the fixed point was determined from plane-parallel Atlas models, and Fields et al. (2003) uses spherical Phoenix models. The intensity profiles of the Phoenix models showed a sharp decrease in intensity at a distance from the distance from the center of the disk that corresponds to the atmospheric extension of the star. Because the square-root law does not model the atmospheric extension; Fields et al. (2003) truncate the radius of the star at the edge of the sharp decrease of intensity, effectively removing the sphericity of the model atmosphere from the intensity profile.

It has been argued that a fixed point is to be expected if one uses a single parameter law to describe the flux-conserved limb-darkening profile (Fields et al., 2003). For example, if one parameterizes the limb-darkening as $I/F = 2[1 + ax(\mu)]$ then the fixed point $\mu_{\rm fixed} = f^{-1}[2\int_0^1 f(\mu')\mu' d\mu']$. Consider instead the general two parameter limb-darkening function

$$\frac{I}{F} = 2[1 + ax(\mu) + by(\mu)], \tag{3.12}$$

and integrate it with $\mu d\mu$ to get

$$1 = 2\left[\frac{1}{2} + a\int_0^1 x(\mu)\mu d\mu + b\int_0^1 y(\mu)\mu d\mu\right]. \tag{3.13}$$

In this case, we can write the unknown parameter a as a function of b

$$a = -b\frac{\int_0^1 y(\mu)\mu d\mu}{\int_0^1 x(\mu)\mu d\mu} \tag{3.14}$$

and the required flux conservation reduces the relation from two free parameters to one. However, for the case where $x(\mu) = 3\mu/2 - 1$ and $y(\mu) = 5\sqrt{\mu}/4 - 1$ (Fields et al., 2003) then

$$a = -b\frac{\int_0^1 (3\mu/2 - 1)\mu d\mu}{\int_0^1 (5\sqrt{\mu}/4 - 1)\mu d\mu} = -b\frac{0}{0}. \tag{3.15}$$

This suggests that the conservation of the flux does not allow us to write a as a function of b. However, the analysis of Fields et al. (2003) does find a fixed point. If we compare two intensity profiles

$$I_1(\mu_0) = I_2(\mu_0), \tag{3.16}$$

$$1 - a_1 - b_1 + \frac{3}{2}a_1\mu_0 + \frac{5}{4}b_1\sqrt{\mu_0} = 1 - a_2 - b_2 + \frac{3}{2}a_2\mu_0 + \frac{5}{4}b_2\sqrt{\mu_0}, \tag{3.17}$$

which yields

$$-(a_1 - a_2) - (b_1 - b_2) + \frac{3}{2}(a_1 - a_2)\mu_0 + \frac{5}{4}(b_1 - b_2)\sqrt{\mu_0} = 0. \tag{3.18}$$

Equation 3.18 may be solved for any two arbitrary intensity profiles if and only if $a_1 = a_2$ and $b_1 = b_2$ or $\Delta a = \alpha\Delta b$ which is a result of $a = \alpha b + \beta$. If we substitute this relation into Equation 3.18 then

$$-\alpha(b_1 - b_2) - (b_1 - b_2) + \frac{3}{2}\alpha(b_1 - b_2)\mu_0 + \frac{5}{4}(b_1 - b_2)\sqrt{\mu_0} = 0, \tag{3.19}$$

or

$$(b_1 - b_2)\left(-1 - \alpha + \frac{3}{2}\alpha\mu_0 + \frac{5}{4}\sqrt{\mu_0}\right) = 0. \tag{3.20}$$

The fixed point is determined from the relation

$$-1 - \alpha + \frac{3}{2}\alpha\mu_0 + \frac{5}{4}\sqrt{\mu_0} = 0 \tag{3.21}$$

and that the fixed point is a function of the slope of $a = \alpha b + \beta$ only. The fixed point requires that the two free parameters are related to each other.

The question is why should a be a function of b? The coefficients a, and b are determined using a general

least squares method where

$$\chi^2 = \sum_i^N [Y_i - af_1(\mu_i) - bf_2(\mu_i)]^2 \tag{3.22}$$

where $Y = I/(2F) - 1$, $f_1 = 3\mu/2 - 1$ and $f_2 = 5\sqrt{\mu}/4 - 1$. The coefficients are determined by taking the derivative of χ^2 with respect to a and b and setting the derivative to be equal to zero. This means

$$\frac{\partial \chi^2}{\partial a} = \sum_i^N \left(\frac{I}{2F} - 1 - af_1(\mu_i) - bf_2(\mu_i)\right) f_1(\mu_i) = 0, \tag{3.23}$$

and

$$\frac{\partial \chi^2}{\partial b} = \sum_i^N \left(\frac{I}{2F} - 1 - af_1(\mu_i) - bf_2(\mu_i)\right) f_2(\mu_i) = 0. \tag{3.24}$$

We multiply Equations 3.23 and 3.24 by $\Delta\mu$ and convert the summation to integration to get

$$\int_0^1 \left(\frac{I}{2F} - 1\right)\left(\frac{3}{2}\mu - 1\right) d\mu - a\int_0^1 \left(\frac{3}{2}\mu - 1\right)^2 d\mu - b\int_0^1 \left(\frac{3}{2} - 1\right)\left(\frac{5}{4}\sqrt{\mu} - 1\right) d\mu = 0, \tag{3.25}$$

and

$$\int_0^1 \left(\frac{I}{2F} - 1\right)\left(\frac{5}{4}\sqrt{\mu} - 1\right) d\mu - a\int_0^1 \left(\frac{3}{2}\mu - 1\right)\left(\frac{5}{4}\sqrt{\mu} - 1\right) d\mu - b\int_0^1 \left(\frac{5}{4}\sqrt{\mu} - 1\right)^2 d\mu = 0. \tag{3.26}$$

Solving the integrals in these relations, we find that

$$1 - \frac{J}{2F} - \frac{1}{4}a - \frac{1}{6}b = 0, \tag{3.27}$$

and

$$\frac{5}{4}\int_0^1 \frac{I}{2F}\mu^{1/2} d\mu + \frac{1}{6} - \frac{J}{2F} - \frac{1}{6}a - \frac{11}{96}b = 0. \tag{3.28}$$

Both relations conserve the quantity $J/2F$, meaning the mean intensity J is that of the model atmosphere because the flux F is conserved by definition. Furthermore the pseudo-moment of the intensity, $\int I\sqrt{\mu}d\mu$, is also conserved from the intensity profile data from model stellar atmospheres. If this pseudo-moment is either a function of a and b or J only then we may solve for $a = f(b)$.

We calculated the pseudo-moment and mean intensity from the cube of SAtlas stellar atmosphere models from the previous chapter for γ Sge, which range in mass from 1.5 to 3.0 $M_\odot$, in luminosity from (1-2) $\times 10^3$ $L_\odot$ and in radius from 60 to 100 $R_\odot$. In Figure 3.1, we show the pseudo-moment plotted as a function of the mean intensity at $\lambda = 555$ *nm*. The choice of this wavelength is somewhat arbitrary, but avoids the weakening of limb-darkening across the stellar disk in the infrared as well as avoiding the large number of spectral lines in the UV. The pseudo-moment appears to be a linear function of the mean intensity, but the range of is very small and it is impractical to compute the linear relation using least-squares fitting.

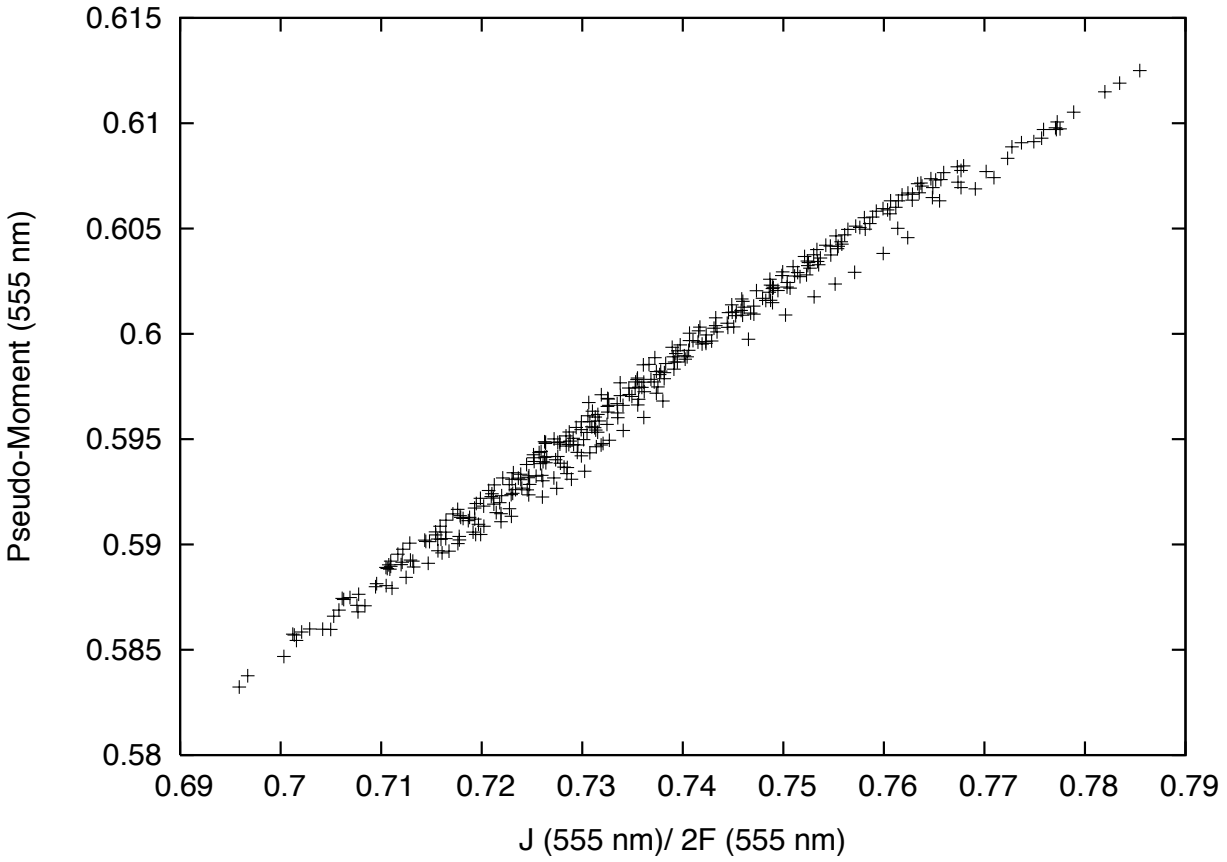

Figure 3.1: Comparison of the pseudo-moment, normalized to have unit Flux, defined in the text and the mean intensity of a cube of SAtlas model atmospheres at $\lambda = 555\ nm$.

Instead, the mean values of the pseudo-moment and the mean intensity are computed, and it is assumed that the ratio of any pseudo-moment to mean intensity is equal to the ratio of the mean values. The mean ratio is 0.811 ± 0.00043. Thus we write

$$\frac{5}{4}\int_0^1 \frac{I}{2F}\mu^{1/2}d\mu = \frac{5}{4}0.811\frac{J}{2F} = 1.014\frac{J}{2F}. \tag{3.29}$$

We now combine Equations 3.27, 3.28, and 3.29 to determine a as a function of b

$$a = -0.688b + 1.082, \tag{3.30}$$

and $\Delta a = -0.688\Delta b$. This function is used with Equation 3.21 to determine the value of the fixed point to be

$$-1 + 0.688 - \frac{3}{2}(0.688)\mu_0 + \frac{5}{4}\sqrt{\mu_0} = 0, \tag{3.31}$$

and rearranging

$$1.065\mu_0^2 - 0.918\mu_0 + 0.097 = 0. \tag{3.32}$$

Solving this polynomial yields *not one* but two fixed points at $\mu_0 = 0.739$ and $\mu_0 = 0.123$.

From this result, we test how the value of the fixed point and the value of $\alpha = \Delta a/\Delta b$ varies with respect to the ratio of the pseudo-moment of the intensity and the mean intensity, represented as $\delta = J^{-1} \int I \sqrt{\mu} d\mu$, shown in Figure 3.2. With the exception of $\delta \approx 0.267$ where the value of α approaches $\pm\infty$, the value of α ranges from -0.72 to -0.65, causing the fixed points to be 0.72-0.74 and 0.08-0.14. Is this range of values reasonable or is $\alpha \rightarrow \pm\infty$ a realistic possibility? In Figure 3.2, the value of α is determined from the combination of Equations 3.27 and 3.28 such that,

$$\alpha = -\frac{(5\delta/4 - 1)/6 + 11/96}{(5\delta/4 - 1)/4 + 1/6}. \tag{3.33}$$

This relation goes to infinity when $\delta \rightarrow 4/15$, however, δ can never be $4/15$. The reason is that $J = \int I d\mu > \int I \sqrt{\mu} d\mu > K$ and hence δ is constrained to be $1 \geq \delta \geq 1/3 > 4/15$ for a spherical atmosphere with a variable Eddington factor $f = K/J \geq 1/3$. It also means that $\delta \leq 1$ and thus we can define the range of possible values for α as $-5/6 \leq \alpha \leq -15/22$. Inserting this range of values for α in Equation 3.21, we find that the fixed point can range from $0.025 \leq \mu_1 \leq 0.130$ and $0.708 \leq \mu_2 \leq 0.741$. This result suggests that the fixed point exists and is stable to differences in the intensity profiles of stellar atmospheres. It also suggests that the fixed point exists regardless of the dominant opacity, contradicting the conjecture by Heyrovsky (2000), meaning that it occurs at all wavelengths as long as the value of $\delta > 1/3$. However, it is necessary to verify the behavior of the fixed point with respect to wavelength to see if the fixed point spans the entire allowed range or only a fraction of the range.

We test the variation of δ, α, and the fixed points by calculating the average value of δ from the cube of models representing γ Sge. The statistical deviation of δ is also calculated, measuring the change of the intensity profile with respect to differences in the gravity, effective temperature and mass of the model atmospheres. This is done for the wavelength range of 100 *nm* to 100 μm. The resultant mean values of δ and α are shown in Figure 3.3 as a function of wavelength. The plot of δ as a function of wavelength, spans a range of $\bar{\delta}_\lambda = 0.72$-$0.82$ and the behavior suggests that it is tracing the average spectral energy distribution of the cube of models that span a narrow range of parameters. The plot of α shows an interesting result for $\lambda < 300$ *nm*, where the uncertainty of α is larger and implies that the fixed point does not exist at these short wavelengths. Other than this uncertainty, the value of $\alpha = -0.698$ is roughly constant at $\lambda > 300$ *nm*. The two solutions for the fixed point, of the intensity distribution is shown in Figure 3.4 and traces the behavior of α as a function of wavelength. Both the negative solution, $\mu_1 \approx 0.113$, and the positive solution, $\mu \approx 0.735$ are roughly constant with respect to wavelength but this result needs to be tested with a grid of model atmospheres spanning a larger range of gravities, effective temperatures and masses. Furthermore it is interesting to test how the value of the fixed point is dependent on these

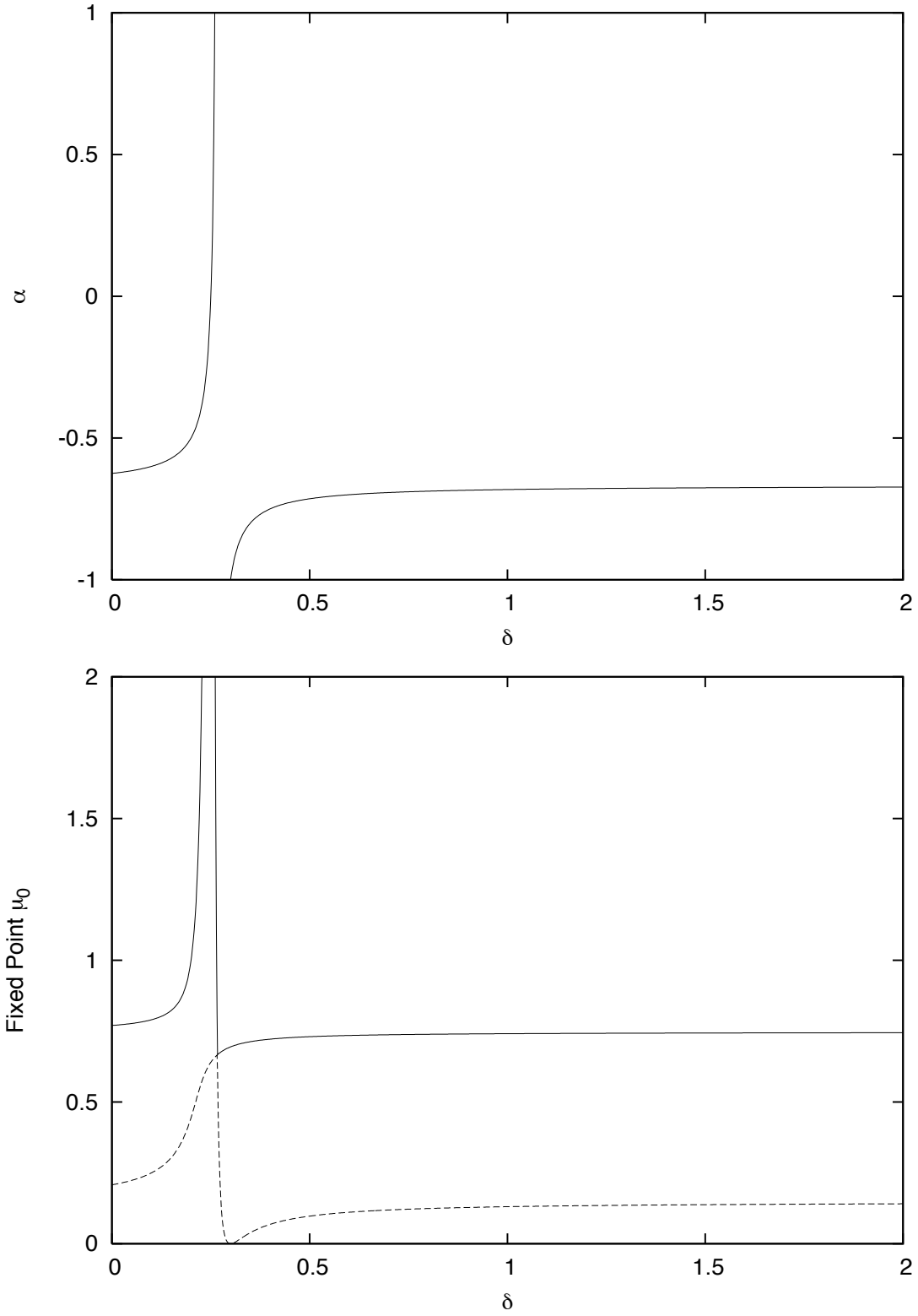

Figure 3.2: The dependence of the fixed-point of the intensity profile μ_0 and the slope of the function $a = \alpha b + \beta$ on the ratio of the pseudo-moment and mean intensity defined as δ.

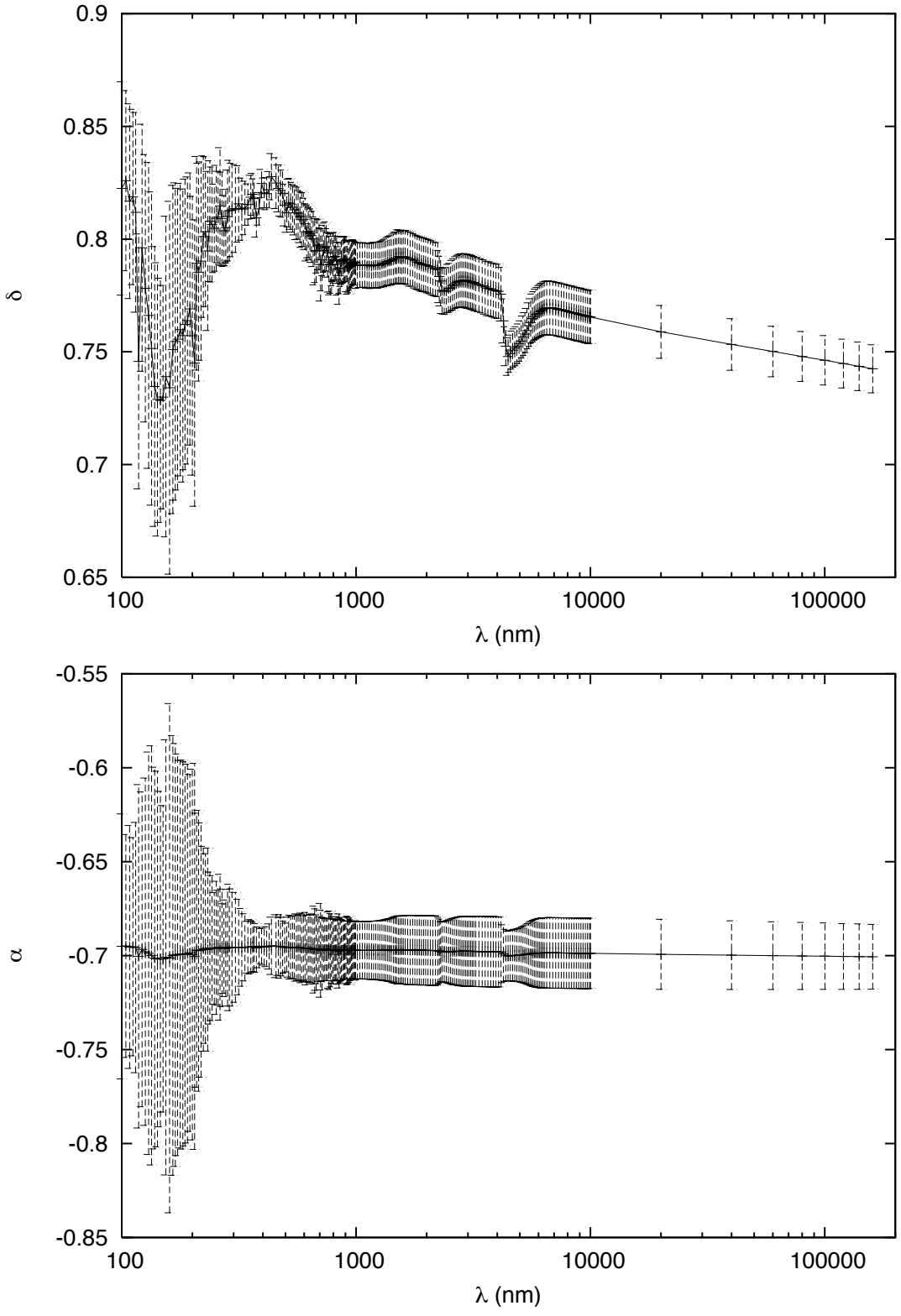

Figure 3.3: (Top) The mean value of the ratio of the pseudo-moment to the mean intensity, δ, determined from the cube of models for γ Sge, as a function of wavelength. (Bottom) The value of α calculated from the mean value of δ, also as a function of wavelength.

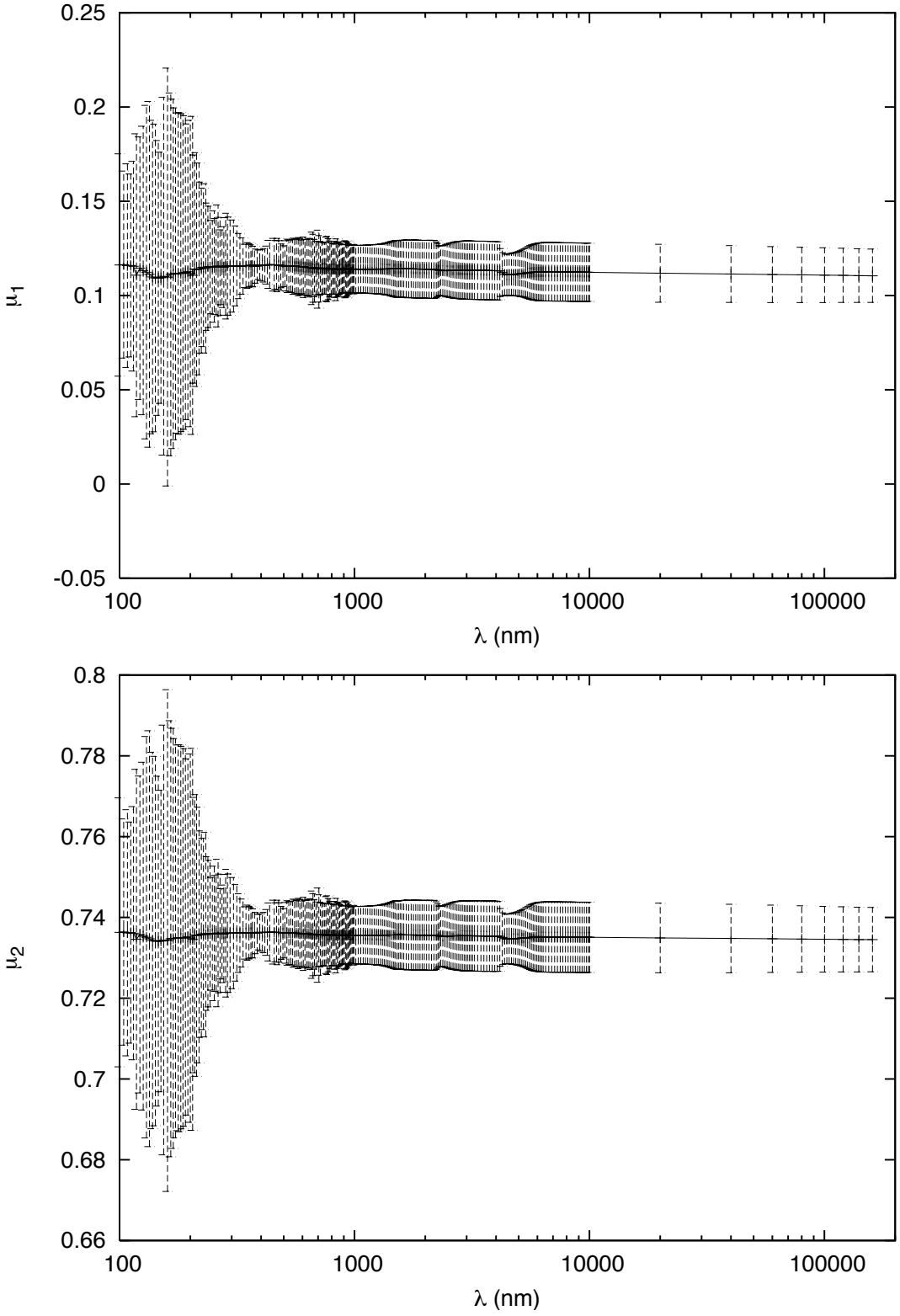

Figure 3.4: The negative (Top) and positive (Bottom) solutions for the fixed point given by Equation 3.21 using the values of α given in Figure 3.3.

global quantities. If there is a significant dependence then we may be able to glean more information from microlensing observations about the atmospheric structure of the observed stars. However, before considering this possibility, it is important to check if the fixed point *actually* exists in the predicted intensity profiles of model stellar atmospheres.

3.4 Limb-darkening and SAtlas Stellar Atmosphere Models

It has been shown that the parameterization of limb-darkening of stars is fraught with pitfalls and have intrinsic properties unique to those parameterizations. For the two-parameter flux-conserving limb-darkening law suggested by Heyrovsky (2000) and Fields et al. (2003), it is shown that the observed fixed point is a result of the law conserving physical properties of the atmospheric models that do not appear to vary significantly. However, it has not yet been shown if this fixed point does or does not appear in the limb-darkening profiles from the model atmospheres. In this section, the intensity as a function of angle μ is compared to the best-fit limb-darkening laws of the form $I/(2F) = 1 - a - b + 3a\mu/2 + 5b\sqrt{\mu}/4$, and the existence of the fixed point is tested using spherically symmetric SAtlas models and plane-parallel Atlas_ODF models (Lester & Neilson, 2008).

We first explore the limb-darkening of the model grid for γ Sge to explore the behavior of the intensity profile as well as to compute the coefficients of the linear plus square root limb-darkening law. In Figure 3.5, we plot the intensity profiles directly taken from the model atmospheres as well as the best-fit limb-darkening laws at $\lambda = 555\ nm$. The model intensity profiles do not have an obvious fixed point but there is a range of μ where the range of intensity is smallest $\Delta I/2F \approx 0.04$. In the plot of the best-fit limb-darkening laws the fixed point is more apparent, where the range of $\Delta I/2F \approx 0.02$. From this analysis, it would appear that the fixed point roughly exists and that fitting the linear plus square root law causes the fixed point to be more pronounced. Because the range of gravity, effective temperature and mass is small, it is not certain if the appearance of a fixed point is real or due to the model atmospheres all being similar.

In order to explore the reality of the fixed point, the intensity profiles are computed for a much larger cube of model stellar atmospheres. Three cubes of model atmospheres have been computed using the SAtlas code with turbulent velocities of 0, 2, and 4 km/s. Each grid uses the effective temperature, mass, and gravity as input. There are four mass bins $M = 2.5$, 5.0, 7.5, and 10.0 $M_\odot$, with the effective temperature ranging from 3000 to 8000 K in steps of 100 K and the gravity ranging from $\log g = -2$ to 3 in steps of 0.25. Each cube of models potentially contains 4284 model atmospheres, but many models do not converge. For $v_{\rm turb} = 0$, there are 2112 model atmospheres, $v_{\rm turb} = 2$ there are 2067 models and form $v_{\rm turb} = 4$ there are 2101 models. The cubes of models cover a significant range of the Hertzsprung-Russell diagram, as shown in Figure 3.6. The intensity profiles for each cube of models are computed with 1000 μ points, more than the 100 points of μ used by Claret (2008) and more than the 17 μ points used by van Hamme (1993).

Using these three cubes of models, the intensity profiles are calculated at $\lambda = 555\ nm$, and shown in

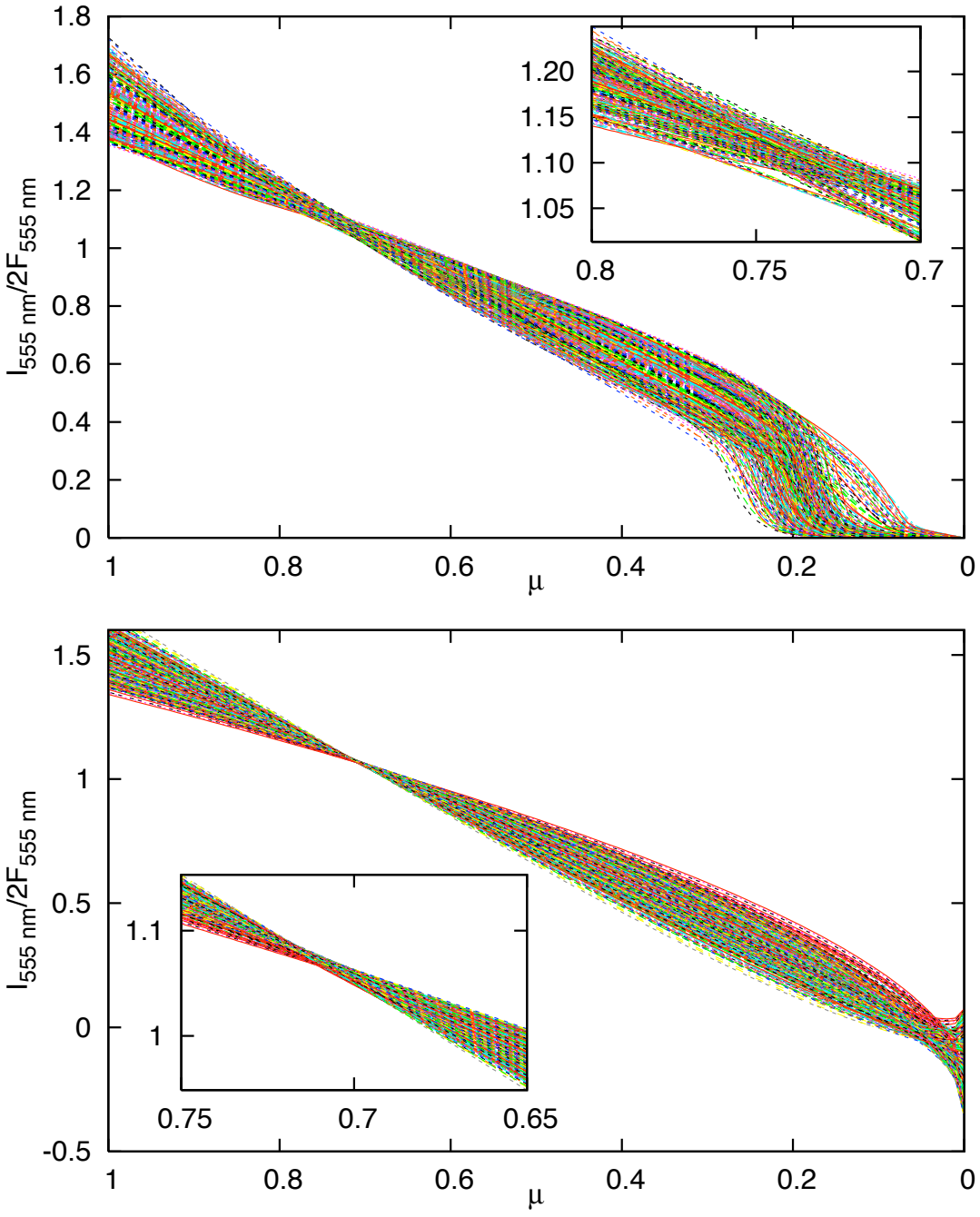

Figure 3.5: (Top) The intensity profiles of each star in the grid of models representing γ Sge at $\lambda = 555$ *nm*. (Bottom) The best-fit linear plus square-root limb-darkening laws calculated from the intensity profiles given above.

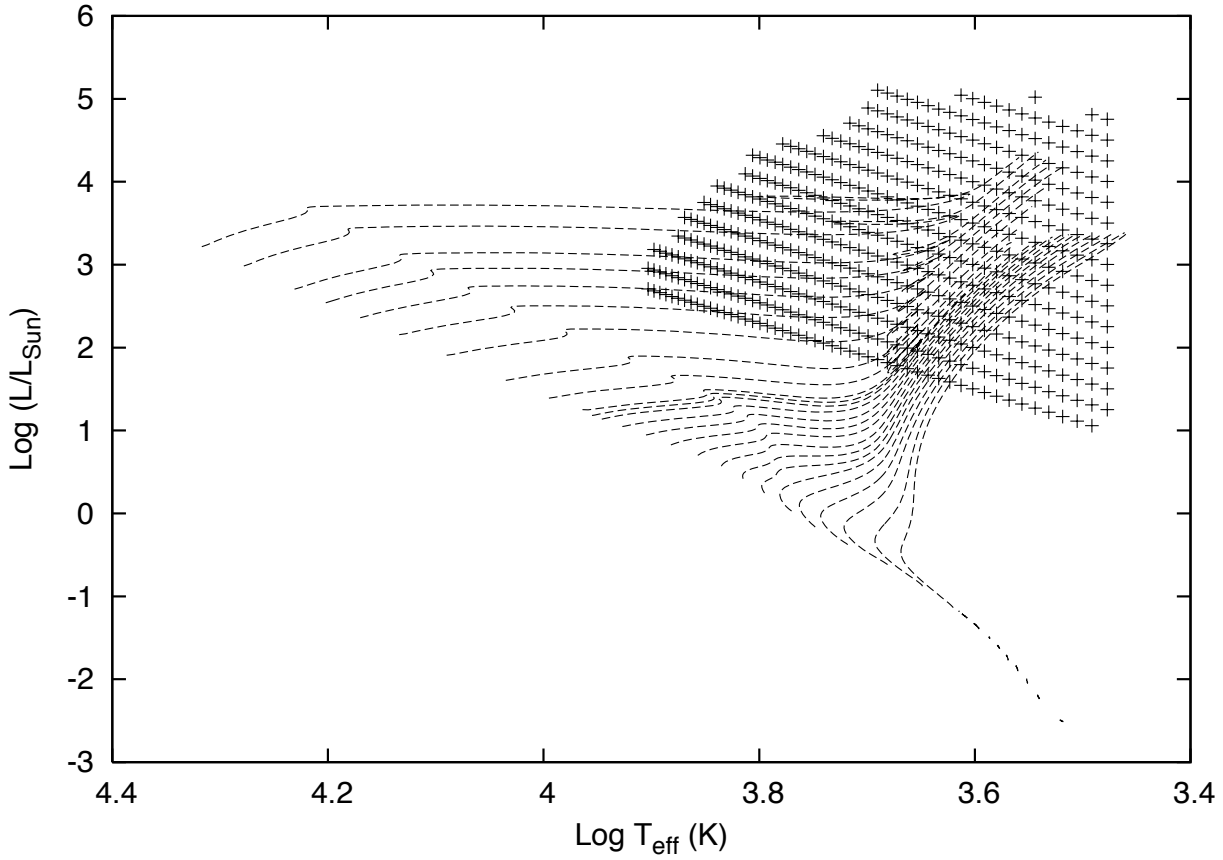

Figure 3.6: The effective temperature and luminosity range of the model stellar atmospheres computed using the SAtlas code along with stellar isochrones from Girardi et al. (2000)..

Figures 3.7, 3.8, and 3.9, along with the best-fit linear plus square-root limb-darkening law. From the model intensity profiles, it is clear that there is no fixed point μ_0 and that the structure of the intensity profile appears to vary significantly with various properties such as gravity and effective temperature. The best-fit limb-darkening laws have a fixed point at approximately $\mu_0 = 0.7$ that is not seen in the model atmospheres. Therefore, it can be concluded that the fixed point is *not* real in general. Even though the fixed point is not apparent in model atmospheres, it does appear in the parameterized law and depends on the mean intensity and the pseudo-moment. This implies a connection to physical stellar properties. It is worth computing the fixed point μ_0 as a function of wavelength, gravity, mass, and effective temperature to learn if there is a dependence that may be exploited with observations.

For the first step we calculate the fixed point of each cube of models at 555 *nm* following the method illustrated earlier. For each cube of models, the mean value of δ, the ratio of the pseudo-moment and the mean intensity, is calculated. For the grid with $v_{\rm turb} = 0$, $\delta = 0.797 \pm 0.028$, meaning the fixed points are $\mu_1 = 0.124 \pm 0.017$ and $\mu_2 = 0.739 \pm 0.010$. The fixed points are the same for the $v_{\rm turb} = 2$, and $v_{\rm turb} = 3$ grids. This averaging over all models suggests that the fixed point is a robust property of the linear plus

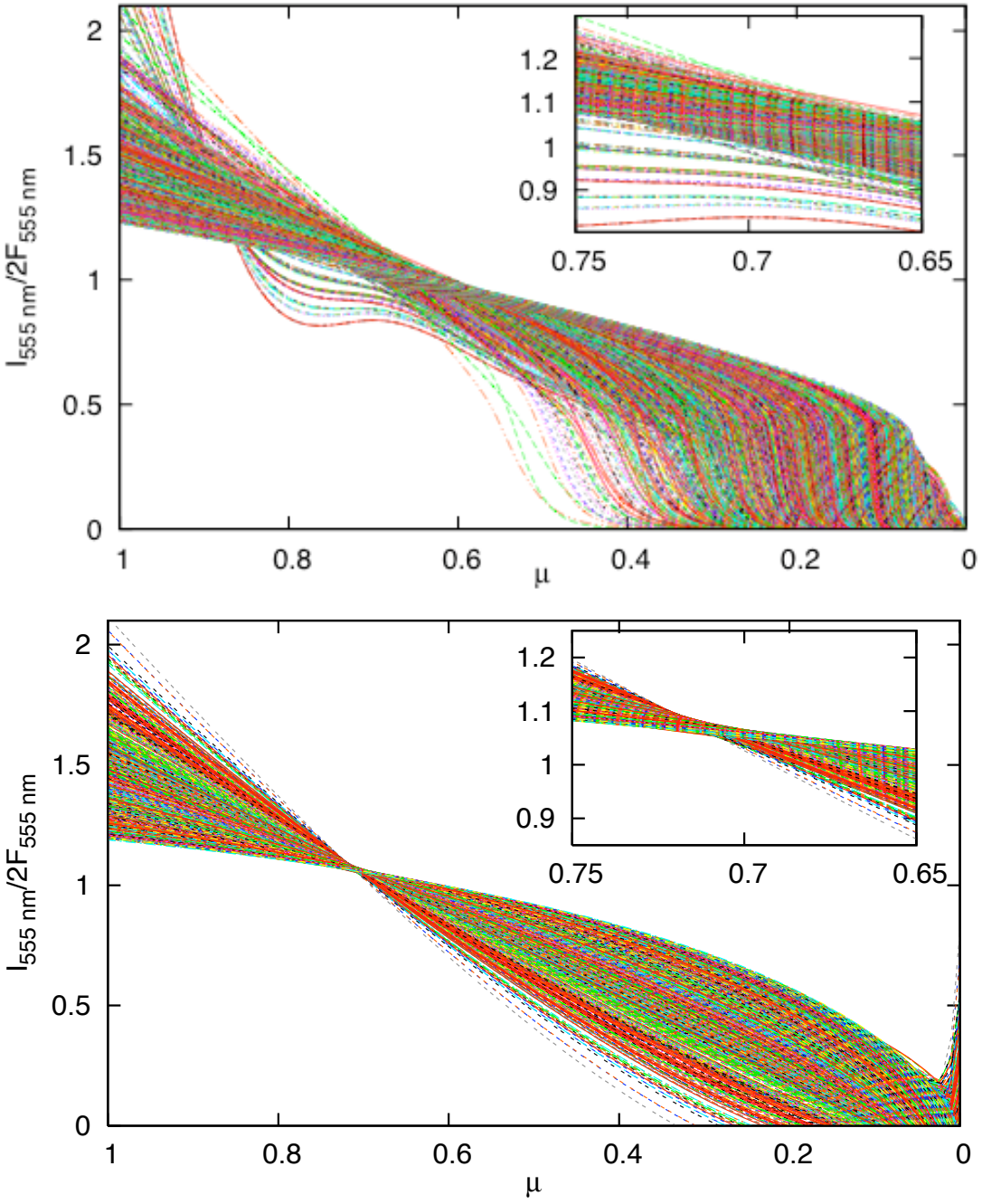

Figure 3.7: (Top) The intensity profiles of each star in the grid of models with $v_{\rm turb} = 0$ at $\lambda = 555\ nm$. (Bottom) The best-fit linear plus square-root limb-darkening laws calculated from the intensity profiles given above.

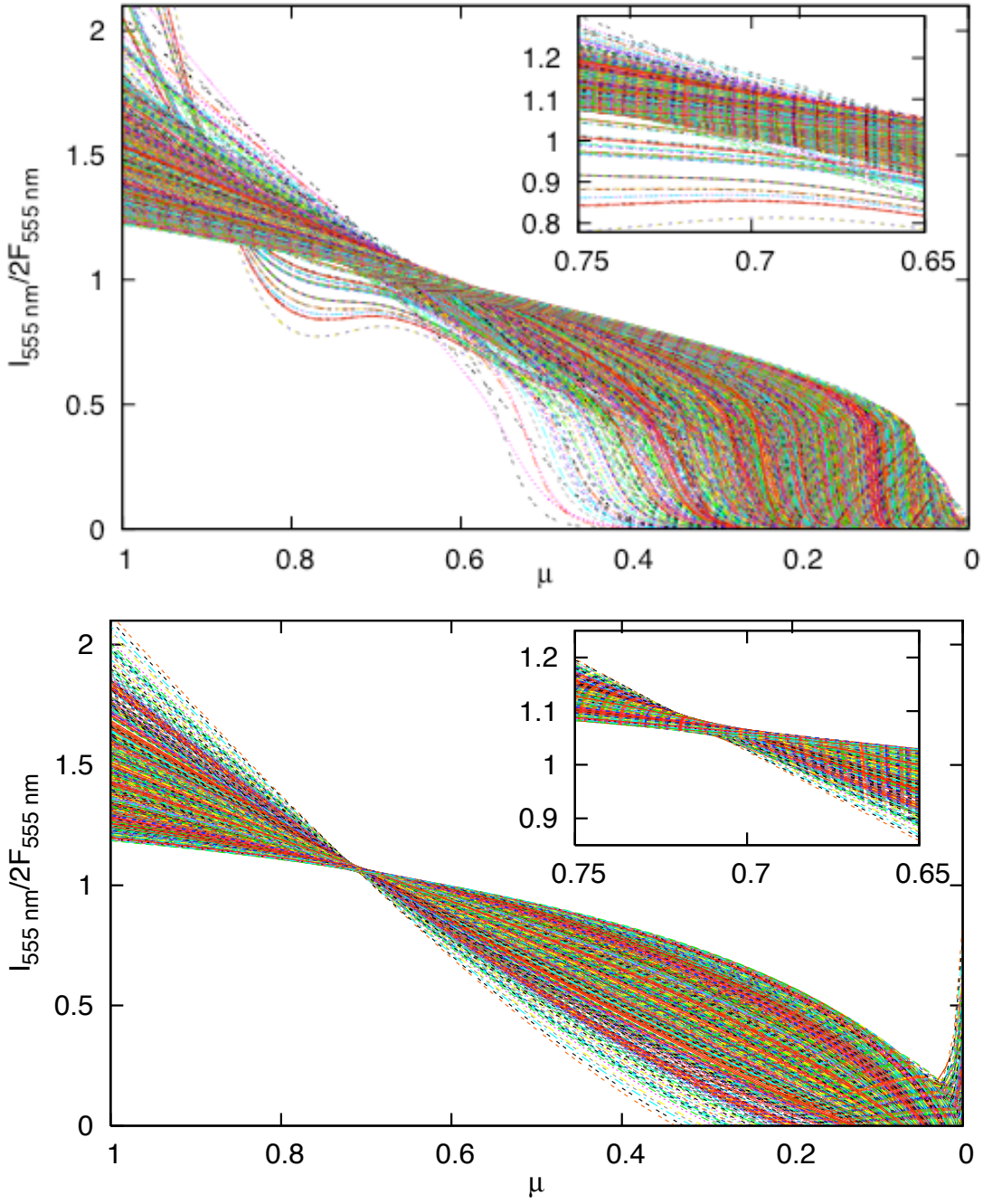

Figure 3.8: (Top) The intensity profiles of each star in the grid of models with $v_{\rm turb}$ = 2 at λ = 555 *nm*. (Bottom) The best-fit linear plus square-root limb-darkening laws calculated from the intensity profiles given above.

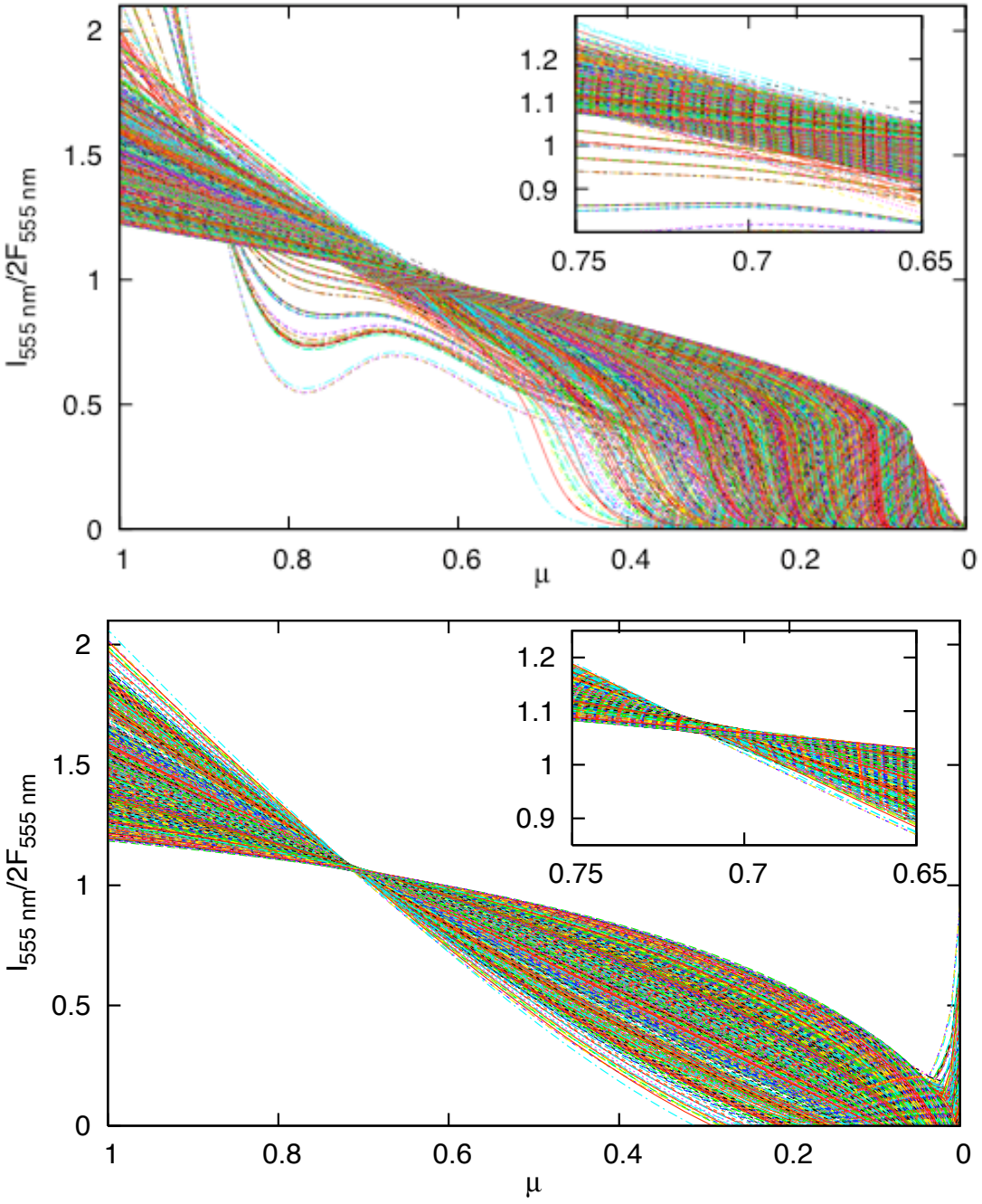

Figure 3.9: (Top) The intensity profiles of each star in the grid of models with $v_{\rm turb}$ = 4 at λ = 555 *nm*. (Bottom) The best-fit linear plus square-root limb-darkening laws calculated from the intensity profiles given above.

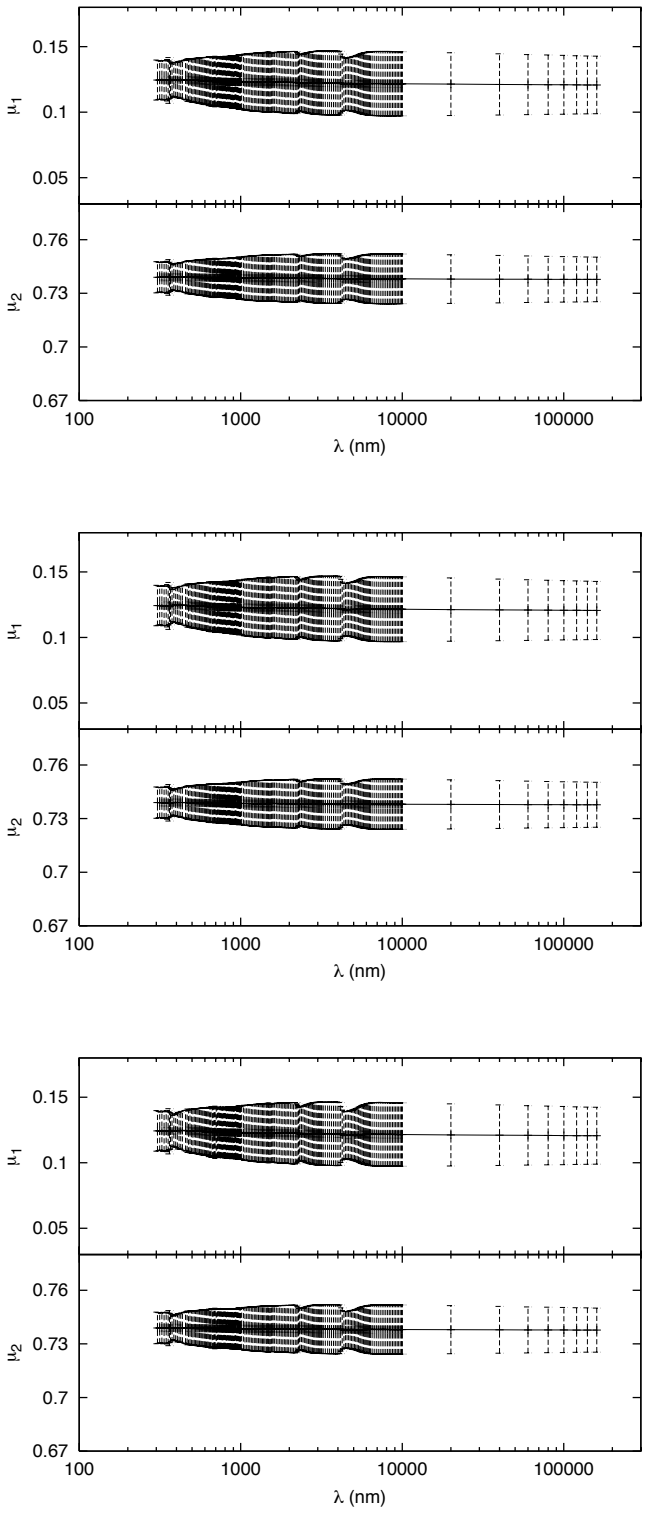

Figure 3.10: The average values of the two fixed points μ_1 and μ_2 for the three cubes of SAtlas models for $v_{\rm turb}$ = 0 km/s (Top) 2 km/s (Middle), and 4 km/s (Bottom).

square-root limb-darkening law. The fixed points are plotted as a function of wavelength from 300 nm to 160 μm for each of the three grids in Figure 3.10. At every wavelength the fixed points are consistent with $\mu_1 = 0.112$ to 0.114 and $\mu_2 = 0.72$ to 0.75 with the error being more than twice as large as was found in the analysis of the γ Sge grid of models. This is further suggestive of a dependence of the fixed point on the global parameters describing the models such as effective temperature, gravity and mass.

To explore this dependence further, we examine the behavior of the fixed point in subsets of the $v_{\rm turb} = 0\ km/s$ such as the the fixed point as a function of effective temperature for a constant gravity. In Figure 3.11 we plot the value of the fixed point and the normalized intensity as a function of the gravity for models with effective temperatures of $3000, 4000, 5000, 6000$, and $7000\ K$. In the plot of the fixed point μ_0 as a function of $\log g$, there is an apparent relation for the model stellar atmospheres with effective temperature $\geq 4000\ K$ but at $3000\ K$ the relation disappears. The same behavior is seen in the plot of the intensity at the fixed point. The lack of apparent relations between the fixed point and the gravity and the intensity at the fixed point and the gravity at $T_{\rm eff} = 3000\ K$ is likely due to a change in the dominant source of continuum opacity in the cool stars. For the hotter stars the opacity source does not change, causing the apparent relations. It should also be noted that the dispersion of the trends between μ_0, $I_0/2F$, and the gravity is related to masses of the model atmospheres. The masses of the models in this work are $2.5, 5.0, 7.5$ and $10.0\ M_\odot$ and the values of both μ_0 and $I_0/2F$ increase with mass.

We now test the dependence of the fixed point and the intensity at the fixed point as a function of effective temperature for fixed values of gravity $\log g = 0, 1, 2$, shown in Figure 3.12. It is clear that the behavior of the fixed point as a function of effective temperature is continuous function for $T_{\rm eff} > 3500\ K$ as well as a dispersion that is dependent on the mass of the model atmosphere. The fixed point, μ_0, is mildly dependent on the value of the effective temperature but is clearly dependent on the gravity of the models, larger gravity atmospheres have larger values of μ_0. The plot of the intensity normalized to the surface brightness shows the same behavior. The intensity is roughly constant with respect to effective temperature for $T_{\rm eff} > 3500\ K$ while the dispersion, again, is due to differences in the mass for each value of $\log g$. It is also worth noting that there appears to be a slight linear dependence of the intensity on the effective temperature for decreasing $\log g$, but the dependence is not significant enough to be pursued further.

It is not surprising that the value of the fixed point and the intensity at the fixed point varies as a function of gravity. In this situation, the gravity is acting as a proxy for the atmospheric extension, where the extension increases as the gravity decreases. When the extension is larger, the slope of the linear plus square-root law is steeper with the intensity approaching zero at a larger value of μ. In this case, intensity profiles with the same gravity but different effective temperature will intersect at larger values of μ and larger values of μ cause larger values of normalized intensity at the fixed point.

The two figures, Figures 3.11 and 3.12 illustrate the how the value of the fixed point and the intensity at the fixed point depends on the gravity, the effective temperature of the model atmospheres as well as the mass of the model atmospheres. The relation between the gravity and μ_0 and $I_0/2F$ is clear and approximately

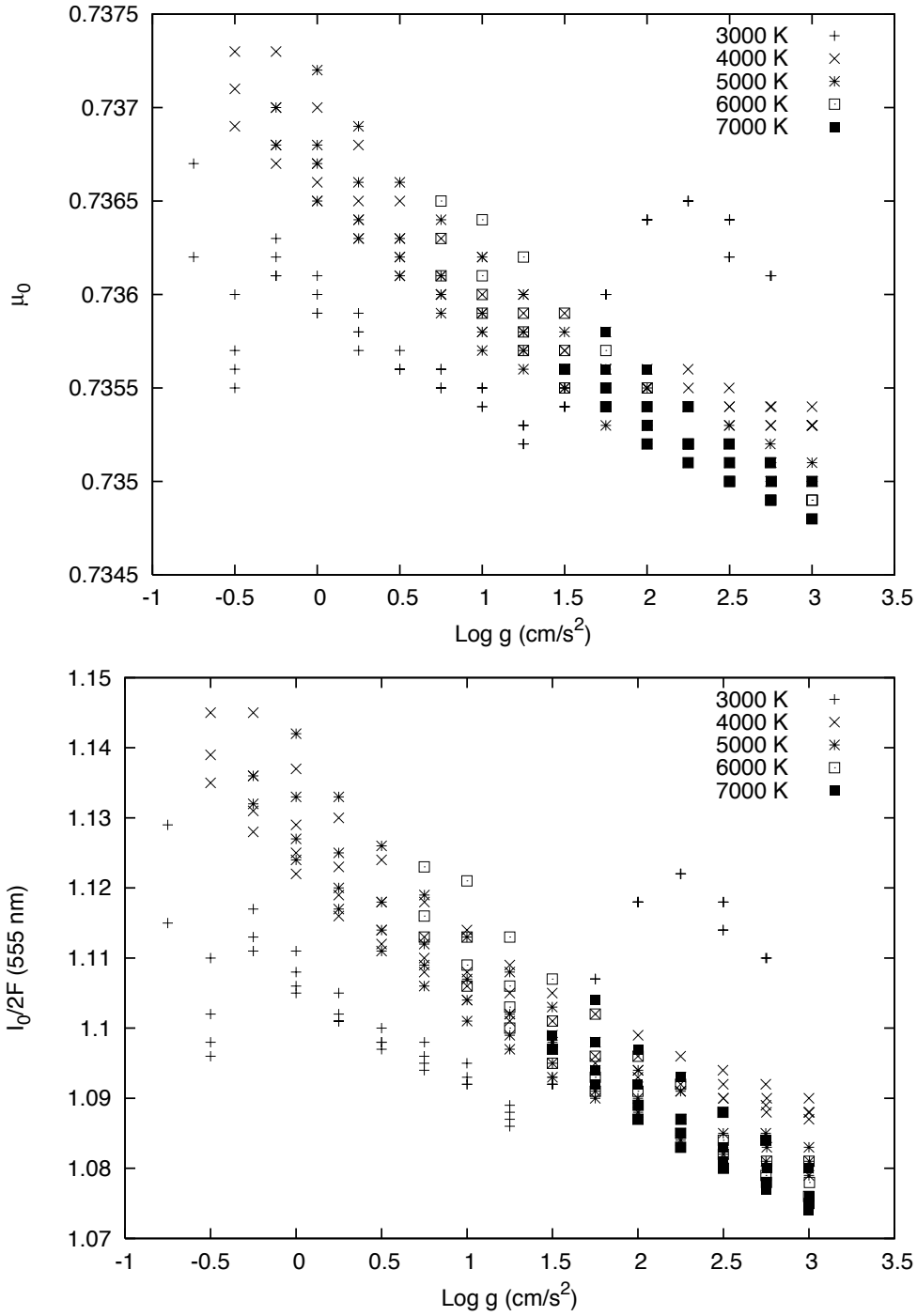

Figure 3.11: (Top) The fixed point of the linear plus square-root limb-darkening law as a function of the gravity of the model stellar atmospheres for different effective temperatures. (Bottom) The intensity at the fixed point at 555 *nm* as a function of gravity.

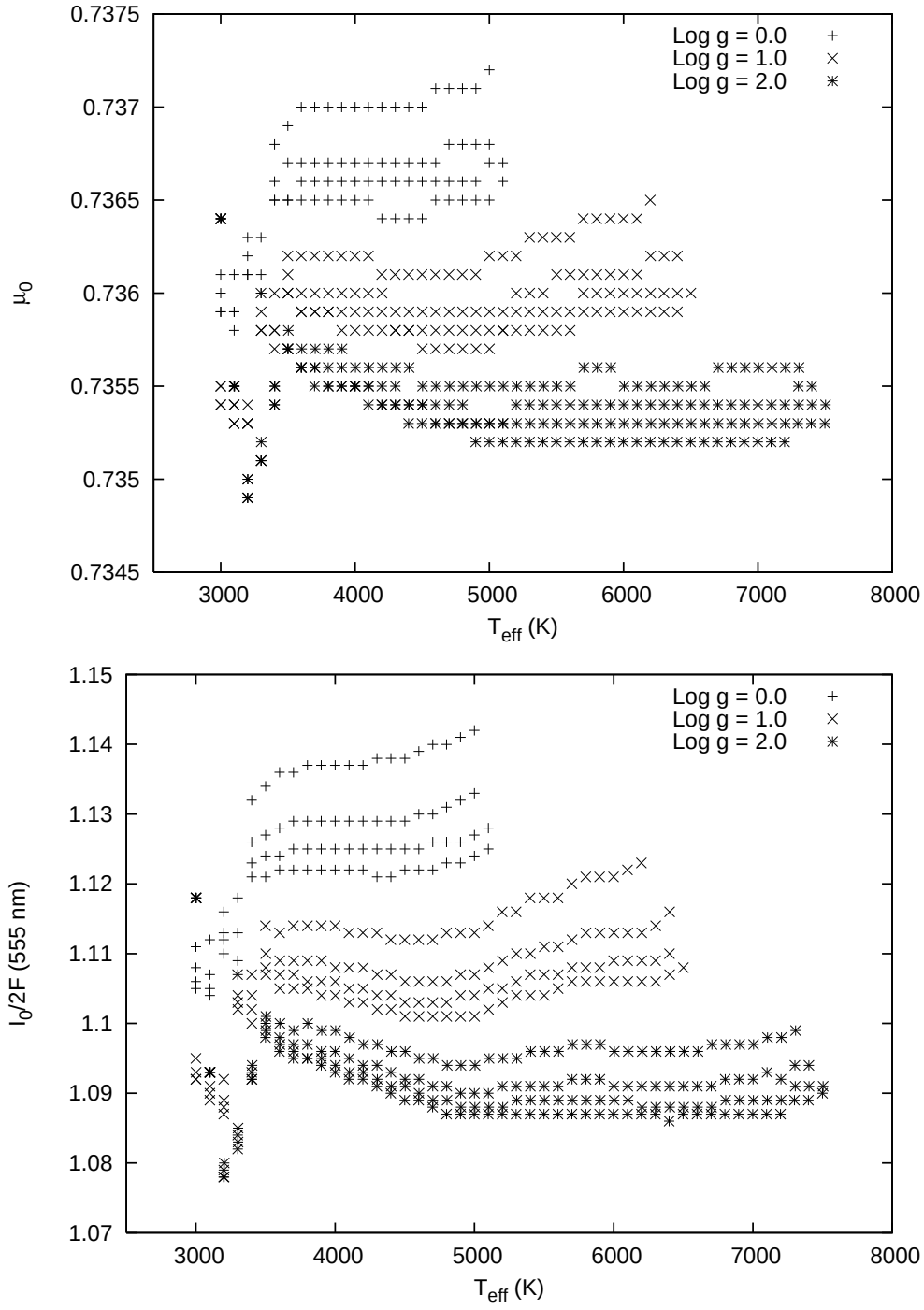

Figure 3.12: (Top) The fixed point of the linear plus square-root limb-darkening law as a function of the effective temperature of the model stellar atmospheres for different values of $\log g$. (Bottom) The intensity at the fixed point at 555 *nm* as a function of effective temperature.

linear, but the dispersion due to the differences in the mass of models makes it difficult to constrain. However, we attempt to minimize the affect the mass has on the relations by exploring how μ_0 and $I_0/2F$ depend on the radius of the models scaled by the mass. The variable R_*/M_* is a more appropriate measure of the atmospheric extension, defined here as the difference between the outer radius of the star at an optical depth of $\tau_{\rm Ross} \rightarrow 0$ and the radius of the star at an optical depth $\tau_{\rm Ross} = 2/3$. This is seen by noting that $d\tau_{\rm Ross} = \chi_{\rm Ross}\rho dr$ and approximating $\rho = \bar{\rho} = M_*/R_*^3$. The opacity has units of cm^2/g suggesting that we can write the opacity to scale as the radius squared per unit mass. However, the opacity at some radius is determined by the composition and hence mean particle mass, more so than the total stellar mass. Therefore, we write $\chi \propto R_*^2/\bar{m}$. The atmospheric extension $\Delta R = R(\tau_{\rm Ross} = 10^{-7}) - R(\tau_{\rm Ross} = 2/3)$ is

$$\Delta R \approx \frac{\Delta\tau_{\rm Ross}}{\chi_{\rm Ross}\rho} = \frac{2/3}{(R_*^2/\bar{m})(M_*/R_*^3)} \propto \frac{R_*}{M_*}. \tag{3.34}$$

This scaling relation is reasonable as long as the effective temperature and density structure in the atmosphere does not change too significantly between different model atmospheres that are being compared because it is assumed that the mean particle mass is roughly constant. It the temperature varies enough then the atmospheric extension will change from the change of mean mass due to ionization or recombination.

Using this scaling relation for the atmospheric extension, the behavior of the fixed point μ_0 and the intensity at the fixed point $I_0/2F$ is shown in Figure 3.13. In the top panel, the fixed point is plotted as a function $\log(R_*/M_*)$ and there appear to be correlations at each given effective temperature with the exception of $T_{\rm eff} = 3000\ K$. This correlation is very similar to that seen in Figure 3.11 between the fixed point and the gravity of the models. However, the dispersion of the correlation with R_*/M_* seems to be much less than the dispersion for the correlation with the gravity itself. The correlation between the intensity at the fixed point and the radius per mass also has less dispersion than the correlation between the intensity at the fixed point and the gravity for different effective temperatures.

The dependence on the effective temperature seen in Figure 3.13 is the same as that seen in the Figures 3.11 and 3.12. When the effective temperature is $< 4000\ K$, there is no correlation, the behavior of the fixed point and the intensity is more random with respect to the radius per mass. This is consistent with the scaling relation derived for the atmospheric extension which is shown to be dependent on the composition via the mean particle mass. When the effective temperature is small ($< 3500\ K$), the opacity becomes more dependent on the density of the gas at each point, implying that a change in gravity of the models leads to significant a change in the mean particle mass and hence the oontinuous opacity. The dominate source of continuous opacity switches from H^- to neutral and diatomic hydrogen. At larger effective temperatures, the change of particle mass is due primarily to changes to the effective temperature only explaining why there are strong correlations between the fixed point and the intensity at specific effective temperatures.

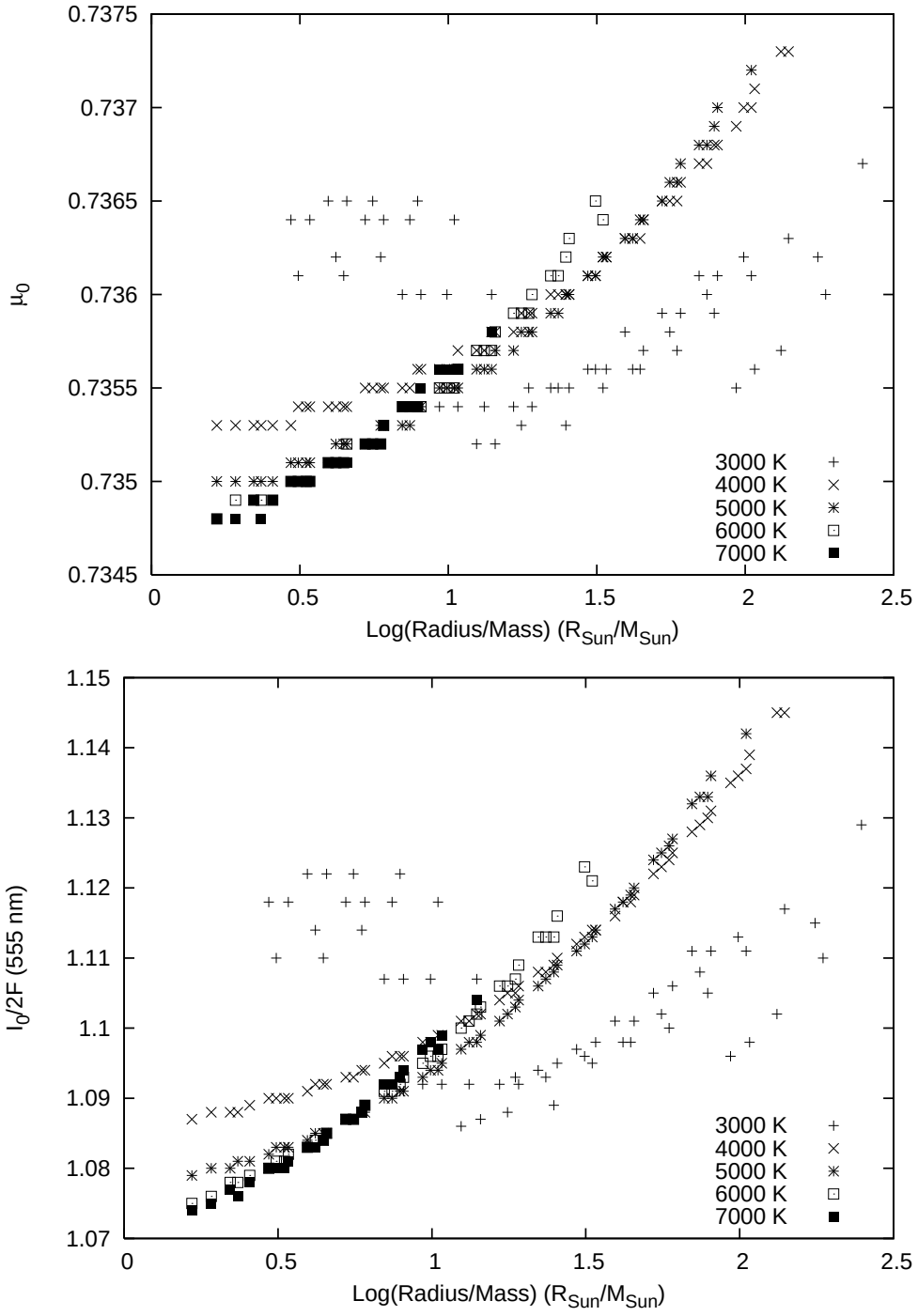

Figure 3.13: (Top) The fixed point of the linear plus square-root limb-darkening law as a function of the radius per mass of the model stellar atmospheres for different values of the effective temperature. (Bottom) The intensity at the fixed point at 555 *nm* as a function of R_*/M_* for different effective temperatures.

Table 3.1: Best Fit Parameters for the Fixed Point and Intensity at the Fixed Point

$T_{\rm eff}$ (K)	a_μ	b_μ	σ_μ
3000	$(-2.0593 \pm 3.726) \times 10^{-5}$	$0.7359 \pm 9.544 \times 10^{-5}$	4.060×10^{-4}
4000	$(4.3284 \pm 0.0476) \times 10^{-4}$	$0.7352 \pm 1.041 \times 10^{-5}$	4.830×10^{-5}
5000	$(5.3943 \pm 0.0404) \times 10^{-4}$	$0.7349 \pm 7.644 \times 10^{-6}$	3.361×10^{-5}
6000	$(7.1074 \pm 0.0987) \times 10^{-4}$	$0.7348 \pm 1.119 \times 10^{-5}$	4.022×10^{-5}
7000	$(8.1628 \pm 0.2155) \times 10^{-4}$	$0.7348 \pm 1.369 \times 10^{-5}$	3.775×10^{-5}
$T_{\rm eff}$ (K)	a_I	b_I	σ_I
3000	$(-0.206 \pm 1.015) \times 10^{-3}$	1.1504 ± 0.025	0.0110
4000	$0.01234 \pm 8.824 \times 10^{-5}$	$1.0861 \pm 1.931 \times 10^{-4}$	8.057×10^{-4}
5000	$0.01530 \pm 6.531 \times 10^{-5}$	$1.0785 \pm 1.232 \times 10^{-4}$	5.417×10^{-4}
6000	$0.02012 \pm 1.982 \times 10^{-4}$	$1.0747 \pm 2.247 \times 10^{-4}$	8.076×10^{-4}
7000	$0.02369 \pm 4.126 \times 10^{-4}$	$1.0740 \pm 2.621 \times 10^{-4}$	7.227×10^{-4}

Because of these correlations, best-fit relations are computed of the form

$$\mu_0 = a_\mu [\log(R_*/M_*)]^2 + b_\mu \tag{3.35}$$

and

$$\frac{I_0}{2F} = a_I [\log(R_*/M_*)]^2 + b_I. \tag{3.36}$$

The best-fit relations are computed for the effective temperatures $3000, 4000, 5000, 6000$, and 7000 K and the best-fit parameters are list in Table 3.1. The relations at $T_{\rm eff} = 3000$ K data are poor fits to the models suggesting that for very cool stars, the fixed point is not an useful measure for stellar properties. However, the remainder of the relations model the data very well, meaning that we can use them to understand observations of limb-darkening, if we have a measure for the effective temperature of that star. In that case, we can measure the parameter R_*/M_* using these two relations plus the best-fit limb-darkening law to observations. First, we guess a value of R_*/M_* and determine the value of μ_0. Using the limb-darkening law representing the observed intensity profile, μ_0 is used to compute $I_0/2F$ and the value of $I_0/2F$ is used to compute a new value of R_*/M_*. The process is iterated until convergence is reached.

3.5 Application of R_*/M_* Method to Microlensing Results

Observations of microlensing produce limb-darkening parameters that can be used to test the method producing an estimate of R_*/M_*. The microlensing event EROS-BLG-2000-5 (An et al., 2002; Fields et al., 2003) was observed in the V, I and H-band as well as the V_E and I_R bands, described by Afonso et al. (2001). Here, we take the computed V-band limb-darkening law from Fields et al. (2003) to predict a value of R_*/M_*. An et al. (2002) use the color $(V-I)_0$ and the fact that the observed star is a K3 giant star to

Table 3.2: Iterative Solution of R_*/M_* for Microlensing Event EROS-BLG-2000-5

Iteration	R_*/M_*	μ_0	$I_0/2F$
1	10	0.73560	1.07264
2	*NaN*	*NaN*	*NaN*

determine an effective temperature of 4200 K.

From the grid of SAtlas model limb-darkening laws, the $(R_*/M_*, \mu_0)$ and $(R_*/M_*, I_0/2F)$ relations are

$$\mu_0 = 4.48857 \times 10^{-4}(\pm 4.684 \times 10^{-6})[\log(R_*/M_*)]^2 + 0.73515(\pm 9.961 \times 10^{-6}) \tag{3.37}$$

and

$$\frac{I_0}{2F} = 0.012781(\pm 9.049 \times 10^{-5})[\log(R_*/M_*)]^2 + 1.08445(\pm 1.925 \times 10^{-4}). \tag{3.38}$$

The V-band limb-darkening relation from Fields et al. (2003) is

$$\frac{I}{2F} = 1 + 0.7856(\pm 0.1058)\left(\frac{3}{2}\mu - 1\right) - 0.1192(\pm 0.1981)\left(\frac{5}{4}\sqrt{\mu} - 1\right). \tag{3.39}$$

We apply the iterative method starting with a value of $\log(R_*/M_*) = 1$. In Table 3.2, the solution at each step using this method is shown. It is clear from the results that the method does not work with this data because the intensity at the fixed point predicted in the first iteration is less than the zero-point of the $(R_*/M_*, I_0/2F)$-relation. While this is a disappointing result, it must be noted that the uncertainty of the best-fit limb-darkening parameters is large relative to the parameters themselves and we have already determined that the two coefficients of the limb-darkening law are related via Equation 3.30, which predicts a much different value of the coefficient of the square-root term. Applying Equation 3.30 to the determined value of $a = 0.7856 \pm 0.1058$ yields $b = 0.4314 \pm 0.1538$, and using this different limb-darkening law, we find a value of $R_*/M_* = 31.5 \pm 0.33$. The results of the iterative solution are given in Table 3.3.

The method proposed seems robust but must be compared to the radius and mass found by An et al. (2002) from kinematic information. Based on the proper motion and radial velocity plus the color and magnitude, the radius was determined to be $R_* = 11.4 \pm 1.0\ R_\odot$. If we include that result then we find a mass of $M_* = 0.36 \pm 0.1\ M_\odot$. This is equivalent to a gravity $\log g = 1.88^{+0.29}_{-0.21}$, more precise than the range of gravity determined by Fields et al. (2003) of $\log g$ = 1.9-2.6.

The computed results are robust assuming we have a precise estimate of the effective temperature. In most cases, it is unlikely that a precise estimate of the effective temperature is possible. The microlensing data are tested again using best-fit relations for the fixed point and the intensity at the fixed point over a larger temperature range, from $T_{\rm eff} = 4000$ to 5000 K, equivalent to an stellar atmosphere having $T_{\rm eff} =$

Table 3.3: Iterative Solution of R_*/M_* for Microlensing Event EROS-BLG-2000-5 With One Free Parameter Limb-Darkening

Iteration	R_*/M_*	μ_0	$I_0/2F$
1	10	0.735598857	1.11233152
2	29.9905291	0.736129174	1.11312315
3	31.4633528	0.736156975	1.11316465
4	31.5419462	0.736158432	1.11316682
5	31.5460701	0.736158508	1.11316694
6	31.5462862	0.736158512	1.11316694
7	31.5462976	0.736158513	1.11316694
8	31.5462982	0.736158513	1.11316694
9	31.5462982	0.736158513	1.11316694
10	31.5462982	0.736158513	1.11316694

$4500 \pm 500\ K$. The two relations, over this temperature range are

$$\mu_0 = 4.79234 \times 10^{-4}(\pm 2.331 \times 10^{-6})[\log(R_*/M_*)]^2 + 0.735064(\pm 4.776 \times 10^{-6}), \tag{3.40}$$

and

$$\frac{I_0}{2F} = 0.0136554(\pm 5.678 \times 10^{-5})[\log(R_*/M_*)]^2 + 1.082060(\pm 1.1182 \times 10^{-4}) \tag{3.41}$$

with dispersions of $\sigma_\mu = 7.1801 \times 10^{-5}$ and $\sigma_I = 1.777 \times 10^{-3}$. The uncertainty of the relations over an effective temperature range of 1000 K is only a factor of 2 larger than the precise relations, while the uncertainties of the slopes and zero-points are similar for both the large range of temperatures and the precise relations. When these two relations are applied, the predicted value of R_*/M_* is $32.30 \pm 0.26\ R_\odot/M_\odot$ and hence a mass $M = 0.35 \pm 0.10\ M_\odot$. This mass agrees with the result from using the relations for $T_{\rm eff} = 4200\ K$ only. The difference between the predicted masses is due to the degeneracy between the dependence of the intensity and fixed point on the effective temperature and R_*/M_*. In fact, the values of the slopes and zero-points of the relations shown in Table 3.1 scale with the effective temperature.

We have discovered a useful method for constraining fundamental parameters of stars where the limb-darkening is determined and parameterized as a linear plus square-root law. The precise results found from the method are surprising when one considers how poorly this type of law fits the computed stellar atmospheres. The downside of this method is that it requires knowledge of one of the degenerate parameters such as the effective temperature or luminosity. However, this formalism is able to constrain stellar parameters using limb-darkening observations even though it is still not possible for limb-darkening observed from microlensing or eclipsing binary stars test for model stellar atmospheres.

3.6 Testing the Limb-darkening Parameterizations with Models

The goal of any limb-darkening law is to produce the most realistic intensity profiles with the fewest free parameters. The results of Claret (2000) and others suggest that a two-parameter limb-darkening law produces satisfactory results, but the best-fit law is different for hotter and cooler stars. The two different laws are linear plus square-root and linear plus quadratic, respectively. Claret (2000) proposed a four-parameter limb-darkening law with the intention of fitting model stellar atmosphere well at all effective temperatures. This limb-darkening law is

$$\frac{I}{I(1)} = 1 - \sum_{i=1}^{4} a_i(1 - \mu^{i/2}), \tag{3.42}$$

such that it is a composite of the square-root and quadratic laws but with an additional term $1 - \mu^{3/2}$. This law has been applied to spherical PHOENIX model atmospheres in the gravity range $\log g$ = 3.5-5.5 and effective temperature range $T_{\rm eff}$ = 5000 to 10000 K(Claret & Hauschildt, 2003), and it is found that the law fits the intensity profiles better than one- and two-parameter limb-darkening laws but not as well as for fits to plane-parallel model atmospheres. The limb-darkening law has not been applied to the spherical model atmosphere with lower gravity and hence larger atmospheric extension. It is expected that the four-parameter law will not fit the data well because of the tail of the intensity profile where the $I/I(1) \rightarrow 0$ at small values of μ.

The intensity as a function of μ for each SATLAS model is fit to the Claret (2000) limb-darkening law at about 300 wavelengths using least squares fitting. The quality of the fit is tested by computing the ratio of the flux from the best-fit law and the flux from the model atmosphere, F_p/F_m. This ratio is shown in Figures 3.14, 3.15 and 3.16 for the set of models with $v_{\rm turb} = 0, 2$, and 4 km/s, respectively, as a function of effective temperature. The flux conservation varies from 0.98-1.01 at short wavelengths to 0.96-1.01 at longer wavelengths. At low effective temperatures, $T_{\rm eff}$ = 3000-3500 K, the flux is not conserved at $\lambda = 435, 555$, and 655 nm. This is most likely due to a change of opacity at these temperatures that dramatically changes the structure of the intensity profile as is seen in the analysis of the linear plus square-root law. The fit of the data is similar for the different turbulent velocities, suggesting that the turbulent velocity has little effect on the intensity structure of the atmosphere.

Because of the significant scatter of the flux ratio as a function of effective temperature, the flux ratio is plotted as a function of gravity $\log g$ in Figures 3.17, 3.18, and 3.19 for the three respective values of turbulent velocity. The flux ratio ranges from 0.99-1.01 for $\log g > 1.5$ for effective temperatures $T_{\rm eff} >$ 3500 K and has a much larger range from 0.96-1 for $\log g < 1.5$. The four-parameter limb-darkening law does not conserve the flux from the model atmosphere at low gravity. The models where the fit fails significantly at low effective temperature, $T_{\rm eff} < 3500$ K is seen at $\log g$ = 2-3. There is also a small difference between the flux ratios for different turbulent velocities at gravities $\log g < 0$ and wavelengths longer than 1 μm. At $v_{\rm turb} = 0$ km/s the flux ratio is as large as $F_p/F_m = 1.01$, while at $v_{\rm turb} = 2$ km/s, the

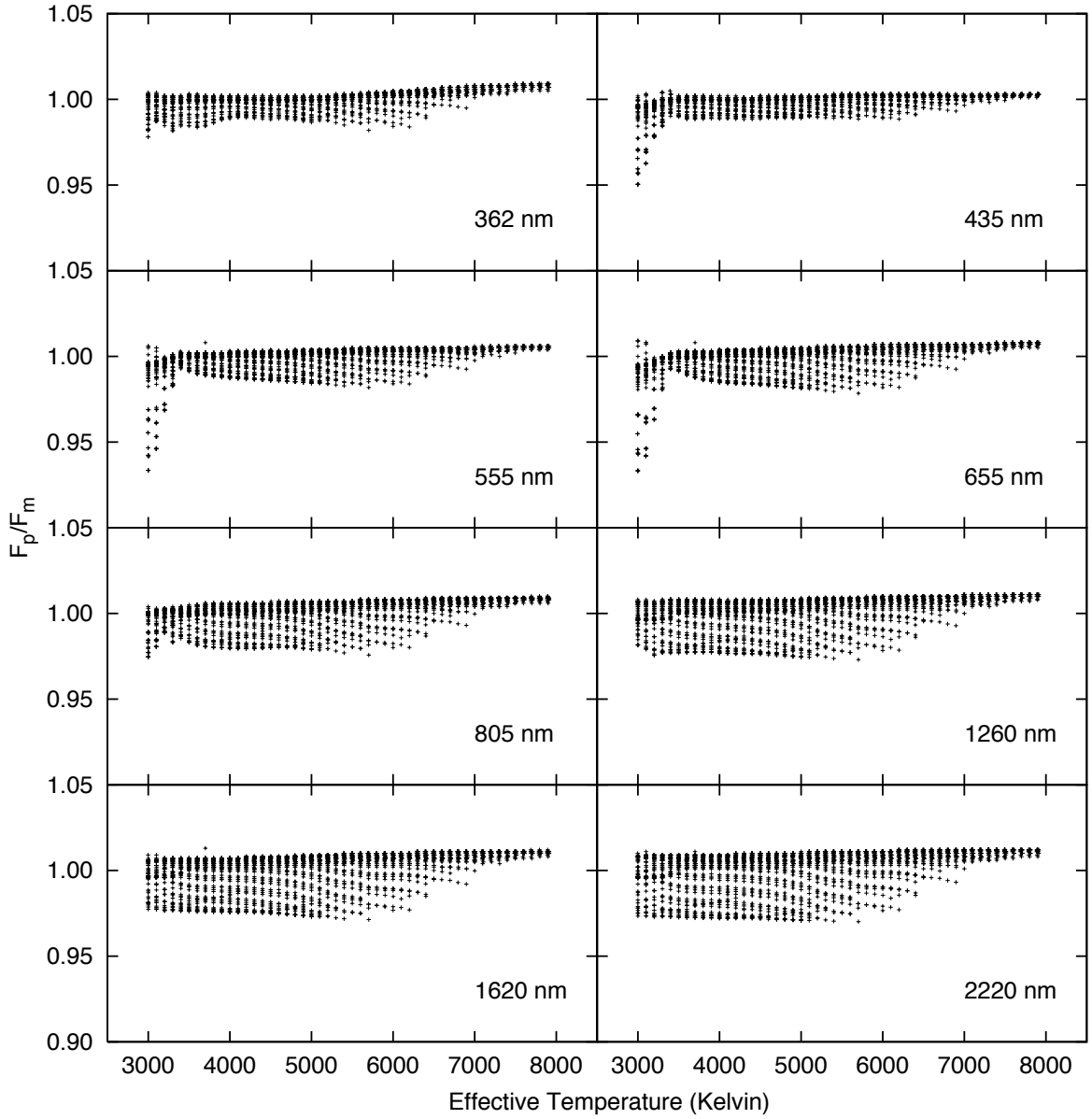

Figure 3.14: Measuring the quality of fit of the four-parameter limb-darkening law, Equation 3.42, with the ratio of the flux from the integration of the limb-darkening law and the flux from the model stellar atmospheres with $v_{\rm turb} = 0\ km/s$ as a function of effective temperature from $T_{\rm eff} = 3000$ to $8000\ K$ for a number of wavelengths. The spread of F_p/F_m at a specific effective temperature is due to difference of gravity and mass between the models.

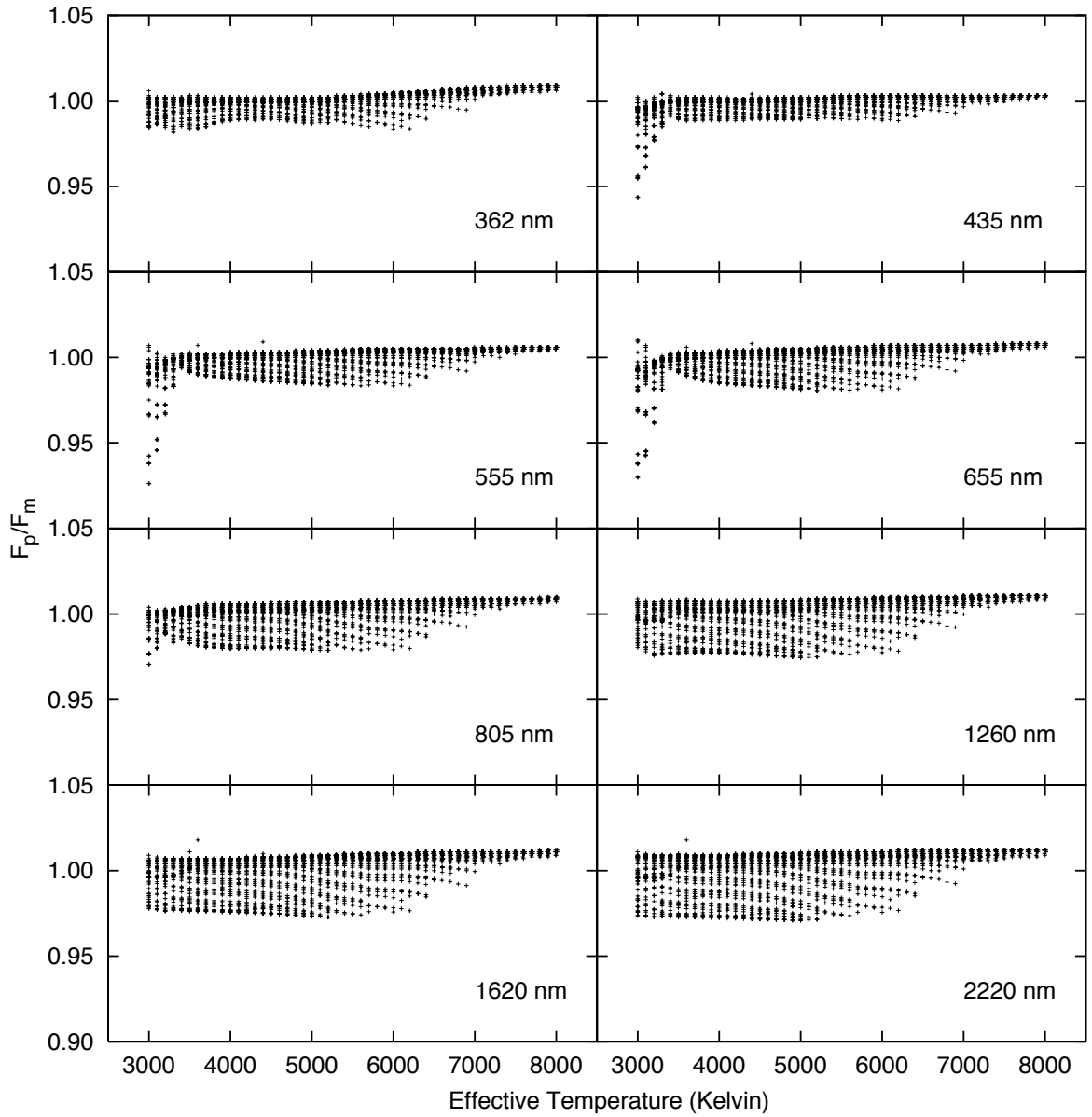

Figure 3.15: Same as Figure 3.14 but for $v_{\rm turb} = 2\ km/s$.

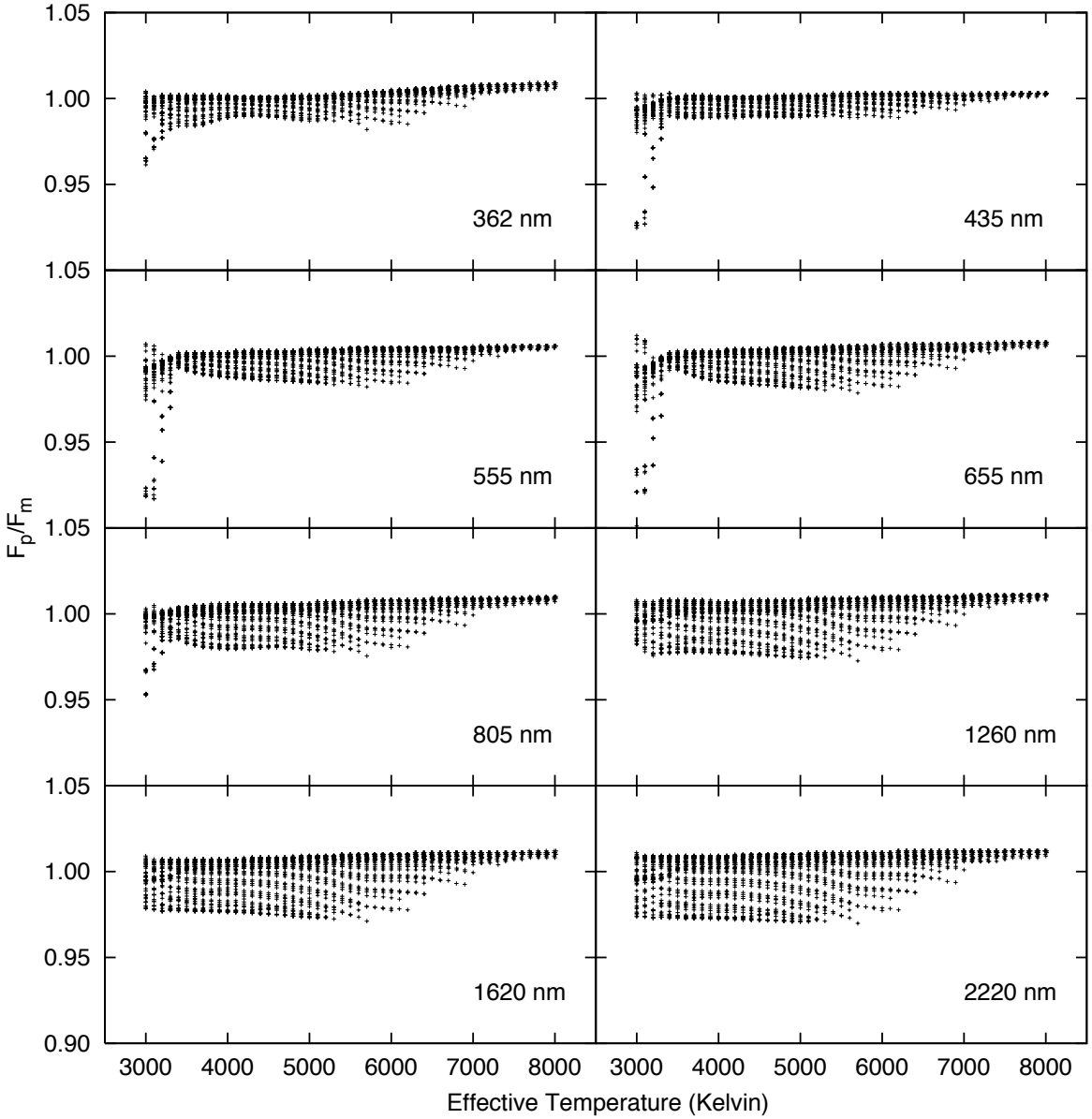

Figure 3.16: Same as Figure 3.14 but for $v_{\rm turb} = 4\ km/s$.

flux ratio is larger, and at $v_{\rm turb} = 4\ km/s$, the flux ratio decreases to be less than unity. This implies there are small differences between intensity profiles of spherical model atmospheres due to differences of turbulent velocity.

It is found that the flux is conserved to the range of $F_p/F_m = 0.96$-1.02 for all spherical model atmospheres. This result is poor in comparison to the fit of the four-parameter limb-darkening law to plane-parallel Atlas model atmospheres from Claret (2000). For the plane-parallel models, the flux ratio deviates from unity by less than 0.0005. This deviation is two orders of magnitude smaller than that seen in the spherical models. The four-parameter law is not ideal for fitting the intensity distribution of spherical atmosphere but is still better than the simpler linear and two-parameter laws discussed. The reason these laws do not fit the spherical models as well as the plane-parallel models is due to the difference between the intensity profiles near the edge of the disk, $\mu \rightarrow 0$. In the plane-parallel models the intensity decreases rapidly to a minimum, $dI/d\mu \rightarrow -\infty$ as $\mu \rightarrow 0$, however in the spherical models, the rapid decrease of intensity occurs at some positive value of μ that depends on the amount of atmospheric extension. As $\mu \rightarrow 0$, the slope $dI/d\mu \rightarrow 0$ asymptotically, suggesting a significantly different structure for the limb-darkening law.

As noted, while the four-parameter law is not ideal, it has been found to be the best representation for the intensity distribution of spherical model atmospheres. It is interesting to compare the coefficients of the limb-darkening law from fits to spherical Atlas models with the coefficients determined by fitting plane-parallel Atlas models (Claret, 2000). Claret (2000) compute limb-darkening laws for Atlas models in the effective temperature range $3500\ K \leq T_{\rm eff} \leq 50000\ K$ in steps of $250\ K$, a gravity range $0 \leq \log g \leq 5$ is steps of 0.5 for a number of compositions and turbulent velocities of $0, 1, 2, 4$, and $8\ km/s$. This set of plane-parallel models overlap with the spherical models in the gravity range $0 \leq \log g \leq 3$ in steps of 0.5 and temperature range of $3500\ K \leq T_{\rm eff} \leq 8000\ K$ in steps of $500\ K$ for turbulent velocities $v_{\rm turb} = 0, 2, 4\ km/s$, and the difference between spherical and plane-parallel models is calculated for each of the four masses of spherical model atmospheres. The difference between the models is measured as the difference between coefficients calculated from the plane-parallel and spherical models.

The difference between the predicted values of the first coefficient a_1 is shown in Figures 3.20, 3.21, and 3.22 for values of $v_{\rm turb} = 0, 2$, and $4\ km/s$ for wavelengths ranging from $360\ nm$ to $2.22\ \mu m$ as a function of gravity $\log g$. The difference $a_1({\rm Sph}) - {\rm a}_1({\rm PP})$ varies significantly as a function of gravity with the difference also depending on the effective temperature and mass of the model. At larger values of $\log g$ the difference between the leading coefficient a_1 as determined from spherical and plane-parallel models is smallest with the spherical coefficient being greater than the plane-parallel coefficient, with the difference increasing with longer wavelength. The difference between the coefficients is most significant a gravities $\log g = 0.5$-1.5 where the spherical coefficient is much smaller than the plane-parallel coefficient. It is interesting that at $\log g = 0$ the difference varies significantly depending on the mass and effective temperature. In fact, at some effective temperatures, the difference between the spherical and plane-parallel values of a_1 are about zero. It is strange that plane-parallel and spherical values of a_1 can agree at $\log g = 0$ but not at $\log g = 0.5$-1.5.

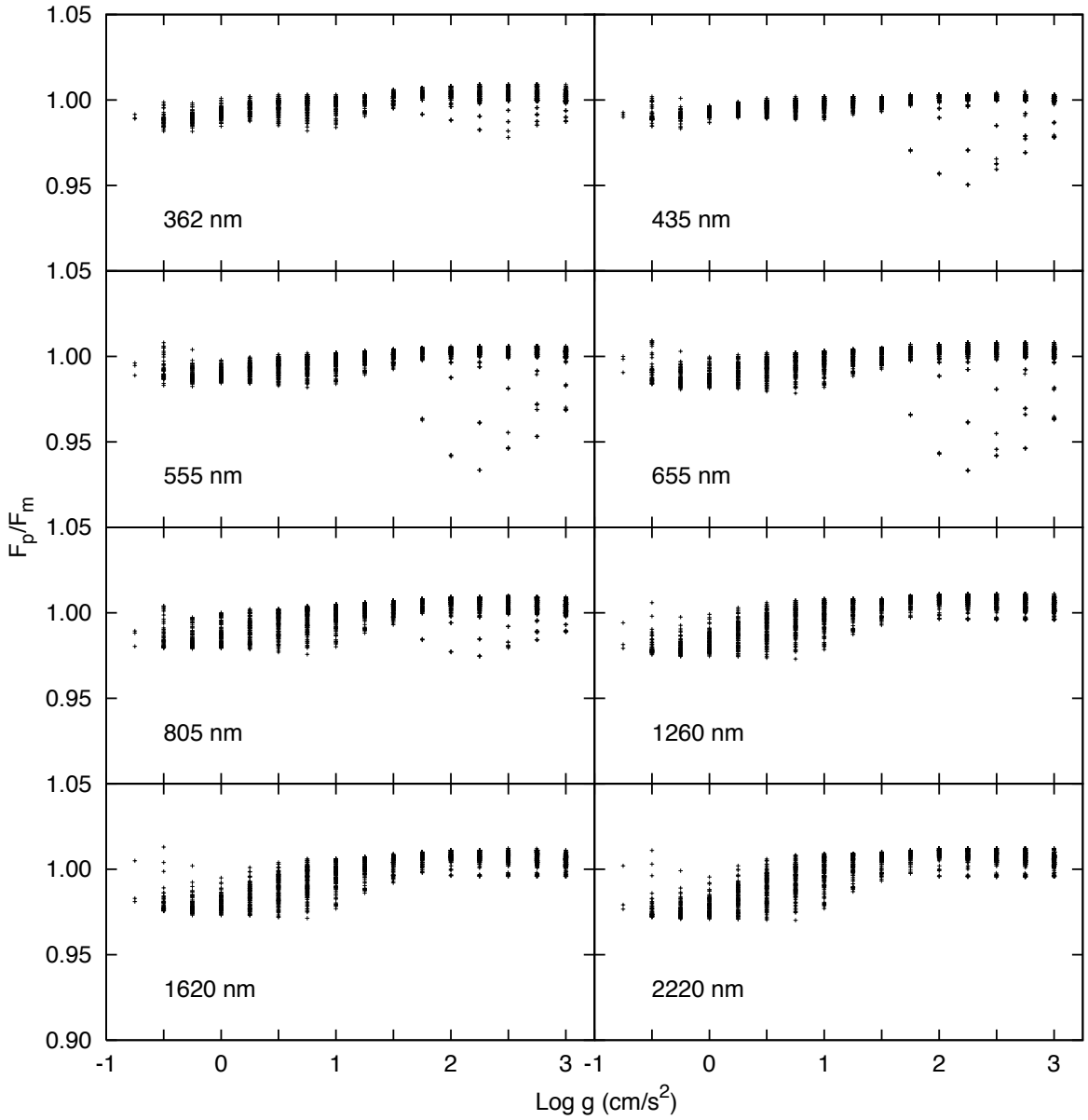

Figure 3.17: Measuring the quality of fit of the four-parameter limb-darkening law, Equation 3.42, with the ratio of the flux from the integration of the limb-darkening law and the flux from the model stellar atmospheres with $v_{\rm turb} = 0\ km/s$ as a function of gravity from $T_{\rm eff} = 3000$ to 8000 K for a number of wavelengths.

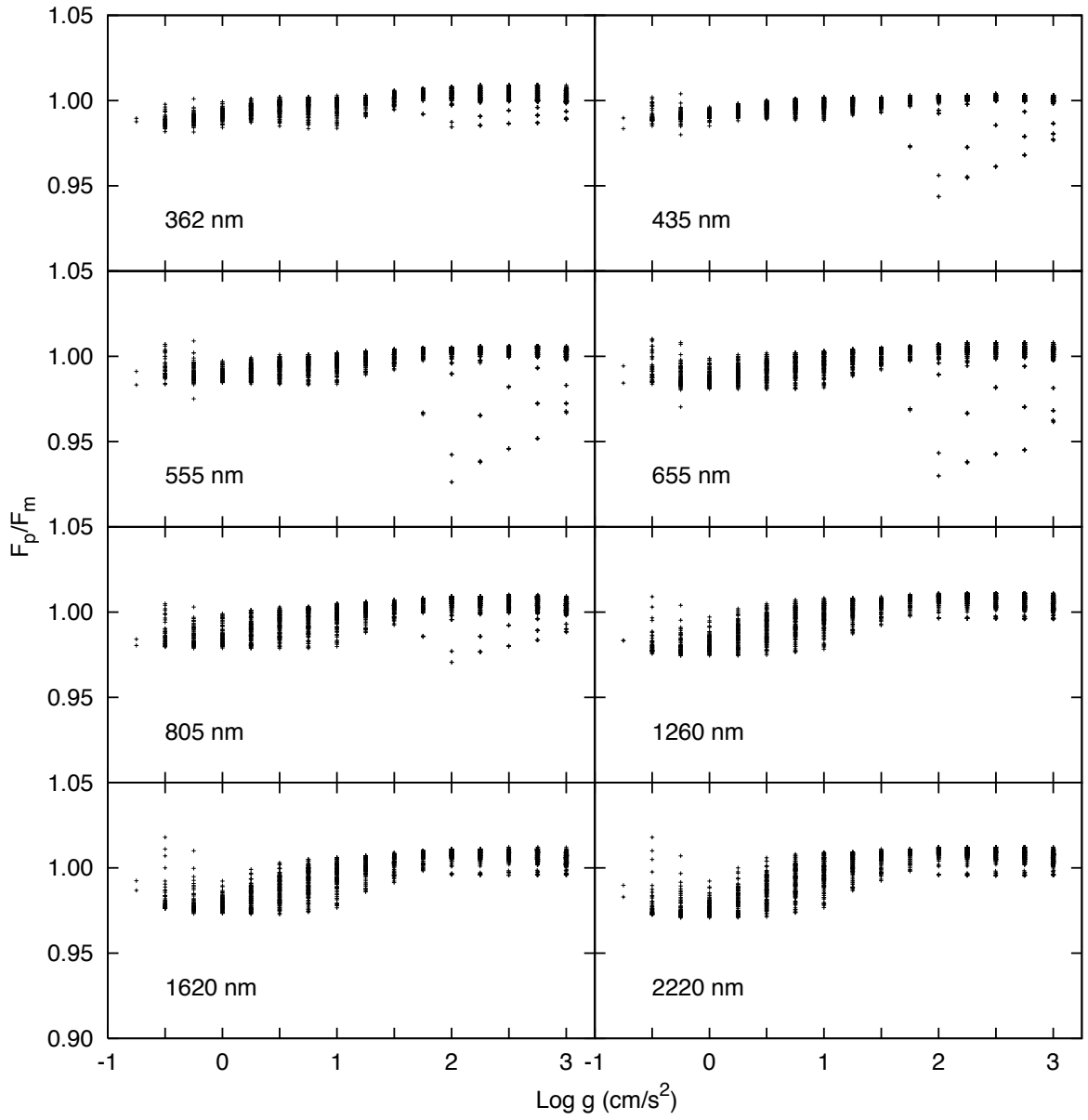

Figure 3.18: Same as Figure 3.17 but for $v_{\rm turb} = 2\ km/s$.

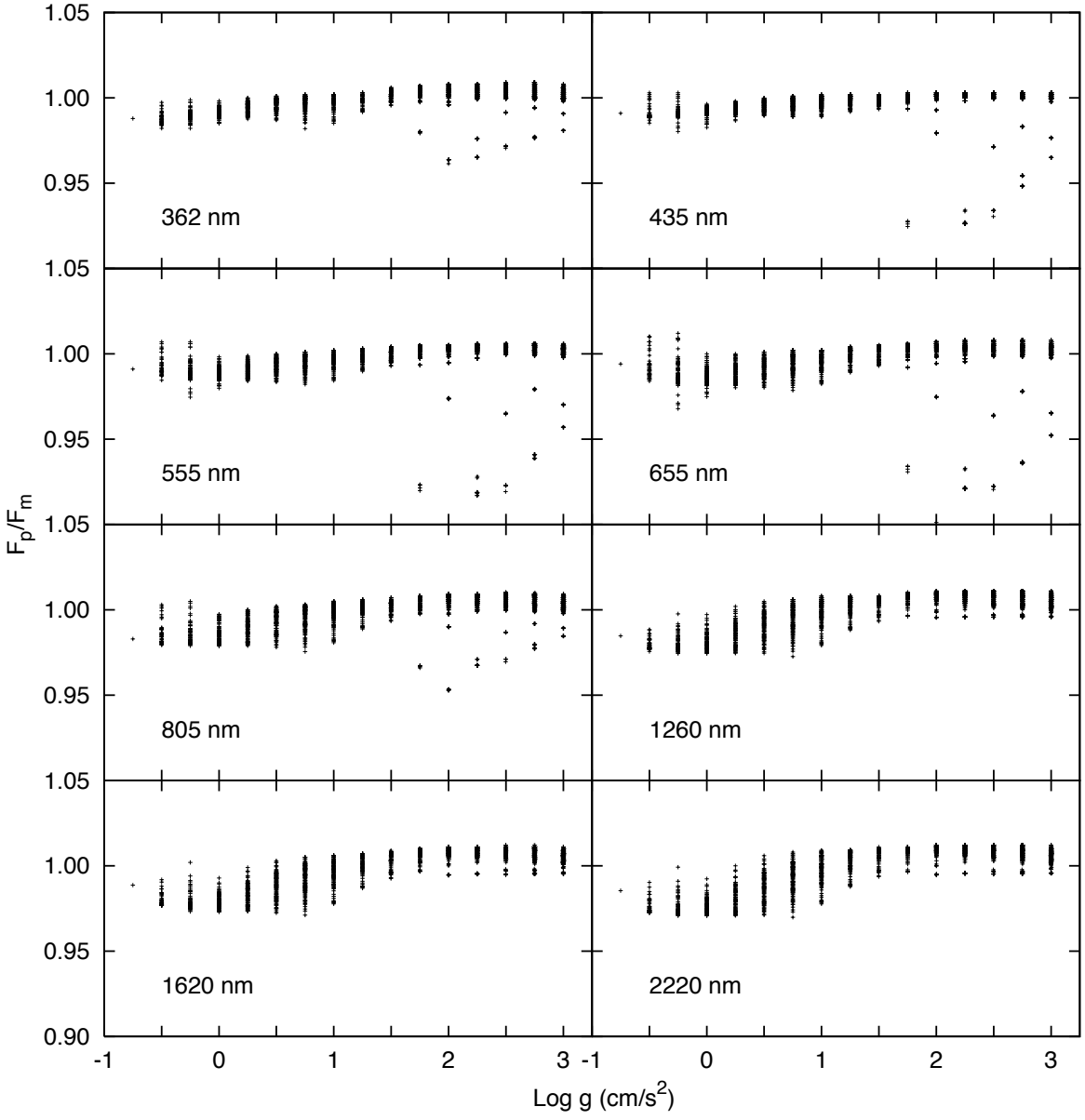

Figure 3.19: Same as Figure 3.17 but for $v_{\rm turb} = 4\ km/s$.

The difference between the second coefficient a_2 calculated from spherical models and that from plane-parallel models is shown as a function of gravity for the three values of turbulent velocity in Figures 3.23, 3.24, and 3.25. The difference for the coefficients a_3 and a_4 are shown in Figures 3.26, 3.27, and 3.28 and Figures 3.29, 3.30, and 3.31, respectively. The difference between a_2 from spherical models and a_2 from plane-parallel models is approximately $-2\times$ value of a_1(Sph) − a$_1$(PP). At $\log g = 3$, the spherical and plane-parallel coefficients approximately agree while the difference is largest at $\log g$ = 0.5-1.5 as well. The values of a_2 roughly agree at shorter wavelengths, $\lambda \leq 555$ *nm* and the differences there are due to the effect of the mass and temperature on the intensity structure. At longer wavelengths the difference is more pronounced as well as the dependence on mass and effective temperature. The strange behavior of a_2(Sph) − a$_2$(PP) at $\log g = 0$ as seen in Figures 3.20-3.22, where for some values of $T_{\rm eff}$ and mass the difference is approximately zero, is apparent here as well.

The computed values a_3(Sph) − a$_3$(PP) show the same behavior as a_1(Sph) − a$_1$(PP), and a_2(Sph) − a$_2$(PP) but ranging from −40 to +40 and the values a_4(Sph) − a$_4$(PP) also show the same behavior as a function of gravity but the range is −20 to +20. It is not surprising that the difference between plane-parallel and spherical coefficients have related behaviors. This may be seen by writing the difference between the intensities for the spherical fit and the plane-parallel fit

$$\frac{I_{\rm Sph}(\mu)}{I_{\rm Sph}(1)} - \frac{I_{\rm PP}(\mu)}{I_{\rm PP}(1)} = \sum_{i=1}^{4} \Delta a_i (1 - \mu^{i/2}). \tag{3.43}$$

While the value of $\Delta I(\mu)$ does not need to be zero, if the fits are reasonable then they should predict the same value of mean intensity, flux, and radiation pressure. Also, the computed value of $I(1)$ does not vary greatly between spherical and plane-parallel models for the same effective temperature and gravity. Therefore, the integrals $\int [\Delta I/I(1)] d\mu$, $\int [\Delta I/I(1)] \mu d\mu$, and $\int [\Delta I/I(1)] \mu^2 d\mu$ are all approximately zero. This yields three equations with four unknown variables

$$0 = \frac{2}{3}\Delta a_1 + \frac{1}{2}\Delta a_2 + \frac{2}{5}\Delta a_3 + \frac{1}{3}\Delta a_4, \tag{3.44}$$

$$0 = \frac{2}{5}\Delta a_1 + \frac{1}{3}\Delta a_2 + \frac{2}{7}\Delta a_3 + \frac{1}{4}\Delta a_4, \tag{3.45}$$

$$0 = \frac{2}{7}\Delta a_1 + \frac{1}{4}\Delta a_2 + \frac{2}{9}\Delta a_3 + \frac{1}{5}\Delta a_4, \tag{3.46}$$

and thus three of the four variables are a function of the fourth variable. The equations are solved for $\Delta a_2, \Delta a_3$, and Δa_4 in terms of Δa_1, yielding $\Delta a_2 \approx -5.5\Delta a_1$, $\Delta a_3 \approx 9\Delta a_1$, and $\Delta a_4 \approx -4.5\Delta a_1$. However, these values are not precise relations because the spherical limb-darkening laws do not agree perfectly with the model intensity profile so there are errors being propagated in this analysis. While the values do not agree perfectly with the results in the figures, it does illustrate the observed trends.

The differences between the coefficients determined from plane-parallel and spherical models show in-

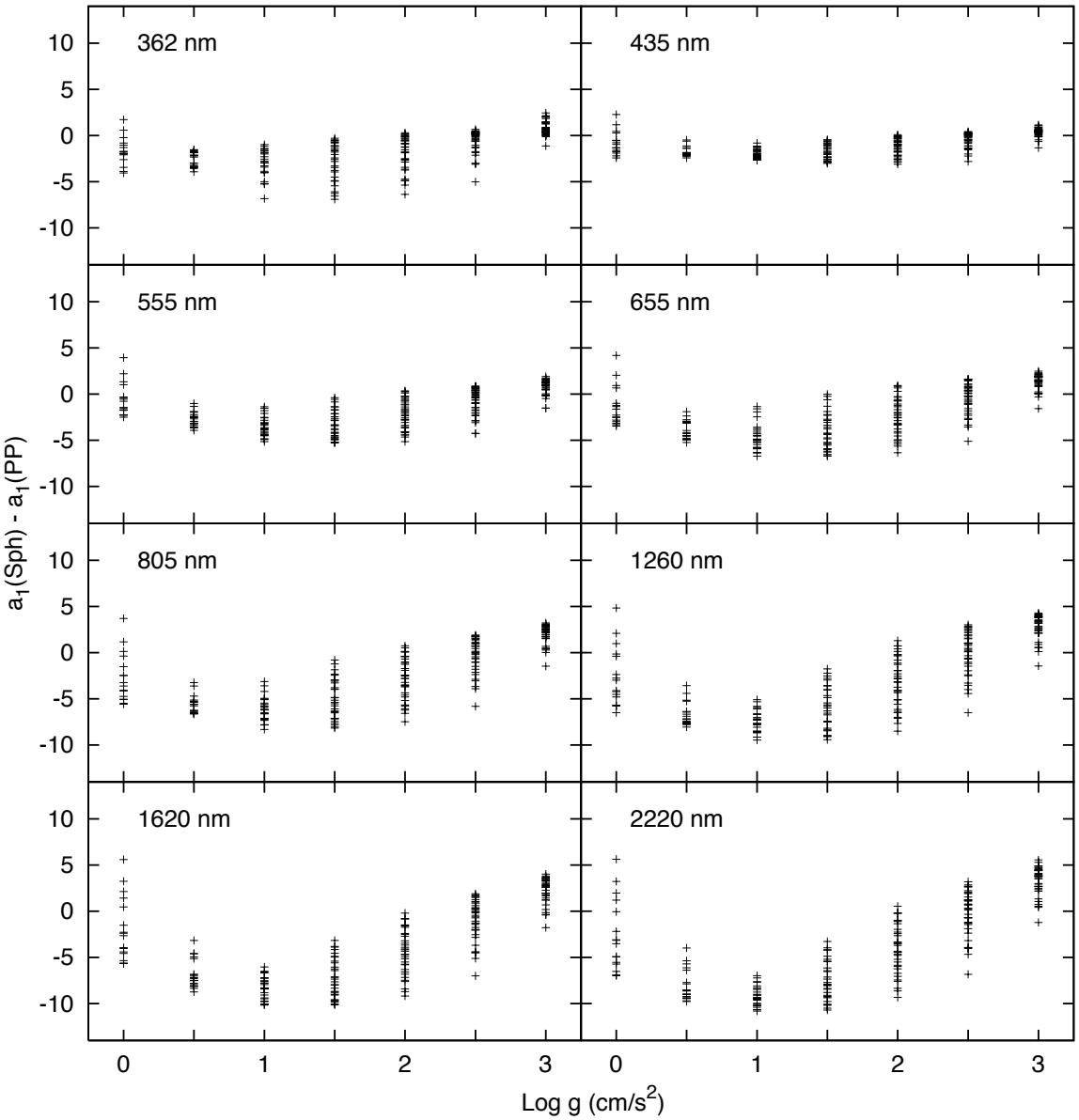

Figure 3.20: Comparison of the first coefficient a_1 from the limb-darkening law, Equation 3.42, derived using plane-parallel model atmospheres (Claret, 2000) and spherically symmetric model atmospheres, $a_1(\mathrm{Sph}) - a_1(\mathrm{PP})$, as a function of gravity for a number of wavelengths and turbulent velocity of 0 km/s. The effective temperature at each gravity ranges from 3000 to 8000 K though at lower gravities this upper limit decreases.

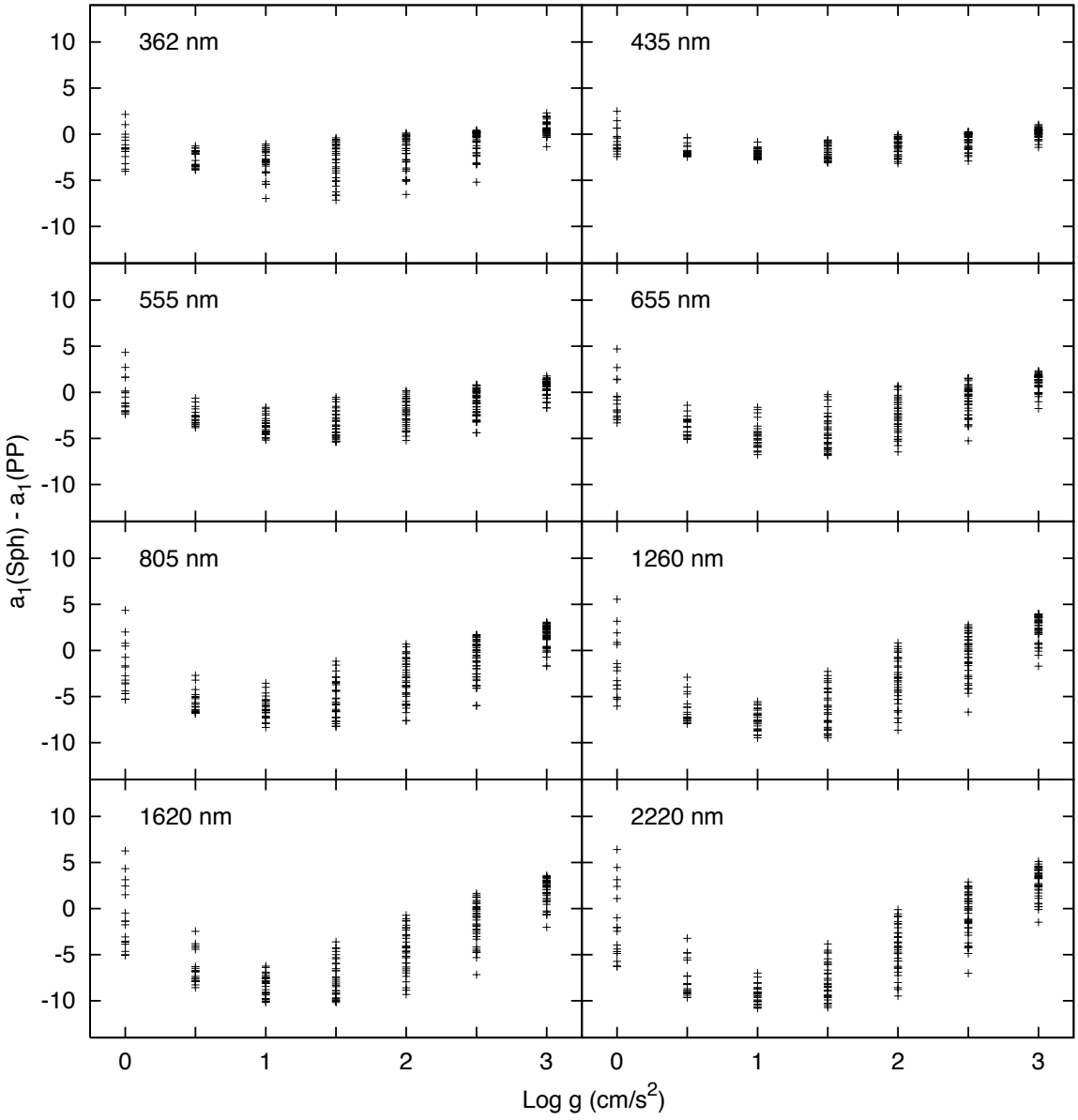

Figure 3.21: Same as Figure 3.20 but for a turbulent velocity of 2 km/s.

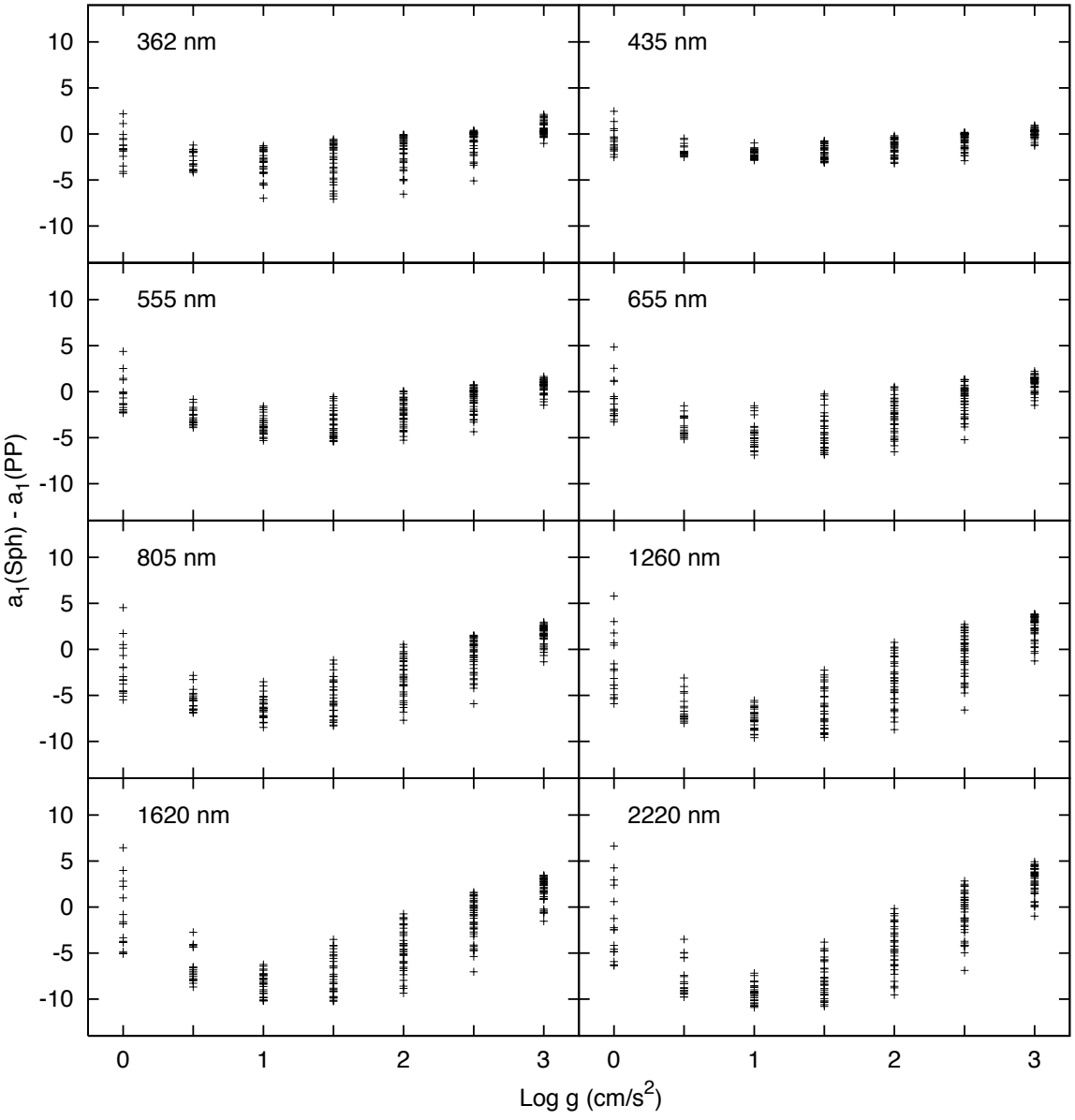

Figure 3.22: Same as Figure 3.20 but for a turbulent velocity of 4 km/s.

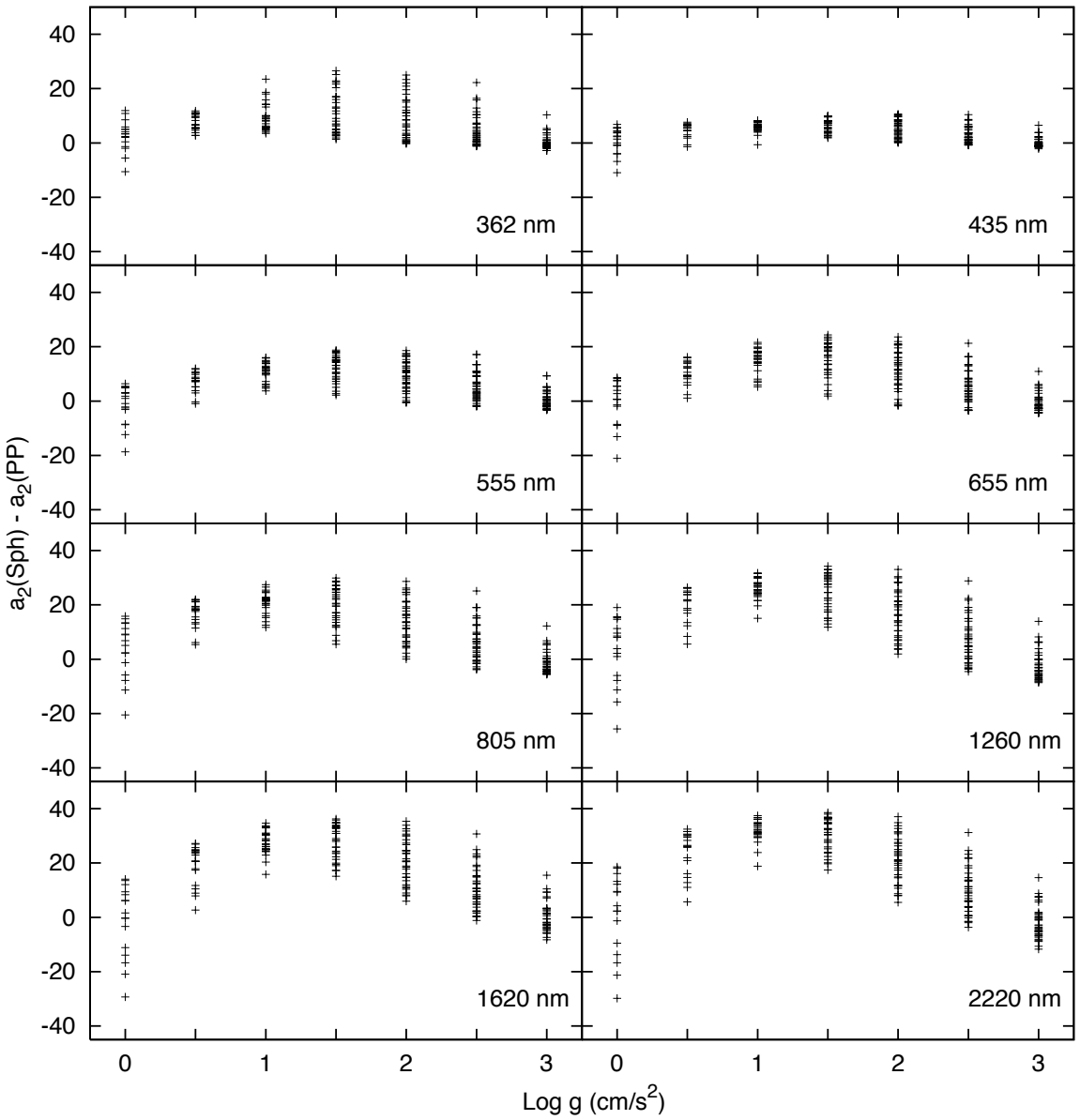

Figure 3.23: Comparison of the second coefficient a_2 from the limb-darkening law, Equation 3.42, derived using plane-parallel model atmospheres (Claret, 2000) and spherically symmetric model atmospheres, $a_2(\mathrm{Sph}) - a_2(\mathrm{PP})$, as a function of gravity for a number of wavelengths and turbulent velocity of 0 km/s.

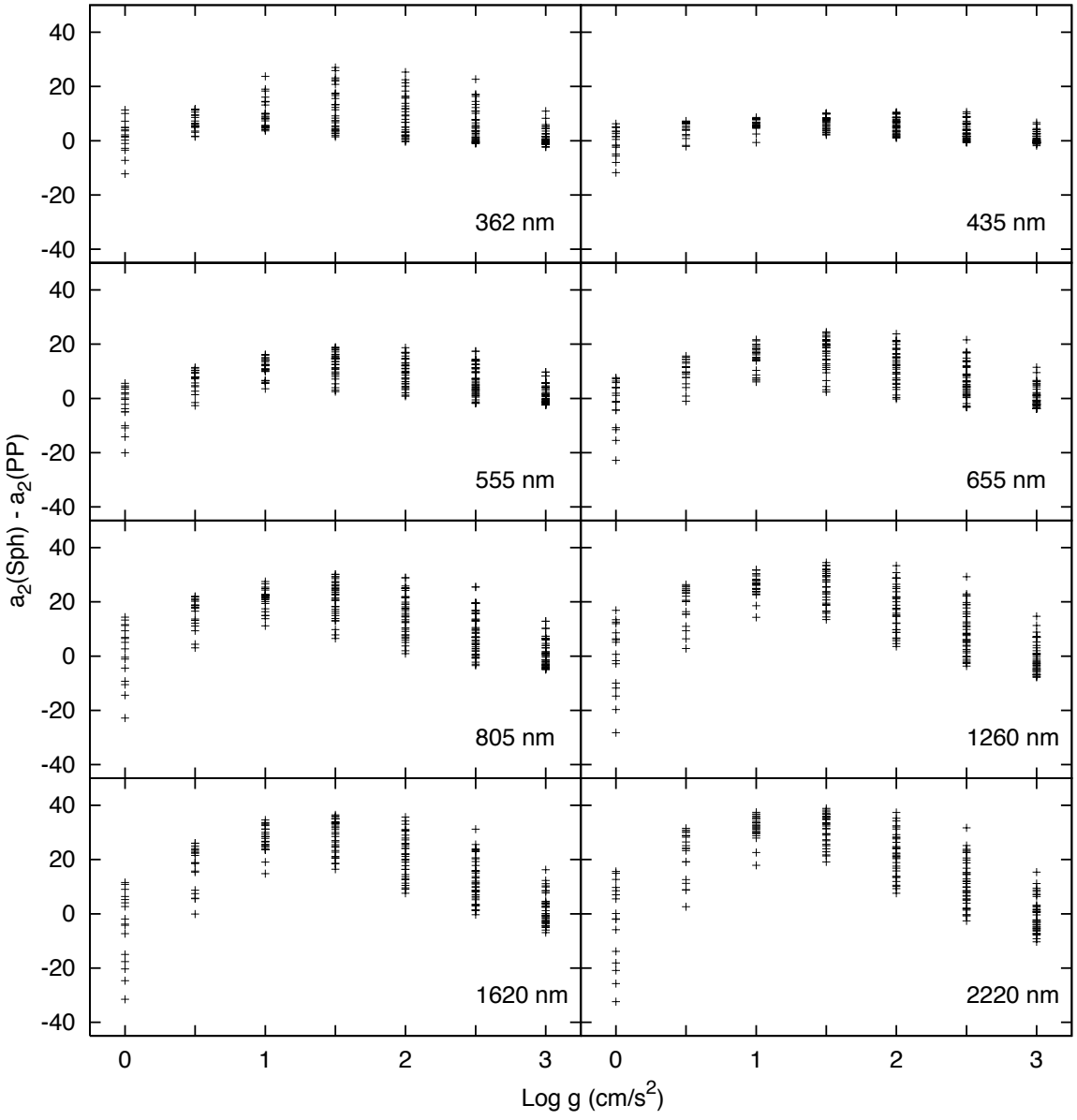

Figure 3.24: Same as Figure 3.23 but for a turbulent velocity of 2 km/s.

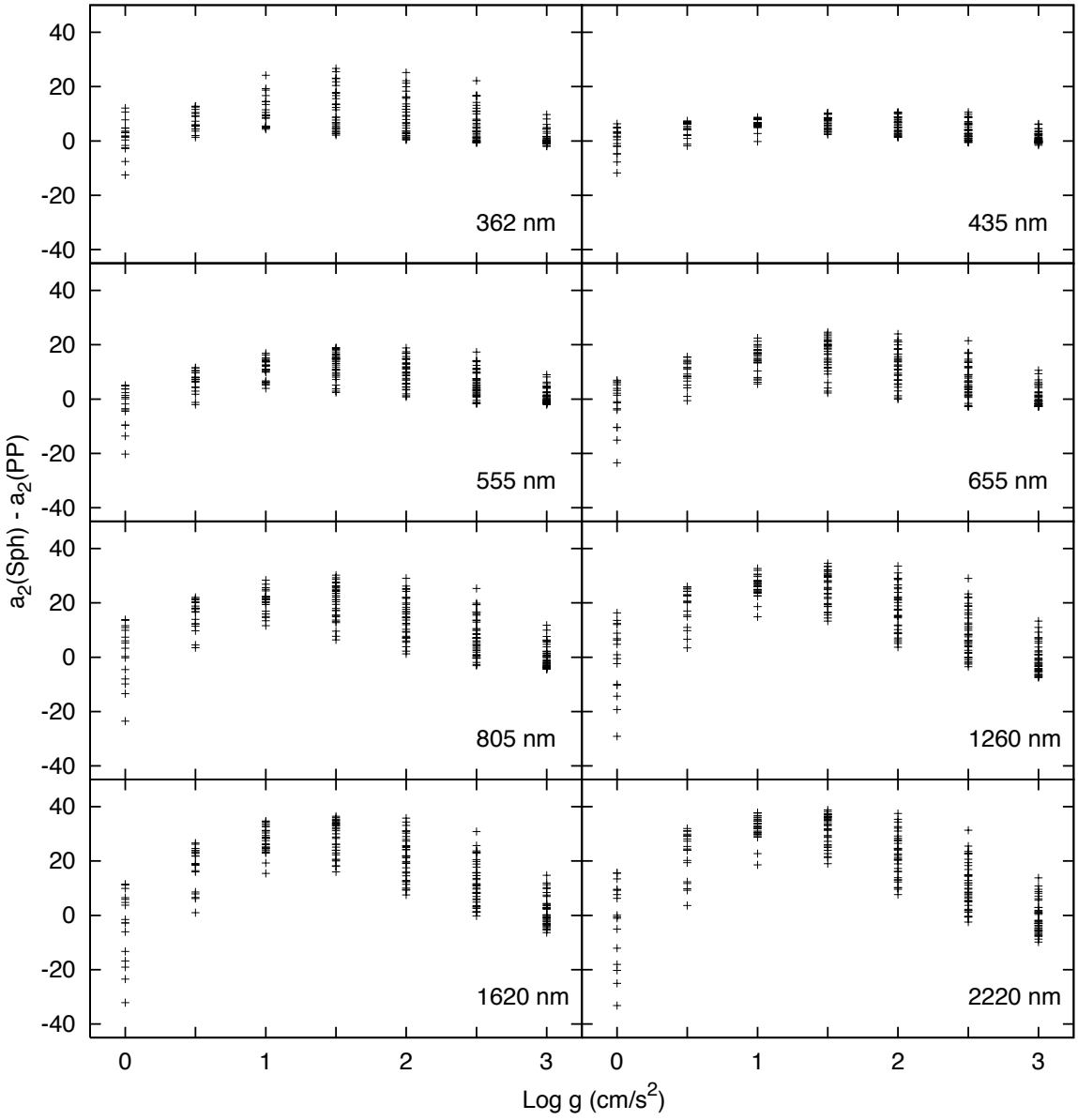

Figure 3.25: Same as Figure 3.23 but for a turbulent velocity of 4 km/s.

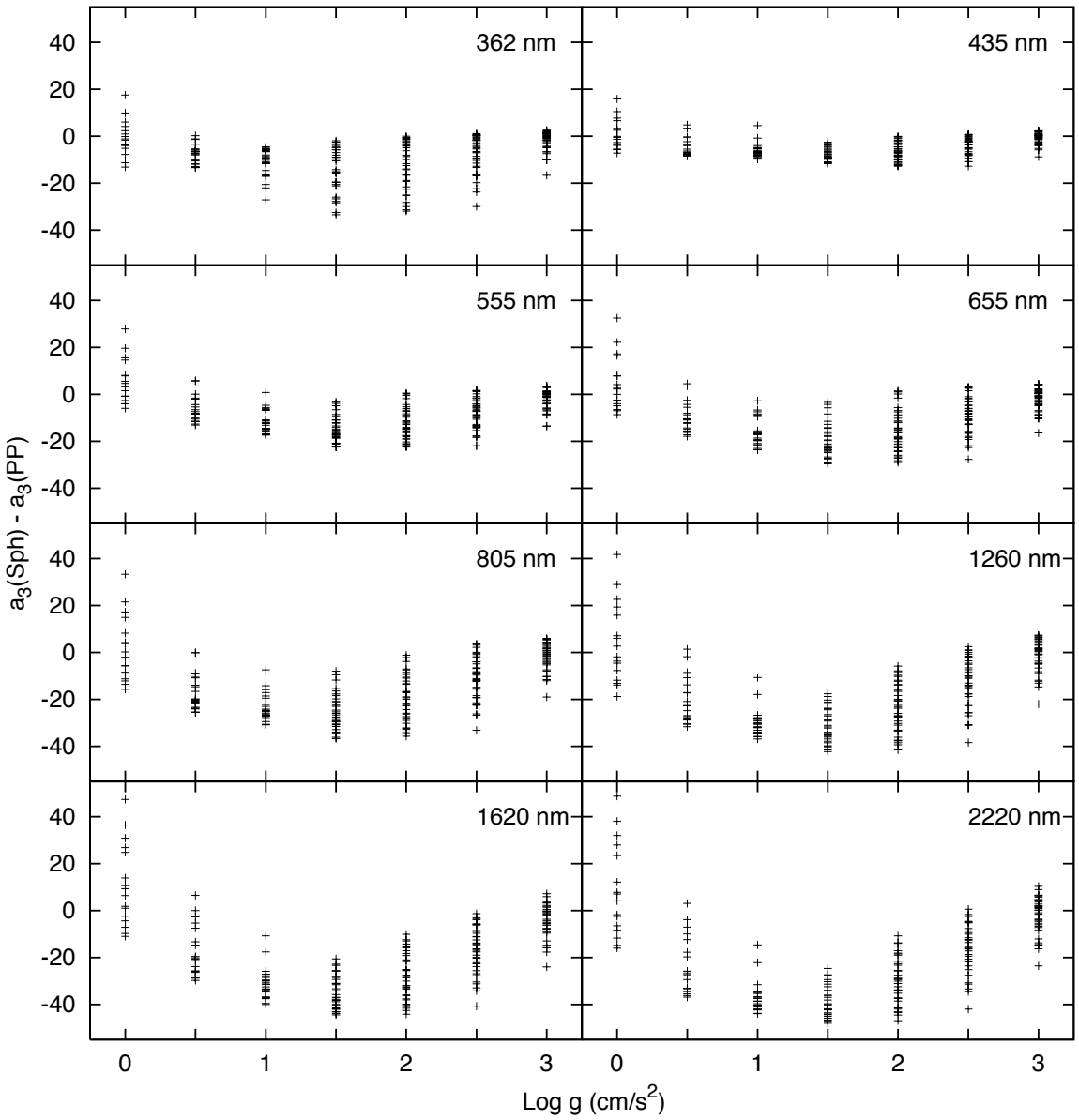

Figure 3.26: Comparison of the third coefficient a_3 from the limb-darkening law, Equation 3.42, derived using plane-parallel model atmospheres (Claret, 2000) and spherically symmetric model atmospheres, a_3(Sph) − a_3(PP), as a function of gravity for a number of wavelengths and turbulent velocity of 0 km/s.

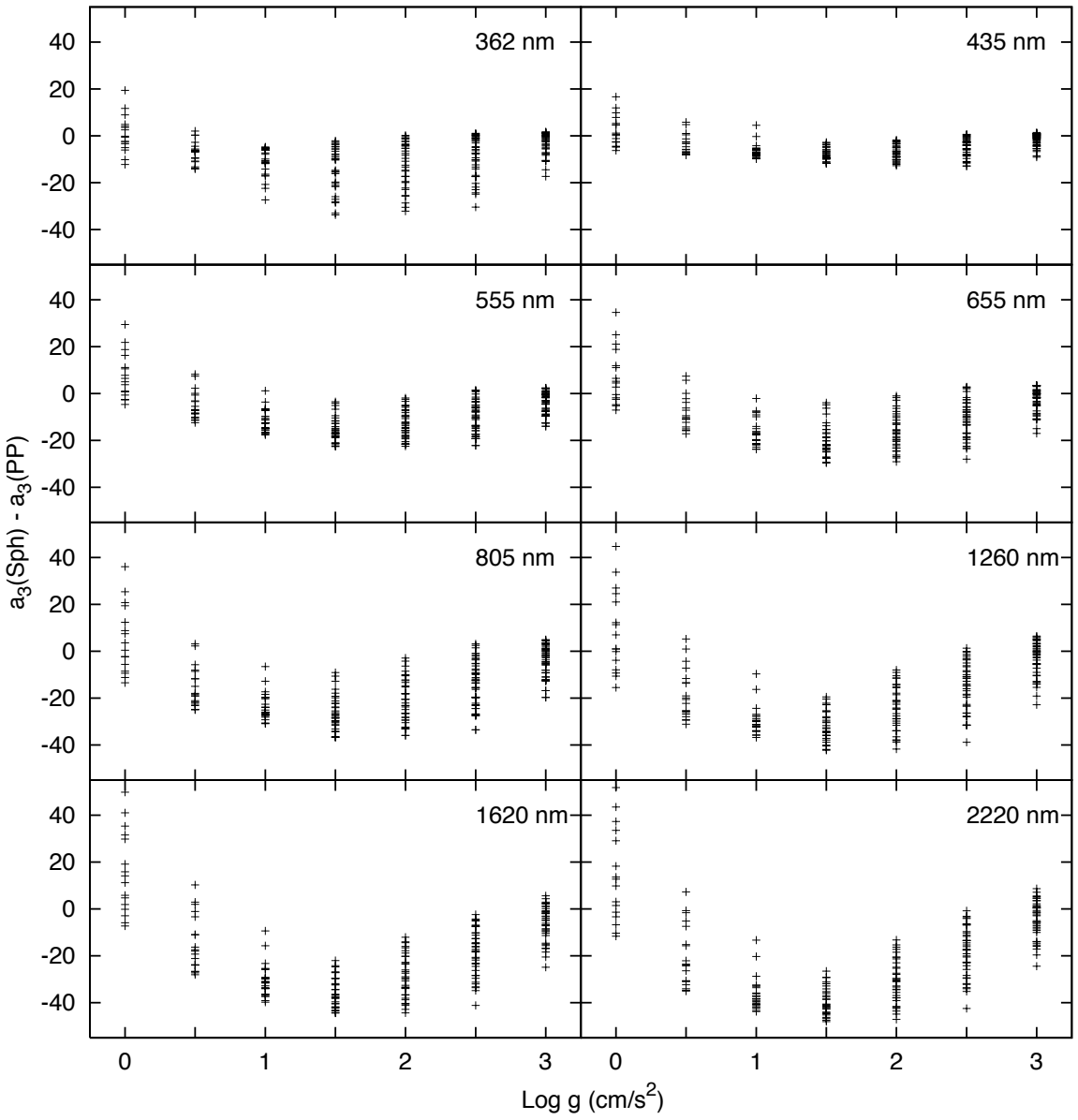

Figure 3.27: Same as Figure 3.26 but for a turbulent velocity of 2 km/s.

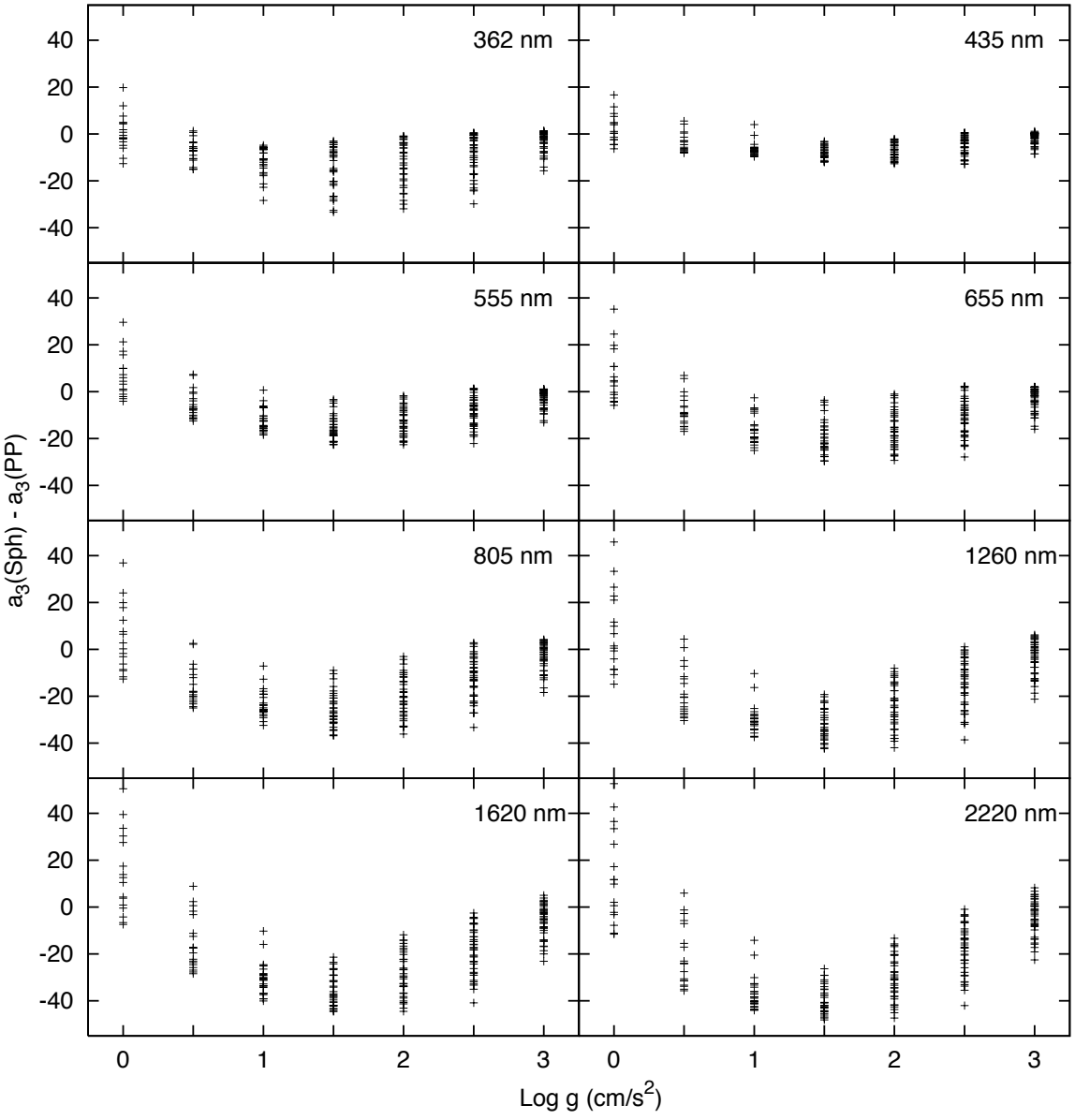

Figure 3.28: Same as Figure 3.26 but for a turbulent velocity of 4 km/s.

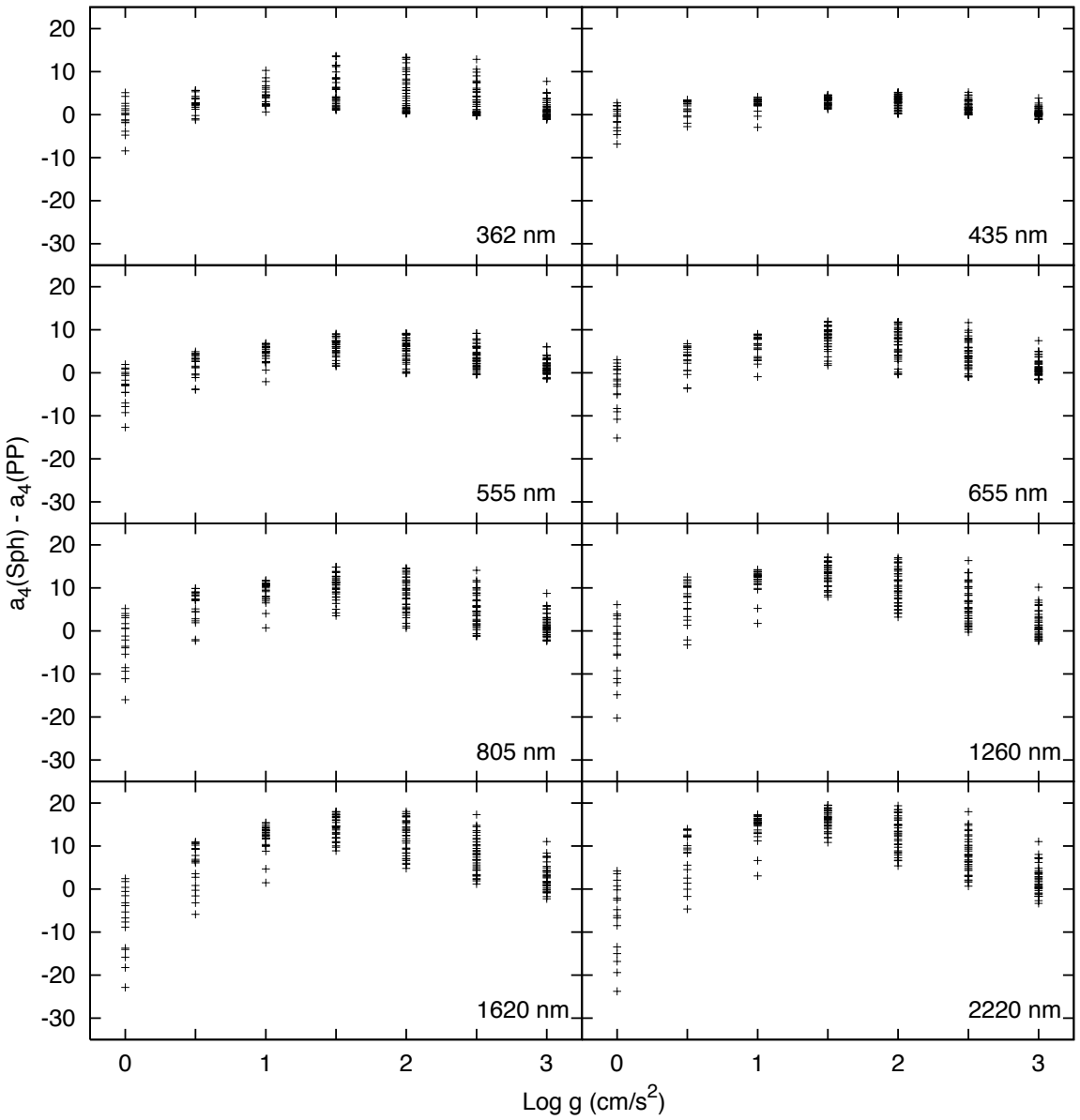

Figure 3.29: Comparison of the fourth coefficient a_4 from the limb-darkening law, Equation 3.42, derived using plane-parallel model atmospheres (Claret, 2000) and spherically symmetric model atmospheres, $a_4(\mathrm{Sph}) - a_4(\mathrm{PP})$, as a function of gravity for a number of wavelengths and turbulent velocity of 0 km/s.

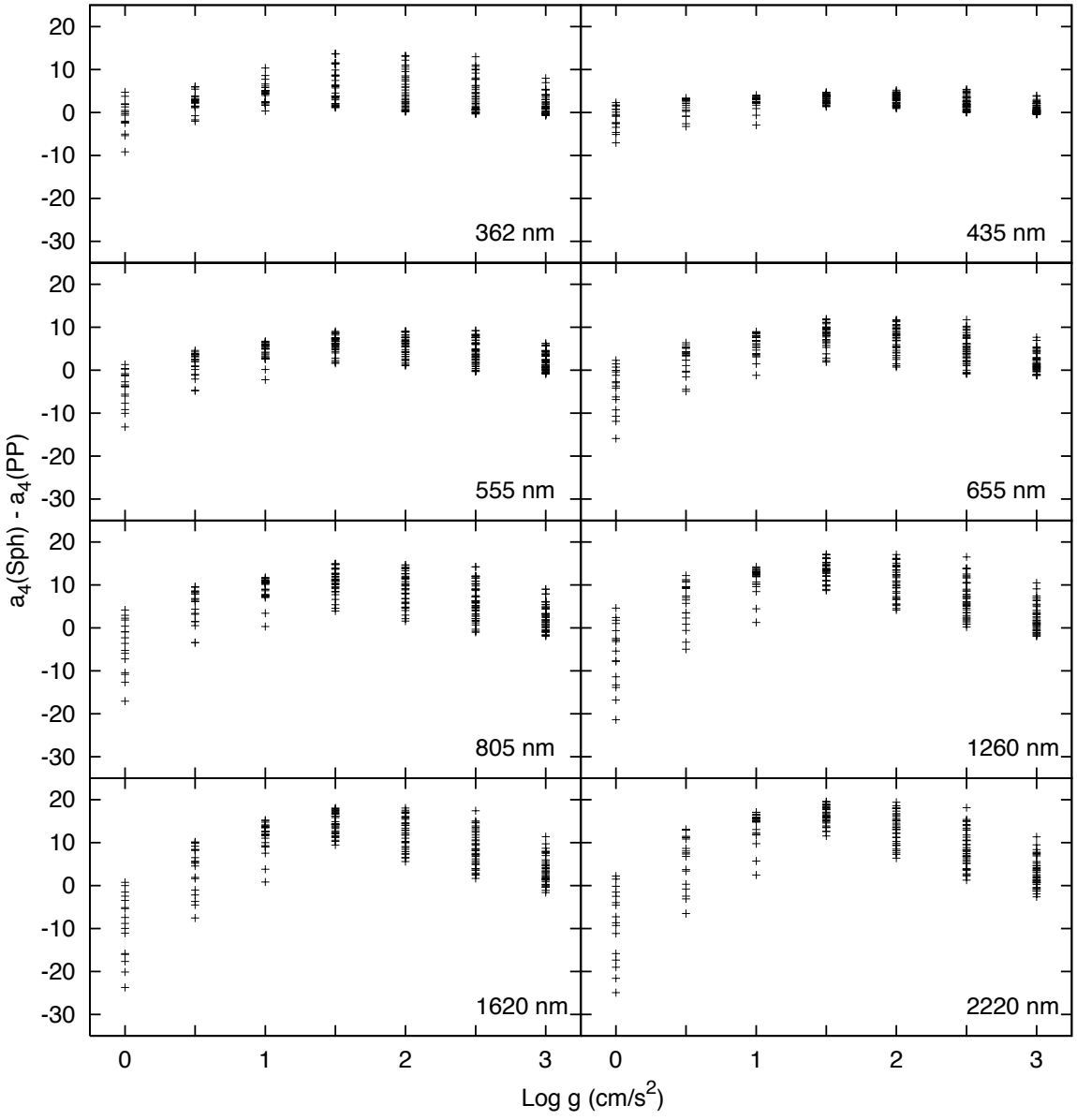

Figure 3.30: Same as Figure 3.29 but for a turbulent velocity of 2 km/s.

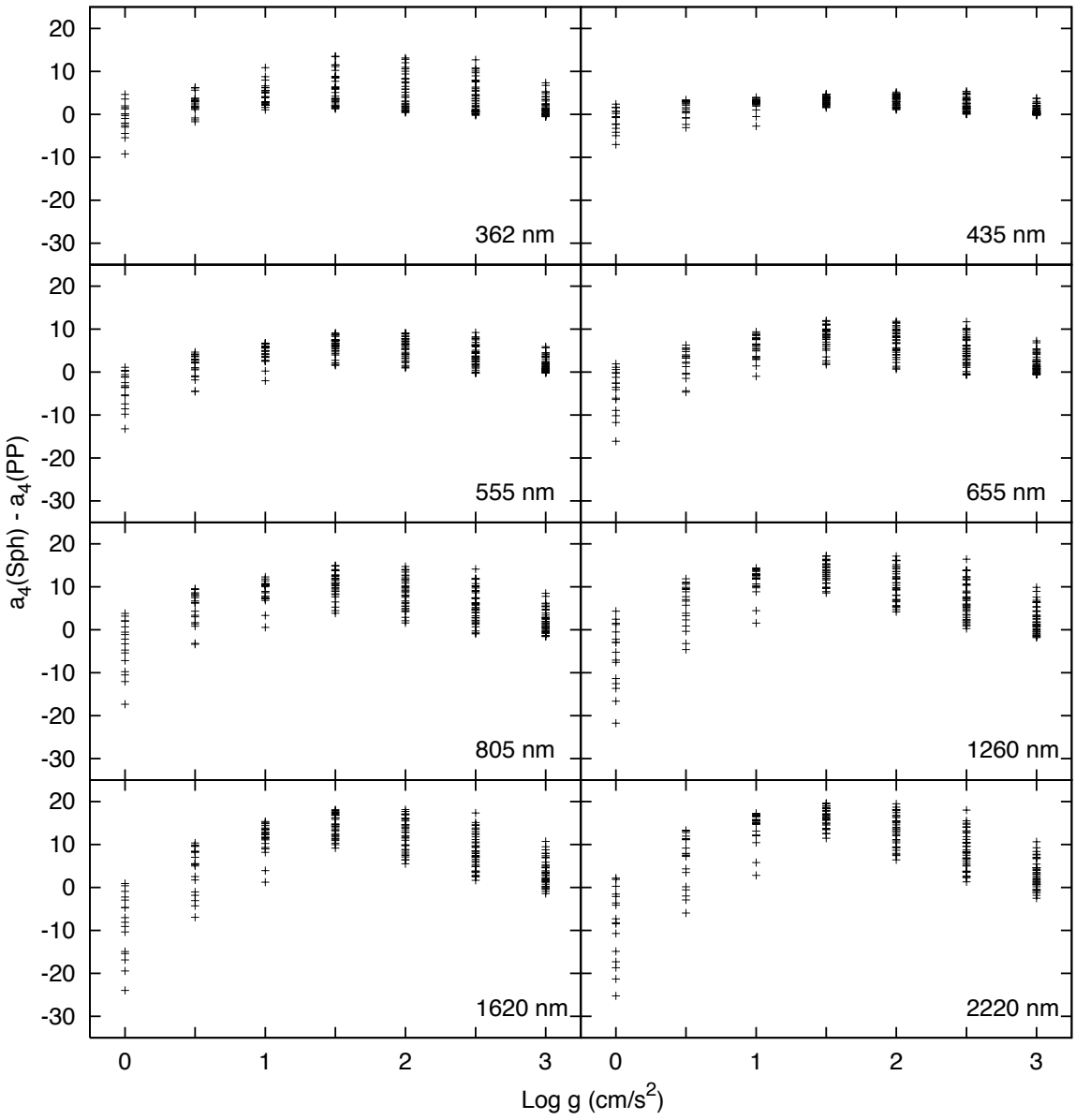

Figure 3.31: Same as Figure 3.29 but for a turbulent velocity of 4 km/s.

teresting behaviors but it is not clear if the behavior is primarily due to the fits to the spherical model models or some combination of the two fits. The behavior of the coefficients determined from spherical models are explored as a function of atmospherical extension defined by the ratio of the radius and mass, R_*/M_*, in Figures 3.32-3.43 for the three values of turbulent velocity $v_{\rm turb} = 0, 2$, and 4 km/s. The coefficients are presented for the same range of wavelengths as before and for effective temperatures ranging from 3500 to 7500 K in steps of 500 K.

The first coefficient a_1 is shown in Figures 3.32, 3.33, and 3.34, where the coefficient is plotted as a function of the atmospheric extension for specific values of effective temperature. The range of values for the coefficient increases with longer wavelength and the rate of change of the coefficient with respect to R_*/M_* tends to be larger. The coefficients also reach a minimum value at about $\log R_*(R_\odot)/M_*(M_\odot) \approx$ 1.5-1.6 at $T_{\rm eff} = 3500$ K with the location of the minimum decreases with increasing effective temperature. It is also worth noting that the values of a_1 do not appear to depend significantly on the turbulent velocity, there is little difference between the coefficient from model atmosphere with $v_{\rm turb} = 0$ km/s and those with $v_{\rm turb} = 4$ km/s. This shows that the turbulent velocity does not contribute significantly to the structure of the intensity profile of model stellar atmospheres.

The second coefficient a_2 is shown in Figures 3.35,3.36, and 3.37. The coefficient shows similar behavior as a function of R_*/M_* and effective temperature as a_1 except that the range of values is from -40 to $+40$ and negative curvature as opposed to a range -10 to $+10$ and positive curvature found for a_1. This relative behavior between a_1 and a_2 is the same as found for the relative behavior of a_1(Sph) − a_1(PP) and a_2(Sph) − a_2(PP) suggesting that the difference between the coefficients from spherical and plane-parallel models is due to the change of structure of the spherical models. The best-fit coefficients for plane-parallel models are constant to within ± 1 with the range of a particular coefficient decreasing with increasing wavelength for a particular effective temperature.

The remaining two coefficients are shown in Figures 3.38, 3.39, and 3.40 and Figures 3.41, 3.42, and 3.43, respectively. The behavior of the coefficients a_3 and a_4 further emphasize the result that the difference between spherical and plane-parallel fits is due primarily to the extension of the atmosphere that cannot be included in the plane-parallel model atmospheres. It is also worth noting that a_3 and a_4 are also insensitive to the values of $v_{\rm turb}$.

The structure of each coefficient as a function of effective temperature and atmospheric extension suggest a method to determine fundamental parameters of star from multi-wavelength observations of limb-darkening using microlensing, eclipsing binaries, planetary transits, etc. If one determines coefficients for the four-parameter law from observations then the coefficients can be used to constrain these parameters. Optical/IR interferometry has the potential for determining the coefficients with sufficient accuracy, however microlensing observations are not precise enough. This result is interesting but it is similar to the method for determining stellar parameters from the linear plus square-root limb-darkening law which has two less free parameters and is hence much simplier.

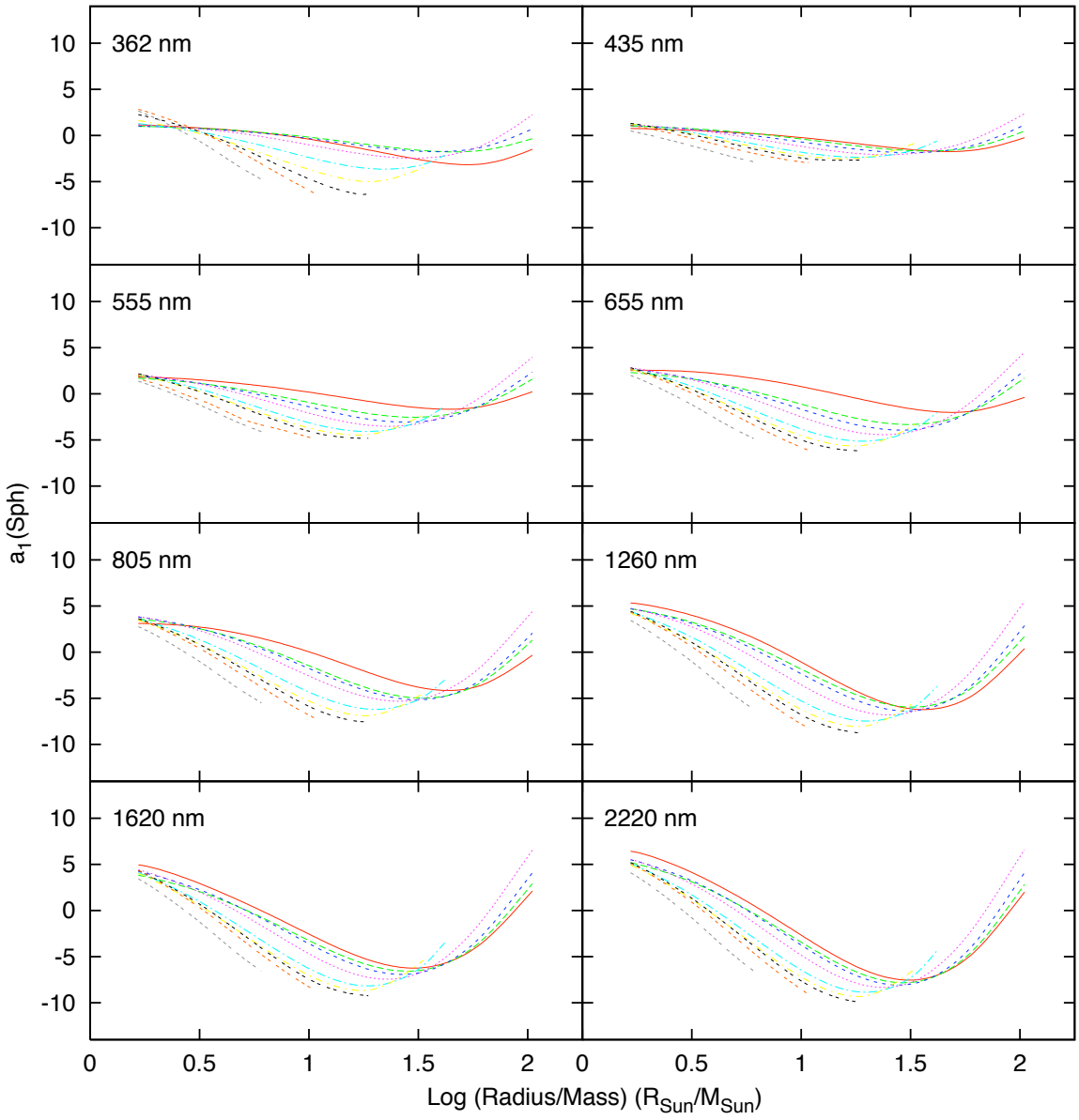

Figure 3.32: The behavior of the first coefficient of the four-parameter limb-darkening law, a_1 with respect to the spherical extension of the stellar atmosphere R_*/M_* for the model atmospheres with a turbulent velocity of 0 km/s. The effective temperatures shown are 3500 K (solid red), 4000 K (green dashed), 4500 K (blue short-dash), 5000 K (purple dotted), 5500 K (aqua dash-dot), 6000 K (yellow short dash-dot), 6500 K (brown two short-dash-space), 7000 K (orange three short-dash-space), and 7500 K (gray four short-dash-space).

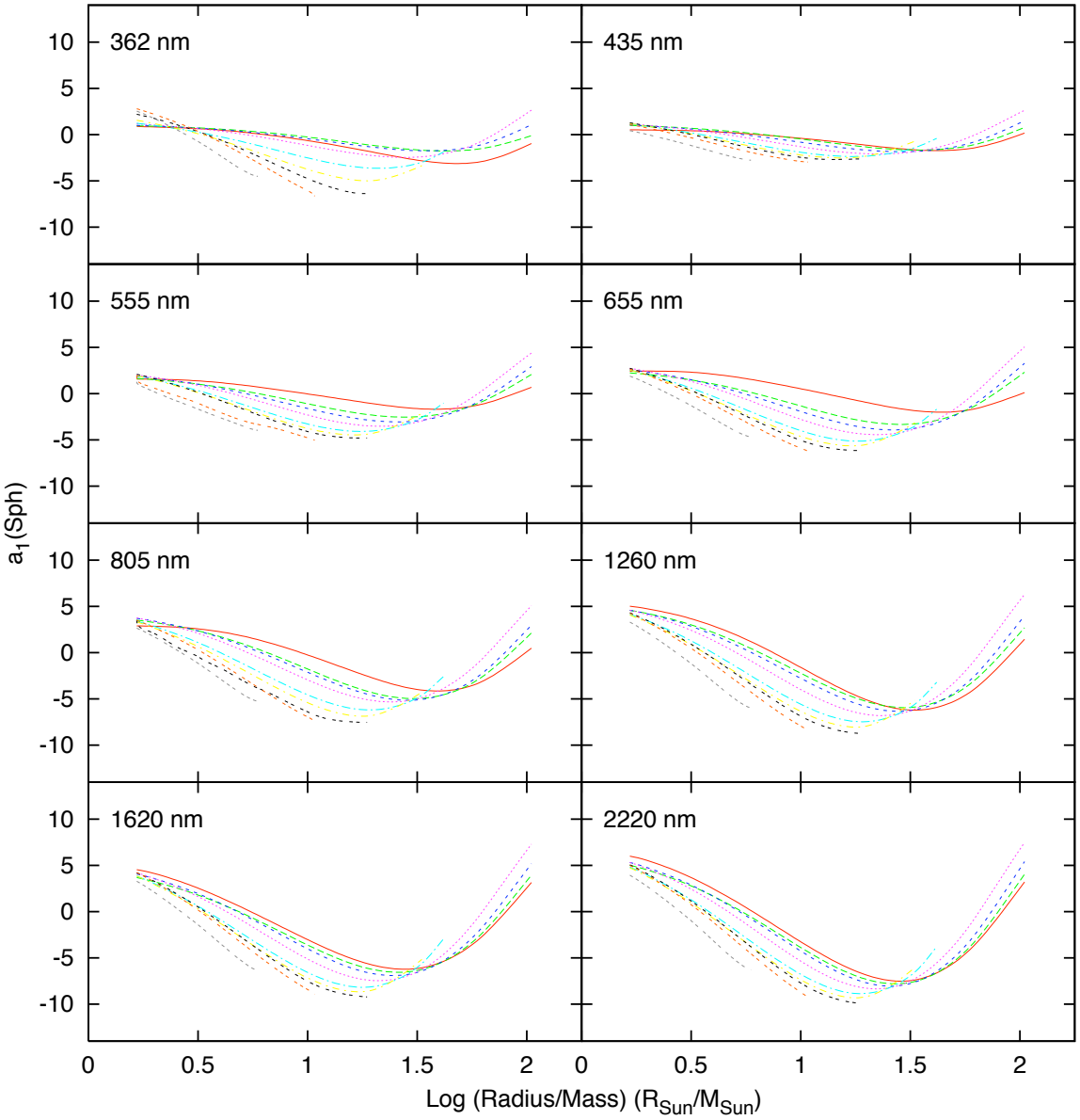

Figure 3.33: Same as Figure 3.32 but for a turbulent velocity of 2 km/s.

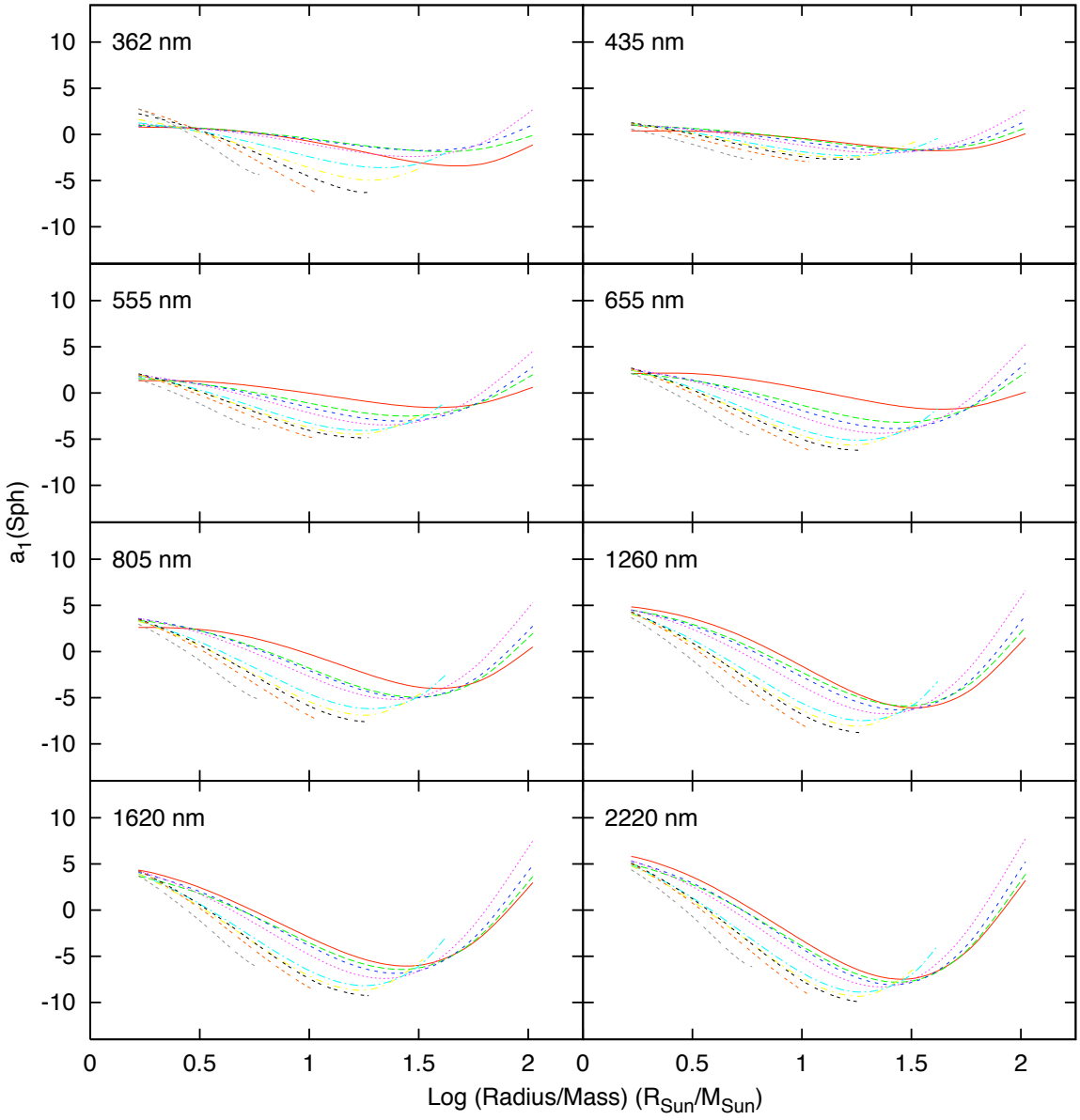

Figure 3.34: Same as Figure 3.32 but for a turbulent velocity of 4 km/s.

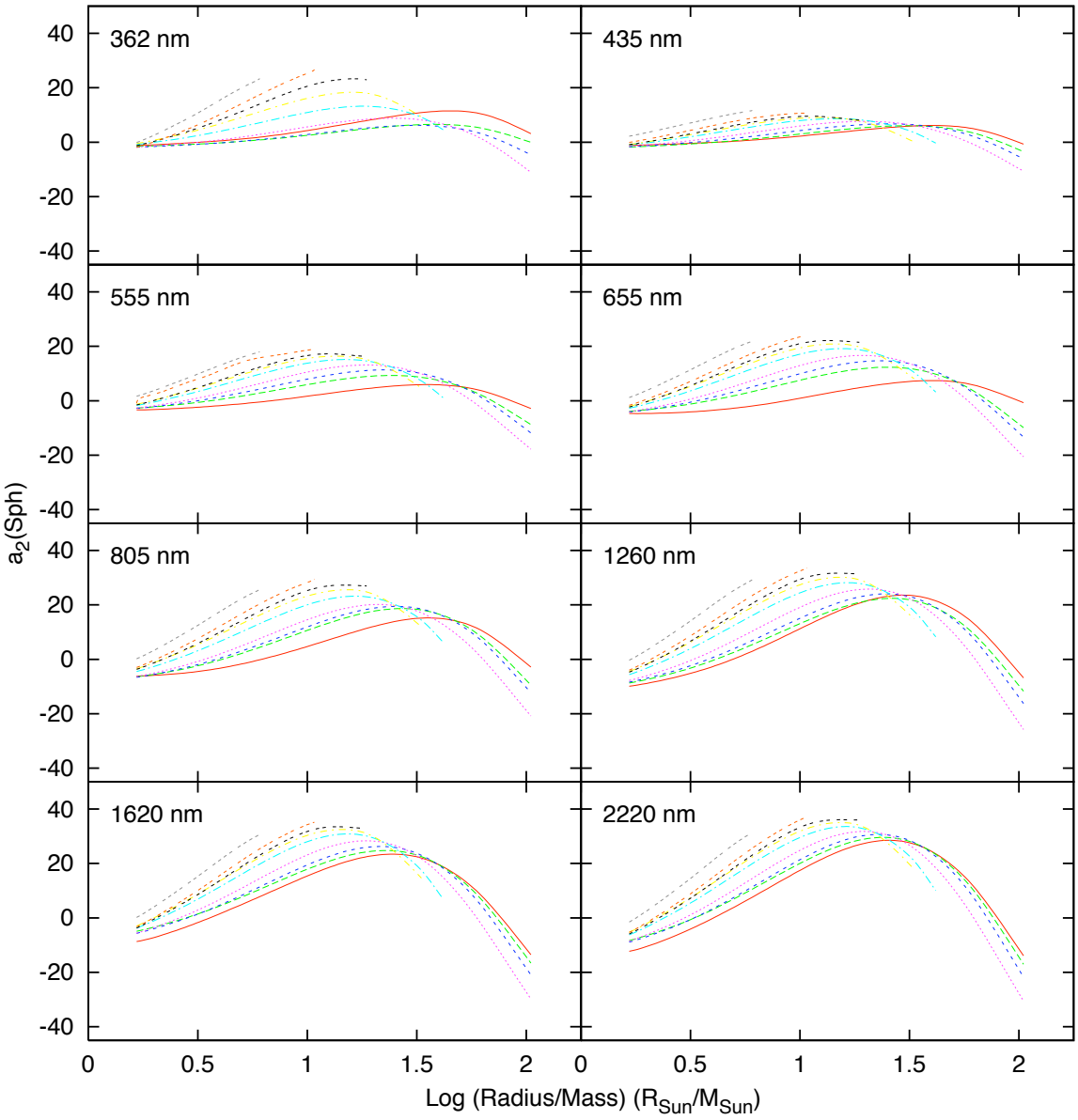

Figure 3.35: The behavior of the first coefficient of the four-parameter limb-darkening law, a_2 with respect to the spherical extension of the stellar atmosphere R_*/M_* for the model atmospheres with a turbulent velocity of 0 km/s.

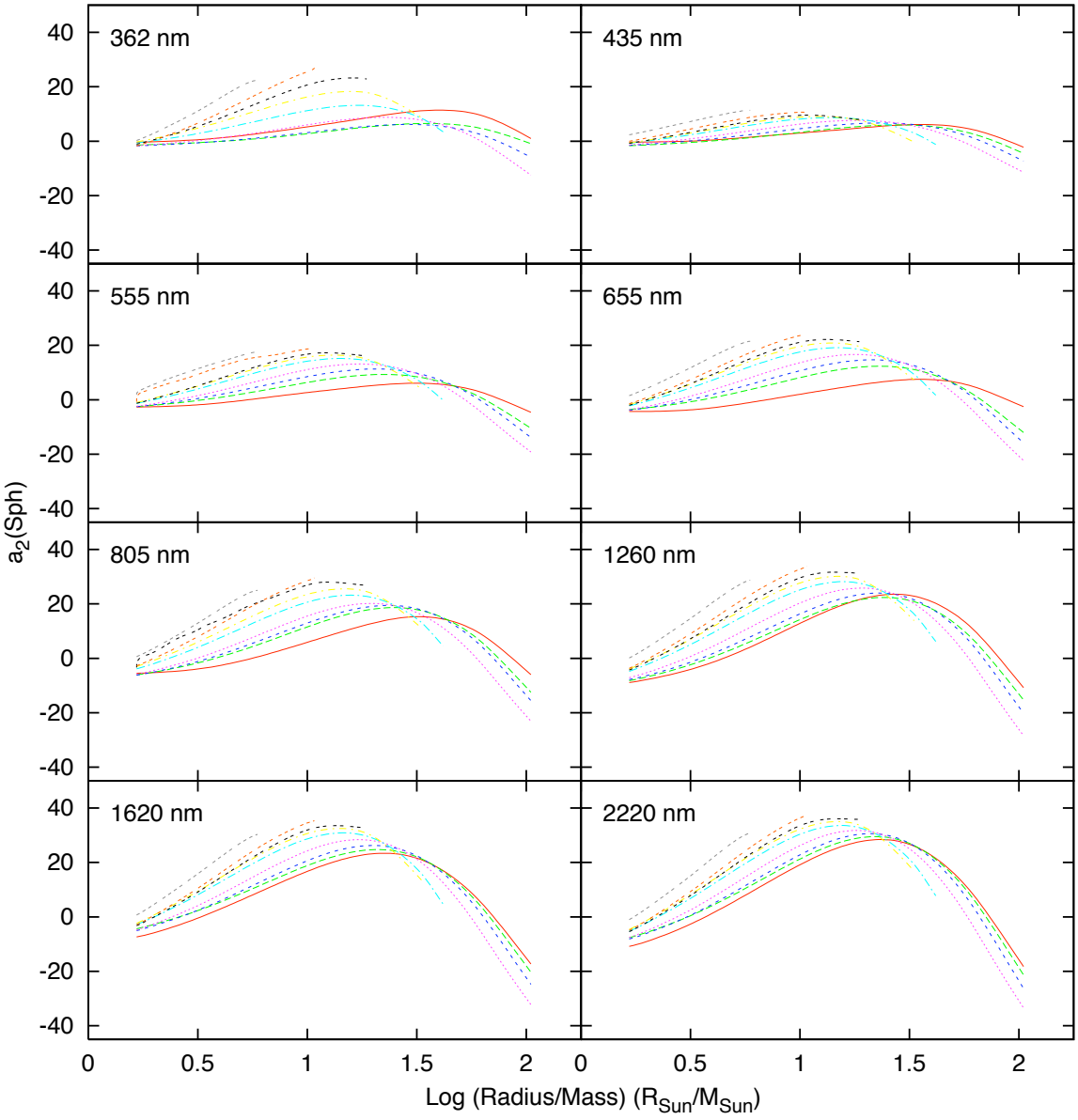

Figure 3.36: Same as Figure 3.35 but for a turbulent velocity of 2 km/s.

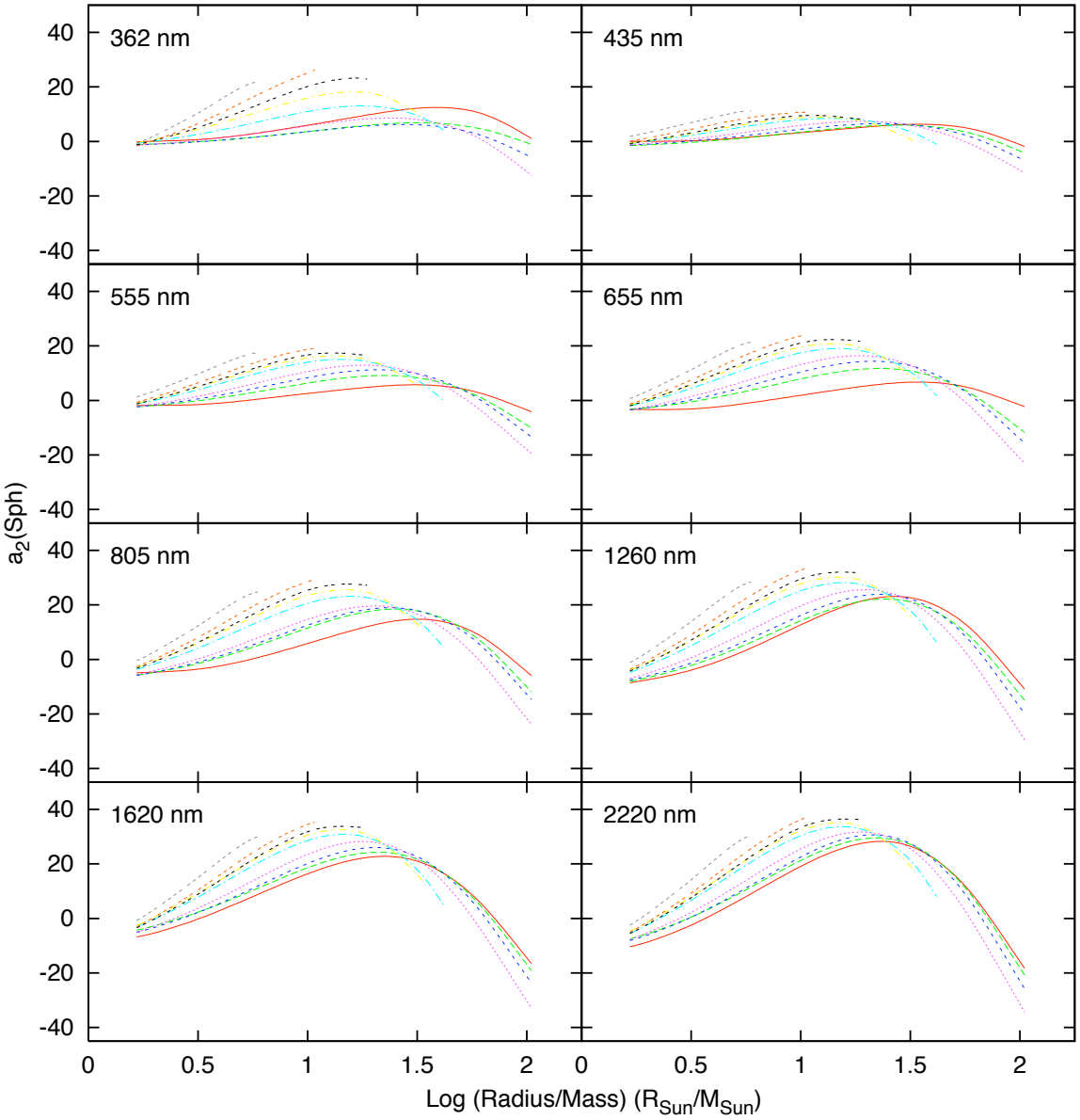

Figure 3.37: Same as Figure 3.35 but for a turbulent velocity of 4 km/s.

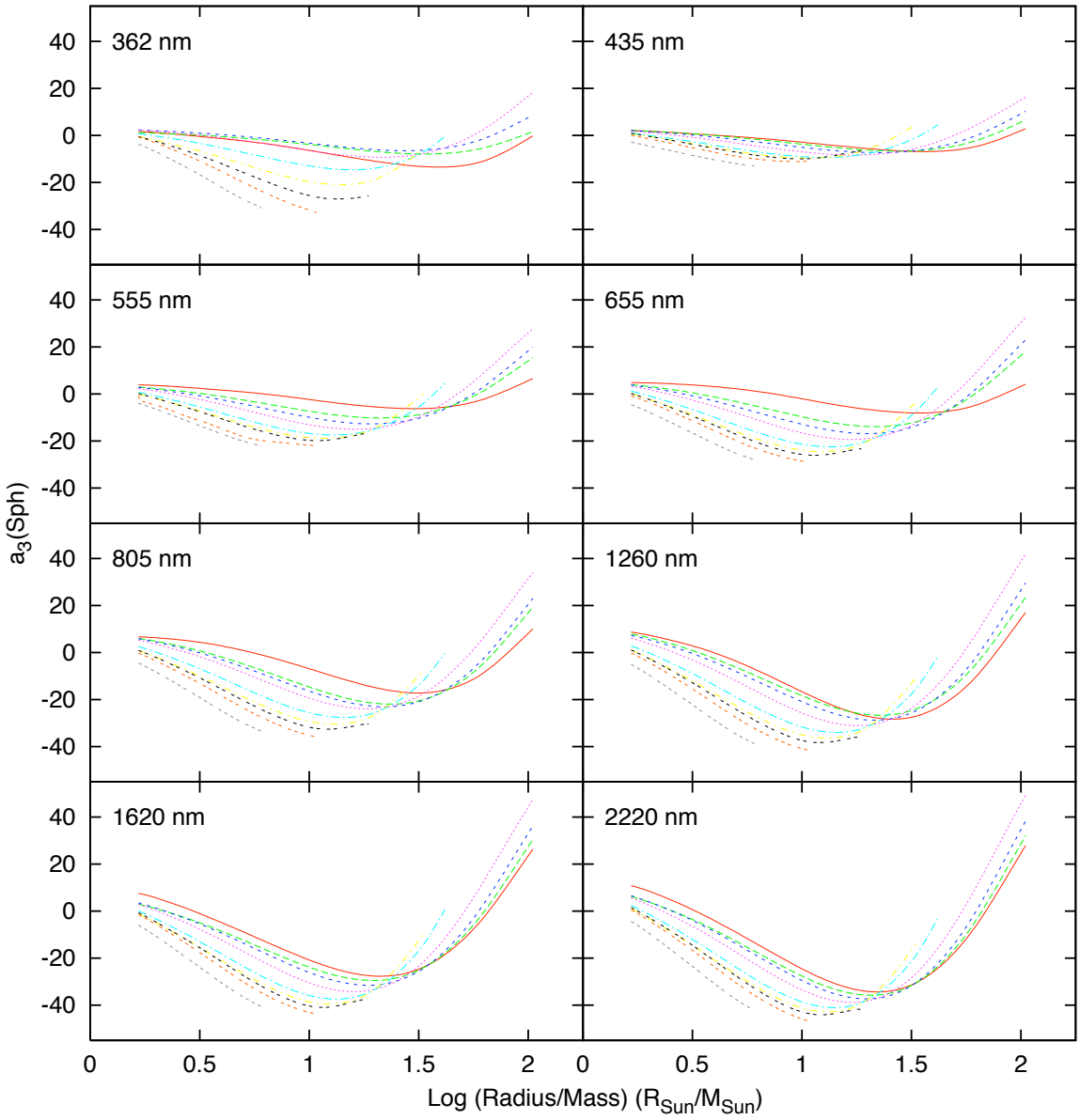

Figure 3.38: The behavior of the first coefficient of the four-parameter limb-darkening law, a_3 with respect to the spherical extension of the stellar atmosphere R_*/M_* for the model atmospheres with a turbulent velocity of 0 km/s.

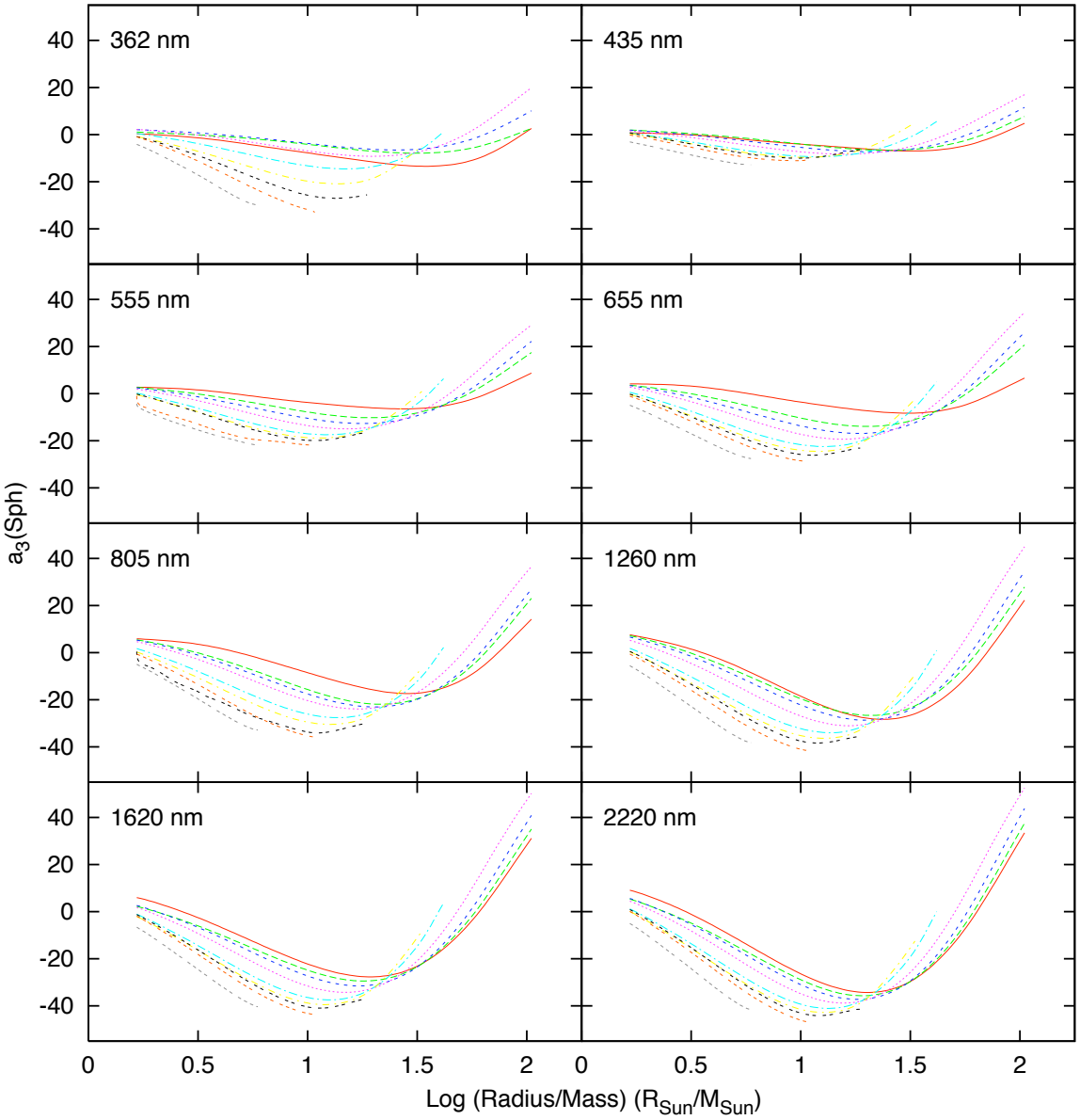

Figure 3.39: Same as Figure 3.38 but for a turbulent velocity of 2 km/s.

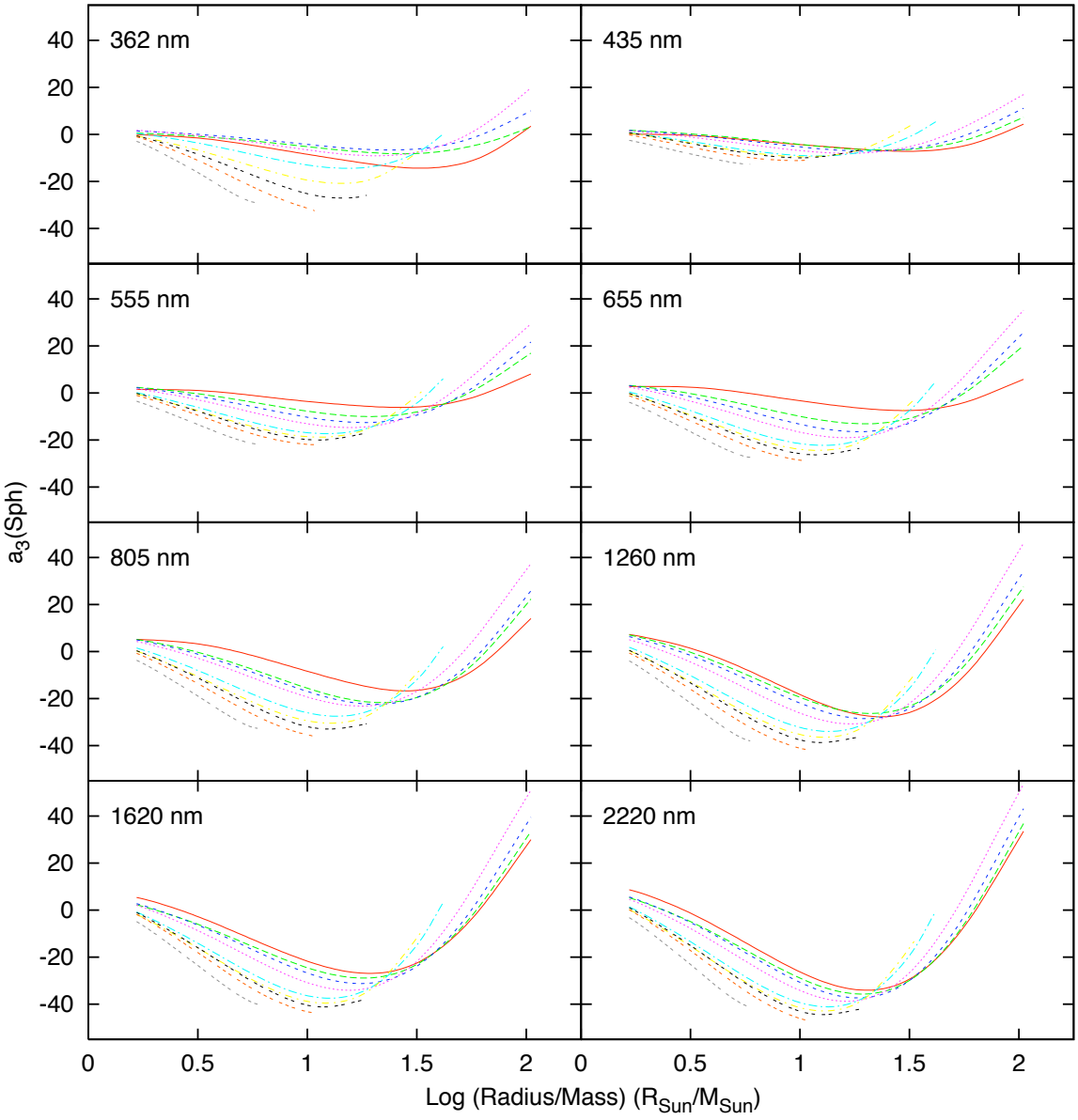

Figure 3.40: Same as Figure 3.38 but for a turbulent velocity of 4 km/s.

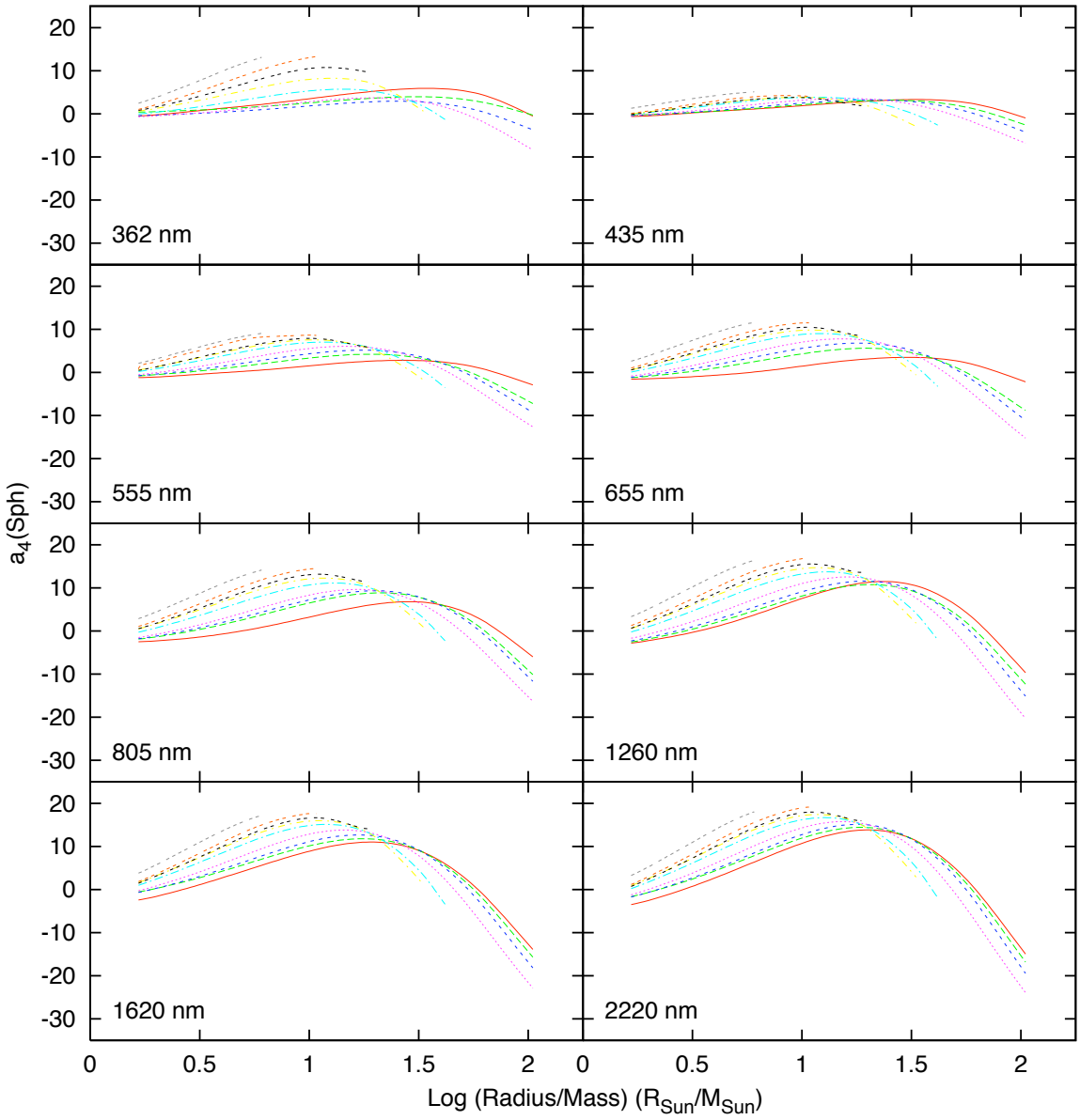

Figure 3.41: The behavior of the first coefficient of the four-parameter limb-darkening law, a_4 with respect to the spherical extension of the stellar atmosphere R_*/M_* for the model atmospheres with a turbulent velocity of 0 km/s.

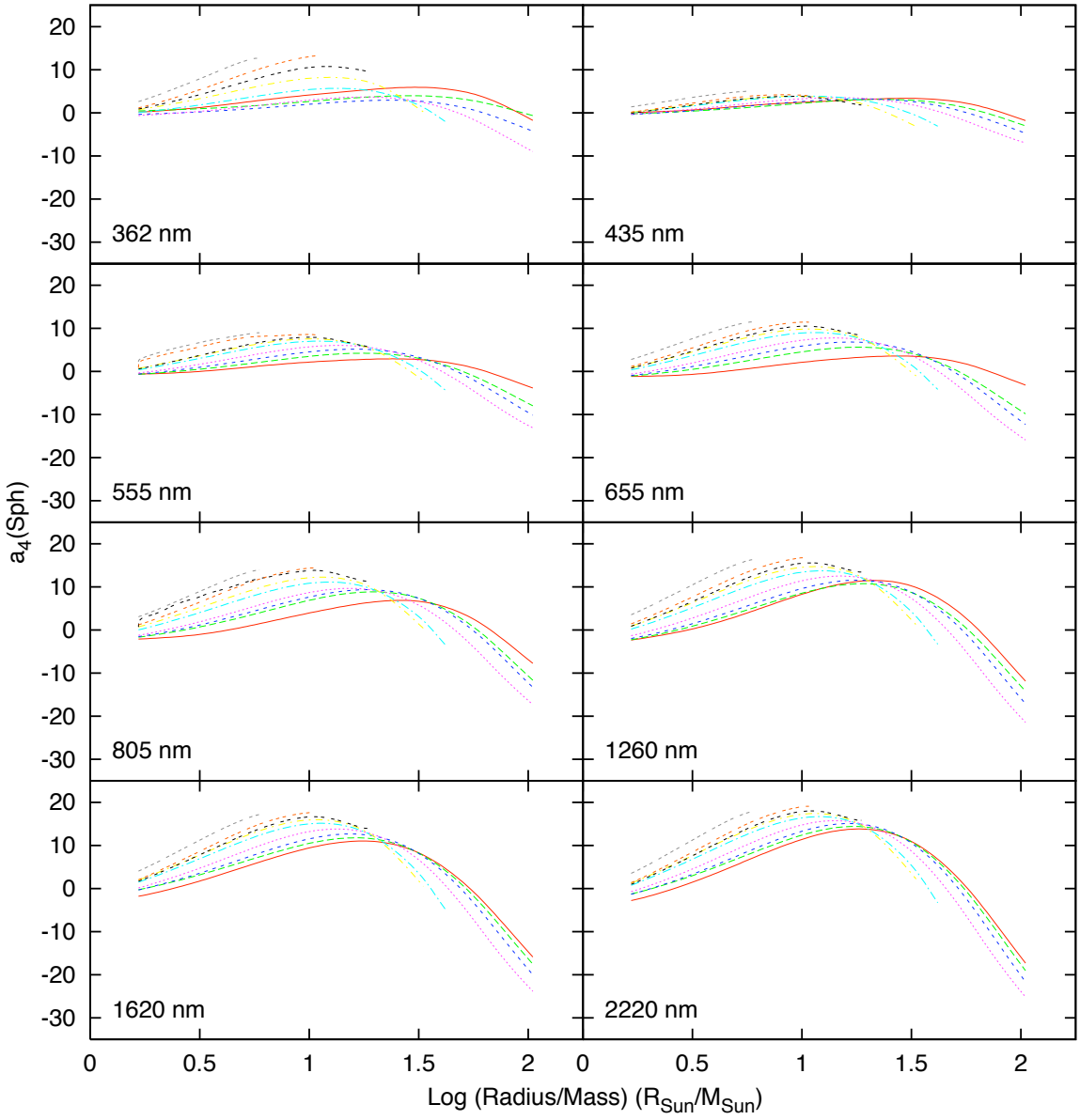

Figure 3.42: Same as Figure 3.41 but for a turbulent velocity of 2 km/s.

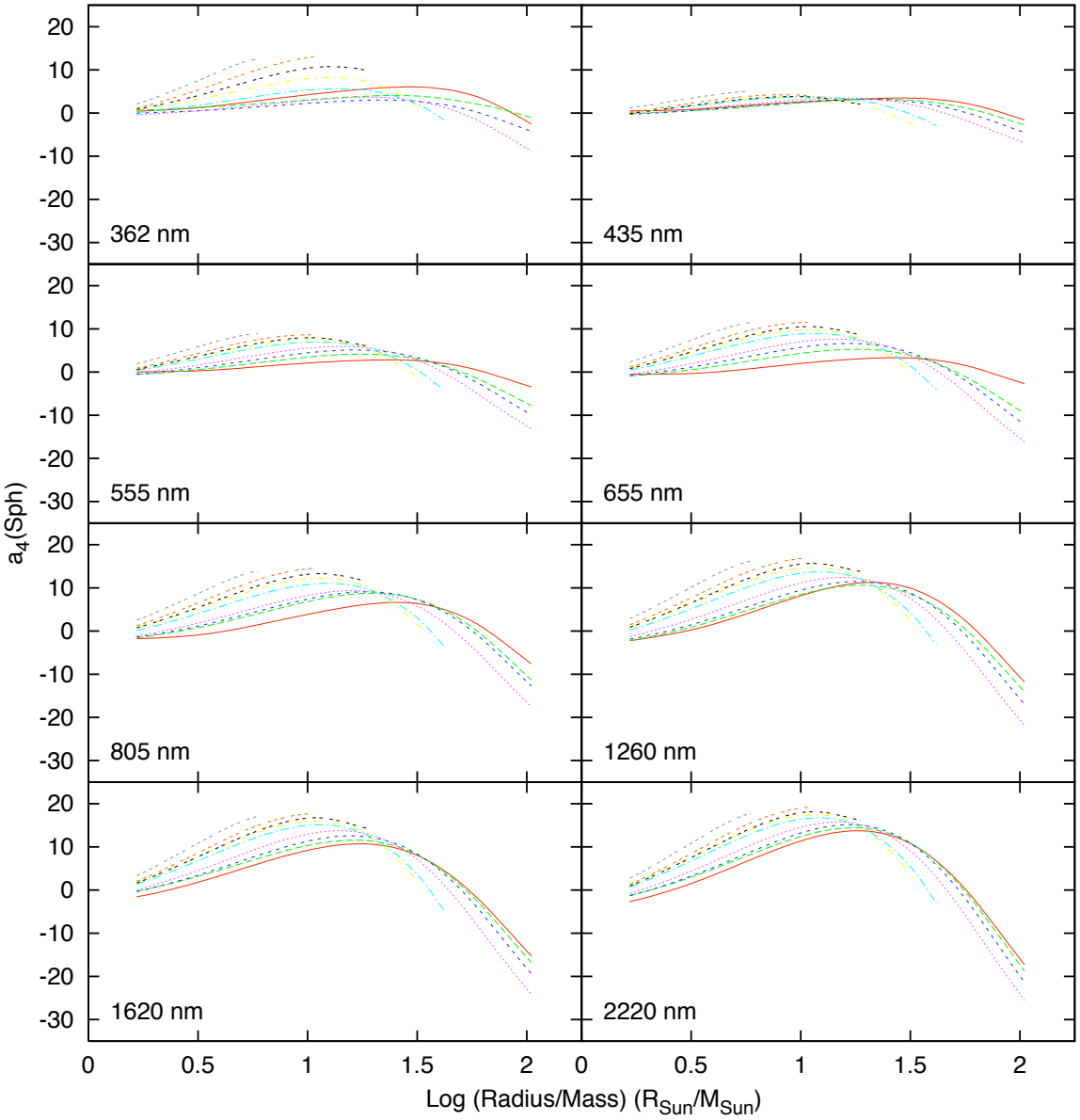

Figure 3.43: Same as Figure 3.32 but for a turbulent velocity of 4 km/s.

3.7 Conclusions

In this chapter, grids of spherical Atlas stellar atmosphere models are computed for the effective temperature range of $T_{\rm eff}$ = 3000-8000 K and gravities $\log g = -2$ to 3 for four different masses and three different values of turbulent velocity. In each model, the center-to-limb intensity distribution is calculated for each wavelength of computation for one thousand points of μ equally spaced from the center to the edge of the disk. This is the largest number of μ-points used for the calculation of the intensity structure ever done.

The intensity structures have been computed with the goal of testing the discovery of Heyrovsky (2000) and Fields et al. (2003) that a flux-conserving linear plus square-root limb-darkening law that represents intensity distribution has a fixed point at some value of μ where laws computed from a grid of plane-parallel model atmospheres all intersect. We test that result be directly plotting the intensity profiles from the spherical grid of models and find that the fixed point does not actually exist. However, when the best-fit limb-darkening laws are plotted there is evidence of a fixed point within some range of $\Delta\mu$. This is different from the plane-parallel laws but still an interesting result to be explored.

It has been demonstrated that the apparent fixed point is a result of least-square fitting where the two free parameters are dependent on two properties of the atmosphere, the mean intensity, J, and the integral $\int I\sqrt{\mu}d\mu$. But for the stellar atmospheres in the temperature range of 4000 K-8000 K the mean intensity is correlated to the psuedo-moment, which means that the two coefficients depend on only one piece of information. Therefore, the two free parameters are not actually free and are correlated. Because of this correlation, it is shown there must be a fixed point.

The non-specific value of the fixed point from spherical models suggest that the additional fundamental parameters that describe the spherical model atmosphere affect the limb-darkening law in a way not seen in the plane-parallel models. This effect is explored by computing the relation between the fixed point, μ_0 and the intensity at the fixed point $I_0/2F$ and the atmospherical extension, defined by the ratio of the radius and mass. Distinct, and precise non-linear relations are found for $\mu_0(R_*/M_*)$ and $I_0/2F(R_*/M_*)$ for specific effective temperatures. This implies a method for determining fundamental parameters for stars using this limb-darkening law. It is argued that if one guesses a value of the fixed point, then uses the limb-darkening law from observations to calculate $I_0/2F$ and then $I_0/2F$ can be used to estimate the value of R_*/M_*. This process can be iterated until the value R_*/M_* converges.

This method was applied to the microlensing results presented by An et al. (2002) and Fields et al. (2003). When the observed values of both coefficients is used, it is found that the method fails. This is because the uncertainty of the observations is large enough to cause the method to fail. However, the coefficients are correlated and if we use the one free parameter and the correlation to constrain the second parameter then the method is shown to succeed to reasonable precision. The method is demonstrated to be a robust tool to help constrain fundamental parameters of stars. This is ironic as the linear plus square-root limb-darkening law is shown to be a poor fit of the intensity distribution of the model atmosphere.

The more precise four-parameter limb-darkening law is also tested in this chapter. The law is fit to grids of models and shown *not* to conserve flux, the flux varies by a few percent, about two orders of magnitude larger than the flux conservation from plane-parallel model atmospheres. However, the four-parameter law is still a reasonable representation of the data when one considers how well other limb-darkeing laws fit the data. The fits to the spherical models show significant differences from the fits to plane-parallel models. The differences are greatest at a gravity of $\log g = 0.5$ to 1.5 but surprisingly tend to agree more at $\log g = 0$. One would expect that as the gravity decreases, the atmospheric extension increases and the intensity structure would deviate more from the plane-parallel intensity structure but this is not what happens. It should be noted that at $\log g = 0$, the differences are more dependent on the mass and effective temperature than at higher gravity, suggesting that a possible change of opacity causes the agreement.

The coefficients of the four-parameter law are compared to the atmospheric extension of the spherical models and the same behavior is seen as with the differences between the spherical and plane-parallel limb-darkening fits. This is because the plane-parallel fits produce roughly constant coefficients while the spherical fits produce a large range of coefficients. The coefficients have a strong dependence on the extension for specific effective temperatures, similar to the correlation seen for the two-parameter limb-darkening law. This implies there is a possible correlation between the four parameters that may be exploited. This possibility was not explored because the method found from the two-parameter law is already robust, uses fewer parameters, and fitting observations with higher order laws tend to produce larger uncertainties.

This work shows how limb-darkening varies as functions of fundamental parameters and demonstrates the power of limb-darkening to constrain fundamental stellar parameters. It is also shown that observations still do not constrain limb-darkening to the necessary precision to allow astronomers to move beyond simple representations of the intensity distribution and yet it is shown that we are not fully exploiting even these simple representations. Even though limb-darkening has been modeled and used as a tool in stellar astrophysics for almost a century, in many ways this tool is still in its infancy.

Chapter 4

Development of the Hydrodynamic Program for Modeling Cepheid Atmospheres

"Computers are useless. They can only give you answers." - Pablo Picasso

4.1 Introduction

The purpose of this is chapter is the describe the one dimensional hydrodynamic program HERMES (Sasselov & Raga, 1992), its strengths and drawbacks and derive the spherically symmetric version of the program. HERMES is designed to calculate the dynamic atmospheres of pulsating stars such as Cepheids. In its non–local thermal equilibrium configuration, the program uses the radiative transfer solver MULTI (Carlsson, 1986), which allows the user to calculate the effect of radiation due to lines from certain atoms and to calculate the effect of pulsation on line profiles.

Sasselov & Raga (1992) discussed the application of HERMES on a model of the Cepheid ζ Gem where line profiles of Mg II at $\lambda = 9226$Å at multiple pulsation phases as well as a comparison of the predicted radial velocity and the observed radial velocity of ζ Gem as a function of phase. Sasselov & Lester (1994c) and Sasselov & Lester (1994b) analyzed the formation of He I λ10830 and the generation of chromospheres in Cepheids using the HERMES program to model the pulsating atmospheres of ζ Gem and η Aql. The hydrodynamic program has also been used to calculate pulsation dependent limb–darkening of l Car for the purpose of predicting the effect of limb–darkening on interferometric estimates of the radii of Cepheids (Sasselov & Karovska, 1994). Evans, Sasselov, & Short (1998b) use the program to model the first overtone pulsator Polaris and compare model of the line profile of Mg II near $\lambda = 2800$Å with observations. More recently, Marengo et al. (2002) used the program to construct updated models to investigate details of limb–

darkening in Cepheids as it relates to pulsation.

For the advances in the understanding of pulsation atmospheres due to the program HERMES, there are also many drawbacks. One of the main drawbacks is the geometry of the program, it is a plane-parallel hydrodynamic program whereas Cepheids have extended atmospheres though it is argued that a spherically geometry is used in Marengo et al. (2002). There are various effects not modeled correctly such as limb–darkening. The hydrodynamic program does not use a complete set of opacities which means a significant amount of the cooling and heating in the atmosphere is ignored and makes it difficult to model spectra. For these reasons and more, it is advantageous to modify the HERMES program to spherical symmetry and combine it with the spherically symmetric version of the ATLAS program (Kurucz, 1993).

The next section in this report is reviews the structure of the HERMES program, how it solves the hydrodynamic problem, the third section discusses the conversion to FORTRAN 90 while the fourth section outline the necessary changes to convert the geometry of the program from planar to spherically symmetric.

4.2 Structure of HERMES

The hydrodynamic program is designed to solve the set of equations denoted by

$$\frac{\partial U}{\partial t} + \frac{\partial F}{\partial m} = G, \tag{4.1}$$

where t is time and m is mass. The quantities U, F and G are vectors

$$U = \begin{pmatrix} \tau \\ u \\ E \end{pmatrix}, \qquad F = \begin{pmatrix} -u \\ P \\ uP \end{pmatrix}, \qquad G = \begin{pmatrix} 0 \\ -g \\ -ug - \Lambda \end{pmatrix}, \tag{4.2}$$

where $\tau = 1/\rho$ is the specific density, u is the velocity, P is the pressure, g is the acceleration due to gravity and Λ is the energy balance due to atomic heating and cooling. These differential equations are for a plane–parallel system. This description is based on the work of Colella & Woodward (1984).

The program is written to solve the set of equations using a multi-ordered Godunov scheme so that it will be second order accurate. A Godunov scheme is designed to solve the set of partial differential equations at time t, defined as $t = (n + 1)\Delta t$ where n is an integer and Δt is the change of time. The equation is solved by knowing the physical quantities as a function of location at time $t = n\Delta t$ where the solution is approximated by a finite grid. The second step is to calculate the solution to the Riemann problem at each grid interface, this is called a flux step. In a plane-parallel stellar atmosphere, this includes solving for the velocity, and pressure. The next step is to use the variables solved at the grid interface to find a time advanced solution to the the state variables τ, u, E. This is a Godunov scheme and it is first order accurate as the variables found at the interface need to be averaged to get solution in the grid at the same points as the state variables. A

second order accurate scheme is found by calculating a Godunov solution on a rougher grid, the change in location, Δm, is larger. This solution is added to the first order solution to determine a second order accurate solution.

The HERMES program can be broken up into ten separate pieces: main, initial, timestep, flux step, extrapolation, large grid flux step, largebin, the second order correction, the reimann solver and interate/reset. The **Main** routine is designed to call the other routines to solve the partial differential equation. It starts by initializing the variables, which includes the change of time Δt, calling the starting stellar atmosphere model, via the initial routine, and calculating the initial flux variables. The main routine follows a loop over the input period of pulsation of the model and starts by calling the timestep routine for each of the three differential equations to calculate the time advanced solutions and then does a flux step to calculate the flux variables at the grid interface at this new time. This is followed by another call to the timestep routine to calculate the state variables at the next time. The values of the state values from the first advance of time are extrapolated to a grid that has a larger difference in mass between grid cells. This is equivalent to extrapolating to a lower spacial resolution. The next step is to calculate the flux variables at the interfaces of the rough grid and then extrapolate the state variable from the original time and source term, G variables to this grid as well at the state variables at the second time step. Then the second order correction is applied to solve for the U at the new time. The variables are then reset, the new solution becomes the input solution, and the loop is iterated to calculate the array U at a new time.

The second component of the hydrodynamic program is the initialization. The input parameters of the program are the starting static model, the period of pulsation of the model and the amplitude of the change of radius. The mean gravity of the starting model, and the number of time steps desired are also input variables. The starting model contains information about the density and temperature as a function of mass. Once the density and temperature are determined then a "piston" is applied to the base of the atmosphere to seed motion. The acceleration due to this piston is calculated in a separate routine called **Gravity**. This routine uses the calculation of the wavefunction for the linear nonadiabatic perturbation of the radius from Buchler, Moskalik, & Kovacs (1990) based on Fourier components. The wavefunction is

$$\Delta r(t) = \Delta r_0\{1 - [\cos(\omega t) + 0.271\cos(2\omega t) + 0.649] + 0.065\cos(3\omega t + 1.802)\} \tag{4.3}$$

and the perturbed velocity and acceleration are just the first and second time derivatives, respectively. The specific density is input from the model and the initial velocity is found from the piston model while the energy is calculated by interpolating a table of potential energy and electron fraction as a function of temperature. The total energy is then the sum of the kinetic and potential energy. Once the state variables are determined then the flux variables are computed followed by the Δt. The change of time is related to the grid cell size, if the velocity large relative to the sound speed then the time required for the gas to move across one grid cell is small. Therefore Δt must be small so that only the nearest cells are required for solving the

partial differential equations, here Δt is defined as

$$\Delta t = \frac{\Delta m}{c_s}. \tag{4.4}$$

The next part of the calculation is to calculate the state variables at time $t = t_0 + \Delta t$. This is done by simply writing the partial differential equation as difference equations. In this case, the state variables at a new time at grid cell i is

$$U_i(t + \Delta t) = U_i(t) - \Delta t \left[\frac{F_i - F_{i-1}}{\Delta m_i} - G_i \right]. \tag{4.5}$$

The flux step is important as it is the physical part of the calculation. In HERMES, the flux step is used to calculate the pressure, gravity and velocity at the interface. The first step is to determine the potential energy, which is just the total energy minus the kinetic energy. The temperature and electron fraction of the gas is found by interpolating values in tables as a function of the potential energy. The pressure is calculated by assuming an ideal gas,

$$p = \frac{k\rho(1 - \chi_e)T}{\bar{\mu}}, \tag{4.6}$$

where k is Boltzmann's constant, $\bar{\mu}$ is the average atomic mass, χ_e is the electron fraction, and ρ and T are the density and temperature respectively. The source function is also determined by calculating the gravity using the **Gravity** subroutine while the energy losses and gains written as Λ is found in the **ALOSS** subroutine. Here the **ALOSS** function calculates the change of energy with respect to time due to the change of temperature. The first step is to account for chromospheric heating, it is calculated based on the temperature structure of input hydrostatic model. This is based on the belief that the chromosphere is a constant phenomenon independent of the pulsation. The heating rate is written as

$$Q_{\text{Gain}} = -\frac{1.131 \times 10^{26} \rho \chi_e^2}{\sqrt{T_i}} \left(\sqrt{\frac{T_i}{T_{rad}}} - 1 \right), \tag{4.7}$$

where the term $\sqrt{T_i/T_{rad}} - 1$ is from the Taylor series expansion of $\exp(-\sqrt{T_i/T_{rad}})$. The quantity T_i is the temperature at some point in the initial model. The energy loss is

$$Q_{\text{Loss}} = \frac{1.131 \times 10^{26} \rho \chi_e^2}{\sqrt{T}} \left(\sqrt{\frac{T}{T_{rad}}} - 1 \right), \tag{4.8}$$

where T is the temperature at some time. The **ALOSS** routine calculates the change of energy at time t due to chromospheric heating as

$$\frac{dE}{dt} = Q_{\text{Gain}} - Q_{\text{Loss}}, \tag{4.9}$$

and this is used to calculate

$$\frac{\Delta E}{kT_{rad}} = \frac{\Delta t}{3} \frac{dE}{dt} \frac{1}{kT_{rad}} \left(\sqrt{\frac{T}{T_{rad}}} - 1 \right)^{-1}. \tag{4.10}$$

The temperature at some layer at a new time due to chromospheric heating is

$$T_{New} = T_{rad}\left[1 + \left(\sqrt{\frac{T}{T_{rad}}} - 1\right)e^{-\Delta E/kT_{rad}}\right]^2. \tag{4.11}$$

A new change of energy is calculated from $E = 3/2kT$ as

$$\frac{dE_{ALOSS}}{dt} = -\frac{3}{2}k\frac{dT}{dt} \approx -\frac{3}{2}k\frac{T_{New} - T}{\Delta t}. \tag{4.12}$$

The **ALOSS** routine then tests the solution to choose whether dE/dt or dE_{ALOSS}/dt is used as the final solution. If both values have the same sign then the routine chooses the quantity with the smallest absolute value; if they have opposite signs then dE/dt is chosen as the final solution in this function.

The flux variables are calculated at the grid cell interface using a Riemann solver. The Riemann solver uses the pressure, specific density, and velocity at the positions i and $i + 1$ as input to calculate the three flux variables at the interface defined at $i + 1/2$. A zeroth order approximation is that the flux variable at the interface is the average of the values at i and $i + 1$. A first order approximation is found by including the motion of gas over time Δt, in that case the effect of gravity must be included

$$P_0 = P_{\rm Avg} - \Delta t c_{s,{\rm Avg}} g = P_{\rm Avg} - \frac{1}{2}(u_i - u_{i+1})c_{\rm Avg}, \tag{4.13}$$

where $c = (\gamma\rho P)^{1/2}$, and an average quantity is the mean of two adjacent zones. However this is not the best solution for the pressure at the interface, especially since the velocity at the grid interface is not known. Colella & Woodward (1984) argue the pressure and velocity at the grid interface can be determined by solving the following set of equations

$$\frac{\bar{P}_{i+1/2} - P_{i+1/2,L}}{W_L} + (\bar{u}_{i+1/2} - u_{i+1/2,L}) = 0, \tag{4.14}$$

$$W_L^2 = \left[\frac{\gamma P^+_{i+1/2}}{\tau^+_{i+1/2}}\right]\left[1 + \frac{\gamma+1}{2\gamma}\left(\frac{\bar{P}_{i+1/2}}{P_{i+1/2,L}} - 1\right)\right], \tag{4.15}$$

$$\frac{\bar{P}_{i+1/2} - P_{i+1/2,R}}{W_R} + (\bar{u}_{i+1/2} - u_{i+1/2,R}) = 0, \tag{4.16}$$

$$W_R^2 = \left[\frac{\gamma P^-_{i+1/2}}{\tau^-_{i+1/2}}\right]\left[1 + \frac{\gamma+1}{2\gamma}\left(\frac{\bar{P}_{i+1/2}}{P_{i+1/2,R}} - 1\right)\right]. \tag{4.17}$$

In this system of equations the variables $P_{i+1/2,L}$, $P_{i+1/2,R}$, $P^+_{i+1/2}$ and $P^-_{i+1/2}$ are generally unique and depend on the geometry of the system. Because the Hermes program is plane-parallel then one can treat these as $P_i = P_{i+1/2,L} = P^-_{i+1/2}$ and likewise for P_{i+1} as well as the velocity and density terms. The variables denoted by a bar are the desired solution at the interface and can be found by using a Newton–Raphson method to iterate towards a solution where the initial guess is P_0. With the pressure and velocity determined at the gird

interface then the flux variables at the interface are known.

Once the flux variables is determined, a second order time step is done in the main routine which calculates the state variables at time $t = t_0 + 2\Delta t$. This is followed by computing the state variables on the larger grids where $dX = dx_i + dx_{i+1}$. The state variables at time t are extrapolated onto this grid. The new grid is defined to have the same number of grid cells and the information is "smoothed". The extrapolation is found using two possible solutions, depending on how large $U_{2j} - U_{2j-1}$ is, where j spans one half the total number of grid cells. If the difference is large then it is smoothed over the two grid cells with

$$U_{L,2j} = U_{L,2j-1} = \frac{\Delta m_{2j-1} U_{2j-1} + \Delta m_{2j} U_{2j}}{\Delta m_{2j} + \Delta m_{2j-1}}, \tag{4.18}$$

while the state variables on the larger grid is

$$U_{L,2j-1} = U_{2j-1} - \frac{(U_{2j} - U_{2j-1})\Delta m_{2j-1}}{\Delta m_{2j} + \Delta m_{2j-1}}, \tag{4.19}$$

$$U_{L,2j} = U_{2j} + \frac{(U_{2j} - U_{2j-1})\Delta m_{2j}}{\Delta m_{2j} + \Delta m_{2j-1}}, \tag{4.20}$$

when $U_{2j} - U_{2j-1}$ is small. These extrapolated values can be then used to calculate the flux variables at the interface on the larger grid. The method is the same as the flux solver on the smaller grid except the Riemann solver is called for the interface between points $2j$ and $2j + 1$ of the variable U_L to determine the flux variables on this larger grid.

The **Largebin** routine takes the source functions G, the state variables U and the predicted values of the state variables after two time steps and smoothes them on the larger grid. This is different then the extrapolation routine, here the large grid variables Q_L are just a weighted average of the variable Q on the smaller grid at points $2j$ and $2j + 1$ and the size of the vector Q_L is half the size of the vector Q. Here the value of Q_L at point j where $j = 2i$ is

$$Q_{L,j} = wQ_{2i} + (1 - w)Q_{2i-1}, \tag{4.21}$$

where $w = \Delta m_{2i-1}/(\Delta m_{2i-1} + \Delta m_{2i})$.

Now the state variables, source functions, flux variables, and the predicted state variables after two time steps are determined on the larger grid. Now it is possible to apply the second order correction to the system. The second order correction starts by using the state variables at time t to solve Equation 4.1 for $UL(t + 2\Delta t)$ at position $j = 2i$

$$U_{LN,j}(t + 2\Delta t) = U_{L,j}(t) - \left(\frac{2\Delta t}{\Delta m_{2i} + \Delta m_{2i-1}}\right)(F_{2i} - F_{2i-1}), \tag{4.22}$$

where the subscript LN refers to new values on the large grid. This is used to correct the value of the

predicted state variable $U_L(t + 2\Delta t)$ that has been smoothed onto the larger grid such that

$$U_{LN2}(t + 2\Delta t) = U_{LN}(t + 2\Delta t) - U_L(t + 2\Delta t). \tag{4.23}$$

However the routine also tests whether the U_{LN2} is very different from $U_{LN} - U_L$ and if the difference between the predicted state variables on the small grid, $u(x + \Delta m, t + 2\Delta t) - u(x, t + 2\Delta t)$ is large. If either of these criteria are large then the second order correction U_{LN2} is set to zero to avoid smoothing out discontinuities in the fluid motion. The correction is then applied to the predicted state variables on the small grid

$$U_{N,2i-1}(t + 2\Delta t) = U_{2i-1}(t + 2\Delta t) + U_{LN2,i}(t + 2\Delta t) \tag{4.24}$$

$$U_{N,2i}(t + 2\Delta t) = U_{2i}(t + 2\Delta t) + U_{LN2,i}(t + 2\Delta t). \tag{4.25}$$

The predicted array U_N is a second order accurate solution to the state variables at time $t + 2\Delta t$.

The final step of one iteration of the Hermes program is to reset the variables to be able to calculate the next time step. This is done by first setting the state variables $U = U_N$ and then followed by relaxing the conditions next to the surface by noting that the surface pressure is known from the input and is treated as constant with time. The state variables at $M - 1$, where $M + 1$ is the constant pressure boundary, are used to calculate a new pressure via the method discussed earlier and the pressure at M is a weighted average of p_{M-1} and the surface pressure. The new pressure at M is used to calculate relaxed state variables at M. This is done so that the pulsation does not cause the calculation to blow up.

4.3 Conversion to Spherical Symmetry

The program is plane-parallel and it is desirable to convert it to spherical symmetry to better model the dynamics of the extended atmospheres of Cepheids. There are two main differences for computing hydrodynamic models in spherical symmetry as opposed to plane-parallel are the structures of the differential equation and the Riemann solver.

The set of differential equations differ with geometery of the problem, Colella & Woodward (1984) derive the set of Equations to be

$$\frac{\partial \tau}{\partial t} - \frac{\partial (r^\alpha u)}{\partial m} = 0, \tag{4.26}$$

$$\frac{\partial u}{\partial t} + r^\alpha \frac{\partial P}{\partial m} = -g, \tag{4.27}$$

$$\frac{\partial E}{\partial t} + \frac{\partial (r^\alpha u P)}{\partial m} = -ug - \Lambda, \tag{4.28}$$

where τ is the specific volume, u is the velocity and E is the total energy per unit volume. The value of α is dependent on the geometry of the system being investigated. A value of $\alpha = 0$ represents a plane-parallel

geometry, $\alpha = 1$ represents cylindrical symmetry and $\alpha = 2$ is spherical symmetry. This can be written in a form similar to Equation 4.1,

$$\frac{\partial U}{\partial t} + H(r)\frac{\partial F}{\partial m} = G, \tag{4.29}$$

where

$$U = \begin{pmatrix} \tau \\ u \\ E \end{pmatrix}, \qquad H = \begin{pmatrix} 1 \\ r^{\alpha} \\ 1 \end{pmatrix} \qquad F = \begin{pmatrix} -r^{\alpha}u \\ P \\ r^{\alpha}uP \end{pmatrix}, \qquad G = \begin{pmatrix} 0 \\ -g \\ -ug - \Lambda \end{pmatrix}. \tag{4.30}$$

The finite difference approximation of Equation 4.29 is

$$U_i(t + \Delta t) = U_i(t) - \Delta t\left[H_i(r)\left(\frac{F_i - F_{i-1}}{\Delta m_i}\right) - G_i\right]. \tag{4.31}$$

This equation will replace the finite difference equation given by Equation 4.5 and equivalently Equation 4.22 in the Hermes program. The addition of the vector H will also require an additional call to the routine **Largebin** where the variables are averaged over grid cells via Equation 4.21. These are the only changes to the program necessary outside of the flux solvers.

The flux solver needs to be changed to account for the geometry. In this case the issue relates to the Riemann solver. In the Hermes program, the pressure and velocity at the grid cell interface is found by solving the set of Equations, 4.14–4.17, where it is assumed the values of $P^{+}_{i+1/2} = P_{i+1/2,R} = P_{i+1}$ and $P^{-}_{i+1/2} = P_{i+1/2,L} = P_i$ and likewise for the velocity. However, the geometry is not plane–parallel, this assumption is not valid. The left (L) and right (R) values as well as the + and − values will be solved following the derivation of Colella & Woodward (1984). The first step is to calculate the left and right values of the pressure and the velocity at the grid interface $i + 1/2$ which is between the grid cells i and $i + 1$. These are given as

$$P_{i+1/2,L} = P^{+}_{i+1/2} + \Delta t c^{+}_{j+1/2} g_i, \tag{4.32}$$

$$P_{i+1/2,R} = P^{-}_{i+1/2} - \Delta t c^{-}_{j+1/2} g_i, \tag{4.33}$$

$$u_{i+1/2,L} = u_{R,i} + \frac{A^{+}_{i+1/2}u^{+}_{i+1/2} - A_{i+1/2}u_{R,i}}{\frac{1}{2}(A^{+}_{i+1/2} + A_{i+1/2})}, \tag{4.34}$$

$$u_{i+1/2,R} = u_{L,i+1} + \frac{A^{-}_{i+1/2}u^{-}_{i+1/2} - A_{i+1/2}u_{L,i+1}}{\frac{1}{2}(A^{-}_{i+1/2} + A_{i+1/2})}. \tag{4.35}$$

The quantity $A_{i+1/2} = r^{\alpha}_{i+1/2}$ represents the geometry of the system. The next step is to write the calculation of $Q^{\pm}$ where Q is some variable, here

$$Q^{+}_{i+1/2} = f^{Q}_{i+1/2,L}(\Delta t c_{s,i}\chi_i), \tag{4.36}$$

$$Q^{-}_{i+1/2} = f^{Q}_{i+1/2,R}(\Delta t c_{s,j+1}\chi_{i+1}), \tag{4.37}$$

where the function f^Q is given as

$$f^Q_{i+1/2,L}(y) = Q_{R,i} - \frac{y}{2\Delta m_i}\left[\Delta Q_i - \left(1 - \frac{2}{3}\frac{y}{\Delta m_i}\right)Q_{6,i}\right], \tag{4.38}$$

$$f^Q_{i+1/2,R}(y) = Q_{L,i+1} - \frac{y}{2\Delta m_{i+1}}\left[\Delta Q_{i+1} - \left(1 - \frac{2}{3}\frac{y}{\Delta m_{i+1}}\right)Q_{6,i+1}\right]. \tag{4.39}$$

The function χ_i is

$$\chi_i = \frac{r^{\alpha+1}_{i+1/2} - r^{\alpha+1}_{i-1/2}}{(\alpha+1)(r_{i+1/2} - r_{i-1/2})}. \tag{4.40}$$

In the function f^Q the variables ΔQ_i and $Q_{6,i}$ are

$$\Delta Q_i = Q_{R,i} - Q_{L,i}, \tag{4.41}$$

$$Q_{6,i} = 6\left[Q_i - \frac{1}{2}(Q_{L,i} + Q_{R,i})\right]. \tag{4.42}$$

The final quantities to be determined are $Q_{L,i}$ and $Q_{R,i}$. These two variables depend on the smoothness of the solution. In smooth parts of the solution, $Q_{L,i+1} = Q_{R,i} = Q_{i+1/2}$, where a third order accurate solution to $Q_{i+1/2}$ is

$$\begin{aligned} Q_{i+1/2} &= Q_i + \frac{\Delta m_i}{\Delta m_i + \Delta m_{i+1}}(Q_{i+1} - Q_i) + \frac{1}{\sum_{j=-1}^{2}\Delta m_{i+j}} \\ &\times\left\{\frac{2\Delta m_{i+1}\Delta m_i}{\Delta m_i + \Delta m_{i+1}}\left[\frac{\Delta m_{i-1} + \Delta m_i}{2\Delta m_i + \Delta m_{i+1}} - \frac{\Delta m_{i+2} + \Delta m_{i+1}}{2\Delta m_{i+1} + \Delta m_i}\right](Q_{i+1} - Q_i)\right. \\ &\left.-\Delta m_i\frac{\Delta m_{i-1} + \Delta m_i}{2\Delta m_i + \Delta m_{i+1}}\delta Q_{i+1} + \Delta m_{i+1}\frac{\Delta m_{i+1} + \Delta m_{i+2}}{\Delta m_i + 2\Delta m_{i+1}}\delta Q_i\right\}, \end{aligned} \tag{4.43}$$

where

$$\begin{aligned} \delta Q_i &= \frac{\Delta m_i}{\Delta m_{i-1} + \Delta m_i + \Delta m_{i+1}} \\ &\times\left[\frac{2\Delta m_{i-1} + \Delta m_i}{\Delta m_{i+1} + \Delta m_i}(Q_{i+1} - Q_i) + \frac{\Delta m_i + 2\Delta m_{i+1}}{\Delta m_{i-1} + \Delta m_i}(Q_i - Q_{i-1})\right]. \end{aligned} \tag{4.44}$$

Colella & Woodward (1984) replace δQ_i with $\delta_m Q_i$ in their calculations to better represent the steepness of discontinuities in the solution and guarantees $Q_{i+1/2}$ is in the range given by Q_i and Q_{i+1} , where

$$\begin{aligned} \delta_m Q_i &= \mathrm{Min}(|\delta Q_i|, 2|Q_i - Q_{i-1}|, 2|Q_{i+1} - Q_i|)\mathrm{Sgn}(\delta Q_i) \\ &\quad \text{if } (Q_{i+1} - Q_i)(Q_i - Q_{i-1}) > 0 \\ &= 0 \quad \text{Otherwise.} \end{aligned} \tag{4.45}$$

If there is a large discontinuity in the range of Q_i and Q_{i+1}, then the definition of $Q_{L,i}$ and $Q_{R,i}$ must change,

and are given by

$$Q_{L,i} = Q_{i-1} + \frac{1}{2}\delta_m Q_{i-1} \qquad Q_{R,i} = Q_{i+1} - \frac{1}{2}\delta_m Q_{i+1}. \tag{4.46}$$

At this point, we have determined all of the necessary components to calculate the pressure and velocity at the grid interface to third order accuracy. The HERMES program, on the other hand, is designed to be second order accurate. If we wish to use the second order approximation then

$$Q_{L,i+1} = Q_{R,i} = Q_{i+1/2} = Q_i + \frac{\Delta m_i}{\Delta m_i + \Delta m_{i+1}}(Q_{i+1} - Q_i) \tag{4.47}$$

in smooth parts of the solution. Where there are discontinuities, the value of $Q_{L,i}$ and $Q_{R,i}$ are

$$Q_{L,i} = Q_{i-1} \qquad Q_{R,i} = Q_{i+1}. \tag{4.48}$$

At this point, there is enough information to calculate the flux values at the grid interface to second order accuracy.

4.4 Combining SATLAS with HERMES

The SATLAS program and spherically symmetric version of the HERMES may be combined to develop a local thermodynamic equilibrium radiative hydrodynamic program for modeling radial pulsation in the atmosphere of a star. Remarkably. accomplishing this merger does not require a dramatic re-writing of both programs. The **Main** routine of the SATLAS can be used as part of the flux solver, since that routine calls the radiative transfer and opacity routines. This means the program requires the radiative transfer routine **josh**, which uses either of two spherical routines designed for the SATLAS program as well as can use a plane-parallel version of the radiative transfer routines if one wishes to save computing time. This second option is being used during testing. The opacity routines include the same routines as they assume only the line and opacities and the equation of state for the atmosphere, not hydrostatic equilibrium. The only routines that make calculations of or assume hydrostatic equilibrium are in the **Main**, **Read** (model input), and the convection routine, The assumptions of hydrostatic equilibrium are removed from the main routine which is converted to a "flux" routine in the RHD program and from the convection routine. It is left in the input routine to provide a consistent starting model atmosphere.

To construct the RHD program, there exist three routines that must be developed. They include a routine for calculating the equation of state, a convergence solver, and new convection routines.

4.4.1 Equation of State

The equation of state is important for computing the gas pressure, temperature, electron number from the known quantities of the composition, density and hence number of atoms, and the energy density of each

layer. This requires assuming the relation between the gas pressure, temperature and number of particles

$$P_g = (\chi_a + \chi_e)kT. \tag{4.49}$$

Fortunately, the Equation of State (EoS) routine does not need to be invented from scratch. The SAtlas program contains an EoS solver for the cases where the atmosphere includes molecular opacities or with atomic opacities only. The EoS solver starts with the gas pressure, temperature and hence total number of particles and iteratively solves for the electron number and then the number of atoms. The iteration procedure starts with a guess for the value of χ_e, usually the value of χ_e from the previous iteration of the model atmosphere. Then the procedure solves the Saha equations for each atom for the given temperature. The solutions of the Saha equations are then added together to get a new value for χ_e. The procedure is iterated until the value of χ_e converges. Once this is found then the value of χ_a and the mass density is calculated at that layer.

For the RHD program, the known variables are the mass density, internal energy density and χ_a with P_g, χ_e and T as the unknowns. To solve for the unknown variables, the internal energy density is used to constrain them via

$$e = 1.5(\chi_a + \chi_e)kT/\rho. \tag{4.50}$$

In this equation the only unknowns are the electron number and temperature. Once these two parameters are found then the gas pressure can computed. The temperature and χ_e are computed by guessing an initial value of T and then using the SAtlas methodology to find the corresponding value of χ_e and then a value of the energy density is predicted. The process is continued for another guess of the temperature and solution for energy density. A root-finding method is then used to compute a final value of the temperature, and χ_e. A similar method is used when molecular opacities are included.

4.4.2 Convergence Solver

The purpose of the convergence solver is to both initiate pulsation via a perturbation to the velocity or acceleration, and to test whether the pulsation is stable and regular. The first routine is called the "kick" routine adds a perturbation to the velocity structure. This perturbation assumes that the model has an initial uniform velocity at each layer in the atmosphere. By having an initial variation of velocity then the mass density and energy density will be affected in the first timestep.

The second routine tests whether the pulsation has reached a regular amplitude. This is done by saving the value of the radius and velocity at the top of the atmosphere for each timestep. As the RHD program iterates, the routine checks the change of velocity. If the velocity at the top of atmosphere changes sign over two iterations then the radius is either at a minimum or maximum. At this time, if the acceleration is positive then the radius is at a minimum and if the acceleration is negative the radius is at a maximum value.

One the minimum and maximum radius is found, the amplitude of pulsation is computed and saved. The process is continued until an arbitrary number of amplitudes are calculated (currently set to 50), and the last two amplitudes are compared. If the amplitude is found to be decaying then RHD program starts anew and inputs a larger value for the "kick". If the radius at the top of the star is too large, for instance double the initial radius of the model then a smaller "kick" is used. The third possibility is if the amplitude is stable within some uncertainty, then the another pulsation period of the atmosphere is computed with output at each step, including the atmospheric structure, limb-darkening as a function of angle and wavelength, the flux and mean intensity as a function of depth and wavelength.

4.4.3 Convective Treatment

The treatment of convection within the RHD program is important because convection is known to modify pulsation in a star. The SAtlas program uses the mixing length theory to model convection which solves for the pressure, velocity and flux due to convection. This formalism can be used in the RHD if one wishes to assume that convection is frozen relative to pulsation. In this scenario, convection does not directly affect the pulsation of the star. For Cepheids, the assumption of frozen convection is a poor one, it is known that convection affects the pulsating structure of Cepheids near the red edge of the Cepheid Instability Strip. However, near the blue edge convection does not interact significantly with the ionization zone so the assumption is not unreasonable. Either way, the assumption is reasonable for the purpose of testing the hydrodynamic program, as is done here.

The second option is based on the methodologies of Stellingwerf (1982a), Kuhfuß (1986) and more recently Smolec & Moskalik (2008). In this methodology, convection is argued to depend on the turbulent energy in each layer of the star. The turbulent energy is treated as a hydrodynamic variable like the mass density, velocity and total energy such that

$$\frac{\partial e_t}{\partial t} + P_t \frac{\partial (r^2 u)}{\partial m} = -4\pi r^2 \frac{\partial F_t}{\partial m}. \tag{4.51}$$

The terms P_t and F_t are the turbulent pressure and the turbulent flux, respectively. In the current test version of the program the flux terms are ignored in the energy equation, so the turbulent energy may be written as

$$\frac{\partial e_t}{\partial t} = -P_t \frac{\partial (r^2 u)}{\partial m}. \tag{4.52}$$

The turbulent pressure is defined by Smolec & Moskalik (2008) to be $P_t = \alpha_t \rho e_t$ where α_t is a free parameter of order unity. Therefore Equation 4.52 may be rewritten as

$$\frac{\partial (\ln e_t)}{\partial t} = -\alpha_t \rho \frac{\partial (r^2 u)}{\partial m}. \tag{4.53}$$

In layers of the star that are convective, the turbulent energy is used to compute the convective flux

$$F_c = -\alpha\alpha_c\rho T c_P e_t^{1/2} \left[\nabla - \nabla_{ad}\right]. \tag{4.54}$$

The convective flux is then added as a source term in for solving the differential equation for the total energy.

The second method has the advantage of being time-dependent and coupled to the velocity field of the star. Hence convection will be allowed to vary with phase and contribute to the energy budget. The disadvantage of the time-dependent model is the number of free parameters. In this simple case for solving the turbulent energy there are three free parameters and if we include the source term for turbulence $F_t = -\alpha\rho\Lambda e_t^{1/2}(\partial e_t/\partial r)$ then the mixing length parameter is introduced as well. While the time-dependent convection is preferable, it still has significant issues to be addressed.

4.5 The Current Status of the RHD Program

As of August 1, 2009, the RHD program has been constructed and is being tested. So far a complete pulsation model has not been produced but significant progress has been made in that direction. The current version of the RHD program is a more simple version than that proposed. The convection is assumed to be frozen with respect to pulsation, the second-order hydrodynamic correction is not used and a plane-parallel radiative transfer algorithm is applied.

The use of frozen convection was discussed in the previous section. The second-order hydrodynamic correction is not used because of errors in earlier versions of the Riemann solver. These errors have been corrected for the first-order calculation but not yet done for the second-order calculation. Since the program is still being tested, correcting these errors do not have high priority. It is also beneficial to not use the second-order solver because incorporating it increases the computing time by a factor of 1.5. At this time, speed is more useful than the second-order correction. This is also the reason for using a plane-parallel radiative transfer routine; the plane-parallel Feautrier solver takes about one second to compute the flux while a spherical Feautrier solver (or Rybicki solver) will take about 150 seconds. Since the program computes an iteration for a timestep of about 50-100 seconds, the number of required iterations to a solution will be order 10^6. This fact suggests that the plane-parallel routine is preferable for computing the test models as well as being used as a first step for computing the final hydrodynamic models. For instance the plane-parallel radiative transfer may be used until regular pulsation is found, then the program switches to spherical radiative transfer and perturbs the original best-fit kick to test if the geometry affects the solution.

In the testing of the program, the most significant issue is due to the temperature range of the opacity table. As the program progresses in time, the temperature of layers near or at the base of the atmosphere increases until the temperature is greater than 2×10^5 K. The standard opacity table used in SAtlas program has a temperature range $1000 < T < 2\times10^5$ and when temperatures are beyond the limits of the table the

program crashes. The solution to this program is to build a new opacity table with a temperature maximum between 0.5-5 $\times 10^6$ K.

With a larger opacity table, the input static models may also be computed to greater depths, though this process is challenging. The static models require conservation of radiative equilibrium at all layers which is enforced by the temperature correction routine, see Chapter 2. However, a temperature correction operates from the surface inwards and at large values of Rosseland optical depth, $\tau_{\rm Ross} > 10^2$-10^3 the temperature correction becomes ineffective. Without radiative equilibrium operating at large depth the temperature structure reaches a plateau instead of increasing with increasing depth. This result would be a poor input model. To work around this problem, an additional temperature correction method is added only at large depths under the assumption that the radiation is effectively blackbody. Thus the luminosity at these layers is $L = 4\pi R^2 \sigma T^4$ and we can solve for the temperature correction based on the luminosity error ΔL to be

$$\Delta T_{BB} = \alpha T \frac{\Delta L}{4L}, \tag{4.55}$$

where α is an efficiency factor designed only to not change the temperature too much. In the SAtlas program, a large correction may lead to an instability in the calculation and the program crashes. If the program does not crash and completes the desired number of iterations, the luminosity error is significantly reduced.

Another issue is related to the convection routine and the computation of thermodynamic quantities. Currently the RHD programs assume a value of $\gamma = 5/3$ throughout the atmosphere, however, this is not ideal and will bury information. The SAtlas program computes the specific heats c_P and c_V in the convection routine by calculating the various thermodynamic derivatives such as $(\partial e/\partial T)_p$ and $(\partial \rho/\partial p)_T$ among others to compute the specific heats. In the SAtlas program, this routine works well and for the input static models predicts sounds speeds of the order 10^5-10^6 cm/s. However, in the RHD program the value of c_V is predicted to be much smaller by about 3-4 orders of magnitude at the surface while the value of c_P is approximately the same for both cases to within 10%. Therefore, the sound speed in the RHD program will be unrealistically large. This problem has been dealt with by assuming $\gamma = 5/3$ everywhere but this is not a permanent solution.

Computations have been made for a Cepheid model atmosphere with solar abundance, $M = 4\ M_\odot$, $L = 2862\ L_\odot$, and $R = 59\ M_\odot$. The model is computed for an Rosseland optical depth of 10^5 corresponded to a temperature of about 19000 K. At the large depths there is still uncertainty due to having large luminosity error, thus the temperature of the model plateaus at large depths. The initial velocity perturbation at every depth is 0.05 km/s. The model is left to run until it fails due to the temperature at some layer being larger than maximum value in the opacity table. In Figure 4.1, the temperature, radius and radiative pressure is shown for the initial static model atmosphere and the hydrodynamic model at its last timestep as a function of gas pressure. The temperature plateau in the static model is apparent and static model ranges from

about 3000 K to 20000 K. This model is arguable completely inappropriate for modeling pulsation as it is just barely deeper than the Helium I ionization zone, however, it is useful for testing. The temperature structure of the final RHD model is very different and contains three temperature inversions and one possible discontinuity. The inversion near the surface is due to the enforced presence of a chromosphere, which is manifested by forcing a small pressure inversion at the top layer. This practice was suggested by Dr. Dimitar Sasselov. The two interior inversions surround a local temperature minimum at 10^4 $dynes/cm^2$ corresponding to $T = 10^4$ K. This appears to be the opacity mechanism operating on the first Heium ionization zone. The radius is shown to vary significantly with the outer layers of the atmosphere having expanding by about 20%. There is also a jump in radius at the He I ionization zone. The radiation pressure traces the temperature structure of the atmosphere in both the static and dynamic cases with the exception of the surface of the dynamic model. The radiation pressure at the surface does not see the chromosphere.

The Lagrangian variables that are computed in the RHD program are shown in Figure 4.2. The mass density is plotted as a function of gas pressure and the discontinuity is seen again at $P_{gas} = 10^4$ $dynes/cm^2$. The mass density is increasing and is consistent the opacity mechanism operating at this layer. The velocity is also shown but no significant velocity gradients are seen about the ionization layer. It is interesting that the velocity for most of the atmosphere is roughly constant, suggesting that no waves have been generated in the atmosphere. The total energy, yet again, shows the impact of the ionization zone but is also increasing with depth below the ionization zone. This is related to the temperature increase at the base of the atmosphere.

Finally, the radius and velocity of the top layer of the model atmosphere is shown as a function of time in Figure 4.3. The velocity is increasing almost linearly with no indication of behaving like a sinusoidal radial velocity curve. Similarly the radius is also increasing, growing by almost 20%. This is a larger amplitude than would be expected, however, to call this an amplitude requires assuming that the input radius is about the mean radius of pulsation. There is no a priori reason for that to be true and it may be more reasonable to expect that the mean radius would be larger than the input because pulsation will "puff up" the atmosphere.

The radiation hydrodynamic program has been developed significantly and is near completion. It is expected that the program will be able to compute complete dynamic atmospheric models of Cepheids in the near future and apply them to the interesting questions such as comparison to interferometric observations of Cepheids.

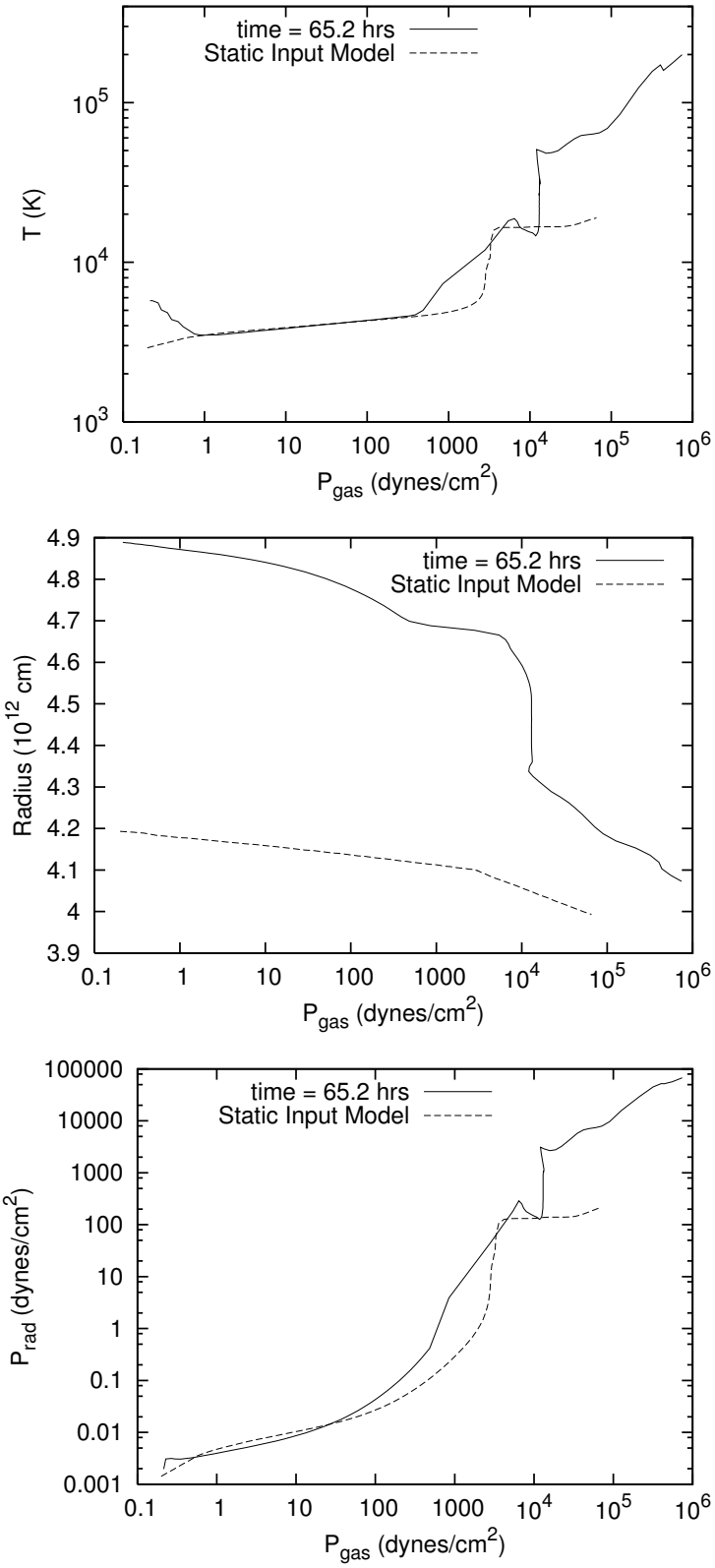

Figure 4.1: The comparison of the temperature, radius, and radiative pressure as a function of the gas pressure from the initial static model atmosphere and the hydrodynamic model atmosphere after approximately 60 hours.

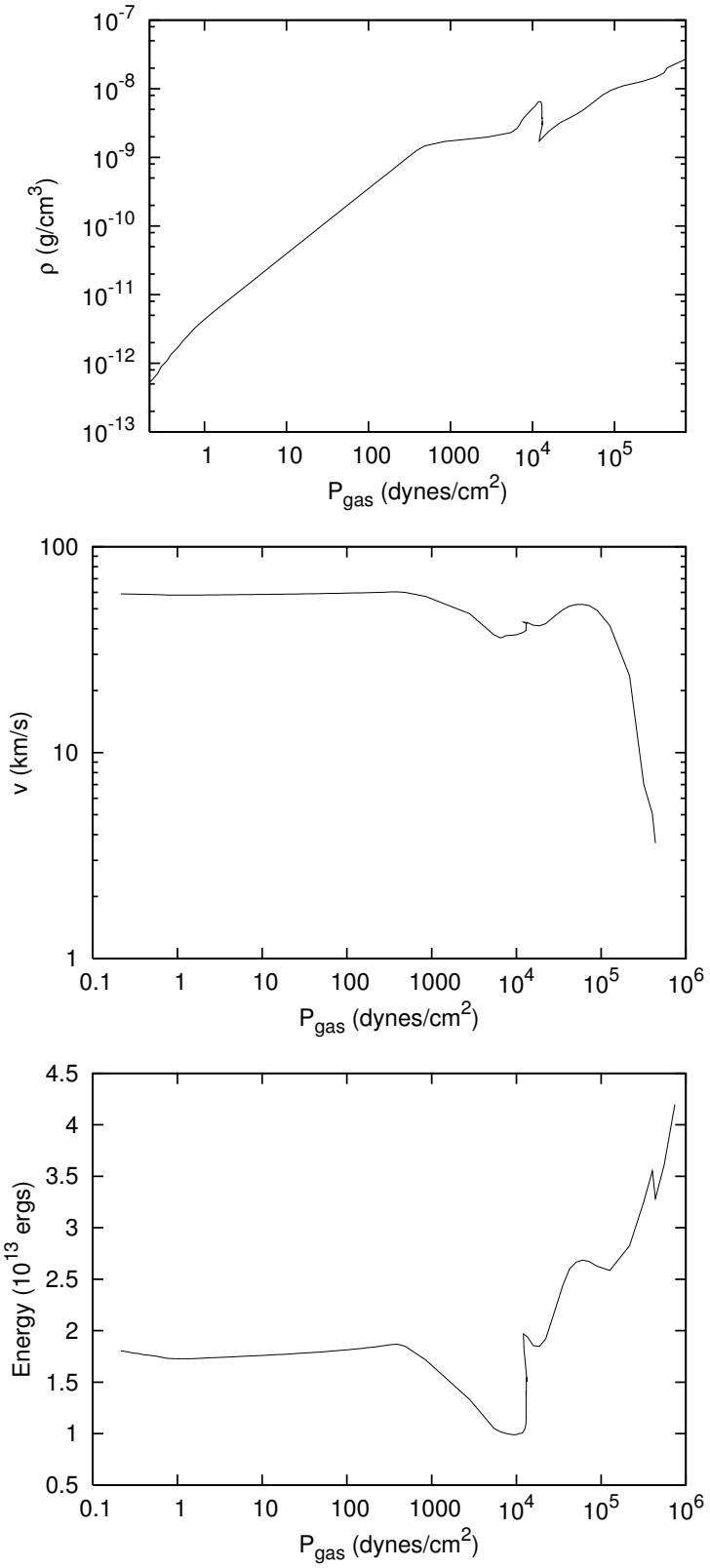

Figure 4.2: The mass density, velocity and total energy of the hydrodynamic model after approximately 60 hours.

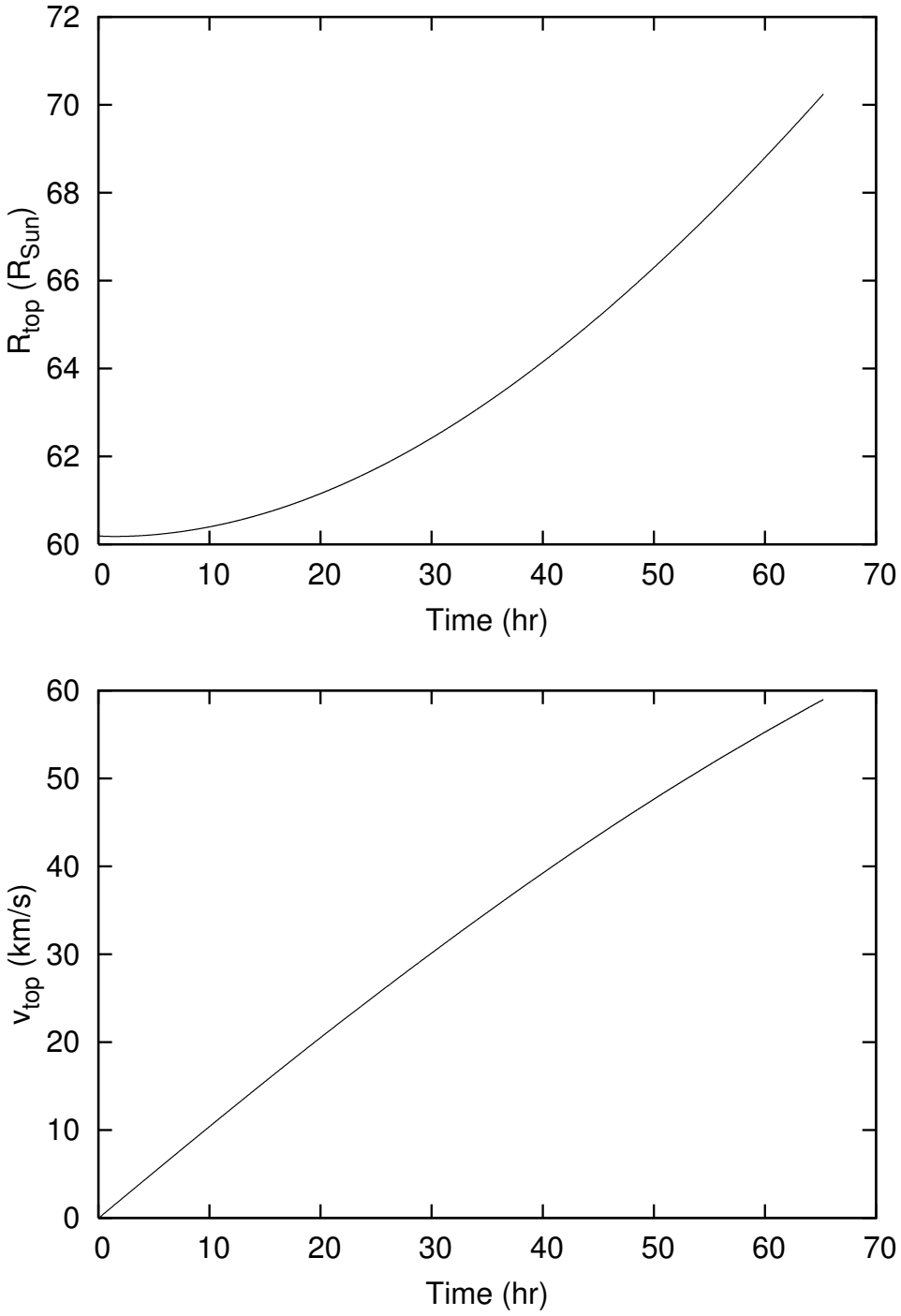

Figure 4.3: The predicted radius and velocity at the top of the model atmosphere as a function of time for the duration of the simulation.

Part II

Cepheid Mass Loss

Chapter 5

The Analytic Derivation of Pulsation-Driven Mass Loss in Cepheids

This chapter is published as:
"On the Enhancement of Mass Loss in Cepheids Due to Radial Pulsation"
Neilson, H.R., & Lester, J.B. 2008, ApJ, 684, 569[1]

"The answer, my friend, is blowin' in the wind..." - Bob Dylan

5.1 Introduction

The observations of circumstellar shells surrounding Cepheids (Kervella et al., 2006; Mérand et al., 2006, 2007) have generated a new set questions regarding the structure and evolution of Cepheids and how these shells are generated. Could these shells be relics from earlier stages of stellar evolution or are they related to Cepheid stage of evolution? Interferometric observations, presented in Mérand et al. (2007), of the non–pulsating yellow supergiant α Persei did not find evidence for circumstellar envelopes and suggests that the shells are not a relic of stellar evolution but are related to Cepheid pulsation.

One possible generation mechanism for these shells is a stellar wind in Cepheids. This is not a particularly new idea, it has been suggested as a solution for the Cepheid mass discrepancy (Brunish & Willson, 1989) and there have been a number of observations that are consistent with mass loss (Deasy, 1988, for example). Because a stellar wind is generated in the atmosphere of a star, then it is important to consider the existence of stellar winds in Cepheids and how the winds are generates to help understand pulsation and dynamics in Cepheid atmospheres.

[1]Neilson & Lester (2008b), reproduced with permission by the American Astronomical Society

5.2 The Driving Mechanism of Cepheid Winds

Mass loss has been studied in other types of variables stars such as luminous blue variables (Guzik et al., 2005), asymptotic giant branch stars (Höfner, 1999), and Miras (Höfner & Dorfi, 1997). Luminous blue variables are hot evolved stars near the Eddington limit that exhibit pulsation variations of brightness of about 0.1 magnitudes and it is argued by Guzik et al. (2005) that these variations are pulsations generated by iron opacities. These pulsations cause regions of the star to exceed the Eddington limit and thus eject mass. This is not the only suggestion; Owocki & van Marle (2008) argues that outbursts might be due to continuum opacities that are modified by differences in density at various times.

Mass loss in asymptotic giant branch stars is believed to be caused by radiation pressure on dust generated in the atmospheres of these stars. This mass loss is affected by pulsation via the injection of pulsation energy (Mattsson et al., 2008), however the amount of mass that is ejected is strongly dependent on dust properties in the stars, for instance Woitke (2007) found that mass loss is negligible in oxygen–rich AGB stars where Iron and Magnesium silicates are important for absorbing radiation. The mass loss mechanism in Miras is believed to be similar to AGB stars, the mass–loss history of the prototype of the class has been modeled this way (Wareing et al., 2007) to explain ultraviolet observations (Martin et al., 2007).

While it may be assumed that Cepheid mass loss is related to pulsation, mass loss be have other driving mechanisms like those implied for other variable stars. The most common mechanisms for driving a stellar wind are: dust driving, radiative line–driving, coronal winds, and magnetic fields (Lamers & Cassinelli, 1999). Dust driving is important in stars where dust can form in the atmosphere. This leads to an increase of the opacity of the star and radiation pressure accelerates the dust away from the star. If the dust is ionized then the particles have a larger effective collisional cross–section and causes more material to be ejected. Since dust must form in the atmosphere for this to be important, the star's effective temperature must be cooler than 2000 K; Cepheids have effective temperatures of order 4000 K – 6500 K. Dust is not a likely factor though it can form some distance from the star where the temperature of the gas is much less when the gas is optically thin.

Radiative line–driving has been explored thoroughly for most stars and is considered to be most important for hotter stars where carbon, nitrogen and oxygen atoms are ionized in the atmosphere causing a larger effective collisional cross–section. The ions are accelerated by radiation and interact with other atoms in the atmosphere, in turn accelerating them outwards. For stars with an effective temperature of order 6000 K, neon, iron, hydrogen and helium may play the role that carbon, nitrogen and oxygen play in hotter stars (Abbott, 1982). Therefore radiative line–driving must be considered in any analysis of mass loss in Cepheids.

To have a coronal wind, a star must have a corona where the temperature is very large. Sasselov & Lester (1994a) and Schmidt & Parsons (1982, 1984a,b) found only weak chromospheres for Cepheids implying there are no hot coronae; coronal driving is an unlikely source.

The presence of magnetic fields is uncertain and controversial in Cepheids. Plachinda (2000) detected a 100 G magnetic field in η Aquilae but Wade et al. (2002) could not verify that result, inferring an upper limit a 10 G field. However, Polaris has recently been observed to be a soft X–ray source, though this may be due to its binary companion; far UV observations of Polaris imply the possible existence of warm winds, shocks or magnetic activity (Engle et al., 2006). Magnetic fields seem an unlikely cause of winds in Cepheids. Thus one needs to be concerned with only one of those four possibilities: radiative line driving.

The purpose of this study is to explore the role radial pulsation plays in driving mass loss in classical Cepheids when coupled with radiative line–driving. Castor, Abbott, & Klein (1975), hereafter CAK, devised a method to solve for the radiation–driven wind structure of a star. Here that method is modified to include a simple function describing additional momentum input into the wind. This chapter describes the derivation of the CAK momentum equation for a pulsating star, including pulsation and shock physics. The shock velocities are taken from a hydrodynamic model of δ Cephei (Fokin et al., 1996) and scaled for other Cepheids.

5.3 Pulsation Enhanced CAK Method

Castor et al. (1975) proposed an isothermal wind model to describe the mass–loss rates and wind structures of stars. The method is a powerful, yet simple, analytical tool for understanding the effects of radiative line driving because it requires knowledge of only the mass, radius and luminosity of the star. The authors assume the forces due to the radiative lines and the pressure gradient are functions of the local velocity gradient; this results in having the conservation of momentum written in a form that can be solved for the velocity as a function of distance from the stellar surface. The CAK wind model is the standard tool for understanding winds in O, B, and A stars (Owocki, 2005; Watanabe et al., 2006) and possibly F and G supergiants (Lamers & Cassinelli, 1999). A review of the analytic derivation can be found in Lamers & Cassinelli (1999).

5.4 Derivation for Pulsation Driven Winds

One can derive the equations governing the mass–loss rate for a radially pulsating star by following the derivation given by Lamers & Cassinelli (1999), who start with the momentum equation for the wind including the effects of continuum and radiative line driving, gravity and gas pressure,

$$v\frac{dv}{dr} = -\frac{GM_*}{r^2} + \frac{1}{\rho}\frac{dp}{dr} + g_e + g_L. \tag{5.1}$$

The functions g_e and g_L describe the radiation force per unit mass due to electron scattering and line opacity respectively. The expression for g_e is

$$g_e = \frac{\sigma_e L_*}{4\pi r^2 c} = \frac{GM_*}{r^2}\Gamma_e \tag{5.2}$$

where $\Gamma_e \equiv \sigma_e L_*/(4\pi c G M_*)$, and $\sigma_e = \sigma_T N(e)$ is the electron scattering opacity as a function of the Thomson scattering opacity and the number of electrons. The electron scattering term is clearly dependent on the composition and temperature of the star, but for this analysis is assumed not to vary significantly. The acceleration due to lines is found by using the Sobolov approximation; the final form is

$$g_L = Cr^{-2}\left(r^2 v\frac{dv}{dr}\right)^{\alpha}, \tag{5.3}$$

where

$$C = \frac{\sigma_e L_* k}{4\pi c}\frac{Z}{Z_\odot}\left[\frac{\sigma_e v_{\rm th}\dot{M}}{4\pi}\right]^{-\alpha}\left[\frac{10^{-11}n_e}{W}\right]^{\delta}. \tag{5.4}$$

The function C is treated as a constant, although this is not strictly true. The parameters α, k and δ are force multiplier parameters calculated using model atmospheres to measure the radiative acceleration due to lines. The values of α and δ tend to be of the order 0.5 and 0.1 respectively, while k can vary significantly: for stars $T_{\rm eff} < 10^4$ K $k \approx 0.1$ (Abbott, 1982; Shimada et al., 1994; Pauldrach et al., 1986). The ratio of the electron density with the geometric dilution factor $W(r) = (1 - \sqrt{1 - R_*/r})/2$ can vary for all stars implying C is not constant, but the ratio has the exponent δ that is small. Therefore the term to the power δ is ignored by assuming it is approximately unity. It should be noted, however, in Cepheids the ionization rate of hydrogen and helium is dependent on the phase of pulsation. The number density of electrons could thus vary as a function of phase and play a small role. If the number density of electrons is increased then the mass–loss rate that is calculated may be larger as a result, but not by more than an order of magnitude because the term Γ_e is much less than unity. Also C has an explicit and implicit metallicity dependence found from calculations on the contributions to radiative line driving for various ions as a function of gravity and effective temperature (Abbott, 1982; Shimada et al., 1994).

The pressure term is rewritten in terms of the velocity by assuming the wind is isothermal

$$\frac{1}{\rho}\frac{dp}{dr} = -\frac{2a^2}{v}\frac{dv}{dr} - \frac{2a^2}{r}, \tag{5.5}$$

where a is the isothermal sound speed. The resulting total form for the conservation of momentum is

$$v\frac{dv}{dr} = -\frac{GM_*(1-\Gamma_e)}{r^2} + \frac{a^2}{v}\frac{dv}{dr} + \frac{2a^2}{r} + Cr^{-2}\left(r^2 v\frac{dv}{dr}\right)^{\alpha}. \tag{5.6}$$

Equation 5.6 does not include the effect of pulsation. Radial pulsation injects momentum into the wind due to the acceleration of the outer layers of the atmosphere of the star. Radial pulsation also generates shocks in the interior that propagate to the surface, depositing energy into the wind. This means there are

two additional sources of acceleration in the atmosphere of the Cepheid. For this derivation, it is assumed the accelerations due to pulsation and shocks are determined at the surface of the star so that they are only a function of time and global parameters. In the wind, these additional acceleration terms are modified by a dissipation factor, $(r/R_*)^{-\nu}$ where $\nu > 0$. Therefore the sum of the acceleration due to pulsation and the acceleration due to shocks are written as $\zeta(r/R_*)^{-\nu}$. The function ζ is the acceleration at the surface of the star due to the sum of the pulsation and shocks that is written in terms of the global quantities of the star. The function is derived in detail in the next section. The full equation for the conservation of momentum including pulsation is

$$rv\frac{dv}{dr} = -\frac{GM_*(1-\Gamma_e)}{r^2} + \frac{a^2}{v}\frac{dv}{dr} + \frac{2a^2}{r} + Cr^{-2}\left(r^2 v\frac{dv}{dr}\right)^{\alpha} + \zeta\left(\frac{r}{R_*}\right)^{-\nu}. \tag{5.7}$$

Rearranging terms and simplifying, Equation 5.7 becomes

$$C\left(r^2 v\frac{dv}{dr}\right)^{\alpha} - \left(1 - \frac{a^2}{v^2}\right)r^2 v\frac{dv}{dr} - GM_*(1-\Gamma_e) + 2a^2 r + \zeta R_*^2\left(\frac{r}{R_*}\right)^{(2-\nu)} = 0. \tag{5.8}$$

Equation 5.8 represents the quasi–static approximation of the momentum equation for the wind of a pulsating star. The differential equation can be solved in a series of snapshots where the velocity calculated is based on the conditions of the star at the given time, however this does not change the mass–loss rate at that instant. The mass–loss rate depends on the velocity and the density of the wind as it is ejected, but the wind does not feed back onto the layers that generate the wind. Therefore the time averaged mass–loss rate can be determined by this quasi–static approximation but the velocity of the wind will be unphysical near the surface of the star. Hence only the change of the luminosity and radius and other quantities dependent on them are considered in the problem.

Because the implicit effects of time are ignored, the differential equation can be solved in the same manner as the non–pulsating form. From Figure 4 of Cassinelli (1979), it is clear there is only one solution to the non–pulsating differential equation, the solution where the velocity as a function of distance from the star satisfies both regularity and singularity conditions at some critical point, r_c. It must be noted the quantity r_c is a mathematical construct for solving the differential equation and is not necessarily a physical quantity. If $F = 0$ represents the momentum equation, Equation 5.8, then

$$\left(\frac{\partial F}{\partial v'}\right)_c = 0 \qquad \text{Singularity Condition} \tag{5.9}$$

$$\left(\frac{\partial F}{\partial r}\right)_c + \left(v'\frac{\partial F}{\partial v}\right)_c = 0 \qquad \text{Regularity Condition,} \tag{5.10}$$

where $'$ denotes the derivative with respect to r. While it may seem that using the velocity structure to determine a valid solution is contradictory with previous statements, this would be a reasonable approximation if the star were non–pulsating. The amount of mass ejected at time t is not be affected by the amount of mass

ejected an instant later. At that instant when the mass is ejected it has a velocity structure for a steady flow that provides a satisfactory solution to the differential equation, though this ignores the effect of clumping. The singular and regularity conditions become

$$\left(1-\frac{a^2}{v_c^2}\right) r_c^2 v_c v_c' = \alpha C \left(r_c^2 v_c v_c'\right)^\alpha , \tag{5.11}$$

$$\begin{aligned} &\frac{2\alpha C}{r_c}\left(r_c^2 v_c v_c'\right)^\alpha - \left(1-\frac{a^2}{v_c^2}\right) 2 r_c v_c v_c' + 2a^2 + \zeta R_* \left(\frac{r_c}{R_*}\right)^{1-\nu} \\ &+\frac{v_c'}{v_c}\left[\alpha C (r_c^2 v_c v_c')^\alpha - \left(1-\frac{a^2}{v_c^2}\right) r_c^2 v_c v_c' - 2\frac{a^2}{v_c^2} r_c^2 v_c v_c'\right] = 0 \end{aligned} \tag{5.12}$$

respectively, where one should recall $d\zeta/dr = 0$ as ζ is defined at the surface of the star.

One may now use the momentum equation and the singularity and regularity conditions to determine the velocity and velocity gradient at the critical point by first substituting the momentum equation into the singularity condition, and eliminating the quantity C,

$$r_c^2 v_c v_c' = \left(\frac{\alpha}{1-\alpha}\right)\left(1-\frac{a^2}{v_c}\right)^{-1}\left[GM_*(1-\Gamma_e) - 2a^2 r_c - \zeta R_*^2 \left(\frac{r_c}{R_*}\right)^{(2-\nu)}\right]. \tag{5.13}$$

Combining the singularity condition with the regularity condition will determine the velocity gradient at the critical point and using that result with Equation 5.13 one finds the velocity at the critical point

$$v_c' = \frac{v_c}{r_c}\left[1 + \frac{\zeta R_*(2-\nu)}{2a^2}\left(\frac{r_c}{R_*}\right)^{(1-\nu)}\right]^{1/2} , \tag{5.14}$$

$$v_c^2 = a^2 + \left[1 + \frac{\zeta R_*(2-\nu)}{2a^2}\left(\frac{r_c}{R_*}\right)^{1-\nu}\right]^{-1/2}\left(\frac{\alpha}{1-\alpha}\right) \tag{5.15}$$

$$\times\left[\frac{GM_*(1-\Gamma_e)}{r_c} - 2a^2 - \zeta R_*\left(\frac{r_c}{R_*}\right)^{1-\nu}\right]. \tag{5.16}$$

These two expressions give the velocity and velocity gradient at the critical point and form a starting point for solving the momentum equation. The expression v_c' is combined with the singularity condition to determine the radiative driving constant C in terms of the radius and velocity at the critical point and various terms

from the momentum equation

$$C = \left(\frac{1}{1-\alpha}\right)\left[1 + \frac{\zeta R_*(2-\nu)}{2a^2}\left(\frac{r}{R_*}\right)^{(1-\nu)}\right]^{-\alpha/2} \frac{1}{r_c^{\alpha} v_c^{2\alpha}} \times \left[GM_*(1-\Gamma_e) - 2a^2 r_c - \zeta R_*^2\left(\frac{r_c}{R_*}\right)^{2-\nu}\right]. \tag{5.17}$$

Equating the two expressions for C, Equation 5.4 and 5.17, and using the function for the critical velocity, Equation 5.15, yields the relation for the mass–loss rate

$$\dot{M} = \left[\frac{\sigma_e L_* k}{4\pi c}\frac{Z}{Z_\odot}(1-\alpha)\right]^{1/\alpha}\left(\frac{4\pi}{\sigma_e v_{th}}\right)\left[GM_*(1-\Gamma_e) - 2a^2 r_c - \zeta R_*^2\left(\frac{r_c}{R_*}\right)^{2-\nu}\right]^{-1/\alpha} \times \left\{a^2 r_c\left[1 + \frac{\zeta R_*(2-\nu)}{2a^2}\left(\frac{r_c}{R_*}\right)^{(1-\nu)}\right]^{1/2} + \left(\frac{\alpha}{1-\alpha}\right)\left[GM_*(1-\Gamma_e) - 2a^2 r_c - \zeta R_*^2\left(\frac{r_c}{R_*}\right)^{2-\nu}\right]\right\}. \tag{5.18}$$

It is now shown the mass–loss rate of a Cepheid can be calculated by knowing the global parameters for the star and the critical point. Lamers & Cassinelli (1999) argue that if one assumes a value for r_c then the velocity structure can be solved and the density structure can be derived from the velocity. The continuum optical depth of the wind is calculated from the density. This lends itself to a condition for the solution of the differential equation. The stellar surface is generally defined where the mean optical depth equals $2/3$, therefore the optical depth of the wind, given by the integration of the density and opacity from infinity to the stellar surface, must be $2/3$. The inclusion of pulsation and shocks, however, means it is not so clear this criterion needs to be satisfied for a wind to be driven. Because there is no ideal criterion to use that will give a clear solution, the optical depth $\tau = 2/3$ will be used. The mass–loss rate is tested and shown to verify that it varies only weakly for different values of the critical point; hence it is reasonable to use the integral of the optical depth as a criterion for solving the momentum equation. Therefore at some phase of pulsation, one can calculate the instantaneous mass loss rate by adopting a value for r_c and solving the wind structure and comparing the velocity predicted at the surface with the velocity due to pulsation; a solution is reached when the two values match.

5.5 Defining the Acceleration Due to Pulsation and Schocks

In deriving the solution for the enhanced mass loss due to pulsation and shocks, it was assumed the function ζ, which represents the sum of the acceleration from both pulsation and shocks, depends only on the global parameters that describe the Cepheid, such as effective temperature, radius, amplitude of radius variation and period of pulsation. In this section, the formulation for the acceleration will be defined and justified.

For simplicity it is advantageous to consider a one–zone model for the radial pulsation of the Cepheid with period P. In that case the radius of the Cepheid as a function of time is written as $\Delta R(t) = -\Delta R\cos(\omega t)$, where ΔR is the amplitude of pulsation. The amplitudes of the nearest Cepheids are readily available from radial velocity studies, and a list has been compiled by Moskalik & Gorynya (2005). The minus sign in the equation defines a phase of zero to correspond to the minimum radius and $\omega = 2\pi/P$ is the angular frequency of pulsation. The acceleration of the surface of the Cepheid due to pulsation is thus

$$a_{\rm puls} = d^2[\Delta R(t)]/dt^2 = \omega^2 \Delta R\cos(\omega t). \tag{5.19}$$

The luminosity varies as a function of time as well. Since there is a well–known phase lag, such that the maximum luminosity occurs roughly a quarter period before the maximum radius, the quasi–adiabatic approximation is used to describe the luminosity such that $\Delta L(t) = \Delta L\sin(\omega t)$. Writing the electron-scattering opacity as a Kramer's law to be $\sigma_e \propto \rho T^{-3.5}$, implies it too varies due to pulsation because both the temperature and density vary as a function of time. Because the temperature goes as $T_{\rm eff} \propto [L_*(t)/(R_*(t)^2]^{1/4}$, the variation of the temperature is

$$\frac{\Delta T_{\rm eff}(t)}{\bar{T}_{\rm eff}} = \frac{1}{4}\frac{\Delta L_*(t)}{\bar{L}_*} - \frac{1}{2}\frac{\Delta R_*(t)}{\bar{R}_*}. \tag{5.20}$$

In addition, the linear perturbation of the density in the one zone model is

$$\frac{\Delta\rho(t)}{\bar{\rho}} = -3\frac{\Delta R_*(t)}{\bar{R}_*}, \tag{5.21}$$

meaning the variation of the electron scattering opacity is

$$\frac{\Delta\sigma_e}{\bar{\sigma_e}} = -\frac{5}{4}\frac{\Delta R}{\bar{R}_*} - \frac{7}{8}\frac{\Delta L}{\bar{L}_*}, \tag{5.22}$$

where variables denoted with a bar are the mean values of the variable over a pulsation period. Also, because the effective temperature will vary as a function of phase then so will the isothermal sound speed, which goes as $a \propto T^{1/2}$. This defines all of the quantities that are assumed to vary due to pulsation.

The role of shocks is not as easily quantified as there is no simple method to describe the acceleration of gas by spherically symmetric shocks. Willson (1976) and Willson & Hill (1979) develop a model for a shock in the atmosphere of long period variables where the shock is periodic with the pulsation. However Mathias et al. (2006) and Sasselov & Lester (1990), for example, find evidence for multiple shocks per period. Also, while the mechanism for generating shocks is understood to be related to both the opacity mechanism and the γ–mechanism, the strength of shocks is uncertain. An analysis of shock behavior in δ Cephei was conducted by Fokin et al. (1996), who modeled the atmosphere of δ Cephei and traced the difference between the post–shock velocity of the gas and the pre–shock velocity of the gas in the frame of reference of the traveling shock as a function of the phase of pulsation. Our work uses that information to estimate the acceleration of the gas in Cepheids due to shocks. Here it is assumed that the velocity of

the shock itself goes to zero at the surface of the Cepheid. This assumption is justified based on evidence that Cepheids have weak chromospheres generated by shocks (Sasselov & Lester, 1994a). Therefore the difference between the velocity of the pre– and post–shocked gas at the stellar surface in the frame of the shock is the same as in the rest frame. It is also assumed that the velocities in Fokin et al. (1996) are valid in a one zone model, i.e. these velocities are at the surface of the Cepheid.

From Matzner & McKee (1999) and Klimishin & Gnatyk (1981), one can assume the pressure of the post–shocked gas is proportional to the mean energy density

$$u^2 = \frac{E}{m}, \tag{5.23}$$

where u, E, m represent the velocity, mean energy density and the mass of the post shock gas, respectively. The mean energy density is roughly constant, while the mass is not. For a central explosion, such as a supernova, one can write the mass as $m \approx \rho r^3$, where r is the scale of the post shock gas from the shock. However, shocks in Cepheids are generated relatively near the surface, therefore we can write the mass as $m \approx \rho R_*^2 \Delta r$, where Δr is the thickness of the shock front. Thus the velocity relative to the sound speed inside the star, c_s, scales as

$$\frac{u}{c_s} = \Omega \left(\frac{m}{M_*} \right)^{-1/2} = \Omega \left(\frac{\rho 4\pi R_*^2 \Delta r}{\bar{\rho} 4\pi R_*^3/3} \right)^{-1/2}, \tag{5.24}$$

where Ω is a constant, and Δr is the mean free path times the pre–shock pressure divided by the change of pressure (Zel'Dovich & Raizer, 1967),

$$\Delta r = l \frac{p}{\Delta p}. \tag{5.25}$$

The pre–shock pressure is $c_s^2 \rho$ at the surface and the change of pressure is the sound speed at the radius where the shock is formed times the change of density. The shock is formed at the partial ionization zone, which has the same temperature for all Cepheids. The mean free path is $1/\kappa\rho$, and the opacity of the shock is also constant. Therefore the thickness of the shock front is

$$\Delta r = \frac{1}{\kappa \Delta \rho} \frac{T_{\rm eff}}{T_{\rm ionization}} = \frac{1}{\kappa \Delta \rho} \frac{L_*^{1/4} R_*^{-1/2}}{L^{1/4}(r) r^{-1/2}} = \frac{1}{\kappa \Delta \rho} \frac{r^{1/2}}{R_*^{1/2}}, \tag{5.26}$$

where the luminosity is the same at both r and R_*, and the radius where the shock is formed is roughly constant for all Cepheids. Thus the speed of the gas due to a shock, given by Equation 5.24, is proportional to

$$u \propto c_s \left(\bar{\rho} R_*^{3/2} \right)^{1/2}. \tag{5.27}$$

Therefore the ratio of the velocity of gas for any Cepheid relative to the prototypical Cepheid, δ Cephei, is

$$\frac{u}{u_\delta} = \frac{c_s \bar{\rho}^{1/2} R_*^{3/4}}{c_{s,\delta} \bar{\rho}_\delta^{1/2} R_\delta^{3/4}}, \tag{5.28}$$

Range of Phase	du/dϕ (km/s/phase)
0 - 0.08	187
0.1 - 0.12	208
0.13 - 0.22	120
0.65 - 0.68	75
0.73 - 0.76	200
0.79 - 0.83	240
0.93 - 1	187

Table 5.1: The change of speed of shocked gas at the surface of δ Cephei with respect to phase of pulsation at different phases. At any phase not within the given ranges the change of speed is zero. The data are taken from Figure 4, Fokin et al. (1996).

where δ refers to δ Cep. The sound speed is proportional to the square root of the effective temperature which, in turn, is proportional to the luminosity and the radius, $T_{\rm eff} \propto L^{1/4} R_*^{-1/2}$. The relative shock speed is now $u/u_\delta = (L*^{1/8}\,\bar{\rho} R_*^{1/2})/(L_\delta^{1/8}\bar{\rho}_\delta R_\delta^{1/2})$. The radius can be expressed in terms of the mean density and the mass, $R_* \propto \bar{\rho}^{-1/3} M^{1/3}$ while the mean density is a function of the period of pulsation $\bar{\rho} = (Q/P_*)^2$ where Q is the pulsation constant. Fernie (1967) found that pulsation constant is not strictly constant, and actually varies as $Q \propto P^{1/8}$. Equation 5.28 is rewritten in terms of the luminosity, period and mass,

$$\frac{u}{u_\delta} = \left(\frac{L_*}{L_\delta}\right)^{1/8} \left(\frac{P_*}{P_\delta}\right)^{-7/24} \left(\frac{M_*}{M_\delta}\right)^{5/12} . \tag{5.29}$$

This defines the velocity of the gas due to shocks at the surface of a Cepheid.

The acceleration of the gas is $a_{\rm shock} = P^{-1} du/d\phi$. In terms of Equation 5.29,

$$a_{\rm shock} = \frac{P^{-1}}{d\phi} du_\delta \left(\frac{L_*}{L_\delta}\right)^{1/8} \left(\frac{P_*}{P_\delta}\right)^{-7/24} \left(\frac{M_*}{M_\delta}\right)^{5/12} , \tag{5.30}$$

where the quantities describing δ Cep are taken from the model computed by Fokin et al. (1996). The values of $du/d\phi$ are listed in Table 5.1, where zero phase corresponds to minimum radius.

Having defined the acceleration of the gas due to shocks and pulsation, the function ζ is

$$\zeta = \Delta R \omega^2 \cos(\omega t) + \frac{P^{-1}}{d\phi} du_\delta \left(\frac{L_*}{L_\delta}\right)^{1/8} \left(\frac{P_*}{P_\delta}\right)^{-7/24} \left(\frac{M_*}{M_\delta}\right)^{5/12} , \tag{5.31}$$

where ζ is dependent only on global parameters: the amplitude of radius variation, luminosity, period, and mass.

5.6 Solution Space of the Wind Equation

It is important to explore the momentum equation's parameter space before applying it to real stars. There may be situations where the combination of parameters do not give a physical solution, which is true for the momentum equation for static stars. There are two regions in the velocity–distance parameter space where there are no solutions: one region is defined where the velocity is subsonic when $GM_*(1-\Gamma_e)-2a^2r < 0$, the other is when the velocity is supersonic too close to the surface of the star where $GM_*(1-\Gamma_e)-2a^2r >> 0$. Cassinelli (1979) reviewed the solution space of a radiative wind. The first case is explored by analyzing how the addition of pulsation affects the Parker point, r_p (Parker, 1958), which is the distance from the star where the effective escape velocity equals the isothermal sound speed. In the pulsating case the Parker point is defined as

$$GM_*(1-\Gamma_e)-2a^2r_p-\zeta R_*^2\left(\frac{r_p}{R_*}\right)^{2-\nu}=0. \tag{5.32}$$

Second, the boundary where the wind becomes supersonic too close to the surface will be explored by analyzing the parameter space of the critical velocity and the derivative of the critical velocity.

The Parker point is an important quantity in the radiative driving momentum equation as the wind solution must be supersonic at a distance less than

$$r < r_p = \frac{GM_*(1-\Gamma_e)}{2a^2}, \tag{5.33}$$

otherwise the velocity gradient $dv/dr < 0$ and the $v(r)$ would go to zero. The inclusion of pulsation adds an extra complication since the Parker point is now defined as the solution to a polynomial equation. In the momentum equation given by Equation 5.8, it is necessary that

$$F(r) = GM_*(1-\Gamma_e)-2a^2r-\zeta R_*^{\nu}r^{2-\nu} > 0 \tag{5.34}$$

when $a^2/v^2 > 1$. Because this function is non–linear, the Parker point is not a complete definition of the instability, especially since it is mathematically plausible to have a solution where r_p is less than the stellar radius R_*. The true Parker point can be defined by using $F(r_p) = 0$ and $dF(r_p)/dr < 0$. The second definition ensures $F(r)$ is decreasing before the Parker point. This is seen if different values of ν are assumed; consider $\nu = 0, 2, 3$, which are the quadratic and linear cases for Equation 5.32 for the Parker point. In the linear case of $\nu = 2$ the Parker point is

$$r_p = \frac{GM_*(1-\Gamma_e)-\zeta R_*^2}{2a^2}. \tag{5.35}$$

In this case the Parker point is modified from the traditional definition to one that oscillates about $GM_*(1-\Gamma_e)/2a^2$. This case does not suffer from multiple solutions, but the cases $\nu = 0, 3$ have two solutions each, where

$$\text{for } \nu = 0, \qquad r_p = \frac{2a^2 \pm \sqrt{4a^4+4\zeta GM_*(1-\Gamma_e)}}{-2\zeta} \tag{5.36}$$

and

$$\text{for } \nu = 3, \qquad r_p = \frac{GM_*(1-\Gamma_e)}{4a^2} \pm \frac{\sqrt{[GM_*(1-\Gamma_e)]^2 - 8a^2\zeta R_*^3}}{-4a^2} \tag{5.37}$$

respectively. These solutions highlight another potential pitfall, the term in the square root may be imaginary depending on the phase of pulsation. In the case of $\nu = 0$, if the phase $0.25 \leq \phi \leq 0.75$ then it is possible for $\zeta < 0$ when the shock acceleration is zero and the acceleration due to pulsation is less than zero. For $\nu = 3$ the Parker point can be imaginary when the function ζ is large as is the case for short period Cepheids or hotter evolved Cepheids. If the Parker radius is imaginary then there may not exist a wind solution at that time as the gravity is less than the outward acceleration implying an instability in the star.

Applying the second criterion for a proper solution for the Parker point, one finds the derivative of Equation 5.32

$$\frac{dF(r_p)}{dr} = -2a^2 - (2-\nu)\zeta R_* \left(\frac{r_p}{R_*}\right)^{1-\nu}. \tag{5.38}$$

Testing this for the case where $\nu = 2$ the derivative is always less than zero. When $\nu = 0$, the Parker point is given by Equation 5.36 and substituting this result to solve for $dF(r_p)/dr$

$$\frac{dF(r_p)}{dr} = \pm\sqrt{a^4 + \zeta GM_*(1-\Gamma_e)} \tag{5.39}$$

implying only the negative square root in the solution for the Parker point as given in 5.37 is the true Parker point. From Equation 5.37, it is clear the Parker point given by the positive square root is less than R_* for most values of ζ.

The second region of interest is based on the wind becoming supersonic too close to the surface of the star, where the boundary is defined as the curve that is tangential to the critical velocity. Therefore Equation 5.15 can be used to analyze any instabilities. There is the obvious possible instability given by the term $\{1 + [\zeta(2-\nu)R_*/2a^2](r_c/R_*)^{1-\nu}\}^{-1/2}$. This term can be imaginary depending on the chosen value of ν and the phase of pulsation. If this is imaginary, then both the critical velocity and the derivative of the critical velocity is complex and the will be no real wind solution. It should be noted that this instability disappears in the case of $\nu = 2$, and it is possible to compute a mass–loss rate at any phase of pulsation.

The conclusion is that there exists time–dependent perturbations to the Parker point and the critical velocities causing no real wind solutions. This is different from the non–pulsating CAK method which does not contain any explicit pitfalls.

5.7 The Power–Law Dependence of the Pulsation and Shock Acceleration

It is important to understand the role the exponent ν plays in the pulsation term of the wind equation. The power law is chosen to represent the dissipation of energy imparted by pulsation as particles in the wind are accelerated outwards. The use of a power law is an approximation of the detailed physics of the dissipation

process. Without having a firm physical determination of ν, it is necessary to determine how sensitive the total mass–loss rate is to an adopted value of ν. One way to test the effect of ν is to derive the change of instantaneous mass–loss rate with respect to ν. This will be done by calculating an approximation of the instantaneous mass–loss rate and solving it for various values of ν.

The sensitivity of the instantaneous mass–loss rate with respect to ν can be measured by the quantity $d \ln \dot{M}/d\nu$. The mass–loss rate is given by Equation 5.18, which can be rewritten in the form $\dot{M} = K_1 A_1^{-1/\alpha}(A_2 + K_2 A_1)$; the term K_1 and $K_2 = \alpha/(1-\alpha)$ are constant multipliers, and A_1 and A_2 are the respective functions of ν. The derivative of the mass–loss rate is

$$\frac{d \ln \dot{M}}{d\nu} = -\frac{1}{\alpha}\frac{1}{A_1}\frac{dA_1}{d\nu} + \frac{dA_2/d\nu + K_2 dA_1/d\nu}{A_2 + K_2 A_1} \tag{5.40}$$

where

$$A_1 = GM_*(1-\Gamma_e) - 2a^2 r_c - \zeta R_*^2 \left(\frac{r_c}{R_*}\right)^{2-\nu}, \tag{5.41}$$

$$A_2 = a^2 r_c \left[1 + \frac{\zeta R_*(2-\nu)}{2a^2}\left(\frac{r_c}{R_*}\right)^{2-\nu}\right]^{1/2}. \tag{5.42}$$

This can be considered one term at a time; starting with A_1

$$\frac{dA_1}{d\nu} = \zeta R_* \left(\frac{r_c}{R_*}\right)^{1-\nu} \ln\left(\frac{r_c}{R_*}\right) \tag{5.43}$$

and

$$\frac{1}{\alpha}\frac{1}{A_1}\frac{dA_1}{d\nu} = \frac{\ln(r_c/R_*)}{\alpha}\left[-1 + \frac{GM_*(1-\Gamma_e)/r_c - 2a^2}{\zeta R_* (r_c/R_*)^{1-\nu}}\right]^{-1}. \tag{5.44}$$

The derivative of the second term is

$$\frac{dA_2}{d\nu} = -\frac{a^2}{2}\left[1 + \frac{\zeta(2-\nu)R_*}{2a^2}\left(\frac{r_c}{R_*}\right)^{(1-\nu)}\right]^{-1/2} \frac{\zeta R_*}{2a^2}\left(\frac{r_c}{R_*}\right)^{(1-\nu)}\left[1 + (2-\nu)\ln\left(\frac{r_c}{R_*}\right)\right]. \tag{5.45}$$

Starting with the result for $dA_1/d\nu$, it can be seen that there is a large change with respect to ν if the pulsation term is of order the effective potential, where the enthalpy term given by the isothermal sound speed is relatively insignificant. In the limit the pulsation term is equal to the effective potential then the ratio approaches one and the term in square brackets goes to zero. Therefore $dA_1/d\nu \to -\infty$ and the derivative of the mass–loss rate will approach infinity. The terms $(dA_2/d\nu)/(A_2 + K_2 A_1)$ and $K_2(dA_1/d\nu)/(A_2 + K_2 A_1)$ can be shown to have a similar behavior. Therefore ν can have a significant effect on the mass–loss rate depending on the combination of parameters.

While the choice of ν affects the mass–loss rate, it also affects the predicted density structure that is used to calculate the continuum optical depth as a criterion for a solution to the momentum equation. Consider the mass loss for a pulsating star from two different dissipation laws given by ν_1 and ν_2 where $\nu_2 > \nu_1$.

For the power–law ν_1 there is a solution given by a corresponding critical point $r_{c,1}$, which satisfies the Singularity and Regularity condition, Equations 5.9 and 5.10 respectively, as well as predicting a density structure such that the continuum optical depth is 2/3. Using the critical point, $r_{c,1}$, to test the solution for the second dissipation law given by ν_2 produces a smaller mass–loss rate. At that choice of critical point, the velocity v_c is larger than that predicted for ν_1 according to Equation 5.15. Similarly the derivative of the velocity at the critical point is larger than in the case of the first dissipation law. At the star's surface, $r = R_*$, the dissipation law does not play a role, implying the momentum equation and the quantity $v(R_*)v'(R_*)$ is approximately the same for both cases. Hence there are three possibilities for the velocity at the surface: the velocity for the second dissipation law is less than, equal, or greater than the velocity for the first dissipation law. If the velocity given by ν_2 is less, then the velocity derivative at the surface is greater, which causes the velocity as a function of distance from the stellar surface to increase too rapidly and not satisfy the Singularity and Regularity conditions at r_c. If the velocity at the surface for ν_2 is greater than or equal to that in the first case then the density structure given by $\rho \propto \dot{M}/v^2$ is smaller at all distances. The continuum optical depth is less than 2/3 for the second dissipation law and thus the critical point r_c that would satisfy the second dissipation is at a larger distance from the star than the critical point in the first case. The larger value of r_c for the case of ν_2 increases the mass–loss rate and acts to cancel the effect of greater dissipation.

The conclusion of these two sections is the dissipation power law will have a significant effect on density and velocity structure but only a minor effect on the mass–loss rate. The effect on mass loss due to dissipation given by the power law is cancelled by forcing a different value of the critical point to satisfy the requirement that the continuum optical depth of the wind is 2/3. So far, the dissipation exponent ν has been treated as a variable where specific cases have been explored, $\nu = 0, 2, 3$. The results show that ν, while not greatly affecting the mass–loss rate, causes complications regarding the Parker point, r_p, except for the case of $\nu = 2$. Therefore, to avoid those pitfalls, the mass loss of pulsating winds will be treated with the dissipation law given by $\nu = 2$.

5.8 Comparison of Pulsating and Non–Pulsating Winds

It is useful to compare the instantaneous mass–loss rate at some phase of pulsation to the mass–loss rate predicted by only radiative driving in a simple case. In this case, one can consider the region of the wind where $v >> a$, ignoring terms of the order a^2/v^2 and assuming the term $2a^2 r << GM_*(1-\Gamma_e) - \zeta R_*^2$ (again ν is assumed to equal 2). These assumptions still allow the solution to probe most of the subcritical region $r < r_c$ as well as the supercritical region $r > r_c$ to large r (Lamers & Cassinelli, 1999), but does limit the solution from describing the case where the $GM_*(1-\Gamma_e) - \zeta R_*^2 \approx 0$. Thus it is possible to rewrite Equation 5.13 as

$$r_c v_c v_c' \approx \left(\frac{\alpha}{1-\alpha}\right)\left[GM_*(1-\Gamma_e) - \zeta R_*^2\right]. \tag{5.46}$$

If it is assumed that the right hand term, over the range specified, does not vary then $r_c v_c v_c'$ is approximately constant meaning rvv' is constant over that range. Therefore the velocity structure of the wind ejected at some instant can be approximated as

$$v^2 = v_c^2 + 2\left(\frac{\alpha}{1-\alpha}\right)\left[GM_*(1-\Gamma_e) - \zeta R_*^2\right]\left(\frac{1}{r_c} - \frac{1}{r}\right). \tag{5.47}$$

Furthermore the term v_c^2 can be replaced with the approximate form of Equation 5.15, such that the velocity as a function of r is

$$v^2 = \left(\frac{\alpha}{1-\alpha}\right)\left\{\left[\frac{GM_*(1-\Gamma_e)}{r_c} - \frac{\zeta R_*^2}{r_c}\right] + 2\left[GM_*(1-\Gamma_e) - \zeta R_*^2\right]\left(\frac{1}{r_c} - \frac{1}{r}\right)\right\}. \tag{5.48}$$

Rearranging and solving for r_c at the surface $r = R_*$ and taking $v(R_*) \approx a$

$$r_c = \frac{3}{2}R_*\left[1 + \frac{1-\alpha}{\alpha}\frac{a^2}{v_{\rm esc,eff}^2}\right]^{-1} \tag{5.49}$$

where $v_{\rm esc,eff}^2 = GM_*(1-\Gamma_e)/R_* - \zeta R_*$. This result is similar to the solution of the critical radius for radiative driving from Lamers & Cassinelli (1999), except the escape velocity is different.

When the function ζ is greater than zero then the effective escape velocity for the pulsating case is smaller than the escape velocity when there is no pulsation implying r_c in the case of pulsating stars is smaller than the critical point for no pulsation. Therefore in the quasi–static pulsating limit one would expect the wind to have a larger acceleration than in the case of only radiative driving. The instantaneous mass–loss rate in the approximate case, using the assumptions given above with Equation 5.18, is

$$\dot{M} = \left(\frac{\sigma_e L_* k}{4\pi c}\frac{Z}{Z_\odot}(1-\alpha)\right)^{1/\alpha}\left(\frac{4\pi}{\sigma_e v_{th}}\right)\left(\frac{\alpha}{1-\alpha}\right)\left[GM_*(1-\Gamma_e) - \zeta R_*^2\right]^{1-1/\alpha}. \tag{5.50}$$

Relative to the approximate mass–loss rate due to radiative driving only, the ratio of mass–loss rates is

$$\frac{\dot{M}_{\rm puls}}{\dot{M}_{\rm rad}} \approx \left[\frac{\sigma_e(t)}{\bar{\sigma}_e}\right]^{-1+1/\alpha}\left[\frac{L_*(t)}{\bar{L}_*}\right]^{1/\alpha}\left(\frac{v_{\rm th}}{\bar{v}_{\rm th}}\right)^{-1}\left[1 - \frac{\zeta R_*^2}{GM_*(1-\Gamma_e)}\right]^{1-1/\alpha}, \tag{5.51}$$

where the quantities denoted with a bar are time averaged over one period of pulsation. It is interesting to note the instantaneous mass–loss rate scales directly with the variations of luminosity to the power of $1/\alpha$, and the electron scattering opacity to the power $-1+1/\alpha$ and inversely with the square root of the temperature through the thermal velocity. More important is the last term in square brackets containing the ratio of the acceleration due to shocks and pulsation and the effective gravitational acceleration. The exponent $1 - 1/\alpha$ is less than zero as α is of order $1/2$, meaning as ζ becomes larger so will the instantaneous mass–loss rate. Furthermore it is clear when ζ is of order the effective gravity the mass–loss rate goes to infinity; however,

this regime violates the assumption $2a^2 r << GM_*(1-\Gamma_e) - \zeta R_*^2$. Still this does illustrate the non–linear behavior of the mass–loss rate due to the added effects of pulsation and shocks.

5.9 Conclusion

The pulsation–enhanced version of the CAK method for calculating the mass–loss rates and velocity structures of winds around Classical Cepheids is a useful tool for testing the impact of mass loss on the structure and evolution of these stars. The method is also applicable to other radially puslating stars such as RR Lyrae, RV Tauri, and R Coronae Borealis stars, to name a few.

In the next chapters, the pulsation–driven mass–loss theory is applied to samples of observed and theoretical model Cepheids to quantify the importance of mass loss. In Chapter 7 the theory is applied to other pulsating variable stars to explore the propensity of mass loss on the instability strip of the H–R Diagram.

Chapter 6

Predicting Mass–Loss Rates of Galactic Cepheids

This chapter is published as:
"On the Enhancement of Mass Loss in Cepheids Due to Radial Pulsation"
Neilson, H.R., & Lester, J.B. 2008, ApJ, 684, 569[1]

"I think there should be a law of Nature to prevent a star from behaving in this absurd way!" - Sir Arthur Eddington

6.1 Introduction

Having derived a analytic method for predicting mass loss in Cepheids in the previous chapter, we wish to apply it to observed Galactic Cepheids and compare the results to observations of infrared excess and mass–loss rates. The Cepheid instability strip spans a large range of mass, radius and luminosity, so to understand the role of mass loss, it is necessary to have a significant number of Cepheid models and observations. That information can be used to calculate mass–loss rates across the instability strip and probe how mass loss evolves with time. The circumstellar shells that have been observed can be modeled as material from the wind that condenses to dust when the temperature reaches approximately 1500 K, as mentioned by Kervella et al. (2006). The dust would absorb light and re-emit isotropically, some of the radiation is toward the observer and thereby causing a flux excess at near infrared and longer wavelengths.

To calculate mass–loss rates using the modified version of the CAK method, it is necessary to know the following parameters: the radius, amplitude of radius variation, luminosity, amplitude of luminosity variation, mass, and the period, along with the metallicity. Furthermore the values of α and k are needed

[1]Neilson & Lester (2008b), reproduced with permission by the American Astronomical Society

Name	Period(d)	M_V	ΔV	Radius ($R_\odot$)	ΔR/R	Mass ($M_\odot$)	T_{eff}(K)
R TrA	3.388	-2.74	0.561	25.3	0.074	2.4	6470
RT Aur	3.724	-2.86	0.803	35.1	0.103	4.7	5640
BF Oph	4.064	-2.97	0.636	34.5	0.101	3.9	5840
V Vel	4.375	-3.06	0.689	32.8	0.116	3.1	6110
T Vul	4.436	-3.08	0.643	38.2	0.100	4.5	5690
V482 Sco	4.529	-3.11	0.652	44.4	0.103	6.4	5320
S Cru	4.688	-3.15	0.690	42.1	0.108	5.3	5510
AP Sgr	5.058	-3.25	0.832	44.0	0.110	5.3	5510
V350 Sgr	5.152	-3.27	0.705	47.8	0.110	6.3	5320
δ Cep	5.370	-3.32	0.838	41.6	0.116	4.2	5800
V Cen	5.495	-3.35	0.804	45.3	0.119	5.0	5820
Y Sgr	5.768	-3.41	0.725	50.0	0.120	6.0	5370
RV Sco	6.067	-3.47	0.824	47.7	0.102	4.9	5570
S TrA	6.324	-3.53	0.768	39.2	0.106	2.8	6230
AW Per	6.456	-3.55	0.812	47.3	0.118	4.4	5700
BB Sgr	6.637	-3.59	0.597	40.3	0.097	2.8	6230
AT Pup	6.668	-3.59	0.904	45.4	0.120	3.8	5870
V Car	6.699	-3.60	0.601	40.6	0.094	2.8	6220
U Sgr	6.745	-3.61	0.717	51.4	0.115	5.1	5540
V496 Aql	6.808	-3.62	0.349	45.5	0.067	3.7	5900
X Sgr	7.014	-3.66	0.590	49.8	0.093	4.4	5720
U Aql	7.031	-3.66	0.757	54.7	0.116	5.6	5440
η Aql	7.178	-3.69	0.799	54.9	0.121	5.5	5510
W Sgr	7.603	-3.76	0.805	63.3	0.121	7.2	5200
RX Cam	7.907	-3.81	0.729	76.0	0.120	10.8	4770
W Gem	7.907	-3.81	0.822	50.7	0.126	3.9	5840
U Vul	7.998	-3.82	0.718	56.5	0.098	5.0	5550
GH Lup	9.268	-4.01	0.192	58.2	0.040	4.3	5710
S Mus	9.660	-4.06	0.500	71.3	0.109	6.8	5220
S Nor	9.750	-4.07	0.640	66.4	0.119	5.6	5420
β Dor	9.840	-4.08	0.630	64.4	0.118	5.1	5550
ζ Gem	10.139	-4.12	0.480	64.9	0.099	5.0	5590
XX Cen	10.965	-4.22	0.924	57.8	0.140	3.3	6020
RX Aur	11.614	-4.29	0.664	63.4	0.122	3.8	5840
TT Aql	13.740	-4.51	1.082	95.8	0.196	8.5	5020
X Cyg	16.368	-4.73	0.986	118.1	0.216	11.1	4760
Y Oph	17.139	-4.78	0.483	93.5	0.080	5.8	5410
VY Car	19.011	-4.91	1.065	108.9	0.220	7.3	5140
RZ Vel	20.417	-5.00	1.181	111.7	0.243	7.0	5210
T Mon	27.040	-5.36	1.028	130.6	0.230	6.8	5230
l Car	35.563	-5.70	0.725	183.7	0.191	10.7	4780
U Car	38.726	- 5.81	1.165	162.2	0.238	6.9	5200
RS Pup	41.400	-5.90	1.105	197.7	0.246	10.3	4820
SV Vul	44.978	-6.00	1.054	235.5	0.246	14.2	4520

Table 6.1: Data for modeling the mass–loss rate behavior of Cepheids. See text for description and references.

Name	$\dot{M}_{\rm puls}(M_\odot/yr)$	$\dot{M}_{\rm rad}(M_\odot/yr)$	Name	$\dot{M}_{\rm puls}(M_\odot/yr)$	$\dot{M}_{\rm rad}(M_\odot/yr)$
R TrA	4.9×10^{-10}	1.2×10^{-11}	η Aql	1.8×10^{-10}	3.6×10^{-11}
RT Aur	2.3×10^{-8}	7.5×10^{-12}	W Sgr	1.3×10^{-10}	3.0×10^{-11}
BF Oph	5.4×10^{-10}	1.1×10^{-11}	RX Cam	8.4×10^{-11}	2.0×10^{-11}
V Vel	1.3×10^{-8}	1.7×10^{-11}	W Gem	3.0×10^{-10}	6.2×10^{-11}
T Vul	1.3×10^{-10}	1.2×10^{-11}	U Vul	1.3×10^{-10}	4.8×10^{-11}
V482 Sco	1.0×10^{-10}	9.0×10^{-12}	GH Lup	1.4×10^{-10}	8.3×10^{-11}
S Cru	2.1×10^{-10}	1.2×10^{-11}	S Mus	1.4×10^{-10}	5.6×10^{-11}
AP Sgr	1.5×10^{-10}	1.4×10^{-11}	S Nor	2.0×10^{-10}	7.0×10^{-11}
V350 Sgr	1.2×10^{-10}	1.2×10^{-11}	β Dor	2.4×10^{-10}	8.3×10^{-11}
δ Cep	3.6×10^{-10}	2.3×10^{-11}	ζ Gem	2.2×10^{-10}	9.5×10^{-11}
V Cen	1.7×10^{-9}	2.7×10^{-11}	XX Cen	7.3×10^{-10}	1.7×10^{-10}
Y Sgr	1.9×10^{-10}	1.7×10^{-11}	RX Aur	4.6×10^{-10}	1.7×10^{-10}
RV Sco	9.3×10^{-11}	2.4×10^{-11}	TT Aql	8.0×10^{-9}	1.1×10^{-10}
S TrA	2.3×10^{-10}	5.0×10^{-11}	X Cyg	7.7×10^{-8}	1.3×10^{-10}
AW Per	1.8×10^{-10}	3.2×10^{-11}	Y Oph	5.1×10^{-10}	3.0×10^{-10}
BB Sgr	2.1×10^{-10}	5.7×10^{-11}	VY Car	4.7×10^{-9}	2.8×10^{-10}
AT Pup	2.4×10^{-10}	4.1×10^{-11}	RZ Vel	3.7×10^{-8}	3.8×10^{-10}
V Car	2.0×10^{-10}	5.8×10^{-11}	T Mon	5.5×10^{-9}	8.1×10^{-10}
V496 Aql	1.0×10^{-10}	4.5×10^{-11}	l Car	2.4×10^{-9}	9.9×10^{-10}
X Sgr	1.2×10^{-10}	4.1×10^{-11}	U Car	1.0×10^{-8}	2.0×10^{-9}
U Sgr	1.4×10^{-10}	3.1×10^{-11}	RS Pup	6.5×10^{-9}	1.6×10^{-9}
U Aql	1.3×10^{-10}	3.1×10^{-11}	SV Vul	4.8×10^{-9}	1.3×10^{-9}

Table 6.2: Predicted mass–loss rates for Cepheids using shock and pulsation dynamics along radiative driving and assuming only radiative driving.

for radiative driving. These parameters are based on the effective temperature and gravity of the star. For this work the parameters chosen are: $\alpha = 0.465$ and $k = 0.064$ from the analysis of Abbott (1982). These values are used for models with temperatures ranging from 4600 K to 6000 K. There is a lack of parameters calculated at effective temperatures less then 6000 K, but α and k are not likely to vary much since the main elements that drive the mass loss radiatively are iron, neon and calcium as well as contributions from hydrogen and helium remain the same (Lamers & Cassinelli, 1999). Molecules may play a small role as molecular opacities are important in AGB star winds, $T_{\rm eff} \approx 3000$ K (Helling et al., 2000), but they are ignored in this analysis.

The amplitude of the radius variation can be determined by integrating the radial velocity profile over one period. Moskalik & Gorynya (2005) compiled a list of viable interferometric targets and calculated the amplitudes of radius variation. The Cepheids on this list that pulsate in the fundamental mode are used here. Since all of the Cepheids in the sample are galactic stars the metallicity is assumed to be solar, $Z = 0.02$, consistent with the shock model from Fokin et al. (1996). Recently, Asplund et al. (2005) have suggested that the solar metallicity might be $Z_\odot = 0.012$, This downward revision is being questioned because it is incompatible with helioseismology. It is unclear how the lower metallicity would affect the shock structure in

the atmosphere of a Cepheid, although if one increases the hydrogen and helium abundances then the shocks generated in the hydrogen and helium ionization fronts might have more energy. An obvious consequence of a lower metallicity is seen in Equation 5.50, where the mass–loss rate explicitly depends on the metallicity, and would lead to the mass–loss rate at lower Z being $1/3$ the mass–loss rate at $Z = 0.02$. However, it is shown other parameters affect the mass loss more significantly. The radius, luminosity and luminosity variation are found in the David Dunlap Observatory Catalogue of Galactic Classical Cepheids (Fernie et al., 1995). The effective temperature iscalculated from the mean luminosity and radius while the mass is calculated using the Period–Mass–Radius relation from Gieren (1989) and Fricke et al. (1972):

$$M_* = [40P(\text{days})]^{-1.49}(R_*/R_\odot)^{2.53}M_\odot. \tag{6.1}$$

The properties of the observed Cepheids are listed in Table 6.1 and the computed mass–loss rates are listed in Table 6.2.

6.2 The Dependence of Mass Loss on the Wind Boundary Conditions

The first test is to compare the sensitivity of the pulsation mass loss to the value of the critical point, r_c. If the mass loss varies significantly as a function of r_c for a given set of parameters then the predicted mass–loss rate will strongly depend on the criterion that the continuum optical depth of the wind be $2/3$. The continuum optical depth is shown in Figure 6.1 (Left) as a function of the critical point, r_c, for two Cepheids in the sample, l Car and δ Cep at minimum radius. The continuum optical depth varies between 0.1 and 1 over a small range of critical points, for δ Cep the range is approximately $0.5R_*$ and for l Car it is about $1.5R_*$. Over the two ranges of critical points, the mass–loss rates vary only about a factor of 2 and 3 as shown in Figure 6.1 (Right). Therefore, the predicted mass–loss rate of a Cepheid is not sensitive to the criterion requiring the continuum optical depth of the wind to be $2/3$.

6.3 Predictions of Mass–Loss Rates of Observed Cepheids

In this section the predicted mass–loss rates, where the wind is driven by the combination of pulsation and shocks, are presented. As a reference, mass–loss rates for this set of observational data are predicted assuming a static stellar surface and the only driving mechanism is radiative with pulsation terms ignored. In Figure 6.2, the mass–loss rates are plotted as a function of pulsation period. The linear relation in the Log–Log plot is striking, if one considers the equation for mass loss in the CAK method in the approximate case given in Section 2 and ignoring pulsation, then

$$\log \dot{M} \approx \left(1 - \frac{1}{\alpha}\right)\log M_* + \frac{1}{\alpha}\log L - \frac{1}{2}\log T_{\text{eff}} + \text{Const.} \tag{6.2}$$

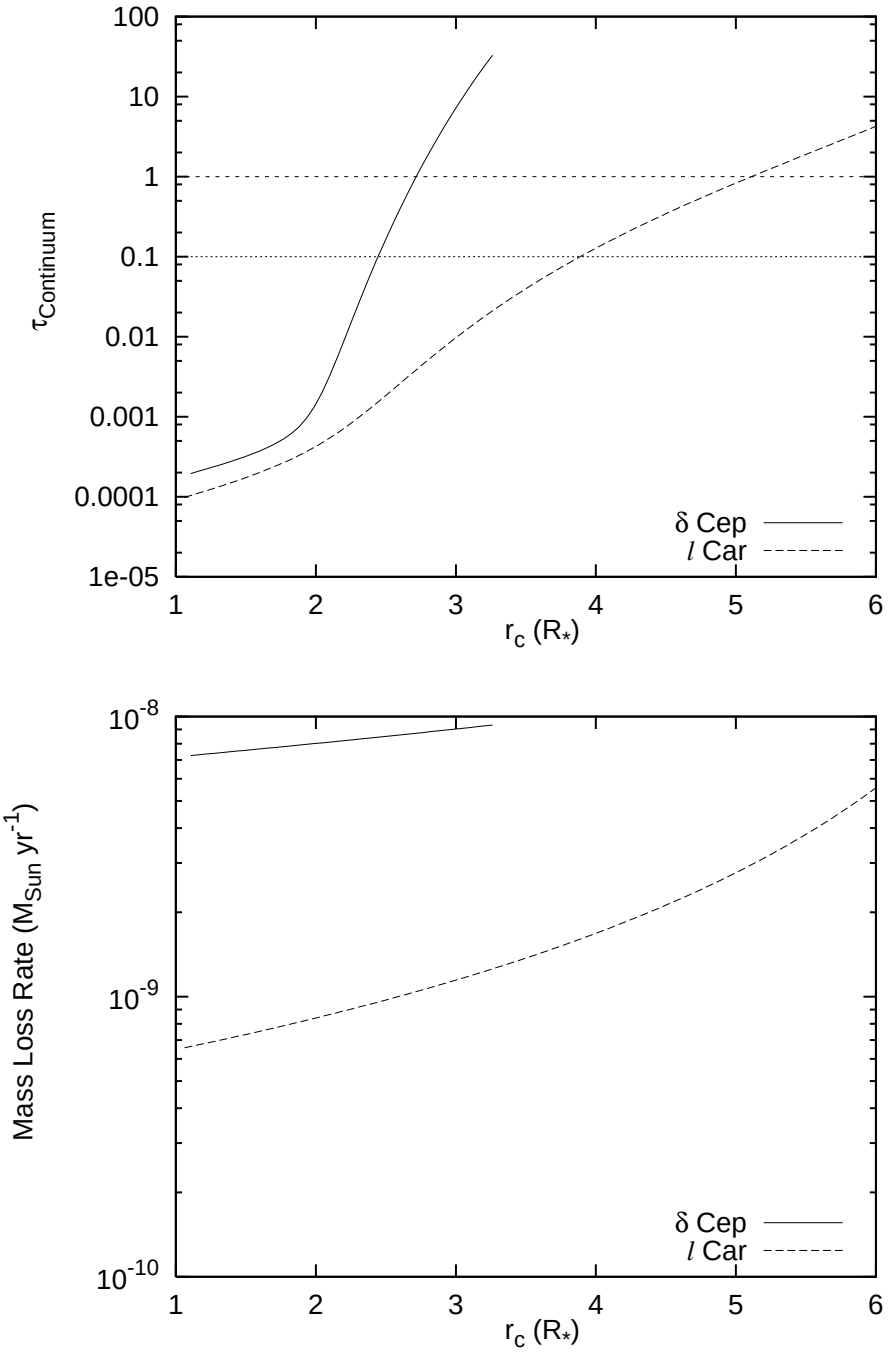

Figure 6.1: (Top) The predicted continuum optical depth of the wind for δ Cep and l Car at minimum radius. The horizontal lines highlight the regime where the τ is of order 2/3. (Bottom) The predicted mass–loss rate for δ Cep and l Car at minimum radius. The rates do not vary significantly with r_c.

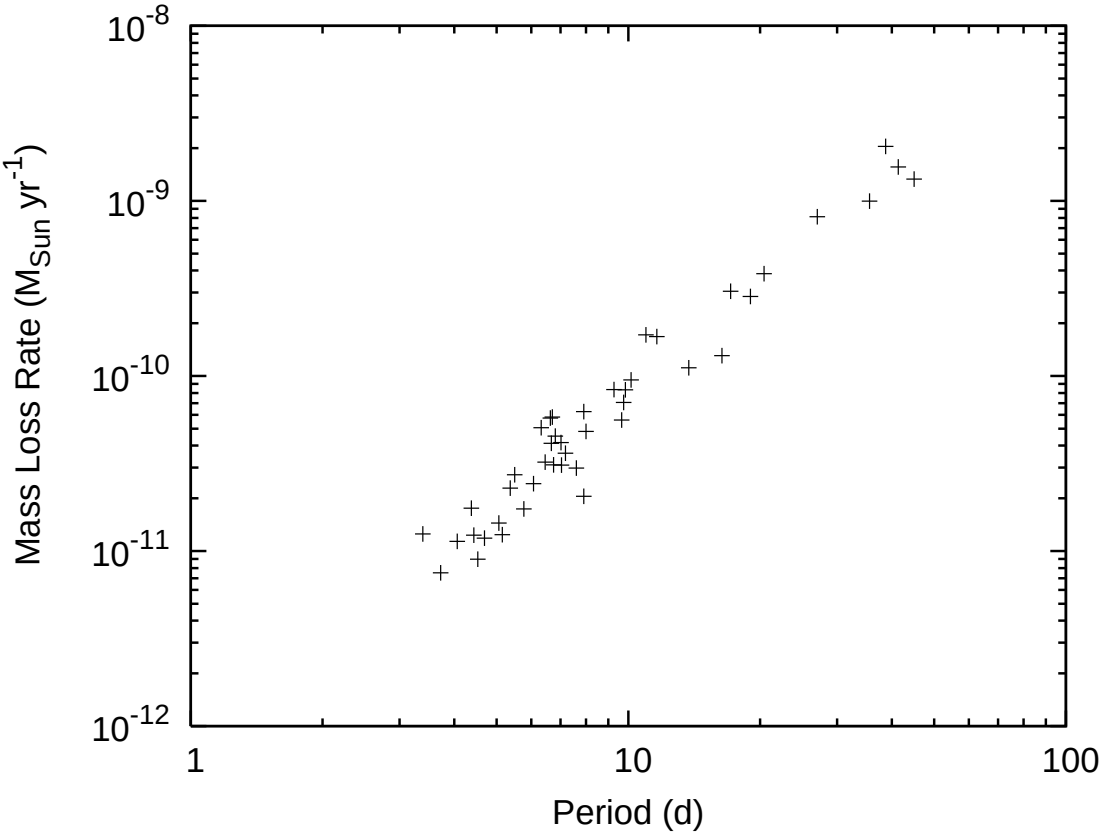

Figure 6.2: The predicted mass–loss rates for Cepheids in the quasi–static approximation using radiative driving as the only mechanism for generating the wind.

The mass can be written in terms of the period and radius via Equation 6.1 and the radius is a function of the effective temperature and luminosity, $R \propto L^{1/2}T^{-2}$. Furthermore the effective temperature can be represented by the color $(B-V)_0$ using the transform from Fry & Carney (1999). The radiative driven mass loss is thus

$$\log \dot{M}_{\rm rad}(M_\odot/yr) = -14.047 + 0.695 \log L(L_\odot) - 0.574(B-V)_0 + 1.71 \log P(d). \tag{6.3}$$

The luminosity can be eliminated using a Period–Luminosity–Color relation from di Benedetto (1995) to obtain an $\dot{M}PC$ relation for the radiative driven mass–loss rates for specific Cepheids,

$$\log \dot{M}_{\rm rad} = -12.11 + 2.69 \log P - 1.16(B-V)_0. \tag{6.4}$$

This relation is for specific Cepheids but to understand the apparent relation of radiative mass loss as a function of period in Figure 6.2, we wish to eliminate the color dependence to derive a statistical representation of the mass–loss rate. Returning to Equation 6.3, the luminosity and the color can be eliminated by using

Period–Luminosity and Period–Color relations from Tammann et al. (2003) yielding

$$\log \dot{M}_{\rm rad} = -12.45 + 2.27 \log P. \tag{6.5}$$

This relation is a theoretical derivation of the radiative driven mass–loss rates for the statistical sample of galactic Cepheids based on best-fit Period–Luminosity and Period–Color relations.

Performing a least squares fit on the predicted radiative driven mass–loss rates as a function of the period as shown in Figure 6.2, one finds

$$\log \dot{M}_{\rm rad}(M_{\odot}/yr) = 2.1 \log P(d) - 12.2. \tag{6.6}$$

The two relations differ but this is to be expected. The derived result ignores the contributions due to continuum radiative driving and assumes that $GM_* >> a^2 r$. The best fit relation will have statistical uncertainties as the majority of the Cepheids examined have periods $P < 10d$. Therefore the best–fit and derived relations for the radiative driven mass–loss rate as a function of period agree and provide a rough lower limit for the mass–loss rates of Cepheids. Furthermore this best–fit relation is equivalent to a Reimer's relation $\dot{M} = \eta L_* R_* / M_*$ (Reimers, 1977), where all quantities are in solar units and time is in years. The standard value is $\eta = 10^{-13}$; for Cepheids this would predict mass–loss rates much larger than found here using the CAK method. Fitting this relation to the radiative driving mass–loss rates determined here, one finds a value of $\eta \approx 4.4 \times 10^{-15}$. Although the η values differ by a factor of 20, the Reimer's relation does not apply to Cepheids.

The second step is to compute the mass–loss rates of Cepheids assuming the contribution from shocks is zero and the wind is accelerated by momentum from pulsation and radiation. The result is shown in Figure 6.3 (Left) where the mass–loss rates due to pulsation but not shocks are plotted alongside the mass–loss rates from radiative driving only. The comparison shows the pulsation does not greatly enhance the mass loss and the result is further highlighted in Figure 6.3 (Right) where the ratio of the two mass–loss rates is also shown. Pulsation does amplify the mass–loss rates but it is a 50% effect at most, which will not produce significant mass loss. The result is not surprising if one considers Equation 5.51 and replaces ζ with just $\omega^2 \Delta R$. Cepheid pulsation can be approximated as a linear perturbation implying the acceleration due to pulsation is much smaller than the gravity of the Cepheid. In that case, the ratio of pulsation mass–loss rates to the radiatively driven mass–loss rates is close to unity. Therefore it is necessary to consider the effect of shocks on the wind.

When the terms describing the shocks and pulsation are included in the calculation, the mass–loss rates change dramatically. This can be seen in Figure 6.4 (Left) where the pulsation mass loss is plotted as a function of period. The mass–loss rates do not follow a simple relation such as a $\dot{M}-P$ relation for radiatively driven mass loss or a Reimer's relation. Some Cepheids have very large mass–loss rates compared to other Cepheids, which can be understood from the approximate version of the mass–loss rate, Equation 6.1. The

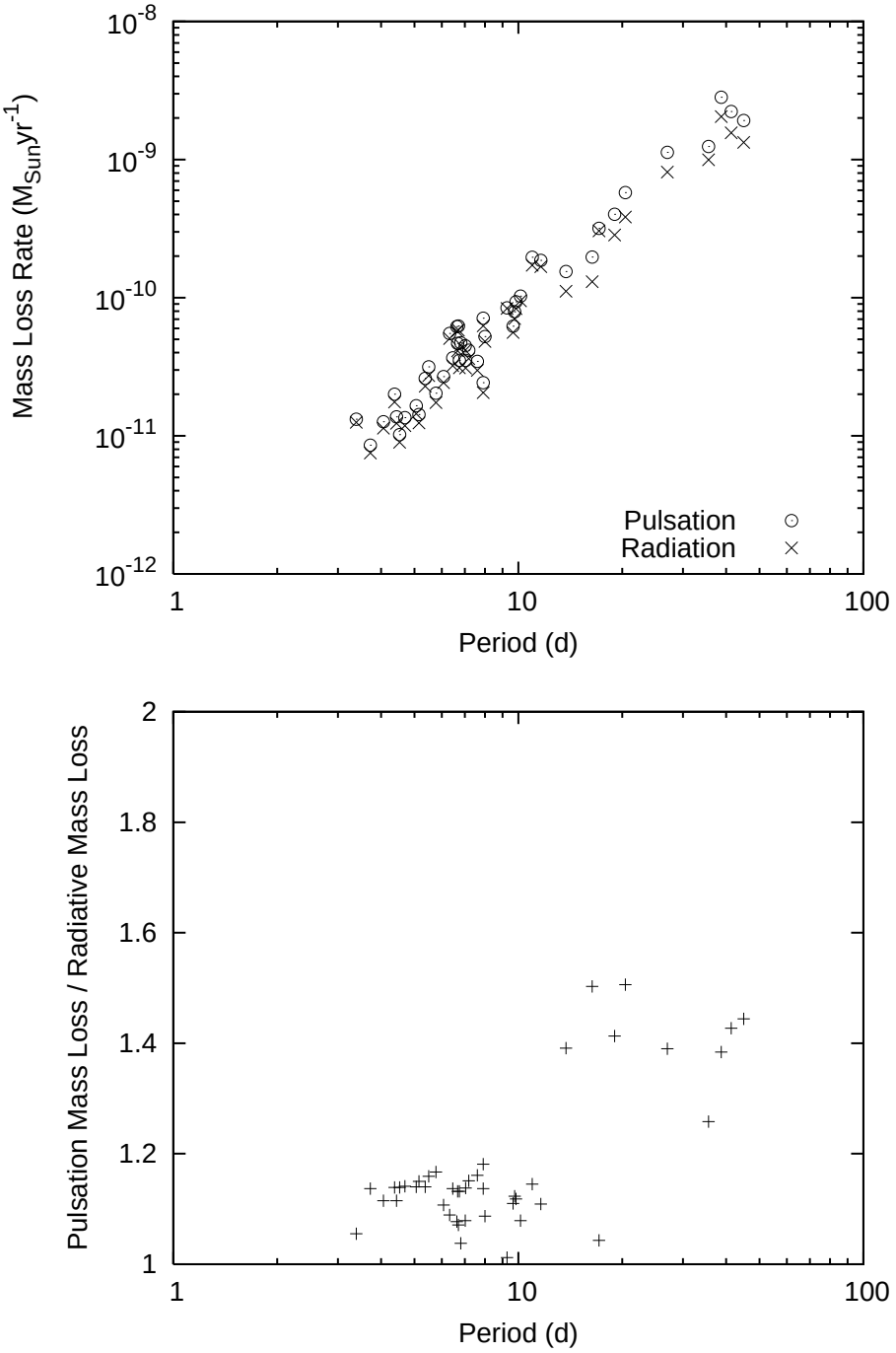

Figure 6.3: (Top) The mass–loss rates for Cepheids using the combination of radiative driving and pulsation but ignoring shocks to generate the wind plotted with the mass–loss rates from only radiative driving for comparison. (Bottom) The ratio of the mass–loss rates computed using pulsation and that using only radiative driving. Accelerating the wind via pulsation does not effect the mass loss significantly by $\lesssim 50\%$. The mass loss is more enhanced for Cepheids with period > 10 days is due to the combination of larger amplitudes of radius variation on average and lower gravity.

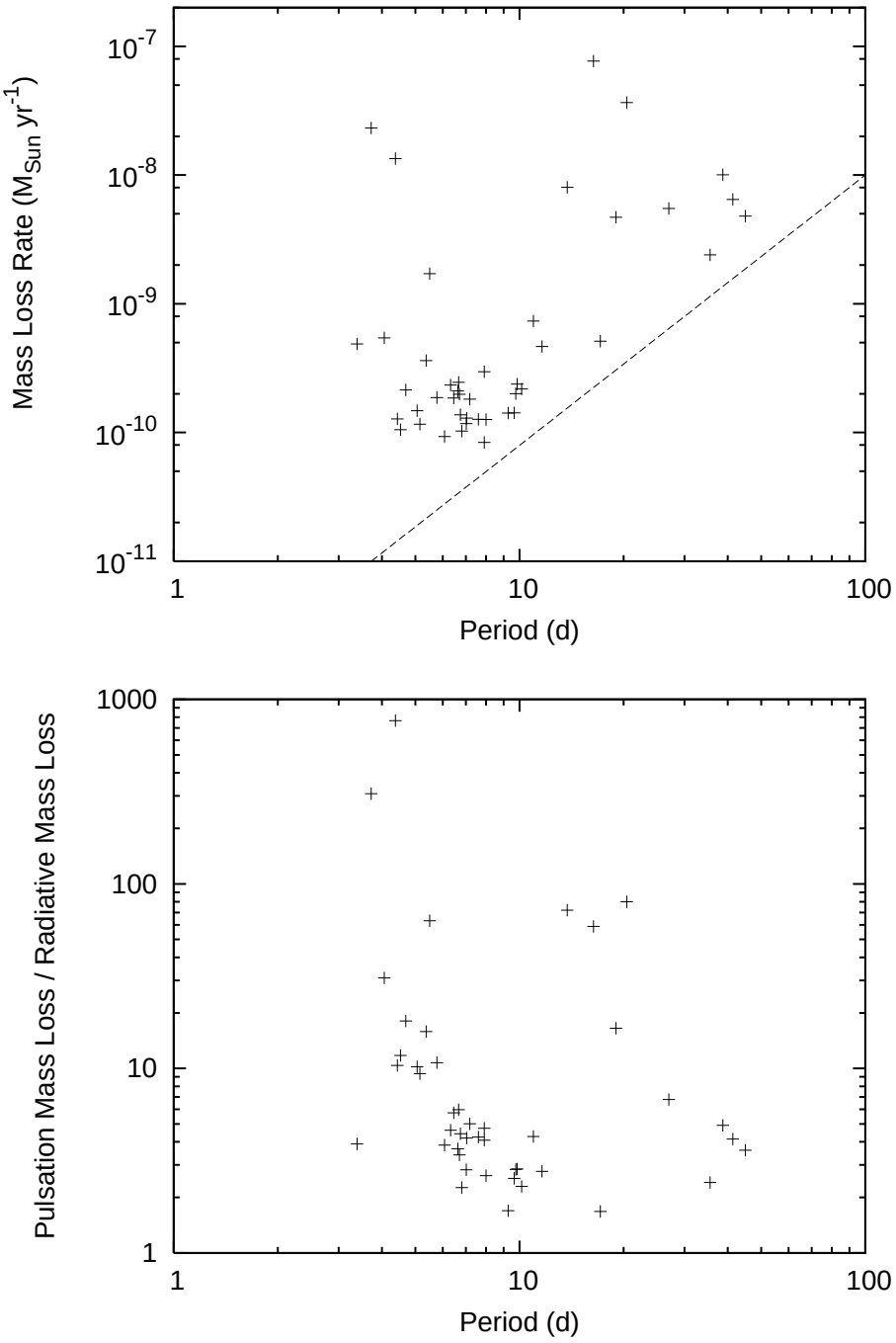

Figure 6.4: (Top) The mass–loss rates for Cepheids using the combination of radiative driving, pulsation and shocks to generate the wind. The dotted line is the least square fit to the radiative driven mass–loss rates shown in Figure 6.2. (Bottom) A comparison of the mass–loss rates computed using pulsation plus shock effects and that using only radiative driving. The wind is strongly enhanced for some Cepheids with the largest enhancement being a factor of approximately 750 and the smallest about 1.7 times.

enhanced mass–loss rate, shown in Figure 6.4 (Right), depends on $(1 - \zeta/g)^{-1}$ if one assumes $\alpha \approx 1/2$, where g is the gravity of the star; the term is maximized when either ζ is large or g is small. The gravity is smallest when the Cepheid is at maximum expansion, $\phi = 0.5$, but the acceleration due to pulsation is at a minimum and the shock amplitude is zero. Therefore ζ at this phase, is acting to decrease the mass–loss rate. The pulsation plus shock function, ζ, is largest at minimum radius where the shock amplitude is large and the acceleration due to pulsation is maximum, meaning both effects contribute. The sum of the two accelerations, which act at similar magnitudes, and the fact that the pulsation depends on the amplitude ΔR implies there is no simple formula for the mass–loss rate.

Only some Cepheids have a dramatic enhancement of mass loss, implying there are restricted regions in the instability strip where Cepheids are more susceptible to lose mass. Figure 6.5 (Left) shows the location of the Cepheids modeled here with the size of the symbols representing the amount of mass loss. The plot shows that larger Cepheids existing in the upper part of instability strip exhibit higher mass–loss rates, as would be expected from the calculations of radiative driving. It is also interesting that the few short period Cepheids with high mass–loss rates are scattered along the effective temperature axis but have consistently lower luminosity, which could be a result of a lower mass and short period contributing to lower gravity and higher pulsation plus shock acceleration respectively. Figure 6.5 (Right) shows the Cepheids on the HR diagram but with the point sizes now representing the amount of mass loss enhancement. The results are striking; there appears to be two bands where the mass loss is enhanced. This may imply the mass loss may be related to which crossing of the instability strip the Cepheid is making.

6.4 Uncertainty Analysis of Modified CAK Method

There are many sources of uncertainty in this analysis. The most important source is the mass for each Cepheid, based on a Period–Mass–Radius relation, which has scatter. Deviations of the mass in the relation to the observed values are important. Consider the Cepheid S Mus, for which a mass of $6.8 M_{\odot}$ is used here; however Evans et al. (2006) find S Mus has a mass of $6.0 \pm 0.4 M_{\odot}$. It is clear from Equation 5.51 that a lower mass will increase the rate of mass loss if all other parameters remain the same. One can test the dependence of the mass–loss rate on the mass of the Cepheid by calculating a set of models with varying mass and holding all other parameters the same. The effect is shown in Figure 6.6 for S Mus, ranging the mass from $5.6 M_{\odot}$ to $6.8 M_{\odot}$. For the larger masses the mass–loss rate is not sensitive to the mass, at $6.8 M_{\odot}$, $\dot{M} = 1.4 \times 10^{-10} M_{\odot}/yr$ and increases by only a factor of five at $6.0 M_{\odot}$. At lower masses, however, the mass–loss rate exhibits a non–linear dependence on the mass increasing by two orders of magnitude from $M = 6.0$ to $M = 5.6 M_{\odot}$. Therefore when the mass–loss rates are large, it is important to have strong constraints on the mass. The analysis also suggests the potential for run-away mass loss, where the mass loss dominates the evolution of the Cepheid. We discuss this possibility is Section 6.7.

The uncertainty in the calculation may be quantified by considering the analytic derivation of the error

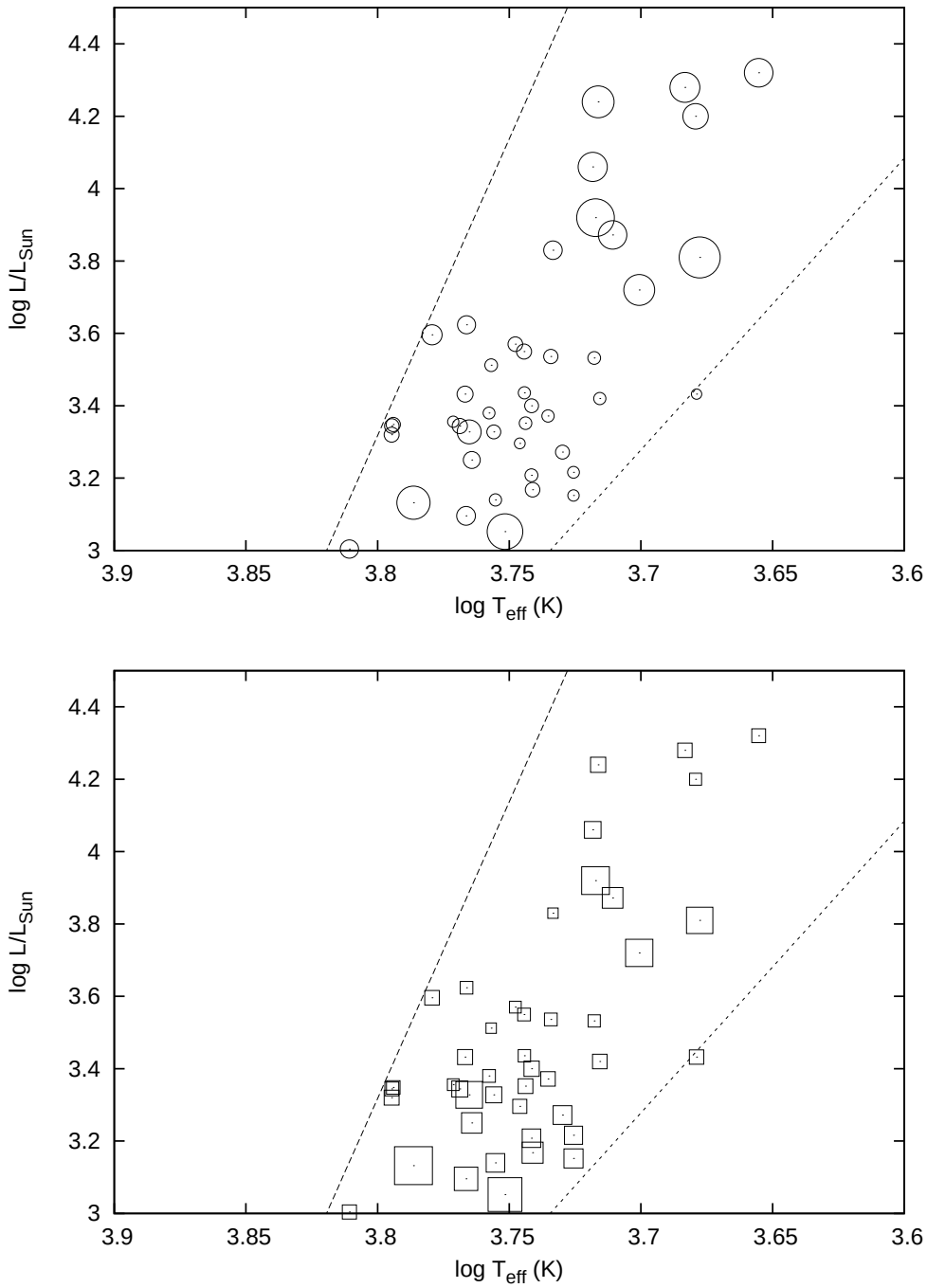

Figure 6.5: The observed Cepheids plotted on a Cepheid instability strip of the HR diagram where the dashed lines represent approximate boundaries. (Top) The size of the circles represent the calculated mass–loss rates for the Cepheids and (Bottom) the size of the squares represent the ratio of the pulsational mass loss and the radiative driven mass loss. All of the brighter Cepheids, $\log L/L_{\odot} \geq 3.7$, have large mass–loss rates, while this is true for only a few of the less bright Cepheids but only a fraction of the luminous Cepheids have their mass loss significantly increased due to pulsation and shocks.

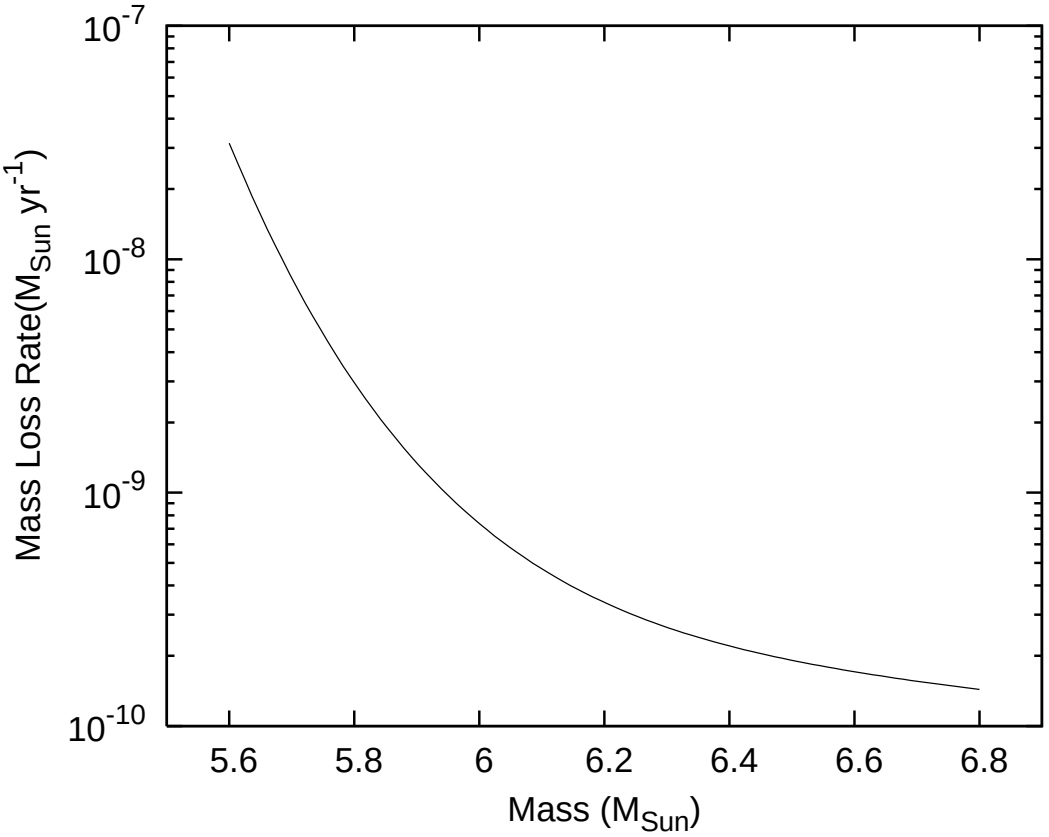

Figure 6.6: The predicted mass–loss rate for S Mus found by holding all necessary parameters describing the Cepheid constant except for the mass, which is allowed to vary.

of the pulsation–driven mass–loss rate based on Equation 5.18, simplified by assuming the quantities $a^2 r_c$ and Γ_e are insignificant. Writing the error as $\Delta F(x_i) = \sqrt{\sum_i (\partial F/\partial x_i)^2 \sigma_{x_i}^2}$ where σ_{x_i} is the error of each quantity,

$$\frac{\sigma_{\dot{M}}}{\dot{M}} = \left[\left(\frac{1}{\alpha L_*} \right)^2 \sigma_L^2 + \left(\frac{1}{2T_{eff}} \right)^2 \sigma_T^2 + \frac{G^2\sigma_M^2 + R_*^4\sigma_\zeta^2 + 4\zeta^2 R_*^2 \sigma_R^2}{(GM_* - \zeta R_*^2)^2} \right]^{1/2} . \tag{6.7}$$

In this equation, it is also assumed that the uncertainty of the period and amplitude of luminosity variation is negligible. The uncertainty of the function ζ is given by

$$\sigma_\zeta = \left\{ [\omega^2 \sigma_{\Delta R}]^2 + \left[\frac{du_\delta}{Pd\phi} \left(\frac{L}{L_\delta} \right)^{1/8} \left(\frac{P}{P_\delta} \right)^{-7/24} \left(\frac{M}{M_\delta} \right)^{5/12} \right]^2 \left[\left(\frac{1}{8} \frac{\sigma_L}{L_*} \right)^2 + \left(\frac{5}{12} \frac{\sigma_M}{M_*} \right)^2 \right] \right\}^{1/2} . \tag{6.8}$$

Upon considering the third term of Equation 6.7, the uncertainty of the mass–loss rate is inversely dependent on the balance of forces $GM_* - \zeta R_*^2$. It was shown in Section 2 that the pulsation driven mass–loss rate is large when the balance of forces is small and likewise $\sigma_{\dot{M}}/\dot{M}$ is also inversely proportional to the balance of forces. This implies that when the mass–loss rate is large due to pulsation and shocks then the error is

Name	$\dot{M}(M_{\odot}/yr)$	Reference
RS Pup	3.5×10^{-6}	Deasy (1988)
l Car	2×10^{-8}	Böhm-Vitense & Love (1994)
R TrA	3×10^{-9}	McAlary & Welch (1986)
S Mus	$< 10^{-9}$	Rodrigues & Böhm-Vitense (1992)
δ Cep	$< 5.5 \times 10^{-9}$	Welch & Duric (1988)
η Aql	$< 6.1 \times 10^{-9}$	Welch & Duric (1988)
T Mon	$< 4.2 \times 10^{-8}$	Welch & Duric (1988)

Table 6.3: The inferred mass–loss rates of various Cepheids from the literature.

even larger. In this case, the uncertainty may be larger by more than an order of magnitude depending on the uncertainty of the mass, radius, luminosity, and amplitude of radius variation. The uncertainty in the effective temperature is not a significant source of error. This implies that the calculation is very sensitive to the values of the parameters used and reiterates the need for more precise values of mass, as well as luminosity and radius.

In this work, the uncertainty of the luminosity is about 10%, the uncertainty of the mass is about 25% to account for the error in the PMR relation, and the uncertainty of the amplitude of variation of radius is about 5% based on the uncertainty of the projection factor (Nardetto et al., 2007). The uncertainty of the effective temperature is $\pm 200K$ while the uncertainty of the radius is calculated from the luminosity and effective temperature errors. The fractional error of the pulsation driven mass–loss rate is shown in Figure 6.7 (Left) as a function of period and the mass–loss rates are plotted as a function of period with error bars in the right panel. This shows that the error of the mass loss is sensitive to the balance of gravity, and the uncertainty of the mass and luminosity has little effect unless they are at least an order of magnitude less. This reiterates the importance of the balance of forces in determining the mass–loss rates. While the uncertainties of the predicted values of the mass–loss rates are large in some cases, the observational determinations of mass–loss rates (as shown in the next section) also have large uncertainties.

6.5 Comparison to Observed Mass–Loss Rates

There have been only a small number of measurements of mass–loss rates for Cepheids. There are two main methods: observing the near and mid–infrared flux excess from dust and using that to determine mass loss, or from emission lines inferring large velocities and particle densities to measure mass loss. The Cepheids with estimated mass–loss rates that are coincident with those used in this work are listed in Table 6.3. By comparing the measurements with the predicted mass–loss rates including pulsation and shocks, it is apparent the predictions are lower than the measured rates by about a factor of 10, except for RS Pup which is a several orders of magnitude different.

For the case of l Car, Böhm-Vitense & Love (1994) used ultraviolet spectra to detect emission lines of

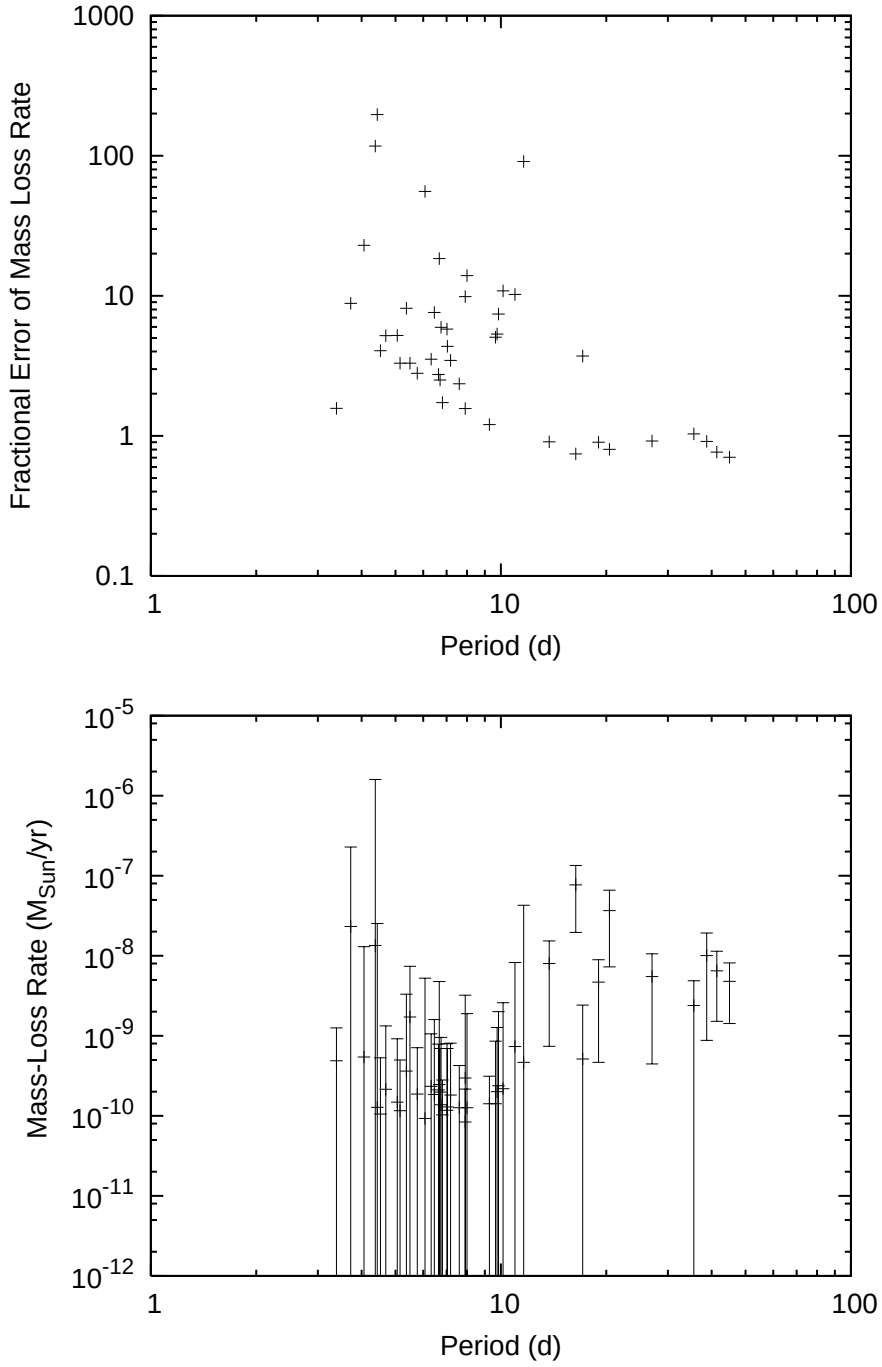

Figure 6.7: (Top) The fractional errors of the pulsation driven mass-loss rates for the sample of galactic Cepheids as a function of period. (Bottom) The mass–loss rates of the Cepheids as a function of period with errors calculated using Equation 6.7 added. The errors appear related to the enhancement of the mass loss due to pulsation and shocks and the plot shows that uncertainty of the mass–loss rate has a similar non–linear behavior as a function of mass as the mass–loss rate which is shown in Figure 6.6.

C II, C IV, Mg II and O I. They argued carbon emission lines provide evidence for mass loss because they require velocities of order 100 km/s to form, which is the same order of magnitude as the escape velocity. The Mg II lines are seen to have two emission components surrounding a broad central absorption profile that is relatively constant with pulsation phase. The width of the central absorption profile of magnesium lines is believed to be a result of circumstellar material or interstellar material or both. Böhm-Vitense & Love (1994) use the velocities inferred from the lines to calculate an optical depth for the absorption shell and thus a column density. The column density depends on the choice of the turbulent velocity, and the uncertainty in the turbulent velocity causes an exponential change in the estimate of the column density; for this reason Böhm-Vitense & Love (1994) argued the mass–loss rate was uncertain by two orders of magnitude. Because Böhm-Vitense & Love (1994) used a value for the turbulent velocity near the lower limit, their mass–loss rate is an upper limit. The mass loss derived by these authors depends also on the distance to l Car, which was taken to be $d = 400\ pc$. However, recent parallax measurements (Benedict et al., 2007) suggest l Car is about 500 pc away, thus lowering this upper limit as well. Given these qualifications, the value of the mass–loss rate predicted here, $2.4 \times 10^{-8} M_{\odot}/yr$, is consistent with the result of Böhm-Vitense & Love (1994).

IUE observations of S Mus (Rodrigues & Böhm-Vitense, 1992) showed features in the absorption profile due to the Cepheid, its B5V companion and possibly the wind from the Cepheid. The authors modeled the line profile by assuming a velocity law for the wind, which they assumed to be spherically symmetric and unperturbed by either pulsation or the companion. Using a β–law for the wind, $v_{\infty}(1 - R_*/r)^{\beta}$, gives a mass–loss rate of approximately $1.1 - 1.3 \times 10^{-10} M_{\odot}/yr$ by fitting the observed absorption profile. Using different velocity laws, such as exponential and power–laws, had a dramatic effect on the mass–loss rate, with the maximum estimate being 2.5×10^5 times larger than the minimum estimate. The result from using the β–law alone is uncertain by a factor of about 6 according to the authors, due to issues of fitting the continuum and the assumed abundances for the system. Therefore the result is an optimistic upper limit. The important conclusion is that our predicted mass loss is small like the observed value, though both may be wrong if the lower limits of the mass determined by Evans et al. (2006) is the true value of the mass as shown in Figure 6.6. The mass–loss rate will still be consistent with that calculated by Rodrigues & Böhm-Vitense (1992).

McAlary & Welch (1986) used IRAS observations to detect Cepheids and found modest infrared excess in several. By assuming the infrared excess is due to dust that formed in a stellar wind, the authors estimated mass–loss rates of the order $10^{-9} - 10^{-8} M_{\odot}/yr$ and worked out the case of R TrA. The calculated mass–loss rate for R TrA is $4 \times 10^{-9} M_{\odot}/yr$, about a factor of 9 greater than that found here. One of the differences in the mass–loss calculation may be due to differences in the choice of stellar radius and temperature, McAlary & Welch (1986) used a larger radius and smaller temperature. A larger radius will affect the calculated density of the shell while the smaller temperature will predict a larger flux excess. Therefore the two estimates for the mass–loss rate of R TrA are probably consistent.

Analysis of IRAS observations was repeated by Deasy (1988) who found mass–loss rates consistent

with the previous work. Furthermore Deasy (1988) derived a mass–loss rate from the geometric structure of the surrounding nebula for RS Pup. The observations of Havlen (1972) showed the reflection nebula was associated with the Cepheid and modeled the nebula as a set of four concentric dust shells, each having a mass of 0.05–0.1$M_{\odot}$. By assuming a velocity for the stellar wind, it is possible to determine a timescale for the shells, but the timescale of the innermost shell is much longer than for the others. This implies the existence of an undetected shell based on the argument the shell timescales are related to the crossing time of a Cepheid on the instability strip. The mass–loss rate is approximated by the dust mass of the shell and the lifetime of the crossing of the instability strip. By assuming a shell mass based on the spacing of shells, the mass of the innermost shell may be overestimated, especially as it has not been detected and the shell is still being generated. Therefore the estimate is a measure of the upper limit of the mass–loss rate.

Welch & Duric (1988) observed a sample of Cepheids at radio wavelengths to measure mass–loss rates. They modeled an ionized wind at temperatures of order 10^4–10^5 K. The mass–loss rate is not sensitive to this assumption. The authors also assume a wind velocity of order 100 km/s, which is not necessarily true. The value is chosen because the observed components of the wind must exist at a radius greater than $4R_*$, meaning a lower wind velocity can be used if the components are older and have moved a further distance from the star. There is also systematic uncertainty about the choice of distances to these Cepheids; parallax measurements indicate a difference of order 20–30% (Feast & Catchpole, 1997; Benedict et al., 2002, 2007). The mass–loss rates are consistent, although the model devised by Welch & Duric (1988) is different than the one used here.

The main conclusion to be drawn from these observed mass–loss rates is they are upper limits, with large uncertainties. These upper limits are orders of magnitude larger than the predicted mass–loss rates derived by assuming only radiative–driving, implying there must be additional driving forces, lending credence to the pulsation + shock mechanism described in this work.

6.6 Model Infrared Excess

The works of McAlary & Welch (1986) and Deasy (1988) both discuss the infrared flux excess of Cepheids in the IRAS bands. Kervella et al. (2006) and Mérand et al. (2006, 2007) discovered excess K–band flux using interferometry, and Evans et al. (2007) discuss using the Spitzer Space Telescope to search for IR excess. Predictions of infrared excess provide a useful test of the mechanism for mass loss in Cepheids.

Infrared excess can be produced in two distinct ways: by hot ionized winds or by cool dusty winds. Since the wind model in this work assumes it is driven by mechanical energy, the wind is not hot so a dusty wind is presumed. The wind is in radiative equilibrium with the Cepheid, so the temperature is dependent on the stellar temperature and is inversely proportional to the square of the distance from the star. Dust forms in the wind when the temperature is near 1500 K, the condensation temperature for dust. Following the discussion from Lamers & Cassinelli (1999) for the luminosity of an optically thin dusty wind, one can

Name	Observed CSE %	Predicted CSE %
δ Cep	1.5 ± 0.4	1.3
l Car	4.2 ± 0.2	1.9
Y Oph	5.0 ± 2.0	0.95

Table 6.4: The flux of circumstellar shells of Cepheids relative to the total flux observed using K–band interferometry compared to the predicted flux of circumstellar shells.

represent the temperature structure as

$$T(r) = T_{\rm eff}\left(\frac{2r}{R_*}\right)^{-2/5}. \tag{6.9}$$

By rearranging, one can determine the condensation radius: for δ Cep this is about $14.7R_*$, while for the coolest Cepheid in the sample, SV Vul, the condensation radius is about $7.9R_*$.

To calculate the dust luminosity, it is assumed that the dust is forming far enough from the star that pulsation and shocks will not affect the structure. From the above calculation, however, this is not an ideal assumption, at least in the inner edge of the dust shell. The total luminosity of the dust at a given frequency is derived by Lamers & Cassinelli (1999),

$$L_\nu = \frac{3}{4\pi}\frac{<a^2>}{<a^3>}\frac{1}{\bar{\rho}_d}\frac{\dot{M}_d}{v_d}Q_\nu^A\int_{r_{\rm min}}^{r_{\rm max}} B_\nu(T_d)\left\{1-\frac{1}{2}\left(1-\sqrt{1-(R_*/r)^2}\right)\right\}dr. \tag{6.10}$$

where the quantities with a subscript d refer to dust. The terms in this expression are evaluated in the following way. The dust is assumed to be graphite with $\rho_d = 2.2 g/cm^3$. The mass–loss rate of dust is one–hundredth of the total mass–loss rate, based on the galactic gas–to–dust mass ratio. Inside the condensation radius the value of $\dot{M}_d$ is zero. The velocity, v_d, is the velocity of the wind at the distances from the star being considered. The value of v_d that is used is the mean terminal velocity of the wind averaged over one period of pulsation. To simplify the integration, $r_{\rm min} = R_*$ and $r_{\rm max} = \infty$; if the velocity is 100 km/s then the wind would travel a distance of order 100 pc in one million years. The dust will contribute to the infrared excess only at a much smaller distance, so the assumption is reasonable. The dust is assumed to have a grain size distribution as given by Mathis et al. (1977), where the number density is $n(a)da \propto Ka^{-3.5}da$. If the grain size ranges from 0.005 μm to 0.25 μm, then the term $< a^2 > / < a^3 >$ is $\approx 40\ \mu m^{-1}$. The absorption efficiency, Q_ν^A, is based on the argument that most of the dust absorption will be at optical wavelengths and will be of order 2 (Jones & Merrill, 1976). Using these values, Equation 6.10 can be used to predict the luminosity of the dust shell in the infrared wavelengths of the VLTI, CHARA, IRAS and Spitzer.

The infrared excess found from interferometric observations of Cepheids is summarized by Mérand et al. (2007), where the authors list the fraction of the total flux contributed by circumstellar shells, defined as the circumstellar emission (CSE) flux. The results for the fundamental pulsating Cepheids are shown in Table 6.4. The non–pulsating supergiant α Per was observed as well and was found to have almost no contribution to the 2.2 μm flux due to circumstellar material. The infrared excess due to the predicted mass loss for

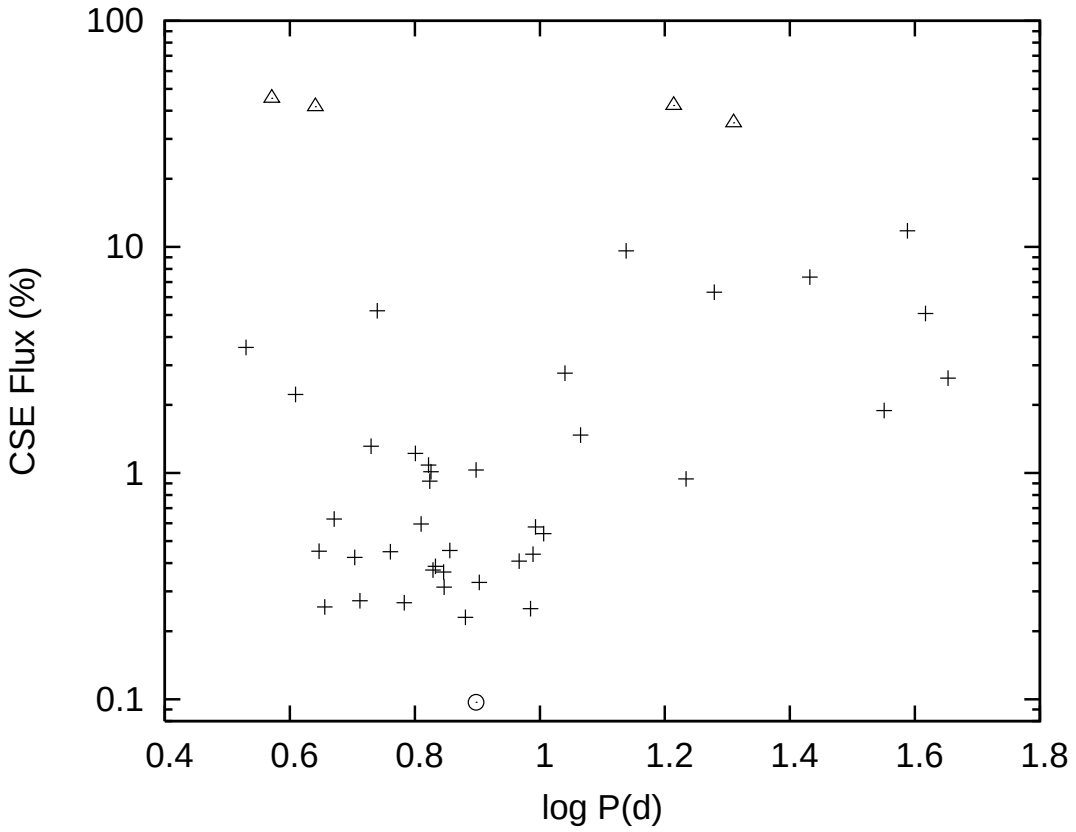

Figure 6.8: The predicted fraction of the total luminosity of a Cepheid contributed by the presence of dust at 2.2 μm. The circle represents the example of the smallest predicted circumstellar emission (CSE) flux, RX Cam, and the triangles represent RT Aur, V Vel, X Cyg and RZ Vel which have the largest predict CSE fluxes of the sample.

the sample of Cepheids at 2.2 μm is shown in Figure 6.8, and the predicted CSE fluxes for the Cepheids observed with interferometry are given in Table 6.4 for comparison. These predictions are of the same order of magnitude as the observed, and differences may be due to the parameters in the dust model. The CSE flux is linearly dependent on the ratio $< a^2 > / < a^3 >$, the mass–loss rate of dust, terminal velocity, grain density, etc.; a small change of any of these parameters will change the prediction. The predicted CSE flux is most different for the cases of Y Oph and *l* Car, which could be related to the uncertainty of the inner radius of the dust shell or to the predicted mass–loss rates being underestimated for these two Cepheids; an increase of the mass–loss rate by a factor of 4 and 2 respectively would match the observations. In the enhanced CAK method this would require a decrease of chosen stellar mass of order of 1 to $1.5 M_{\odot}$ or an increase of stellar radius of order 7–$15 R_{\odot}$, or some combination of the two, both of which are within the range of observational uncertainty. All things considered, the dust model is a consistent fit to the observations and the difference between the predicted and observed CSE is small. The predicted CSE fluxes of the sample Cepheids span a significant range, 0% to 50%, due to the combination of the fundamental parameters. This prediction can

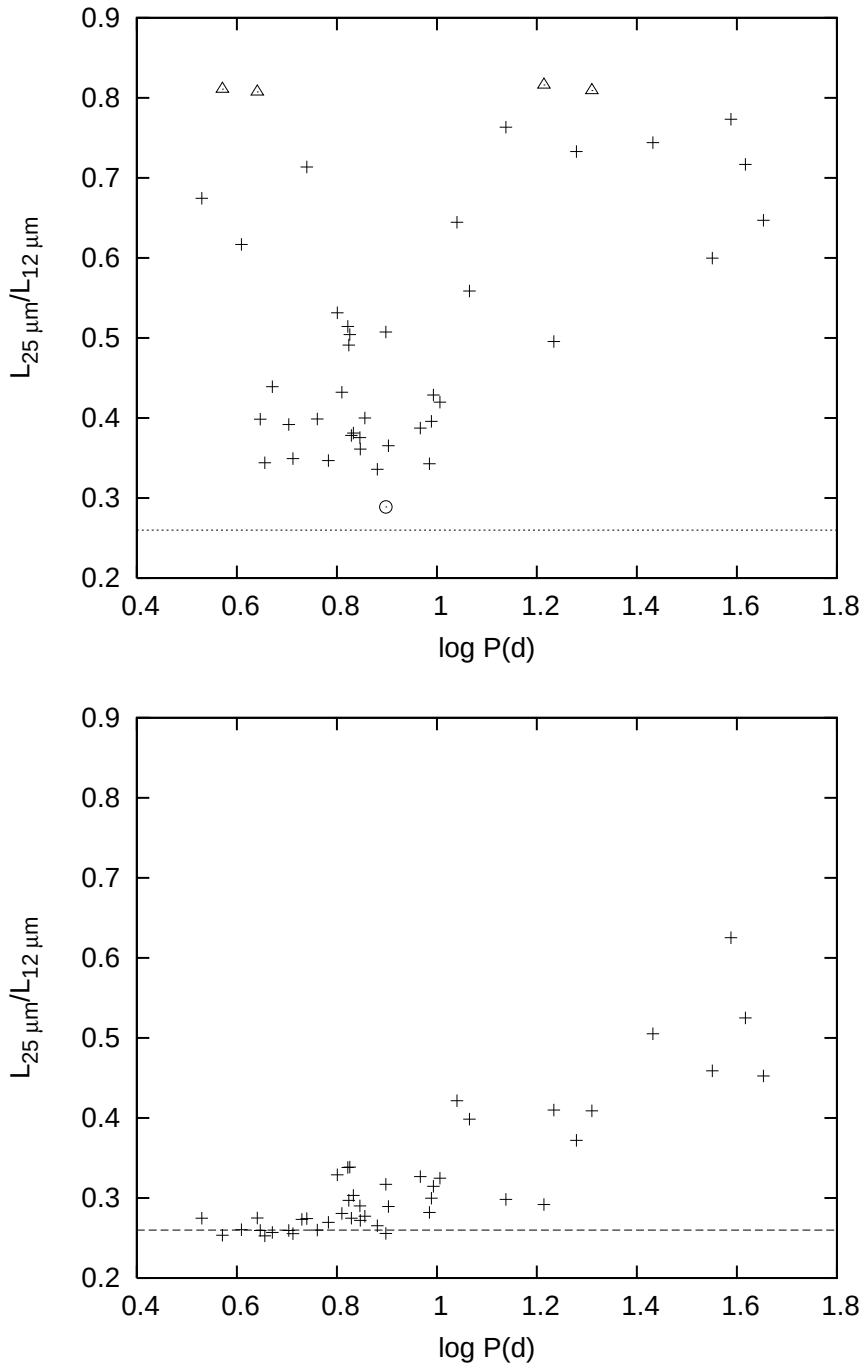

Figure 6.9: (Top) The ratio of the luminosity of the wind at 25 μm and 12 μm based on the predicted pulsation mass–loss rates. The ratio of the luminosity at these wavelengths is about 0.26 when there is no infrared excess, represented by the dashed line. The Cepheid, RX Cam, is represented by the circle at $\log P \approx 0.9$ with the smallest infrared excess of the sample. The triangles represent the largest predicted flux excess for the Cepheids for RT Aur, V Vel, X Cyg and RZ Vel. (Bottom) The ratio of the luminosity of the wind at 25 μm and 12 μm for the predicted mass–loss rates based on radiative driving alone. The ratio of the luminosity at these wavelengths is about 0.26 when there is no infrared excess, represented by the dashed line.

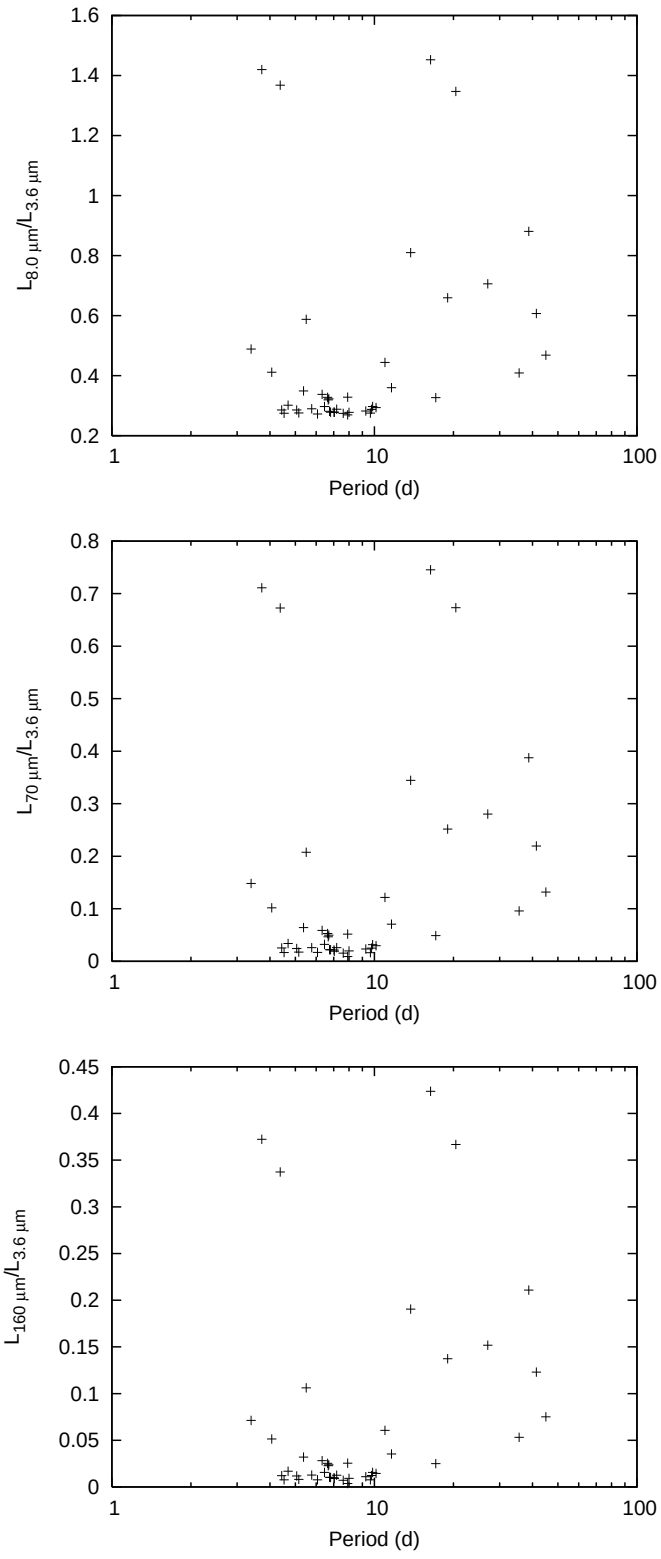

Figure 6.10: The ratio of the predicted luminosity at 8.0 μm (Top), 70 μm (Middle), and 160 μm (Bottom) relative to the predicted 3.6 μm luminosity of the sample of Cepheids.

be tested.

The IRAS observations provide fluxes in its four bands for a large sample of Cepheids. Deasy (1988) found the ratio of $F(25\ \mu m)/F(12\ \mu m)$ ranges from roughly 0.25 to 0.8. The lower end is the expected ratio from just blackbody radiation with no excess radiation (Figure 1 of that paper). The ratio of the infrared excesses from the predicted mass–loss rates is given in Figure 6.9 (Left). It is striking that the ratio of fluxes exhibit the same range of values as in Deasy (1988). This agreement is encouraging as the luminosity of the dust at these two wavelengths is much less sensitive to the dust parameters, and the contributing dust is much farther from the inner boundary of the dust shell. The infrared excess predicted for just radiative driven mass loss is shown in Figure 6.9 (Right), where the maximum excess is significantly less than that predicted for pulsation plus shock driven mass loss, and this prediction does not agree with the range of infrared excesses found by Deasy (1988). This is further evidence that mass loss in Cepheids is driven by pulsation and not just radiation. Note there appears to be a minimum in the flux ratio in Figure 6.9 (Left) near $\log P \approx 0.9$, which corresponds to $\log L/L_{\odot} \approx 3.5$; this reflects the lack of mass–loss enhancement due to pulsation at that luminosity, which is consistent with the behavior as shown in Figure 6.5.

Figures 6.8 and 6.9 (Left) show that the mass–loss rates and dust model can reproduce the existing interferometric and IRAS observations, but the Spitzer Space Telescope can now provide new results. Therefore it is useful to predict the infrared excess at wavelengths observed by Spitzer. The luminosity of the Cepheids with dust shells are plotted in Figure 6.10, relative to the 3.6 μm luminosity, at wavelengths 8, 70, and 160 μm, respectively. The combination of the four wavelengths provide a test of mass–loss enhancement. At 8 μm, the excess is due to mass loss being enhanced by both pulsation and shocks and radiative driving at longer periods. This would provide a test for the period dependence of mass loss. Observations at the longer wavelengths provide a measure of smaller mass–loss rates because fluxes at these wavelengths are in the tail end of the stellar blackbody function as well as a measure of the size of the circumstellar shell.

There are extreme values of the predicted flux excess; from Figures 6.9 (Left) and 6.10 it is clear one Cepheid, at period $\log P = 0.9$, has minimal flux excess shown as a circle in the figures. This is the model for RX Cam, where the predicted mass–loss rate is 8.4×10^{-11}, which is most likely due to the estimate of the mass $M = 10.8 M_{\odot}$. The infrared excess and mass–loss rate may easily be underestimated, but the result does show it is possible for Cepheids to have a low infrared excess similar to non–pulsating yellow supergiants. On the other hand, there are a number of Cepheids predicted to have very large IR excess, where the dust luminosity contributes most of the total luminosity at that wavelength. From Figure 6.9 (Left), there are four Cepheids with a CSE flux of order 50%: the short–period Cepheids RT Aur and V Vel and the 10–20 day period Cepheids X Cyg and RZ Vel. The two short period Cepheids have a large enhancement of mass loss, both by almost 10^3 times and hence the infrared excess is large. The same is true for the longer period Cepheids but to a lesser extent. It is unlikely the excesses are overestimated, if it is assumed the mass–loss rates are reasonable. Both V Vel and RT Aur have large effective temperatures for Cepheids, meaning the condensation radius is significantly large that it is not affected by the pulsation and shocks, supporting the

predicted results. In all, the dust model discussed implies the measured infrared excesses and CSE fluxes can have a very large range, making it more challenging to use near–IR interferometry for distance estimates.

6.7 Mass Loss and Period Change

The rate of period change of a Cepheid is a measure of its evolution on the instability strip due to the rate of change of effective temperature and luminosity or equivalently the change of radius and luminosity. The period change of Cepheids has been investigated by Turner et al. (2006) where the period change is

$$\frac{\dot{P}}{P} = \frac{6}{7}\frac{\dot{L}_*}{L_*} - \frac{24}{7}\frac{\dot{T}_{\rm eff}}{T_{\rm eff}} \tag{6.11}$$

based on the Period–Mean Density relation and the small period dependence of the pulsation constant $Q \propto P^{1/8}$ (Fernie, 1967). This relation assumes the mass of the Cepheid is constant with respect to time. Starting with the Period–Mean Density relation, the period change can be re–derived to include mass loss,

$$\frac{7}{8}\frac{\dot{P}}{P} + \frac{1}{2}\frac{\dot{M}_*}{M_*} - \frac{3}{2}\frac{\dot{R}_*}{R_*} = 0. \tag{6.12}$$

Substituting the luminosity and effective temperature for the radius for comparison to the result of Turner et al. (2006), this relation becomes

$$\frac{\dot{P}}{P} = -\frac{4}{7}\frac{\dot{M}}{M_*} + \frac{6}{7}\frac{\dot{L}_*}{L_*} - \frac{24}{7}\frac{\dot{T}_{\rm eff}}{T_{\rm eff}}. \tag{6.13}$$

This new relation implies the change of period is due to both evolution and mass loss. We have substituted the mass-loss rate of the wind, $\dot{M}$ for the star's moss-loss rate, $\dot{M}_*$ in this relation. Because the change of mass of a Cepheid is negative, the mass loss will always act to increase the period of pulsation.

The comparison of the observed and theoretical period change of Cepheids by Turner et al. (2006) showed models provide a reasonable fit to the observations overall. There are, however, exceptions; one is the large number of Cepheids with a negative period change that is smaller in magnitude than that predicted by the models. This difference also appears in the comparison of positive period change but the difference is smaller. It is likely the models overestimate the rate of evolution, but a lower absolute rate of period change on the second crossing of the instability strip could be related to mass loss, which would increase the period change. The role of mass loss on period change can be tested by plotting the fractional difference $(\dot{P}/P - 4\dot{M}/7M)/(\dot{P}/P)$ as a function of the fractional period change. Observed values of the period change for some of the sample of Cepheids are given in Table 6.5 taken from the literature (Fernie, 1993; Turner et al., 1999; Berdnikov & Ignatova, 2000; Turner & Berdnikov, 2004; Turner et al., 2005) and the comparison is shown in Figure 6.11. Mass loss is a contributing factor to those Cepheids where the fractional difference is different from unity. From Figure 6.11, there are only two Cepheids where the mass–loss rate would

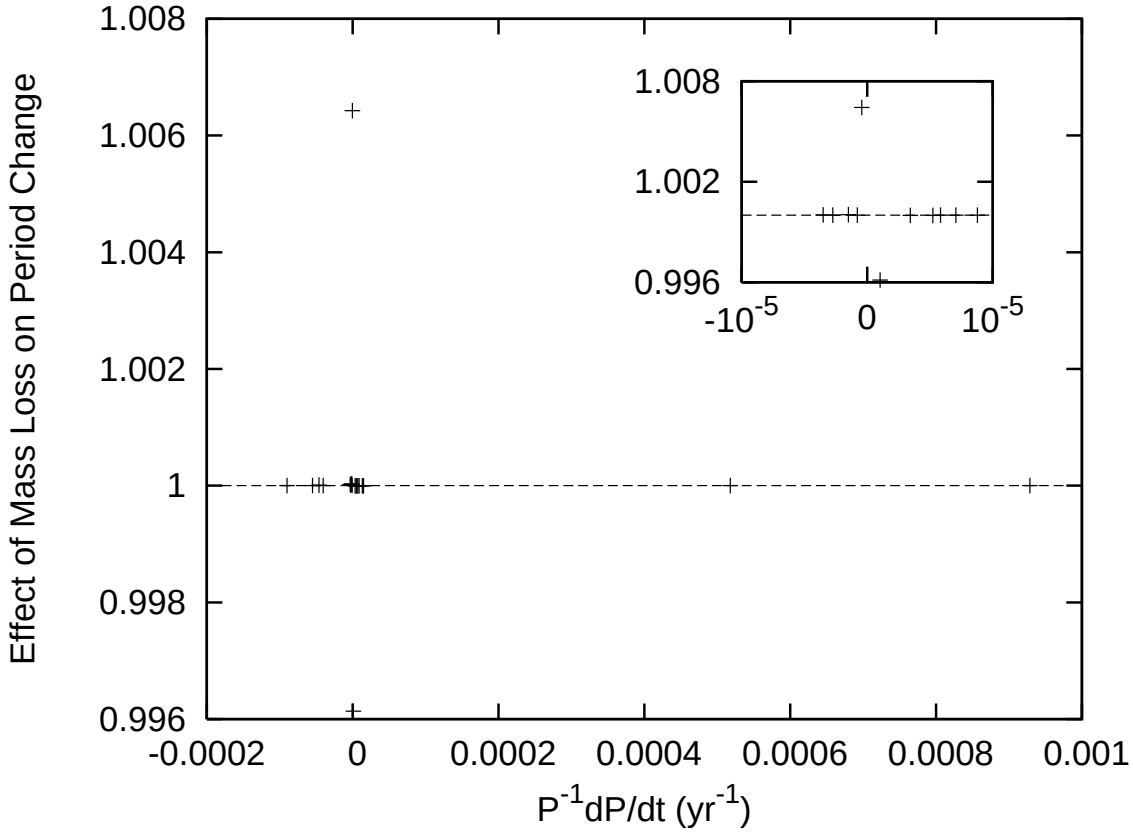

Figure 6.11: The fractional contribution of mass loss towards the period change for Cepheids as a function of period change. Cepheids with a period change not affected by the mass–loss rate would fall on the dashed line. Deviations from the dashed line measure how much mass loss plays a role.

affect the period change of order 1%, X Cyg and RT Aur; both of which have large mass–loss rates and small rates of period change. For the case of RT Aur, it should be noted the rate of period change was recently determined to be $\dot{P} = 0.082\ s/yr$ implying the Cepheid is on its third crossing of the instability strip (Turner et al., 2007). This new result differs from the rate of period change used here, $\dot{P} = -0.14\ s/yr$, but the magnitude of period change is still small, and mass loss will still contribute to the rate of period change. It can be inferred that mass loss does not play a significant role in changing their periods, complementing the result of Turner et al. (2006).

The large mass–loss rates correlate to the minimal absolute period change of Cepheids. This point is emphasized in Figure 6.12, where the enhancement of the mass loss by shocks plus pulsation is plotted against $\dot{P}/P$. This implies mass loss is most enhanced when the Cepheid is evolving slowly through the instability strip. This correlation can be produced in several ways. For example, when the mass–loss rate is large one might expect the radius of the Cepheid to be large, causing the gravity to be lower. A larger radius would also correspond to a larger luminosity, and a larger luminosity would mean a lower rate of period

Name	$\dot{P}(s/yr)$	Name	$\dot{P}(s/yr)$
U Aql	4.29	Y Oph	766.82
η Aql	3.24	BF Oph	−1.23
RT Aur	−0.14	V350 Sgr	1.53
VY Car	−75.92	U Sgr	5.11
δ Cep	−0.7	W Sgr	3.84
X Cyg	1.45	X Sgr	7.96
β Dor	12.83	R TrA	0.23
ζ Gem	−78.88	T Vul	1.05
W Gem	−27.66	SV Vul	−214.3
T Mon	2169.72		

Table 6.5: The rate of period change for some Cepheids with modeled mass loss.

change according to Equation 6.13. Another way to get a small period change is for the Cepheid to be at the blue edge of the instability strip where both the temperature and luminosity are largest for that crossing, meaning the ratios $\dot{T}_{\rm eff}/T_{\rm eff}$ and $\dot{L}_*/L_*$ are small. At that point in the instability strip, the period is smallest, increasing the acceleration of gas due to both shocks and pulsation, which could increase the mass–loss rate. The first explanation is seen in Figure 6.5 for the Cepheids with large mass–loss rates, but there are no examples of the second explanation. The fact that there are few Cepheids from the sample evolving near the blue edge may account for this as well as the possibility mass loss may only be extreme very early upon entering the instability strip, making it very unlikely to catch one in the process.

The minimal role of mass loss upon the period change implies the period change is primarily due to evolution. Near the blue edge of the instability strip the rate of evolution slows as the fractional change of luminosity and temperature is small. Also near the blue edge, one might expect the mass–loss rate to be large because the period is lower, causing the acceleration due to pulsation and shocks to be larger. For Cepheids on the second crossing, the rate of period change is $\dot{P} < 0$, but near the blue edge of the crossing, mass loss will tend to decrease the absolute value of the rate of period change, and potentially even manage to change the sign of the rate of period change. This can be tested by considering a sample of Cepheids where the period change is small and consistent with third crossing; the Cepheid X Cyg is likely on its third crossing with $\dot{P} = 1.52\ s/yr$. For X Cyg to be on its second crossing its mass–loss rate would need to be $\dot{M} \geq 2.1 \times 10^{-5} M_\odot/yr$; much too large, in the range observed for Wolf–Rayet stars. The Cepheid SX Car is another Cepheid consistent with being on the third crossing (Turner et al., 2005), with $\dot{P} = 0.07\ s/yr$, period of 4.86 days and an inferred upper mass limit of $5.7 M_\odot$ (Turner, 1996). This would require of minimum mass–loss rate of $\dot{M} = 1.67 \times 10^{-6} M_\odot/yr$, which is an order of magnitude larger than the limit seen in Figure 6.4. It has been shown that it is possible for mass loss to significantly affect the rate of period change at certain parts of the instability strip.

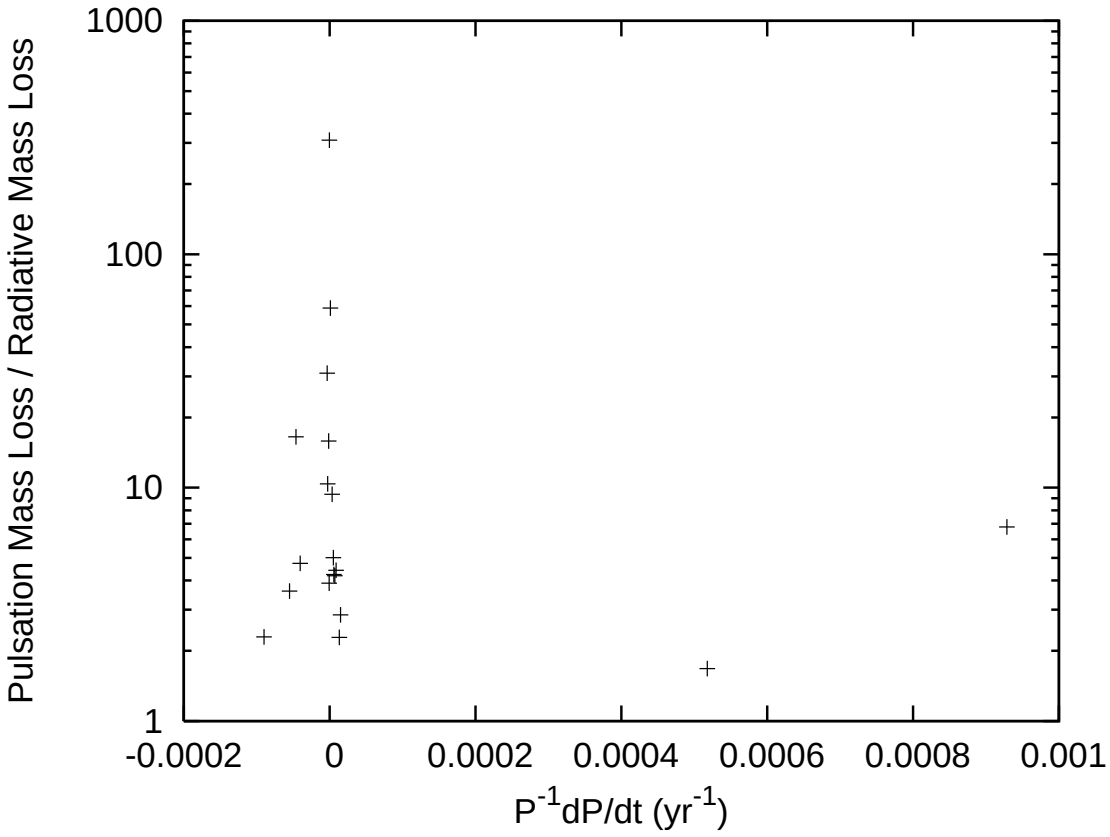

Figure 6.12: The enhancement of the mass loss, the ratio of the shock/pulsation mass loss and the mass loss from radiative driving, as a function of the period change $\dot{P}/P$.

6.8 Conclusions

In this study, an analytic method is presented to describe the mass–loss rates of Cepheids using as input the global parameters that describe a Cepheid. The derivation is based on the method for solving radiatively driven winds with additional energy supplied by shocks and pulsation. It is assumed the wind is spherically symmetric, quasi–static and uses the Sobolev approximation. The limits of the derivation are explored where in the simplest case the mass–loss rate is dependent on the ratio of the pulsation plus shocks and the effective gravity. It is shown mass loss can be enhanced by up to three orders of magnitude.

The analytic method was tested using a set of Cepheids for which the necessary global parameters are given in the literature. For reference, the mass–loss rates, based on only radiative driving, were also calculated. The energy added from pulsation and shocks increases the mass–loss rates, in some cases by orders of magnitude, predicting rates in closer agreement with those inferred from observations. Furthermore the mass–loss behavior of Cepheids as a function of period is described, where the long period Cepheids have mass loss dominated by radiative driving but the short period Cepheids have a large range of mass–loss

rates. The large range of values implies the mass loss for short period Cepheids depend on the evolutionary state of the Cepheid.

The model provides reasonable estimates of mass–loss rates of Cepheids but there are uncertainties. The mass is the largest uncertainty, as it is difficult to measure in general, so a Period–Mass–Radius relation is used. The value of the radius also has an impact; the larger the radius, the lower the gravity and hence the larger the mass–loss rate but observed radii of Cepheids are precise with an uncertainty of a few percent (Gieren et al., 1997). There is uncertainty added due to the radiative driving coefficients α and k. The mass–loss rate depends on the exponent α, and variations of α can cause the predicted mass–loss rates to vary. The value of k is less important because it is small and $\dot{M} \propto k^{1/\alpha}$. More detailed analysis of the mass loss of Cepheids would benefit from calculations of α and k at temperatures and gravities consistent with Cepheids over a finer grid.

For some Cepheids, the mass loss seems to be driven primarily by the shocks generated in the atmosphere by pulsation. The rates calculated are dependent on the accuracy of the pulsating atmosphere model by Fokin et al. (1996). Errors in the model of a Cepheid atmosphere with mass $M = 5.7 M_{\odot}$, and $T_{\rm eff} = 5750$ K will affect other calculations; the mass–loss rates will be wrong due to the relative scaling. It would be useful to verify the accuracy of the model of the shocks in pulsating atmospheres. Furthermore, models of pulsating atmospheres could be used to calculate the mass loss of the Cepheid directly to provide a consistency test of the analytic method.

The shock model may also be tested with observations. Shocks propagating in a stellar atmosphere cause the layers in the star to move and this is reflected in the broadening of lines in a spectrum. Mathias et al. (2006) analyzed the time varying spectra of X Sgr and found evidence for two, possibly three, shocks moving through the atmosphere of the Cepheid in one pulsation period. This result suggests spectroscopic observations of a Cepheid with intense phase coverage would provide information for understanding shocks in Cepheids. X-ray and UV observations are important because shocks moving in the atmosphere will ionize material which could be detected as X-ray and UV variability (Engle et al., 2006). The observations would provide a test for any hydrodynamic model of shocks in a Cepheid atmosphere.

It would be interesting to apply the theory of pulsation and shock induced mass loss to first overtone Cepheids and other radial pulsating variables. As first overtone pulsation occurs at an earlier stage of pulsation than fundamental pulsation, analysis of mass loss in first overtone pulsating Cepheids would shed more light on the contribution of mass loss on the problem of the Cepheid mass discrepancy and would contribute to the understanding of Cepheid evolution. However, the shock model of Fokin et al. (1996), that underlies this analysis, is valid only for fundamental pulsation and thus cannot be realistically applied to first overtone pulsation. With an appropriate shock model, shock induced mass loss can be investigated with this theory.

The dust model proposed here provides a consistent match with existing observations. In particular, the calculation of the ratio of the luminosity at wavelengths 25 μm and 12 μm exhibits the same behavior as shown by Deasy (1988). The results, however, are dependent on the choice of dust parameters such as mean

grain size. New observations from Spitzer and at sub–millimeter wavelengths would provide constraints on the properties of the dust in the wind and on the mass–loss rates of Cepheids. Sub–mm observations would also provide information on the age of Cepheids. Consider RS Pup with four observed shells, each associated with a particular crossing on the instability strip; a very strong sub–mm excess may indicate a large amount of cool dust in these shells. Thus the amount of sub–mm excess may trace the mass–loss history of the Cepheid and its age.

The connection between mass loss and evolution has been explored for the observed Cepheids. It was shown the period change of a Cepheid is dependent on the mass–loss rate at that time. However, for all the Cepheids with period changes quoted, the mass–loss rate provides an insignificant contribution, and, furthermore, the Cepheids with the largest calculated mass–loss rates have the slowest absolute value of period change. This connection needs to be explored in greater detail with a larger set of observations.

Mass loss in the instability strip is an important concept to understand if one is to determine the physical structure and the cause of the mass discrepancy of Cepheids. It is also important to constrain mass loss for observations in the near–IR and longer wavelengths if the period–luminosity relation is to be precise to a few percent, which is a motivation of interferometric observations. The analytical model of mass loss of the Cepheids investigated here imply shocks and pulsation play a strong role driving the wind and increase the mass–loss rate by orders of magnitude.

Chapter 7

Predicting Mass–Loss Rates of Theoretical Cepheids with Varying Metallicity

This chapter is published as:

"On the Enhancement of Mass Loss in Cepheids Due to Radial Pulsation. II. The Effect of Metallicity"

Neilson, H.R., & Lester, J.B. 2009, ApJ, 690, 1829[1]

"Eat, drink and be merry, for tomorrow ye diet." - William Gilmore Beymer

7.1 Introduction

In the previous chapter, it was shown that mass loss is important in Galactic Cepheids, with mass–loss rates ranging from 10^{-10} to $10^{-7} M_{\odot}/yr$. At thesis rate, the Cepheids can lose about $1 M_{\odot}$, therefore potentially solving the Cepheid mass discrepancy. However, for mass loss to explain the Cepheid mass discrepancy, one needs to understand the behavior of mass loss as a function of metallicity.

The Cepheid mass discrepancy has been calculated for Galactic, and Large and Small Magellanic Cloud Cepheids. Keller & Wood (2002) explore the mass discrepancy of LMC Bump Cepheids using non–linear pulsation models and find a mass discrepancy of about 20%. Keller & Wood (2006) determined that the mass discrepancy for SMC Cepheids is about 20% for Cepheids with mass 5–7$M_{\odot}$, while the discrepancy for LMC Cepheids is about 17%, determined by matching MACHO and OGLE observations with non–linear pulsation models with varying mass and metallicity. This observation has been verified for the LMC (Testa et al., 2007), and it also agrees qualitatively with the analysis of Cordier et al. (2002). This suggests mass loss is a solution to the mass discrepancy if mass loss either is more efficient or at least similar at lower

[1] Neilson & Lester (2009), reproduced with permission by the American Astronomical Society

metallicity as at solar metallicity.

In this chapter, the dependence of Cepheid mass loss on the metallicity is explored using pulsation–enhanced CAK method derived in Chapter 6. The first step is to use the approximate solution for the mass–loss rate and compare how the mass–loss rates differ for different metallicities. In the second part of this chapter, the mass–loss rates are calculated for theoretical Cepheid models with Galactic, LMC and SMC metallicity (Bono et al., 2000b).

7.2 The Metallicity Dependence of the Analytical Mass Loss Relation

This approximate solution for the mass–loss rate of a pulsating star can be used to evaluate the dependence on metallicity. Consider first the dependence of mass loss on metallicity for winds driven by radiation alone. In this case the mass–loss rate is given by Equation 2.10 with $\zeta = 0$ at all phases of pulsation. For Cepheids evolving on the second crossing of the instability strip the luminosity is proportional to the mass, with the same dependence for different metallicities (Castellani et al., 1992; Girardi et al., 2000). The instability strip is somewhat hotter for smaller metallicities (Bono et al., 2000b), but there is significant overlap for the metallicities in question. Therefore the temperature range does not contribute significantly. If we consider two Cepheids with differing metallicities but same mass and luminosity then from Equation 2.10 with $\zeta = 0$ the comparison of the mass–loss rates for two metallicities Z_1 and Z_2 is

$$\frac{\dot{M}_1}{\dot{M}_2} = \left(\frac{Z_1}{Z_2}\right)^{1/\alpha} . \tag{7.1}$$

This implies that Cepheids in the LMC and SMC would have lower mass–loss rates then those in the Milky Way as the relative metallicity for the LMC is 0.4 and for the SMC is 0.2. Because $\alpha = 0.465$, $\dot{M}_{\rm LMC}/\dot{M}_{\rm MW} = 0.139$ and $\dot{M}_{\rm SMC}/\dot{M}_{\rm MW} = 0.031$. Thus the radiative–driven mass–loss rates in the LMC and SMC are very small relative to the Milky Way. However the metallicity is important in the calculation of pulsation–driven mass–loss rates as well as radiative–driven mass–loss rates. If we again consider Equation 2.10 to describe the ratio of mass–loss rates for two different metallicities then

$$\frac{\dot{M}_1}{\dot{M}_2} = \left(\frac{Z_1}{Z_2}\right)^{1/\alpha} \left[\frac{GM_1(1-\Gamma_{e,1}) - \zeta_1 R_1^2}{GM_2(1-\Gamma_{e,2}) - \zeta_2 R_2^2}\right]^{1-1/\alpha} . \tag{7.2}$$

This can be rewritten as

$$\frac{\dot{M}_1}{\dot{M}_2} = \left(\frac{Z_1}{Z_2}\right)^{1/\alpha} \left[\left(\frac{g_{\rm eff,1}}{g_{\rm eff,2}}\right)\left(\frac{1 - a_{\rm puls,1}/g_{\rm eff,1} - a_{\rm Shock,1}/g_{\rm eff,1}}{1 - a_{\rm puls,2}/g_{\rm eff,2} - a_{\rm Shock,2}/g_{\rm eff,2}}\right)\right]^{1-1/\alpha} , \tag{7.3}$$

where the terms $a_{\rm Shock}$ and a_p are the shock and the pulsation acceleration terms of the function ζ respectively, and $g_{\rm eff}$ is the effective gravity, $GM(1-\Gamma_e)$. The ratio of the shock acceleration to the effective gravity

is

$$\frac{a_{\rm Shock}}{g_{\rm eff}} = \frac{du_\delta}{Pd\phi}\left(\frac{L}{L_\delta}\right)^{1/8}\left(\frac{P}{P_\delta}\right)^{-7/24}\left(\frac{M}{M_\delta}\right)^{5/12}\left[\frac{R^2}{GM(1-\Gamma_e)}\right] = C_0 P^{-1.29} M^{-0.58} R^2, \tag{7.4}$$

and the ratio of the pulsation acceleration and the effective gravity is

$$\frac{a_{\rm puls}}{g_{\rm eff}} = \frac{2\pi\Delta R R^2}{GM(1-\Gamma_e)}. \tag{7.5}$$

The ratio of the analytic mass–loss rates can be used to test the behavior of a Magellanic Cloud Cepheid relative to a Galactic Cepheid, and to investigate if pulsation–driven mass loss is significant for lower metallicities. To do this, Equation 7.3 must be rewritten such that all variables are in relative non–dimensional units. Consider two Cepheids, labeled 1 and 2, and express the ratio of the pulsation acceleration for the Cepheid number 2 be in terms of the effective gravity, called a_p. Second, write the balance of force for Cepheid number 2 as the non–dimensional parameter $F = 1 - a_p - a_{\rm Shock,2}/g_{\rm eff,2}$. Also it is assumed that $\Gamma_e \approx 0$ and can be ignored in the calculation because the electron number is small for stars with effective temperatures ranging from 4000 to $6000K$. The small electron number causes an acceleration that is small relative to the gravity. The acceleration due to pulsation for Cepheid 1 relative to Cepheid 2 is

$$\frac{a_{\rm puls,1}}{g_{\rm eff,1}} = a_p\left(\frac{\Delta R_1}{\Delta R_2}\right)\left(\frac{R_1}{R_2}\right)^2\left(\frac{P_1}{P_2}\right)^{-2}\left(\frac{M_1}{M_2}\right)^{-1}, \tag{7.6}$$

and the ratio of the shock acceleration and the effective gravity is

$$\frac{a_{\rm Shock,1}}{g_{\rm eff,1}} = (1 - a_p - F)\left(\frac{P_1}{P_2}\right)^{-1.29}\left(\frac{M_1}{M_2}\right)^{-0.58}\left(\frac{R_1}{R_2}\right)^2. \tag{7.7}$$

Substituting these results into Equation 7.3 and writing all quantities with a subscript of 1 in units of the quantities denoted with a subscript of 2, the relative mass–loss rate of Cepheid 1 is

$$\begin{aligned}&\dot{M}_1(\dot{M}_2) = Z_1^{1/\alpha} \times \\ &\left\{\left(\frac{M_1}{F}\right)\left(1 - a_p\Delta R_1 R_1^2 P_1^{-2} M_1^{-1} - (1 - a_p - F)P_1^{-1.29} M_1^{-0.58} R_1^2\right)\right\}^{1-1/\alpha}.\end{aligned} \tag{7.8}$$

Equation 7.8 can be used to probe the mass–loss rates for low metallicity Cepheids as a function of relative period with the following free parameters: a_p, F, M_1, R_1, and ΔR_1.

If the metallicity Z_1 is less than unity then the relative mass–loss rates, $\dot{M}_1$, tend to be smaller based on the explicit dependence of metallicity. However, the ratio of mass–loss rates may be greater than or equal to unity if the term inside the curly brackets is significantly less than one. This term is significantly less than one only when

$$1 - a_p\Delta R_1 R_1^2 P_1^{-2} M_1^{-1} - (1 - a_p - F)P_1^{-1.29} M_1^{-0.58} R_1^2 << 1, \tag{7.9}$$

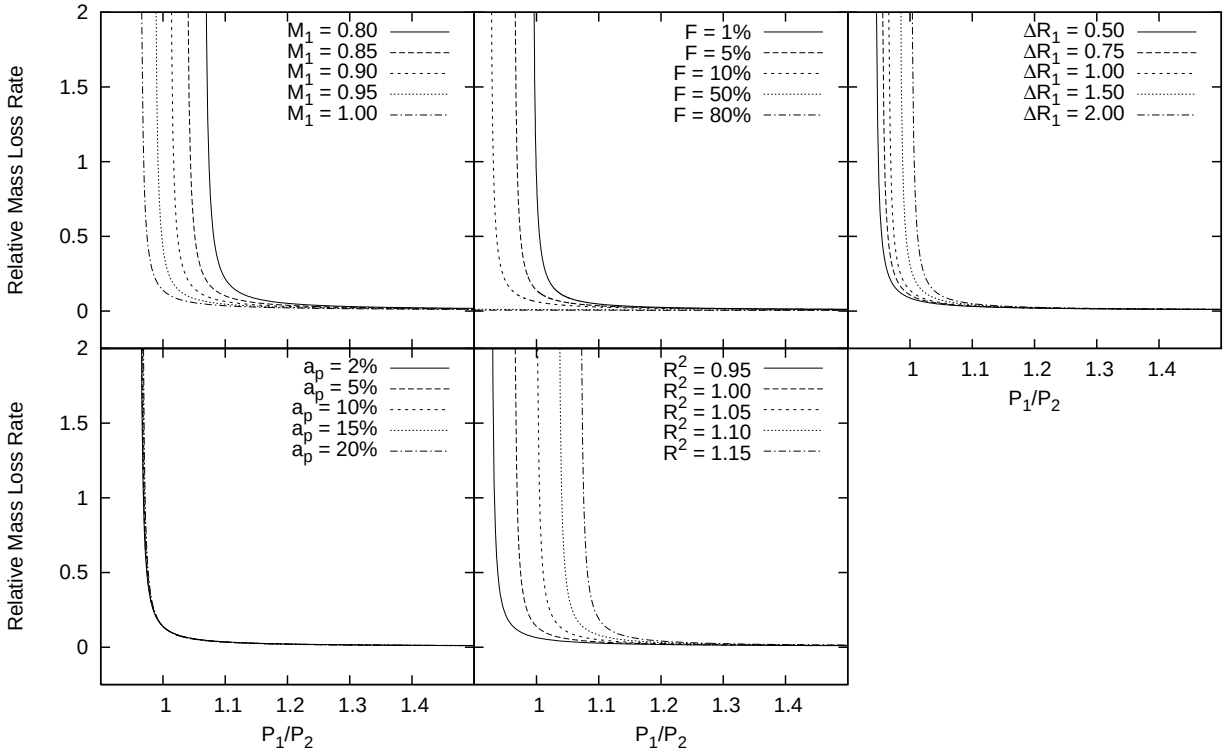

Figure 7.1: The mass–loss rate of a LMC Cepheid relative to a similar Cepheid with solar metallicity as a function of period and the effect of varying the other parameters. When the parameters are held constant, they are $R_1 = 1$, $M_1 = 1$, $\Delta R_1 = 1$, $F = 5\%$, and $a_p = 5\%$.

and furthermore this term must be smaller than the balance of forces, F. There are many ways for this function to be small, one of which is the relative period. If $P_1 < 1$ and R_1 and M_1 are approximately unity, then this function is less than one; however how much less than one P_1 needs to be will depend on the values of a_p and F. The value of a_p, the ratio of the acceleration due to pulsation to the effective gravity, is generally in the range 0 to 0.1 for Galactic Cepheids. Therefore a_p plays only a small role in affecting the mass–loss rate, implying that the shock acceleration term is the dominate term, which means the parameter F needs to be small to satisfy Equation 7.9. A small value of F suggests that the balance of forces for the reference Galactic Cepheid is small and the mass–loss rate is large.

The inequality given by Equation 7.9 is satisfied when the relative radius is greater than unity or when the mass is less than unity, but this also requires that the value of F be small. Varying the amplitude of radius pulsation affects the result as well; if the amplitude is greater than unity for lower metallicity then the pulsation terms increases linearly and thus decreases Equation 7.9. The result of varying the values of a_p, F, R_1^2, M_1, and ΔR_1 in Equation 7.8 gives the mass–loss rate of Cepheid 1, $\dot{M}_1$, shown in Figure 7.1 as a function of P_1 for the relative metallicity of the LMC to the Milky Way. From the plots, it is clear that the relative mass–loss rate can become very large even at lower metallicity. Applying the same analysis for the mass loss of SMC Cepheids relative to Galactic Cepheids the curves shows similar behavior. The

effect of the metallicity in the analysis is to shift the curve up and down along the mass–loss rate axis. For a relative mass–loss rate of unity the relative period is approximately the same for both Cepheids with LMC metallicity and Cepheids with SMC metallicity since it is in the nonlinear regime given by the term in the curly brackets in Equation 7.8.

The mass–loss rates are larger at lower metallicity if the shocks are more efficient. These shocks are generated from waves in the hydrogen and helium partial ionization zones of Cepheids and at lower metallicity the partial ionization zones produce more energy when the layers become ionized. This is because of the larger fractional mass hydrogen and helium. Therefore the shocks have more momentum to input into the wind. Also, the shocks will maintain more energy as radiative cooling will depend on the amount of metals. The lower metallicity and possibly larger abundance of helium also affect the global properties of Cepheids (Marconi et al., 2005), such as the pulsation period, and these metallicity–dependent global properties appear in the shock acceleration formula making it implicitly metallicity dependent.

7.3 Comparison of the Analytic Predictions with Observations

It has been argued that pulsation–driven mass loss generally decreases for lower metallicities, but there are combinations of parameters that predict larger relative mass–loss rates. One might ask what the parameters describing Magellanic Cloud Cepheids would predict.

The average relative period of the LMC and SMC Cepheids can be determined using the metallicity correction. The metallicity correction is a constant that is added to the Period–Luminosity relation to account for the fact that Cepheids with different metallicities have different luminosities for the same pulsation period. The Hubble Key Project on the Extragalactic Distance Scale (Kennicutt et al., 1998) used the Period–Luminosity relation to determine the distance to galaxies in the local group, but it required a correction for the metallicity of approximately $\delta(m - M)/\delta[M/H] = -0.25$ mag/dex. This correction factor has been verified by other studies (Tammann et al., 2003; Sakai et al., 2004; Groenewegen et al., 2004; Romaniello et al., 2005; Groenewegen & Salaris, 2003; Gieren et al., 2005) but the exact value is uncertain. For instance, fecent theoretical studies using non–linear hydrodynamic models find the period–luminosity relation depends significantly on the metallicity as well as on the helium abundance (Fiorentino et al., 2002; Marconi et al., 2005). Sasselov et al. (1997) argued that the metallicity correction, $\delta\mu$, could be written as a function of Z,

$$\delta\mu = 0.44 \log\left(\frac{Z}{Z_{\rm LMC}}\right). \tag{7.10}$$

Combining this with the period–luminosity relation for the LMC,

$$M_V = -2.760(\log P - 1) - 4.218, \tag{7.11}$$

(Freedman et al., 2001), one finds the period ratio for the LMC and SMC relative to Milky Way Cepheids

with the same luminosity to be $P_{\rm LMC}/P_{\rm MW} \sim 1.16$ and $P_{\rm SMC}/P_{\rm MW} \sim 1.30$.

The relative mass of Cepheids in the LMC and SMC can be estimated by comparing the mass discrepancy in the Magellanic Clouds and the Milky Way (Keller & Wood, 2006). The mass discrepancy is a function of metallicity implying that for the same luminosity the mass of Cepheids is a function of metallicity. Therefore the mass of SMC Cepheids may be up to approximately 3% smaller than LMC Cepheids, which in turn is about 3% smaller than Galactic Cepheids.

The values of the relative radius and relative amplitude of radius variation are difficult to approximate. Radial velocity observations suggest that the radii of Cepheids in the Magellanic Clouds follow a similar Period–Radius relation as Galactic Cepheids (Storm et al., 2004, 2005). Therefore varying these parameters can provide a test of mass loss with the period ratios quoted for the LMC and SMC. Figure 7.2 shows the relative mass–loss rate for LMC (Left Panel) and SMC (Right Panel) Cepheids as a function of the mean radius for corresponding relative period. The analysis assumes the value of F is 0.01, $\Delta R_1 = 1.15$, and $a_p = 0.05$. Each curve represents the possible relative mass range suggested by mass discrepancy studies, 0.96 to 1 for the LMC and 0.92 to 1 for the SMC. The results are insensitive to small variations of F, ΔR_1, and a_p, implying that mass loss in the Clouds is significant if the radii of Cepheids are about 10% and 16% larger in the LMC and SMC respectively than Galactic Cepheids with the same luminosity. This may be tested by measuring the angular diameters of Cepheids using interferometry, Mourard et al. (2008a) argued that it is possible to measure these angular diameters with the Very Large Telescope Interferometer using differential interferometry techniques.

The plausibility of this required larger radius may be checked by considering the observed Period–Radius (PR) relation (Gieren et al., 1999; Groenewegen, 2007). The PR relation for Galactic, LMC and SMC Cepheids is

$$\log R = 0.68 \log P + 1.146, \tag{7.12}$$

and for the period ratios of 1.16 and 1.3 the relative LMC and SMC Cepheid radius is 1.1 and 1.2 respectively. This implies that it is possible that LMC and SMC Cepheids have larger mass–loss rates than Galactic Cepheids when the mass loss of the Galactic Cepheid is significant.

The metallicity correction that is determined using theoretical models suggests that metal–poor Cepheids are more luminous for the same period. In other words, the periods of metal–poor Cepheids are shorter for the same luminosity (Fiorentino et al., 2002). In this case the value of P_1 is less than unity. The relative mass–loss rate will be greater than unity for LMC and SMC Cepheids as long as the other parameters are $R_1 \geq 1$, $\Delta R_1 \geq 1$ and $M_1 \leq 1$.

This analysis has shown that it is possible for metal–poor Cepheids to have significant mass loss, similar to and even greater than the mass–loss rates for Galactic Cepheids for both relative period regimes suggested by theoretical and observed values of the metallicity correction of the Period–Luminosity relation.

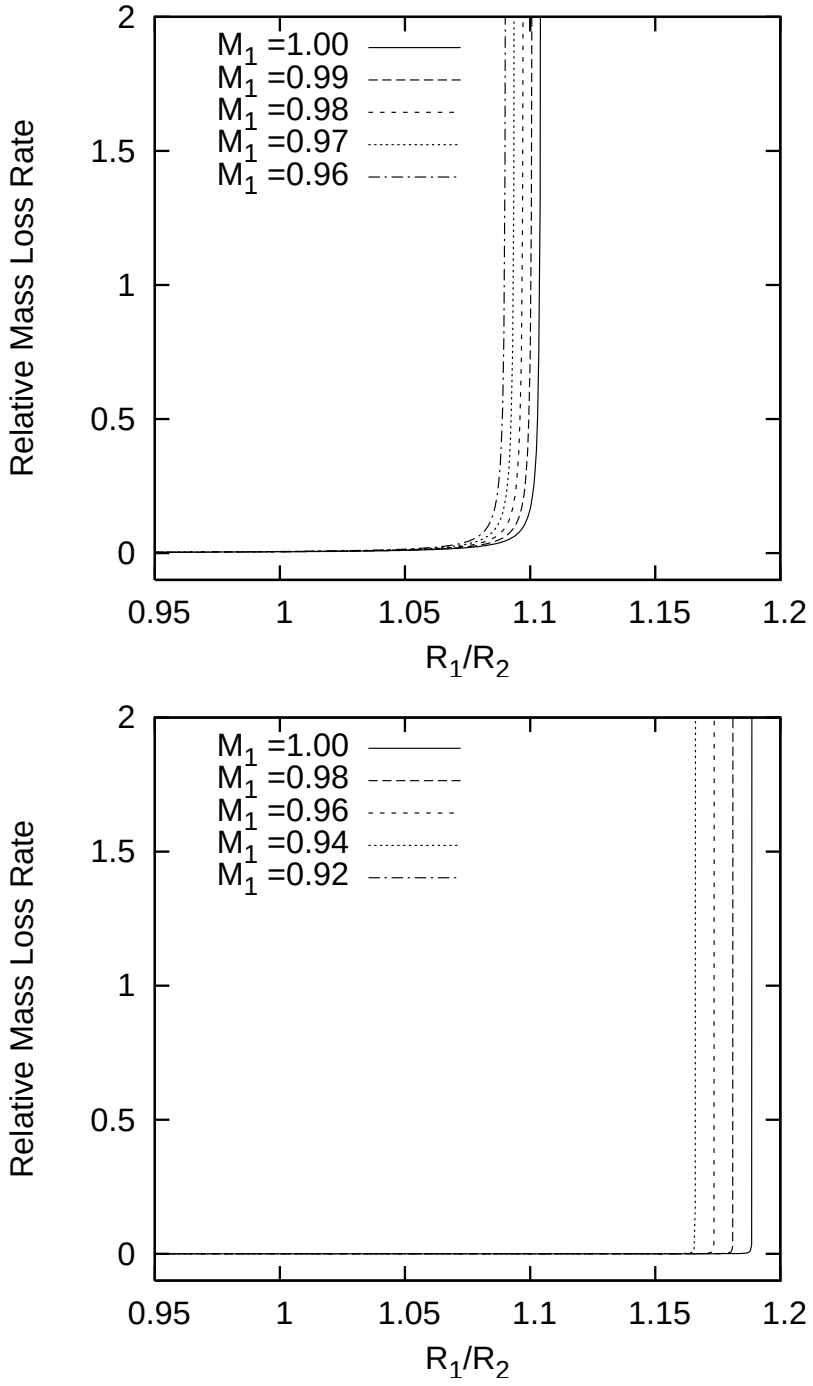

Figure 7.2: The relative mass–loss rates for LMC (Left Panel) and SMC (Right Panel) Cepheid as a function of relative radius with period ratios $P_{\rm LMC}/P_{\rm MW} = 1.16$ and $P_{\rm SMC}/P_{\rm MW} = 1.3$ respectively.

7.4 Predicting Mass–Loss Rates For Theoretical Model Cepheids

The previous analysis is suggestive, but it can be carried further to determine, quantitatively, how much larger the mass–loss rates are for LMC and SMC Cepheids, at least in the regime where the periods of LMC and SMC Cepheids are smaller than those of Milky Way Cepheids for the same luminosity. To compute the mass–loss rate for a Cepheid, it is necessary to know the following parameters that describe the Cepheid: the mass, luminosity, radius, and pulsation period, as well as the amplitudes of the variation of the luminosity and radius. While these quantities have been determined for many Galactic Cepheids (Moskalik & Gorynya, 2005), this has not been done for LMC and SMC Cepheids. Therefore theoretical models of Cepheids from Bono et al. (2000b) are used to predict mass–loss rates. The method of solving the mass loss in the pulsating case is derived in Paper I.

The models include all the necessary information to calculate pulsation–driven mass–loss rates using the enhanced CAK method. There are two types of models describing the mass–luminosity relations: one is based on canonical stellar evolution models, and the second assumes convective core overshoot, which results in a larger luminosity for the same mass as the canonical models. This does not mean the models necessarily represent only convective core overshoot; for instance the steeper mass–luminosity relation could also represent mass loss during stages of evolution before the second crossing of the instability strip. The masses of the models are $5, 7, 9$ and $11 M_{\odot}$ and span the temperature range of the instability strip.

The mass–loss rates for model Cepheids in the Milky Way, LMC and SMC are shown in Figure 7.3 as a function of pulsation period for the canonical models, along with the ratio of the pulsation mass–loss rates and the radiative–driven mass–loss rates. The ratio, the enhancement of mass loss, is a measure of the dependence of the wind on the pulsation plus shock terms in the mass–loss calculation. The points labeled as LMC or SMC Maximum are based on model Cepheids where the pulsation period is so small that the sum of the acceleration due to pulsation and shocks is greater than the effective gravity of the Cepheid. In this limit the calculation of the mass–loss rate becomes imaginary. These points are calculated by using the same parameters from the model Cepheid but increasing the period by steps of 0.01 day until the calculation is stable. The physical justification for this is based on how the rate of change of period depends on mass loss. It was shown in Paper I that mass loss acts to increase the rate of period change, making it more positive. For most Cepheids, the contribution to the period change due to mass loss is small compared to the contribution due to evolution, but for Cepheids near the blue edge of the instability strip the effect of evolution on period change decreases, making the contribution of mass loss more significant. The period is also smaller, further increasing the mass–loss rate and the effect of mass loss on the period change.

The mass–loss rates for the SMC models shown in Figure 7.3 are larger than that for LMC and Milky Way at periods about 3.5 days, denoted by LMC and SMC Maximum in the figures. This is also true at periods near 20 days. These periods correspond to masses of 5 and $9 M_{\odot}$ respectively. The increase of mass–loss rates with decreasing metallicity is clear in these two cases, but for the other models the effect is

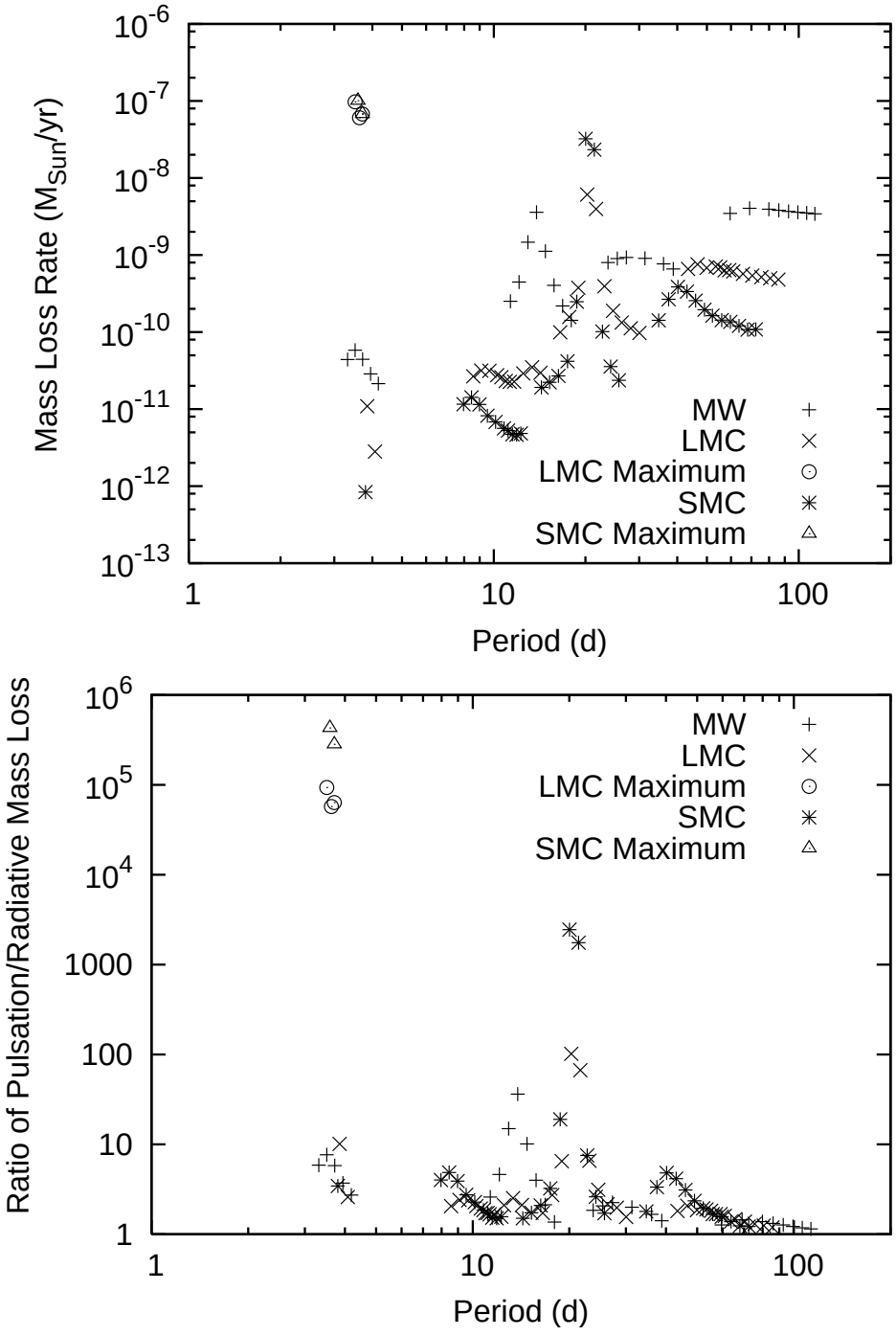

Figure 7.3: (Left Panel) The predicted mass–loss rates of the theoretical Cepheid models with a canonical mass–luminosity relation (Bono et al., 2000b). (Right Panel) The enhancement of the mass loss as given by the ratio of the pulsation–driven mass–loss rate to the radiative–driven mass–loss rate that ignores pulsation effects. The points given in the key as LMC/SMC Maximum are explained in the text.

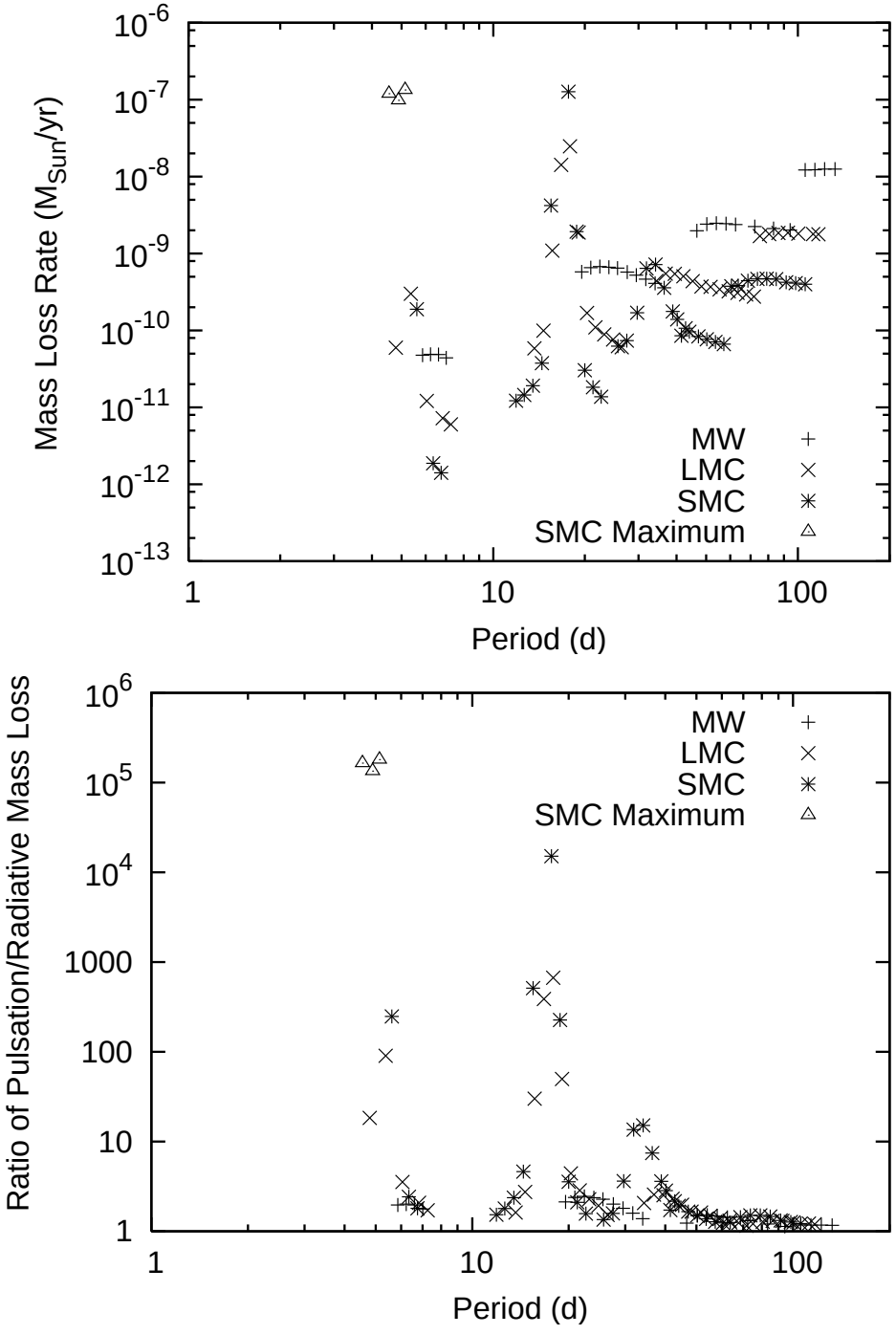

Figure 7.4: Same as Figure 7.3 but for Cepheid models assuming a convective overshoot mass–luminosity relation.

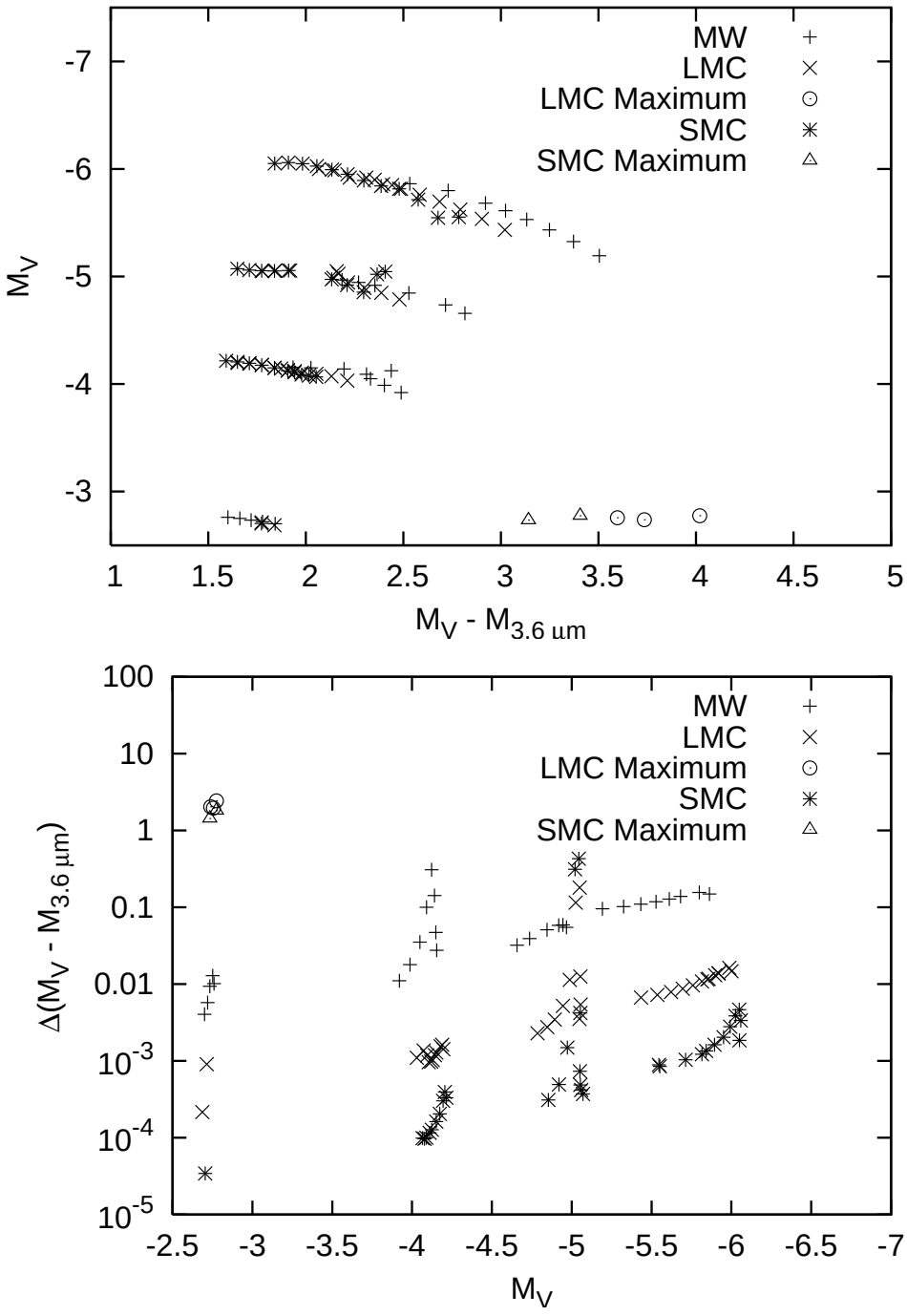

Figure 7.5: (Left Panel) The color–magnitude plot of the model Cepheids based on the canonical mass–luminosity relation. Cepheids with large mass–loss rates have significant color excess. The different sequences are for different masses, the brightest Cepheids are the most massive. (Right Panel) The color excess due to dust in the circumstellar shells.

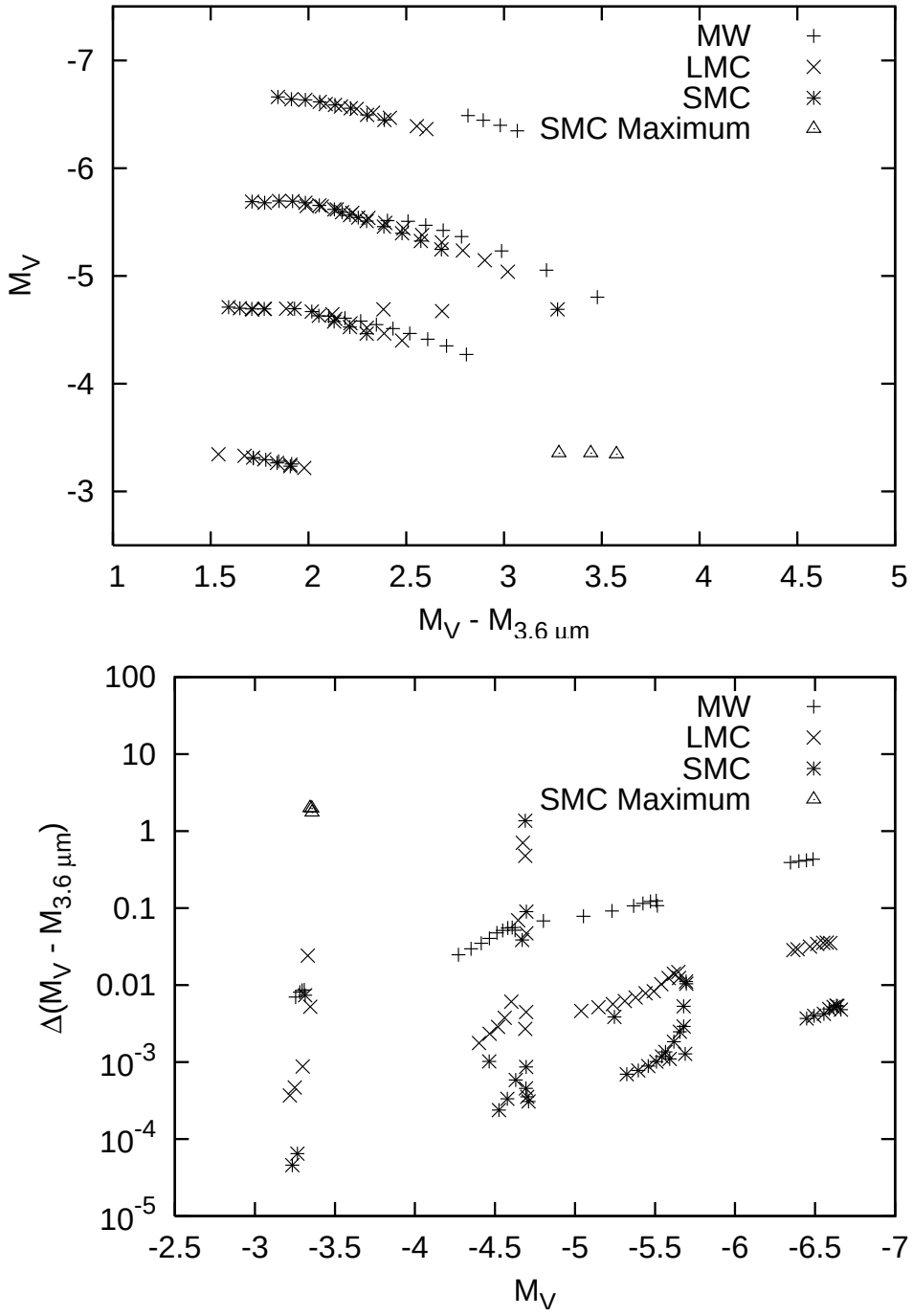

Figure 7.6: Same a Figure 7.5 but for the model Cepheids with the convective overshooting mass–luminosity relation.

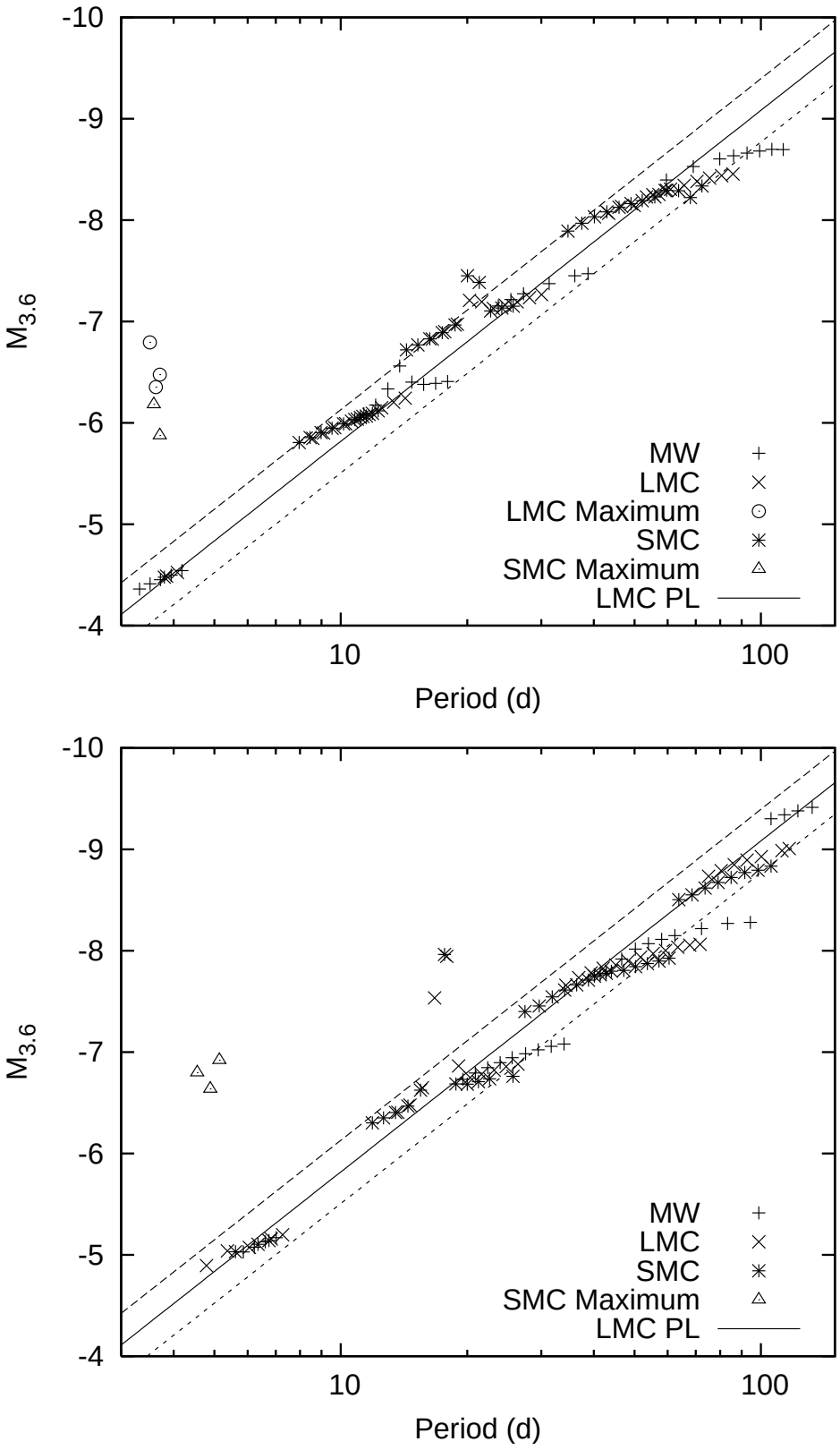

Figure 7.7: The Luminosity at 3.6 μm of the theoretical Cepheid models from Bono et al. (2000b) including the effect of mass loss for the three values of the metallicity. The models with a canonical mass–luminosity relation is shown in the Left Panel while the convective core overshooting models are shown in the Right Panel. The LMC Period–Luminosity relation from Ngeow & Kanbur (2008) with the 3σ deviation is shown for comparison.

not as obvious. It is interesting that the long period Cepheids have lower mass–loss rates with decreasing metallicity. This is consistent with the observation that the mass discrepancy of Cepheids decrease with increasing period for the Milky Way (Caputo et al., 2005), and it suggests similar behavior for LMC and SMC Cepheids. The mass–loss enhancement, in the right panel of Figure 7.3, shows that the mass loss in the SMC Cepheids is more sensitive to the effects of pulsation for Cepheids in the LMC and Milky Way; for Cepheids with periods near 10 days the SMC mass loss is enhanced by a factor of 10 relative to the LMC. This verifies the the argument that when mass loss is enhanced by pulsation for Galactic Cepheids, the mass loss is further amplified for similar Cepheids at the same position on the instability strip but with lower metallicities.

The analysis is repeated with the steeper mass–luminosity relation associated with convective core overshoot and is shown in Figure 7.4. The dependence of pulsation–driven mass loss on metallicity is more clear in this case. The mass–loss rates for SMC Cepheids may be larger than those of the LMC and the Milky Way for periods up to about 20 days which is consistent with the result shown in Figure 7.3. For periods greater than 20 days, the mass–loss rate decreases as a function of metallicity where pulsation and shocks are not as effective. The mass–loss enhancement, shown in the right panel of Figure 7.4, implies pulsation is more efficient for driving mass loss as metallicity decreases. The mass–loss rates are also largely independent of the mass–luminosity relation for the theoretical Cepheid models.

7.5 Predictions of Infrared Excess Due to Mass Loss

It has been hypothesized that mass loss is important in LMC and SMC Cepheids. In Paper I, the circumstellar shells that have been observed as infrared excess in Galactic Cepheids were modeled as dust forming in the winds of Cepheids. This luminosity depends on the fraction of the total amount of gas that forms dust, the dust–to–gas ratio, which for the Milky Way is approximately $1/100$. This quantity is dependent on the composition of the gas, meaning the dust–to–gas ratio is smaller for the lower metallicity of the LMC and SMC. For this work the dust–to–gas ratio is assumed to scale linearly with the relative metallicity, meaning that the ratio for the LMC is $1/250$ and SMC is $1/500$. However these are maximum values for the dust–to–gas ratios; for instance Clayton & Martin (1985) found the LMC dust–to–gas ratio is about $1/400$ and Weingartner & Draine (2001) determined that the ratio is about $1/1000$. These chosen dust–to–gas values are the maximum values but are uncertain by only about a factor of 5.

If mass loss is important in LMC and SMC Cepheids then the winds should produce observable infrared excess. A Color–Magnitude Diagram, M_V versus $M_V - M_{3.6\mu m}$, is shown in Figure 7.5 for the Cepheid models based on the canonical mass–luminosity relation. Along with that plot, the difference of the colors due to the star plus circumstellar shell relative to the star alone is also shown in the right panel. Because the luminosity of a circumstellar shell is due to dust, it will have minimal effect on the value M_V, but the dust contributes significantly to the 3.6 μm luminosity. Therefore color excess increases if the mass–loss rate is

large.

The color–excess analysis is repeated for the convective core overshoot models and is shown in Figure 7.6. In this case, the color excess is more pronounced though for only a few points. In both cases, the color excess due to circumstellar shells is significant. If mass loss is important in LMC and SMC Cepheids then observations of a large population of Cepheids should be able test this model.

Infrared excess may also affect the infrared Period–Luminosity relation. The Period–Luminosity relation for the LMC was recently presented by both Ngeow & Kanbur (2008) and Freedman et al. (2008) in IRAC bands using SAGE data (Meixner et al., 2006). The PL relation was also determined in J, H and K–bands by Persson et al. (2004) for a sample of 92 Cepheids. In Ngeow & Kanbur (2008) and Persson et al. (2004) blending is an important issue because of the lower resolution of the infrared observations; while Freedman et al. (2008) avoids the issue by using a subsample from Persson et al. (2004). Blending acts to make the Cepheid appear more luminous in the infrared, just as mass loss would do, making the two difficult to distinguish from photometry. In Figure 7.7, the luminosities of the theoretical Cepheids, including infrared excess due to mass loss are plotted as a function of period for the Galactic, LMC and SMC sample at 3.6 μm. The 3.6 μm PL relation for the LMC (Ngeow & Kanbur, 2008) is also plotted with dotted lines representing 3σ deviation. For the model LMC Cepheids with the canonical mass–luminosity relation, there are two regimes where the luminosity is 3σ larger than the luminosity from the observed PL relation. There are two Cepheids at a period of about 15 days and the two near four days having the maximum possible mass–loss rate with a luminosity four magnitudes larger than that given by the PL relation. The models with convective overshooting, shown in the Right Panel of Figure 7.7, show a similar behavior at 15 days, but at shorter periods the luminosity of the LMC Cepheids are consistent with the PL relation.

In the analysis of Ngeow & Kanbur (2008), a number of Cepheids are removed from the determination of the infrared PL relation because the IR brightness is too large. This is presumably due to blending, however infrared excess due to mass loss has the same effect. The predicted luminosity of the model Cepheids is consistent with the range of luminosities of these outliers, providing possible observational agreement.

The computation of mass–loss rates of the theoretical Cepheid models predicts that at some points on the second crossing of the instability strip the mass–loss rates are increased by up to three orders of magnitude. This significant increase agrees with the result in the section 2.

7.6 Mass Loss and the Mass Discrepancy

It has been shown that mass loss increases as metallicity decreases for theoretical models of Cepheids. This result is consistent with the observations of mass discrepancy as a function of metallicity (Keller & Wood, 2006; Keller, 2008). Furthermore the dependence of mass loss on metallicity is found to change for larger periods where the mass–loss enhancement becomes less significant. Along with the fact that more massive Cepheids spend less time on the instability strip than less massive Cepheids, this result is potentially

consistent with the observation that the mass discrepancy is constant (Keller, 2008) or decreases (Caputo et al., 2005) as a function of mass. The model of mass loss being driven by radial pulsation and shocks is consistent with the behavior of mass discrepancy between pulsation and evolution calculations as a function of both mass and metallicity. But can mass loss predict the actual measured differences of mass?

For mass loss to be the solution it must be able to account for a difference of approximately $1M_{\odot}$ for Cepheids with an evolutionary mass of $5M_{\odot}$ and $0 - 2M_{\odot}$ for Cepheids with an evolutionary mass $11M_{\odot}$ in the Milky Way. The lower limit represents the mass discrepancy with the dependence on mass that is predicted by Caputo et al. (2005) and the upper limit is due to the constant mass discrepancy argued by Keller (2008). For LMC Cepheids the mass difference is approximately $1 - 1.5M_{\odot}$ for $5M_{\odot}$ Cepheids and $0 - 2.5M_{\odot}$ for $11M_{\odot}$ Cepheids, while for SMC Cepheids the mass difference is $1 - 2M_{\odot}$ and $0 - 3M_{\odot}$ respectively.

A timescale is required to determine the average mass–loss rates needed to account for mass discrepancy. This timescale is assumed to be the evolutionary lifetime on the second crossing: about 25 Myr for a $5M_{\odot}$ Galactic Cepheid and about 2 Myr for an $11M_{\odot}$ Galactic Cepheid (Bono et al., 2006). Furthermore, it is assumed that the evolutionary timescales are similar in the LMC and SMC. In that case, a $5M_{\odot}$ Cepheid would need to lose mass at an average rate of 4×10^{-8} in the Galaxy, 6×10^{-8} in the LMC and $8\times10^{-8}M_{\odot}/yr$ in the SMC, to account for the maximum mass difference. For an $11M_{\odot}$ Cepheid, the average mass–loss rate needs to be $0 - 1\times10^{-6}$, $0 - 1.2\times10^{-6}$ and $0 - 1.5\times10^{-6}M_{\odot}/yr$. According to the theory of radiative–driven mass loss, which dominates over the pulsation effects at long period, the mass–loss rate is of order $10^{-8}M_{\odot}$, far less than the maximum value of the average mass–loss rate that is required. The mass–loss rate for l Car has been estimated to be $< 2\times10^{-8}M_{\odot}/yr$ (Böhm-Vitense & Love, 1994), and for RS Pup the rate is estimated to be $< 3.5\times10^{-6}M_{\odot}/yr$ (Deasy, 1988).

The challenge for explaining the mass discrepancy with mass loss is thus the large–mass regime. However, this challenge disappears if the mass discrepancy is a decreasing function of mass, as found by Caputo et al. (2005). The mass discrepancy does not need to be zero at large mass, but it must be smaller than the 17% argued by Keller (2008) to agree with predictions from pulsation–driven mass loss. If the mass discrepancy is smaller for large mass Cepheids, then an average mass–loss rate of the order $10^{-8}M_{\odot}/yr$ may resolve the difference.

At smaller mass, $M < 9M_{\odot}$, the theory of pulsation–driven mass loss predicts mass–loss rates of order $10^{-8}M_{\odot}/yr$ consistent with the average required mass–loss rate for the mass discrepancy. It is not obvious, however, that the average mass–loss rate for Cepheids over the first and second crossing is this large. The predicted mass–loss rates of the model Galactic Cepheids from Bono et al. (2000b) is generally too small, but there are a number of examples of significant mass loss in short period Cepheids in Paper I.

In the LMC and SMC the mass discrepancy at smaller mass is 17 – 25%, and the required average mass–loss rate to explain this is $6 - 8\times10^{-8}M_{\odot}/yr$. At 10 – 20 day periods the mass–loss rates of the theoretical Cepheid models is greater or equal to this required average, as shown in Figure 7.3, but only

for two of the points of on the evolutionary track of the LMC and SMC Cepheid. For the shorter period LMC/SMC Cepheids the mass loss was shown to be unstable for some of the models, but this was solved by using slightly larger values for the period of pulsation for a maximum value of the mass–loss rate. These maximum values are of the order $10^{-7} M_{\odot}$ implying that it is possible to account for the required amount of mass loss.

It is worth noting that pulsation–driven mass loss predicts that the mass loss decreases with metallicity at long periods. If mass loss is the solution to the mass discrepancy then the mass discrepancy must decrease as a function of mass at a larger rate for the LMC and SMC than for the Milky Way, against the assertion of Keller (2008) that the mass discrepancy is constant with mass. The mass discrepancy may be constant for periods up to 20 days where the mass loss is dominated by pulsation and shocks. At longer periods, the mass loss depends primarily on radiative driving, which decreases as $(Z/Z_{\odot})^2$, thus implying a smaller mass discrepancy in the SMC and LMC compared to the Milky Way.

The results of this work imply it is possible for mass loss to account for the mass discrepancy but the evidence is circumstantial. However, mass loss accounts for at least some of the mass discrepancy according to this theory. In that case, it could be argued the remaining mass discrepancy is due to convective core overshoot which in turn affects mass loss. The most significant effect of convective core overshoot on the global parameters is the ratio of the luminosity and mass, where this ratio is larger for more overshoot. This larger ratio causes a larger contribution to the acceleration of the wind via the continuum opacity which in turn increases the mass–loss rate of all Cepheids. By comparing the mass–loss rates in Figures 7.3 and 7.4, it is reasonable to argue that mass loss is important even if the helium core is larger due to convective core overshoot in Cepheid progenitors. The two possible explanations may be differentiated by determining the mass discrepancy for long period ($P > 30d$), massive Cepheids; if the discrepancy is smaller at large masses then mass loss is a probable solution.

7.7 Conclusions

The hypothesis that mass loss is important for the lower metallicity Cepheids in the LMC and SMC has been investigated in this chapter. This has been done by rewriting the analytic method for computing pulsation–driven mass–loss rates as a ratio of mass–loss rates for two Cepheids that are alike in effective temperature and luminosity but with different metallicities, and allowing the other parameters to vary, such as the radius and the period of pulsation. This leads to a parameter space that can be tested to understand the potential behavior of Cepheids at lower metallicity. Over the majority of the parameter space the relative mass–loss of the two Cepheids is less than unity, reflecting the explicit dependence on metallicity. However, there exists two regimes where the relative mass–loss may be larger for lower metallicity. The first regime is where the relative mass is less than unity and the relative radius is larger than unity, and thus the ratio of the pulsation periods may be greater than unity. The other regime is where the pulsation period of the lower metallicity

Cepheid is less than that of the Cepheid with solar metallicity and the ratios of the mass and radius are approximately unity. There is an additional parameter constraining this result. The mass loss is only larger for the lower metallicity Cepheid if the mass loss is significant for the similar solar–metallicity Cepheid. In other words, if mass loss is significantly amplified by pulsation for the solar metallicity Cepheid then the mass loss may be further amplified by pulsation for the lower metallicity Cepheid.

We tested if the parameter space that caused the pulsation amplification of mass loss is consistent with with properties of LMC and SMC Cepheids. This was done using the metallicity correction of the Period–Luminosity relation to determine periods of LMC and SMC Cepheids relative to Galactic Cepheids with the same luminosity. Also we used the Period–Radius relation to determine how the radius changes for the lower metallicity Cepheids. The metallicity correction suggests that lower metallicity Cepheids have longer pulsations periods than Galactic Cepheids and the longer pulsation periods imply that the radii of lower metallicity Cepheids are larger than Galactic Cepheids for the same luminosity. These behaviors are consistent with mass–loss rates being further amplified implying mass loss is important for LMC and SMC Cepheids.

We have calculated mass–loss rates for theoretical models of Large, and Small Magellanic Cloud, and Galactic Cepheids using the method presented in Paper I. It should be noted that the theoretical models use stellar evolution calculations that do not include mass loss in earlier stages of evolution. This affects the Cepheid mass–luminosity relation. It is not clear how the pulsation–driven mass–loss rates of massive ($M > 10M_{\odot}$) Cepheids would change if we use the non–linear mass–luminosity relation of Keller (2008). The non–linear mass–luminosity relation suggests that at large mass the luminosity is less for a given mass than what is predicted by Caputo et al. (2005). This would suggest that pulsation–driven mass–loss rate would be less, but it is unclear what the pulsation period would be in this case. The pulsation period of a Cepheid following the non–linear mass–luminosity relation may be smaller than the period of a Cepheid following the linear mass–luminosity relation. If the period is smaller then the shocks that help drive mass–loss are more efficient and the mass–loss rate may increase. It would be very interesting to test this possibility.

In the calculation of the mass–loss rates, it was found that the peak mass–loss rates in the second crossing of the instability strip in the SMC is almost a factor of 10 larger than in the LMC, which in turn, is almost 10 times larger than that in the Milky Way. Furthermore it was found that the period of about 10–20 days is the point where the dependence of mass loss on metallicity changes sign. This result may be interpreted as the mass loss being amplified significantly for the shorter period Cepheids and radiative driving being the dominant driving mechanism in longer period Cepheids. The larger mass–loss rates for lower metallicity Cepheids is consistent with the conclusion that mass loss may be amplified more by pulsation at lower metallicity.

It is believed that dust forms in the wind of a Cepheid, generating an infrared excess. From the predicted mass–loss rates of theoretical models of Cepheids, we compute Color Magnitude Diagrams as an observational prediction. The result, however, depends on both the dust–to–gas ratio and the mass–loss rate. The

color excess computed here is thus the maximum value because the dust–to–gas ratio used in this work is the maximum value. The dust–to–gas ratio may be a few times to an order of magnitude less, implying the color excess may be about a factor of 2–3 less. The predicted 3.6 μm luminosity computed from the sum of the stellar and circumstellar shell luminosities was found to be consistent with the observed infrared Period–Luminosity relation at 3.6 μm (Ngeow & Kanbur, 2008; Freedman et al., 2008) as well as possibly agreeing with the set of Cepheids from Ngeow & Kanbur (2008) that were considered outliers with much larger luminosities due to blending effects.

The ability of mass loss to explain the mass discrepancy has also been explored. It is shown that pulsation–driven mass loss is a possible explanation, but there still is not enough information to say this with certainty. The most difficult aspect to explain is the 17% mass discrepancy at large mass where the predicted mass–loss rates are smaller than the necessary values of $10^{-6} M_{\odot}/yr$. However, the 17% mass discrepancy is an upper limit and the mass discrepancy at large masses range from 17% down to zero. At smaller masses the pulsation–driven mass loss is consistent with a mass discrepancy of 17%. For the LMC and SMC the mass–loss rates increase, implying mass loss can also explain the metallicity dependence of the mass discrepancy.

The results of this work suggest that it is possible for mass–loss rates of lower metallicity Cepheids in the LMC and SMC to be greater than the mass–loss rates of similar Galactic Cepheids. This result is counterintuitive, one might expect mass loss to scale as the metallicity. However, the pulsation period, radius and other parameters that describe a Cepheid and its mass loss also have dependencies on the metallicity, and the combination of these parameters and the dependencies cause the mass–loss rates to be potentially more significant. Furthermore, the amount of mass loss predicted for Magellanic Cloud Cepheids is consistent with the observed behavior of the mass discrepancy of Cepheids as a function of metallicity from Keller & Wood (2006) as well as the dependence on mass Caputo et al. (2005). Therefore mass loss cannot be discounted as a possible contribution to the mass discrepancy. The amount of mass loss calculated using the pulsation mass–loss model is significant but there is not enough information to argue mass loss alone resolves the mass discrepancy. This needs to be tested by with a large number of nonlinear pulsation models of Cepheids on both the first and second crossing to account for the effect of mass loss of the evolution of the period.

Chapter 8

Testing Mass Loss in Large Magellanic Cloud Cepheids using Infrared and Optical Observations

This chapter is published as:
"Testing Mass Loss in Large Magellanic Cloud Cepheids Using Infrared and Optical Observations"
Neilson, H.R., Ngeow, C.-C., Kanbur, S.M., & Lester, J.B. 2009, ApJ, 692, 81[1]

> *"Dusting is a good example of the futility of trying to put things right. As soon as you dust, the fact of your next dusting has already been established.."* - George Carlin

8.1 Introduction

Cepheids are powerful standard candles because they follow a Period–Luminosity (PL) relation. This relation has been determined using Cepheids in the Large Magallanic Cloud (LMC) in optical and near infrared bands (Laney & Stobie, 1994). LMC Cepheids also provide insight into stellar astrophysics as they have lower metallicity relative to Galactic Cepheids, which has an effect on the pulsation of Cepheids.

Recently, infrared PL relations have been derived using Spitzer observations from the SAGE program (Meixner et al., 2006) by Ngeow & Kanbur (2008) and by Freedman et al. (2008) and with the Epoch 2 SAGE observations by Ngeow et al. (2008); Madore et al. (2008) . These infrared PL relations are important for extragalactic studies, and this will be even more so when the James Web Space Telescope begins operation. The infrared PL relations are powerful tools because metallicity does not contribute significantly (Freedman et al., 2008) and because the pulsation amplitude decreases in the infrared. However, there is

[1]Neilson et al. (2009), reproduced with permission by the American Astronomical Society

significant evidence of infrared excess in Cepheids (Deasy, 1988; Evans et al., 2007; Kervella et al., 2006; Mérand et al., 2006, 2007). The observations of infrared excess imply that there may be an additional uncertainty in infrared PL relations, and the excesses may play a role in LMC Cepheids.

The purpose of this chapter is to test if there is infrared excess in the sample of Cepheids with SAGE observations from Ngeow & Kanbur (2008) caused by a stellar wind. It is argued that at some large distance from the surface of the Cepheid, the wind cools enough that a small fraction of the gas condenses into a dust shell that produces an infrared excess. The dust shells that surround Cepheids are optically thin because they form at large distances from the Cepheids. For instance, a Cepheid with $T_{\rm eff} = 6000\ K$ will have a condensation radius of $r_c/R_* = 0.5(T_c/T_{\rm eff})^{-5/2} = 16$, assuming a condensation temperature of 1500 K. At the distance where dust forms, the dust shells are optically thin, and do not contribute to the extinction of starlight.

The mass–loss hypothesis causing infrared excess in LMC Cepheids is tested using SAGE observations in the IRAC bands combined with OGLE II observations of B,V, and I (Udalski et al., 1999a,b). The next section outlines the observations and the model describing circumstellar dust created in a stellar wind that causes infrared excess. The process for determining the mass–loss rates is also described. The results are given in Section 3 and the predicted infrared PL relations are described in Section 4. The fifth section will explore possible driving mechanisms for mass loss in LMC Cepheids, testing if the predicted mass–loss rates are consistent with the analytic model for mass loss derived in Chapter 6.

8.2 The Data and Mass Loss Model

We use OGLE II and SAGE observations of LMC Cepheids to determine mass–loss rates. The OGLE II data are for B, V and I magnitudes while the SAGE magnitudes are in IRAC bands at wavelengths 3.6, 4.5, 5.8 and 8.0 μm. The SAGE data is adopted from Ngeow & Kanbur (2008), which consist of 730 OGLE II LMC Cepheids with $\log P > 0.4$. However we only use 488 of these Cepheids that have at least 3 IRAC bands and 2 of the BVI bands from this dataset. The SAGE data are compiled by matching the position of OGLE II Cepheids with positions of infrared sources in the SAGE observations. Ngeow & Kanbur (2008) match sources if they are within 3.5 arcseconds of the position of the OGLE II Cepheids. Figure 8.1 show the infrared PL relations constructed using the IRAC magnitudes. A number of (mostly short period) Cepheids appear to deviate from the infrared PL relations, implying there is some infrared excess.

The are three possible causes of the infrared flux excess: (1) blending of stars in SAGE observations, (2) false matches of the infrared sources to the OGLE II Cepheids, (3) or circumstellar dust shells forming at a significant distance from the Cepheids in a stellar wind. It is possible that false matches contaminate the sample, and we check this in Figure 8.2 where the magnitude residuals of the IR Period–Luminosity relations determined by Ngeow & Kanbur (2008) are shown as a function of the separation between the OGLE II and SAGE positions. Although the search radius used in Ngeow & Kanbur (2008) is rather large,

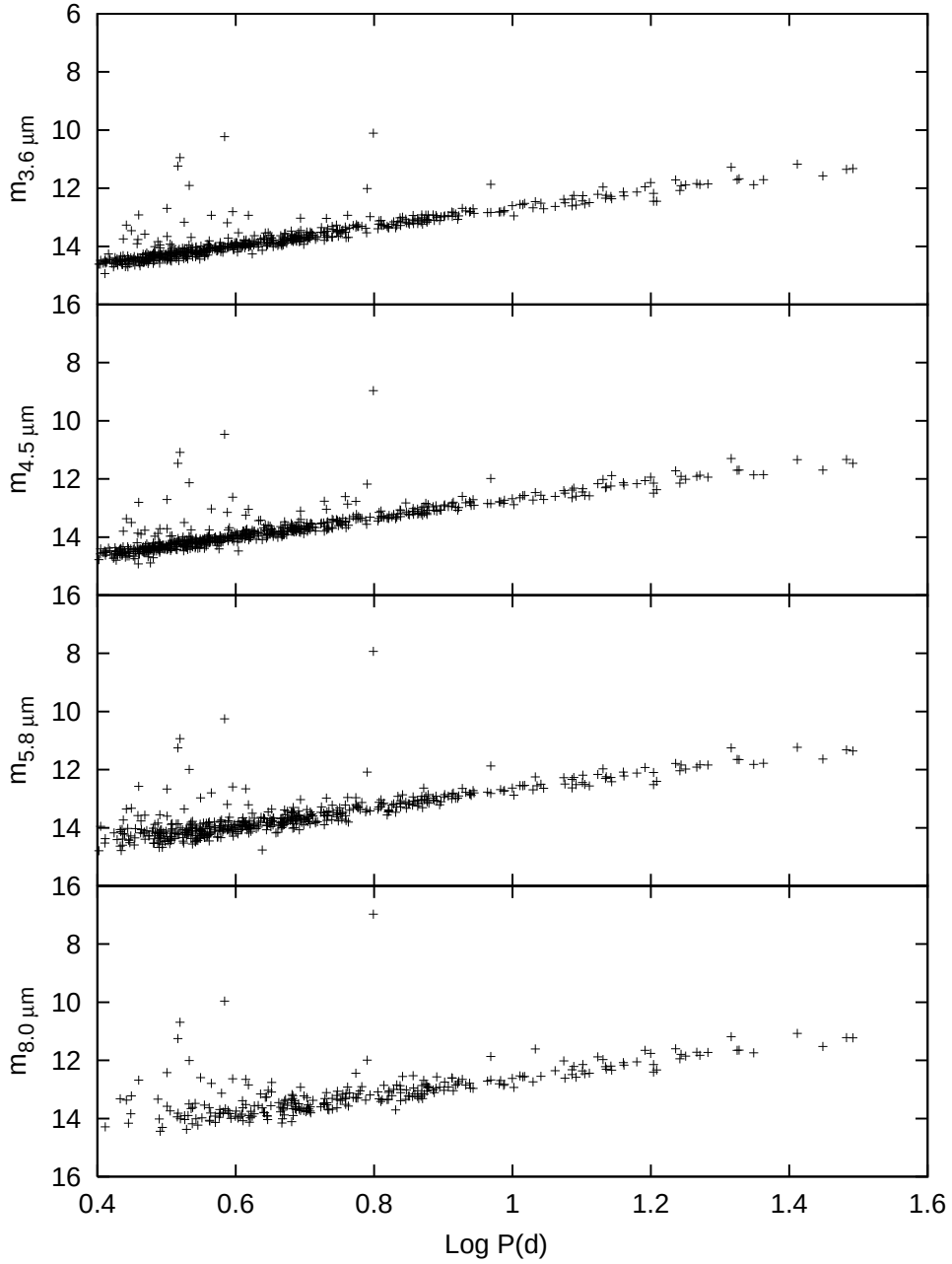

Figure 8.1: The observed brightnesses of LMC Cepheids in the infrared as a function of period.

most of the matched objects have a separation less than 0.77 arcseconds [as demonstrated in the Figure 1 and Table 1 in Ngeow & Kanbur (2008)]. The potential for false matches is only significant for a small fraction of the total sample of Ngeow & Kanbur (2008), and in the sample used here, only ten of the 488 Cepheid matches have a separation greater than 1.3 arcseconds, which is the separation where the matches almost all have large residuals to the fit of the PL relation. There is another asymmetry apparent in Figure 8.2 where the residuals have a separation less than 0.4 arcseconds. In this work, we keep the two samples, but identify them in the figures when important.

We can test if the infrared excess is due to mass loss by calculating the sum of the infrared luminosity of the Cepheid and the luminosity of the dust that is generated in the wind, given by

$$L_{\nu,\mathrm{Shell}} = \frac{3}{4\pi}\frac{< a^2 >}{< a^3 >}\frac{1}{\bar{\rho}}\frac{\dot{M}_d}{v_d}Q_\nu^A \int_{R_*}^{\infty} B_\nu(T_d)[1 - W(r)]dr. \tag{8.1}$$

The dust shell luminosity is proportional to the ratio of the mean cross section, $< a^2 >$, and volume, $< a^3 >$, of the dust particles, and inversely proportional to the mass density of dust particles, $\bar{\rho}$. The dust mass–loss rate is given by $\dot{M}_d$, the dust velocity is v_d, and Q_ν^A is the absorption efficiency. The term in the integral is the product of the blackbody radiation of the dust with temperature T_d and the geometric dilution factor $W(r) = [1 - \sqrt{1 - (R_*/r)^2}]/2$ at a distance r from the surface of the Cepheid.

To predict the dust shell luminosity, we need to specify the properties of the dust. The dust grain size is assumed to range from 0.005 μm to 0.25 μm, which yields a value $< a^2 > / < a^3 > \approx 40\ \mu m$ based on the method of Mathis et al. (1977). Assuming the dust is primarily graphite, the absorption will be concentrated at optical wavelengths, giving an absorption efficiency of $Q_\nu^A \approx 2$. This further implies that the mean density of the grains is $\bar{\rho} = 2.2\ g/cm^3$. The dust velocity, equivalent to the terminal velocity of a wind, is about 100 km/s, approximately equivalent to the escape velocity of a Cepheid. The integral is computed from the surface of a Cepheid but dust does not form in the wind until the material is at a condensation distance $r_c = (R_*/2)(T_*/1500K)^{5/2}$, where dust condenses at a temperature of $1500K$. The dust temperature at distance r from the star, greater than the condensation distance, is $T_d(r) = T_* W(r)^{1/5}$. This leaves the dust mass–loss rate, stellar radius and effective temperature as unknowns in Equation 8.1.

The gas mass–loss rate is found by assuming a dust–to–gas ratio. The typical ratio assumed for the Milky Way ISM is 1/100, and this ratio was used in previous studies for mass–loss in Galactic Cepheids (McAlary & Welch, 1986). The dust–to–gas ratio in the LMC must be significantly smaller than 1/100 because the formation of dust depends on the metallicity of the gas. For this work, a value of the LMC dust–to–gas ratio is assumed to be 1/250 found by scaling the Milky Way dust–to–gas ratio by the ratio of the average LMC metallicity of $Z = 0.008$ to the standard solar metallicity $Z_\odot = 0.02$. This choice of dust–to–gas ratio leads to a gas mass–loss rate that is a lower limit. The dust–to–gas ratio in the LMC has been observed to be approximately one quarter the Galactic value (Clayton & Martin, 1985) to about one tenth the Galactic value (Weingartner & Draine, 2001). Therefore a gas mass–loss rate may be smaller than

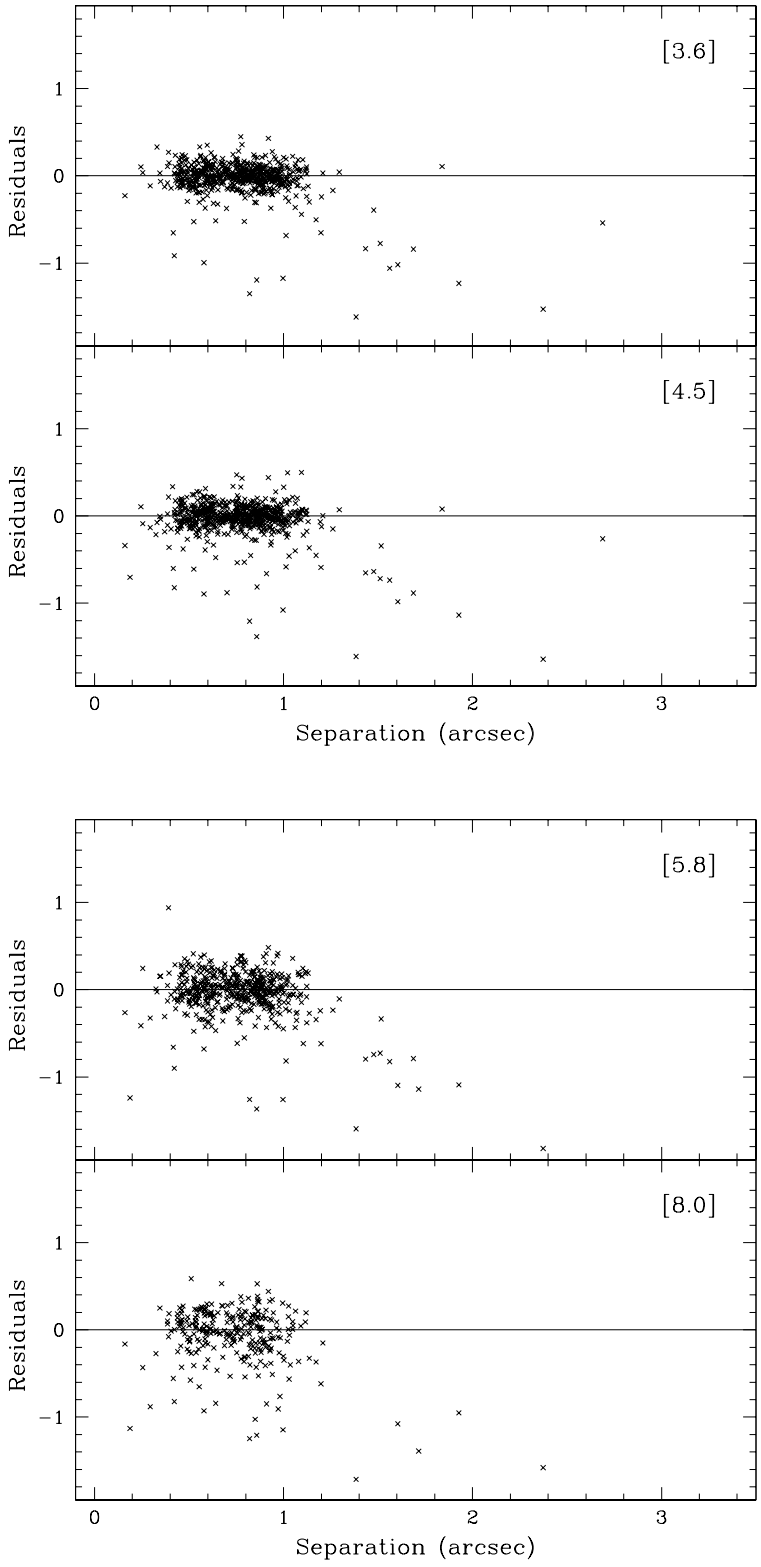

Figure 8.2: The apparent magnitude residuals of the fits of the PL relations from Ngeow & Kanbur (2008) as a function of the separation of the positions of OGLE II Cepheids and the infrared sources for (Top) 3.6 and 4.5 μm and (Bottom) 5.8 and 8.0 μm.

would be predicted using other dust–to–gas ratios. The dust velocity, which is also the terminal velocity of the gas wind, is chosen to be approximately the escape velocity, but the dust velocity may range from about 75–150 km/s, leading to an uncertainty of about 50%.

The mean luminosity of a Cepheid at frequency ν is given by

$$L_{\nu,\mathrm{Star}} = 4\pi R_*^2 \pi B_\nu(T_{\mathrm{eff}}), \tag{8.2}$$

meaning the stellar luminosity is dependent on the radius and effective temperature. We check if a blackbody is a reasonable approximation by comparing blackbody B, V, I brightnesses with the B,V, and I from a Atlas stellar atmosphere mode Kurucz (1979) with an effective temperature of $6000K$ and $\log g = 1$. The model atmosphere is consistent with Cepheid properties and the B,V, I agree with blackbody estimates to within a few tenths of a magnitude. The infrared observations are well approximated by a blackbody brightness because these wavelengths are in the tail of the blackbody function at 6000 K. The different predicted brightnesses will affect the uncertainty of the mass–loss model but not greatly. This leaves three unknown variables for fitting the observations: the dust mass–loss rate, the stellar radius and the effective temperature. The effective temperature may be determined using the relation determined by Beaulieu et al. (2001)

$$\log T_{\mathrm{eff}} = 3.930122 + 0.006776 \log P - 0.2487(V - I)_0. \tag{8.3}$$

The relation is dependent on the pulsation period and de–reddened color.

To compare the predicted total luminosity (stellar plus shell) of the LMC Cepheids with the observed fluxes, we need to adopt a distance modulus. Our choice is 18.5 ± 0.1 for the LMC, which is approximately the mean distance modulus (Catelan & Cortés, 2008; Clement et al., 2008, for example), although the value ranges from 18.4 to 18.7.

The errors for the optical and infrared observations are likely to be negligible compared to other uncertainties, so we assume that the error for each optical wavelength is 0.1 magnitudes, due to the uncertainty of the distance to the Cepheids to determine the absolute magnitudes and the error for the infrared observations is 0.2 magnitudes based on the distance uncertainty. The main sources of error are the thickness of the LMC (Lah et al., 2005), error in the observations themselves and that the infrared observations may not be the mean brightness of Cepheids. In fact, a thickness of about 5% of the distance to the LMC corresponds to an error of 0.1 mag.

The BVI observations are also de–reddened while it is assumed that the extinction of the infrared light is negligible. The color excess $E(B - V)$ is given in the OGLE II data for each Cepheid and is on average ≈ 0.15. The extinction for the BVI is calculated in the same way as in Udalski et al. (1999b), while the extinction in the infrared is significantly less than 0.1 magnitudes.

8.3 Quality of Fit of Mass–Loss Rates

Having described the method for predicting stellar fluxes over the seven bands, we fit the mean radius and dust mass–loss rate, and hence the gas mass–loss rate, using χ^2 fitting, for each Cepheid in the sample. The value of χ^2 is given as

$$\chi^2 = \frac{1}{N-f}\sum_{i}^{N}\left(\frac{M_{\lambda_i}(\text{Predicted}) - \text{M}_{\lambda_\text{i}}(\text{Observed})}{\sigma_i}\right)^2, \tag{8.4}$$

where N is the number of observations and f is the number of unknowns. The χ^2 fits are calculated for a range of stellar radii based on the Period–Radius relation (Gieren et al., 1999)

$$\log R/R_\odot = 0.68 \log P(d) + 1.146. \tag{8.5}$$

and varying that radius by ±20%. The dust mass–loss rate is fit for a specific mean radius by finding a minimum value of χ^2 using a root–finding algorithm. Before we attempt to fit the dust mass–loss rate, we first apply the χ^2 fitting to the range of mean radii alone as a reference. The values of χ^2 and predicted radii in this method are shown in Figure 8.3.

Fitting the radius alone to the observations seems to provide a reasonable fit, but one may argue that the uncertainty of the fit is related to the fact that the SAGE observations are single epoch and are not mean brightness at these wavelengths. We test this by χ^2 fitting the radius and a quantity dm. This variable represents the difference between the observed infrared magnitude and the mean brightness of the Cepheids. The values of dm are assumed to vary from −0.5 to 0.5 magnitudes dimmer, where a negative value of dm implies the mean brightness is brighter than what is observed. The chosen range of values are exaggerated as the full brightness amplitude of a Cepheid at IRAC wavelengths is < 0.4 the amplitude in the visible. The largest full amplitude in the visible is 1.2 magnitudes, meaning the infrared variable dm will be $-0.25 < dm < 0.25$ in reality, and for the majority of Cepheids the range of dm is much smaller. We show in Figure 8.4 the predicted values of dm as a function of period. If the hypothesized infrared excess were due primarily to the fact that the infrared observations are single epoch then about 50% of the sample would predict $dm \leq 0$ and 50% ≥ 0. The results in Figure 8.4 show a preference for $dm > 0$, with 68% of the total sample having $dm > 0$ and 13% preferring $dm = 0$. Therefore, we take this as proof of an infrared excess in the SAGE sample.

The next step is to determine the best–fit radius and mass–loss rate for the sample of Cepheids. The χ^2 fits are presented as a function of pulsation period in Figure 8.5 along with the gas mass–loss rate. The mass–loss rates range from 10^{-12} to $10^{-8} M_\odot/yr$, with the values of χ^2 ranging from about 1.1 to about 23. The large majority of Cepheids appear well fit by a mass–loss model that forms dust at some distance from the surface of the Cepheid. These predicted mass–loss rates are significant, $10^{-9} M_\odot/yr$, and, depending on

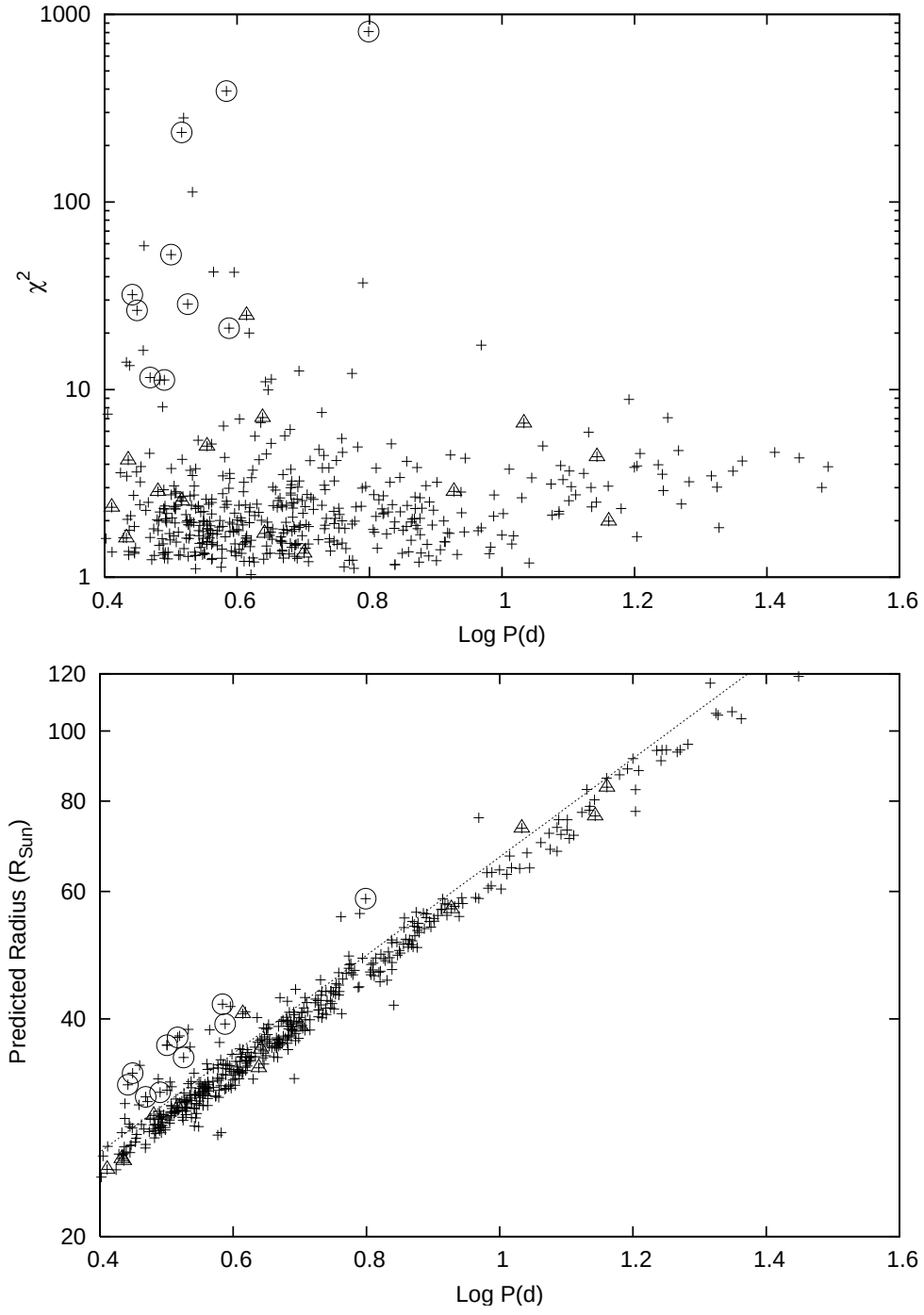

Figure 8.3: (Top) The χ^2 fit of the observations with best–fit mean radius only. (Bottom) The predicted radii of the sample of Cepheids with the Period–Radius relation (Gieren et al., 1999) shown as a dotted line. The circled points are the Cepheids that are considered most likely to be false associations while the triangles represent the Cepheids with separation between OGLE II and SAGE coordinates of less than 0.4 arcseconds.

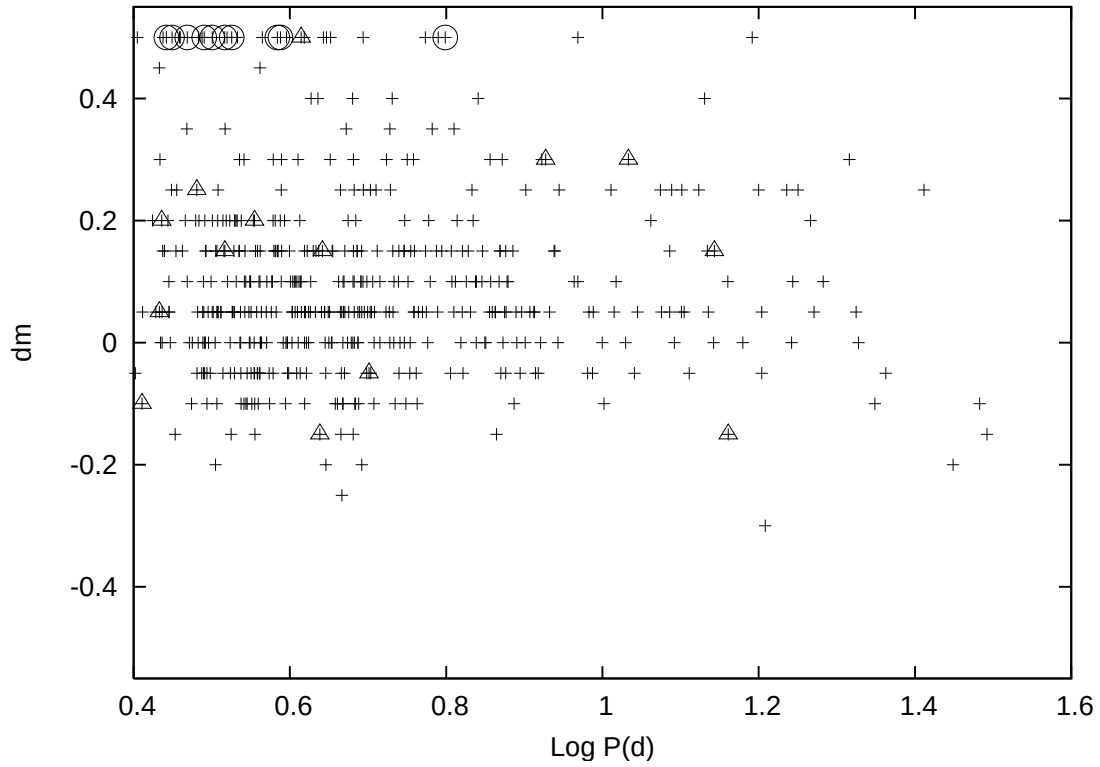

Figure 8.4: The best–fit values of *dm*, the predicted differences between the mean brightness and observed brightness at infrared wavelengths. Circled points are the likely false associations and triangles represent separations less 0.4 arcseconds.

the dust–to–gas ratio and dust grain properties, the gas mass–loss rates may be an order of magnitude larger or even more. These gas mass–loss rates are the minimum mass–loss rates for the LMC Cepheids.

We also quantify the uncertainty of the mass–loss rates caused by the unknown phase of the infrared observations by computing the best χ^2 fits for the mass–loss rate, radius and the quantity *dm* that was defined earlier, and we compute the values of $\delta \ln(\dot{M})/\delta(dm)$ for a random, with respect to period, subsample of 100 of the Cepheids. This error is a function of both the pulsation amplitude, and the mass–loss rate. We show the values of $\delta \ln(\dot{M})/\delta(dm)$ as a function of $\dot{M}$ in Figure 8.6. The uncertainty is related to the mass–loss rate, and, as one would expect, the uncertainty of the pulsation amplitude is less important for larger predicted mass–loss rates. We highlight the boundary where the uncertainty of the mass–loss rate is 100% for a pulsation amplitude of 0.5 magnitudes which represents the maximum infrared pulsation amplitude. This implies that Cepheids with predicted mass–loss rates $> 10^{-9} M_{\odot}/yr$ have infrared excesses that cannot be explained solely by pulsation phase, and a number of Cepheids with mass–loss rates $< 10^{-9} M_{\odot}/yr$ have uncertainties $\delta \ln(\dot{M})/\delta(dm) < 4$. As the IR pulsation amplitudes become known we will be able to probe smaller mass–loss rates with more certainty.

The model is also tested by comparing the two parameter fits, with the mass–loss rate and radius as

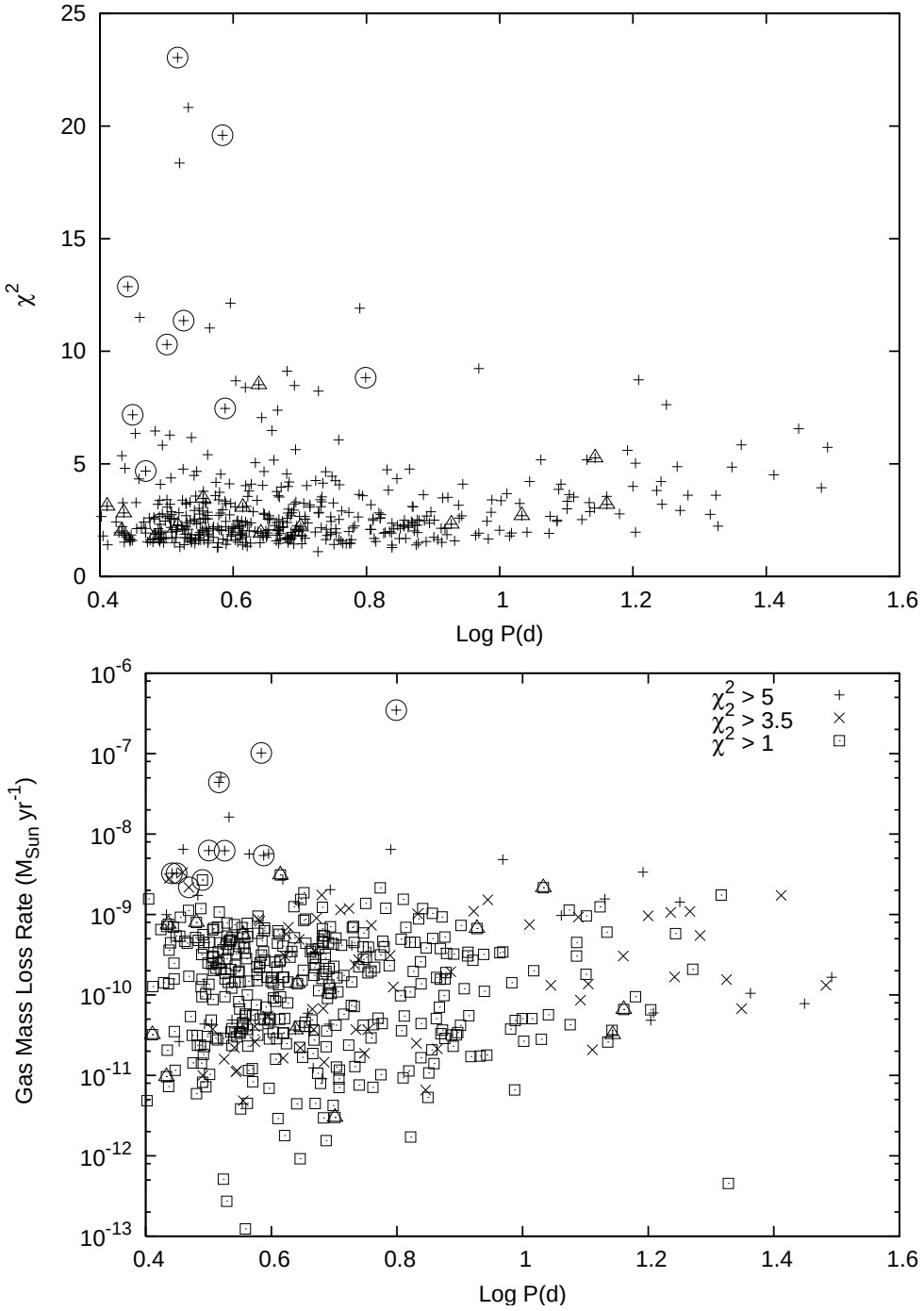

Figure 8.5: (Top) The χ^2 of the observation with best–fit mean stellar radius and mass–loss rate. (Bottom) The gas mass–loss rates of the sample of Cepheids, binned into different χ^2 groups. Those points circled are the possible false associations.

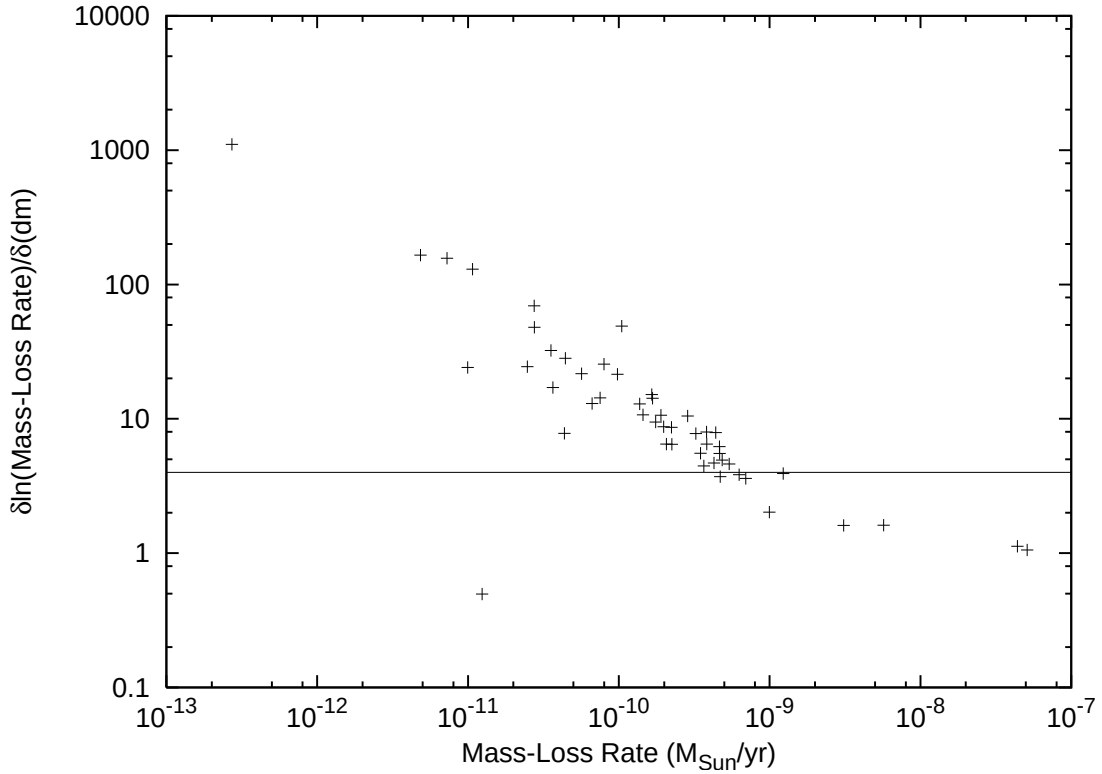

Figure 8.6: The uncertainty of the mass–loss rates due to the difference between the observed infrared brightness and the unknown mean brightness of the Cepheids as a function of mass–loss rate. The horizontal line refers to an uncertainty of 100% for a full pulsation amplitude of 0.5 mag.

the two degrees of freedom, to fits using just the radius as the only degree of freedom. We use the F–test to quantify the significance of the mass–loss model. The F–test is described by Kanbur & Ngeow (2004); Ngeow & Kanbur (2008, and references therein) and for each Cepheid we calculate the value of F. For the majority of Cepheids, the fit of the radius has only six degrees of freedom while the mass–loss model has five. Some of the Cepheids have one less degree of freedom for each model respectively. The values of F are shown in Figure 8.7 against the values of χ^2 for the mass–loss model. The values of $F > 5$ mean that we can state with 95% confidence that the mass–loss model is significant relative to fitting the radius alone. This provides no information into the possibility of blending, for instance, so we also take a cut of models with a value of $\chi^2 < 5$. This corresponds to the upper left quadrant of Figure 8.7 which contains 44 Cepheids. Therefore we state with 95% confidence that approximately 9% of the sample of LMC Cepheids have circumstellar dust shells caused by stellar winds.

It is shown that 44 of the Cepheids are consistent with the mass–loss model, implying that the remainder of the sample is consistent with no mass loss. However the value of F is a function of the mass–loss rate, with F increasing with $\dot{M}$, as shown in Figure 8.7. Cepheids with values of $F < 9$ and $\chi^2 < 5$ in the lower left quadrant of Figure 8.7 with $\chi^2 < 5$ are consistent with mass loss but the observational errors are too

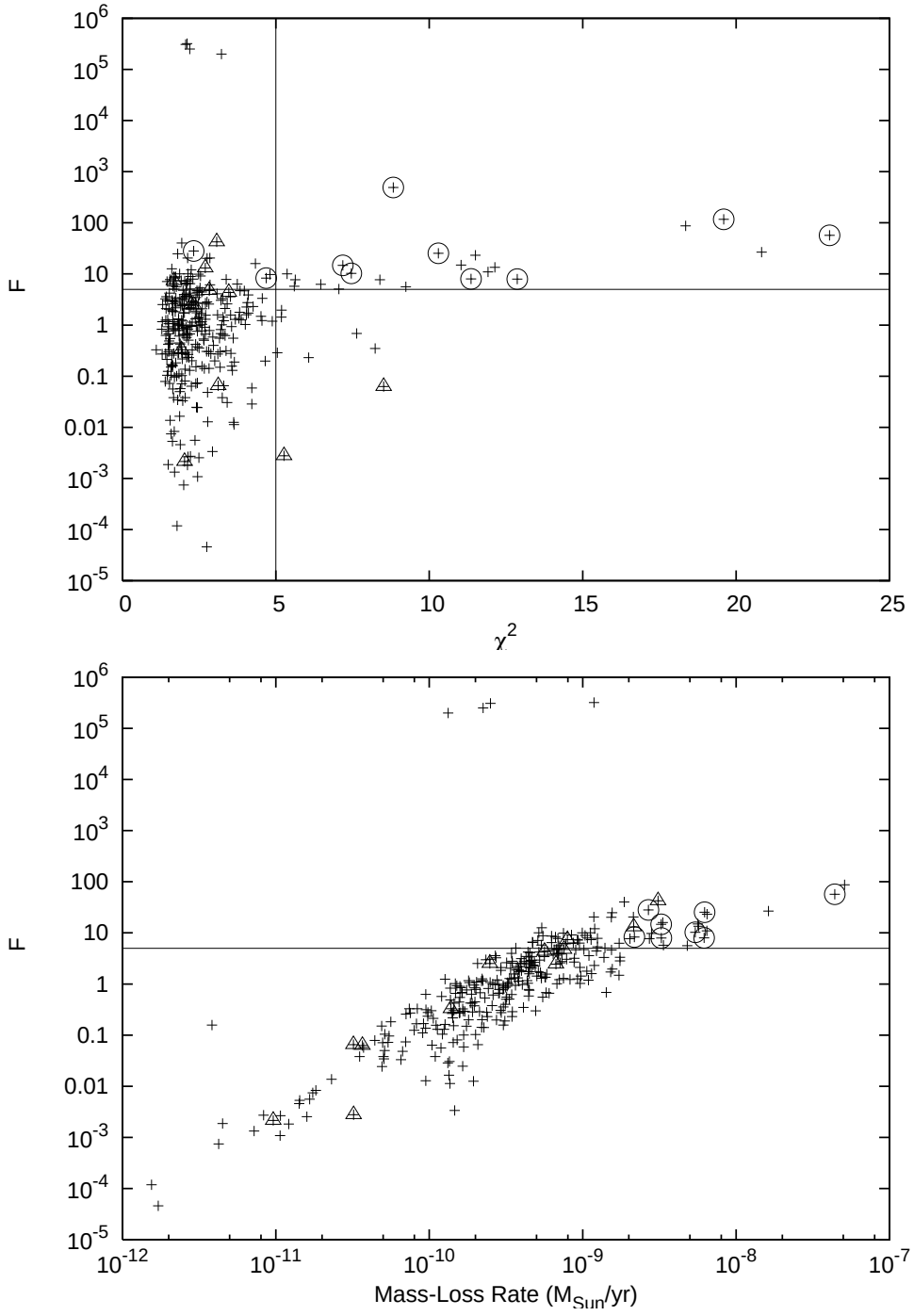

Figure 8.7: (Top) Calculation of the F–test for each Cepheid in the sample plotted in terms of the value of χ^2 from the mass–loss model. The horizontal line represents the 95% confidence level that the mass–loss model is distinguished from fitting the mean radius only. The vertical line is a represents a cut–off of $\chi^2 = 5$ where we interpret $\chi^2 < 5$ as a reasonable fit. (Bottom) The values of F as a function of the predicted mass–loss rates. The circled points represent those Cepheids that are likely false associations of the infrared observations and the triangles represent those with separations less than 0.4 arcseconds.

Table 8.1: Best Fit Parameters for Predicted PL Relations

Type	λ (μm)	Slope	Zero Point	Dispersion
Linear	3.6	-3.145 ± 0.024	15.993 ± 0.017	0.110
	4.5	-3.159 ± 0.023	15.921 ± 0.017	0.108
	5.8	-3.170 ± 0.023	15.924 ± 0.017	0.107
	8.0	-3.181 ± 0.023	15.929 ± 0.017	0.105
Non–	3.6	-3.248 ± 0.038	16.057 ± 0.025	0.107
Linear	4.5	-3.259 ± 0.038	15.983 ± 0.025	0.105
$P < 10d$	5.8	-3.268 ± 0.037	15.984 ± 0.025	0.104
	8.0	-3.276 ± 0.037	15.988 ± 0.024	0.103
Non–	3.6	-2.971 ± 0.123	15.815 ± 0.146	0.125
Linear	4.5	-2.989 ± 0.121	15.747 ± 0.143	0.122
$P > 10d$	5.8	-3.005 ± 0.119	15.754 ± 0.141	0.120
	8.0	-3.019 ± 0.118	15.763 ± 0.140	0.118

large to state with certainty that all LMC Cepheids are undergoing mass loss. This suggests that the model needs to be tested with time series infrared observations to constrain the pulsation amplitude and reduce the uncertainty of the infrared observations. In the next section, we test what effect mass loss might have on the infrared PL relation if the hypothesis is correct.

8.4 The Effect of Mass Loss on Infrared Period Luminosity Relations

It has been postulated that mass loss generates dust in a circumstellar shell surrounding a Cepheid and this, in turn, affects the infrared PL relation. By using the predicted stellar luminosities of the sample of Cepheids, we compute the stellar PL relations, $m_\lambda = a \log P + b$, and compare them with results from Ngeow & Kanbur (2008) and Freedman et al. (2008). We also test the data for non–linearity in the infrared PL relations. In the fit, we do not include the Cepheids with large separations that were noted in the previous section, however, we do include those with separation less than 0.4 arcseconds because they have randomly distributed mass–loss rates, in Figure 8.5, and hence have randomly distributed infrared excesses.

The predicted stellar luminosities of the LMC Cepheids in the mass-loss model are shown in Figure 8.8, together with a comparison of the linear and non–linear PL relations with the relations from Ngeow & Kanbur (2008) and Freedman et al. (2008). The non–linear PL relation is defined as two linear relations, the first for the period range of 1 to 10 days while the second is for the longer period range (Ngeow et al., 2005). The slopes, zero–points and dispersions of the fits for the linear and non–linear fits are given in Table 2.1.

The linear PL relations have smaller dispersion than the PL relations from Ngeow & Kanbur (2008) for the two longer wavelengths and slightly larger dispersion for the two shorter infrared wavelengths. There are also notable differences in the slopes and the zero points. The zero points of the predicted 3.6 and 4.5 μm

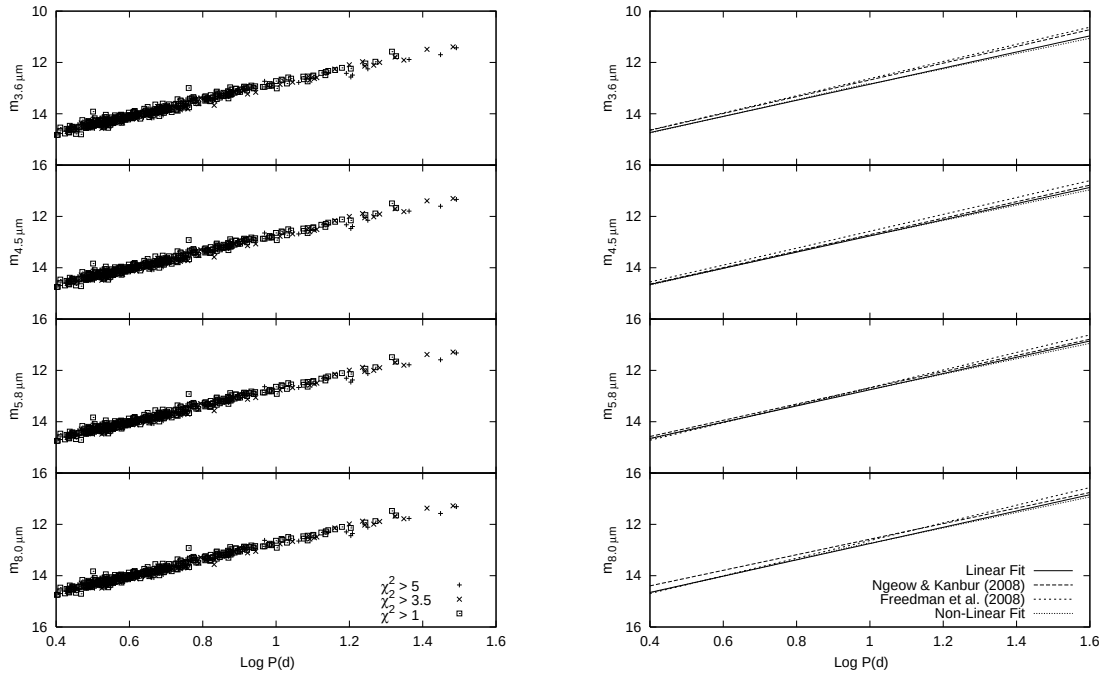

Figure 8.8: (Left) The predicted stellar brightnesses of the LMC Cepheids as a function of period. (Right) The Comparison of the best–fit linear and non–linear PL relations to the relations determined by Ngeow & Kanbur (2008) and Freedman et al. (2008) where we removed Cepheids with separation greater than 1.3 arcseconds.

PL relations are approximately the same as those determined by Ngeow & Kanbur (2008), while at longer wavelengths the differences are significant and also the predicted zero points tend to be a little brighter than the zero–points found by Freedman et al. (2008). This is consistent with mass loss causing larger infrared excesses at longer wavelengths. The predicted slopes range from −3.14 at shorter wavelengths to −3.18 at longer wavelengths. This is a small change of slope as a function of wavelength, and it is roughly consistent with a constant slope within the errors given n Table 2.1. The slopes from Ngeow & Kanbur (2008) show the opposite behavior with the slopes becoming less steep with longer wavelength, contrary to the arguments in Freedman et al. (2008) who maintain the slope of the PL relation should be steeper as a function of wavelength and approaches an asymptotic limit. In both cases the uncertainty of the slope is similar, ranging from 0.017 to 0.048 with increasing wavelength for Ngeow & Kanbur (2008), and about an average of 0.03 for Freedman et al. (2008). Therefore the slopes from these two works and those predicted here do not agree within the uncertainty.

This shift in the behavior of the slopes of the infrared PL relations is due the removal of infrared excess caused by mass loss. This is best seen at 8.0 μm where the slope changes from about −3 (Ngeow & Kanbur, 2008) to −3.18 when the contribution of brightness due to mass loss is removed, although the observed slope of −3 may also be due to incompleteness of the data at the faint end of the PL relation. The implication is that mass loss in short period Cepheids contributes significant luminosity, increasing the zero point and

causing a shallower slope because the majority of the Cepheids in the sample have periods less than ten days. The shallower slope implies that mass loss contributes fractionally less to the total infrared luminosity at longer periods because the stellar luminosity is already so large.

The analysis in the previous section showed that the mass loss hypothesis is statistically unique from fitting only the radius of the Cepheid for about 44 Cepheids in the sample, or conversely that the majority of Cepheids in the sample are statistically consistent with zero mass loss. From this realization, we wish to compare the observed infrared brightness that we fit our model with and the predicted infrared brightness of the Cepheids. The comparison is shown in Figure 8.9 for the 8.0 μm data. At this wavelength the differences is most apparent because a dust shell contributes a larger fraction of the total flux at longer wavelengths. We also compute best–fit linear relations for the observed data where the Cepheids with large separation and the 44 Cepheids where mass loss is shown to be likely are not used in the fitting. This relation is $m_{8.0\mu m}(\text{Observed}) = -2.905 \log \text{P} + 15.530$ with a standard deviation of 0.219. For comparison, we derive the best–fit data using all of the 8.0 μm data from Ngeow & Kanbur (2008) and find $m_{8.0\mu m}(\text{Complete}) = -2.473 \log P + 15.058$ with a standard deviation of 0.602. The relations given in Ngeow & Kanbur (2008) are determined using an iterative fitting method where a best–fit relation is determined and then any Cepheids with a brightness that is more than 3σ different are removed and a new PL relation is computed and the process repeats until the PL relation converges. Here, we compute the PL relation using all of the data without the iterative approach, The linear relations are shown in Figure 8.9. Although we are only able to confidently state that 44 of the Cepheids are consistent with the mass–loss model, we note that there are significant differences between the predicted stellar brightnesses and observed data, and that these differences are reflected in the infrared PL relations. It is also interesting that these 44 Cepheids are observed to be brighter than the majority of the sample but there are a number of Cepheids with similar brightness that are statistically consistent with zero mass loss.

The data are tested for non–linearity in the infrared PL relations. The hypothesis that the infrared PL relations are non–linear is tested with the F–test, as described in Kanbur & Ngeow (2004); Ngeow & Kanbur (2008, and references therein) by comparing a PL relation of the form

$$m_\lambda = \begin{cases} a \log P + b & \log P < 1 \\ c \log P + d & \log P > 1 \end{cases} \tag{8.6}$$

with the standard linear PL relation with two degrees of freedom. If the value of $F > 3$, the PL relations are non–linear with 95% confidence. Our values of F, with increasing wavelength, are 7.89, 5.93, 5.78, and 5.50. The predicted stellar PL relations are thus consistent with being non–linear with a period break at 10 days. The predicted slopes and zero–points are given in Table 2.1. However there are two possible sources of error. The first is that we are assuming blackbody radiation that ignores any infrared absorption lines that may affect the structure of the PL relations. The second is that there are significantly less data for periods greater than 10 days (approximately 50 data points).

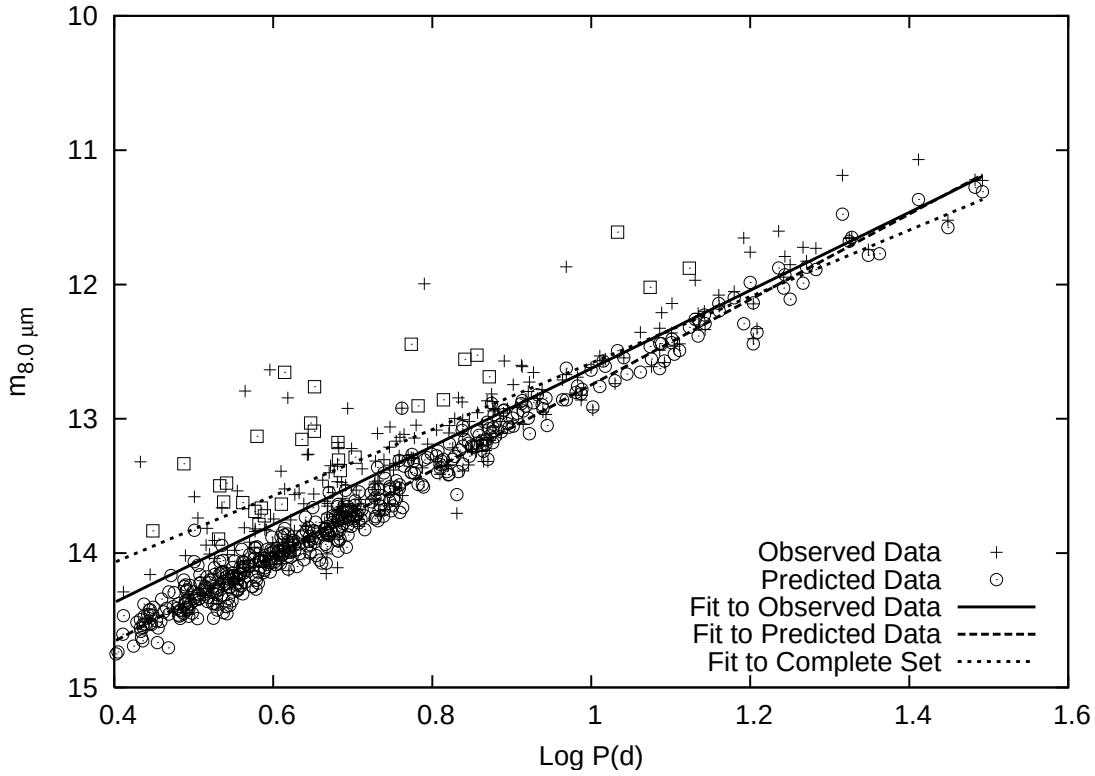

Figure 8.9: Comparison of the predicted stellar and the observed fluxes of the sample of Cepheids. The 44 Cepheids where the mass–loss model is statistically unique are shown as squares. The lines represent the predicted stellar flux, the observed stellar flux of the sample and that of the complete set from Ngeow & Kanbur (2008).

The non–linearity is related to the fact that the luminosities are given by the effective temperature; using the OGLE II data to derive effective temperatures may cause a non–linear Period–Temperature relation because of non–linearity in the OGLE II $(V - I)$ Period–Color relation (Kanbur & Ngeow, 2004). This non–linear Period–Temperature relation causes non–linearity in the infrared predictions. This implies that the PL relations given by only the stellar component is non–linear in the wavelength range of 3.6 to 8.0 μm based on blackbody arguments, contradicting the results of Ngeow & Kanbur (2008) and Ngeow & Kanbur (2006) for the K–band PL relation. There are two plausible reasons why this contradiction is found. Kanbur et al. (2004) argue the non–linearity is due to the hydrogen ionization front (HIF) interacting with the photosphere, causing significant temperature variations in the layers of the Cepheids that emit mostly in the optical; at longer wavelengths this interaction becomes less significant. This implies that the mean effective temperature at shorter periods is affected by the HIF while at longer periods the effective temperature is just what would be expected for a non–pulsating star. At infrared wavelengths, most of the radiation is emitted higher in the stellar atmosphere farther from the effects of the HIF, which leads to a more linear PL relation and is hence more dependent on the Period–Radius relation, which is linear. This would explain why the values of F for the non-linear relations decrease with longer wavelength, the IR PL relations are becoming

more consistent with a surface brightness related to the linear Period–Radius relation. The non–linearity of the predicted data may just be reflecting the non–linearity in the optical wavelengths because the variations of the effective temperature over the pulsation period is ignored.

The second possibility is that mass loss causes larger infrared excess for shorter period Cepheids than for longer period Cepheids even though the mass–loss rates are similar for short ($P < 10d$) and long ($P > 10d$) period Cepheids. The short period Cepheids have smaller radii leading to smaller, more dense circumstellar shells. The more dense shells cause greater infrared excess. This greater infrared excess in shorter period Cepheids makes them appear brighter on average, which increases the zero point of the infrared PL relation; because the relative infrared excess decreases with longer period, the slope of the PL relation will appear shallower, with the effect being more prominent at longer wavelength. This idea may explain the marginal linearity found in the K–band PL relation. Infrared excess in Galactic Cepheids has been observed using K–band interferometry (Kervella et al., 2006; Mérand et al., 2006, 2007) so it is likely infrared excess plays a role in the LMC Cepheids at this wavelength. This would imply that the K–band PL relation is actually non–linear and this non–linearity is being masked by the infrared excess. This argument also explains the results of the tests of non–linearity in the IRAC PL relations in Ngeow & Kanbur (2008), in particular the non–linear PL relation at 8.0 μm. The authors found that the slope of the non–linear PL relation for $P < 10d$ is shallower than the slope of the linear relation at 8.0 μm with a more luminous zero point. The non–linear PL relations for $P < 10d$ in the optical and near–IR all display the opposite behavior with respect to the linear PL relations. This non–linear relation at 8.0 μm is due to the same process that causes the other IRAC PL relations to appear linear except the process is more significant at longer wavelengths.

It has been shown that mass loss provides a significant contribution to the infrared brightness of LMC Cepheids and affects the structure of infrared PL relations. Without the contribution of mass loss, the slopes of the linear PL relations are steeper with increasing wavelength albeit at a small rate differing from the slopes becoming more shallow as found by Ngeow & Kanbur (2008). Applying the F–test to the predicted data implies that the infrared PL relations are non–linear, though this result requires further testing. However most of the Cepheids have predicted mass–loss rates that are statistically consistent with zero implying this result is preliminary and needs to be tested further with more data with smaller uncertainties.

8.5 What is the Driving Mechanism?

Up to this point, we have investigated the ability of mass loss to match the OGLE II and SAGE observations of LMC Cepheids, and how the resulting estimates of infrared excess affects the structure of the PL relations. This has been done *without* assuming a driving mechanism of the Cepheid wind. There are a number of possible methods for stars to drive mass loss, but only two are likely for Cepheids: radiative driving and pulsation driving, which was discussed in Chapter 6. It is not feasible to apply the pulsation–driving model to this set of data as we do not have knowledge of the pulsation amplitudes or masses to which the model is

sensitive. However we can test whether a *radiative*–driven stellar wind can match the predicted mass–loss rates using the method of Castor, Abbott, & Klein (1975).

The calculation of the mass–loss rate for a radiative–driven stellar wind is reviewed in Lamers & Cassinelli (1999), and discussed in Chapter 6. To conduct the calculation the mass, luminosity, radius and effective temperature are needed; the radii are determined by the χ^2 fitting, the effective temperatures are given by the relation from Beaulieu et al. (2001) and the luminosity is found from the radius and effective temperature. The mass is unknown so the radiative–driven mass–loss rates are found using a number of masses via mass–luminosity relations from Bono et al. (2000b), where $L = M^n$ in solar units. The mass–loss rates found from the observations are shown in the left panel of Figure 8.10, plotted with the best–fit relations for radiative–driven mass–loss rates found with the following mass–luminosity relations, where $n = 4.4, 4.7, 5.0$, and 6.0. The value of $n = 4.4$ represents the mass–luminosity relation from stellar evolution calculations, while $n = 4.7$ and 5.0 represent the mass–luminosity relations relating to mass found using pulsation calculations, and $n = 6.0$ is used as an extreme case. An example of the values of the radiative–driven mass–loss rates is shown in the right panel of Figure 8.10 for the case of $n = 4.7$. Radiative–driven mass–loss rates for other values of $n > 4.7$ will increase the rates and for $n < 4.7$ will decrease the rates by a roughly constant amount for each Cepheid.

The radiative–driven mass–loss rates are significantly smaller than the mass–loss rates determined from the observations. At short periods of approximately 5 days, the radiative mass–loss rates are about 10^3 to 10^5 times lower. However, at periods greater than 30 days the radiative–driven mass–loss rates are of similar order as the calculations. This implies that the mass–loss cannot be driven by radiative lines alone at short period; there must be another driving mechanism. This differs at longer period, but it should be noted that the mass–loss rates found from the observations are the minimum value based on the dust–to–gas ratio. This means that the predicted gas mass–loss rates from infrared observations may be larger than the *radiative*–driven mass–loss rates.

As a further test of whether the mass loss is consistent with radiative driving we compute the circumstellar flux from dust created in a radiative–driven wind and added that to the predicted blackbody fluxes to compute infrared PL relations. These relations are predictions of what would be observed if the mass loss is consistent with radiative driving. The fitted relations at the four wavelengths 3.6, 4.5, 5.8, and 8.0 μm have slopes and y–intercepts that are equivalent to the IR PL relations derived from the predicted stellar fluxes alone within the error of the fits. For instance the slope and y–intercept of the 8.0 μm relation is -3.139 ± 0.024 and 15.988 ± 0.017, differing by only a few thousandths from the 8.0 μm PL relation determined from the predicted stellar fluxes alone. Radiative driving does not explain the significant infrared excess of 44 Cepheids that are explained by mass loss.

The amount of mass loss from the LMC Cepheids do not agree with radiative–driving calculations, and the mass loss is more consistent with the pulsation–driven model if one considers the magnitude of the mass–loss rates and the amount of scatter, especially for the 44 Cepheids where the mass–loss model is

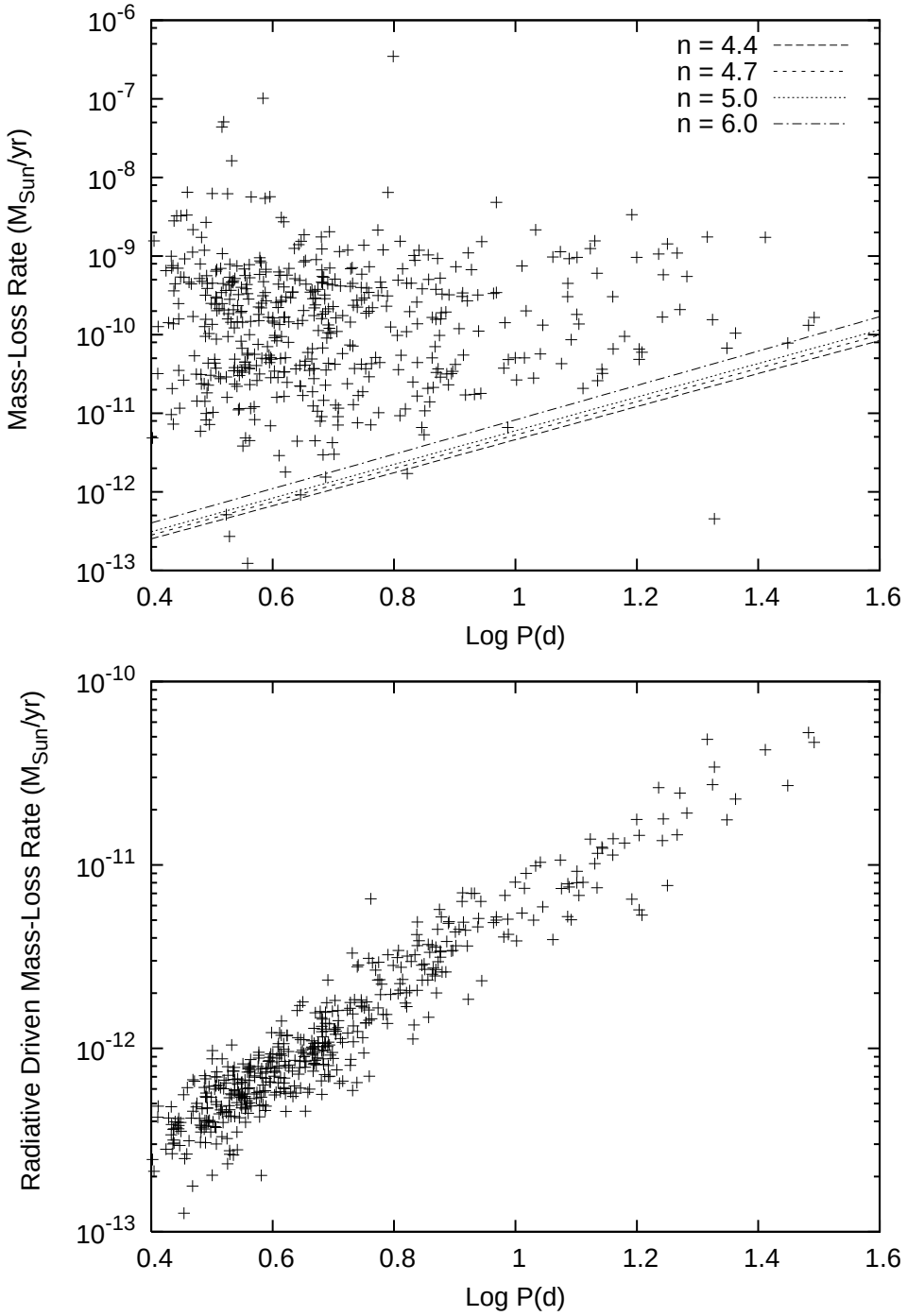

Figure 8.10: (Top) The comparison of the mass–loss rates found from the infrared observations with best–fit linear relations representing mass–loss rates found from radiative–driving calculations, and (Bottom) the radiative–driven mass–loss rates for the mass–luminosity relation where $n = 4.7$.

unique. The remainder of the sample cannot be distinguished statistically from pulsation driving, radiative driving or no mass loss. However, if one invokes no mass loss or radiative driving then it is more difficult to explain the behavior of the 44 Cepheids. Pulsation–driven mass loss predicts that mass loss is driven by shocks generated in a pulsating atmosphere and the shocks tend to be more efficient at hotter effective temperatures. This would explain the large range of mass–loss rates at similar pulsation periods. The pulsation–driven mass–loss rates tend to be orders of magnitude larger than radiative–driven mass–loss rates as shown for observations of Galactic Cepheids and theoretical models of Galactic, LMC and SMC Cepheids at shorter periods. We conclude that the mass–loss rates found in this work provide evidence for the model of pulsation–driven mass loss.

8.6 Discussion and Conclusions

It is hypothesized that LMC Cepheids have significant infrared excess based on infrared observations of the LMC from the SAGE survey, and that the infrared excess is caused by dust forming in a Cepheid wind at a large distance from the surface of the star. The idea was tested using OGLE II BVI observations along with IRAC observations of the Cepheids to best–fit radii and dust mass–loss rates of the LMC Cepheids. The effective temperatures are determined using a temperature–color–period relation from Beaulieu et al. (2001).

The predicted gas mass–loss rates are significant with an average about 10^{-10} to $10^{-9} M_{\odot}/yr$ and may possibly be as high as $10^{-7} M_{\odot}/yr$, depending on the value of the dust–to–gas ratio. These mass–loss rates are not consistent with have radiative line–driving as the primary driving mechanism for the LMC Cepheids. The rates, instead, provide evidence for shocks and pulsation driving the mass loss when compared to the analytic pulsation–driven wind model.

The mass–loss model is compared to the fit of the observations with radii alone, and it is shown that a model fitting only the radius may be rejected with 95% confidence relative to the mass–loss model for 44 Cepheids but this means that the remainder of the sample is consistent with no mass loss. Therefore the results and arguments in the work based on the mass–loss model should be regarded with caution. For almost every case the predictions are limited by the uncertainties of the distance modulus and the IR pulsation amplitude. This comparison of the two models using the F–test is dependent on the mass–loss rate, and this shows we detect reliable infrared excess if the mass–loss rate is $> 10^{-10} M_{\odot}/yr$. Because of the dependence of the F–test on the mass–loss rate we explored what effect mass loss would have on the infrared PL relation. The mass–loss model would benefit from infrared observations over the period of pulsation to determine the mean brightness, which would decrease the uncertainty of the infrared brightnesses.

The large mass–loss rates of LMC Cepheids may explain the Cepheid mass discrepancy in the LMC. The pulsation masses tend to be about 20% smaller than evolution masses in the LMC (Keller, 2008), which translates to a difference of about $1 M_{\odot}$ for lowest mass Cepheids up to a few solar masses for the

most massive Cepheids. The mass–loss rates found in this work agree with the discrepancy for low mass Cepheids to an order of magnitude because the evolutionary timescale for a Cepheid on its second crossing is of order ten million years. However the mass–loss rates are too small to be consistent with a 20% mass discrepancy for the more massive Cepheids. It should be noted that the mass discrepancy in LMC Cepheids is measured from Cepheids with periods less than $20d$, which have evolutionary masses from about 4 to $7M_{\odot}$ (Bono et al., 2000b). The mass discrepancy has not been measured for more massive LMC Cepheids.

It has also been found that mass loss affects the infrared PL relations. Using the predicted stellar luminosities we constructed new infrared PL relations that do not have infrared excess. These relations differ from those determined by Ngeow & Kanbur (2008) with differences in the zero point and the slope. The IR PL relations from Ngeow & Kanbur (2008) have slopes that become smaller at longer wavelength inconsistent with the argument that the slope of the PL relation should approach a constant maximum value at longer wavelength base on the Period–Radius relation (Freedman et al., 2008). The slopes in this work are all about -3.15 with a small amount of steepening at longer wavelength. This would imply a constant slope near that value which is also inconsistent with the slope derived from the PR relation.

Using the F–test, there is evidence for non–linearity in the relations similar to the non–linear structure found in optical PL relations. Mass loss acts to linearize the PL relation at 3.6, 4.5, and 5.8 μm, while at 8.0 μm the PL relation is non–linear with a slope that is shallower at $P < 10d$ than for $P > 10d$ which implies the infrared excess is becoming more important at longer wavelength. Mass loss may also explain why the K–band PL relation is marginally linear Ngeow & Kanbur (2006).

The resulting effect that mass loss has on infrared observations of Cepheids implies serious consequences for infrared Period–Luminosity relations if they are to be used for high precision astrophysics. One of the reasons for using infrared PL relations is that they are less sensitive to metallicity than optical relations and hence do not need to be corrected for each galaxy (Sasselov et al., 1997). The metallicity correction is a significant source of uncertainty in studies of the Hubble Constant (Freedman et al., 2001) and an infrared PL relation that avoids this uncertainty would be a powerful tool. However, we have shown that mass loss affects the scatter and the structure of the PL relation. The scatter increases the uncertainty of any distance determination, but more importantly the fractional amount of dust generated in a wind depends on metallicity. The amount of mass loss may also depend on metallicity, as suggested in Chapter 8. These two issues imply the Period–Luminosity relation depends on metallicity at infrared wavelengths as well as at optical wavelengths though to what extent is currently unknown.

Part III

Summary

Chapter 9

Conclusions and Future Work

"All my life I've had one dream, to achieve my many goals." - Homer Simpson

9.1 Introduction

The work presented in this dissertation focuses on two objectives, the first is the development of a radiative hydrodynamic program based on a new spherically symmetric version of the ATLAS stellar atmospheres program as well as a study of limb-darkening in the model atmospheres. The second part of the dissertation is the theoretical study of Cepheid mass loss and the formation of circumstellar envelopes. The results and conclusions of these two parts are discussed in their respective chapters and is not repeated here. Instead, the purpose of this final chapter is to review the implications of this work from a more global perspective and to discuss future directions of research.

9.2 The Big Picture

9.2.1 The Mass-Loss Model

The results of this dissertation cover a diverse range of topics in stellar astrophysics but they all share a common thread. They provide insight into the atmospheres of Cepheids and similar stars, and motivate the need for more complete models to produce synthetic spectra and synthetic optical interferometric visibilities to compare with observations presented by Nardetto et al. (2006), Nardetto et al. (2007), Nardetto et al. (2008a), Nardetto et al. (2008b), and Nardetto et al. (2009), and Kervella et al. (2004d), Kervella et al. (2006), Mérand et al. (2006), and Mérand et al. (2007), as well as future observations from the next generation of telescopes and interferometers.

One of the more interesting questions regarding Cepheid structure and evolution is the Cepheid mass discrepancy. In Chapters 6 and 7, it was found that the difference between the evolutionary and pulsation masses is consistent with predicted mass-loss rates due to pulsation driving. Under the hypothesis that mass

loss is the source of the discrepancy, a star will evolve off of the main sequence and enter the Cepheid Instability Strip for the first time. Upon entering the Instability Strip the star has a mass that is consistent with stellar evolution calculations. The star evolves through the first crossing in about 10^6 years and loses some of its mass, up to 0.1 $M_\odot$. The star eventually returns to the Instability Strip to begin its second crossing and spends about 10^7 years losing more mass, up to 1 $M_\odot$. It is in the second crossing where observers are most likely to observe a Cepheid because that is the stage of evolution where stars spend the most time in crossing the Instability Strip. It is at this point where stellar pulsation models are fit to observations and predict a smaller mass Cepheid than standard stellar evolution calculations. The stellar pulsation masses also agrees with dynamical masses as well. Therefore, the mass-loss model suggests that the Cepheid mass discrepancy could be solved by incorporating some sort of pulsation-driven mass-loss prescription in the stellar evolution calculations. The model is also consistent with the existence of circumstellar envelopes where dust forms at a large distance from the star creating an infrared excess.

This picture appears to solve the Cepheid mass discrepancy but mass discrepancy, itself, is not consistently determined, for instance, see the differing results of Caputo et al. (2005) and Keller (2008). The difference between those two results is due to the different assumptions for the Cepheid mass-luminosity relation from different stellar evolution calculations. It is important to quantify the mass discrepancy to better precision to provide better constraints for any hypothesis for the source of the Cepheid mass discrepancy. Essentially, we return to the need for more and better Cepheid models.

The mass-loss model is a potential explanation for the Cepheid mass discrepancy and the existence of circumstellar envelopes but there is nothing in the theory derived in Chapter 5 that is specific to Cepheids only. The theory requires that a star be radially pulsating, to have shocks propagate through the atmosphere and that the star be hot enough for radiative driving to contribute to the mass-loss rate. Therefore, the mass-loss theory, in principle, is applicable to a plethora of radially pulsating stars including RR Lyraes, Type II Cepheids, R Coronae Borealis stars, β Cephei stars, Luminous Blue Variables, yellow hypergiants, and potentially even red supergiants. For instance, preliminary tests of RR Lyrae mass loss have been computed for theoretical models from Bono et al. (1997) with mass $M = 0.75, 0.65, 0.58\ M_\odot$ corresponding to a metallicity of $Z = 0.0001, 0.001, 0.06$, respectively, and are shown in Figure 9.1. In the RR Lyrae models, the mass-loss rates are enhanced by up to eight orders of magnitude due to the presence of shocks in the atmospheres of these stars. This result suggests that mass loss may be important to the evolution of RR Lyrae stars and other stars on the Horizontal Branch but also suggests a luminosity and metallicity dependence. For RR Lyrae stars with the same metallicity, the mass-loss rates are larger for the those with smaller luminosity which corresponds to a shorter period. The RR Lyraes with smaller metallicity have a larger range of mass-loss rates, similar to what was found for Cepheid models in Chapter 6.

Mass loss in RR Lyrae stars was suggested by Koopmann et al. (1994) to be a solution for the problem of the color dispersion of Horizontal Branch stars in Globular Clusters (Clementini et al., 2004; Dotter, 2008; Caloi & D'Antona, 2008) which is a RR Lyrae analogue to the Cepheid mass discrepancy. The standard

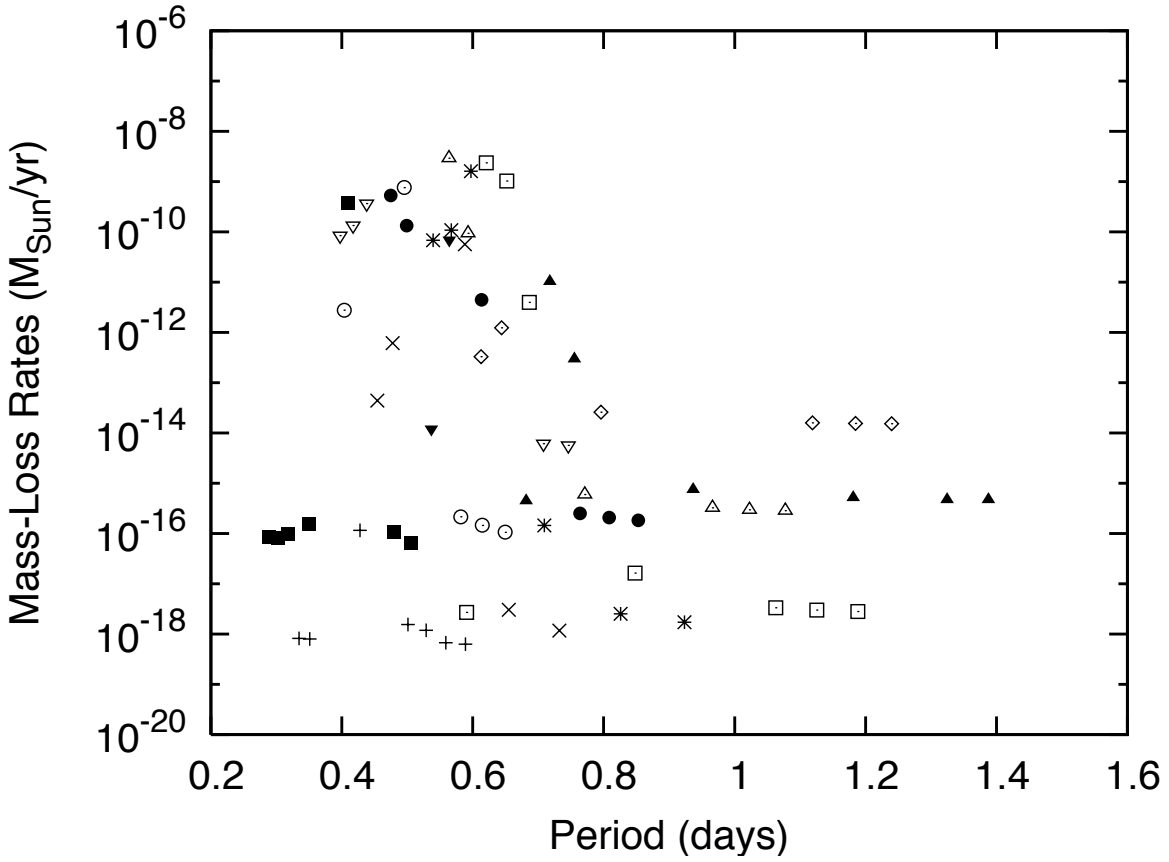

Figure 9.1: Predicted mass-loss rates for theoretical models of RR Lyrae variables using the mass-loss theory derived in Chapter 5. The different symbols refer to different combinations of luminosity and metallicity for a star. The '+' signs refer to $L = 1.61\ L_{\odot}$ and $Z = 0.0001$, 'x' refers to $L = 1.72\ L_{\odot}$ and $Z = 0.0001$, the stars refer to $L = 1.81\ L_{\odot}$ and $Z = 0.0001$, open squares are $L = 1.91\ L_{\odot}$ and $Z = 0.0001$, filled squares are $L = 1.51\ L_{\odot}$ and $Z = 0.001$, open circles are $L = 1.61\ L_{\odot}$ and $Z = 0.001$, filled circles are $L = 1.72\ L_{\odot}$ and $Z = 0.001$, open triangles pointing up are $L = 1.81\ L_{\odot}$ and $Z = 0.001$, closed triangles pointing up are $L = 1.91\ L_{\odot}$ and $Z = 0.001$, open downward triangles are $L = 1.61\ L_{\odot}$ and $Z = 0.006$, filled downward triangles are $L = 1.77\ L_{\odot}$ and $Z = 0.006$, and open diamonds are $L = 1.81\ L_{\odot}$ and $Z = 0.006$.

assumption is that the color dispersion is due to a dispersion of mass on the Horizontal Branch which is explained to be due to a gaussian distribution of mass loss on the Red Giant Branch caused by a distribution of stellar helium abundances. However, this work suggests that RR Lyrae stars may contribute to the color dispersion. There is also the possibility that the shocks and mass loss might explain asymmetries in the distribution of RR Lyrae rates of period change and even some of the stochastic period changes due to the shocks changing the structure of RR Lyrae atmospheres. These results are speculative but do show how the mass-loss model can apply to RR Lyrae stars as easily as it has for Cepheids.

Mass loss is believed to be important in the R Coronae Borealis stars. The light curves of these stars show a periodic sharp decrease in luminosity by a few magnitudes that is believed to be due to the formation of a dust cloud in the line-of-sight of the observer (Clayton, 1996). However, the mechanism for ejecting the required amount of mass to cause this large decline in brightness is not known except that there must be some time-dependent enhancement (Clayton et al., 2003, 2004). The mass-loss theory may be applied here to test if pulsation has a significant effect on the mass-loss rate at certain phases and determine if enhanced mass loss causes the decline. This is also an interesting test because RCB stars are both very similar to Cepheids and very different. The RCB stars are hydrogen deficient and have mass $M \approx 0.8\ M_{\odot}$ but the cool ($\log T_{\rm eff} \approx 3.9$) RCB stars have pulsations excited by the κ-mechanism in the helium ionization zones. The RCB stars provide an unique case study for pulsation-driven mass loss at extreme compositions.

The RCB stars appear to undergo explosive mass loss. A number of massive stars also display the same phenomenon, such as Luminous Blue Variables and yellow hypergiants. The prototypical LBV, η Carinae, has been observed to have numerous explosive mass-loss events (Smith et al., 2003), which has been argued to be a precursor to a supernovae event by Smith (2008). Another LBV, AG Carinae, has been observed to have significant mass loss, $\dot{M} \approx 10^{-6}$ - $10^{-5}\ M_{\odot}/yr$ (Groh et al., 2009). There are three suggested mechanisms for eruptive mass loss in LBVs. One possible mechanism is super-Eddington continuum driving (van Marle et al., 2008), in which a star may have super-Eddington luminosity if the atmosphere is porous with regions of clumped matter and optically-thin, low density regions. In that case, the star can be super-Eddington and have significant mass loss and be gravitationally stable. Harpaz & Soker (2009) proposed a different scenario related to the presence of a close companion causing wind Roche-Lobe overflow (Mohamed & Podsiadlowski, 2007) and the formation of a core magnetic field that can enhance the mass loss. The third possibility is that LBV pulsation affects the structure of the star causing it to exceed the Eddington luminosity in the iron bump region of the star. When the star exceeds the Eddington luminosity locally, it may lead to an explosive outburst (Onifer & Guzik, 2008). The third possibility may be tested using the pulsation-driven mass-loss theory. The yellow hypergiants are another target for the mass-loss theory. Recent observations of IRC+10420 suggest mass-loss rates of the order $10^{-4}\ M_{\odot}/yr$ (Dinh-V.-Trung et al., 2009) The star ρ Cassiopeiae has also been observed to have outburst behavior with a mass-loss rate of $0.5\ M_{\odot}$ in one outburst over 200 days (Lobel et al., 2005).

Understanding mass loss in Cepheids and RR Lyraes provides insights into stellar evolution and stellar

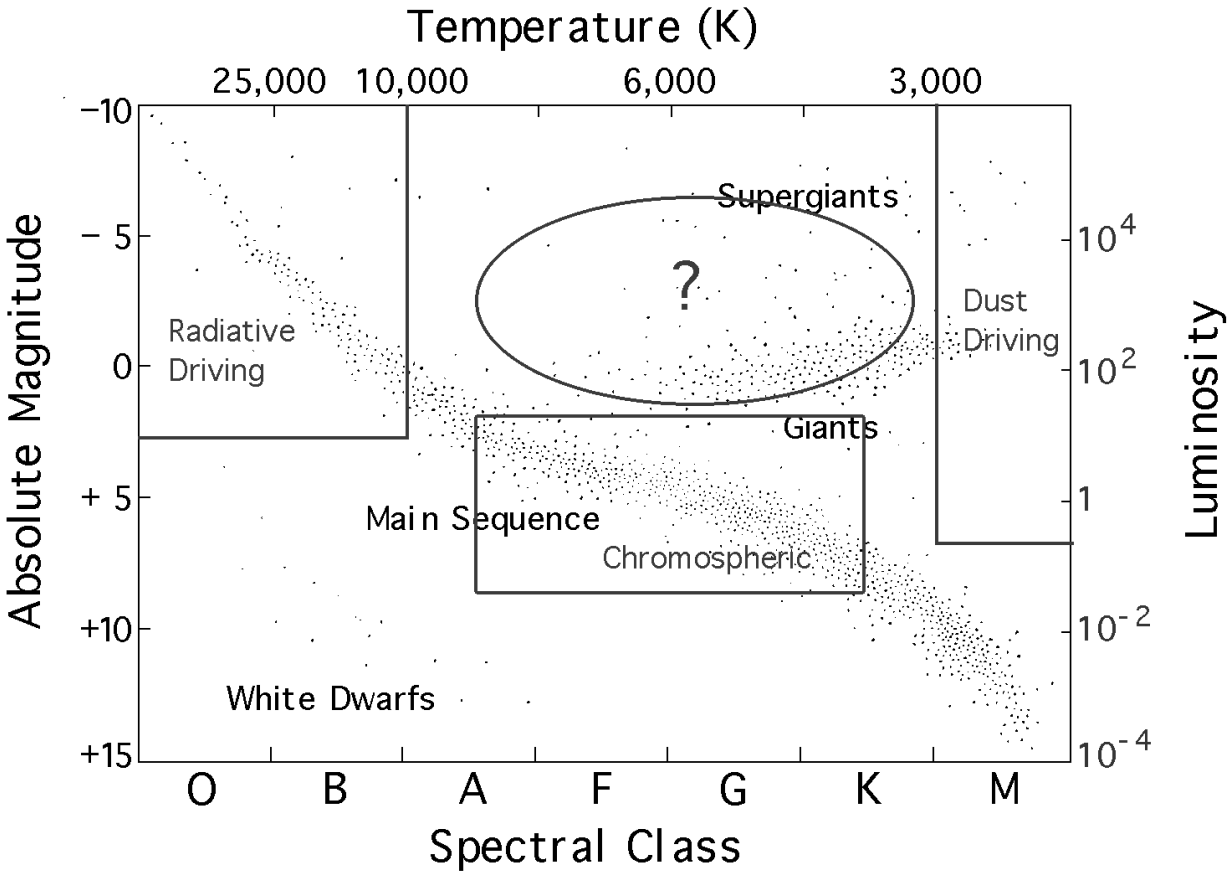

Figure 9.2: An outline of mass-loss mechanisms on the Hertzsprung-Russell diagram.

structure of these stars and stars of similar mass and composition. By studying pulsation-enhanced mass loss in the yellow hypergiants and LBV stars, one can understand the past evolution but also tells us about the circumstellar environments around supernovae. These massive stars will explode and the explosion will interact with the environment around it and explain some of the different classes of supernovae that are observed, such as the Type IIn supernovae denoted by a luminosity curve with a flattened maximum and a slow decline.

The mass-loss model can be applied to each of these different classes of variable star and as well as others and potentially teach us about this aspect of stellar evolution. However, applying the mass-loss model to these objects is a test of a mass-loss mechanism that is not understood. In fact, it is arguable that mass loss is only understood in three regimes: 1) hot stars undergoing radiative-driving, 2) cool stars undergoing dust driving, and 3) late-type stars with chromosphere having solar-like mass loss. In Figure 9.2, the HR Diagram is shown outlining these regions and showing a large hole where mass loss is not understood centered on the Cepheid Instability Strip, and while not shown includes the very massive stars.

The mass-loss theory proposed in this dissertation is a plausible explanation for mass loss in Classical

Cepheids and even RR Lyrae stars. Because of the assumptions in the theory it is a possible explanation for mass loss in other radially pulsating variable stars. The question then is not if radially pulsating stars lose mass, but it is how efficient is radial pulsation at driving mass loss.

9.2.2 Pulsation-Radiation Hydrodynamics

The first part of the dissertation focused on the development of the spherically symmetric stellar atmosphere program SAtlas and its conversion to a one-dimensional radiation hydrodynamic program. In this work, the RHD program is assumed to be in local thermodynamic equilibrium and is based on the scheme proposed by Colella & Woodward (1984). The purpose for constructing the RHD program is to model the dynamic atmospheres of Cepheids and compute time-dependent spectra and interferometric visibilities for comparison with observations. By doing so, we may gain a deeper understanding of the pulsation-induced dynamics that occurs in Cepheids.

Just like the mass-loss model, there is nothing in the RHD program that limits it to only Cepheids. It can be applied to any physical system for which there is radial motion that is non-relativistic and where LTE is a reasonable assumption. Therefore, it is expected that atmospheric dynamics can be modeled for any star without dust ($T_{\rm eff} > 3000\ K$) and any star cooler than early B-type ($T_{\rm eff} < 20000\ K$). This temperature range is similar to the temperature range shown in Figure 9.2 for the mass-loss theory, meaning the RHD program is able to model Type-II Cepheids, RR Lyrae stars, RCB stars (with the exception of the dust cloud), yellow hypergiants, the cool edge of the LBV and β Cephei Instability Regions, and possibly even the red supergiant pulsations.

The challenge of the color dispersion of the Horizontal Branch stars in Globular Clusters can be addressed using RHD model atmospheres. For a set of time dependent spectra of RR Lyrae stars, the composition, mean luminosity, mean radius, and mass may be determined from static models as a first trial solution. Then pulsating hydrodynamic models may be fit to the observations and provide more precise results. The models can constrain the mass of the a small population of RR Lyraes and quantify the mass dispersion and predict a resultant color dispersion.

For the case of RCB stars, the models may be used to explore pulsation of star with essentially no hydrogen as well as test the hypothesis that the sharp declines in brightness may be related to the pulsation or may occur at different phases as suggested Fernie (2000). While the program cannot model the formation of the dust cloud, it can test for non-periodic instabilities in the atmosphere. Similarly, the program may be applied to LBV stars (of S Doradus type) to search for the formation of super-Eddington layers near the top of the envelop that can lead to a mass eruption. Pulsation and spectroscopy of yellow hypergiants may be modeled with the RHD program to compare with time-series observations (Lobel et al., 2005).

These are just a few examples of how the RHD program can be applied to different classes of radially pulsating stars. However, we can apply the hydrodynamic program to explore the behavior of the helium ionization zones on pulsation across the HR diagram where LTE may be assumed. In doing this, we can

gain an understanding of atmospheric turbulence, and the dependence of pulsation on mass, and luminosity, and evolution. The process may be repeated for some types of stars that pulsate because of the iron bump and build connections between these types of stars.

The radiative hydrodynamic program is a tool for stellar astrophysics that can be used to study stellar evolution and structure. However, this tool is just one leg of a three legged table. When the program is used in concert with time-series spectroscopic and interferometric observations, we can probe the details of atmospheric dynamics and pulsation to unprecedented detail.

9.3 Future Directions

This dissertation has focused on the study of limb-darkening, mass loss and dynamics in Cepheids. However, this work is less about the Cepheids themselves, and more about the development of tools for studying mass loss and atmospheric dynamics in pulsating stars. The mass-loss theory is an analytic model for understanding the driving mechanism for winds in Cepheids and other radially pulsating stars. The RHD program is designed to study dynamic atmospheres with complete atomic and molecular opacities under the assumption of local thermodynamic equilibrium. Both tools are applicable to a diverse range of pulsating variable stars.

The mass-loss theory has been shown to be an effective tool but it is only as useful as the input parameters used and there are few stars as well-observed or as well-modeled as Cepheids. Therefore, we have taken the theory almost to the limits of its applicability. The remaining applications of the theory focus around parameter studies.

One such example is to continue the work regarding mass loss in RR Lyrae stars. This project would be approached in a similar manner as the research presented in Chapter 6. In this case, we can test the metallicity dependence of the mass-loss rates and compare the dependency to the measurements of the color (mass) dispersion for Horizontal Branch stars in Globular Clusters as a function of metallicity. If the two dependencies are similar then we have found a new, possible explanation for color dispersion. A second test is to compute the contribution of mass loss to the rate of period change and compare this to the distribution of observed rates of period change of RR Lyrae stars. If the observed distribution has an asymmetry (meaning an equal number of star with an increasing rate as the number with a decreasing period) similar to that suggested by the mass loss then we have found another argument in favor of mass loss.

Another example is the application of the theory to RCB stars as a test of the hypothesis for the sharp decrease of brightness due to a dust cloud forming in the line-of-sight. A parameter study of the global variables may be undertaken to understand the pulsation properties necessary to eject enough mass to cause such a large decrease of brightness. In the study, a number of parameters will be allowed to vary while still corresponding to observed values such as the luminosity, effective temperature, mass, and pulsation amplitudes. The results might yield hints into the structure of these stars and the mass-loss mechanism.

These two projects are relatively small in scale, primarily because of the limitations of the mass-loss theory. The radiative hydrodynamic program has many more possible directions to pursue. The prospective projects can be classified into two groups: code development and applications. There are four directions to development, including the conversion to time-dependent convection, the conversion of the opacity sampling version SAtlas program to include hydrodynamics, the development of a type of adaptive mesh refinement for the RHD program, and the addition of circumstellar layers to model pulsation-induced mass loss.

The development of the time-dependent convection routines was discussed in Chapter 4 and is not repeated. The conversion of the opacity sampling version of the stellar atmospheres program is important for detailed analyses of the composition of pulsating stars such as the carbon, nitrogen, and oxygen enhancement in some Cepheids (Wallerstein et al., 2000), and the metallicity gradient of the Milky Way disk seen using Cepheids (Pedicelli et al., 2009). A second use of the opacity sampling version of the program is that the static version allows for chemical stratification which may be of interest in some pulsating variables as well.

An adaptive mesh would be a powerful tool for resolving large density enhancements and the formation of shocks in the model dynamic atmospheres as well as helping to resolve the partial ionization zones where the density builds up in the pulsation cycle. The addition of an adaptive mesh does not require any new routines, the static stellar atmospheres program contains a routine that interpolates various quantities after each iteration a maps them onto a uniform grid of Rosseland optical depth. This routine is ideal for this problem as it can be used to map the necessary quantities in the RHD program onto a grid defined by $\tau_{\rm Ross}$ or column density $\int \rho dr$. In that case, regions of high density will have a better spacial resolution.

The fourth development is the most challenging but also the most interesting. One of my research goals is to model mass loss in Cepheids and other pulsating variable stars using the RHD program. To do this, the program will need to be extended to include the circumstellar environment of the star and to devise a soft boundary condition where mass can be allowed to leave the star. However, if this program is developed, it will be a more powerful tool for understanding dynamic stellar atmospheres and will be able to model the star from the wind region to the atmosphere to pulsation driving regions in the star. The program can be used to explain mass loss across the HR diagram.

There are also a number of applications of the RHD program, many more than can be discussed. Instead, four different projects are mentioned. The first project is the continuation of the theme of this dissertation, which is the modeling of Cepheid atmospheres. For this, we wish to compute a small grid of dynamic atmospheres varying in parameters. Using this grid, a number of issues can be explored such as the projection factor and limb-darkening which have already been discussed. There are other issues such as the line asymmetry of the $H\alpha$ line profiles along with other spectral features. One project of interest is being studied in collaboration with Dr. Chow-Choong Ngeow and Dr, Shashi Kanbur is the structure of the Leavitt Law. It is argued that the P-L relation is non-linear and that the source of the non-linearity is due to the interaction between the hydrogen ionization zone and the photosphere (Simon et al., 1993). In short-period Cepheids

($P < 10$ days) the hydrogen ionization zone interacts with the photosphere and modifies the effective temperature of the star while in long-period Cepheids the ionization zone does not interact with the photosphere so that the effective temperature is the same as that for an equivalent static star. This leads to a non-linearity in the P-L relation. The hypothesis is easily tested by a sample of models that range in pulsation period.

The program will also be used to model the atmospheres of RR Lyrae stars with a particular emphasis on modeling the nearest one, that being RR Lyrae itself. The purpose of studying the prototype is to predict the global properties of the star such as the radius and luminosity for comparison with Baade-Wesselink distance determinations and in advance of interferometric observations that will eventually be done as facilities grow. The second goal of this project is to test if the Blazhko effect can be found in the models due to the presence of shocks as opposed to non-radial pulsations or magnetic fields as suggested by Chadid et al. (2008).

At the suggestion of Dr. John Percy, the primary star in the eclipsing binary system ϵ Aurigae is an ideal candidate to be modeled using both the static SAtlas and the RHD programs. The primary is an F0 supergiant that appears to undergo Cepheid-like pulsation (Carroll et al., 1991). Furthermore, the star has been observed using interferometry yielding a second measurement of limb-darkening (Stencel et al., 2008), the first being the eclipse of the star. Combining these observations with the results shown in Chapter 3 and *Hipparcos* parallax, we have a measure of the mass of the supergiant independent of the measurement from the eclipsing binary. Using these results, one can test for radial pulsation in the supergiant and predict its impact on the eclipsing binary light curve.

The fourth project is being done in collaboration with Dr. Geoff Clayton, studying the spectra of RCB stars and, in particular, the time-dependent profile of the He I λ10830 line. It is believed that the structure of the He I line is related to the light curve of the star itself and that the line itself shows evidence of mass outflows (Clayton et al., 2003). Therefore, modeling the line profile from a pulsation model provides a significant constraint on understanding if and how the line is a diagnostic of mass loss. In this work, Dr. Clayton has obtained spectra using the UK Infrared Telescope for twelve RCB stars where the line profiles can be fit.

These projects are just a beginning for studying atmospheric dynamics in variable stars, and when the hydrodynamic program is modified to include mass loss, there will be many more questions that may be addressed including the formation of circumstellar envelopes surrounding Cepheids, and mass loss from RCB stars. Yet another project is the study of 20 $M_{\odot}$ stars that lose significant mass over their evolution. When one becomes a red supergiant, the star is found to have unstable pulsations and these pulsations may trigger substantial mass loss that could change what type of supernova progenitor it is. This is particularly interesting because of the results by Smartt et al. (2009) that is a survey of supernovae progenitors and find that the maximum mass of a red supergiant to undergo Type II-P supernova is $< 16.5 \pm 1.5$ $M_{\odot}$, while red supergiants with masses between 25 - 30 $M_{\odot}$ become Wolf-Rayet stars. This leaves a gap of about 5-10 $M_{\odot}$ that is not understood. One possibility being explored in collaboration with Dr. Sung-Chul Yoon is that Red Supergiants with progenitor masses in this regime lose sufficient mass to create the observed gap and one

mechanism is that pulsation may help drive this mass. This is where the RHD program modified to include mass loss is a powerful tool to help model evolution of the star by deriving pulsation-enhanced mass-loss prescriptions for the stellar evolution calculations.

This dissertation has described the development of the spherically symmetric version of the SAtlas program, its conversion to a radiative hydrodynamics program as well as the development of a theory for pulsation-driven mass loss. The SAtlas program has been applied to interferometric observations, showing it to be competitive with other, more detailed programs. It has been used to study limb-darkening and limb-darkening parameterizations and has been used to derive a method to compute the ratio of the radius to the mass of stars from limb-darkening parameterizations. The mass-loss theory has been used to study mass loss in Cepheids and provide a plausible explanation for the mass discrepancy and the existence of circumstellar envelopes. However, these results are not an end in themselves, they raise new questions about the structure of stars and Cepheids, in particular. New tools have been developed that can be applied to a much more diverse range of stars than done here and explore more questions in detail. This dissertation is not an end to a research project, it is just the beginning.

Bibliography

Abbot, C. G., Fowle, F. E., & Aldrich, L. B. 1913, ApJ, 38, 181

Abbott, D. C. 1982, ApJ, 259, 282

Abbott, D. C. & Hummer, D. G. 1985, ApJ, 294, 286

Abe, F., Bennett, D. P., Bond, I. A., Calitz, J. J., Claret, A., Cook, K. H., Furuta, Y., Gal-Yam, A., Glicenstein, J.-F., Hearnshaw, J. B., Hauschildt, P. H., Kent, D., Kilmartin, P. M., Kurata, Y., Masuda, K., Maoz, D., Matsubara, Y., Meintjes, P. J., Moniez, M., Muraki, Y., Noda, S., Ofek, E. O., Okajima, K., Philpott, L., Rattenbury, N. J., Rhie, S. H., Sako, T., Sullivan, D. J., Sumi, T., Terndrup, D. M., Tristram, P. J., Yanagisawa, T., & Yock, P. C. M. 2003, A&A, 411, L493

Abt, H. A. 1959, ApJ, 130, 769

Abt, H. A. & Levy, S. G. 1970, PASP, 82, 334

Adams, W. S. & Russell, H. N. 1928, ApJ, 68, 9

Afonso, C., Albert, J. N., Andersen, J., Ansari, R., Aubourg, É., Bareyre, P., Bauer, F., Blanc, G., Bouquet, A., Char, S., Charlot, X., Couchot, F., Coutures, C., Derue, F., Ferlet, R., Fouqué, P., Glicenstein, J. F., Goldman, B., Gould, A., Graff, D., Gros, M., Haissinski, J., Hamilton, J. C., Hardin, D., de Kat, J., Kim, A., Lasserre, T., LeGuillou, L., Lesquoy, É., Loup, C., Magneville, C., Mansoux, B., Marquette, J. B., Maurice, É., Milsztajn, A., Moniez, M., Palanque-Delabrouille, N., Perdereau, O., Prévot, L., Regnault, N., Rich, J., Spiro, M., Vidal-Madjar, A., Vigroux, L., Zylberajch, S., & The EROS collaboration. 2001, A&A, 378, 1014

Aikawa, T. & Antonello, E. 2000a, A&A, 363, 593

—. 2000b, A&A, 363, 601

Airy, G. B. 1863, MNRAS, 23, 188

Al-Naimiy, H. M. 1978, Ap&SS, 53, 181

Albrecht, S. 1907, ApJ, 25, 330

Albrow, M. D., Beaulieu, J.-P., Caldwell, J. A. R., Dominik, M., Greenhill, J., Hill, K., Kane, S., Martin, R., Menzies, J., Naber, R. M., Pel, J.-W., Pollard, K., Sackett, P. D., Sahu, K. C., Vermaak, P., Watson, R., Williams, A., & Sahu, M. S. 1999, ApJ, 522, 1011

Alcock, C., Allsman, R. A., Alves, D., Axelrod, T. S., Becker, A. C., Bennett, D. P., Cook, K. H., Freeman, K. C., Griest, K., Lehner, M. J., Marshall, S. L., Minniti, D., Peterson, B. A., Pratt, M. R., Quinn, P. J., Rodgers, A. W., Rorabeck, A., Sutherland, W., Tomaney, A., Vandehei, T., Welch, D. L., & The MACHO Collaboration. 1999, ApJ, 511, 185

Alcock, C., Allsman, R. A., Alves, D. R., Becker, A. C., Bennett, D. P., Cook, K. H., Drake, A. J., Freeman, K. C., Griest, K., Hawley, S. L., Keller, S., Lehner, M. J., Lepischak, D., Marshall, S. L., Minniti, D., Nelson, C. A., Peterson, B. A., Popowski, P., Pratt, M. R., Quinn, P. J., Rodgers, A. W., Suntzeff, N., Sutherland, W., Vandehei, T., & Welch, D. L. 2002, ApJ, 573, 338

Alekseeva, G. A., Arkharov, A. A., Galkin, V. D., Hagen-Thorn, E. I., Nikanorova, L. N., Novikov, V. V., Novopashenny, V. B., Pakhomov, V. P., Ruban, E. V., & Shechegolev, D. E. 1997, Baltic Astronomy, 6, 481

Allard, F. & Hauschildt, P. H. 1995, ApJ, 445, 433

Allard, F., Hauschildt, P. H., Alexander, D. R., & Starrfield, S. 1997, ARAA, 35, 137

Allard, F., Hauschildt, P. H., Baraffe, I., & Chabrier, G. 1996, ApJL, 465, L123+

Allard, F., Hauschildt, P. H., Miller, S., & Tennyson, J. 1994, ApJL, 426, L39

Allard, F., Hauschildt, P. H., & Schweitzer, A. 2000, ApJ, 539, 366

Aller, L. H. 1942, ApJ, 96, 321

An, J. H., Albrow, M. D., Beaulieu, J.-P., Caldwell, J. A. R., DePoy, D. L., Dominik, M., Gaudi, B. S., Gould, A., Greenhill, J., Hill, K., Kane, S., Martin, R., Menzies, J., Pogge, R. W., Pollard, K. R., Sackett, P. D., Sahu, K. C., Vermaak, P., Watson, R., & Williams, A. 2002, ApJ, 572, 521

Anderson, L. S. 1985, ApJ, 298, 848

Antonello, E. & Aikawa, T. 1993, A&A, 279, 119

—. 1995, A&A, 302, 105

Argeländer, F. W. A. 1843, Uranometria nova : Stellae per Mediam Europam SOLIS oculis conspicuae secundum veras lucis magnitudines E coelo ipso descriptae, ed. F. W. A. Argelander

—. 1857, Astronomische Nachrichten, 45, 97

—. 1859, Bonner Sternverzeichnis, 1., ed. F. W. A. Argelander

Asplund, M., Grevesse, N., & Sauval, A. J. 2005, in Astronomical Society of the Pacific Conference Series, Vol. 336, Cosmic Abundances as Records of Stellar Evolution and Nucleosynthesis, ed. T. G. Barnes, III & F. N. Bash, 25–+

Auer, L. 1976, Journal of Quantitative Spectroscopy and Radiative Transfer, 16, 931

Auer, L. H. & Mihalas, D. 1970, MNRAS, 149, 65

Aufdenberg, J. P., Hauschildt, P. H., & Baron, E. 1999, MNRAS, 302, 599

Aufdenberg, J. P., Ludwig, H.-G., & Kervella, P. 2005, ApJ, 633, 424

Auman, Jr., J. R. 1969, ApJ, 157, 799

Avrett, E. H. 1964, SAO Special Report, 167, 83

Avrett, E. H. & Krook, M. 1963, ApJ, 137, 874

Baade, W. 1926, Astronomische Nachrichten, 228, 359

—. 1956, PASP, 68, 5

Backhouse, T. W. 1882, The Observatory, 5, 56

Baker, N. & Kippenhahn, R. 1962, Zeitschrift fur Astrophysik, 54, 114

—. 1965, ApJ, 142, 868

Bappu, M. K. V. & Raghavan, N. 1969, MNRAS, 142, 295

Barban, C., Goupil, M. J., Van't Veer-Menneret, C., Garrido, R., Kupka, F., & Heiter, U. 2003, A&A, 405, 1095

Barbier, D. 1946, Annales d'Astrophysique, 9, 173

Barman, T. S., Hauschildt, P. H., & Allard, F. 2004, ApJ, 614, 338

Baron, E., Hauschildt, P. H., Nugent, P., & Branch, D. 1996, MNRAS, 283, 297

Barrell, S. L. 1982, MNRAS, 200, 127

Bauer, F., Afonso, C., Albert, J. N., Alard, C., Andersen, J., Ansari, R., Aubourg, É., Bareyre, P., Beaulieu, J. P., Bouquet, A., Char, S., Charlot, X., Couchot, F., Coutures, C., Derue, F., Ferlet, R., Gaucherel, C., Glicenstein, J. F., Goldman, B., Gould, A., Graff, D., Gros, M., Haissinski, J., Hamilton, J. C., Hardin, D., de Kat, J., Kim, A., Lasserre, T., Lesquoy, É., Loup, C., Magneville, C., Mansoux, B., Marquette, J. B., Maurice, É., Milsztajn, A., Moniez, M., Palanque-Delabrouille, N., Perdereau, O., Prévot, L., Renault, C., Regnault, N., Rich, J., Spiro, M., Vidal-Madjar, A., Vigroux, L., & Zylberajch, S. 1999, A&A, 348, 175

Beaulieu, J. P., Buchler, J. R., & Kolláth, Z. 2001, A&A, 373, 164

Beaulieu, J. P., Grison, P., Tobin, W., Pritchard, J. D., Ferlet, R., Lepeintre, F., Vidal-Madjar, A., Maurice, E., Prevot, L., Gry, C., Guibert, J., Moreau, O., Tajhamady, F., Aubourg, E., Bareyre, P., Coutures, C., Gros, M., Laurent, B., Lachieze-Rey, M., Lesquoy, E., Magneville, C., Milsztajn, A., Moscoso, L., Queinnec, F., Renault, C., Rich, J., Spiro, M., Vigroux, L., Zylberajch, S., Ansari, R., Cavalier, F., & Moniez, M. 1995, A&A, 303, 137

Bell, R. A., Eriksson, K., Gustafsson, B., & Nordlund, A. 1976, A&AS, 23, 37

Bell, R. A. & Rodgers, A. W. 1964, MNRAS, 128, 365

—. 1967, MNRAS, 135, 121

Belopolsky, A. 1895, ApJ, 1, 160

—. 1899, Astronomische Nachrichten, 149, 239

—. 1900, Astronomische Nachrichten, 152, 199

Benedict, G. F., McArthur, B. E., Feast, M. W., Barnes, T. G., Harrison, T. E., Patterson, R. J., Menzies, J. W., Bean, J. L., & Freedman, W. L. 2007, AJ, 133, 1810

Benedict, G. F., McArthur, B. E., Fredrick, L. W., Harrison, T. E., Slesnick, C. L., Rhee, J., Patterson, R. J., Skrutskie, M. F., Franz, O. G., Wasserman, L. H., Jefferys, W. H., Nelan, E., van Altena, W., Shelus, P. J., Hemenway, P. D., Duncombe, R. L., Story, D., Whipple, A. L., & Bradley, A. J. 2002, AJ, 124, 1695

Berdnikov, L. N. & Ignatova, V. V. 2000, in Astronomical Society of the Pacific Conference Series, Vol. 203, IAU Colloq. 176: The Impact of Large-Scale Surveys on Pulsating Star Research, ed. L. Szabados & D. Kurtz, 244–245

Biermann, L. 1933, Veroeffentlichungen der Universitaets-Sternwarte zu Goettingen, 3, 45

Birmingham, J. 1877, The Observatory, 1, 17

Bleksley, A. E. H. 1936, Astronomische Nachrichten, 260, 165

Bohannan, B., Abbott, D. C., Voels, S. A., & Hummer, D. G. 1986, ApJ, 308, 728

Böhm-Vitense, E. 1964, SAO Special Report, 167, 99

—. 1967, ApJ, 150, 483

Böhm-Vitense, E. 1994, AJ, 107, 673

Böhm-Vitense, E., Clark, M., Cottrell, P. L., & Wallerstein, G. 1990, AJ, 99, 353

Böhm-Vitense, E., Evans, N. R., Carpenter, K., Albrow, M. D., Cottrell, P. L., Robinson, R., & Beck-Winchatz, B. 1998, ApJ, 505, 903

Böhm-Vitense, E., Evans, N. R., Carpenter, K., Morgan, S., Beck-Winchatz, B., & Robinson, R. 1997a, AJ, 114, 1176

Böhm-Vitense, E. & Love, S. G. 1994, ApJ, 420, 401

Böhm-Vitense, E. & Parsons, S. B. 1983, ApJ, 266, 171

Böhm-Vitense, E., Remage Evans, N., Carpenter, K., Beck-Winchatz, B., & Robinson, R. 1997b, ApJ, 477, 916

Bond, H. E. & Sparks, W. B. 2009, A&A, 495, 371

Bono, G., Caputo, F., & Castellani, V. 2006, Memorie della Societa Astronomica Italiana, 77, 207

Bono, G., Caputo, F., Castellani, V., & Marconi, M. 1997, A&AS, 121, 327

—. 1999a, ApJ, 512, 711

Bono, G., Castellani, V., & Marconi, M. 2000a, ApJ, 529, 293

—. 2000b, ApJ, 529, 293

Bono, G., Gieren, W. P., Marconi, M., Fouqué, P., & Caputo, F. 2001, ApJ, 563, 319

Bono, G., Marconi, M., & Stellingwerf, R. F. 1999b, ApJS, 122, 167

—. 2000c, A&A, 360, 245

Bowen, G. H. 1988, ApJ, 329, 299

Bowen, G. H. & Willson, L. A. 1991, ApJL, 375, L53

Breger, M. 1970, AJ, 75, 239

—. 1980, Space Science Reviews, 27, 431

—. 2006, Communications in Asteroseismology, 148, 52

Breitfellner, M. G. & Gillet, D. 1993a, A&A, 277, 524

—. 1993b, A&A, 277, 553

—. 1993c, A&A, 277, 541

Bressan, A., Fagotto, F., Bertelli, G., & Chiosi, C. 1993, A&AS, 100, 647

Browning, M. K. 2008, ApJ, 676, 1262

Brunish, W. M. & Willson, L. A. 1987, in Lecture Notes in Physics, Berlin Springer Verlag, Vol. 274, Stellar Pulsation, ed. A. N. Cox, W. M. Sparks, & S. G. Starrfield, 27–+

Brunish, W. M. & Willson, L. A. 1989, in IAU Colloq. 111: The Use of pulsating stars in fundamental problems of astronomy, ed. E. G. Schmidt, 252–+

Bruntt, H., Evans, N. R., Stello, D., Penny, A. J., Eaton, J. A., Buzasi, D. L., Sasselov, D. D., Preston, H. L., & Miller-Ricci, E. 2008, ApJ, 683, 433

Buchler, J. R. 2008, ApJ, 680, 1412

—. 2009, ArXiv e-prints

Buchler, J. R., Goupil, M. J., & Piciullo, R. 1997, ApJL, 491, L99+

Buchler, J. R., Kolláth, Z., & Beaulieu, J.-P. 2004, A&A, 423, 643

Buchler, J. R. & Kovacs, G. 1986, ApJ, 303, 749

Buchler, J. R., Moskalik, P., & Kovacs, G. 1990, ApJ, 351, 617

Buchler, J. R. & Szabó, R. 2007, ApJ, 660, 723

Burki, G. & Mayor, M. 1980, A&A, 91, 115

Cacciari, C. 2009, Memorie della Societa Astronomica Italiana, 80, 97

Caccin, R., Onnembo, A., Russo, G., & Sollazzo, C. 1981, A&A, 97, 104

Caffau, E., Maiorca, E., Bonifacio, P., Faraggiana, R., Steffen, M., Ludwig, H.-G., Kamp, I., & Busso, M. 2009, A&A, 498, 877

Caloi, V. & D'Antona, F. 2008, ApJ, 673, 847

Campbell, W. W. 1901, ApJ, 13, 90

—. 1907, ApJ, 25, 59

Cannon, A. J. & Pickering, E. C. 1901, Annals of Harvard College Observatory, 28, 129

—. 1912, Annals of Harvard College Observatory, 56, 65

Cantiello, M., Langer, N., Brott, I., de Koter, A., Shore, S. N., Vink, J. S., Voegler, A., Lennon, D. J., & Yoon, S.-C. 2009, A&A, 499, 279

Canuto, V. M., Goldman, I., & Mazzitelli, I. 1996, ApJ, 473, 550

Caputo, F., Bono, G., Fiorentino, G., Marconi, M., & Musella, I. 2005, ApJ, 629, 1021

Caputo, F., Marconi, M., & Musella, I. 2000a, A&A, 354, 610

Caputo, F., Marconi, M., Musella, I., & Santolamazza, P. 2000b, A&A, 359, 1059

Caputo, F., Marconi, M., & Ripepi, V. 1999, ApJ, 525, 784

Carbon, D. F. & Gingerich, O. 1969, in Theory and Observation of Normal Stellar Atmospheres, ed. O. Gingerich, 377–+

Carlsson, M. 1986, Uppsala Astronomical Observatory Reports, 33

Carroll, S. M., Guinan, E. F., McCook, G. P., & Donahue, R. A. 1991, ApJ, 367, 278

Carson, T. R. & Stothers, R. 1976, ApJ, 204, 461

Carson, T. R. & Stothers, R. B. 1988, ApJ, 328, 196

Cassinelli, J. P. 1971, ApJ, 165, 265

—. 1979, ARAA, 17, 275

Castellani, V., Chieffi, A., & Straniero, O. 1992, ApJS, 78, 517

Castor, J. I. 1972, ApJ, 178, 779

Castor, J. I., Abbott, D. C., & Klein, R. I. 1975, ApJ, 195, 157

Catelan, M. & Cortés, C. 2008, ApJL, 676, L135

Chabrier, G., Barman, T., Baraffe, I., Allard, F., & Hauschildt, P. H. 2004, ApJL, 603, L53

Chadid, M., Vernin, J., & Gillet, D. 2008, A&A, 491, 537

Chandrasekhar, S. 1934, MNRAS, 94, 444

Chapman, R. D. 1966, ApJ, 143, 61

Christensen-Dalsgaard, J. 2003, Lecture Notes on Stellar Oscillations, 5th Ed. (Denmark: Institut for Fysik og Astronomi, 2003)

Christy, R. F. 1966a, ApJ, 144, 108

—. 1966b, ApJ, 145, 340

Claret, A. 1998, A&A, 335, 647

—. 2000, A&A, 363, 1081

—. 2003, A&A, 401, 657

—. 2004, A&A, 428, 1001

—. 2008, A&A, 482, 259

Claret, A., Diaz-Cordoves, J., & Gimenez, A. 1995, A&AS, 114, 247

Claret, A. & Hauschildt, P. H. 2003, A&A, 412, 241

Clayton, G. C. 1996, PASP, 108, 225

Clayton, G. C., Geballe, T. R., & Bianchi, L. 2003, ApJ, 595, 412

Clayton, G. C., Geballe, T. R., & Bianchi, L. 2004, in Astronomical Society of the Pacific Conference Series, Vol. 313, Asymmetrical Planetary Nebulae III: Winds, Structure and the Thunderbird, ed. M. Meixner, J. H. Kastner, B. Balick, & N. Soker, 569–+

Clayton, G. C. & Martin, P. G. 1985, ApJ, 288, 558

Clement, C. M., Xu, X., & Muzzin, A. V. 2008, AJ, 135, 83

Clementini, G., Corwin, T. M., Carney, B. W., & Sumerel, A. N. 2004, AJ, 127, 938

Clerke, A. M. 1903, The Observatory, 26, 206

Cogan, B. C. 1970, ApJ, 162, 139

Cohen, M., Witteborn, F. C., Carbon, D. F., Davies, J. K., Wooden, D. H., & Bregman, J. D. 1996, AJ, 112, 2274

Colella, P. & Woodward, P. R. 1984, Journal of Computational Physics, 54, 174

Collins, II, G. W. 1965, ApJ, 142, 265

Compton, A. H. 1923a, Phys. Rev, 21, 483+

—. 1923b, Phil. Mag., 46, 414+

Cordier, D., Lebreton, Y., Goupil, M.-J., Lejeune, T., Beaulieu, J.-P., & Arenou, F. 2002, A&A, 392, 169

Cowling, T. G. 1934, MNRAS, 94, 768

—. 1935, MNRAS, 96, 42

Cox, A. N. 1979, ApJ, 229, 212

Cox, A. N., Deupree, R. G., King, D. S., & Hodson, S. W. 1977, ApJL, 214, L127

Cox, A. N., Hodson, S. W., & King, D. S. 1978a, ApJ, 224, 607

Cox, A. N., Hodson, S. W., & Michaud, G. 1978b, ApJ, 222, 621

Cox, J. P. 1955, ApJ, 122, 286

—. 1958, ApJ, 127, 194

—. 1959, ApJ, 130, 296

—. 1960, ApJ, 132, 594

—. 1963, ApJ, 138, 487

Cox, J. P., Cox, A. N., Olsen, K. H., King, D. S., & Eilers, D. D. 1966, ApJ, 144, 1038

Cox, J. P., King, D. S., & Stellingwerf, R. F. 1972, ApJ, 171, 93

Cox, J. P. & Whitney, C. 1958, ApJ, 127, 561

Curtiss, R. H. 1904, PASP, 16, 243

Dartayet, M. & Landi Dessy, J. 1952, ApJ, 115, 279

Davis, J., Tango, W. J., & Booth, A. J. 2000, MNRAS, 318, 387

Deasy, H. P. 1988, MNRAS, 231, 673

Deupree, R. G. 1978, ApJ, 223, 982

—. 1980, ApJ, 236, 225

di Benedetto, G. P. 1995, ApJ, 452, 195

Di Benedetto, G. P. 2005, MNRAS, 357, 174

Diaz-Cordoves, J., Claret, A., & Gimenez, A. 1995, A&AS, 110, 329

Diaz-Cordoves, J. & Gimenez, A. 1992, A&A, 259, 227

Dinh-V.-Trung, Muller, S., Lim, J., Kwok, S., & Muthu, C. 2009, ApJ, 697, 409

Dirac, P. A. M. 1925, MNRAS, 85, 825

Dominik, M. 2004, MNRAS, 352, 1315

Donati, G. B. 1863, MNRAS, 23, 100

Dotter, A. 2008, ApJL, 687, L21

Duncan, J. C. 1909, Lick Observatory Bulletin, 5, 120

Dunkley, J., Komatsu, E., Nolta, M. R., Spergel, D. N., Larson, D., Hinshaw, G., Page, L., Bennett, C. L., Gold, B., Jarosik, N., Weiland, J. L., Halpern, M., Hill, R. S., Kogut, A., Limon, M., Meyer, S. S., Tucker, G. S., Wollack, E., & Wright, E. L. 2009, ApJS, 180, 306

Dyck, H. M., Benson, J. A., van Belle, G. T., & Ridgway, S. T. 1996, AJ, 111, 1705

Dziembowski, W. A. & Mizerski, T. 2004, Acta Astronomica, 54, 363

Edberg, S. J., Laskin, R. A., Marr, IV, J. C., Unwin, S. C., & Shao, M. 2007, in Society of Photo-Optical Instrumentation Engineers (SPIE) Conference Series, Vol. 6693, Society of Photo-Optical Instrumentation Engineers (SPIE) Conference Series

Eddington, A. S. 1917a, MNRAS, 77, 596

—. 1917b, The Observatory, 40, 290

—. 1918, MNRAS, 79, 2

—. 1919a, The Observatory, 42, 338

—. 1919b, MNRAS, 79, 177

—. 1926, The Internal Constitution of the Stars, ed. A. S. Eddington

Eddington, Sir, A. S. 1930, MNRAS, 91, 109

—. 1941, MNRAS, 101, 182

Edgar, J. A. 1933, MNRAS, 93, 422

Eggert, J. 1919, Phys. Zeitschrift, 20, 570+

Emden, R. 1907, Gaskugeln Anwendungen der Mechanischen Warmen-theorie auf Kosmologie und Meteorologische Probleme (Leipzig: Teubner)

Engle, S. G., Guinan, E. F., Depasquale, J., & Evans, N. 2009, in American Institute of Physics Conference Series, Vol. 1135, American Institute of Physics Conference Series, ed. M. E. van Steenberg, G. Sonneborn, H. W. Moos, & W. P. Blair, 192–197

Engle, S. G., Guinan, E. F., & Evans, N. R. 2006, in Bulletin of the American Astronomical Society, Vol. 38, Bulletin of the American Astronomical Society, 942–+

Epstein, I. 1950, ApJ, 112, 6

Evans, N. R. 1976, ApJ, 209, 135

Evans, N. R., Barmby, P., Marengo, M., Bono, G., Welch, D., & Romaniello, M. 2007, in American Astronomical Society Meeting Abstracts, Vol. 210, American Astronomical Society Meeting Abstracts, #13.05–+

Evans, N. R., Böhm-Vitense, E., Carpenter, K., Beck-Winchatz, B., & Robinson, R. 1997, PASP, 109, 789

—. 1998a, ApJ, 494, 768

Evans, N. R. & Bolton, C. T. 1990, ApJ, 356, 630

Evans, N. R., Massa, D., Fullerton, A., Sonneborn, G., & Iping, R. 2006, ApJ, 647, 1387

Evans, N. R., Sasselov, D., & Short, C. I. 1998b, in Astronomical Society of the Pacific Conference Series, Vol. 154, Cool Stars, Stellar Systems, and the Sun, ed. R. A. Donahue & J. A. Bookbinder, 745–+

Evans, N. R., Schaefer, G. H., Bond, H. E., Bono, G., Karovska, M., Nelan, E., Sasselov, D., & Mason, B. D. 2008, AJ, 136, 1137

Faulkner, D. J. 1977, ApJ, 216, 49

Feast, M. W. 2008, MNRAS, 387, L33

Feast, M. W. & Catchpole, R. M. 1997, MNRAS, 286, L1

Feast, M. W., Whitelock, P. A., & Carter, B. S. 1990, MNRAS, 247, 227

Feautrier, P. 1964, C.R. Acad. Sci. Paris, 258, 3189

Fernie, J. D. 1967, AJ, 72, 1327

—. 1969, PASP, 81, 707

—. 1993, Informational Bulletin on Variable Stars, 3854, 1

Fernie, J. D. 2000, in IAU Symposium, Vol. 177, The Carbon Star Phenomenon, ed. R. F. Wing, 191–+

Fernie, J. D., Evans, N. R., Beattie, B., & Seager, S. 1995, Informational Bulletin on Variable Stars, 4148, 1

Feuchtinger, M., Buchler, J. R., & Kolláth, Z. 2000, ApJ, 544, 1056

Fields, D. L., Albrow, M. D., An, J., Beaulieu, J.-P., Caldwell, J. A. R., DePoy, D. L., Dominik, M., Gaudi, B. S., Gould, A., Greenhill, J., Hill, K., Jørgensen, U. G., Kane, S., Martin, R., Menzies, J., Pogge, R. W., Pollard, K. R., Sackett, P. D., Sahu, K. C., Vermaak, P., Watson, R., Williams, A., Glicenstein, J.-F., & Hauschildt, P. H. 2003, ApJ, 596, 1305

Fiorentino, G., Caputo, F., Marconi, M., & Musella, I. 2002, ApJ, 576, 402

Fiorentino, G., Marconi, M., Musella, I., & Caputo, F. 2007, A&A, 476, 863

Fokin, A. B. 1991, MNRAS, 250, 258

—. 1992, MNRAS, 256, 26

Fokin, A. B. & Gillet, D. 1994, A&A, 290, 875

—. 1997, A&A, 325, 1013

Fokin, A. B., Gillet, D., & Breitfellner, M. G. 1996, A&A, 307, 503

Fors, O. 2006, PhD thesis, AA(Departament d'Astronomia i Meteorologia, Universitat de Barcelona, Martí i Franqués 1, 08028 Barcelona, Spain; Observatori Fabra, Camí de l'Observatori s/n, 08035 Barcelona, Spain)

Fouqué, P., Arriagada, P., Storm, J., Barnes, T. G., Nardetto, N., Mérand, A., Kervella, P., Gieren, W., Bersier, D., Benedict, G. F., & McArthur, B. E. 2007, A&A, 476, 73

Fouque, P. & Gieren, W. P. 1997, A&A, 320, 799

Freedman, W. L. & Madore, B. F. 1990, ApJ, 365, 186

Freedman, W. L., Madore, B. F., Gibson, B. K., Ferrarese, L., Kelson, D. D., Sakai, S., Mould, J. R., Kennicutt, Jr., R. C., Ford, H. C., Graham, J. A., Huchra, J. P., Hughes, S. M. G., Illingworth, G. D., Macri, L. M., & Stetson, P. B. 2001, ApJ, 553, 47

Freedman, W. L., Madore, B. F., Mould, J. R., Hill, R., Ferrarese, L., Kennicutt, R. C., Saha, A., Stetson, P. B., Graham, J. A., Ford, H., Hoessel, J. G., Huchra, J., Hughes, S. M., & Illingworth, G. D. 1994, Nature, 371, 757

Freedman, W. L., Madore, B. F., Rigby, J., Persson, S. E., & Sturch, L. 2008, ApJ, 679, 71

Freytag, B., Steffen, M., & Dorch, B. 2002, Astronomische Nachrichten, 323, 213

Fricke, K., Stobie, R. S., & Strittmatter, P. A. 1971, MNRAS, 154, 23

—. 1972, ApJ, 171, 593

Frost, E. B. 1907, ApJ, 25, 59

Fry, A. M. & Carney, B. W. 1999, AJ, 118, 1806

Fuhrmeister, B., Schmitt, J. H. M. M., & Hauschildt, P. H. 2005, A&A, 439, 1137

Fuhrmeister, B., Short, C. I., & Hauschildt, P. H. 2006, A&A, 452, 1083

Gascoigne, S. C. B. 1969, MNRAS, 146, 1

Gautschy, A. 2003, The History of Radial Stellar Pulsation.

Gerasimovic, B. P. 1931, AJ, 41, 17

Gieren, W., Storm, J., Barnes, III, T. G., Fouqué, P., Pietrzyński, G., & Kienzle, F. 2005, ApJ, 627, 224

Gieren, W. P. 1989, A&A, 225, 381

Gieren, W. P., Fouque, P., & Gomez, M. 1998, ApJ, 496, 17

Gieren, W. P., Fouque, P., & Gomez, M. I. 1997, ApJ, 488, 74

Gieren, W. P., Moffett, T. J., & Barnes, III, T. G. 1999, ApJ, 512, 553

Gingerich, O. 1963, ApJ, 138, 576

Girardi, L., Bressan, A., Bertelli, G., & Chiosi, C. 2000, A&AS, 141, 371

Glushneva, I. N., Doroshenko, V. T., Fetisova, T. S., Khruzina, T. S., Kolotilov, E. A., Mossakovskaya, L. V., Ovchinnikov, S. L., & Voloshina, I. B. 1998a, VizieR Online Data Catalog, 3208, 0

Glushneva, I. N., Doroshenko, V. T., Fetisova, T. S., Khruzina, T. S., Kolotilov, E. A., Mossakovskaya, L. V., Shenavrin, V. I., Voloshina, I. B., Biryukov, V. V., & Shenavrina, L. S. 1998b, VizieR Online Data Catalog, 3207, 0

Godon, P., Sion, E. M., Barrett, P. E., & Linnell, A. P. 2009, ApJ, 699, 1229

Gonczi, G. 1981, A&A, 96, 138

—. 1982, A&A, 110, 1

Gonczi, G. & Osaki, Y. 1980, A&A, 84, 304

Goodricke, J. & Bayer. 1786, Royal Society of London Philosophical Transactions Series I, 76, 48

Gough, D. O. 1977, ApJ, 214, 196

Gray, D. F. 2009, ApJ, 697, 1032

Gray, D. F. & Stevenson, K. B. 2007, PASP, 119, 398

Gray, R. & Corbally, C. 2009, Stellar Spectral Classification (Princeton: Princeton University Press)

Grevesse, N. & Sauval, A. J. 1998, Space Science Reviews, 85, 161

Groenewegen, M. A. T. 2007, A&A, 474, 975

Groenewegen, M. A. T., Romaniello, M., Primas, F., & Mottini, M. 2004, A&A, 420, 655

Groenewegen, M. A. T. & Salaris, M. 2003, A&A, 410, 887

Groh, J. H., Hillier, D. J., Damineli, A., Whitelock, P. A., Marang, F., & Rossi, C. 2009, ApJ, 698, 1698

Grupp, F. 2004a, A&A, 420, 289

—. 2004b, A&A, 426, 309

Gusev, E. B. 1967, Information Bulletin on Variable Stars, 186, 1

Gustafsson, B. 1989, ARAA, 27, 701

Gustafsson, B., Bell, R. A., Eriksson, K., & Nordlund, A. 1975, A&A, 42, 407

Gustafsson, B., Edvardsson, B., Eriksson, K., Jørgensen, U. G., Nordlund, Å., & Plez, B. 2008, A&A, 486, 951

Guzik, J. A., Cox, A. N., & Despain, K. M. 2005, in ASP Conf. Ser. 332: The Fate of the Most Massive Stars, ed. R. Humphreys & K. Stanek, 263–+

Haefner, R. 1975, A&A, 45, 287

Hamann, W.-R. 1985, A&A, 148, 364

Harpaz, A. & Soker, N. 2009, New Astronomy, 14, 539

Hauschildt, P. H. 1992, Journal of Quantitative Spectroscopy and Radiative Transfer, 47, 433

—. 1993, Journal of Quantitative Spectroscopy and Radiative Transfer, 50, 301

Hauschildt, P. H., Allard, F., Alexander, D. R., & Baron, E. 1997a, ApJ, 488, 428

Hauschildt, P. H., Allard, F., & Baron, E. 1999a, ApJ, 512, 377

Hauschildt, P. H., Allard, F., Ferguson, J., Baron, E., & Alexander, D. R. 1999b, ApJ, 525, 871

Hauschildt, P. H., Baron, E., & Allard, F. 1997b, ApJ, 483, 390

Hauschildt, P. H., Baron, E., Starrfield, S., & Allard, F. 1996, ApJ, 462, 386

Hauschildt, P. H., Starrfield, S., Shore, S. N., Gonzalez-Riestra, R., Sonneborn, G., & Allard, F. 1994, AJ, 108, 1008

Havlen, R. J. 1972, A&A, 16, 252

Hearnshaw, J. B. 1986, The analysis of starlight: One hundred and fifty years of astronomical spectroscopy, ed. J. B. Hearnshaw

Helling, C., Dehn, M., Woitke, P., & Hauschildt, P. H. 2008, ApJL, 675, L105

Helling, C., Winters, J. M., & Sedlmayr, E. 2000, A&A, 358, 651

Henroteau, F. 1925, JRASC, 19, 81

Henyey, L., Vardya, M. S., & Bodenheimer, P. 1965, ApJ, 142, 841

Herbig, G. H. 1952a, PASP, 64, 302

—. 1952b, ApJ, 116, 369

Herbig, G. H. & Moore, J. H. 1952, ApJ, 116, 348

Hertzsprung, E. 1905, Zeitschrift für Wissenschaftliche Photographie, 3, 429

—. 1907, Zeitschrift für Wissenschaftliche Photographie, 5, 86

—. 1914, Astronomische Nachrichten, 196, 201

—. 1926, BAIN, 3, 115

Heyrovsky, D. 2000, PhD thesis, AA(HARVARD UNIVERSITY)

Heyrovský, D. 2007, ApJ, 656, 483

Hill, S. J. & Willson, L. A. 1979, ApJ, 229, 1029

Hillier, D. J. 1990, A&A, 231, 116

Ho, P. Y. & Ho, P.-Y. 1962, Vistas in Astronomy, 5, 127

Hoffleit, D. 1986, Journal of the American Association of Variable Star Observers (JAAVSO), 15, 77

Höfner, S. 1999, in IAU Symp. 191: Asymptotic Giant Branch Stars, ed. T. Le Bertre, A. Lebre, & C. Waelkens, 159–+

Höfner, S. & Dorfi, E. A. 1997, A&A, 319, 648

Huang, M., Sion, E. M., & Szkody, P. 1995, AJ, 109, 1746

Huang, R. Q. & Weigert, A. 1983, A&A, 127, 309

Hubble, E. P. 1925, The Observatory, 48, 139

Hubeny, I. 1988, Computer Physics Communications, 52, 103

Hubeny, I., Hummer, D. G., & Lanz, T. 1994, A&A, 282, 151

Hubeny, I. & Lanz, T. 1995, ApJ, 439, 875

Huegelmeyer, S. D., Dreizler, S., Homeier, D., & Hauschildt, P. 2009, ArXiv e-prints

Huffer, C. M. & Eggen, O. J. 1947, ApJ, 106, 106

Huggins, W. 1864, Royal Society of London Philosophical Transactions Series I, 154, 139

Huggins, W. & Miller, W. A. 1864, Royal Society of London Philosophical Transactions Series I, 154, 413

Hughes, E. M. 1931, Harvard College Observatory Bulletin, 883, 32

Hummer, D. G. & Rybicki, G. B. 1971, MNRAS, 152, 1

Hundt, E., Schmid-Burgk, J., Scholz, M., & Kodaira, K. 1975, A&A, 41, 37

Hunger, K. 1955, Zeitschrift fur Astrophysik, 36, 42

Hunger, K. & van Blerkom, D. 1967, Zeitschrift fur Astrophysik, 66, 185

Husfeld, D., Kudritzki, R. P., Simon, K. P., & Clegg, R. E. S. 1984, A&A, 134, 139

Iben, I. J. 1965, ApJ, 142, 1447

Iben, I. J. & Tuggle, R. S. 1972a, ApJ, 178, 441

—. 1972b, ApJ, 173, 135

Iglesias, C. A. & Rogers, F. J. 1991, ApJL, 371, L73

Irwin, J. B. 1963, ApJ, 138, 1104

Jacobsen, T. S. 1926, Lick Observatory Bulletin, 12, 138

—. 1949, JRASC, 43, 142

—. 1950, PASP, 62, 269

Jeans, J. H. 1925, MNRAS, 85, 797

Jeffers, S. V., Aufdenberg, J. P., Hussain, G. A. J., Cameron, A. C., & Holzwarth, V. R. 2006, MNRAS, 367, 1308

Johnson, G. 2005, Miss Leavitt's Stars: The Untold Story of the Woman Who Discovered How to Measure the Universe (New York: W.W. Norton (Atlas Books), 2005)

Johnson, H. L. & Mitchell, R. I. 1975, Revista Mexicana de Astronomia y Astrofisica, 1, 299

Johnson, H. R., Bernat, A. P., & Krupp, B. M. 1980, ApJS, 42, 501

Johnson, H. R., Collins, J. G., Krupp, B., & Bell, R. A. 1977, ApJ, 212, 760

Johnson, H. R. & Krupp, B. M. 1976, ApJ, 206, 201

Jones, T. W. & Merrill, K. M. 1976, ApJ, 209, 509

Joy, A. H. 1937, ApJ, 86, 363

Joy, A. H. & Wilson, R. E. 1949, ApJ, 109, 231

Kamp, L. W. & Deupree, R. G. 1979, PASP, 91, 681

Kamper, K. W. 1996, JRASC, 90, 140

Kanbur, S. M. & Ngeow, C.-C. 2004, MNRAS, 350, 962

Kanbur, S. M., Ngeow, C.-C., & Buchler, J. R. 2004, MNRAS, 354, 212

Kanbur, S. M. & Simon, N. R. 1994, ApJ, 420, 880

Kapteyn, J. C. & van Rhijn, P. J. 1922, BAIN, 1, 37

Karp, A. H. 1975a, ApJ, 199, 448

—. 1975b, ApJ, 200, 354

—. 1975c, ApJ, 201, 641

Keller, C. F. & Mutschlecner, J. P. 1970, ApJ, 161, 217

Keller, S. C. 2008, ArXiv e-prints, 801

Keller, S. C. & Wood, P. R. 2002, ApJ, 578, 144

—. 2006, ApJ, 642, 834

Kennicutt, Jr., R. C., Stetson, P. B., Saha, A., Kelson, D., Rawson, D. M., Sakai, S., Madore, B. F., Mould, J. R., Freedman, W. L., Bresolin, F., Ferrarese, L., Ford, H., Gibson, B. K., Graham, J. A., Han, M., Harding, P., Hoessel, J. G., Huchra, J. P., Hughes, S. M. G., Illingworth, G. D., Macri, L. M., Phelps, R. L., Silbermann, N. A., Turner, A. M., & Wood, P. R. 1998, ApJ, 498, 181

Kervella, P., Bersier, D., Mourard, D., Nardetto, N., & Coudé du Foresto, V. 2004a, A&A, 423, 327

Kervella, P., Bersier, D., Mourard, D., Nardetto, N., Fouqué, P., & Coudé du Foresto, V. 2004b, A&A, 428, 587

Kervella, P., Coude du Foresto, V., Glindemann, A., & Hofmann, R. 2000, in Presented at the Society of Photo-Optical Instrumentation Engineers (SPIE) Conference, Vol. 4006, Proc. SPIE Vol. 4006, p. 31-42, Interferometry in Optical Astronomy, Pierre J. Lena; Andreas Quirrenbach; Eds., ed. P. J. Lena & A. Quirrenbach, 31–42

Kervella, P., Coudé du Foresto, V., Perrin, G., Schöller, M., Traub, W. A., & Lacasse, M. G. 2001, A&A, 367, 876

Kervella, P., Coudé du Foresto, V., Traub, W. A., & Lacasse, M. G. 1999, in Astronomical Society of the Pacific Conference Series, Vol. 194, Working on the Fringe: Optical and IR Interferometry from Ground and Space, ed. S. Unwin & R. Stachnik, 22–+

Kervella, P., Fouqué, P., Storm, J., Gieren, W. P., Bersier, D., Mourard, D., Nardetto, N., & du Coudé Foresto, V. 2004c, ApJL, 604, L113

Kervella, P., Mérand, A., & Gallenne, A. 2009, ArXiv e-prints

Kervella, P., Mérand, A., Perrin, G., & Coudé Du Foresto, V. 2006, A&A, 448, 623

Kervella, P., Mérand, A., Szabados, L., Fouqué, P., Bersier, D., Pompei, E., & Perrin, G. 2008, A&A, 480, 167

Kervella, P., Nardetto, N., Bersier, D., Mourard, D., & Coudé du Foresto, V. 2004d, A&A, 416, 941

King, D. S., Hansen, C. J., Ross, R. R., & Cox, J. P. 1975, ApJ, 195, 467

Klimishin, I. A. & Gnatyk, B. I. 1981, Astrophysics, 17, 306

Klinglesmith, D. A. 1967, AJ, 72, 808

Klinglesmith, D. A. & Sobieski, S. 1970, AJ, 75, 175

Klinkerfues, E. F. W. 1865, Nachr. d. K. Gesellscharf d. Wissenschaften u. d. Georg-Augusts Univ., 21, 1+

Kluyver, H. A. 1935, BAIN, 7, 265

Knutson, H. A., Charbonneau, D., Noyes, R. W., Brown, T. M., & Gilliland, R. L. 2007, ApJ, 655, 564

Koen, C. 2001, MNRAS, 322, 97

Kogure, T. 1962, PASJ, 14, 247

Kollath, Z., Beaulieu, J. P., Buchler, J. R., & Yecko, P. 1998, ApJL, 502, L55+

Koopmann, R. A., Lee, Y.-W., Demarque, P., & Howard, J. M. 1994, ApJ, 423, 380

Kovács, G. & Buchler, J. R. 1989, ApJ, 346, 898

Kovtyukh, V. V., Andrievsky, S. M., Luck, R. E., & Gorlova, N. I. 2003, A&A, 401, 661

Kraft, R. P. 1957, ApJ, 125, 336

Krishna Swamy, K. S. 1970, ApJ, 162, 259

Krook, M. 1938, MNRAS, 98, 204

Krupp, B. M., Collins, J. G., & Johnson, H. R. 1978, ApJ, 219, 963

Kuhfuß, R. 1986, A&A, 160, 116

Kuiper, G. P. 1938, ApJ, 88, 472

Kukarkin, B. 1937, Astr. Zhurnal U.S.S.R, 14, 125+

Kunasz, P. B., Hummer, D. G., & Mihalas, D. 1975, ApJ, 202, 92

Kurucz, R. L. 1969, ApJ, 156, 235

—. 1970a, SAO Special Report, 309

—. 1970b, Atlas: A computer program for calculating model stellar atmospheres, ed. R. L. Kurucz

—. 1970c, SAO Special Report, 309

—. 1979, ApJS, 40, 1

Kurucz, R. L. 1990, in 3rd International Collogium of the Royal Netherlands Academy of Arts and Sciences, ed. J. E. Hansen, 20–+

Kurucz, R. L. 1993, in Astronomical Society of the Pacific Conference Series, Vol. 44, IAU Colloq. 138: Peculiar versus Normal Phenomena in A-type and Related Stars, ed. M. M. Dworetsky, F. Castelli, & R. Faraggiana, 87–+

Kurucz, R. L. 1996, in IAU Symposium, Vol. 176, Stellar Surface Structure, ed. K. G. Strassmeier & J. L. Linsky, 523–+

Kurucz, R. L., van Dishoeck, E. F., & Tarafdar, S. P. 1987, ApJ, 322, 992

Lah, P., Kiss, L. L., & Bedding, T. R. 2005, MNRAS, 359, L42

Lamers, H. J. G. L. M. & Cassinelli, J. P. 1999, Introduction to Stellar Winds (Introduction to Stellar Winds, by Henny J. G. L. M. Lamers and Joseph P. Cassinelli, pp. 452. ISBN 0521593980. Cambridge, UK: Cambridge University Press, June 1999.)

Landstreet, J. D., Asplund, M., Spite, M., Balachandran, S. B., Berdyugina, S. V., Hauschildt, P. H., Ludwig, H. G., Mashonkina, L. I., Nagendra, K. N., Puls, J., Randich, M. S., & Tautvaisiene, G. 2008, Transactions of the International Astronomical Union, Series A, 27, 222

Lane, B. F., Creech-Eakman, M. J., & Nordgren, T. E. 2002, ApJ, 573, 330

Lane, B. F., Kuchner, M. J., Boden, A. F., Creech-Eakman, M., & Kulkarni, S. R. 2000, Nature, 407, 485

Laney, C. D. & Stobie, R. S. 1994, MNRAS, 266, 441

—. 1995, MNRAS, 274, 337

Lanz, T. & Hubeny, I. 1995, ApJ, 439, 905

—. 2003, ApJS, 146, 417

—. 2007, ApJS, 169, 83

Lautman, D. A. 1957, ApJ, 126, 537

Leavitt, H. S. 1908, Annals of Harvard College Observatory, 60, 87

Leavitt, H. S. & Pickering, E. C. 1912, Harvard College Observatory Circular, 173, 1

Ledoux, P. 1941, ApJ, 94, 537

Ledoux, P., Simon, R., & Bielaire, J. 1955, Annales d'Astrophysique, 18, 65

Leotta-Janin, C. 1967, BAIN, 19, 169

Lester, J. B., Lane, M. C., & Kurucz, R. L. 1982, ApJ, 260, 272

Lester, J. B. & Neilson, H. R. 2008, A&A, 491, 633

Lloyd Evans, T. 1968, MNRAS, 141, 109

Lobel, A., Aufdenberg, J. P., Ilyin, I., & Rosenbush, A. E. 2005, in ESA Special Publication, Vol. 560, 13th Cambridge Workshop on Cool Stars, Stellar Systems and the Sun, ed. F. Favata, G. A. J. Hussain, & B. Battrick, 771–+

Lockyer, J. N. 1889, MNRAS, 49, 221

—. 1893, Royal Society of London Philosophical Transactions Series A, 184, 675

Lockyer, N. 1899, Astronomische Nachrichten, 149, 387

Lockyer, Sir, N. 1903, MNRAS, 64, A23+

Lord Kelvin. 1890, Mathematical and Physical Papers vol III (London: C.J. Clay and Sons)

Lucy, L. B. 1964, SAO Special Report, 167, 93

Lundblad, R. 1923, ApJ, 58, 113

Lundmark, K. 1931, Zeitschrift fur Astrophysik, 3, 313

Madore, B. F. 1985, ApJ, 298, 340

Madore, B. F. & Freedman, W. L. 2009, ApJ, 696, 1498

Madore, B. F., Freedman, W. L., Rigby, J., Persson, S. E., Sturch, L., & Mager, V. 2009, ApJ, 695, 988

Madore, B. F., Freedman, W. L., Rigby, J., Persson, S. E., Sturch, L., & Major, V. 2008, ArXiv e-prints

Manduca, A. 1979, A&AS, 36, 411

Manduca, A., Bell, R. A., & Gustafsson, B. 1977, A&A, 61, 809

Marconi, M., Musella, I., & Fiorentino, G. 2005, ApJ, 632, 590

Marengo, M., Evans, N. R., Barmby, P., Bono, G., & Welch, D. 2009, in The Evolving ISM in the Milky Way and Nearby Galaxies

Marengo, M., Karovska, M., Sasselov, D. D., Papaliolios, C., Armstrong, J. T., & Nordgren, T. E. 2003, ApJ, 589, 968

Marengo, M., Karovska, M., Sasselov, D. D., & Sanchez, M. 2004, ApJ, 603, 285

Marengo, M., Sasselov, D. D., Karovska, M., Papaliolios, C., & Armstrong, J. T. 2002, ApJ, 567, 1131

Martin, D. C., Seibert, M., Neill, J. D., Schiminovich, D., Forster, K., Rich, R. M., Welsh, B. Y., Madore, B. F., Wheatley, J. M., Morrissey, P., & Barlow, T. A. 2007, Nature, 448, 780

Mathias, P., Gillet, D., Fokin, A. B., Nardetto, N., Kervella, P., & Mourard, D. 2006, A&A, 457, 575

Mathis, J. S., Rumpl, W., & Nordsieck, K. H. 1977, ApJ, 217, 425

Mattsson, L., Wahlin, R., Höfner, S., & Eriksson, K. 2008, ArXiv e-prints, 804

Matzner, C. D. & McKee, C. F. 1999, ApJ, 510, 379

Maury, A. C. & Pickering, E. C. 1897, Annals of Harvard College Observatory, 28, 1

McAlary, C. W. & Welch, D. L. 1986, AJ, 91, 1209

McCrea, W. H. 1931, MNRAS, 91, 836

Meixner, M., Gordon, K. D., Indebetouw, R., Hora, J. L., Whitney, B., Blum, R., Reach, W., Bernard, J.-P., Meade, M., Babler, B., Engelbracht, C. W., For, B.-Q., Misselt, K., Vijh, U., Leitherer, C., Cohen, M., Churchwell, E. B., Boulanger, F., Frogel, J. A., Fukui, Y., Gallagher, J., Gorjian, V., Harris, J., Kelly, D., Kawamura, A., Kim, S., Latter, W. B., Madden, S., Markwick-Kemper, C., Mizuno, A., Mizuno, N., Mould, J., Nota, A., Oey, M. S., Olsen, K., Onishi, T., Paladini, R., Panagia, N., Perez-Gonzalez, P., Shibai, H., Sato, S., Smith, L., Staveley-Smith, L., Tielens, A. G. G. M., Ueta, T., Dyk, S. V., Volk, K., Werner, M., & Zaritsky, D. 2006, AJ, 132, 2268

Menzel, D. H. & Milne, E. A. 1966, Selected papers on the transfer of radiation, ed. D. H. Menzel & E. A. Milne

Mérand, A., Aufdenberg, J. P., Kervella, P., Foresto, V. C. d., ten Brummelaar, T. A., McAlister, H. A., Sturmann, L., Sturmann, J., & Turner, N. H. 2007, ApJ, 664, 1093

Mérand, A., Kervella, P., Coudé Du Foresto, V., Perrin, G., Ridgway, S. T., Aufdenberg, J. P., Ten Brummelaar, T. A., McAlister, H. A., Sturmann, L., Sturmann, J., Turner, N. H., & Berger, D. H. 2006, A&A, 453, 155

Mérand, A., Kervella, P., Coudé Du Foresto, V., Ridgway, S. T., Aufdenberg, J. P., Ten Brummelaar, T. A., Berger, D. H., Sturmann, J., Sturmann, L., Turner, N. H., & McAlister, H. A. 2005, A&A, 438, L9

Mihalas, D. 1965, ApJS, 11, 184

—. 1967a, ApJ, 149, 169

—. 1967b, ApJ, 150, 909

—. 1968, ApJ, 153, 317

—. 1978, Stellar atmospheres /2nd edition/ (San Francisco, W. H. Freeman and Co., 1978. 650 p.)

Mihalas, D. 1994, in Astronomical Society of the Pacific Conference Series, Vol. 60, The MK Process at 50 Years: A Powerful Tool for Astrophysical Insight, ed. C. J. Corbally, R. O. Gray, & R. F. Garrison, 41–+

Mihalas, D. 2003, in Astronomical Society of the Pacific Conference Series, Vol. 288, Stellar Atmosphere Modeling, ed. I. Hubeny, D. Mihalas, & K. Werner, 471–+

Mihalas, D. & Auer, L. H. 1970, ApJ, 160, 1161

Mihalas, D. & Hummer, D. G. 1974, ApJS, 28, 343

Mihalas, D. & Kunasz, P. B. 1978, ApJ, 219, 635

Mihalas, D., Kunasz, P. B., & Hummer, D. G. 1975, ApJ, 202, 465

—. 1976a, ApJ, 203, 647

—. 1976b, ApJ, 206, 515

—. 1976c, ApJ, 210, 419

Mihalas, D. & Stone, M. E. 1968, ApJ, 151, 293

Millis, R. L. 1969, Lowell Observatory Bulletin, 7, 113

Milne, E. A. 1926, MNRAS, 87, 43

—. 1928a, MNRAS, 89, 17

—. 1928b, MNRAS, 89, 3

—. 1930, Thermodynamics of the stars, ed. E. A. Milne

Milnes, R. 1848, Life, Letters and Literary Remains of John Keats (New York: Putnam)

Mitchell, Jr., W. E. 1959, ApJ, 129, 93

Moffett, T. J. & Barnes, III, T. J. 1987, ApJ, 323, 280

Mohamed, S. & Podsiadlowski, P. 2007, in Astronomical Society of the Pacific Conference Series, Vol. 372, 15th European Workshop on White Dwarfs, ed. R. Napiwotzki & M. R. Burleigh, 397–+

Moore, J. H. 1929, PASP, 41, 56

Morgan, S. M. & Welch, D. L. 1997, AJ, 114, 1183

Moskalik, P., Buchler, J. R., & Marom, A. 1992, ApJ, 385, 685

Moskalik, P. & Gorynya, N. A. 2005, Acta Astronomica, 55, 247

Moskalik, P. & Kolaczkowski, Z. 2008, Communications in Asteroseismology, 157, 343

Mourard, D., Bonneau, D., Koechlin, L., Labeyrie, A., Morand, F., Stee, P., Tallon-Bosc, I., & Vakili, F. 1997, A&A, 317, 789

Mourard, D., Nardetto, N., Lagarde, S., Petrov, R., Bonneau, D., & Millour, F. 2008a, in The Power of Optical/IR Interferometry: Recent Scientific Results and 2nd Generation, ed. A. Richichi, F. Delplancke, F. Paresce, & A. Chelli, 477–+

Mourard, D., Perraut, K., Bonneau, D., Clausse, J. M., Stee, P., Tallon-Bosc, I., Kervella, P., Hughes, Y., Marcotto, A., Blazit, A., Chesneau, O., Domiciano de Souza, A., Foy, R., Hénault, F., Mattei, D., Merlin, G., Roussel, A., Tallon, M., Thiebaut, E., McAlister, H., ten Brummelaar, T., Sturmann, J., Sturmann, L., Turner, N., Farrington, C., & Goldfinger, P. J. 2008b, in Society of Photo-Optical Instrumentation Engineers (SPIE) Conference Series, Vol. 7013, Society of Photo-Optical Instrumentation Engineers (SPIE) Conference Series

Nardetto, N., Fokin, A., Mourard, D., Mathias, P., Kervella, P., & Bersier, D. 2004, A&A, 428, 131

Nardetto, N., Gieren, W., Kervella, P., Fouque, P., Storm, J., Pietrzynski, G., Mourard, D., & Queloz, D. 2009, ArXiv e-prints

Nardetto, N., Groh, J. H., Kraus, S., Millour, F., & Gillet, D. 2008a, A&A, 489, 1263

Nardetto, N., Mourard, D., Kervella, P., Mathias, P., Mérand, A., & Bersier, D. 2006, A&A, 453, 309

Nardetto, N., Mourard, D., Mathias, P., Fokin, A., & Gillet, D. 2007, A&A, 471, 661

Nardetto, N., Stoekl, A., Bersier, D., & Barnes, T. G. 2008b, A&A, 489, 1255

Natale, G., Marconi, M., & Bono, G. 2008, ApJL, 674, L93

Neilson, H. R. & Lester, J. B. 2008a, A&A, 490, 807

—. 2008b, ApJ, 684, 569

—. 2009, ApJ, 690, 1829

Neilson, H. R., Ngeow, C.-C., Kanbur, S. M., & Lester, J. B. 2009, ApJ, 692, 81

Ngeow, C. & Kanbur, S. M. 2006, ApJ, 650, 180

—. 2008, ApJ, 679, 76

Ngeow, C., Kanbur, S. M., Neilson, H. R., Nanthakumar, A., & Buonaccorsi, J. 2008, ApJ

Ngeow, C.-C. 2005, PhD thesis, University of Massachusetts Amherst, United States – Massachusetts

Ngeow, C.-C., Kanbur, S. M., Neilson, H. R., Nanthakumar, A., & Buonaccorsi, J. 2009, ApJ, 693, 691

Ngeow, C.-C., Kanbur, S. M., Nikolaev, S., Buonaccorsi, J., Cook, K. H., & Welch, D. L. 2005, MNRAS, 363, 831

Nordgren, T. E., Germain, M. E., Sudol, J. J., Hindsley, R. B., Armstrong, J. T., & Hajian, A. R. 2000, in Astronomical Society of the Pacific Conference Series, Vol. 203, IAU Colloq. 176: The Impact of Large-Scale Surveys on Pulsating Star Research, ed. L. Szabados & D. Kurtz, 152–156

Nordlund, A. 1974, A&A, 32, 407

Nordlund, Å., Stein, R. F., & Asplund, M. 2009, Living Reviews in Solar Physics, 6, 2

Okunev, B. 1929, Astronomische Nachrichten, 236, 313

Onifer, A. J. & Guzik, J. A. 2008, in IAU Symposium, Vol. 250, IAU Symposium, ed. F. Bresolin, P. A. Crowther, & J. Puls, 83–88

Oosterhoff, P. T. 1957a, BAIN, 13, 320

—. 1957b, BAIN, 13, 317

—. 1964, BAIN, 17, 448

Osawa, K. 1956, ApJ, 123, 513

Owocki, S. 2005, in ASP Conf. Ser. 332: The Fate of the Most Massive Stars, ed. R. Humphreys & K. Stanek, 169–+

Owocki, S. P. & van Marle, A. J. 2008, ArXiv e-prints, 801

Parker, E. N. 1958, ApJ, 128, 664

Parsons, S. B. 1972, ApJ, 174, 57

—. 1980, ApJ, 239, 555

Pauldrach, A. & Herrero, A. 1988, A&A, 199, 262

Pauldrach, A., Puls, J., & Kudritzki, R. P. 1986, A&A, 164, 86

Payne, C. H. 1925, PhD thesis, AA(RADCLIFFE COLLEGE.)

Payne-Gaposchkin, C. & Gaposchkin, S. 1966, Vistas in Astronomy, 8, 191

Pecker, J.-C. 1950, Annales d'Astrophysique, 13, 433

—. 1965, ARAA, 3, 135

Pedicelli, S., Bono, G., Lemasle, B., Francois, P., Groenewegen, M., Lub, J., Pel, J. W., Laney, D., Piersimoni, A., Romaniello, M., Buonanno, R., Caputo, F., Cassisi, S., Castelli, F., Leurini, S., Pietrinferni, A., Primas, F., & Pritchard, J. 2009, ArXiv e-prints

Peraiah, A. 1973, Ap&SS, 23, 159

Percy, J. R. & Evans, N. R. 1980, AJ, 85, 1509

Perrine, C. D. 1919, ApJ, 50, 81

Perryman, M. A. C. & ESA, eds. 1997, ESA Special Publication, Vol. 1200, The HIPPARCOS and TYCHO catalogues. Astrometric and photometric star catalogues derived from the ESA HIPPARCOS Space Astrometry Mission

Persson, S. E., Madore, B. F., Krzemiński, W., Freedman, W. L., Roth, M., & Murphy, D. C. 2004, AJ, 128, 2239

Petersen, J. O. 1973, A&A, 27, 89

Petrie, R. M. 1934, Publications of Michigan Observatory, 5, 9

—. 1937, Publications of Michigan Observatory, 6, 37

Petroni, S., Bono, G., Marconi, M., & Stellingwerf, R. F. 2003, ApJ, 599, 522

Pickering, E. C. 1880, Proceedings of the American Academy of Arts and Sciences, 16, 1+

—. 1881, The Observatory, 4, 225

—. 1890, Annals of Harvard College Observatory, 27, 1

—. 1903, Annals of Harvard College Observatory, 48, 91

Pickering, E. C. & Bailey, S. I. 1895, ApJ, 2, 321

Plachinda, S. I. 2000, A&A, 360, 642

Plaskett, H. H. 1936, MNRAS, 96, 402

Plummer, H. C. 1913, MNRAS, 73, 661

Plummer, H. G. 1914, MNRAS, 74, 660

Popper, D. M. 1984, AJ, 89, 132

Provencal, J. L., Shipman, H. L., Thejll, P., & Vennes, S. 2000, ApJ, 542, 1041

Puls, J. 1991, A&A, 248, 581

Puls, J. & Herrero, A. 1988, A&A, 204, 219

Reimers, D. 1977, in IAU Colloq. 42: The Interaction of Variable Stars with their Environment, ed. R. Kippenhahn, J. Rahe, & W. Strohmeier, 559–+

Richichi, A., Fors, O., & Mason, E. 2008a, A&A, 489, 1441

Richichi, A., Fors, O., Mason, E., Stegmeier, J., & Chandrasekhar, T. 2008b, A&A, 489, 1399

Richichi, A., Fors, O., Merino, M., Otazu, X., Núñez, J., Prades, A., Thiele, U., Pérez-Ramírez, D., & Montojo, F. J. 2006, A&A, 445, 1081

Ritter, A. 1879, Ann. d. Physik und Chemie, neue Folge, 8, 179+

Roberts, A. W. 1895, ApJ, 2, 283

Robinson, L. V. & Shapley, H. 1940, Annals of Harvard College Observatory, 90, 27

Rodgers, A. W. 1970, MNRAS, 151, 133

Rodgers, A. W. & Bell, R. A. 1964, MNRAS, 127, 471

—. 1967, MNRAS, 136, 91

—. 1968, MNRAS, 138, 23

Rodrigues, L. L. & Böhm-Vitense, E. 1992, ApJ, 401, 695

Romaniello, M., Primas, F., Mottini, M., Groenewegen, M., Bono, G., & François, P. 2005, A&A, 429, L37

Rosseland, S. 1925, ApJ, 61, 424

—. 1931, Avhand. Det Norske Videnskaps-Akad. i Oslo I. Mat.-Naturv. Klasse, Volume 5, p. 1-50, 5, 1

—. 1949, The pulsation theory of variable stars., ed. S. Rosseland

Rudkjøbing, M. H. 1947, On the atmospheres of the B-stars., ed. M. H. Rudkjobing

Russell, H. N. 1902, ApJ, 15, 252

—. 1912a, ApJ, 35, 315

—. 1912b, ApJ, 36, 54

—. 1913a, The Observatory, 36, 324

—. 1913b, Science, ns, 37, 651+

—. 1929, ApJ, 70, 11

—. 1945, ApJ, 102, 1

Russell, H. N., Adams, W. S., & Moore, C. E. 1928, ApJ, 68, 1

Russell, H. N. & Shapley, H. 1912a, ApJ, 36, 385

Russell, I. H. N. & Shapley, H. 1912b, ApJ, 36, 239

Rutherfurd, L. 1863, Amer. Jour. of Sci. and Arts, 35, 71

Rybicki, G. B. 1971, Journal of Quantitative Spectroscopy and Radiative Transfer, 11, 589

Rybicki, G. B. & Hummer, D. G. 1991, A&A, 245, 171

Sabbey, C. N., Sasselov, D. D., Fieldus, M. S., Lester, J. B., Venn, K. A., & Butler, R. P. 1995, ApJ, 446, 250

Saha, M. N. 1921, Royal Society of London Proceedings Series A, 99, 135

Sakai, S., Ferrarese, L., Kennicutt, Jr., R. C., & Saha, A. 2004, ApJ, 608, 42

Sandage, A., Saha, A., Tammann, G. A., Labhardt, L., Schwengeler, H., Panagia, N., & Macchetto, F. D. 1994, ApJL, 423, L13

Sandage, A. & Tammann, G. A. 1968, ApJ, 151, 531

Sandage, A., Tammann, G. A., & Reindl, B. 2004, A&A, 424, 43

Sandage, A. R. 1953, AJ, 58, 61

Sanford, R. F. 1930, ApJ, 72, 46

—. 1935a, ApJ, 81, 140

—. 1935b, ApJ, 81, 132

Sasselov, D. & Karovska, M. 1994, ApJ, 432, 367

Sasselov, D. D., Beaulieu, J. P., Renault, C., Grison, P., Ferlet, R., Vidal-Madjar, A., Maurice, E., Prevot, L., Aubourg, E., Bareyre, P., Brehin, S., Coutures, C., Delabrouille, N., de Kat, J., Gros, M., Laurent, B., Lachieze-Rey, M., Lesquoy, E., Magneville, C., Milsztajn, A., Moscoso, L., Queinnec, F., Rich, J., Spiro, M., Vigroux, L., Zylberajch, S., Ansari, R., Cavalier, F., Moniez, M., Gry, C., Guibert, J., Moreau, O., & Tajhmady, F. 1997, A&A, 324, 471

Sasselov, D. D., Fieldus, M. S., & Lester, J. B. 1989, ApJL, 337, L29

Sasselov, D. D. & Lester, J. B. 1990, ApJ, 362, 333

—. 1994a, ApJ, 423, 795

—. 1994b, ApJ, 423, 795

—. 1994c, ApJ, 423, 785

Sasselov, D. D. & Raga, A. 1992, in Astronomical Society of the Pacific Conference Series, Vol. 26, Cool Stars, Stellar Systems, and the Sun, ed. M. S. Giampapa & J. A. Bookbinder, 549–+

Sastri, V. K. & Stothers, R. 1978, ApJ, 225, 939

Schmid-Burgk, J. & Scholz, M. 1975, A&A, 41, 41

Schmidt, E. G. 1970, ApJ, 162, 871

Schmidt, E. G. & Parsons, S. B. 1982, ApJS, 48, 185

—. 1984a, ApJ, 279, 215

—. 1984b, ApJ, 279, 202

Schmidt, E. G. & Weiler, E. J. 1979, AJ, 84, 231

Schuster, A. 1905, ApJ, 21, 1

Schwarszchild, K. 1900, Pub. Kuffner Obs., 5, 100+

Schwarzschild, K. 1906, Nachrichten von der Königlichen Gesellschaft der Wissenschaften zu Göttingen. Math.-phys. Kalsse, 195, 41

—. 1914, Sitzungsherichte der Königlichen Preussischen Akademie der Wissenschaften, 2, 1183

Schwarzschild, M. 1936, Zeitschrift fur Astrophysik, 11, 152

—. 1938, Harvard College Observatory Circular, 429, 1

Schwarzschild, M., Schwarzschild, B., & Adams, W. S. 1948, ApJ, 108, 207

Scott, R. M. 1942, ApJ, 95, 58

Secchi, A. 1875, Astronomical register, 13, 208

Sen, H. K. 1948, ApJ, 107, 404

Serkowski, K. 1961, AJ, 66, 405

Shane, W. W. 1958, ApJ, 127, 573

Shapley, H. 1914, ApJ, 40, 448

—. 1916, ApJ, 44, 273

—. 1918, ApJ, 48, 279

—. 1919, ApJ, 49, 24

—. 1934, MNRAS, 94, 791

—. 1940, Proceedings of the National Academy of Science, 26, 541

Shapley, H. & Nicholson, S. B. 1919, Proceedings of the National Academy of Science, 5, 417

Shimada, M. R., Ito, M., Hirata, B., & Horaguchi, T. 1994, in IAU Symp. 162: Pulsation; Rotation; and Mass Loss in Early-Type Stars, ed. L. A. Balona, H. F. Henrichs, & J. M. Le Contel, 487–+

Shook, G. A. 1914, ApJ, 39, 277

Short, C. I. & Hauschildt, P. H. 2005, ApJ, 618, 926

—. 2006, ApJ, 641, 494

—. 2009, ApJ, 691, 1634

Shulyak, D., Tsymbal, V., Ryabchikova, T., Stütz, C., & Weiss, W. W. 2004, A&A, 428, 993

Simon, N. R. & Kanbur, S. M. 1994, ApJ, 429, 772

Simon, N. R., Kanbur, S. M., & Mihalas, D. 1993, ApJ, 414, 310

Smartt, S. J., Eldridge, J. J., Crockett, R. M., & Maund, J. R. 2009, MNRAS, 395, 1409

Smith, N. 2008, in IAU Symposium, Vol. 250, IAU Symposium, ed. F. Bresolin, P. A. Crowther, & J. Puls, 193–200

Smith, N., Davidson, K., Gull, T. R., Ishibashi, K., & Hillier, D. J. 2003, ApJ, 586, 432

Smolec, R. & Moskalik, P. 2008, Acta Astronomica, 58, 193

Sneden, C., Johnson, H. R., & Krupp, B. M. 1976, ApJ, 204, 281

Soszynski, I., Poleski, R., Udalski, A., Szymanski, M. K., Kubiak, M., Pietrzynski, G., Wyrzykowski, L., Szewczyk, O., & Ulaczyk, K. 2008, Acta Astronomica, 58, 163

Southworth, J. 2008, MNRAS, 386, 1644

Southworth, J., Bruntt, H., & Buzasi, D. L. 2007, A&A, 467, 1215

Stebbins, J. 1945, Contributions from the Mount Wilson Observatory / Carnegie Institution of Washington, 704, 1

Stellingwerf, R. F. 1982a, ApJ, 262, 339

—. 1982b, ApJ, 262, 330

Stencel, R. E., Creech-Eakman, M., Hart, A., Hopkins, J. L., Kloppenborg, B. K., & Mais, D. E. 2008, ApJL, 689, L137

Stobie, R. S. 1969a, MNRAS, 144, 461

—. 1969b, MNRAS, 144, 485

—. 1969c, MNRAS, 144, 511

—. 1977, MNRAS, 180, 631

Storm, J., Carney, B. W., Gieren, W. P., Fouqué, P., Freedman, W. L., Madore, B. F., & Habgood, M. J. 2004, A&A, 415, 521

Storm, J., Gieren, W. P., Fouqué, P., Barnes, III, T. G., & Gómez, M. 2005, A&A, 440, 487

Stothers, R. 1979, ApJ, 229, 1023

—. 1982, ApJ, 255, 227

Stothers, R. B. 2006, ApJ, 652, 643

—. 2009, ApJL, 696, L37

Strom, S. E. 1964, SAO Special Report, 167, 294

—. 1967, ApJ, 150, 637

—. 1969, ApJ, 156, 177

Strom, S. E. & Avrett, E. H. 1964a, ApJ, 140, 1381

—. 1964b, ApJ, 140, 1381

—. 1965, ApJS, 12, 1

Strömgren, B. 1940, On the Chemical Composition of the Solar Atmosphere, 218–+

Strömgren, B. 1944, Kgl. Dans. Vid. Selsk., 21

Swan, W. 1856, Phil. Mag., 6, 448

Swihart, T. L. 1956, ApJ, 123, 139

Tammann, G. A., Sandage, A., & Reindl, B. 2003, A&A, 404, 423

Tango, W. J. & Davis, J. 2002, MNRAS, 333, 642

Terashita, V. & Matsushima, S. 1966, ApJS, 13, 461

Testa, V., Marconi, M., Musella, I., Ripepi, V., Dall'Ora, M., Ferraro, F. R., Mucciarelli, A., Mateo, M., & Côté, P. 2007, A&A, 462, 599

Tingley, B., Thurl, C., & Sackett, P. 2006, A&A, 445, L27

Torres, G. & Sandberg Lacy, C. H. 2009, AJ, 137, 507

Trumpler, R. J. 1930, PASP, 42, 267

Turner, D. G. 1996, JRASC, 90, 82

Turner, D. G., Abdel-Sabour Abdel-Latif, M., & Berdnikov, L. N. 2006, PASP, 118, 410

Turner, D. G. & Berdnikov, L. N. 2004, A&A, 423, 335

Turner, D. G., Bryukhanov, I. S., Balyuk, I. I., Gain, A. M., Grabovsky, R. A., Grigorenko, V. D., Klochko, I. V., Kosa-Kiss, A., Kosinsky, A. S., Kushmar, I. J., Mamedov, V. T., Narkevich, N. A., Pogosyants, A. J., Semenyuta, A. S., Sergey, I. M., Schukin, V. V., Strigelsky, J. B., Tamello, V. G., Lane, D. J., & Majaess, D. J. 2007, ArXiv e-prints, 709

Turner, D. G., Forbes, D., van den Bergh, S., Younger, P. F., & Berdnikov, L. N. 2005, AJ, 130, 1194

Turner, D. G., Horsford, A. J., & MacMillan, J. D. 1999, Journal of the American Association of Variable Star Observers (JAAVSO), 27, 5

Tycner, C. & Lester, J. B. 2002, PASP, 114, 330

Udalski, A., Soszynski, I., Szymanski, M., Kubiak, M., Pietrzynski, G., Wozniak, P., & Zebrun, K. 1999a, Acta Astronomica, 49, 1

—. 1999b, Acta Astronomica, 49, 45

—. 1999c, Acta Astronomica, 49, 437

—. 1999b, Acta Astronomica, 49, 223

Udalski, A., Szymanski, M., Kubiak, M., Pietrzynski, G., Soszynski, I., Wozniak, P., & Zebrun, K. 1999a, Acta Astronomica, 49, 201

Ueno, S. & Matsushima, S. 1950, PASJ, 2, 32

Underhill, A. B. 1950, AJ, 55, 185

—. 1957, Publications of the Dominion Astrophysical Observatory Victoria, 10, 357

Unno, W. 1967, PASJ, 19, 140

Unsöld, A. 1927, Zeitschrift für Physik, 44, 793

—. 1928, Zeitschrift für Physik, 46, 782

Unsöld, A. 1930, Zeitschrift fur Astrophysik, 1, 138

—. 1934a, Zeitschrift fur Astrophysik, 8, 32

—. 1934b, Zeitschrift fur Astrophysik, 8, 225

van den Bergh, S. 1966, AJ, 71, 990

van Hamme, W. 1993, AJ, 106, 2096

van Hoof, A. 1948, ApJ, 108, 160

van Marle, A. J., Owocki, S. P., & Shaviv, N. J. 2008, MNRAS, 389, 1353

van't Veer, F. 1960, L'assombrissement centre-bord des etoiles. (Utrecht, Drukkerij Schotanus & Jens, 1960.), 3–+

Vogel, H. 1873, Astronomische Nachrichten, 82, 291

Vogel, H. C. 1874, Astronomische Nachrichten, 84, 113

Wade, G. A., Chadid, M., Shorlin, S. L. S., Bagnulo, S., & Weiss, W. W. 2002, A&A, 392, L17

Wade, R. A. & Rucinski, S. M. 1985, A&AS, 60, 471

Wallerstein, G., Matt, S., & Gonzalez, G. 2000, MNRAS, 311, 414

Wareing, C. J., Zijlstra, A. A., O'Brien, T. J., & Seibert, M. 2007, ApJL, 670, L125

Watanabe, S., Sako, M., Ishida, M., Ishisaki, Y., Kahn, S. M., Kohmura, T., Nagase, F., Paerels, F., & Takahashi, T. 2006, ApJ, 651, 421

Watanabe, T. & Kodaira, K. 1978, PASJ, 30, 21

—. 1979, PASJ, 31, 61

Weaver, H. 1954, AJ, 59, 375

Weingartner, J. C. & Draine, B. T. 2001, ApJ, 548, 296

Welch, D. L., Alcock, C., Allsman, R. A., Alves, D. R., Axelrod, T. A., Becker, A., Bennett, D. P., Cook, K. H., Freeman, K. C., Griest, K., Gurern, J. A., Lehner, M. J., Marshall, S. L., Minniti, D., Peterson, B. A., Pratt, M. R., Quinn, P. J., Rodgers, A. W., Rorabeck, A., Stubbs, C. W., & Sutherland, W. 1997, in Variables Stars and the Astrophysical Returns of the Microlensing Surveys, ed. R. Ferlet, J.-P. Maillard, & B. Raban, 205–+

Welch, D. L. & Duric, N. 1988, AJ, 95, 1794

Welch, D. L., McAlary, C. W., Madore, B. F., McLaren, R. A., & Neugebauer, G. 1985, ApJ, 292, 217

Welch, D. L., Wieland, F., McAlary, C. W., McGonegal, R., Madore, B. F., McLaren, R. A., & Neugebauer, G. 1984, ApJS, 54, 547

Werner, K. & Husfeld, D. 1985, A&A, 148, 417

Wesselink, A. J. 1946, BAIN, 10, 91

—. 1947, BAIN, 10, 256

Whipple, F. L. 1932, Lick Observatory Bulletin, 16, 1

Wielen, R., Jahreiß, H., Dettbarn, C., Lenhardt, H., & Schwan, H. 2000, A&A, 360, 399

Wildt, R. 1939, ApJ, 90, 611

Willson, L. A. 1976, ApJ, 205, 172

Willson, L. A. & Bowen, G. H. 1986, in Lecture Notes in Physics, Berlin Springer Verlag, Vol. 254, Cool Stars, Stellar Systems and the Sun, ed. M. Zeilik & D. M. Gibson, 385–+

Willson, L. A. & Hill, S. J. 1979, ApJ, 228, 854

Wilsing, J. & Scheiner, J. 1909, Publikationen des Astrophysikalischen Observatoriums zu Potsdam, 56

Wilsing, J., Scheiner, J., & Munch, W. 1919, Publikationen des Astrophysikalischen Observatoriums zu Potsdam, 74

Wittkowski, M., Aufdenberg, J. P., Driebe, T., Roccatagliata, V., Szeifert, T., & Wolff, B. 2006a, A&A, 460, 855

Wittkowski, M., Aufdenberg, J. P., & Kervella, P. 2004, A&A, 413, 711

Wittkowski, M., Hummel, C. A., Aufdenberg, J. P., & Roccatagliata, V. 2006b, A&A, 460, 843

Woitke, P. 2007, in Astronomical Society of the Pacific Conference Series, Vol. 378, Why Galaxies Care About AGB Stars: Their Importance as Actors and Probes, ed. F. Kerschbaum, C. Charbonnel, & R. F. Wing, 156–+

Wolf, R. 1863, MNRAS, 23, 207

Woltjer, Jr., J. 1936, BAIN, 8, 17

—. 1937, BAIN, 8, 193

Wood, P. R., Arnold, A., & Sebo, K. M. 1997, ApJL, 485, L25+

Woolley, R. & Carter, B. 1973, MNRAS, 162, 379

Wylie, C. C. 1922, ApJ, 56, 217

Wyse, A. B. 1939, PASP, 51, 328

Xu, H. Y. & Li, Y. 2004, A&A, 418, 213

Yecko, P. A., Kollath, Z., & Buchler, J. R. 1998, A&A, 336, 553

Zel'Dovich, Y. B. & Raizer, Y. P. 1967, Physics of shock waves and high-temperature hydrodynamic phenomena (New York: Academic Press, 1966/1967, edited by Hayes, W.D.; Probstein, Ronald F.)

Zhevakin, S. A. 1948, PhD thesis, Leningrad University

—. 1953, Astron. J. (USSR), 30, 161

—. 1954a, Astron. J. (USSR), 31, 141

—. 1954b, Astron. J. (USSR), 31, 355

—. 1959a, Soviet Astronomy, 3, 267

—. 1959b, Soviet Astronomy, 3, 913

—. 1959c, Soviet Astronomy, 3, 389

—. 1963, ARAA, 1, 367

Part IV

Appendices

Appendix A

Methods for Calculating Spherically Symmetric Radiative Transfer

A.1 Introduction

Radiative transfer is a fundamental field in astrophysics; one of the most common applications is in modeling atmospheres of stars. The star is normally treated as a plane parallel semi–infinite slab to simplify the problem and make the computation quick. This assumption is adequate if the size of the atmosphere is small compared to the radius of a star, one example where this is true is the Sun. For giant and supergiant stars, however, the assumption breaks down; the atmosphere is a significant fraction of the star's radius. One way to solve for the radiation field is to relax one's assumption from a plane–parallel atmosphere to a spherically symmetric atmosphere. The equation of radiative transfer in the plane–parallel case is

$$\mu \frac{dI_\nu(z,\mu)}{dz} = \chi_\nu(z)(S_\nu(z) - I_\nu(z,\mu)) \tag{A.1}$$

while for spherical symmetry the equation of transfer is

$$\mu \frac{\partial I_\nu(r,\mu)}{\partial r} + \frac{1-\mu^2}{r}\frac{\partial I_\nu(r,\mu)}{\partial \mu} = \chi_\nu(S_\nu(r) - I_\nu(r,\mu)). \tag{A.2}$$

Upon inspection of both equations, it is clearly more difficult to determine the intensity in a spherically symmetric atmosphere as opposed to a plane–parallel atmosphere. The purpose of this report is to give a detailed derivation of a solution to the spherically symmetric equation of radiative transfer.

A.2 Geometry

The equation of transfer is spherical symmetry is dependent on two differential terms. Solving this equation is difficult and undesirable; the problem would be tractable if it could be reduced from two dimensions to one. Hummer & Rybicki (1971) did just this by defining a coordinate system (z, p) where $z = r\mu$ and $p = \sqrt{r^2 - z^2}$. If one were to observe a star, rays of light would travel along z at constant p along the line–of–sight towards the observer.

One can now transform the equation of transfer by noticing

$$\frac{d}{dz} = \frac{\partial}{\partial r}\frac{dr}{dz} + \frac{\partial}{\partial \mu}\frac{d\mu}{dz} \tag{A.3}$$

where

$$\frac{dr}{dz} = \frac{d}{dz}\sqrt{p^2 + z^2} = \frac{z}{\sqrt{p^2 + z^2}} = \frac{z}{r} = \mu \tag{A.4}$$

and

$$\frac{d\mu}{dz} = \frac{d}{dz}\left(\frac{z}{r}\right) = \frac{1}{r} - \frac{z}{r^2}\frac{dz}{dr} = \frac{1}{r} - \frac{\mu}{r}\mu = \frac{1-\mu^2}{r}. \tag{A.5}$$

Therefore

$$\frac{d}{dz} = \mu\frac{\partial}{\partial r} + \frac{1-\mu^2}{r}\frac{\partial}{\partial \mu} \tag{A.6}$$

and

$$\mu\frac{\partial I_\nu(r,\mu)}{\partial r} + \frac{1-\mu^2}{r}\frac{\partial I_\nu(r,\mu)}{\partial \mu} = \frac{dI_\nu(z)}{dz} = \chi_\nu(S_\nu(r) - I_\nu(z)) \tag{A.7}$$

for some constant p. There exist many techniques for solving the transfer equation of this form such as long and short characteristics, and Rybicki (1971) and Feautrier (1964) solutions. This appendix will focus on the method of Feautrier solution by developing a second order differential equation, and the reorganization to the Rybicki solution. The Hermitian method, Auer (1976) for solving the equation of radiative transfer is also discussed.

A.3 Derivation

This derivation is based on the outline given by Mihalas (1978). The first step to simplify the problem is to write the transfer equation along the ray towards the observer, I_ν^+ and y away from the observer along the ray, I_ν^-. I_ν^+ adds intensity along the ray towards the observer while I_ν^- removes intensity. Therefore the gradient of the intensities are

$$\pm\frac{dI_\nu(\pm z)}{dz} = \chi_\nu(S_\nu - I_\nu^\pm) \tag{A.8}$$

or writing $-\chi_\nu dz = d\tau_{\nu,z}$ denoting the optical depth along a ray (written as $d\tau_\nu$ for the remainder of this report)

$$\mp \frac{dI_\nu^\pm}{d\tau_\nu} = S_\nu - I_\nu^\pm. \tag{A.9}$$

Next one can define mean intensity–like and flux–like intensities u and v as

$$u = \frac{1}{2}\left(I_\nu^+ + I_\nu^-\right) \tag{A.10}$$

and

$$v = \frac{1}{2}\left(I_\nu^+ - I_\nu^-\right) \tag{A.11}$$

meaning $I_\nu^+ = u + v$ and $I_\nu^- = u - v$. By adding the two equations in Equation A.9, one finds

$$-\frac{dI_\nu^+}{d\tau_\nu} + \frac{dI_\nu^-}{d\tau_\nu} = -\frac{d(u+v)}{d\tau_\nu} + \frac{d(u-v)}{d\tau_\nu} = -2\frac{dv}{d\tau_\nu} = 2S_\nu - I_\nu^+ - I_\nu^- = 2S_\nu - u - v - u + v = 2S_\nu - 2u \tag{A.12}$$

or

$$\frac{dv}{d\tau_\nu} = u - S_\nu. \tag{A.13}$$

Likewise one can subtract the two equations of Equation A.9

$$-\frac{dI_\nu^+}{d\tau_\nu} - \frac{dI_\nu^-}{d\tau_\nu} = -\frac{d(u+v)}{d\tau_\nu} - \frac{d(u-v)}{d\tau_\nu} = -2\frac{du}{d\tau_\nu} = -I_\nu^+ + I_\nu^- = -u - v + u - v = 2v \tag{A.14}$$

or

$$\frac{du}{d\tau_\nu} = v. \tag{A.15}$$

Substituting Equation A.15 into Equation A.13,

$$\frac{d^2u}{d\tau_\nu} = u - S_\nu \tag{A.16}$$

is the second–order differential equation we wish to solve.

It is important to consider the boundary conditions, in a spherically symmetric atmosphere there are three: one at the surface of the star, one at the core of the star ($p \leq R_{core}$) and one at $z = 0$ when $p > R_{core}$. Consider first the surface boundary condition, where it can be assumed there is no irradiation from external sources. In this case $I_\nu^-(R_*) = 0$ meaning the mean intensity–like intensity is the same as the flux–like intensity, $u(R_*) = v(R_*)$. Combining this information with Equation A.15 leads to the surface condition

$$\left.\frac{du}{d\tau_\nu}\right|_{r=R_*} = u(R_*). \tag{A.17}$$

The core condition, at depth along the ray z_{max}, can be determined by assuming the intensity at the core

boundary can be approximated by the diffusion approximation. Using Equation A.15 and substituting $v = I_\nu^+ - u$

$$\left.\frac{du}{d\tau_\nu}\right|_{r=R_c} = I_\nu^+ - u(R_c) = B(R_c) + \frac{z_{max}}{R_c}\left(\frac{1}{\chi_\nu}\left|\frac{\partial B}{\partial r}\right|\right)_{R_c} - u(R_c). \tag{A.18}$$

The third boundary condition is determined based on the symmetry of the problem, at $z = z_{max}, p > R_c$. Consider a ray towards the observer; this ray will have intensity I_ν at point $z_{max} - \epsilon$ where $\epsilon << z_{max}$. A ray at the same point p but pointing away from the observer will have the same intensity I_ν at point $z_{max} + \epsilon$. Therefore

$$I_\nu^+(z_{max} - \epsilon) + I_\nu^-(z_{max} - \epsilon) = I_\nu^+(z_{max} + \epsilon) + I_\nu^-(z_{max} + \epsilon). \tag{A.19}$$

Note that in the frame of the observer $I_\nu^-(z_{max} + \epsilon)$ points away the observer and $I_\nu^+(z_{max} + \epsilon)$ points towards. Since the intensities are the same and the star is symmetric then the outgoing radiation must be the same, meaning $I_\nu^+(z_{max} - \epsilon) = I_\nu^-(z_{max} + \epsilon)$ and likewise for the radiation towards $z = z_{max}$. This implies in the limit as $\epsilon \to 0$ then $I_\nu^+(z_{max}) = I_\nu^-(z_{max})$ and because of symmetry $v(z_{max}) = 0$. Therefore the boundary condition can again be given by Equation 15

$$\left.\frac{du}{d\tau_\nu}\right|_{z=z_{max}, p>R_c} = 0. \tag{A.20}$$

Now there are four equations for solving the radiative transfer. The next step is to derive difference equations representing the differential equations to solve the system computationally.

A.4 Numerical Derivation

In this section a numerical method is derived for solving the radiative transfer. The first step is to define the first and second derivatives of a quantity. For some variable X the first derivative with respect to τ_ν along a ray at point $d + 1/2$ is

$$\frac{dX}{d\tau_\nu} = \frac{\Delta X}{\Delta \tau_\nu} = \frac{X_{d+1} - X_d}{\Delta \tau_{d+1/2}}. \tag{A.21}$$

where $\Delta\tau_{d+1/2} = 0.5(\chi_{d+1} + \chi_d)|z_{d+1} - z_d|$. The second derivative at point d is

$$\frac{d^2X}{d\tau_\nu^2} = \frac{(dX/d\tau)_{d+1/2} - (dX/d\tau)_{d-1/2}}{0.5(\Delta\tau_{d+1/2} + \Delta\tau_{d-1/2})} = \frac{2}{\Delta\tau_{d+1/2} + \Delta\tau_{d-1/2}}\left(\frac{X_{d+1} - X_d}{\Delta\tau_{d+1/2}} - \frac{X_d - X_{d-1}}{\Delta\tau_{d-1/2}}\right) \tag{A.22}$$

and let $t_d \equiv \Delta\tau_{d+1/2} + \Delta\tau_{d-1/2}$ for simpilicity. One can apply these equalities to Equation A.16 to derive a difference equation to solve for u

$$\frac{d^2u}{d\tau_\nu^2} = \frac{2}{t_d}\left(\frac{u_{d+1} - u_d}{\Delta\tau_{d+1/2}} - \frac{u_d - u_{d-1}}{\Delta\tau_{d-1/2}}\right) = u_d - S_d \tag{A.23}$$

The source function can be written in the form

$$S_d(r) = \alpha_d(r)J_d(r) + \beta_d(r) = \alpha_d \int_0^1 u_d d\mu + \beta_d(r) = \alpha_d \sum_n w_{dn}u_{dn} + \beta_d(r) \tag{A.24}$$

where u_{dn} is the mean intensity–like intensity at point d along ray at point p_n. The difference equation is now

$$\frac{2}{t_d}\left(\frac{u_{d+1} - u_d}{\Delta\tau_{d+1/2}} - \frac{u_d - u_{d-1}}{\Delta\tau_{d-1/2}}\right) = u_d - \alpha_d \sum_n w_{dn}u_{dn} - \beta_d(r) \tag{A.25}$$

and rearranging

$$\begin{aligned} -\frac{2}{t_d}\frac{1}{\Delta\tau_{d-1/2}}u_{d-1} + \left[\frac{2}{t_d}\left(\frac{1}{\Delta\tau_{d+1/2}} + \frac{1}{\Delta\tau_{d-1/2}}\right) + 1 - \alpha_d \sum_n w_{dn}\right]u_{dn} \\ - \frac{2}{t_d}\frac{1}{\Delta\tau_{d+1/2}}u_{d+1} = \beta_d. \end{aligned} \tag{A.26}$$

One can treat the mean intensity–like intensities at depth d for each ray as a vector $\mathbf{u}_d = \{u_{d1}, u_{d2}, ...u_{dN}\}$ then each of the coefficients in Equation A.26 can be treated as elements in a matrix. Define matrix $\mathbf{A}_d$ with elements

$$A_{ii} = \frac{2}{t_i}\frac{1}{\Delta\tau_{i-1/2}} \tag{A.27}$$

where $i = 2...N - 1$ and all non–diagonal terms are zero. Likewise matrix $\mathbf{C}_d$ is defined with elements

$$C_{ii} = \frac{2}{t_i}\frac{1}{\Delta\tau_{i+1/2}} \tag{A.28}$$

where $i = 2...N - 1$ and all non–diagonal terms are again zero representing the third term of Equation A.26. The second term of Equation A.26 requires a full matrix, $\mathbf{B}_d$, as opposed to the preceding two matrices. The diagonal terms of $\mathbf{B}_d$ are

$$B_{ii} = \frac{2}{t_i}\left(\frac{1}{\Delta\tau_{i+1/2}} + \frac{1}{\Delta\tau_{i-1/2}}\right) + 1 - \alpha_i w_{ii} \tag{A.29}$$

and the non–diagonal terms are

$$B_{ij}(i \neq j) = -\alpha_j w_{ij}. \tag{A.30}$$

Using these matrices and letting $\mathbf{L}_d$ be a vector containing the thermal terms of Equation 26 one finds

$$-\mathbf{A}_d u_{d-1} + \mathbf{B}_d u_d - \mathbf{C}_d u_{d+1} = \mathbf{L}_d. \tag{A.31}$$

Thus the difference equations representing the solution to the equation of transfer in a stellar atmosphere is now derived. The next step is to determine difference equation representations of the boundary conditions.

Consider the surface condition given by Equation A.17, written in terms of differences becomes

$$\frac{u_2 - u_1}{\Delta\tau_{3/2}} = u_1 \tag{A.32}$$

however this representation is only first order accurate. Consider the Taylor series expansion of u near the surface

$$u_2 = u_1 + \Delta\tau_{3/2}\left.\frac{du}{d\tau}\right|_1 + \frac{\Delta\tau_{3/2}^2}{2}\left.\frac{d^2u}{d\tau^2}\right|_1 = u_1 + \Delta\tau_{3/2}u_1 + \frac{\Delta\tau_{3/2}^2}{2}(u_1 - S_1) \tag{A.33}$$

where Equations A.15 and A.17 are used. Rearranging and inserting Equation A.24

$$\left(1 + \frac{2}{\Delta\tau_{3/2}^2} + \frac{2}{\Delta\tau_{3/2}} - \alpha_1\sum_n w_{1n}\right)u_1 - \frac{2}{\Delta\tau_{3/2}^2}u_2 = \beta_1 \tag{A.34}$$

and then the matrices in Equation A.31 have elements

$$B_{11} = 1 + \frac{2}{\Delta\tau_{3/2}^2} + \frac{2}{\Delta\tau_{3/2}} - \alpha_1 w_{11}, \tag{A.35}$$

$$B_{1n}(n \neq 1) = -\alpha_1 w_{1n} \tag{A.36}$$

and

$$C_{11} = \frac{2}{\Delta\tau_{3/2}^2}. \tag{A.37}$$

The matrix $\mathbf{A}_1$ is zero and the elements L_{1n} are β_1. The next boundary condition to be considered is the interior condition where $p > R_c$. Directly applying the difference relations to Equation A.20 will lead again to only a first–order accurate solution so again it is necessary to apply a Taylor series expansion

$$u_{D-1} = u_D + \Delta\tau_{D-1/2}\left.\frac{du}{d\tau}\right|_D + \frac{\Delta\tau_{D-1/2}^2}{2}\left.\frac{d^2u}{d\tau^2}\right|_D = u_D + \frac{\Delta\tau_{D-1/2}^2}{2}(u_D - S_D) \tag{A.38}$$

and rearranging

$$-\frac{2}{\Delta\tau_{D-1/2}^2}u_{D-1/2} + \left(1 + \frac{2}{\Delta\tau_{D-1/2}^2} - \sum_n \alpha_D w_{Dn}\right)u_{Dn} = \beta_D. \tag{A.39}$$

Therefore the matrices can be written with elements

$$A_{ii} = \frac{2}{\Delta\tau_{i-1/2}^2}, \tag{A.40}$$

$$B_{ii} = \left(1 + \frac{2}{\Delta\tau_{i-1/2}^2} - \alpha_i w_i\right) \tag{A.41}$$

with non–diagonal elements

$$B_{ij}(i \neq j) = -\alpha_j w_j \tag{A.42}$$

and the matrix C_D is zero and $L_i = \beta_i$. The third condition is at the core boundary, and again a taylor series expansion is applied to obtain second order accuracy

$$\begin{aligned} u_{D-1} &= u_D + \Delta\tau_{D-1/2} \left.\frac{du}{d\tau}\right|_D + \frac{\Delta\tau_{D-1/2}{}^2}{2} \left.\frac{d^2u}{d\tau^2}\right|_D \\ &= u_D + \Delta\tau_{D-1/2}\left(B_D + \frac{z_D}{R_c}\left(\frac{1}{\chi_D}\left|\frac{\partial B}{\partial r}\right|\right)_D - u_D\right) + \frac{\Delta\tau^2_{D-1/2}}{2}(u_D - S_D) \end{aligned} \tag{A.43}$$

and rearranging

$$\begin{aligned} -\frac{2}{\Delta\tau^2_{D-1/2}}u_{D-1} + \left(\frac{2}{\Delta\tau^2_{D-1/2}} - \frac{2}{\Delta\tau_{D-1/2}} + 1 - \alpha_D \sum_n w_{Dn}\right)u_{Dn} \\ = \beta_D - \frac{\Delta\tau_{D-1/2}}{2}\left(B_D + \frac{z_D}{R_c}\left(\frac{1}{\chi_D}\left|\frac{\partial B}{\partial r}\right|\right)_D\right). \end{aligned} \tag{A.44}$$

Therefore

$$A_{ii} = \frac{2}{\tau^2_{D-1/2}} \tag{A.45}$$

and

$$B_{ii} = \frac{2}{\Delta\tau^2_{i-1/2}} - \frac{2}{\Delta\tau_{i-1/2}} + 1 - \alpha_i w_{ii} \tag{A.46}$$

with non–diagonal terms

$$B_{ij}(i \neq j) = -\alpha_j w_{ij}. \tag{A.47}$$

Again $C_{ij} = 0$ but $L_i = \beta_i - \Delta\tau_{i-1/2}/2(B_i + (z_i/R_c)(\partial B/\partial r)|_{r=R_c}$. Now all of the necessary elements are known and the vectors **u** can be solved at all depths.

A.5 Feautrier Solution

At the surface the matrix equation is

$$B_1 u_1 - C_1 u_2 = L_1 \tag{A.48}$$

and one can solve this for u_1 to get

$$u_1 = B_1^{-1} L_1 + B_1^{-1} C_1 u_2 = v_1 + D_1 u_2. \tag{A.49}$$

One can then substitute u_1 into $-A_2u_1 + B_2u_2 - C_2u_3 = L_3$ to solve for u_2

$$-A_2v_1 - A_2D_1u_2 + B_2u_2 - C_2u_3 = L_3 \tag{A.50}$$

and then

$$u_2 = (-A_2D_1 + B_2)^{-1}(L_3 + A_2v_1) + (-A_2D_1 + B_2)^{-1}C_2u_3 = v_2 + D_2u_3. \tag{A.51}$$

This process can be continued until

$$u_{D-1} = v_{D-1} + D_{D-1}u_D \tag{A.52}$$

and substituting this into the next equation

$$-A_Dv_{D-1} - A_DD_{D-1}u_D + B_Du_D = L_D. \tag{A.53}$$

Therefore one can solve u_D in terms of known quantities and once u_D is known one can use back substitution to solve u_{D-1} and so on to u_1. This method has the benefit of solving for the mean intensity–like intensities and hence the mean intensity, flux, and source function without using an iterative process. The mean intensity is

$$J_d = \sum_n w_{dn}u_{dn} \tag{A.54}$$

and the flux is

$$H_d = \sum_n w_{dn}\mu_n v_{dn} \tag{A.55}$$

and the source function can be calculated using Equation A.24. Thus the quantities are now known and the radiation field in the atmosphere is determined.

A.6 Rybicki Solution

The Rybicki solution for solving the equation of radiative transfer is very similar to the Feautrier solution. Consider Equation A.24 where the source function is defined, and let the source function be redefined as

$$S_d(r) = \alpha_d \sum_n w_{dn}u_{dn} + \beta_d(r) = \alpha_d\bar{J}_d + \beta_d(r) \tag{A.56}$$

then Equation A.26 changes to

$$\begin{aligned} -\frac{2}{t_d}\frac{1}{\Delta\tau_{d-1/2}}u_{d-1} + \left[\frac{2}{t_d}\left(\frac{1}{\Delta\tau_{d+1/2}} + \frac{1}{\Delta\tau_{d-1/2}}\right) + 1\right]u_d \\ - \frac{2}{t_d}\frac{1}{\Delta\tau_{d+1/2}}u_{d+1} + \alpha_d\bar{J}_d = \beta_d. \end{aligned} \tag{A.57}$$

The boundary conditions, Equations A.34, A.39 and A.44 are rewritten as

$$\left(1+\frac{2}{\Delta\tau_{3/2}^2}+\frac{2}{\Delta\tau_{3/2}}\right)u_1-\frac{2}{\Delta\tau_{3/2}^2}u_2-\alpha_1\bar{J}_1=\beta_1, \tag{A.58}$$

$$-\frac{2}{\Delta\tau_{D-1/2}^2}u_{D-1/2}+\left(1+\frac{2}{\Delta\tau_{D-1/2}^2}\right)u_D-\alpha_D\bar{J}_D=\beta_D, \tag{A.59}$$

and

$$-\frac{2}{\Delta\tau_{D-1/2}^2}u_{D-1}+\left(\frac{2}{\Delta\tau_{D-1/2}^2}-\frac{2}{\Delta\tau_{D-1/2}}+1\right)u_D-\alpha_D\bar{J}_D = \beta_D-\frac{\Delta\tau_{D-1/2}}{2}\left(B_D+\frac{z_D}{R_c}\left(\frac{1}{\chi_D}\left|\frac{\partial B}{\partial r}\right|\right)_D\right). \tag{A.60}$$

For a frequency ν_i, these equations can be written in the form

$$A_d u_{d-1}+B_d u_d+C_d u_{d+1}-\alpha_d\bar{J}_d=L_d \tag{A.61}$$

where the surface boundary condition is

$$B_2u_1+C_1u_2-\alpha_1\bar{J}_1=L_1 \tag{A.62}$$

and the inner boundary condition is

$$A_D u_{D-1}+B_D u_D-\alpha_D\bar{J}_D=L_D. \tag{A.63}$$

The mean intensity variable $\bar{J}$ contains frequency dependent variables. One may define the vectors $\mathbf{u}_i = (u_1, u_2, \ldots, u_D)^T$, $\bar{\mathbf{J}}_i = (\bar{J}_1, \bar{J}_2, \ldots, \bar{J}_D)^T$, $\mathbf{K}_i = (L_1, L_2, \ldots, L_D)^T$, $\mathbf{U}_i = (-\alpha_1, -\alpha_2, \ldots, -\alpha_D)$ and the matrix

$$\mathbf{T_i}=\begin{pmatrix} B_1 & C_1 & 0 & 0 & \cdots & 0 \\ A_2 & B_2 & C_2 & 0 & \cdots & 0 \\ 0 & A_3 & B_3 & C_3 & \cdots & 0 \\ \vdots & & & \ddots & & \vdots \\ 0 & 0 & \cdots & 0 & A_D & B_D \end{pmatrix}, \tag{A.64}$$

all at frequency i. Equations A.61, A.62 and A.63 may be written as

$$\mathbf{T}_i\mathbf{u}_i+\mathbf{U}_i\bar{\mathbf{J}}=\mathbf{K}_i \tag{A.65}$$

but the quantity $\bar{\mathbf{J}}$ is still unknown. From its definition, this quantity is

$$\bar{J}_d = \sum_i w_i \phi_{di} u_{di} \tag{A.66}$$

and the vector can written as

$$\sum_i \mathbf{V}_i \mathbf{u}_i - \bar{\mathbf{J}} = 0. \tag{A.67}$$

Combining this with Equation A.65, we are left with the set of equations

$$\begin{pmatrix} \mathbf{T}_1 & 0 & 0 & \cdots & 0 & \mathbf{U}_1 \\ 0 & \mathbf{T}_2 & 0 & \cdots & 0 & \mathbf{U}_2 \\ 0 & 0 & \mathbf{T}_3 & \cdots & 0 & \mathbf{U}_3 \\ \vdots & & \ddots & & \vdots & \\ 0 & 0 & 0 & \cdots & \mathbf{T}_N & \mathbf{U}_N \\ \mathbf{V}_1 & \mathbf{V}_2 & \mathbf{V}_3 & \cdots & \mathbf{V}_N & 0 \end{pmatrix} \begin{pmatrix} \mathbf{u}_1 \\ \mathbf{u}_2 \\ \mathbf{u}_3 \\ \vdots \\ \mathbf{u}_N \\ \bar{\mathbf{J}} \end{pmatrix} = \begin{pmatrix} \mathbf{K}_1 \\ \mathbf{K}_2 \\ \mathbf{K}_3 \\ \vdots \\ \mathbf{K}_N \\ 0 \end{pmatrix}. \tag{A.68}$$

This system of equations may be solved by noting that

$$\mathbf{u}_i = \mathbf{T}_i^{-1} \mathbf{K}_i - \mathbf{T}_i^{-1} \mathbf{U}_i \bar{\mathbf{J}} \tag{A.69}$$

and by substituting the relations for $\mathbf{u}_i$ into Equation A.64 then one may calculate the vector $\bar{\mathbf{J}}$. Once this vector is known then the mean–like intensities u_{di} are easily calculated.

A.7 Hermitian Method Solution

Auer (1976) proposed an alternative method for solving the second order differential equation for the mean–like intensity variable u. The method is similar to that previously stated for solving for u at point d except that it includes information about the second derivative of u at points $d-1$ and $d+1$. The added information makes the solution fourth order accurate and is of the form

$$a_d u_{d-1} + b_d u_d + c_d u_{d+1} + j_d u''_{d-1} + k_d u''_d + l_d u''_{d+1} \approx 0 \tag{A.70}$$

where the coefficients are unknown. They can be determined by substituting a taylor series expansion for u in terms of u_d. Therefore

$$u_{d-1} = u_d - u'_d \Delta\tau_{d-1} + \frac{1}{2} u''_d \Delta\tau^2_{d-1} - \frac{1}{6} u'''_d \Delta\tau^3_{d-1} + \frac{1}{24} u^{(iv)}_d \Delta\tau^4_{d-1} \tag{A.71}$$

$$u_{d+1} = u_d + u'_d \Delta\tau_d + \frac{1}{2} u''_d \Delta\tau^2_d + \frac{1}{6} u'''_d \Delta\tau^3_d + \frac{1}{24} u^{(iv)}_d \Delta\tau^4_d \tag{A.72}$$

$$u''_{d-1} = u''_d - u'''_d \Delta\tau_{d-1} + \frac{1}{2} u^{(iv)}_d \Delta\tau^2_{d-1} \tag{A.73}$$

$$u''_{d+1} = u''_d + u'''_d \Delta\tau_d + \frac{1}{2} u^{(iv)}_d \Delta\tau^2_d. \tag{A.74}$$

Substituting these four equations into Equation A.70 and rearranging

$$\begin{aligned}
&(a_d + b_d + c_d)u_d + (c_d\Delta\tau_d - a_d\Delta\tau_{d-1})u'_d + \\
&\left(\frac{1}{2}\Delta\tau^2_{d-1}a_d + \frac{1}{2}\Delta\tau^2_d c_d + j_d + k_d + l_d\right)u''_d + \\
&\left(-\frac{1}{6}\Delta\tau^3_{d-1}a_d + \frac{1}{6}\Delta\tau^3_d c_d - \Delta\tau_{d-1} j_d + \Delta\tau_d l_d\right)u'''_d + \\
&\left(\frac{1}{24}\Delta\tau^4_{d-1}a_d + \frac{1}{24}\Delta\tau_d c_d + \frac{1}{2}\Delta\tau^2_{d-1} j_d + \frac{1}{2}\Delta\tau^2_d l_d\right)u^{(iv)}_d = 0
\end{aligned} \tag{A.75}$$

For Equation A.75 to be true for all u_d and it's derivatives then each term in brackets must be identically zero and since this leads to five equations with six unknowns, one variable is arbitrary. It is easily shown that

$$a_d = -\frac{2}{(\Delta\tau_{d-1} + \Delta\tau_d)\Delta\tau_{d-1}} \tag{A.76}$$

$$c_d = \frac{2}{(\Delta\tau_{d-1} + \Delta\tau_d)\Delta\tau_d} \tag{A.77}$$

$$b_d = \frac{2}{\Delta\tau_{d-1} + \Delta\tau_d}\left(\frac{1}{\tau_{d-1}} - \frac{1}{\tau_d}\right) \tag{A.78}$$

$$j_d = \frac{1}{6}\left(1 - \frac{\Delta\tau^2_d}{(\Delta\tau_{d-1} + \Delta\tau_d)\Delta\tau_{d-1}}\right) \tag{A.79}$$

$$l_d = \frac{1}{6}\left(1 + \frac{\Delta\tau^2_{d-1}}{(\Delta\tau_{d-1} + \Delta\tau_d)\Delta\tau_d}\right) \tag{A.80}$$

and

$$k_d = 1 - \frac{1}{6(\Delta\tau_{d-1} + \Delta\tau_d)}\left(\frac{\Delta\tau^2_{d-1}}{\Delta\tau_d} - \frac{\Delta\tau^2_d}{\Delta\tau_{d-1}}\right). \tag{A.81}$$

Returning to Equation A.70 and substituting Equation A.16 and Equation A.24 to account for the source function, one gets

$$\begin{aligned}
&(a_d + j_d)u_{d-1} + (b_d + k_d)u_d + (c_d + l_d)u_{d+1} - j_d\alpha_{d-1}\sum_n w_{d-1,n}u_{d-1,n} \\
&- k_d\alpha_d\sum_n w_{dn}u_{dn} - l_d\alpha_{d+1}\sum_n w_{d+1,n}u_{d+1,n} = j_d\beta_{d-1} + k_d\beta_d + l_d\beta_{d+1}.
\end{aligned} \tag{A.82}$$

Casting this in the form of Equation A.31 one can write the values of the elements of the matrices $\mathbf{A}_d, \mathbf{B}_d, \mathbf{C}_d, \mathbf{L}_d$. The diagonal elements of $\mathbf{A}_d$ are

$$A_{ii} = \frac{2}{(\Delta\tau_{i-1} + \Delta\tau_i)\Delta\tau_{i-1}} - \frac{1}{6}\left(1 - \frac{\Delta\tau_i^2}{(\Delta\tau_{i-1} + \Delta\tau_i)\Delta\tau_{i-1}}\right)(1 - \alpha_{i-1}w_{ii}) \tag{A.83}$$

while the non–diagonal terms are

$$A_{ij}(i \neq j) = \frac{1}{6}\left(1 - \frac{\Delta\tau_i^2}{(\Delta\tau_{i-1} + \Delta\tau_i)\Delta\tau_{i-1}}\right)\alpha_i w_{ij}. \tag{A.84}$$

The diagonal and non–diagonal elements of $\mathbf{B}_d$ are

$$B_{ii} = \frac{2}{\Delta\tau_{d-1} + \Delta\tau_d}\left(\frac{1}{\tau_{i-1}} - \frac{1}{\tau_i}\right) + \left[1 - \frac{1}{6(\Delta\tau_{i-1} + \Delta\tau_i)}\left(\frac{\Delta\tau_{i-1}^2}{\Delta\tau_i} - \frac{\Delta\tau_i^2}{\Delta\tau_{i-1}}\right)\right](1 - \alpha_i w_{ii}) \tag{A.85}$$

$$B_{ij} = -\left[1 - \frac{1}{6(\Delta\tau_{i-1} + \Delta\tau_i)}\left(\frac{\Delta\tau_{i-1}^2}{\Delta\tau_i} - \frac{\Delta\tau_i^2}{\Delta\tau_{i-1}}\right)\right]\alpha_i w_{ij} \tag{A.86}$$

and for the matrix $\mathbf{C}_d$

$$C_{ii} = -\frac{2}{(\Delta\tau_{i-1} + \Delta\tau_i)\Delta\tau_i} - \frac{1}{6}\left(1 + \frac{\Delta\tau_{i-1}^2}{(\Delta\tau_{i-1} + \Delta\tau_i)\Delta\tau_i}\right)(1 - \alpha_i w_{ii}) \tag{A.87}$$

$$C_{ij} = \frac{1}{6}\left(1 + \frac{\Delta\tau_{i-1}^2}{(\Delta\tau_{i-1} + \Delta\tau_i)\Delta\tau_i}\right)\alpha_i w_{ij}. \tag{A.88}$$

The matrix containing the thermal terms is

$$\begin{aligned} L_i = {} & \frac{1}{6}\left(1 - \frac{\Delta\tau_i^2}{(\Delta\tau_{i-1} + \Delta\tau_i)\Delta\tau_{i-1}}\right)\beta_{i-1} + \left[1 - \frac{1}{6(\Delta\tau_{i-1} + \Delta\tau_i)}\left(\frac{\Delta\tau_{i-1}^2}{\Delta\tau_i} - \frac{\Delta\tau_i^2}{\Delta\tau_{i-1}}\right)\right]\beta_i \\ & + \frac{1}{6}\left(1 + \frac{\Delta\tau_{i-1}^2}{(\Delta\tau_{i-1} + \Delta\tau_i)\Delta\tau_i}\right)\beta_{i+1}. \end{aligned} \tag{A.89}$$

The next step is to consider the boundary conditions. It is desirable to use the maximum amount of information to solve the boundaries. Unfortunately to make any of the three conditions fourth–order accurate would require extra information and the matrix for solving the system of equations will not be tridiagonal. The boundaries can be approximated to third order accuracy. The surface boundary condition is give by Equation A.17 and can be cast in the form

$$a_1 u_1 + b_1 u_2 + u_1' + j_1 u_1'' + k_1 u_2'' \tag{A.90}$$

and expanding u_2 and u_2''

$$u_2 \approx u_1 + \Delta\tau_1 u_1' + \frac{1}{2}\Delta\tau_1^2 u_1'' + \frac{1}{6}\Delta\tau_1^3 u_1''' \tag{A.91}$$

$$u_2'' \approx u_1'' + \Delta\tau_1 u_1'''. \tag{A.92}$$

Substituting these two results and rearranging Equation A.90

$$(a_1 + b_1)u_1 + (1 + \Delta\tau_1 b_1)u_1' + \left(\frac{1}{2}\Delta\tau_1^2 b_1 + j_1 + k_1\right)u_1'' + \left(\frac{1}{6}\Delta\tau_1^3 b_1 + \Delta\tau_1 k_1\right)u_1''' = 0. \tag{A.93}$$

This yields four equations and four unknowns, the choice of the coefficient of u_1' to be 1 is arbitrary, in the same manner as the derivation previous. The variables are thus

$$a_1 = \frac{1}{\Delta\tau_1} \tag{A.94}$$

$$b_1 = -\frac{1}{\Delta\tau_1} \tag{A.95}$$

$$j_1 = \frac{\Delta\tau_1}{3} \tag{A.96}$$

$$k_1 = \frac{\Delta\tau_1}{6}. \tag{A.97}$$

Returning to Equation A.91 and inserting these values, the surface boundary equation and Equationeq:a23, one finds

$$\left(\frac{\Delta\tau_1}{3} + \frac{1}{\Delta\tau_1} + 1\right)u_1 + \left(\frac{\Delta\tau_1}{6} - \frac{1}{\Delta\tau_1}\right)u_2 - \alpha_1 \sum_i w_{1i}u_{1i} - \alpha_2 \sum_i w_{2i}u_{2i} = \frac{\Delta\tau_1}{3}\left(\beta_1 + \frac{\beta_2}{2}\right). \tag{A.98}$$

Hence the matrices $\mathbf{B}_1$ and $\mathbf{C}_1$ can be written with elements

$$B_{1j} = \delta_{1j}\left(\frac{\Delta\tau_1}{3} + \frac{1}{\Delta\tau_1} + 1\right) - \alpha_1 w_{1j} \tag{A.99}$$

$$C_{1j} = -\delta_{1j}\left(\frac{\Delta\tau_1}{6} - \frac{1}{\Delta\tau_1}\right) - \alpha_2 w_{2j}. \tag{A.100}$$

The thermal term is

$$L_1 = \frac{\Delta\tau_1}{3}\left(\beta_1 + \frac{\beta_2}{2}\right). \tag{A.101}$$

The inner boundary where $p > R_c$ will be similar to the surface boundary, with the same equation to be solved with a different choice of arbitrary constant,

$$a_D u_{D-1} + b_D u_D - u_D' + j_D u_{D-1}'' + k_D u_D'' = 0 \tag{A.102}$$

and expanding u_{D-1} and u_{D-1}''

$$u_{D-1} \approx u_D - \Delta\tau_D u_D' + \frac{1}{2}\Delta\tau_D^2 u_D'' - \frac{1}{6}\Delta\tau_D^3 u_D''' \tag{A.103}$$

$$u''_{D-1} \approx u''_D - \Delta\tau_D u'''_D \tag{A.104}$$

which yields values for the coefficients as

$$a_D = -\frac{1}{\Delta\tau_D} \tag{A.105}$$

$$b_D = \frac{1}{\Delta\tau_D} \tag{A.106}$$

$$j_D = \frac{\Delta\tau_D}{3} \tag{A.107}$$

$$k_D = \frac{\Delta\tau_D}{6}. \tag{A.108}$$

The matrix components for the Feautrier solution are

$$A_{Dj} = \delta_{Dj}\left(\frac{1}{\Delta\tau_D} - \frac{\Delta\tau_D}{3}\right) + \frac{\alpha_{D-1}\Delta\tau_D}{3} w_{D-1,j} \tag{A.109}$$

$$B_{Dj} = \delta_{Dj}\left(\frac{1}{\Delta\tau_D} + \frac{\Delta\tau_D}{6}\right) - \frac{\alpha_D\Delta\tau_D}{6} w_{Dj} \tag{A.110}$$

and the thermal term is

$$L_D = \frac{\Delta\tau_D}{3}\left(\beta_{D-1} + \frac{\beta_D}{2}\right). \tag{A.111}$$

The core boundary condition is given by the diffusion approximation, Equation A.18, and using the same relation given above, Equation A.102. The values of a_D, b_D, j_D, and k_D will be the same as that given by Equations A.105, A.106, A.107, and A.108. Therefore the matrix elements can be written as

$$A_{Dj} = \delta_{Dj}\left(\frac{1}{\Delta\tau_D} - \frac{\Delta\tau_D}{3}\right) + \frac{\alpha_{D-1}\Delta\tau_D}{3} w_{D-1,j} \tag{A.112}$$

$$B_{Dj} = \delta_{Dj}\left(1 + \frac{1}{\Delta\tau_D} + \frac{\Delta\tau_D}{6}\right) - \frac{\alpha_D\Delta\tau_D}{6} w_{Dj} \tag{A.113}$$

and

$$L_{Dj} = \frac{\Delta\tau_D}{3}\left(\beta_{D-1} + \frac{\beta_D}{2}\right) + B_D(T) + \frac{z_D}{R_c}\left(\frac{1}{\chi_D}\left|\frac{\partial B(T)}{\partial r}\right|\right)_D. \tag{A.114}$$

Thus a second method for solving the radiative transfer is derived. This can be solved using the Feautrier method or reorganized to be solved using the Rybicki method.

Appendix B

Derivation of Spherically Symmetric Temperature Correction

B.1 Introduction

The temperature correction is an important element in the calculation of a stellar atmosphere. The calculation of a model stellar atmosphere is an iterative process to produce a structure where the flux is conserved. The purpose of a temperature correction routine is to adjust the starting temperature structure of the atmosphere by using the difference between the calculated bolometric flux and the desired bolometric flux. For a plane–parallel geometry the correct structure produces a divergentless bolometric flux,

$$\nabla \cdot \int_0^\infty F_\nu d\nu = 0 \tag{B.1}$$

and in a spherically symmetric atmosphere this becomes

$$\nabla \cdot \left[r^2 \int_0^\infty F_\nu d\nu \right] = 0. \tag{B.2}$$

Using the constraint of radiative equilibrium, it is possible to derive a number of temperature correction methods. One of the more simple methods is based on the alternative form of the condition of radiative equilibrium

$$\int_0^\infty k_\nu B_\nu(T) d\nu = \int_0^\infty k_\nu J_\nu d\nu. \tag{B.3}$$

If the temperature structure and the mean intensity that were calculated in a previous iteration do not satisfy the condition of radiative equilibrium then one can write $T_{eq} = T + \Delta T$ where T_{eq} is the temperature as a function of depth that will satisfy radiative equilibrium and ΔT is the difference between the temperature

calculated and the temperature for equilibrium. Therefore

$$B_\nu(T_{eq}) = B_\nu(T + \Delta T) \approx B_\nu(T) + \Delta T \frac{\partial B_\nu(T)}{\partial T} \tag{B.4}$$

and substituting into Equation B.3,

$$\int_0^\infty k_\nu \left[B_\nu(T) + \Delta T \frac{\partial B_\nu(T)}{\partial T} \right] d\nu = \int_0^\infty k_\nu J_\nu d\nu. \tag{B.5}$$

Solving for ΔT

$$\Delta T = \frac{\int_0^\infty k_\nu [J_\nu - B_\nu(T)] d\nu}{\int_0^\infty k_\nu [\partial B_\nu(T)/\partial T] d\nu}. \tag{B.6}$$

One could use this method to iterate a stellar atmosphere but it has many drawbacks. It can be shown the mean intensity is a function of B_ν if this is approximately the source function

$$J_\nu(\tau_\nu) \propto \int B_\nu(T) e^{-(t-\tau_\nu)/\mu} dt \tag{B.7}$$

where $\mu = \cos\theta$ is the angle between the point on the stellar disk where the intensity emerges and the center of the disk. Equation B.7 implies that deep in the atmosphere the $J_\nu \rightarrow B_\nu(T)$ and the change of temperature will approach zero. Another failure, according to Mihalas (1978), is the method assumes the mean intensity is correct at all depths when in fact, if one assumes that $B_\nu = B_\nu(T + \Delta T)$ then Equation B.7 is wrong and needs to be replaced by,

$$J_\nu(\tau'_\nu) \propto \int B_\nu(T + \Delta T) e^{-(t-\tau'_\nu)/\mu} dt \tag{B.8}$$

suggesting a better temperature correction method would need to include changes in the optical depth.

B.2 Avrett–Krook Temperature Correction

Avrett (1964) derived a temperature correction method that included the optical depth for a plane–parallel model atmosphere. It was done by assuming the following perturbations

$$\tau \rightarrow \tau^{(0)} + \tau^{(1)} \tag{B.9}$$

$$I_\nu \rightarrow I_\nu^{(0)} + I_\nu^{(1)} \tag{B.10}$$

$$T \rightarrow T^{(0)} + T^{(1)} \tag{B.11}$$

and the following expansions

$$k_\nu[\tau^{(0)} + \tau^{(1)}] = k_\nu[\tau^{(0)}] + \tau^{(1)} \frac{\partial k_\nu}{\partial \tau^{(0)}} \tag{B.12}$$

$$B_\nu[T^{(0)} + T^{(1)}] = B_\nu[T^{(0)}] + T^{(1)} \frac{\partial B_\nu}{\partial T^{(0)}} \tag{B.13}$$

inserted into the equation of radiation transfer. One can then derive relations solving for $\tau^{(1)}$ and $T^{(1)}$

$$\frac{\partial \tau^{(1)}}{\partial \tau^{(0)}} + \tau^{(1)} \left(\int_0^\infty \frac{\partial k_\nu}{\partial \tau^{(0)}} H_\nu^{(0)} d\nu \Big/ \int_0^\infty k_\nu H_\nu^{(0)} d\nu \right) = \left(1 - \frac{\mathcal{H}}{H^{(0)}}\right) - \frac{1}{\sqrt{3}} \int_0^\infty k_\nu [J_\nu^{(0)} - B_\nu(T^{(0)})] d\nu \Big/ \int_0^\infty k_\nu H_\nu^{(0)} d\nu \tag{B.14}$$

and

$$T^{(1)} = \left\{ (1 + \tau^{(1)}) \int_0^\infty k_\nu [J_\nu^{(0)} - B_\nu(T^{(0)})] d\nu - \sqrt{3} \left(1 - \frac{\mathcal{H}}{H^{(0)}}\right) \int_0^\infty k_\nu H_\nu^{(0)} d\nu + \frac{\partial \tau^{(1)}}{\partial \tau^{(0)}} \int_0^\infty \frac{\partial k_\nu}{\partial \tau^{(0)}} [J_\nu^{(0)} - B_\nu(T^{(0)}] d\nu \right\} \Big/ \int_0^\infty k_\nu \frac{\partial B_\nu}{\partial T^{(0)}} d\nu \tag{B.15}$$

where $H_\nu^{(0)}$ and $J_\nu^{(0)}$is the calculated flux and mean intensity and $\mathcal{H}$ is the desired bolometric flux. This method has been shown to be robust, however, it is not designed to include the effects of convection. Kurucz (1970c) includes the effects of convection on the perturbation of the flux and hence on the temperature structure of the atmosphere.

The purpose of this report is to derive a spherically symmetric version of the Avrett–Krook temperature correction method and incorporate the effects of convection. The next section will focus on the formal derivation and the fourth section will attempt to construct the temperature correction scheme including convection following the formalism of Kurucz (1970c). The fifth section will discuss the additional temperature correction schemes employed in the ATLAS code.

B.3 Formal Derivation

The Avrett–Krook temperature correction method is based on perturbing the intensity, the temperature and the independent measure of depth in the atmosphere, be it the optical depth, column density or the radius. For this derivation the radius will be used as the independent variable. Therefore the perturbations are:

$$I_\nu \rightarrow I_\nu^{(0)} + I_\nu^{(1)} \tag{B.16}$$

$$r \rightarrow r^{(0)} + r^{(1)} \tag{B.17}$$

$$T \rightarrow T^{(0)} + T^{(1)} \tag{B.18}$$

and expanding the total opacity k_ν and the source function S_ν (as opposed to the blackbody function B_ν) with respect to their explicit dependencies, following the derivation of Avrett (1964),

$$k_\nu(r) \approx k_\nu[r^{(0)}] + r^{(1)}\frac{\partial k_\nu[r^{(0)}]}{\partial r^{(0)}} \tag{B.19}$$

$$S_\nu(r,T) \approx S_\nu[r^{(0)},T^{(0)}] + r^{(1)}\frac{\partial S_\nu[r^{(0)},T^{(0)}]}{\partial r^{(0)}} + T^{(1)}\frac{\partial S_\nu[r^{(0)},T^{(0)}]}{\partial T^{(0)}}. \tag{B.20}$$

The spherical equation of radiative transfer is

$$\mu\frac{\partial I_\nu}{\partial r} + \frac{(1-\mu^2)}{r}\frac{\partial I_\nu}{\partial \mu} = k_\nu(S_\nu - I_\nu), \tag{B.21}$$

and substituting the perturbed and expanded quantities yields

$$\frac{\mu}{1+r^{(1)\prime}}\frac{\partial[I_\nu^{(0)}+I_\nu^{(1)}]}{\partial r^{(0)}} + \frac{(1-\mu^2)}{[r^{(0)}+r^{(1)}]}\frac{\partial[I_\nu^{(0)}+I_\nu^{(1)}]}{\partial \mu} = [k_\nu + r^{(1)}k_\nu'][S_\nu + r^{(1)}S_\nu' + T^{(1)}\dot{S}_\nu - I_\nu^{(0)} - I_\nu^{(1)}] \tag{B.22}$$

where '$\prime$' is the derivative with respect to $r^{(0)}$ and '$\cdot$' refers to the derivative with respect to $T^{(0)}$. Because $r^{(1)} << r^{(0)}$ then one can approximate

$$[r^{(0)}+r^{(1)}]^{-1} \approx \frac{1}{r^{(0)}}\left[1 - \frac{r^{(1)}}{r^{(0)}}\right] \tag{B.23}$$

and inserting into Equation B.22 and rearranging terms, ignoring terms of second order perturbation,

$$\begin{aligned}
&\mu\frac{\partial I_\nu^{(0)}}{\partial r^{(0)}} + \frac{(1-\mu^2)}{r^{(0)}}\frac{\partial I_\nu^{(0)}}{\partial \mu} + \mu\frac{\partial I_\nu^{(1)}}{\partial r^{(0)}} - \frac{(1-\mu^2)}{r^{(0)}}\frac{r^{(1)}}{r^{(0)}}\frac{\partial I_\nu^{(0)}}{\partial \mu} \\
&+r^{(1)\prime}\frac{(1-\mu^2)}{r^{(0)}}\frac{\partial I_\nu^{(0)}}{\partial \mu} + \frac{(1-\mu^2)}{r^{(0)}}\frac{\partial I_\nu^{(1)}}{\partial \mu} = \\
&k_\nu[S_\nu - I_\nu^{(0)}] + (r^{(1)\prime}k_\nu + r^{(1)}k_\nu')[S_\nu - I_\nu^{(0)}] + k_\nu[r^{(1)}S_\nu' + T^{(1)}\dot{S}_\nu - I_\nu^{(1)}].
\end{aligned} \tag{B.24}$$

It is clear

$$\mu\frac{\partial I_\nu^{(0)}}{\partial r^{(0)}} + \frac{(1-\mu^2)}{r^{(0)}}\frac{\partial I_\nu^{(0)}}{\partial \mu} = k_\nu(S_\nu - I_\nu^{(0)}) \tag{B.25}$$

and thus these terms cancel out of Equation B.24 leaving

$$\begin{aligned}
&\mu\frac{\partial I_\nu^{(1)}}{\partial r^{(0)}} + \frac{(1-\mu^2)}{r^{(0)}}\left[r^{(1)\prime} - \frac{r^{(1)}}{r^{(0)}}\right]\frac{\partial I_\nu^{(0)}}{\partial \mu} + \frac{(1-\mu^2)}{r^{(0)}}\frac{\partial I_\nu^{(1)}}{\partial \mu} \\
&\qquad = [r^{(1)\prime}k_\nu + r^{(1)}k_\nu'][S_\nu - I_\nu^{(0)})] + k_\nu[r^{(1)}S_\nu' + T^{(1)}\dot{S}_\nu - I_\nu^{(1)}].
\end{aligned} \tag{B.26}$$

as the first–order perturbation of the equation of radiative transfer.

The next step is to calculate the zero and first moments of the perturbed equation. This is done by integrating Equation 26 with respect to μ. The integral of the first term is

$$\frac{1}{2}\int_{-1}^{1}\mu\frac{\partial I_\nu^{(1)}}{\partial r^{(0)}}d\mu = \frac{\partial}{\partial r^{(0)}}\frac{1}{2}\int_{-1}^{1}\mu I_\nu^{(1)}d\mu = \frac{\partial H_\nu^{(1)}}{\partial r^{(0)}}, \tag{B.27}$$

the second term is

$$\begin{aligned}\frac{1}{2}\int_{-1}^{1}\frac{(1-\mu^2)}{r^{(0)}}\left[r^{(1)\prime}-\frac{r^{(1)}}{r^{(0)}}\right]\frac{\partial I_\nu^{(0)}}{\partial\mu}d\mu &= \left[r^{(1)\prime}-\frac{r^{(1)}}{r^{(0)}}\right]\frac{1}{2r^{(0)}}\int_{-1}^{1}(1-\mu^2)\frac{\partial I_\nu^{(0)}}{\partial\mu}d\mu \\ &= (r^{(0)})^{-1}\left[r^{(1)\prime}-\frac{r^{(1)}}{r^{(0)}}\right]\left[\frac{1}{2}I_\nu(1-\mu^2)\Big|_{-1}^{1}+\int_{-1}^{1}\mu I_\nu^{(0)}d\mu\right] \\ &= \left[r^{(1)\prime}-\frac{r^{(1)}}{r^{(0)}}\right]\frac{2H_\nu^{(0)}}{r^{(0)}}\end{aligned} \tag{B.28}$$

and similarly the third term is

$$\frac{1}{2}\int_{-1}^{1}\frac{1-\mu^2}{r^{(0)}}\frac{\partial I_\nu^{(1)}}{\partial\mu}d\mu = \frac{2H_\nu^{(1)}}{r^{(0)}} \tag{B.29}$$

The integral, with respect to μ, of the right–hand side is

$$\begin{aligned}&\frac{1}{2}\int_{-1}^{1}\left\{(r^{(1)\prime}k_\nu + r^{(1)}k_\nu')[S_\nu - I_\nu^{(0)}] + k_\nu[r^{(1)}S_\nu' + T^{(1)}\dot{S}_\nu - I_\nu^{(1)}]\right\}d\mu \\ &\qquad = [r^{(1)\prime}k_\nu + r^{(1)}k_\nu'][S_\nu - J_\nu^{(0)}] + k_\nu[r^{(1)}S_\nu' + T^{(1)}\dot{S}_\nu - J_\nu^{(1)}].\end{aligned} \tag{B.30}$$

and thus the first order perturbation of the zero order moment equation is

$$\frac{\partial H_\nu^{(1)}}{\partial r^{(0)}} + \left[r^{(1)\prime}-\frac{r^{(1)}}{r^{(0)}}\right]\frac{2H_\nu^{(0)}}{r^{(0)}} + \frac{2H_\nu^{(1)}}{r^{(0)}} = [r^{(1)\prime}k_\nu + r^{(1)}k_\nu'][S_\nu - J_\nu^{(0)}] + k_\nu[r^{(1)}S_\nu' + T^{(1)}\dot{S}_\nu - J_\nu^{(1)}]. \tag{B.31}$$

The perturbation of the first moment equation can be found by integrating Equation B.26 with $\mu d\mu$. The integral of the first term is

$$\frac{1}{2}\int_{-1}^{1}\mu^2\frac{\partial I_\nu^{(1)}}{\partial r^{(0)}}d\mu = \frac{\partial}{\partial r^{(0)}}\frac{1}{2}\int_{-1}^{1}\mu^2 I_\nu^{(1)}d\mu = \frac{\partial K_\nu^{(1)}}{\partial r^{(0)}}, \tag{B.32}$$

the second term is

$$\begin{aligned}&\frac{1}{2}\int_{-1}^{1}\frac{(1-\mu^2)}{r^{(0)}}\left(r^{(1)\prime}-\frac{r^{(1)}}{r^{(0)}}\right)\frac{\partial I_\nu^{(0)}}{\partial\mu}\mu d\mu = \left[r^{(1)\prime}-\frac{r^{(1)}}{r^{(0)}}\right]\frac{1}{2r^{(0)}}\int_{-1}^{1}(\mu-\mu^3)\frac{\partial I_\nu^{(0)}}{\partial\mu}d\mu \\ &= \left[r^{(1)\prime}-\frac{r^{(1)}}{r^{(0)}}\right]\frac{1}{2r^{(0)}}\left[I_\nu^{(0)}(\mu-\mu^3)\Big|_{-1}^{1}+\int_{-1}^{1}(3\mu^2-1)I_\nu^{(0)}d\mu\right] \\ &= \left[r^{(1)\prime}-\frac{r^{(1)}}{r^{(0)}}\right]\left[\frac{3K_\nu^{(0)}-J_\nu^{(0)}}{r^{(0)}}\right]\end{aligned} \tag{B.33}$$

and the third term

$$\frac{1}{2}\int_{-1}^{1}\frac{(1-\mu^2)}{r^{(0)}}\frac{\partial I_\nu^{(1)}}{\partial\mu}\mu d\mu = \frac{[3K_\nu^{(1)} - J_\nu^{(1)}]}{r^{(0)}} \tag{B.34}$$

and the right–hand side is

$$\frac{1}{2}\int_{-1}^{1}\left\{[r^{(1)\prime}k_\nu + r^{(1)}k_\nu'](S_\nu - I_\nu^{(0)}) + k_\nu[r^{(1)}S_\nu' + T^{(1)}\dot{S}_\nu - I_\nu^{(1)}]\right\}\mu d\mu$$
$$= -[r^{(1)\prime}k_\nu + r^{(1)}k_\nu']H_\nu^{(0)} - k_\nu H_\nu^{(1)}. \tag{B.35}$$

Therefore the perturbation of the first moment equation is

$$\frac{\partial K_\nu^{(1)}}{\partial r^{(0)}} + \frac{[3K_\nu^{(1)} - J_\nu^{(1)}]}{r^{(0)}} = -[r^{(1)\prime}k_\nu + r^{(1)}k_\nu']H_\nu^{(0)} - k_\nu H_\nu^{(1)} - \left[r^{(1)\prime} - \frac{r^{(1)}}{r^{(0)}}\right]\frac{3K_\nu^{(0)} - J_\nu^{(0)}}{r^{(0)}}. \tag{B.36}$$

Equation B.36 is frequency dependent meaning any solution of it to determine the change of temperature would require the temperature to be frequency dependent and that would be non–physical. Therefore it is desirable to integrate Equation B.36 over all frequencies

$$\int_0^\infty\left\{\frac{\partial K_\nu^{(1)}}{\partial r^{(0)}} + \frac{[3K_\nu^{(1)} - J_\nu^{(1)}]}{r^{(0)}}\right\}d\nu$$
$$= -\int_0^\infty\left\{(r^{(1)\prime}k_\nu + r^{(1)}k_\nu')H_\nu^{(0)} + k_\nu H_\nu^{(1)} + \left[r^{(1)\prime} - \frac{r^{(1)}}{r^{(0)}}\right]\frac{3K_\nu^{(0)} - J_\nu^{(0)}}{r^{(0)}}\right\}d\nu \tag{B.37}$$

and one can choose $r^{(1)}$ such that

$$\int_0^\infty\frac{1}{k_\nu}\left\{\frac{\partial K_\nu^{(1)}}{\partial r^{(0)}} + \frac{[3K_\nu^{(1)} - J_\nu^{(1)}]}{r^{(0)}}\right\}d\nu = 0 \tag{B.38}$$

and thus, dividing by k_ν

$$\left\{H^{(0)} + \frac{1}{r^{(0)}}\int_0^\infty\left[\frac{3K_\nu^{(0)} - J_\nu^{(0))}}{k_\nu}\right]d\nu\right\}r^{(1)\prime}$$
$$+\left[\int_0^\infty\frac{k_\nu'}{k_\nu}H_\nu^{(0)}d\nu - \frac{1}{[r^{(0)}]^2}\int_0^\infty\left(\frac{[3K_\nu^{(0)} - J_\nu^{(0)}]}{k_\nu}\right)d\nu\right]r^{(1)} + H^{(1)} = 0. \tag{B.39}$$

This is equivalent to assuming that the Eddington approximation holds for the perturbed values $3K_\nu^{(1)} \approx J_\nu^{(1)}$ and that the gradient of $K^{(1)}$ is negligible. Really choosing the function $r^{(1)}$ such that Equation B.38 is satisfied is based on the desire to correct the structure. For instance, if the correction is unnecessary then the all perturbed values would be zero. This constraint thus requires the structure to converge. Also $H^{(1)} = \mathcal{H} - H^{(0)}$ thus eliminating $H^{(1)}$ from the equation. As a result $r^{(1)}$ is the solution to the differential equation

$$a[r^{(0)}]r^{(1)\prime} + b[r^{(0)}]r^{(1)} + c[r^{(0)}] = 0 \tag{B.40}$$

which has a general solution

$$r^{(1)}[r^{(0)}] = -e^{-\int \frac{b}{a} d\tilde{r}} \int \frac{c}{a} e^{\int \frac{b}{a} d\tilde{\tilde{r}}} d\tilde{r} \tag{B.41}$$

where

$$a[r^{(0)}] = H^{(0)} + \int_0^\infty \left[\frac{3K_\nu^{(0)} - J_\nu^{(0))}}{k_\nu r^{(0)}} \right] d\nu \tag{B.42}$$

$$b[r^{(0)}] = \int_0^\infty \frac{k'_\nu}{k_\nu} H_\nu^{(0)} d\nu - \int_0^\infty \left[\frac{3K_\nu^{(0)} - J_\nu^{(0))}}{k_\nu [r^{(0)}]^2} \right] d\nu \tag{B.43}$$

$$c[r^{(0)}] = \mathcal{H} - H^{(0)}. \tag{B.44}$$

This is the solution for the perturbation of the variable describing depth of the atmosphere.

The next step is to use the solution for $r^{(1)}$ to help find the function describing the perturbation of the temperature $T^{(1)}$. To do this, consider the perturbation of the zero moment, Equation B.31, integrating with respect with frequency

$$\frac{1}{[r^{(0)}]^2} \frac{d[r^{(0)}]^2 H^{(1)}}{dr^{(0)}} + \left[r^{(1)\prime} - \frac{r^{(1)}}{r^{(0)}} \right] \frac{2H^{(0)}}{r^{(0)}} = \int_0^\infty \left\{ [r^{(1)\prime} k_\nu + r^{(1)} k'_\nu][S_\nu - J_\nu^{(0)}] + k_\nu [r^{(1)} S'_\nu + T^{(1)} \dot{S}_\nu - J_\nu^{(1)}] \right\} d\nu. \tag{B.45}$$

In Equation B.45 there are three unknown quantities $H^{(1)}$, $J_\nu^{(1)}$ and $T^{(1)}$. $H^{(1)}$ can be replaced by $H^{(1)} = \mathcal{H} - H^{(0)}$ and noting that $r^2\mathcal{H}$ is conserved, meaning $d(r^2\mathcal{H})/dr = 0$. Determining $J_\nu^{(1)}$ is more difficult and requires making two assumptions. The first is that the integral, Equation B.38, is satisfied by

$$\frac{\partial K_\nu^{(1)}}{\partial r^{(0)}} + \frac{3K_\nu^{(1)} - J_\nu^{(1)}}{r^{(0)}} = 0 \tag{B.46}$$

for all frequencies. The variable Eddington factors (Mihalas, 1978) are $h_\nu \equiv H_\nu^{(0)}/J_\nu^{(0)}$ and $f_\nu \equiv K_\nu^{(0)}/J_\nu^{(0)}$ and assuming that the perturbed quantities follow the same relations then,

$$H_\nu^{(1)} = h_\nu J_\nu^{(1)} = H_\nu^{(0)} \frac{J_\nu^{(1)}}{J_\nu^{(0)}}, \tag{B.47}$$

$$K_\nu^{(1)} = f_\nu J_\nu^{(1)} = K_\nu^{(0)} \frac{J_\nu^{(1)}}{J_\nu^{(0)}}. \tag{B.48}$$

Using Equation B.48 in Equation B.46 yields

$$\frac{\partial [f_\nu J_\nu^{(1)}]}{\partial r^{(0)}} + \frac{3f_\nu - 1}{r^{(0)}} J_\nu^{(1)} = 0 \tag{B.49}$$

which has a solution

$$J_\nu^{(1)}[r^{(0)}] = J_\nu^{(1)}(R)\exp\left[-\int_R^{r^{(0)}}\left(\frac{f_\nu'}{f_\nu}+\frac{3f_\nu-1}{f_\nu r}\right)dr\right]. \tag{B.50}$$

Thus we have a solution for $J_\nu^{(1)}$ at all points but the surface. To find a solution for $J^{(1)}(R)$, the other Eddington factor is used, Equation B.47, but then $H_\nu^{(1)}(R)$ needs to be determined instead. $H_\nu^{(1)}(R)$ can be determined by substituting values of $r^{(1)\prime}(R)$ and $r^{(1)}(R)$ into Equation B.36 and using the assumption in Equation B.46 meaning

$$[r^{(1)\prime}k_\nu + r^{(1)}k_\nu']H_\nu^{(0)} + k_\nu H_\nu^{(1)} + \left[r^{(1)\prime} - \frac{r^{(1)}}{r^{(0)}}\right]\frac{3K_\nu^{(0)} - J_\nu^{(0)}}{r^{(0)}} = 0. \tag{B.51}$$

At the surface $r^{(1)}(R)$ must be zero, meaning

$$H_\nu^{(1)}(R) = -\frac{r^{(1)\prime}(R)}{k_\nu(R)}\left\{k_\nu(R)H_\nu^{(0)}(R) + \frac{3K_\nu^{(0)}(R) - J_\nu^{(0)}(R)}{R}\right\} \tag{B.52}$$

and noting $r^{(1)}$ is found from Equation B.39 where $r^{(1)}(R) = 0$

$$r^{(1)\prime}(R) = -\left[\mathcal{H} - H^{(0)}(R)\right]\left\{H^{(0)}(R) + \int_0^\infty\left[\frac{3K_\nu^{(0)} - J_\nu^{(0)}}{k_\nu R}\right]d\nu\right\}^{-1}. \tag{B.53}$$

Using this result with Equations B.47 and B.52, one finds

$$J_\nu^{(1)}(R) = \frac{H_\nu^{(1)}(R)}{h_\nu(R)} = -\frac{r^{(1)\prime}(R)}{h_\nu(R)}\left[H_\nu^{(0)}(R) + \frac{3K_\nu^{(0)}(R) - J_\nu^{(0)}(R)}{k_\nu(R)R}\right] \tag{B.54}$$

and thus it is now possible to determine $J_\nu^{(1)}[r^{(0)}]$, Equation B.50 and hence the temperature correction $T^{(1)}$ from Equation B.45

$$\begin{aligned}T^{(1)} = &\left[\int_0^\infty k_\nu \dot{S}_\nu d\nu\right]^{-1}\left[-\frac{1}{[r^{(0)}]^2}\frac{d[r^{(0)}]^2H^{(0)}}{dr^{(0)}} + \right.\\ &\left.\left[r^{(1)\prime} - \frac{r^{(1)}}{r^{(0)}}\right]\frac{2H^{(0)}}{r^{(0)}} - \int_0^\infty\left\{[r^{(1)\prime}k_\nu + r^{(1)}k_\nu'][S_\nu - J_\nu^{(0)}] + k_\nu[r^{(1)}S_\nu' - J_\nu^{(1)}]\right\}d\nu\right].\end{aligned} \tag{B.55}$$

This is the formal derivation of the temperature correction for a spherically symmetric model atmosphere. In the derivation, however, the flux due to convection is ignored. The next section will focus on how convection can be included.

B.4 Temperature Correction for ATLAS

The plane–parallel version of ATLAS uses the column density, M, and the Rossland optical depth, τ_R, as the independent variable as opposed to the radius. The first moment of the spherical equation of transfer becomes,

$$\rho\frac{\partial K_\nu}{\partial M}+\frac{J_\nu-3K_\nu}{r}=k_\nu H_\nu. \tag{B.56}$$

The following quantities will be perturbed:

$$M \rightarrow M+dM \tag{B.57}$$
$$K_\nu \rightarrow K_\nu+dK_\nu \tag{B.58}$$
$$J_\nu \rightarrow J_\nu+dJ_\nu \tag{B.59}$$
$$k_\nu \rightarrow k_\nu+dM\frac{\partial k_\nu}{\partial M} \tag{B.60}$$
$$r \rightarrow r+dr \tag{B.61}$$
$$H_\nu \rightarrow H_\nu+dH_\nu. \tag{B.62}$$

and

$$\frac{\partial}{\partial M}\rightarrow\frac{\partial}{\partial M}\left(1+\frac{\partial(dM)}{\partial M}\right)^{-1}. \tag{B.63}$$

It is important to write the derivation of the temperature correction in the notation of Kurucz (1970c). Let us return to Equation B.39 and switch notation, here $r^{(0)}, J^{(0)}, H^{(0)}$ and $K^{(0)}$ become r, J, H, K while $r^{(1)}, J^{(1)}, H^{(1)}$ and $K^{(1)}$ become dr, dJ, dH, dK. Also it must be noted that the column density is $\partial M=-\rho\partial r$ and

$$\frac{\partial k_\nu}{\partial r}=\frac{\partial k_\nu}{\partial M}\frac{\partial M}{\partial r}=-\rho\frac{\partial k_\nu}{\partial M}. \tag{B.64}$$

The perturbed quantity dM can be written as $-\rho dr$ implying

$$\frac{\partial(dr)}{\partial r}=\frac{\rho^{-1}\partial(-dM)}{\rho^{-1}\partial(-M)}=\frac{\partial(dM)}{\partial M}. \tag{B.65}$$

Therefore Equation B.39 becomes

$$\begin{aligned}&\left\{H+\frac{1}{r}\int_0^\infty\left[\frac{3K_\nu-J_\nu}{k_\nu}\right]d\nu\right\}dM'\\&+\left[\int_0^\infty\frac{k'_\nu}{k_\nu}H_\nu d\nu+\frac{1}{r^2}\int_0^\infty\left(\frac{3K_\nu-J_\nu}{\rho k_\nu}\right)d\nu\right]dM+dH=0\end{aligned} \tag{B.66}$$

where derivatives noted by $'$ are now with respect to column density. The solution to the differential equation has the same form as Equation B.41 and in Kurucz's notation

$$dM = e^{-\int g(M)dM} \int_0^M \frac{dM}{\text{Coeff}_{dM'}} e^{\int g(y)dy} dM \tag{B.67}$$

where

$$g(M) = \frac{\text{Coeff}_{dM}}{\text{Coeff}_{dM'}} \tag{B.68}$$

and the coefficients are given by Equation B.66. This derivation, however, is for the radiative flux and need to include the convective flux, given by Kurucz (1970c) as

$$H_{\text{CONV}} = AT \frac{(\nabla - \nabla_{ad})^3}{[BT^6 + (\nabla - \nabla_{ad})]^{3/2}} \Sigma^{3/2} \tag{B.69}$$

where

$$A = \frac{1}{4\pi} \frac{1}{2} \rho C_P T \left(\frac{l}{h}\right) \sqrt{\frac{1}{8} g h \left(\frac{l}{h}\right)^2 \left(\frac{d \ln \rho}{d \ln T}\right)_P}, \tag{B.70}$$

$$B = \frac{D}{T^6} = \frac{1}{2} \left[\frac{32\sqrt{2}\sigma T}{k_{\text{Ross}} \rho h 8\pi A}\right]^2 \tag{B.71}$$

and

$$\Sigma = \frac{1}{2} + \frac{1 \cdot 1}{2 \cdot 4} \left[\frac{(\nabla - \nabla_{ad})}{BT^6 + (\nabla - \nabla_{ad})}\right]^2 + \frac{1 \cdot 1 \cdot 3}{2 \cdot 4 \cdot 6} \left[\frac{(\nabla - \nabla_{ad})}{BT^6 + (\nabla - \nabla_{ad})}\right]^4 + \ldots \tag{B.72}$$

and (l/h) refers to the mixing length parameter. None of these quantities is explicitly dependent on the geometry of the stellar atmosphere and thus will not change in a spherically symmetric stellar atmosphere model. Therefore the relation for the perturbation of the convective flux and the perturbation of the column density given by Kurucz (1970c) can be implemented here,

$$\begin{aligned} dH_{\text{CONV}} = -H_{\text{CONV}} \frac{dT}{dM} \frac{1}{T} \left\{ \left[1 - \frac{9D}{D + (\nabla - \nabla_{ad})}\right] + \frac{3}{2(\nabla - \nabla_{ad})} \frac{d\nabla}{dM} \left[1 + \frac{D}{D + (\nabla - \nabla_{ad})}\right] \right\} dM \\ - H_{\text{CONV}} \frac{3\nabla}{2(\nabla - \nabla_{ad})} \left[1 + \frac{D}{D + (\nabla - \nabla_{ad})}\right] \frac{\partial (dM)}{\partial M}. \end{aligned} \tag{B.73}$$

This can be used by noting the actual flux is

$$\mathcal{H} = H_{\text{RAD}} + dH_{\text{RAD}} + H_{\text{CONV}} + dH_{\text{CONV}} \tag{B.74}$$

and in the differential equation, Equation B.66 $H \rightarrow H_{\rm RAD}$ and $dH \rightarrow dH_{\rm RAD}$ then the differential equation becomes

$$\left\{H_{\rm RAD} - \int_0^\infty \frac{J_\nu - 3K_\nu}{k_\nu r} d\nu + H_{\rm CONV} \frac{3\nabla}{2(\nabla - \nabla_{ad})}\left[1 + \frac{D}{D + (\nabla - \nabla_{ad})}\right]\right\} \frac{\partial(dM)}{\partial M} + \left\{H_{\rm CONV} \frac{dT}{dM}\frac{1}{T}\left[\left(1 - \frac{9D}{D + (\nabla - \nabla_{ad})}\right) + \frac{3}{2(\nabla - \nabla_{ad})}\frac{d\nabla}{dM}\left(1 + \frac{D}{D + (\nabla - \nabla_{ad})}\right)\right] + \int_0^\infty \frac{k'_\nu}{k_\nu} H_{{\rm RAD},\nu} d\nu - \int_0^\infty \frac{J_\nu - 3K_\nu}{\rho k_\nu r^2} d\nu\right\} dM + \mathcal{H} - H_{\rm RAD} - H_{\rm CONV} = 0. \tag{B.75}$$

The solution to this differential equation is the same as before except the coefficients are now changed. This differential equation is similar to that given by Kurucz (1970c) except for the terms $-\int_0^\infty (J_\nu - 3K_\nu)/k_\nu r d\nu$ and $-\int_0^\infty (J_\nu - 3K_\nu)/\rho k_\nu r^2 d\nu$. The change of temperature in the ATLAS code is computed using the relation $dT = (\partial T/\partial M) dM$. This relation can be used instead of Equation B.55. Therefore there is only a minimal change to the numerical code required.

The ATLAS code uses another temperature correction scheme near the surface where the flux error is not very sensitive to the temperature. Here the flux derivative is used with the $r^{(1)}$ operator to find the change of temperature excluding the case of convection. For the plane–parallel case (Kurucz, 1970c)

$$\frac{dH_\nu}{dM} = k_\nu (J_\nu - S_\nu) \tag{B.76}$$

and it is assumed the source function is of the form

$$S_\nu = \alpha_\nu J_\nu + (1 - \alpha_\nu) B_\nu(T) \tag{B.77}$$

and $J_\nu = \Lambda_\nu[S_\nu]$ then the source function can be written as

$$S_\nu = (1 - \alpha_\nu \Lambda_\nu)^{-1} (1 - \alpha_\nu) B_\nu(T). \tag{B.78}$$

The moment equation becomes

$$\frac{dH_\nu}{dM} = k_\nu (\Lambda_\nu - 1)(1 - \alpha_\nu \Lambda_\nu)^{-1} (1 - \alpha_\nu) B_\nu(T). \tag{B.79}$$

One can expand $B_\nu \rightarrow B_\nu + dB_\nu/dT \Delta T$ ignoring the dependence on T for any other variable and insert it into the moment equation

$$\frac{dH_\nu}{dM} + \frac{d(\Delta H_\nu)}{dM} = k_\nu (\Lambda_\nu - 1)(1 - \alpha_\nu \Lambda_\nu)^{-1} (1 - \alpha_\nu)\left(B_\nu(T) + \frac{dB_\nu}{dT}\Delta T\right). \tag{B.80}$$

Since $\mathcal{H} = H + \Delta H$, if Equation B.80 is integrated with respect to frequency, the change of temperature is

$$\Delta T_\Lambda = \frac{d\mathcal{H}/dM - \int_0^\infty k_\nu (J_\nu - S_\nu) d\nu}{\int_0^\infty k_\nu [(\Lambda_{\nu,\mathrm{diag}} - 1)/(1 - \alpha_\nu \Lambda_{\nu,\mathrm{diag}})](1 - \alpha_\nu)(dB_\nu/dT) d\nu}. \tag{B.81}$$

In spherical symmetry, if one assumes the diagonal elements of Λ_ν do not change then only the moment equation is different

$$\frac{d(r^2 H_\nu)}{dM} = k_\nu r^2 (J_\nu - S_\nu) \tag{B.82}$$

and the temperature correction becomes

$$\Delta T_\Lambda = \frac{d(r^2\mathcal{H})/r^2 dM - \int_0^\infty k_\nu (J_\nu - S_\nu) d\nu}{\int_0^\infty k_\nu [(\Lambda_{\nu,\mathrm{diag}} - 1)/(1 - \alpha_\nu \Lambda_{\nu,\mathrm{diag}})](1 - \alpha_\nu)(dB_\nu/dT) d\nu}. \tag{B.83}$$

A third temperature correction is used in the ATLAS code to smooth the region where the other two correction schemes overlap. This is based on the relation $H = \sigma T^4$ and expanding that to first order gives

$$\Delta T = \frac{T \Delta H}{4\mathcal{H}}. \tag{B.84}$$

This correction scheme will not change in a spherically symmetric atmosphere so it can be applied as is.